

0830-H-10

0312

NAS155:3089

NASA Conference Publication 3089

FEB 23 1991

# Current Collection From Space Plasmas

*Proceedings of a workshop held at  
the Tom Bevil Center  
University of Alabama in Huntsville  
Huntsville, Alabama  
April 24-25, 1989*

PN

---

NASA

# Current Collection From Space Plasmas

*Edited by*  
N. Singh and K. H. Wright, Jr.  
*University of Alabama in Huntsville*  
*Huntsville, Alabama*

N. H. Stone  
*NASA George C. Marshall Space Flight Center*  
*Marshall Space Flight Center, Alabama*

Proceedings of a workshop sponsored by  
the NASA George C. Marshall Space Flight Center  
and the University of Alabama in Huntsville  
and held at the Tom Bevil Center  
University of Alabama in Huntsville  
Huntsville, Alabama  
April 24-25, 1989



National Aeronautics and  
Space Administration  
Office of Management  
Scientific and Technical  
Information Division

1990

I

## PREFACE

Many space applications require an in-depth understanding of the current collection properties of a body immersed in a plasma. Examples of such applications include electrostatic probes, charge neutralization on space vehicles, operation of plasma particle detectors, charged-particle beam injections from a spacecraft, high-voltage power systems in space, and the electrodynamic effects on large conducting bodies or long conducting tethers in space. Early investigations of current collection processes were motivated by the use of electric probes for plasma diagnostics. These investigations led to the development of probe theories with simple geometries and idealized plasma models. In recent years there is renewed interest in this field due, primarily, to the ability to conduct active experiments in space and the need for charge neutralization on space vehicles. For example, the problem of charge neutralization was the topic of a previous workshop convened by N. A. Sflekos and J. L. Burch at the Southwest Research Institute in August 1985. However, the overall problem of current collection by a body in space remains an open issue.

The first Tethered Satellite System mission (TSS-1) is concerned with the electrodynamic behavior of a long conducting tether in space. This objective will require a thorough knowledge of the physical processes affecting current collection by a highly biased conducting body in a low Earth orbit, including the processes producing a general disturbance of the plasma around the body and, specifically, the plasma sheath structure at relatively high voltages. Supporting theoretical predictions of the behavior of these processes are crucial in planning experiments for the mission and the subsequent post-flight data analysis. However, it is generally recognized that the theoretical treatment of current collection in a plasma is a formidable task. Complications in theoretical treatments arise due to the magnetic field, the relative motion between the collector and the plasma, and the shape and size of the collector and its surface properties. At high voltages, additional effects must be addressed that include the ionization of neutral particles in the sheath and the secondary emission of particles from the collecting surface. The dynamic features of the sheath and modification of current collection due to waves and instabilities are further complicating factors. It is because of these complicating factors that the problem of current collection in a plasma remains an open issue and in view of the fundamental importance of the current collection processes to the TSS-1 mission, it was felt that an assessment of the present state of knowledge on the subject should be made. This led to the First Workshop on Current Collection from Space Plasmas held on April 24-25, 1989, at the Tom Bevil Center on the campus of the University of Alabama in Huntsville.

The intent of the workshop was to assemble experts on various topics related to the problem of current collection for deliberations that would elucidate the present understanding of the overall current collection problem. Open discussions would be initiated through invited talks, posters sessions, and a panel discussion. A complete list of the participants and the papers presented in the workshop is given in these proceedings. A brief summary of the papers is given below.

E. C. Whipple reviewed the theories on current collection without a magnetic field. J. G. Laframboise and L. J. Sonmor reviewed the theories which include magnetic field effects. The effect of plasma drift motion on current collection was illustrated by N. Singh and B. Vashi. W.-W. Lei presented the effects on current collection due to a plasma with an anisotropic velocity distribution. E. P. Szuszczewicz dealt with models of current collection in relation to experimental realities that must be considered in performing plasma measurements.

R. L. Stenzel and J. M. Urrutia presented a summary of laboratory experiments on the dynamic aspects of current collection in a tethered electrode configuration, including the issue of closure for the current.

The topic of plasma contactors and its related aspect of plasma discharge was addressed in several papers. P. Wilbur reviewed laboratory experiments on plasma contactors based on hollow-cathode devices. The theoretical aspects of plasma contactors were discussed in papers by M. Gerver et al. and I. Katz and V. A. Davis. An abstract by D. Cooke on double layers in contactor plasmas is also included.

One of the issues of considerable interest is the effect of neutral atoms and molecules on current collection at high voltages. J. A. Antoniades and coauthors discussed results from laboratory experiments on this topic. W. J. Raitt and coauthors presented results from the SPEAR-1 sounding rocket experiment and compared the measured currents with the predictions from theories. An abstract by P. J. Palmadesso on some of the theoretical aspects of the experiments is also included. These papers are also of relevance to the topic of plasma contactors.

In space applications involving large manned vehicles, the offgassing of contaminant atoms and molecules, at times, plays a significant role in modifying both the ambient plasma and neutral gas environments. This topic was discussed by J. M. Grebowsky and A. Schaefer. The dynamics of neutral gas clouds in plasmas was discussed by C. K. Goertz and G. Lu.

The topic of charged particle beam injections, with and without the presence of a neutral gas, and the associated phenomena of charging and return currents was discussed in papers by R. C. Olsen, R. M. Winglee, and K. S. Hwang and N. Singh. Gilchrist et al. presented a synopsis of results from the CHARGE-2 rocket experiments, in which the effects of a nitrogen gas release on the current collection was studied.

Computer modeling of current collection in various laboratory and space flight scenarios was presented by M. J. Mandell and coauthors. G. A. Jongeward and coauthors presented a computer software design tool for space power systems which includes many of the physical processes discussed above.

The workshop was sponsored by the NASA/Marshall Space Flight Center and the University of Alabama in Huntsville, whose financial support is gratefully acknowledged. Special thanks are due to A. Pouliakas for his enthusiastic support in organizing the workshop. We are also grateful to the session chairpersons (L.R.O. Storey, N. H. Stone, and C. Purvis) and to K. S. Hwang and B. Vashi for their assistance during the course of planning and conducting the workshop.

N. Singh  
Dept. of Electrical and Computer Engineering  
(also at the Center for Space Plasma and Aeronomics Research)  
The University of Alabama in Huntsville

K. H. Wright, Jr.  
Center for Space Plasma and Aeronomics Research  
The University of Alabama in Huntsville

N. H. Stone  
Space Science Laboratory/ES53  
NASA/Marshall Space Flight Center

## LIST OF ATTENDEES

John Antoniades  
Dept. of Physics  
University of Maryland  
College Park, MD 20742

Ralph Carruth  
EH12  
NASA/MSFC  
Huntsville, AL 35812

R. Hugh Comfort  
CSPAR  
University of Alabama in Huntsville  
Huntsville, AL 35899

David Cooke  
Space Physics Division  
AFGL/PHK  
Hanscom AFB, MA 01731

Victoria A. Davis  
S-CUBED  
P.O. Box 1620  
La Jolla, CA 92038-1620

M. J. Gerver  
Plasma Fusion Center  
MIT  
Cambridge, MA 02139

C. K. Goertz  
Dept. of Physics & Astronomy  
University of Iowa  
Iowa City, IA 52242

Rod Greaves  
Dept. of Physics  
University of Maryland  
College Park, MD 20742

Joe Grebowsky  
Code 614  
NASA/GSFC  
Greenbelt, MD 20771

Daniel Hastings  
Dept. of Aeronautics & Astronautics  
MIT  
Cambridge, MA 02139

C. W. Ho  
Dept. of Physics  
University of Alabama in Huntsville  
Huntsville, AL 35899

James Horwitz  
CSPAR  
University of Alabama in Huntsville  
Huntsville, AL 35899

K. S. Hwang  
CSPAR  
University of Alabama in Huntsville  
Huntsville, AL 35899

Gary A. Jongeward  
S-CUBED  
P.O. Box 1620  
La Jolla, CA 92038-1620

Ira Katz  
S-CUBED  
P.O. Box 1620  
La Jolla, CA 92038-1620

Jim Laframboise  
Dept. of Physics  
York University  
4700 Keele St.  
North York, Ontario, Canada M3J 1P3

Leroy Larry, Jr.  
Dept. of Physics  
University of Alabama in Huntsville  
Huntsville, AL 35899

Wei-wei Li  
CASS  
University of California, San Diego  
La Jolla, CA 92093

Myron J. Mandell  
S-CUBED  
P.O. Box 1620  
La Jolla, CA 92038-1620

Tom Moore  
ES53  
NASA/MSFC  
Huntsville, AL 35812

**Neil Myers**  
CASS  
Utah State University  
Logan, UT 84322

**R. C. Olsen**  
Physics Dept. (61-Os)  
Naval Postgraduate School  
Monterey, CA 93943

**Peter Palmadesso**  
Code 4780  
Naval Research Laboratory  
4555 Overlook Avenue  
Washington, DC 20375

**Carolyn Purvis**  
MS 302-1  
NASA/LeRC  
2100 Brookpark Road  
Cleveland, OH 44135

**David Reasoner**  
ES53  
NASA/MSFC  
Huntsville, AL 35812

**Nagendra Singh**  
Dept. of Electrical & Computer Eng.  
University of Alabama in Huntsville  
Huntsville, AL 35899

**David Snyder**  
MS 302-1  
NASA/LeRC  
2100 Brookpark Road  
Cleveland, OH 44135

**Reiner Stenzel**  
Dept. of Physics  
UCLA  
Los Angeles, CA 90024

**Nobie H. Stone**  
ES53  
NASA/MSFC  
Huntsville, AL 35812

**Owen Story**  
Code ES  
NASA/Hdqs.  
Washington, DC 20546

**Edward Szuszczewicz**  
SAIC  
1710 Goodridge Drive  
P.O. Box 1303  
McLean, VA 22102

**Bharat Vashi**  
Dept. of Electrical & Computer Eng.  
University of Alabama in Huntsville  
Huntsville, AL 35899

**Jason Vaughn**  
EH12  
NASA/MSFC  
Huntsville, AL 35812

**John J. Wachs**  
CSSD-H-DT  
106 Wynn Dr.  
Huntsville, AL 35805

**Elden Whipple**  
CASS  
University of California, San Diego  
La Jolla, CA 92093

**Paul Wilbur**  
Dept. of Mechanical Engineering  
Colorado State University  
Fort Collins, CO 80523

**Gordon Wilson**  
CSPAR  
University of Alabama in Huntsville  
Huntsville, AL 35899

**R. M. Winglee**  
Dept. of APAS  
University of Colorado  
Boulder, CO 80309-0391

**K. H. Wright, Jr.**  
CSPAR  
University of Alabama in Huntsville  
Huntsville, AL 35899

**S. T. Wu**  
CSPAR  
University of Alabama in Huntsville  
Huntsville, AL 35899

## TABLE OF CONTENTS

	Page
LIST OF ATTENDEES .....	v
CURRENT COLLECTION FROM AN UNMAGNETIZED PLASMA: A TUTORIAL E. C. Whipple .....	1
CURRENT COLLECTION IN A MAGNETOPLASMA J. G. Laframboise and L. J. Sonmor .....	13
CURRENT COLLECTION IN A FLOWING MAGNETOPLASMA N. Singh and B. I. Vashi .....	50
CURRENT COLLECTION IN AN ANISOTROPIC PLASMA W.-w. Li .....	74
MEASUREMENT REALITIES OF CURRENT COLLECTION IN DYNAMIC SPACE PLASMA ENVIRONMENTS E. P. Szuszczewicz .....	88
LABORATORY EXPERIMENTS ON CURRENT FLOW BETWEEN STATIONARY AND MOVING ELECTRODES IN MAGNETOPLASMAS R. L. Stenzel and J. M. Urrutia .....	125
LABORATORY EXPERIMENTS ON PLASMA CONTACTORS P. J. Wilbur and J. D. Williams .....	128
THEORY OF PLASMA CONTACTORS IN GROUND-BASED EXPERIMENTS AND LOW EARTH ORBIT M. J. Gerver, D. E. Hastings, and M. R. Oberhardt .....	150
PHYSICAL PROCESSES ASSOCIATED WITH CURRENT COLLECTION BY PLASMA CONTACTORS I. Katz and V. A. Davis .....	190
DOUBLE LAYERS IN CONTACTOR PLASMAS D. L. Cooke .....	201
CURRENT COLLECTION BY HIGH VOLTAGE ANODES IN NEAR IONOSPHERIC CONDITIONS J. A. Antoniades, R. G. Greaves, D. A. Boyd, and R. Ellis .....	202
SPEAR-1, AN EXPERIMENT TO MEASURE CURRENT COLLECTION IN THE IONOSPHERE BY HIGH VOLTAGE BIASED CONDUCTORS W. J. Raitt, N. B. Myers, J. A. Roberts, and D. C. Thompson .....	214
CURRENT COLLECTION BY A SPHERICAL HIGH VOLTAGE PROBE: ELECTRON TRAPPING AND COLLECTIVE PROCESSES P. J. Palmadesso .....	232

TABLE OF CONTENTS (Concluded)

	Page
OBSERVATIONS OF THERMAL ION INFLUXES ABOUT THE SPACE SHUTTLE J. M. Grebowsky and A. Schaefer .....	233
INTERACTION OF A NEUTRAL CLOUD MOVING THROUGH A MAGNETIZED PLASMA C. K. Goertz and G. Lu .....	256
CURRENT LIMITING MECHANISMS IN ELECTRON AND ION BEAM EXPERIMENTS R. C. Olsen .....	276
EFFECTS OF NEUTRAL GAS RELEASE ON CURRENT COLLECTION DURING THE CHARGE-2 ROCKET EXPERIMENT B. E. Gilchrist, P. M. Banks, T. Neubert, P. R. Williamson, N. B. Myers, W. J. Raitt, and S. Sasaki .....	305
EFFECTS OF NEUTRAL GAS RELEASES ON ELECTRON BEAM INJECTION FROM ELECTRICALLY TETHERED SPACECRAFT R. M. Winglee .....	308
PRESSURE AND CURRENT BALANCE CONDITIONS DURING ELECTRON BEAM INJECTIONS FROM SPACECRAFT K. S. Hwang and N. Singh .....	320
NASCAP/LEO CALCULATIONS OF CURRENT COLLECTION M. J. Mandell, I. Katz, V. A. Davis, and R. A. Kuharski .....	334
THE ENVIRONMENT POWER SYSTEM ANALYSIS TOOL DEVELOPMENT PROGRAM G. A. Jongeward, R. A. Kuharski, E. M. Kennedy, K. G. Wilcox, N. J. Stevens, R. M. Putnam, and J. C. Roche .....	352

## AUTHOR INDEX

- J. A. Antoniades 202  
P. M. Banks 305  
D. A. Boyd 202  
D. L. Cooke 201  
V. A. Davis 190, 334  
R. Ellis 202  
M. J. Gerver 150  
B. E. Gilchrist 305  
C. K. Goertz 256  
R. G. Greaves 202  
J. M. Grebowksy 233  
D. E. Hastings 150  
K. S. Hwang 320  
G. A. Jongeward 352  
I. Katz 190, 334  
E. M. Kennedy 352  
R. A. Kuharski 334, 352  
J. G. Laframboise 13  
Wei-wei Li 74  
G. Lu 256  
M. J. Mandell 334  
N. B. Myers 214, 305  
T. Neubert 305
- M. R. Oberhardt 150  
R. C. Olsen 276  
P. J. Palmadesso 232  
R. M. Putnam 352  
W. J. Raitt 214, 305  
J. A. Roberts 214  
J. C. Roche 352  
S. Sasaki 305  
A. Schaefer 233  
N. Singh 50, 320  
L. J. Sonmor 13  
R. L. Stenzel 125  
N. J. Stevens 352  
E. P. Szusczewicz 88  
D. C. Thompson 214  
J. M. Urrutia 125  
B. I. Vashi 50  
E. C. Whipple 1  
P. J. Wilbur 128  
K. G. Wilcox 352  
J. D. Williams 128  
P. R. Williamson 305  
R. M. Winglee 308

# CURRENT COLLECTION FROM AN UNMAGNETIZED PLASMA : A TUTORIAL

Elden C. Whipple

Center for Astrophysics and Space Science  
University of California at San Diego  
La Jolla, CA 92093

**Abstract.** The current collected by a body in an unmagnetized plasma depends in general on: (1) the properties of the plasma; (2) the properties of the body; and (3) the properties of any neutral species that are present. The important plasma properties are the velocity distributions of the plasma particles at a location remote from the body (at "infinity"), and the Debye length which determines the importance of plasma space charge effects. The important body properties are its surface characteristics, namely the conductivity and secondary yield coefficients. The neutral species affect the current through collisions which impede the flow of current and possibly through ionization of the neutrals which can enhance the current. The technique for calculating the current collected by a body in a plasma will be reviewed with special attention given to the distinction between orbit limited and space charge limited regimes, the asymptotic variation of the potential with distance from a body, and the concept of a sheath.

## Orbit Limited Currents

Consider a body in a plasma where the Debye length is much larger than the body dimensions so that the potential can be taken to be a Coulomb potential. To simplify the discussion we will consider the body to be a sphere and will first look at how the sphere attracts particles from a monoenergetic beam. Figure 1 shows how the trajectories are bent by the attractive potential distribution. In a spherically symmetric potential distribution there are two constants of the motion, the total energy  $E$  and the angular momentum  $J$ . As the angular momentum is varied, there is a critical trajectory which just barely grazes the sphere. The impact parameter of this trajectory,  $r_0$ , defines the radius of an "effective cross-section" for collection of particles. Any particles with angular momentum (or impact parameter) less than that for the critical trajectory will be collected. Therefore the cross-section for collection and the current to the sphere can be obtained from the expressions for the total energy and angular momentum, as shown in Figure 1.

Note that in the derivation of the expression for the current that no explicit use was made of the inverse square dependence of the potential. Therefore a linear cur-

rent voltage relation holds for any monotonic attractive potential distribution about a sphere provided that trajectories exist at all energies which come from infinity and are tangent to the surface of the sphere. This linear relation between current and an attractive voltage holds for any particle velocity distribution since any particle velocity distribution can be decomposed into superimposed beams. The condition that trajectories exist at all energies which come from infinity and graze the surface of the attracting body is the defining condition for "orbit limited" currents. Laframboise and Parker (1973) have shown that prolate and oblate spheroids also exhibit orbit limited behavior in the Laplace limit as long as the major-to-minor axis ratios are less than 1.653 and 2.537 respectively.

Orbit limited behavior also holds for any monotonic repelling potential about a convex object since every grazing orbit connects to infinity. However, the current to a repelling object is not linear since the particles in the plasma with energies less than the potential energy of the body will not reach it. For a Maxwellian plasma, the attracted and repelled currents are

$$I = I_0(1 - e\phi/kT), \text{ for } e\phi < 0 \quad (1)$$

$$I = I_0 \exp(-e\phi/kT), \text{ for } e\phi > 0 \quad (2)$$

where  $I_0$  is the random current to the body when it is at zero potential.

#### Sheath Limited Currents

When the Debye length in the plasma is on the order of or less than the body dimension, then there may not be any trajectories at a given energy which come from the plasma and are tangent to the surface of the body. This is illustrated in Figure 2 where there is a critical trajectory, defined as the non-impacting trajectory which approaches closest to the body for particles with a given energy. Trajectories with less angular momentum will all impact the body at angles of incidence which are not grazing angles. In such a case the critical trajectory defines an "absorption radius" (or absorption boundary) but this can not be easily used to obtain the current since each energy will in general define a different absorption radius. When this kind of behavior occurs the currents are said to be "sheath-limited".

The problem of obtaining sheath-limited currents is difficult since it involves finding the potential distribution from Poisson's equation which is self-consistent

with the space charge. Bernstein and Rabinowitz (1959) first showed how to do this and Laframboise (1966) has applied their method to a Maxwellian plasma to obtain currents to spheres and cylinders for various values of plasma parameters. The method makes use of the "effective potential for radial motion",  $U(r)$ , defined as follows:

$$E = \frac{1}{2}mv_r^2 + \frac{1}{2}mv_\theta^2 + e\phi(r) = \frac{1}{2}mv_r^2 + \frac{J^2}{2mr^2} + e\phi(r) \quad (3)$$

$$J = mr v_\theta \quad (4)$$

then

$$v_r = \sqrt{\frac{2}{m}[E - U(r)]} \quad (5)$$

where

$$U(r) = e\phi(r) + \frac{J^2}{2mr^2} \quad (6)$$

and where the radial and angular components of velocity are  $v_r$  and  $v_\theta$ . The second term in (6) is the repelling "centrifugal potential" which can give rise to potential barriers as shown in Figure 3. When the attractive electrostatic potential is weaker than  $(1/r^2)$  then a maximum in the effective potential does not exist outside the probe surface. However, when the electrostatic potential is stronger than the inverse square potential, then potential barriers can exist for angular momenta greater than zero. Particle trajectories can be pictured in Figure 3 as horizontal lines of constant total energy which are reflected when they are incident on the effective potential curve for a particular angular momentum  $J$ . Barriers in the effective potential will repel particles with positive energies and thus reduce the current. Consequently sheath limited currents are always smaller than the orbit limited currents at a given potential. Orbit limited behavior can be seen to exist whenever the electrostatic potential falls off more weakly than an inverse square potential at every radius.

Figures 4 and 5 illustrate how the various types of trajectories which can occur for a given potential variation can be translated into a picture in the velocity space defined by the energy  $E$  and square of the angular momentum ( $J^2$ ). Moments of the particle velocity distribution such as the particle density and current involve integrals over the distribution function, and the boundaries in the  $(E, J^2)$  plane between the different types of trajectories must be used in the limits of these integrals. For example, in Figure 4 trajectories of type 1 are populated by incoming plasma particles, and possibly by outgoing secondary particles from the probe surface. Those of type 2 are plasma particles which do not reach the probe. Type 4

consists of particles trapped in closed orbits about the probe, and type 3 consists of secondary particles which are emitted from and return to the probe. In Figure 5 for the sheath limited case, trapped particles do not exist, and type 3 trajectories are for particles which are repelled by a potential barrier and return to the plasma. This type of analysis has been used to calculate the current, space charge, and potential distribution about probes where both plasma particles and secondary particles contributed (Chang and Bienkowski, 1970; Schroder 1973; Tunaley and Jones, 1973; Whipple 1976; Parker, 1976).

Figure 6 shows currents obtained for inverse power law potential variations (Parker and Whipple, 1967). These potentials are not self-consistent but they illustrate nicely how the current decreases as the power  $n$  increases. Note how there is only one, linear curve for  $n <= 2$ . Figure 7 from Laframboise (1966) shows self-consistent currents to a sphere for various values of the probe radius to Debye length ratio.

When the particle velocity distribution is not isotropic, it may still be a reasonable approximation to use a spherically symmetric potential in order to calculate the current. Godard (1975) has used the potential distributions obtained by Laframboise (1966) for a stationary body to calculate the currents for a drifting Maxwellian plasma. These results, shown for a sphere in Figure 8, are appropriate for a positive ion currents to an attractive spherical satellite moving through the ionospheric plasma. Note especially that the current can in some cases initially decrease as the speed ratio of the body increases from zero. This effect is significant in calculating the "gyrophase drift" of a charged dust grain in a magnetic field (Northrop et al., 1989).

#### The Concept of a Sheath Edge

Intuitively, a sheath is the region close to a charged body where most of the potential drop occurs and where there is significant space charge. The concept of a "sheath edge" is useful because it defines a surface where the potential is close to the plasma potential and where the current can be estimated and equated (or related to) the total current to the body. The concept of a sheath is most useful when the body potential is high and when the Debye length is small compared to the body size. The sheath edge is usually defined as the place where the potential is  $(kT/2e)$  so that outside this surface a quasi-neutral solution can be used for the potential. Swift and Schwar (1970) have reviewed work based on the concept of a finite thickness sheath.

The most important application of the sheath concept to current collection is

the Langmuir-Blodgett (1923, 1924) derivation of the familiar (3/2) power law for the collected current:

$$I = C(V)^{3/2} \quad (7)$$

Angular momentum effects are neglected in this derivation. It is assumed that the particles are all emitted from one electrode with either zero or very small radial velocities, and that the particles follow the electric field lines to the collector. With these assumptions it is possible to relate the charge density to the current by means of the continuity equation. When the inner electrode is taken to be the collector, then the outer electrode position can be interpreted as the edge of the sheath for applications where a single collector is placed in a plasma.

The three-halves power law in equation (7) may seem to contradict the earlier statement that the maximum current drawn by a body is the orbit-limited current which is linear with voltage. However, the derivation of the current in (7) is for a given ratio of emitter and collector radii. This ratio is contained in the constant C in (7). When the sheath edge around a body in a plasma is taken to be the emitter, the current increases as the potential on the body is increased because the sheath grows larger. The way in which the sheath radius can be estimated for various regimes in space has been discussed in some detail by Parker (1980).

#### Asymptotic Potential Variation

In the distant plasma far from a spherical body the electrostatic potential varies asymptotically as

$$V = C/r^2 \quad (8)$$

where V is the potential, r the radial distance, and C a constant.

This behavior is obtained from the so-called "plasma solution", where the asymptotic forms of the ion and electron densities are obtained in terms of the local potential and distance, and then quasi-neutrality of the plasma is invoked. Both the ion and electron densities involve terms depending on the potential such as the Boltzmann factor, and solid angle factors depending on the distance,  $(1 - r_p^2/r^2)$ , where  $r_p$  is the radius of the body. In the limit as r becomes large, the potential enters the density terms linearly and this gives the first-order asymptotic variation of the potential as  $(1/r^2)$ .

In a numerical scheme for obtaining the potential distribution from Poisson's equation where a floating condition is necessary as a boundary condition at a finite distance, then this inverse square potential is the appropriate one to use. Laframboise (1966) has discussed the application of this condition and has given examples of calculations showing how the accuracy of the solutions depends on the distance of the boundary. Parker and Sullivan (1974) have also used this condition.

The value of C in (8) depends on the assumed plasma conditions. Various authors have obtained different expressions (Bernstein and Rabinowitz, 1958; Lam, 1965; Chang and Biekowski, 1970).

### Present Issues Involving Current Collection

Finally, we list some of the issues involving current collection which are receiving attention at the present time. These issues have arisen in context of active space experiments where large potentials may occur or where large structures may be used:

1. What determines the current for large attractive potentials? Large potentials have been envisaged for high-power solar arrays. They also can occur when energetic charged particle beams are emitted.
2. Large potentials on spacecraft may involve dipole configurations with overlapping sheaths. What are the collected currents in such configurations? Katz et al. (1989) have recently calculated the current through a dipolar sheath and found good agreement with data.
3. The presence of neutral gas (from the neutral atmosphere, vehicle venting or outgassing, etc.) provides opportunities for ionization and therefore large currents. How can this effect be calculated?
4. Application to tether configurations: in large extended geometries, the spacecraft and tether form a circuit element with the current loop being completed through the plasma. How does the current flow in the plasma to complete the circuit?

Acknowledgments. This work was supported by NASA grant NGL 05-005-007.

## References

- Bernstein, I. B., and I. N. Rabinowitz, Theory of electrostatic probes in a low-density plasma, *Phys. Fluids*, **2**, 112, 1959.
- Chang, K. W., and G. K. Bienkowski, Effects of electron emission on electrostatic probes at arbitrary pressures, *Phys. Fluids*, **13**, 902, 1970.
- Godard, R., A Symmetrical Model for Cylindrical and Spherical Collectors in a Flowing Collisionless Plasma, *Ph. D. Thesis*, York University, Toronto, 1975.
- Katz, I., G. A. Jongeward, V. A. Davis, M. J. Mandell, R. A. Kuharski, J. R. Lilley, Jr., W. J. Raitt, D. L. Cooke, R. B. Torbert, G. Larson, and D. Rau, Structure of the Bipolar Plasma Sheath Generated by SPEAR I, *J. Geophys. Res.* **94**, 1450-1458, February 1, 1989.
- Laframboise, J. G., Theory of spherical and cylindrical Langmuir probes in a collisionless, Maxwellian plasma at rest, University of Toronto Institute for Aerospace Studies, *Rep. No. 100*, 1966.
- Laframboise, J., G., and L. W. Parker, Probe design for orbit-limited current collection, *Phys. Fluids*, **16**, 629, 1973.
- Lam, S. H., Unified theory for the Langmuir probe in a collisionless plasma, *Phys. Fluids*, **8**, 73, 1965.
- Langmuir, I., and K. B. Blodgett, Currents limited by space charge between coaxial cylinders, *Phys. Rev.*, **22**, 347, 1923.
- Langmuir, I., and K. B. Blodgett, Currents limited by space charge between concentric spheres, *Phys. Rev.*, **24**, 49, 1924.
- Northrop, T. G., D. A. Mendis and Les Schaffer, Gyrophase Drifts and the Orbital Evolution of Dust at Jupiter's Gossamer Ring, *Icarus*, 1989.
- Parker, L. W., Theory of Electron Emission Effects in Symmetric Probe and Spacecraft Sheaths, *AFGL Rep. TR-76-024*, 1976.
- Parker, L. W., Plasmashield-Photosheath Theory for Large High-Voltage Space Structures, in Space Systems and Their Interactions with Earth's Space Environment, Editors, H. B. Garrett and C. P. Pike, *Progress in Astronautics and Aeronautics*, Vol 71, 477-522, 1980.

Parker, L. W., and E. C. Whipple, Theory of a Satellite Electrostatic Probe, *Annals of Physics*, 44, 126, 1967.

Swift, J. D., and M. J. R. Schwar, *Electrical Probes for Plasma Diagnostics*, Iliffe Books, Ltd., London, 1970.

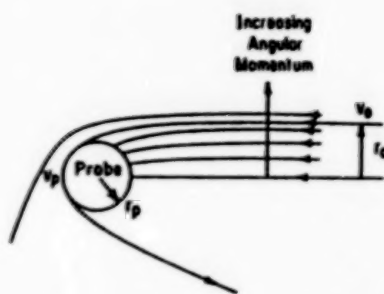
Tunaley, J. K. E., and J. Jones, The Photoelectron Sheath Around a spherical body, in *Photon and Particle Interactions With Surfaces in Space*, ed. by R. J. L. Grard, p. 59, D. Reidel, Dordrecht, Netherlands, 1973.

Whipple, E. C., Theory of the Spherically Symmetric Photoelectron Sheath: A Thick Sheath Approximation and comparison With the ATS 6 Observation of a Potential Barrier, *J. Geophys. Res.*, 81, 601, 1976.

An Attractive Coulomb Potential: ( $e\phi_r < 0$ )

2 Dynamic Constants of Motion:

$$\begin{cases} E = \frac{1}{2}mv_0^2 = \frac{1}{2}mv_p^2 + e\phi_r \\ J = mv_0r_0 = mv_p r_p \end{cases}$$



$$\text{"Effective" Cross-section} = \pi r_p^2 = \frac{\pi r_0^2}{\frac{J^2}{mv_0^2}} = \frac{\pi r_0^2 v_0^2}{mv_0^2 r_0^2} = \pi r_p^2 \left(\frac{v_0^2}{r_0^2}\right)$$

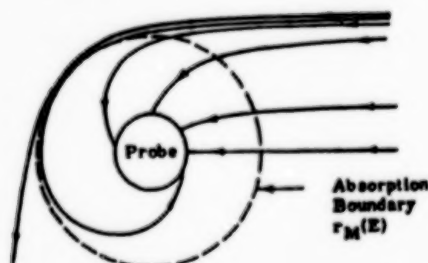
$$\text{But } \left(\frac{v_p^2}{v_0^2}\right) = \left(\frac{\frac{1}{2}mv_p^2}{\frac{1}{2}mv_0^2}\right) = \frac{E - e\phi_r}{E} = 1 - \frac{e\phi_r}{E}$$

$$\text{Cross-section} = \pi r_p^2 \left[1 - \frac{e\phi_r}{E}\right]$$

$$\text{Current from mono-energetic beam is } I_s \left[1 - \frac{e\phi_r}{E}\right] \implies \text{for MB f(v)} \quad I = I_s \left[1 - \frac{e\phi_r}{E}\right]$$

1. Behavior of particles in an attractive Coulomb potential.

A More General Attractive Potential

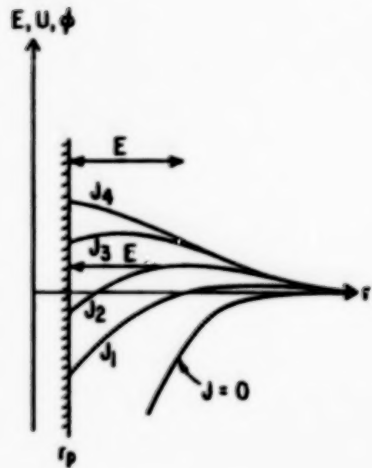


There may not be any trajectories (for a given energy) which come from  $\infty$  and are tangent to the probe.

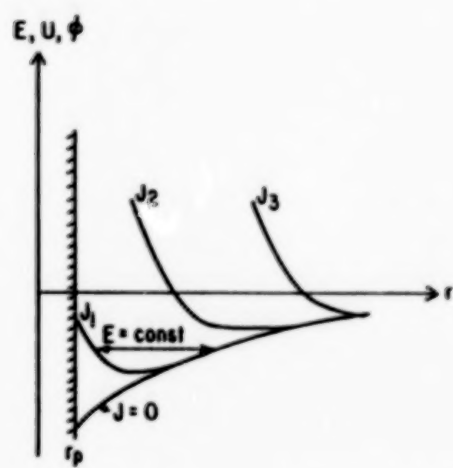
The last (least  $J$ ) non-impacting trajectory, for a given energy, defines an "absorption boundary" for that energy.

2. Behavior of particles in a more general attractive potential.

$$\text{EFFECTIVE POTENTIAL: } U(r) = e\phi(r) + \frac{J^2}{2mr^2}$$



$\phi(r)$  stronger than  $(1/r^2)$

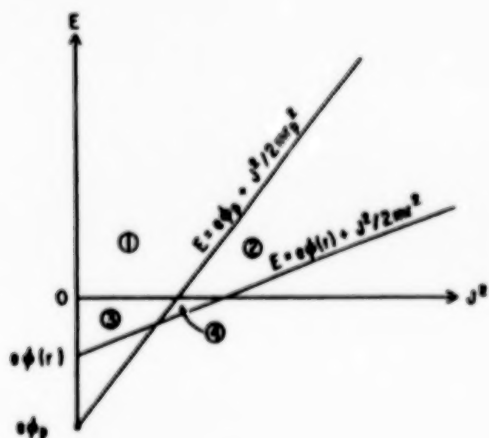
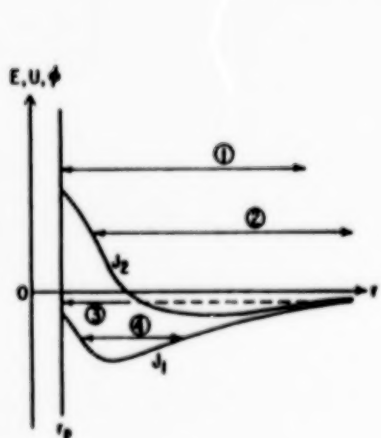


$\phi(r)$  weaker than  $(1/r^2)$

### 3. The effective potential $U(r)$ for radial motion.

Moments (density, flux) are integrals in velocity ( $E, J^2$ ) space.

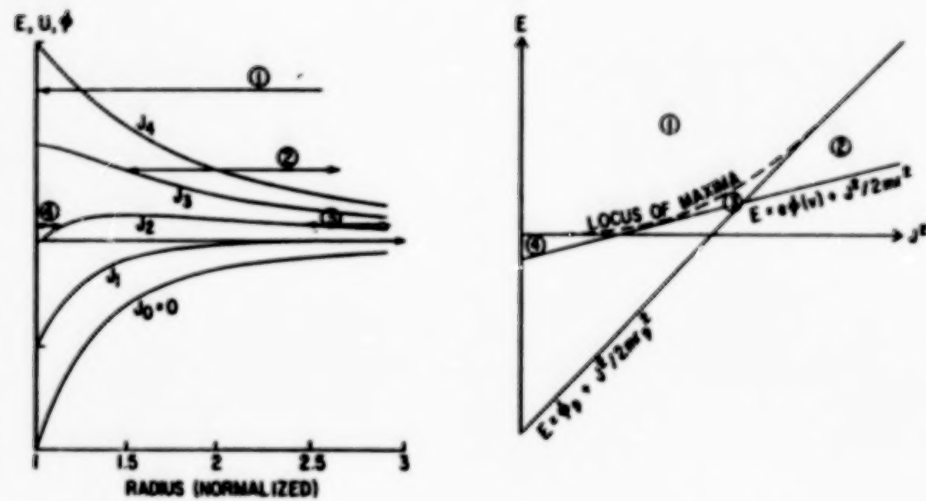
$$M \sim \int \int f(E, J^2) dE dJ^2$$



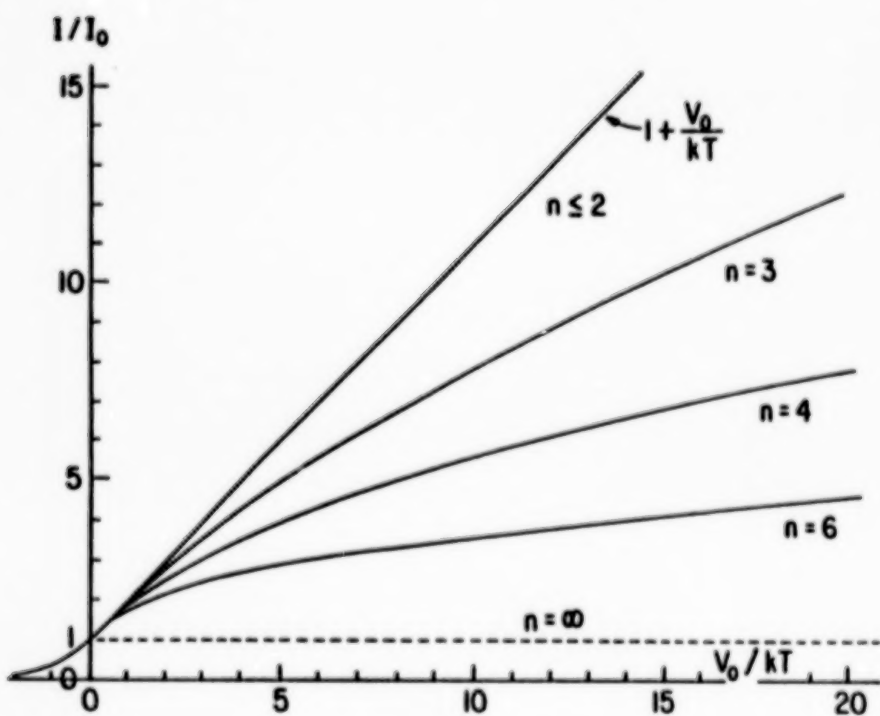
### POSSIBLE TRAJECTORIES FOR THE ORBIT - LIMITED CASE

#### 4. Classification of trajectories for orbit-limited trajectories.

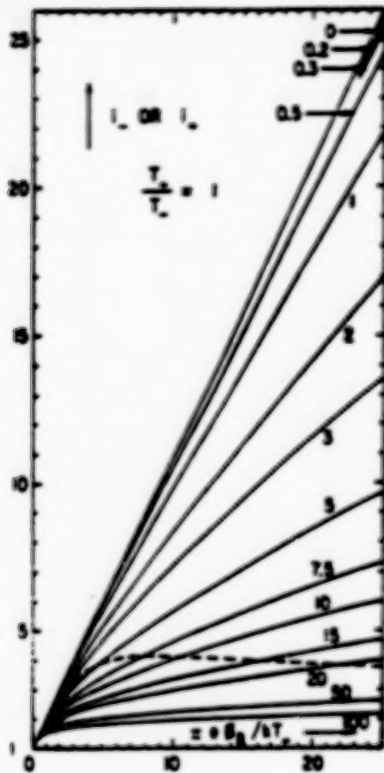
POSSIBLE TRAJECTORIES FOR THE SHEATH-LIMITED CASE



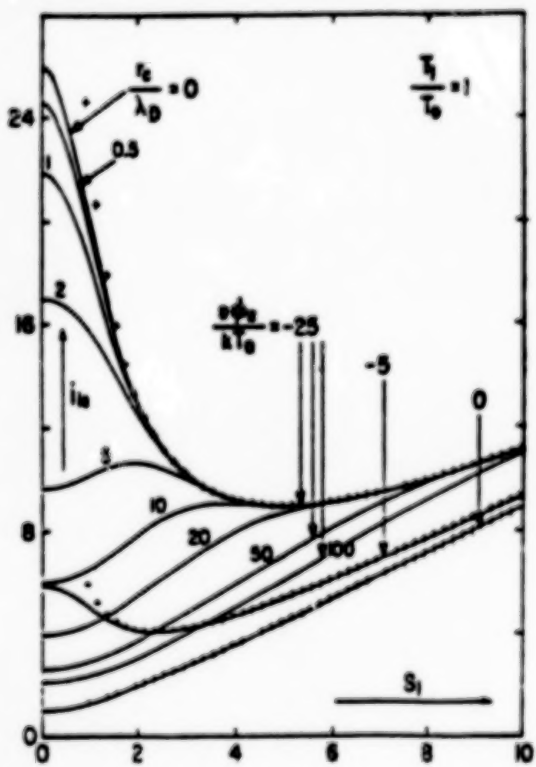
5. Classification of trajectories for sheath-limited trajectories.



6. Current-voltage curves for an inverse power law potential with a Maxwellian velocity distribution (from Parker and Whipple, 1967).



7. Ion or electron current vs. probe potential for various ratios of probe radius to ion or electron Debye length; dotted curve shows trapped-orbit boundary (from Laframboise, 1966).



8. Ion current vs. ion speed ratio with ratios of probe radius to Debye length and probe potential to electron temperature as parameters. The crosses represent the asymptotic solution (from Godard, 1975).

# CURRENT COLLECTION IN A MAGNETOPLASMA

J.G. Laframboise and L.J. Sonmor

Physics Department, York University  
Downsview, Ontario, Canada M3J 1P3

## ABSTRACT

We present a survey of a very incomplete subject. Our presentation is intended in part as an introduction to topics to be covered in greater detail by others later in this Workshop. The best-developed and simplest theories for current collection are steady-state collisionless theories, and these must be understood before departures from them can be analyzed usefully, so we begin with a review of them. We include some recent numerical results by one of us (L.J.S.) which indicate that steady-state collisionless Laplace-limit currents remain substantially below the Parker-Murphy (1967) canonical upper bound out to very large electrode potentials, and approach it as a limit only very slowly if at all. Attempts to correct this theory for space-charge effects lead to potential disturbances which extend to infinite distance along the electrode's magnetic shadow, unless collisional effects are also taken into account. However, even a small amount of relative plasma drift motion, such as that involved in a typical rocket experiment, can change this conclusion fundamentally. It is widely believed that time-averaged current collection may be increased by effects of plasma turbulence, and we review the available evidence for and against this contention. Steady-state collisionless particle dynamics predicts the existence of a toroidal region of trapped orbits which surrounds the electrode. Light emissions from this region have been photographed, indicating that collisional ionization may also occur there, and this, and/or scattering by collisions or possibly turbulent fluctuations in this region, may also increase current collection by the electrode. We also discuss effects on particle motions near the electrode, associated with "breakdown of magnetic insulation" in the region of large electric fields near it.

## 1. INTRODUCTION

Even without magnetic-field effects, the problem of predicting current collection by objects ("probes") in plasmas is one of the most formidable in plasma physics. Reasonably complete solutions of it exist only for very simple geometries, in the limits of large and small mean-free-paths, and in the absence of flow effects. For objects in space plasmas, this situation has been summarized by E.C. Whipple in the preceding paper.

When magnetic-field effects are introduced, the problem becomes notoriously intractable. As one would expect, available treatments of it generally involve extreme simplifications. For space applications, the collisionless approximation seems not extreme but instead inevitable. However, we shall see that even in cases of large mean-free-paths, magnetic fields can cause collisional effects to become important.

In spite of this, collisionless theories form the most important category of available theories, and also must be understood before departures from them can be usefully analyzed. Accordingly, a review of collisionless, steady-state theories (Section 2) forms the next part of this presentation. It seems inevitable also to make a further division of such theories, into ones for the zero-space-charge,

or large-Debye-length, limit (one would expect these to be the simplest), and those for finite Debye length. However, even this division is complicated by magnetic-field effects. It turns out that a strictly collisionless theory cannot be exact in cases of finite Debye length, because the disturbance of electric potential produced by the object then extends infinitely far along the magnetic-field direction. However, this conclusion is modified radically by even a small amount of relative plasma drift motion. This situation is discussed in more detail in Sections 3 and 7. Our review includes the work of Sanmartin (1970), who has himself given an extensive review of older theories. A review of probe use in fusion plasmas has been given by Stangeby (1989).

It has often been asked whether any steady-state theory can give a correct prediction, in view of the tendency of fluctuations, or "plasma turbulence", to carry charge across magnetic field lines in magnetic-confinement fusion experiments. Measured return currents in electron-beam-emission experiments in space have frequently been in excess of predicted values from steady-state theory, and such observations have often been cited in support of this view. An alternative explanation, involving energization of ambient electrons by an interaction with the beam, is supported by results of the CHARGE-2 (Myers *et al*, 1989) and SPEAR I (Katz *et al*, 1989) rocket experiments. We discuss this question in Section 4.

Collisional ionization may cause important increases in current collection beyond those predicted by steady-state collisionless theory. The presence of a magnetic field greatly increases phase-space volumes available to particles on "trapped" orbits near the probe, and the long lifetimes of trapped particles in these regions greatly increase opportunities for collisional ionization to occur. The observation of "toroidal glow" regions around spherical probes in low-pressure laboratory magnetoplasmas (W.J. Raitt and A. Konradi, private communication, 1987; Antoniades and Greaves, paper appearing later in these Proceedings) lends support to this idea. Ionization may produce "explosive" growth of the probe's sheath (Lai *et al*, 1985; Cooke and Katz, 1988). Independently of collisional ionization, the existence of trapped orbits also increases the opportunity for current collection to be increased by particle scattering, both collisional and turbulent. We discuss collisional-ionization and collisional-scattering effects in more detail in Section 5.

Enhanced current collection by a probe at large attractive potentials requires increased transport of particles across magnetic-field lines, and this phenomenon is often called "breakdown of magnetic insulation". A brief discussion of some aspects of this phenomenon appears in Section 6.

If the probe is a large object compared with the ambient Debye length, and is moving rapidly compared with the ion thermal speed as in the proposed Tethered Satellite Experiment, a variety of complicated phenomena can occur near it. This situation has been studied by Thompson (1985). A discussion of it appears in Section 7. Unexpectedly, this discussion leads to an inference that even the small relative drift velocities characteristic of rocket experiments can modify radically the processes governing collection of electrons, and can "revalidate" collisionless theories of such collection. A separate issue is the enhancement of current collection by the use of a "plasma contactor" (4 papers, by Hastings, Wilbur and Williams, Katz and Davis, and Cooke, respectively, which appear later in these Proceedings).

Some concluding remarks appear in Section 8.

Much of our discussion in this paper is directed toward current collection at large positive electrode voltages. Interest in predicting such collection has recently increased because of applications to the design of high-voltage power systems for use in space and also because of large induced voltages expected in the Shuttle Electrodynamic Tether experiment.

## 2. COLLISIONLESS STEADY-STATE THEORIES

In this Section, we consider a spherical probe in a collisionless plasma containing a uniform magnetic field  $\mathbf{B}$ . We give brief summaries of the treatments of Parker and Murphy (1967) and Rubinstein and Laframboise (1982, 1983) and of new results by one of us (L.J.S.). We also summarize results of an analogous treatment which has been done for an infinite cylindrical probe inclined at an arbitrary angle to  $\mathbf{B}$ , by Laframboise and Rubinstein (1976) and Rubinstein and Laframboise (1978). For the spherical-probe case, we choose cylindrical coordinates  $(r, \theta, z)$  centred on the probe, with the  $z$  axis aligned with  $\mathbf{B}$ . In the presence of  $\mathbf{B}$ , our situation no longer has spherical symmetry, and this makes our task much more difficult. However, it still has rotational symmetry about the direction of  $\mathbf{B}$ , and therefore the electric potential  $\phi$  will be independent of  $\theta$ . In this situation, there are two constants of collisionless particle motion, the total energy  $E$ , given by:

$$E = \frac{1}{2}m(\dot{r}^2 + r^2\dot{\theta}^2 + \dot{z}^2) + q\phi(r, z) \quad (1)$$

and the canonical angular momentum component  $J$  about the  $z$  axis, given by

$$J = mr^2\dot{\theta} + \frac{1}{2}qBr^2 = mr^2\left(\dot{\theta} + \frac{1}{2}\omega\right) \quad (2)$$

where  $m$  and  $q$  are particle mass and charge, and  $\omega = qB/m$  is the particle's gyrofrequency. We also define the absolute gyrofrequency  $\omega_c = |\omega| = eB/m$ , where  $e$  is the magnitude of unit electronic charge.

We eliminate  $\dot{\theta}$  from these two equations, and obtain:

$$E = \frac{1}{2}m(\dot{r}^2 + \dot{z}^2) + q\phi(r, z) + \frac{m}{2}\left[\frac{J}{mr} - \frac{\omega r}{2}\right]^2 \quad (3)$$

The first term on the right of (3) is the kinetic energy of particle motion in the  $(r, z)$  plane. The remaining two terms are then the "effective potential"

$$U(r, z) \equiv q\phi(r, z) + \frac{m}{2}\left[\frac{J}{mr} - \frac{\omega r}{2}\right]^2 \quad (4)$$

for particle motion in the same plane. Since the kinetic energy must be nonnegative, it follows that a particle having a particular  $E$  and  $J$  will be confined to those regions of the  $(r, z)$  plane for which  $E \geq U(r, z)$ , i.e., inside the particle's "magnetic bottle". Some examples of the general appearance of magnetic bottles are shown in Fig. 1.

Some properties of magnetic bottles follow readily from inspection of Eq. (3); see also Section IV of Rubinstein and Laframboise (1982). These are as follows:

- (1) Magnetic bottles have rotational symmetry about the  $z$  axis, i.e. their boundaries are independent of  $\theta$ .
- (2) A particle orbit (having a given  $E$  and  $J$ ) can touch the boundary of its magnetic bottle only if  $\dot{r}$  and  $\dot{z}$  are both zero at the same point on the orbit. Since this is very unlikely, particle orbits generally do not do so.

(3) We define a radius  $r_o$  by the relation:

$$J = \frac{1}{2}m\omega r_o^2 \quad (5)$$

(if  $\omega > 0$ ). In Eq. (4), the last term in  $U(r, z)$  will then vanish at  $r = r_o$ , and is positive for  $r \neq r_o$ , increasing without limit as  $r \rightarrow 0$  (unless  $J = 0$ ) or as  $r \rightarrow \infty$ . Therefore, particles for which  $J \neq 0$  are prevented from reaching the  $z$  axis.

(4) For  $\omega > 0$ , particle orbits for which  $J < 0$  encircle the  $z$  axis once per gyration; orbits for which  $J > 0$  do not.

(5) A nonencircling orbit having energy  $E$  and canonical angular momentum  $J$  will have the same projection in the  $(r, z)$  plane, and also the same magnetic bottle, as those of an encircling orbit having the corresponding values  $E + \omega J = E + \frac{1}{2}m\omega^2 r_o^2$  and  $-J$ . In a strong magnetic field, an encircling orbit will have a much larger energy and also a much larger gyroradius than the corresponding nonencircling orbit, and encircling orbits will then make vanishing contributions to number densities and fluxes.

We now present a derivation of the Parker and Murphy (1967) canonical upper-bound current. Besides the assumption of collisionless, steady-state conditions, their work contained two additional ones. They assumed that any particle whose magnetic bottle intersects the probe is itself collected, and they ignored the effect of a particle's thermal motion at infinity on the question of whether such an intersection exists for that particle. The first assumption results in their current expression being an upper bound on the corresponding exact value. The second assumption amounts to taking the limit  $E \rightarrow 0$  in Eq. (3). We shall see that this approximation does not lead to an upper bound, so actual currents can exceed the Parker and Murphy (1967) values. When this approximation is made, particles having the largest  $J$  for which collection occurs then have a magnetic bottle similar in appearance to that shown as (a) in Fig. 1, but with one important difference: the condition  $E \rightarrow 0$  means that at large  $|z|$ , the inner and outer surfaces of the bottle collapse onto the common radius  $r_o$ . To find the value of  $r_o$ , we make the further substitutions  $\dot{r} = 0$ ,  $\dot{\theta} = 0$ ,  $r = r_p$ , and  $\phi = \phi_p$  in Eq. (3), where  $\phi_p$  is the probe's potential relative to space,  $r_p$  is its radius, and  $q\phi_p < 0$  for an attractive probe potential for the particle species considered. We then substitute for  $J$  using Eq. (5). We obtain:

$$\left(\frac{r_o}{r_p}\right)^2 = 1 \pm \left(\frac{8|q\phi_p|}{m\omega^2 r_p^2}\right)^{\frac{1}{2}} \quad (6)$$

The positive sign corresponds to tangency of the bottle's inner surface with the probe, as shown in Fig. 1a.

We now note that with Parker and Murphy's approximations, the collected current is equal to the product of the random thermal particle flux with the combined area  $2\pi r_o^2$  of the two disks of radius  $r_o$ , located at  $z = \pm\infty$ , through which all collected particles of charge  $q$  must pass.

In terms of the random current  $I_R = 4\pi r_p^2 q n_\infty (kT/2\pi m)^{\frac{1}{2}}$ , and using Eq. (6), we now obtain:

$$i \equiv \frac{I}{I_R} = \frac{1}{2} + \frac{1}{2} \left(\frac{8|q\phi_p|}{m\omega^2 r_p^2}\right)^{\frac{1}{2}} \quad (7)$$

where  $k$  is Boltzmann's constant, and  $T$  and  $n_\infty$  are the temperature and ambient number density of the attracted particles. Apart from notation, this is the same as Eq. (13) of Parker and Murphy (1967).

If effects of thermal motion are included, then Eq. (7) is no longer an upper bound on the (collisionless, steady-state) probe current, although we shall see that it remains a good approximate upper bound for large potentials and large magnetic fields. Calculation of the canonical upper bound including thermal-motion effects is much more cumbersome. It has been done by Rubinstein and Laframboise (1982). Here we give only their result, which is in analytic form, as follows:

$$i = i_1 + i_2 \quad (8)$$

where  $i_1$  and  $i_2$  are the (normalized) currents due to nonencircling and encircling particles, respectively, given by:

$$\begin{aligned} i_1 &= \frac{\sqrt{\pi}}{2\sigma} \left( \frac{3}{2} - \psi_p \right) \operatorname{erfc} \left( \sqrt{\psi_p} \right) \exp \left( \psi_p \right) + \frac{3}{2} \frac{\sqrt{\psi_p}}{\sigma} + \frac{1}{2} \\ i_2 &= F_1 \left( 1 + 2 \frac{\sqrt{\psi_p}}{\sigma} \right) + F_2 \left( 1 + 2 \frac{\sqrt{\psi_p}}{\sigma} \right) + \frac{1}{2\sigma^2} \end{aligned} \quad (9)$$

$$\begin{aligned} F_1(u) &= -\frac{1}{4} \left( \sigma^2 u^2 + 2u + \frac{2}{\sigma^2} \right) \exp \left( -\sigma^2 u \right) \\ F_2(u) &= \frac{\sqrt{\pi}}{4} \left[ 2\sigma + \frac{1}{\sigma} \left( 3 - 2\psi_p \right) \right] \operatorname{erfc} \left[ \left( \sigma^2 u + \psi_p \right)^{\frac{1}{2}} \right] \exp \left( \psi_p \right) \\ &\quad + \frac{1}{2} \left\{ \left[ \frac{3}{\sigma} + 2\sigma(1+u) \right] \left( \sigma^2 u + \psi_p \right)^{\frac{1}{2}} - 3 - 2\psi_p \right. \\ &\quad \left. - \sigma^2 \left( 3u + \frac{1}{2} \right) \right\} \exp \left( -\sigma^2 u \right) \\ \sigma &= \frac{1}{2} \sqrt{\pi} \beta \end{aligned} \quad (10)$$

where  $\beta = r_p/\bar{a} = r_p|\omega|(2m/\pi kT)^{\frac{1}{2}}$  is the ratio of probe radius to mean attracted-particle gyroradius, and  $\psi_p = -q\phi_p/kT \geq 0$  is dimensionless probe potential. Rubinstein and Laframboise (1982) also obtained a corresponding analytic result for repelling probe potentials  $\psi_p < 0$ , given by their Eqs. (30), (36), and (37), and plotted in their Fig. 10. In contrast with the usual exponential variation of collected current at these potentials, their result shows a "rounding of the knee" of the probe's current-voltage characteristic at small negative  $\psi_p$ . In the limit of large attractive potentials  $\psi_p \gg 1$ , Eqs. (8) – (10) reduce to:

$$i = \frac{1}{2} + \frac{\sqrt{\psi_p}}{\sigma} + \frac{1}{2\sigma^2} \quad (11)$$

The first two terms of this are the same as the Parker and Murphy (1967) result. The last term is a contribution from encircling orbits, which vanishes in the limit of strong magnetic fields:  $\beta \rightarrow \infty$ . A comparison of the Parker-Murphy (1967) canonical upper bound with results of Rubinstein and Laframboise (1982) for attracted-species currents is shown in Fig. 2. The increasing curves in Fig. 2 show least upper-bound currents. The portions of these curves to the right of the "kinks" (discontinuities of slope) are the canonical upper bounds given by Eqs. (8) – (10). The portions to the left of the kinks are "helical" upper bounds also calculated by them, and based on an

assumption that particle orbits are helices near the probe. The decreasing curves are adiabatic-limit (effectively lower-bound) currents also calculated by them, also assuming helical orbits near the probe, but assuming a "one-dimensional" rather than "three-dimensional" velocity-space cutoff. For a probe at space potential,  $\psi_p = 0$ , the upper-bound and adiabatic-limit currents coincide, and are the same as those given in Fig. 17 of Whipple (1965). For any given value of  $\beta$ , we see that the upper-bound and lower-bound curves separate rapidly as  $\psi_p$  increases. This is clearly an unsatisfactory situation, but it appears to represent the best that can be done without resorting to the expense of numerical orbit integration. We present results of such a calculation below.

As mentioned above, the adiabatic-limit currents decrease as  $\psi_p$  increases. This "negative-resistance" behavior results from the fact that in the adiabatic limit, the kinetic-energy gain of incoming particles goes entirely into increased speed parallel to  $\mathbf{B}$ . This increases the pitch of their orbits. Some orbits whose pitch becomes greater than roughly the probe diameter can now bypass the probe, and current collection will be decreased. When  $\psi_p$  is small, we also expect the actual currents to approach the adiabatic-limit currents, since the adiabatic-limit condition is that changes in the probe sheath electric field are small over an average particle gyroradius. We further expect that as  $\psi_p$  becomes more positive, adiabatic-limit conditions will break down, and collected currents will then rise toward the upper-bound values.

We therefore expect the current-voltage characteristics to be "N-shaped". Such behavior was predicted qualitatively by Laframboise and Rubinstein (1976) and Rubinstein and Laframboise (1982), and more recently seen in data from spherical electrostatic probes on the University of Iowa Plasma Diagnostics Package flown on several Shuttle flights (G.B. Murphy, private communication, 1983). We present later in this Section a quantitative prediction of such characteristics.

Figure 3 shows the same comparison of the Parker and Murphy (1967) and Rubinstein and Laframboise (1982) upper-bound currents over a larger range of attractive probe potentials. It is evident from this Figure, and also from Eq. (11), that these bounds do not coalesce at large potentials, but only for large magnetic fields.

Corresponding upper and lower bounds on current have been calculated for an infinite-cylindrical probe inclined at an arbitrary angle to  $\mathbf{B}$  by Laframboise and Rubinstein (1976) and Rubinstein and Laframboise (1978), and for spheroids and finite cylinders, including disks, whose axis of symmetry is aligned with  $\mathbf{B}$ , by Rubinstein and Laframboise (1983). In all cases, their helical upper-bound and adiabatic-limit currents depend on all aspects of probe shape, whereas their canonical upper-bound currents depend only on the probe cross-section perpendicular to  $\mathbf{B}$ . We reproduce here only their result for the canonical upper-bound current to an infinite cylindrical probe. For the cylindrical case only, we redefine  $I$  and  $I_R$  to be the current and the random current  $2\pi r_p q n_\infty (kT/2\pi m)^{1/2}$ , respectively, both per unit probe length. For the attracted particles ( $\psi_p \geq 0$ ), their result [Rubinstein and Laframboise, 1978, Eqs. (10) and (11)] is:

$$i = \frac{2}{\pi} \sin \theta + \frac{1}{\pi^{3/2} \beta} \left[ (3 - 2\psi_p) \sqrt{\pi} \operatorname{erfc}(\sqrt{\psi_p}) \exp(\psi_p) + 6\sqrt{\psi_p} \right] \quad (12)$$

where  $\theta$  is the angle between the probe axis and the direction of  $\mathbf{B}$ . For large  $\psi_p$ :

$$i \rightarrow \frac{2}{\pi} \sin \theta + \frac{4}{\pi^{3/2}} \frac{\sqrt{\psi_p}}{\beta} = \frac{2}{\pi} \sin \theta + \left( \frac{8|q\phi_p|}{\pi^2 m \omega^2 r_p^2} \right)^{1/2} \quad (13)$$

A corresponding result for repelling probe potentials  $\psi_p < 0$  is given by their Eq. (13). The most remarkable feature of our Eq. (13) is that it gives the same one-half-power dependence of probe

current on probe potential as in the spherical case [Eqs. (7) and (11)], in spite of the difference in probe shape. As in the spherical case, the canonical upper bound may not be the least upper bound, especially at small  $\beta$  and  $\psi_p$ ; see Figs. 2 and 3 of Rubinstein and Laframboise (1978). Equations (12) and (13) should be useful for estimation of currents collected by tether wires in space.

All of this leaves unanswered so far the question of how nearly the actual current collection approaches these upper-bound values. For cylindrical probes, experimental data presented in Fig. 4 of Szuszczewicz and Takacs (1979) provide a partial answer to this question. They found that adiabatic conditions are easily violated in the cylindrical configuration. For spherical probes in the limit of large Debye length (Laplace-potential limit), we present results from an exact numerical calculation of probe currents by one of us (L.J. Sonmor, Ph.D. thesis, in preparation). This calculation is "exact" in the sense that in the limit of zero discretization and roundoff errors, it would produce results corresponding exactly to the physical assumptions made.

In the Laplace-potential limit, an important computational advantage can be gained by scaling the collisionless charged-particle orbits. These obey the equation of motion  $m\ddot{\mathbf{r}} = q(\mathbf{E} + \dot{\mathbf{r}} \times \mathbf{B})$ . We introduce the scaled position vector  $\tilde{\mathbf{r}} = \mathbf{r}/(|m\phi_p r_p/qB^2|)^{1/3}$  and time  $\tau = (qB/m)t$ . This equation then reduces to:

$$\frac{d^2\tilde{\mathbf{r}}}{d\tau^2} = \pm \frac{\mathbf{i}_r \dot{r} + \mathbf{i}_z \dot{z}}{(\dot{r}^2 + \dot{z}^2)^{3/2}} + \frac{d\tilde{\mathbf{r}}}{d\tau} \times \mathbf{i}_z \quad (14)$$

which contains no free parameters. The calculation method then involves integration of (14) for various scaled initial positions  $\tilde{\mathbf{r}}$  and velocities  $d\tilde{\mathbf{r}}/d\tau$  on a plane  $\tilde{z} = \text{constant}$  located sufficiently far from the origin of coordinates. This yields a data base of distances of closest approach to the origin. The appropriate integration over this data base then yields the current-voltage characteristics ( $i$  vs  $\psi_p$  for various  $\beta$ ). Separate data bases must be created for attractive and repulsive probe potentials. To obtain values of  $i$  having a relative accuracy of 1% or better required the integration of about two million such orbits, and this consumed about 25 hours of CPU time on the University of Toronto CRAY X-MP computer.

Results from this calculation are shown in Figures 4-7. Figures 4(a) - (d) show representative particle orbits, together with their corresponding magnetic-bottle boundaries. The orbits shown all have positive total energies ( $E > 0$ ) so they all originate at  $z = \pm\infty$ . As we mentioned following Eq. (4), such orbits generally do not touch their bottle boundaries, but they evidently come very close to them near points of reversal of  $z$  velocity, because  $|\dot{r}|$  and  $|\dot{z}|$  can be simultaneously very small near such points. Our earlier discussion implies that actual currents will equal canonical-upper-bound values [Eqs. (8) - (10)] if every orbit reaches the point closest to the origin on its bottle boundary, but that in general, orbits do not do so. Comparison of Figures 4(b) - (d) shows that the nearness of an orbit's approach to this point can be very sensitive to its initial phase. Figures 4(a) - (d) also show significant violation of the adiabatic-limit approximation, including, in (b) - (d), reversals of  $z$ -velocity.

Figures 5 and 6 show attracted-particle current-voltage characteristics for smaller and larger ranges of attractive probe potential, respectively, and for two different values of  $\beta$ . Also shown are the Rubinstein and Laframboise (1982) canonical upper bound [Eqs. (8) - (10)], and, in Figs. 5(a) and (b), their helical upper bound and adiabatic limit. Features visible in Figs. 5(a) and (b) include, as predicted above, a negative-resistance region in the attracted-particle current-voltage characteristic. When  $\beta = 3$ , this region extends over a larger range of probe potentials than when  $\beta = 1$ .

In this region, the slope of the exact characteristic appears to be less negative than that of the adiabatic-limit curve everywhere, even at small potentials. One can identify three possible reasons for this. One of these is that the mechanism causing this behavior, namely that some orbits miss the probe because they are "stretched", i.e., their pitch is increased near it, does not operate as effectively for the real orbits as for the helical ones assumed in the adiabatic-limit calculation. Another is that nonadiabatic effects also cause some particle gyroradii to increase (Fig. 4), allowing more particles to be collected. A third possible reason is radial drift motions caused by electric-field inhomogeneities (Fig. 4a). A current-collection theory based on such drift motions was developed by Parker and Murphy (1967, Fig. 2 and Table 1).

Figures 5 and 6 appear to leave unresolved the important question of whether the exact currents approach the canonical upper-bound values at large attractive potentials or remain substantially below them. This question is examined directly in Fig. 7, but the outcome is still not clear. What is clear from Fig. 7 is that even if the actual currents approach the canonical upper-bound currents at large potentials, the approach is so slow as to be irrelevant to most practical purposes. It is noteworthy that at the largest probe potential shown in Fig. 7, i.e.  $\psi_p = 500$ , the Parker-Murphy (1967) canonical-bound values are much closer to the Rubinstein-Laframboise (1982) values than the exact currents are, so the latter currents also remain substantially below the corresponding Parker-Murphy values. Some evidence of the level of numerical errors in these "exact" results also appears in Figs. 6(a) and 6(b).

An important limitation of the exact results shown in Figs. 4-7 is that they apply only in the Large-Debye-length limit. As the Debye length is decreased, space-charge effects influence more and more strongly the potential disturbance around the probe. As a result, this potential becomes progressively more "short-range", with increased electric fields in the sheath region near the probe, and decreased fields in the presheath region farther away (see below, however). M.J. Mandell (private communication, 1989) has suggested that in this situation, the current collection may increase above the values shown in Figs. 5-7 toward the canonical-upper-bound values, because adiabatic-limit conditions now are more strongly violated near the probe, and this permits incoming particles to acquire larger gyroradii, so that more of them are collected. This is in contrast with the nonmagnetic situation, in which attracted-species current collection decreases with decreasing Debye length; see, for example, the preceding paper by E.C. Whipple.

Figure 7 contains a feature which may illuminate this question. This Figure shows a "crossover" of the current-voltage curves for various values of  $\beta$  as the probe voltage  $\psi_p$  increases, with the currents for the largest  $\beta$  values becoming the closest ones to the upper-bound currents at the largest  $\psi_p$  values shown. If one considers the magnetic bottles which correspond to the attracted-particle energies making the most important current contributions at large  $\psi_p$ , then among these bottles, those which correspond to the largest  $\beta$  values will have the least relative widening (Figs. 1 and 4) near  $z = 0$ . Figure 7 therefore implies a tendency for bottles with the least widening to be the "most filled" by the orbits confined inside them. If this tendency carries through to situations in which space-charge effects are important, it will tend to counteract the mechanism described in the preceding paragraph, and the attracted-species current may then decrease rather than increase with decreasing Debye length as in the nonmagnetic case. Another mechanism which may act in the same direction is the tendency of magnetic bottles to form "bulges" or even disjoint "bubbles" as a result of space-charge effects on the probe sheath potential distribution (Section 5).

### 3. COMBINED EFFECTS OF SPACE-CHARGE AND COLLISIONS

In some presheath locations, a decrease in Debye length will produce an increased rather than decreased electric field. To see why, we consider the depletion of particles at large distances from a spherical probe, caused by the probe's current collection. If  $\mathbf{B} = \mathbf{0}$ , this depletion occurs equally in all directions for both ions and electrons, and therefore results in a spherically-symmetric distribution of net space charge and therefore of potential. If  $\mathbf{B} \neq \mathbf{0}$ , it occurs predominantly along and adjacent to the probe's "magnetic shadow". In other words, we expect that at large  $|z|$ , both the ion and electron density disturbances (in the collisionless limit) will become functions only of the cylindrical radius  $r$ . In contrast with the nonmagnetic case, however, these disturbances will have different dependences on  $r$  for the ions and electrons, because the much smaller average gyroradius of the electrons will cause the electron depletion to be confined much more closely to the magnetic shadow itself, whereas the ion depletion will be more widespread (Fig. 8). If the Debye length is finite, the resulting charge imbalances will produce a potential disturbance which will also depend only on  $r$  at large  $|z|$ . Unless the probe potential is very negative, this disturbance will be positive in sign (Sanmartin, 1970). In the absence of collisions (and assuming steady-state conditions), no mechanism exists to cause the charge-density disturbances to decay with increasing  $|z|$ , and the resulting potential disturbance must therefore also extend to infinity in both directions along the probe's magnetic shadow. This further implies that if the charged-particle mean-free-paths are finite, no matter how large they are, collisions will ultimately repopulate the depleted regions as  $|z| \rightarrow \infty$ . Some of these collisionally-reddirected particles will travel toward the probe. In doing so, they will produce effects on both the space-charge density near it and on current collection by it. Some of the same particles will have negative values of the total energy  $E$  defined in Eq. (1); if the potential disturbance is positive in sign, this can happen only for electrons. These particles cannot escape from the probe's potential disturbance unless it extends to infinity or they undergo another collision; otherwise the  $z$  component of their velocity, if initially directed away from the probe, must eventually reverse. The electron current reaching the probe will therefore include a contribution due to electrons which have negative total energies. In contrast with the situation for  $\mathbf{B} = \mathbf{0}$ , this contribution will persist rather than vanish in the limit of large mean-free-paths; increasing the mean-free-path will result merely in a corresponding increase of the scale of distances over which collisions provide this contribution.

We therefore conclude that a collisionless, finite-Debye-length theory cannot be formulated for a probe in a magnetoplasma, unless some approximation is made (discussions with H.A. Cohen, unpublished). On the other hand, effects of this may be negligible in at least some real situations. For example, the calculations reported by Katz *et al* (1989), which were done in support of the SPEAR I electrostatic probe measurements using the NASCAP/LEO and POLAR simulation programs, gave good agreement (within about 4% in the case of the more-accurate POLAR calculations) with these measurements (see their Fig. 10), and these were collisionless calculations. The NASCAP/LEO calculations used analytic approximations for space-charge densities in the sheaths around the SPEAR I probes and rocket body, whereas POLAR calculated these densities by tracking particle orbits inward from sheath edges. It is noteworthy also that all the theory which we have discussed so far has been for a nondrifting ambient plasma. In Section 7, we discuss a description by Thompson (1985) of the disturbed region around a high-voltage orbiting object. Thompson's description implies that a drift transverse to  $\mathbf{B}$ , even at much less than orbital speed, may change fundamentally the structure of this disturbed region, and a completely collisionless calculation of collected current then may still be applicable. We discuss this question in more detail in Section 7. Here we confine our discussion to nondrifting situations.

The most thorough available treatment of the combined effects of collisions and space-charge on probe current is that of Sanmartin (1970), who performed an asymptotic analysis on this problem, using ion and electron collision models based on cumulative small-angle scattering by multiple Coulomb encounters. In his treatment, electron collection by the probe is limited by the fluxes of electrons which are supplied by collisions to the above-mentioned two regions (one for  $z > 0$  and one for  $z < 0$ ) of positive potentials in the probe's magnetic shadow. To be collected, these electrons must also cross a potential barrier which exists between each of these regions and the probe when the probe potential is close enough to space potential. This barrier exists because at such probe potentials, each region is more positive than at either the probe or infinity, *i.e.*, there is an "overshoot" in the potential distribution as a function of  $|z|$  in each region (Fig. 9). The most important effect of this situation on the probe current near space potential is to decrease the electron collection, thereby "rounding the knee" of the probe's current-voltage characteristics as computed by Sanmartin. His results for the electron-current characteristics are reproduced in Fig. 10. Sanmartin's treatment assumes that the ion-to-electron temperature ratio is close to unity, the electron average gyroradius  $\bar{a}$  and the Debye length  $\lambda_D$  are both  $\ll r_p$ , and  $r_p \lesssim$  both the mean free path for multiple small-angle Coulomb collisions and the ion average gyroradius. In his analysis, the magnetic shadow region on each side of the probe is divided into: an outer layer which extends to infinity, is quasineutral and collision-dominated, and in which the potential rises to a maximum value as one approaches the probe; an intermediate layer, also quasineutral, across which the potential is uniform and whose thickness is of the order of the local electron mean free path; and an inner layer which is collisionless and in which the potential decreases steeply to its value on the probe. Sanmartin's approximations include a point-to-point matching of the particle fluxes as a function of  $r$  across the intermediate layer. For electrons, this is done by equating his Eqs. (44) and (65) for these fluxes. The result is to exclude the possibility of an attraction-region increase in current collection due to effects of particle orbital motions, so his attraction-region currents saturate at  $i = \frac{1}{2}$  as  $\psi_p \rightarrow \infty$ , in contradiction with the results discussed in Section 2. His theory in its present form therefore is useful primarily for probe potentials close to space potential when  $r_p \gg \lambda_D$  and the magnetic field is large enough that  $\beta = r_p/\bar{a} \gg 1$  (See, however, the last paragraph of Section 4). For a probe at space potential,  $\psi_p = 0$ , the currents predicted by him (Fig. 10) are much lower than the collisionless currents given by Fig. 17 of Whipple (1965) for the case  $r_p \ll \lambda_D$ . At present, there is no theory available for probes in magnetoplasmas which includes effects of particle orbital motions together with collisional and space-charge effects, and we have seen (Section 2) that at larger probe potentials, orbital-motion effects become increasingly important.

#### 4. EFFECTS OF PLASMA TURBULENCE

A persistent and widespread suspicion has been that when probe potential is sufficiently positive, spontaneous fluctuations or "plasma turbulence", driven by the large electron-density gradients which then exist near the edges of the probe's magnetic shadow, will transport charged particles transversely to  $\mathbf{B}$  and produce probe currents much larger than those predicted by the steady-state theories described in Sections 2 and 3. The existence of probe-induced spontaneous fluctuations, for probes having a sufficiently large positive bias, is well-established by laboratory observations (Balmain, 1972; Urrutia and Stenzel, 1986; Stenzel, 1988). Spontaneous density fluctuations of up to a few percent amplitude have also been observed in the disturbed region around the Shuttle Orbiter (Murphy *et al.*, 1986). What is less clear is whether such fluctuations can increase substantially the time-averaged currents collected by probes.

For a long time, only one theoretical treatment, due to Linson (1969), has been available which includes predictions of plasma turbulence effects on current collection by a probe. An alternative formulation by P.J. Palmadesso appears later in these Proceedings.

Linson's (1969) treatment is semi-empirical because it depends on a parameter whose value is inferred from experimental data rather than predicted. Linson suggests that the unneutralized electron population in the sheath region around a probe having a large positive bias may be subject to a gyroresonant instability whose onset depends on a sufficiently large value of the parameter:

$$Q = \omega_e^2 / \omega_c^2 \quad (15)$$

where  $\omega_e = (n_e e^2 / m_e \epsilon_0)^{1/2}$  is the electron plasma frequency,  $\omega_c = eB/m_e$  is the electron gyrofrequency,  $m_e$  and  $n_e$  are electron mass and number density, and  $\epsilon_0$  is the permittivity of space. Linson cites evidence that the onset of this instability occurs when  $Q$  is close to or somewhat smaller than 1; ionospheric values of  $Q$  are generally greater than 1. Linson then assumes that the resulting turbulent diffusion produces a region of uniform electron density around the probe (Fig. 11), that this region is greatly extended in the  $z$  direction, and that electric fields parallel to  $z$  are small compared to those perpendicular to  $z$ . Assuming also that ions are completely excluded from this region then permits him to write a cylindrically-symmetric Poisson equation:

$$\frac{1}{r} \frac{d}{dr} \left( r \frac{d\phi}{dr} \right) = \frac{en_e}{\epsilon_0} \quad (16)$$

for potentials within it. He solves this equation subject to the boundary conditions:

$$\phi = \phi_p \text{ when } r = r_p \quad (17)$$

$$\phi = 0, \frac{d\phi}{dr} = 0 \text{ when } r = r_s \quad (18)$$

Equation (16) is of only second order, so with three boundary conditions given in Eqs. (17) and (18), this system of equations is overdetermined. Solving it therefore also provides a value for the sheath radius  $r_s$ . We obtain:

$$\phi_p = \frac{1}{2} Q \phi^* \left\{ \left( \frac{r_s}{r_p} \right)^2 \left[ \ln \left( \frac{r_s}{r_p} \right)^2 - 1 \right] + 1 \right\} \quad (19)$$

where  $\phi^* = \frac{1}{2} m_e \omega_c^2 r_p^2 / e$ . This result is Linson's Eq. (13). It provides an implicit relation for  $r_s$  as a function of the probe potential  $\phi_p$ . Linson then proposes, as an upper bound on probe current, the random current incident on both ends of a flux tube of radius  $r_s$ . In terms of the random current  $I_R$  defined just prior to Eq. (6), Linson's upper-bound current is now given by:

$$i = I/I_R = \frac{1}{2} \left( r_s / r_p \right)^2 \quad (20)$$

Figure 12, which is a reproduction of Linson's Figure 3, shows a comparison of the currents given by Linson's treatment for  $Q = \frac{1}{4}$  and 1 with those given by the result of Parker and Murphy (1967) [our Eq. (7)] and by the nonmagnetic, spherically-symmetric, space-charge-limited theory of Langmuir and Blodgett (1924). This Figure suggests that turbulent transport produces a major increase in the probe's electron collection, perhaps to values close to the nonmagnetic ones.

Experimental evidence for this contention has been ambiguous until recently. This is in spite of the launching, since 1969, of no fewer than 25 separate rocket and satellite experiments which included measurements of the potential acquired by surfaces of the vehicle when an electron beam was emitted from it. Reviews of these experiments have been given by Winckler (1980), Linson (1982), Szuszczewicz (1985), and Maehlum (1988). During the same period, space experiments have also been performed which involved either the emission of ion beams, with measurements of the resulting vehicle surface potentials, or the application of a differential bias which caused one part of the vehicle to acquire a large negative potential relative to space, with the resulting ion collection current measured. In such cases, magnetic-field effects on ion collection are relatively small because of the relatively large average gyroradii of ions. Of greater importance in these cases are effects of relative ion drift motion. Exact collisionless theory for ion collection in the presence of ion drift is relatively incomplete. A review of available approximate theories for this situation has been given by Godard and Laframboise (1983). Substantial disagreement exists between these theories and experimental results (Makita and Kuriki 1977, 1978) but the approximations in the theories are severe enough that this does not constitute evidence that the collisionless, steady-state model is invalid for ion collection. In contrast with this, the electron current-voltage observations generally imply currents exceeding the Parker and Murphy (1967) values. The amount of excess current appears to increase with ambient electron density. Popadopoulos and Szuszczewicz (1986) have proposed that a collective interaction between the beam and the ambient plasma may energize some of the ambient electrons, and these then provide a greatly increased return current to the vehicle because of their much larger velocities.

This hypothesis is supported by the results of the recent CHARGE-2 (Myers *et al*, 1989) and SPEAR I (Katz *et al*, 1989) rocket experiments. In the CHARGE-2 experiment, the payload was separated into two sections joined by an insulated conducting tether. One of the sections carried a 1 keV electron gun. The sections were separated by up to 426m across the geomagnetic field. Return current collection was observed for positive potentials up to 1 kV on both sections. In all measurements, return currents to the section carrying the gun exceeded Parker-Murphy (1967) values, while those to the other section agreed well with these values. In the SPEAR I experiment, no beam was emitted. SPEAR I carried two spherical electrostatic probes of radius 10cm, separated from each other by 1m and from the rocket body by 3m. Positive voltages up to 45.3kV were applied to one of the two spheres. In the results presented by Katz *et al* (1989), the other sphere was grounded to the rocket body. Also grounded to the rocket body was a stem which supported both probes and was separated from them by resistive bushings of length 1m. Katz *et al* (1989) calculated that when a 46kV bias was applied to one sphere, the rocket body and the other sphere floated at -8.3kV, and the biased sphere then floated at 37.7kV. The measured current-voltage curve gives a current of 52 mA at this voltage. This is about twice the Parker-Murphy (1967) value [Eq. (7)] for these conditions, but the calculations of Katz *et al* (1989) indicate that this discrepancy results from the breaking of canonical angular momentum conservation [Eq. (2)] by the strong asymmetry of the sheath around the probe; this asymmetry in turn is produced by the presence of the oppositely-biased large rocket body and other probe (I. Katz, private communication, 1989). The results of this experiment therefore can be interpreted as providing further support for the validity of the canonical upper bound on current collection [In these experiments, the correction term  $\frac{1}{2}/\sigma^2$  in Eq. (11) was negligible, so the canonical upper bound was essentially equal to the Parker and Murphy (1967) upper bound given by Eq. (7)]. This in turn indicates an absence of significant turbulent-transport effects on such currents in the absence of beam-induced disturbances, contrary to the hypothesis advanced at the beginning of this Section.

However, Palmadesso (paper appearing later in these Proceedings) has pointed out that one

expects turbulent-transport effects to become important only when the region of large electric fields near the probe extends radially beyond the region in which the probe is readily accessible to particles on the basis of steady-state fields only. For the radii of these two regions, he uses the nonmagnetic spherical sheath solution of Langmuir and Blodgett (1924) and the Parker-Murphy (1967) radius  $r_o$ , given by Eq. (6) with a positive sign, respectively. He points out that the Langmuir-Blodgett radius is initially smaller but grows more rapidly as probe potential increases, so one should expect significant turbulent transport effects only for large enough values of probe potential. This appears to indicate that turbulent transport may yet prove to be important at large enough positive voltages, so the indications to the contrary provided by the CHARGE-2 and SPEAR I experiments may not be conclusive.

This apparent absence of turbulent-transport effects in space situations runs counter to widespread expectations, as we noted at the beginning of this Section. An example of such expectations is a discussion by Stangeby (1989, Sec. IIIA) of particle transport across magnetic fields in magnetic-confinement fusion experiments. Stangeby summarizes the evidence for the well-known conclusion that such transport generally agrees with the empirically-obtained Bohm value (Bohm *et al*, 1949), and is much larger than the "classical" value which forms the basis of the Sanmartin (1970) theory discussed in Sec. 3. However, probe use in fusion plasmas generally involves very different conditions than in space (P.C. Stangeby, private communication, 1990). Because of interpretive difficulties, probes in fusion plasmas are generally operated at voltages below floating potential (Stangeby and McCracken, 1990, Figures 2.4 and 2.5). Ion and electron densities are then nearly equal to each other almost to the probe surface, whereas in the CHARGE-2 and SPEAR I situations, the probes were surrounded by large electron sheaths. This difference presumably affects the turbulent-transport mechanisms involved, but these are understood very poorly, so firm conclusions cannot be drawn.

## 5. PARTICLE TRAPPING AND THE "TOROIDAL GLOW" REGION

We have seen that imposition of a magnetic field changes fundamentally the characteristic motions of charged particles in the disturbed region around a probe (Sections 2 and 3). An important consequence of this is a qualitative increase in the possibilities for trapping of attracted particles in this region. This in turn creates the possibility of significant increases in probe current because of collisional or turbulent scattering into and out of this region, or collisional ionization of neutrals in it. We examine each of these aspects of this situation separately.

We illustrate in Fig. 13 the region of space in which particle trapping occurs in the presence of a magnetic field. For the attracted-particle species [ $q\phi_p < 0$ ], this Figure shows the general appearance of "open" magnetic bottles which extend to  $z = \pm\infty$  and correspond to  $E > 0$ , and "closed" ones which correspond to  $E < 0$ , all drawn for a particular value of  $J$  which is chosen such that the bottle for  $E = 0$  marginally fails to intersect the probe. Since  $\phi = 0$  at infinity,  $E > 0$  for all particles coming from the ambient plasma. Therefore, in the absence of collisions, the "trapped-orbit" ( $E < 0$ ) region of one-particle phase space, corresponding to closed magnetic bottles such as those shown in Fig. 13, must remain unpopulated. However, if a particle is scattered into this region, by either a collision or (possibly) a turbulent scattering event, it will remain there until another such event scatters it out again. If the collision frequency is very small, such a particle is likely to remain there for a very long time. Therefore, even in the limit of small collision frequency, a steady-state particle population will build up in the trapped-orbit region. This population will not be larger than the equilibrium value given by the usual Boltzmann factor, but this bound permits very large attracted-species populations if potentials near the probe are very large. This population will always remain less than the equilibrium value, because particles can also be scattered out of

it into "collection" orbits which intersect the probe. Assuming that the probe is nonemissive, this sets up a net unbalanced flux of particles into it, using the trapped orbits as an intermediary stage (Fig. 14), and therefore detailed balancing cannot occur, and an equilibrium population of these orbits cannot be attained. This unbalanced flux also constitutes an additional current to the probe. So far, the problem of calculating this current is completely unsolved.

In the absence of a magnetic field, approaches to this problem have been made by Wasserstrom *et al* (1965), Chou *et al* (1966), Bienkowski and Chang (1968), Self and Shih (1968), Talbot and Chou (1969), Thornton (1971), Shih and Levi (1971), Parker (1973), Friedland and Kagan (1979), and others, using various approximations. A review of most of this work has been given by Chung *et al* (1975, Section 2.5).

Our depiction in Fig. 14 of the intermediary role of trapped orbits is schematic, and applies whether or not a magnetic field is present, even though the orbits when  $\mathbf{B} \neq \mathbf{0}$  will generally be more complicated than those shown. However, one feature of the trapping phenomenon is fundamentally different when  $\mathbf{B} \neq \mathbf{0}$ . In either the nonmagnetic or magnetic case, the term  $q\phi(r, z)$  in Eq. (4) will have a local minimum as a function of  $z$  at  $z = 0$  for each  $r$ , so trapping will occur, *i.e.* the effective potential  $U(r, z)$  in Eq. (4) will have a local minimum, if the last term in Eq. (4) has a minimum outside the probe as a function of  $r$  for at least some values of  $J$ . Inspection of this term shows that in the nonmagnetic case ( $\omega = 0$ ), this term has minima only if  $|q\phi(r, z)|$  decreases more slowly as a function of  $r$  than an inverse-square potential  $\phi = \text{const. } r^{-2}$  over at least some range of  $r$  values (Mott-Smith and Langmuir, 1926; Bernstein and Rabinowitz, 1959; Laframboise, 1966; Laframboise and Parker, 1973). Accumulation of a trapped-particle population adds space charge of a sign opposite to that on the probe surface, and this causes the sheath potential to steepen, tending to destroy the conditions necessary for trapped orbits to exist, and thereby limiting their population (Laframboise, 1966, Section VIII). However, in the magnetic case, the last term in Eq. (4) always has minima as a function of  $r$ . A steepening of the potential therefore can modify the resulting minima of the effective potential  $U(r, z)$ , but cannot destroy them. We therefore expect trapped-orbit effects to be much more important when significant magnetic fields are present.

We have so far not mentioned what may be the most important consequence of trapped-orbit population. Particles scattered into the trapped-orbit region will be accelerated by large electric fields in this region if the probe potential is large. In the more central regions of the closed magnetic bottle accessible to each particle, it will then have enough kinetic energy to cause collisional ionization of neutrals. If the attracted particles are electrons, this will occur for probe potentials above a few hundred volts. Some of the new charged particles thus produced will be on collection orbits (Fig. 14), and this can produce a substantial increase in probe current. Another consequence of energetic collisions in the trapped-orbit region is light emission. Such emission was first observed as a "toroidal glow" region, in a laboratory experiment by W.J. Raitt and A. Konradi (private communication, 1987). The toroidal-glow phenomenon has since been studied in detail by Antoniades and Greaves (paper appearing later in these Proceedings), who have also observed the above-mentioned increase in probe current. They have observed these phenomena in a test chamber which was large enough to permit a well-developed trapped-orbit region to exist around the probe, but they did not see them in tests done in a smaller chamber. So far, these phenomena have not been observed in space. Antoniades and Greaves discuss in detail the conditions under which one can expect them to occur. One feature of the toroidal-glow region, which may be expected on the basis of Fig. 13, is that it should have "pointed ends" in the  $\pm z$  directions, and this feature is evident in photographs of it presented in their paper.

When the magnetic field is sufficiently weak, their results show that the toroidal-glow region disappears and either no discharge or a spherically-symmetric discharge occurs. If the ambient

neutral density is large enough, the establishment of a spherically-symmetric discharge, around a probe at a large positive voltage, involves a process of "explosive sheath ionization", which has been studied by Lai *et al* (1985) and Cooke and Katz (1988). In this process, electrons created by ionization of neutrals in the sheath migrate quickly to the probe, while similarly-created ions accelerate slowly away from it. This results in a net positive contribution to the space charge in the probe sheath. This contribution enlarges the sheath and thereby enlarges the region in which the electrons have been accelerated through a sufficient change of potential to ionize neutrals. This results in more net positive space charge and a consequent runaway sheath expansion.

Magnetic-bottle shapes similar to those shown in Figs. 1, 4, and 13 do not exhaust all possibilities. The dependence of  $|\phi(r, z)|$  on  $r$  for  $z \approx 0$  in a steady-state situation invariably involves a steep decrease toward space potential in the sheath region, followed by a much less rapid decrease in the presheath region beyond the sheath edge. For some values of  $J$ , the effective potential  $U(r, z)$  for the attracted particle species in Eq. 4 may then have, instead of a single minimum as a function of  $r$  for  $z = 0$ , two minima separated by a maximum. Depending on the value of  $E$ , this can cause the corresponding magnetic bottles to have "bulges" or even disjoint "bubble" regions (Fig. 15). In the latter case, particles travelling along collisionless orbits from infinity will be unable to enter these "bubble" regions even though permitted by their values of  $E$  and  $J$  to exist there. In the case of "bulges", such particles are likely to be partly prevented from entering the bottle regions closest to the probe; a similar effect was discussed in connection with bottle "widening" at the end of Section 2. To some extent, all of these effects will limit access to the probe of attracted-species particles which initially (*i.e.* far from the probe) move along orbits located outside the probe's magnetic shadow. This may possibly invalidate the conjecture, mentioned at the end of Section 2, that space-charge effects on the potential  $\phi(r, z)$  may cause the current collection to increase above the Laplace-limit values calculated by Sonmor (see Section 2), toward the canonical-upper-bound values. However, the SPEAR I and CHARGE-2 current-collection values discussed in Sections 3 and 4 appear to show good agreement with the canonical-upper-bound values, so at present there is no clear experimental evidence for a collected-current decrease caused by the formation of "bulges" and the breakup of magnetic bottles into disjoint "bubble" regions. As noted in Section 2, the numerical results of Sonmor support the idea that this may occur. However, a definitive answer to this question will require a more specific investigation of it than any done so far.

## 6. BREAKDOWN OF MAGNETIC INSULATION

"Magnetic insulation" is the tendency of a magnetic field to inhibit the transport of charged particles across magnetic flux surfaces. In Sections 2-5, we have considered various ways in which magnetic insulation can break down and current collection by a probe can increase as probe voltage becomes more attractive for the particle species considered (most specifically, the electrons). We have examined effects of violation of adiabatic invariance (Section 2), collisions (Sections 3 and 5), self-excited fluctuations (Sections 4 and 5) and particle trapping combined with collisions, fluctuations, or collisional ionization (Section 5). Here we take a different view of the collisionless particle motions treated in Section 2 (discussions with D.L. Cooke, unpublished). We consider specifically the motions of particles in the trapped-orbit or "toroidal glow" region discussed in Section 5. For particles which have a small enough  $z$ -component of velocity, one may expect these motions to be well-approximated by a circumferential  $\mathbf{E} \times \mathbf{B}$  drift with superposed gyromotion in the plane  $z = 0$ , together with small oscillations about this plane. However, we now show that this is not necessarily the case.

To show this, we note that the usual analysis for particle motion in uniform crossed  $\mathbf{E}$  and  $\mathbf{B}$  fields (see, for instance, Tanenbaum, 1967, Section 1.4) yields an  $\mathbf{E} \times \mathbf{B}$  drift velocity

$\mathbf{v}_d = (\mathbf{E} \times \mathbf{B})/B^2$ . The magnitude of  $\mathbf{v}_d$  is  $E/B$ . This can easily exceed the speed of light. This happens when  $E > Bc$ . For  $B = 0.3$  Gauss =  $3 \times 10^{-5} T$ , corresponding to the low-latitude ionosphere, and  $c = 3 \times 10^8 m/sec$ , this inequality becomes  $E > 9000V/m$ . The SPEAR I probes had radius  $r_p = 10cm$ . Ignoring space-charge effects gives a surface electric field  $E_r$  on these probes given by  $E_r = -(d\phi/dr)_p = \phi_p/r_p$ . The above-mentioned inequality is then fulfilled when the probe potential  $\phi_p > 900V$ . Since space-charge effects can be expected to increase electric fields near a probe, this inequality would have been fulfilled at even lower probe voltages in the SPEAR I experiment. Since drift velocities greater than the speed of light are impossible, something is clearly wrong with this analysis.

What is wrong is that the usual derivation of  $\mathbf{v}_d$  is non-relativistic. For planar geometry, the correct approach to the derivation of  $\mathbf{v}_d$  involves use of a Lorentz transformation (Longmire, 1963, p. 30; Jackson, 1975, pp. 582-584), which can eliminate the component of  $\mathbf{E}$  perpendicular to  $\mathbf{B}$ , yielding the usual  $\mathbf{E} \times \mathbf{B}$  drift result, only if  $E < Bc$ . If  $E > Bc$ , a Lorentz transformation to a frame moving at velocity  $\mathbf{E} \times \mathbf{B}/E^2$  (rather than  $\mathbf{E} \times \mathbf{B}/B^2$ ) now eliminates the component of  $\mathbf{B}$  perpendicular to  $\mathbf{E}$ . In this frame, particles now accelerate indefinitely parallel to  $\mathbf{E}$ , so no magnetic-insulation effect is predicted. The situations treated here do not involve probe potentials large enough to produce strong relativistic effects, but what is instead implied is that orbit curvatures due to the magnetic field become so slight that electron motions become dominated by electric-field inhomogeneities associated with the rotational symmetry of the probe's potential distribution. Therefore, the non-relativistic magnetic-bottle analysis of Section 2 still applies, and still predicts that radially-inward motion toward a probe will eventually be limited, except for particles having a zero value of the canonical angular momentum component  $J$  defined in Eq. (2). Palmadesso (paper appearing later in these Proceedings) has numerically calculated particle orbits in model spherical-probe sheath potentials in magnetic fields, and these orbits display both of the phenomena just described, namely the breakdown of  $\mathbf{E} \times \mathbf{B}$  drift in strong electric fields, and the limitation of the resulting radially-inward motion because of conservation of  $J$ . The same phenomena are visible also in results from the NASCAP/LEO simulation of SPEAR I flight conditions, presented by Katz *et al* (1989). We have reproduced their Figures 8(a) and (b) herein as Figures 16(a) and (b). Figure 16(a) shows their calculated bipolar-sheath potential contours for a 46kV bias on one spherical probe and a -6kV assumed floating potential for the SPEAR I rocket body. Figure 16(b) shows the trajectory of an electron in the potential of Figure 16(a). A sudden transition from  $\mathbf{E} \times \mathbf{B}$  drift motion to accelerated motion is clearly visible, as also is orbital motion caused by nonzero angular momentum, closer to the probe.

## 7. PHENOMENA AROUND LARGE ORBITING OBJECTS AT HIGH VOLTAGES

Our discussion so far has been directed primarily toward rocket experiments involving large positive electrode voltages. In such experiments, effects of spacecraft motion (relative plasma drift) on sheath structure and current collection are generally thought to be unimportant. A very different situation arises in the planned Electrodynamic Tether experiment, which is part of the Shuttle-borne Tethered Satellite System (T.S.S.). In this experiment, it is planned to deploy an insulated conductive tether of up to 20km length, extended vertically upward from the Orbiter's cargo bay. At the end of the tether is to be located a conductive spherical subsatellite. One expected consequence of this arrangement is the generation of large-scale systems of low-frequency plasma waves in the ionosphere (Banks *et al*, 1981; Raitt *et al*, 1983; Grossi, 1984; Rasmussen *et al*, 1985; Urrutia and Stenzel, 1989; Stenzel and Urrutia, 1989). Another experimental objective, more closely related to our present discussion, is to investigate whether induced currents in the tether due to its motion across the geomagnetic field can provide a useful source of electric power in space.

This depends on achieving as large as possible an electron current collection by the subsatellite, either passively or with the aid of a low-energy plasma source known as a "plasma contactor". Here we consider only passive current collection; the performance of plasma contactors is analysed in four papers, by Hastings, Wilbur and Williams, Katz and Davis, and Cooke, respectively, which appear later in these Proceedings. In the Orbiter's reference frame, the ambient plasma contains an upwardly-directed  $\mathbf{v} \times \mathbf{B}$  electric field of about  $0.24V/m$ , where  $\mathbf{v}$  is the Orbiter's orbital velocity. The Orbiter is to carry an electron emitter (Banks *et al.*, 1981; Raitt *et al.*, 1983) which is intended to keep its potential close to that of its surroundings. The subsatellite will then acquire a potential up to about  $5kV$  positive with respect to its surroundings.

The planned diameter of the subsatellite is  $1.4m$  (Raitt *et al.*, 1983). Much larger subsatellites (conductive balloons) have also been considered (Williamson and Banks, 1976; Banks *et al.*, 1981). In either event, the subsatellite's radius will be large compared with both the average gyroradius and the Debye length of ambient electrons. The situation around the subsatellite therefore appears likely to be similar to that analyzed by Sanmartin (1970; our Section 3), except that the ions and electrons will now have a drift speed  $U = 8km/sec$  relative to the subsatellite. Since the mean thermal speeds  $\bar{v}_i$  and  $\bar{v}_e$  of ambient ions and electrons are roughly  $1km/sec$  and  $300km/sec$ , respectively, drift effects would appear likely to be important for ions but negligible for electrons. However, in the case of electrons, this conclusion turns out to be untrue. The following discussion is based in large part on a treatment by Thompson (1985), and also on unpublished work by W.B. Thompson.

In the nondrifting situation analyzed by Sanmartin (1970; our Section 3), electron depletion by the probe created a positive potential disturbance which extended in both directions along the probe's magnetic shadow without attenuation until distances of the order of an electron mean free path were reached. However, in low-Earth-orbit conditions, electrons drift at speed  $U$  toward the upstream surface of this positive-potential region. They then enter this region, migrate along it to the subsatellite, and are collected. The flux associated with this drift, integrated over this surface out to a distance of order  $L = D\bar{v}_e/U$  in both directions from the subsatellite, where  $D = 2r_p$  is the subsatellite's diameter, then supplies the subsatellite's electron collection current. The speed and direction of this drift will be modified near this surface by electric fields associated with the potential change across it. The upstream surface of the positive-potential region (on each side of the subsatellite) now is no longer parallel to  $\mathbf{B}$  but is "swept back" relative to  $\mathbf{B}$  by a small angle  $\theta \approx \tan^{-1}(U/\bar{v}_e)$  (Fig. 17). This implies that the region of positive potentials now tapers to zero width in a distance of order  $L$  along each of the directions parallel and antiparallel to  $\mathbf{B}$ . This distance will be large compared to  $D$ , but generally much smaller than the electron mean-free-path, so in this situation, a self-consistent collisionless treatment can be formulated. Positive ions striking the upstream side of this region reflect forward from it (Fig. 17), creating conditions conducive to two-stream instability just forward of it. Whether such instability has any substantial effect on electron collection has not been determined. The same repulsion of ions from the positive-potential region also creates an extensive ion-depleted wake region on its downstream side, and this wake region can be expected to contain negative potentials (Fig. 17). In Thompson's description, the total length of this wake region parallel to  $\mathbf{B}$ , i.e. transverse to the relative plasma drift, will be of order  $2L$ .

From our viewpoint, the most important question regarding the treatments of Sanmartin (1970) and Thompson (1985) is whether they lead to different predictions for electron collection by the subsatellite. Sanmartin's theory includes collisions, and therefore leads to the populating of orbits which have negative total energies with respect to space potential and therefore cannot be populated by particles moving collisionlessly from infinity. In fact, the electron population reaching the probe in Sanmartin's treatment is a Maxwellian, with a reduced density factor [his Eq. (65)]

which at the probe depends on position perpendicular to  $\mathbf{B}$  (our  $r$  coordinate in Section 2 and elsewhere). Therefore, in Sanmartin's description, most of the electron current reaching the probe is carried by negative-total-energy electrons.

The collisionless description given by Thompson (1985), and summarized above, is very different. In this description, the definition of space potential is more complicated because in a reference frame fixed on the subsatellite, there exists an ambient  $\mathbf{v} \times \mathbf{B}$  electric field of about  $0.24V/m$ . However, this does not substantially affect what we can conclude about the velocity distribution of electrons reaching the subsatellite. This remains as follows: all electron orbits not connecting back to infinity are unpopulated. This includes all negative-total-energy orbits, and also those positive-total-energy orbits which are caused to return to the subsatellite by electric or magnetic fields. The positive-total-energy orbits which connect back to infinity have populations which are a function of their ambient velocities. This function is just the drifting Maxwellian velocity distribution of the ambient plasma. However, the drift velocity of these electrons is, as we have seen, very small compared to their mean thermal velocity, and even though this "small" amount of drift is crucial to the construction of a self-consistent collisionless treatment, it nonetheless has a negligible effect on the population of those orbits which connect back to infinity. This population can therefore be regarded as isotropic, *i.e.* dependent only on the total energy of each electron impacting the subsatellite, and this energy is conserved along the electron's orbit, again assuming that the electron has not passed through a region of significant time-dependent fluctuations (Section 4). If this is the case, we then have complete knowledge of the velocity distribution of impacting electrons if we know the "cutoff boundaries" in velocity space which separate the orbits which connect back to the ambient plasma from those which do not (Laframboise and Parker, 1973). This last question in turn is easy to resolve if electron acceleration into the positive-potential region is adiabatic (gyroradius  $\ll$  scale of changes in the electric field  $\mathbf{E}$ ), because the cutoff boundary is then "one-dimensional", *i.e.*, if the  $z$  direction is again parallel to  $\mathbf{B}$ , electron orbits arriving at the subsatellite surface are populated only for  $v_z$  values such that  $\frac{1}{2}m_e v_z^2 - e\phi_p > 0$ , where  $\phi_p$  is the subsatellite's potential relative to space (Laframboise and Parker, 1973; Laframboise and Rubinstein, 1976; Rubinstein and Laframboise, 1982; see also Section 2). All of this now implies that with these approximations, the velocity distribution of impacting electrons is just an "accelerated half-Maxwellian", and the electron current collected by the subsatellite is just the random current collected by the projection of its area onto a plane perpendicular to  $\mathbf{B}$ . The dimensionless current  $i$  defined in Eq. (7) is then just equal to  $\frac{1}{2}$ .

However, this estimate may be much too small, because it excludes any correction for nonadiabatic effects on electron motions near the subsatellite; these were discussed in Section 2. It may seem surprising that such effects should be significant, because the average ambient-electron gyroradius  $\bar{a}$  is much smaller than the subsatellite radius  $r_p$ . For  $r_p = 0.7m$ ,  $B = 0.3G = 3 \times 10^{-4}T$ , and  $kT_e = 0.1eV$ , the ratio  $\beta = r_p/\bar{a}$  defined following Eq. (10) is equal to 22.2. In spite of this, for a subsatellite potential  $\phi_p = 5keV$ , The Parker-Murphy (1967) upper-bound value for  $i$ , given by either Eq. (7) or the first two terms of Eq. (11), is 11.86; the correction given by the third term of Eq. (11) is insignificant. For this value of  $\beta$  and for the value  $\psi_p = 5 \times 10^4$  implied by the parameter values just given, the numerical results of Sonmor given in Fig. 7 appear to indicate that the actual current will be very close to this upper-bound value. One cannot infer a firm conclusion on this point because the Sonmor results are for a Laplace potential distribution (infinite Debye length), rather than for the actual sheath potential distribution around the subsatellite, and no clear information exists on whether actual currents will be larger or smaller than the corresponding Laplace-limit currents (Sections 2 and 5). Nonetheless, the wide disparity between the values of  $\frac{1}{2}$  and 11.86, given just above for  $i$ , suggests that nonadiabatic effects on electron motions near the subsatellite are very strong, and therefore the actual velocity-space cutoff boundary for electrons ar-

riving at the subsatellite is very different from that given by the "one-dimensional" cutoff-boundary relation noted above. However, this conclusion in turn could be affected strongly by the breakup of magnetic bottles into disjoint regions, which we noted in Section 5 and in Fig. 15, so it still requires detailed numerical verification.

For increasingly large subsatellite diameters  $D$ , the half-length  $L$  of the positive-potential region increases in proportion. It is instructive to ask at what value of  $D$  does  $L$  become large enough that a transition will occur from the collisionless description of Thompson (1985) to the collisional one of Sanmartin (1970). To calculate the electron mean-free-path, we use the classical Spitzer (1962, Chapter 5) results for the electron collision frequency in a fully-ionized gas. To use these results, we consider an electron "test particle" whose velocity  $v_e$  is given by  $mv_e^2 = 3kT_e$ , i.e. which has kinetic energy equal to the average value for electrons at temperature  $T_e$ .

We include contributions to its cumulative angular scattering from both ambient electrons and ambient ions. For ambient-electron density  $n_e = 10^5/cm^3$  and temperature  $T_e = 0.1eV$ , Eq. (5.22) of Spitzer (1956) gives an electron mean-free-path  $\lambda_e = 725m$  for cumulative angular scattering. We have just seen that the most important distinction between the collisionless and collisional descriptions is likely to be the energy distribution of electrons in the positive-potential regions. Another important mean-free-path therefore is that for energy exchange among electrons, also defined by Spitzer (1956, Eq. 5.25). Bearing in mind that electron-electron encounters change the electron energy distribution much more rapidly than do electron-ion encounters, a recalculation of Table 5.3 of Spitzer (1956) to include ion effects indicates that the energy-exchange mean-free-path is only moderately larger than  $\lambda_e$  for most electrons.

A good approximate criterion for collisionless current collection by the subsatellite therefore is that  $L \ll \lambda_e$ . With the above-mentioned relation  $L = D\bar{v}_e/U$  and the values  $U = 8km/sec$  and  $\bar{v}_e = 300km/sec$ , this criterion reduces to  $D \ll 19m$ . This result implies that collisional effects can become significant for balloon subsatellite diameters which are within the realm of possibility.

In rocket experiments,  $U$  is generally much smaller, and this criterion then becomes much more severe. For  $U = 1km/sec$ , we obtain  $D \ll 2.4m$ . The SPEAR I probes (Sections 3, 4, and 6), whose diameters were 20cm, are comfortably within this limit, so we infer that even the relatively small amount of spacecraft motion present in the SPEAR I experiment was enough to ensure that current collection by these probes was essentially a collisionless process. The collecting portion of the CHARGE-2 daughter payload (Myers *et al*, 1989) was somewhat larger, with a largest dimension of 82 cm, but was still within the above-mentioned approximate limit. As mentioned in Sections 3 and 4, current collection in both experiments appeared to be described well by collisionless, steady-state theory. A surprising prediction of the discussion in this Section is the extreme sensitivity of this conclusion to very small values of ambient-electron drift motion. The effects of this drift motion appear to remove the apparent contradiction between the conclusion of most of our discussion in Section 3 (which applied in the strict absence of drift) and the apparent success of collisionless, steady-state theory in both of these experiments. To put this interpretation on a firmer basis will require the development of a theory which is capable of making quantitative predictions of collected current in the transitional regime between the collisionless situation described by Thompson (1985) and the collisionally-influenced one of Sanmartin (1970).

## 8. CONCLUSIONS

Our discussion in Sections 2-7 has revealed subtle and surprising aspects of the problem of predicting current collection by probes in the space magnetoplasma. Many of these aspects involve unresolved issues. They include the following:

- (1) The attraction-region current-voltage characteristic of a probe in a magnetoplasma can contain a "negative-resistance region" near space potential (Section 2).
- (2) Numerical calculations of collisionless, steady-state, Laplace-limit currents indicate that these remain substantially below the canonical-upper-bound current values even at large attractive potentials. Implications for current collection in more realistic potentials are not clear (Sections 2 and 5).
- (3) In a nondrifting plasma, no current-collection theory is possible which includes space-charge effects but not interparticle collisions, no matter how large the ambient charged-particle mean-free-paths are (Section 3). However, even a very small amount of relative plasma drift, such as that involved in a typical rocket experiment, can change this conclusion fundamentally (Section 7).
- (4) Plasma turbulence appears to have an important influence on current collection by probes in fusion plasmas but not in space plasmas. Such turbulence is not understood well enough to explain why (Section 4).
- (5) Space-charge effects, which tend to steepen the sheath potential profile near a probe, decrease attracted-particle collection in nonmagnetic situations, but may possibly increase it in magnetic ones (Section 2). However, formation of "bulges" and breakup of magnetic bottles into disjoint "bubble" regions by such space-charge effects may reverse this effect. Presently available experimental results and theory do not provide sufficient evidence to indicate whether an increase or a decrease actually occurs (Section 5).
- (6) The existence of trapped-orbit regions around a probe provides pathways for additional current collection due to collisional ionization, collisional scattering, and possibly turbulent scattering. The first of these is undoubtedly important; no predictions are available for the other two (Section 5).
- (7) Circumferential " $\mathbf{E} \times \mathbf{B}$  drifting" motion can break down in the strong electric fields that exist near a probe, and be replaced by radially-accelerated motion. This motion in turn can be limited by angular-momentum effects closer to the probe (Section 6).

## ACKNOWLEDGMENTS

We are grateful to many people, including J. Antoniades, H.A. Cohen, D.L. Cooke, I. Katz, M.J. Mandell, G.B. Murphy, L.W. Parker, W.J. Raitt, P.C. Stangeby, W.B. Thompson, and E.C. Whipple, for valuable discussions and comments. Various aspects of this work were supported by the U.S. Air Force Geophysics Laboratory under Contract No. F19628-85-K-0043, the U.S. Naval Surface Weapons Center under Contract No. N60921-86-C-A226 (Auburn University Space Power Institute Subcontract No. 86-209), the Institute for Space and Terrestrial Science of Ontario under Project Number 182-10, and the Natural Sciences and Engineering Research Council of Canada under Operating Grant A-4638 and Supercomputers Access Grant 120. We wish to thank the Ontario Centre for Large-Scale Computation for the use of their facilities and for valuable technical assistance.

## REFERENCES

- Balmain, K.G., Probe-Triggered Audiofrequency Plasma Oscillations, IEEE Transactions on Antennas and Propagation AP-20, 400, 1972.
- Banks, P.M., P.R. Williamson, and K.-I. Oyama, Electrical behavior of a Shuttle Electrodynamic Tether System (SETS), Planet. Space Sci. 29, 139, 1981.
- Bernstein, I.B., and I.N. Rabinowitz, Theory of electrostatic probes in a low-density plasma, Phys. Fluids 2, 112, 1959.
- Bienkowski, G.K., and K.-W. Chang, Asymptotic theory of a spherical electrostatic probe in a stationary weakly ionized plasma, Phys. Fluids 11, 784, 1968.
- Bohm, D., E.H.S. Burhop, and H.S.W. Massey, The use of probes for plasma exploration in strong magnetic fields. In: The Characteristics of Electrical Discharges in Magnetic Fields, edited by A. Guthrie and R.K. Wakerling, pp. 13-76, McGraw-Hill, New York, 1949.
- Chou, Y.S., L. Talbot, and D.R. Willis, Kinetic theory of a spherical electrostatic probe in a stationary plasma, Phys. Fluids 9, 2150, 1966.
- Chung, P.M., L. Talbot, and K.J. Tournay, Electric Probes in Stationary and Flowing Plasmas: Theory and Application. Springer-Verlag, New York, 1975.
- Cooke, D.L., and I. Katz, Ionization-induced instability in an electron-collecting sheath, J. Spacecraft and Rockets 25, 132, 1988.
- Friedland, L., and Yu. M. Kagan, The theory of electron current to a spherical probe at intermediate pressures, J. Phys. D: Appl. Phys. 12, 739, 1979.
- Godard, R., and J.G. Laframboise, Total current to cylindrical collectors in collisionless plasma flow, Planet. Space Sci. 31, 275, 1983.
- Grossi, M.D., Spaceborne long vertical wire as a self-powered ULF/ELF radiator, IEEE Journal of Oceanic Engineering OE-9, 211, 1984.
- Jackson, J.D., Classical Electrodynamics, 2nd Ed., Wiley, New York, 1975.
- Katz, I., G.A. Jongeward, V.A. Davis, M.J. Mandell, R.A. Kuharski, J.R. Lilley, Jr., W.J. Raitt, D.L. Cooke, R.B. Torbert, G. Larson, and D. Rau, Structure of the bipolar plasma sheath generated by SPEAR I, J. Geophys. Res. 94, 1450, 1989.

- Laframboise, J.G., Theory of spherical and cylindrical Langmuir probes in a collisionless, Maxwellian plasma at rest. Institute for Aerospace Studies, University of Toronto, Report No. 100, 1966.
- Laframboise, J.G., and L.W. Parker, Probe design for orbit-limited current collection, *Phys. Fluids* 16, 629, 1973.
- Laframboise, J.G., and Rubinstein, J., Theory of a cylindrical probe in a collisionless magneto-plasma, *Phys. Fluids* 19, 1900, 1976.
- Lai, S.T., H.A. Cohen, K.H. Bhavnani, and M. Tautz, Sheath ionization model of beam emissions from large spacecraft. In: *Spacecraft Environmental Interactions Technology 1983*, edited by C.K. Purvis and C.P. Pike, NASA Conf. Publ. 2359/Rep. AFGL-TR-85-0018, pp. 253-262, Air Force Geophys. Lab., Hanscom Air Force Base, Mass., 1985.
- Langmuir, I., and K.B. Blodgett, Currents limited by space charge between concentric spheres, *Phys. Rev.* 23, 49, 1924.
- Linson, L.M., Current-voltage characteristics of an electron-emitting satellite in the ionosphere, *J. Geophys. Res.* 74, 2368, 1969.
- Linson, L.M., Charge neutralization as studied experimentally and theoretically. In: *Artificial particle beams in space plasma studies*, edited by B. Grandal, pp. 573-595, NATO Advanced Study Institutes Series B: Physics, Volume 79, Plenum, New York, 1982.
- Longmire, C.L., *Elementary Plasma Physics*, Wiley/Interscience, New York, 1963.
- Maehlum, B.N., Beam-Plasma Experiments, *Computer Physics Communications* 49, 119, 1988.
- Makita, H., and K. Kuriki, Comparative study of spherical and cylindrical drift probes. In: *Proc. 10th International Symposium on Rarefied Gas Dynamics*, edited by J. Leith Potter, pp. 1007-1014, *Progress in Astronautics and Aeronautics*, Vol. 51, Amer. Inst. of Astronautics and Aeronautics, New York, 1977.
- Makita, H., and K. Kuriki, Current collection by spherical Langmuir probes drifting in a collisionless plasma, *Phys. Fluids* 21, 1279, 1978.
- Mott-Smith, H.M., and I. Langmuir, The theory of collectors in gaseous discharges. *Phys. Rev.* 28, 727, 1926.
- Murphy, G.B., J. Pickett, N. D'Angelo, and W.S. Kurth, Measurements of plasma parameters in the vicinity of the space shuttle, *Planet. Space Sci.* 34, 993, 1986.
- Myers, N.B., W.J. Raitt, B.E. Gilchrist, P.M. Banks, T. Neubert, P.R. Williamson, and S. Sasaki, A comparison of current-voltage relationships of collectors in the Earth's ionosphere with and without electron beam emission, *Geophys. Res. Lett.* 16, 365, 1989.
- Papadopoulos, K., and E.P. Szuszczewicz, Current understanding and issues on electron beam injection in space, COSPAR General Assembly 1986.
- Parker, L.W., and B.L. Murphy, Potential buildup on an electron-emitting ionospheric satellite, *J. Geophys. Res.* 72, 1631, 1967.
- Parker, L.W., Computer Solutions in Electrostatic Probe Theory. I. Spherical Symmetry with Collisions. Air Force Avionics Laboratory, Wright-Patterson Air Force Base, Ohio, Report No. AFAL-TR-72- 222, Part 1, 1973.

- Parker, L.W., Computer Method for Satellite Plasma Sheath in Steady-State Spherical Symmetry, Air Force Geophysics Laboratory, Hanscom Air Force Base, Mass., Report No. AFCRL-TR-75-0410, 1975.
- Raitt, W.J., P.M. Banks, and P.R. Williamson, Electrodynamic tether experiments in the ionosphere. In: Active Experiments in space, edited by W.R. Burke, European Space Agency Publ. ESA SP-195, pp. 361-367, 1983.
- Rasmussen, C.E., P.M. Banks, and K.J. Harker, The excitation of plasma waves by a current source moving in a magnetized plasma: the MHD approximation, *J. Geophys. Res.* 90, 505, 1985.
- Rubinstein, J., and J.G. Laframboise, Upper-bound current to a cylindrical probe in a collisionless magnetoplasma, *Phys. Fluids* 21, 1655, 1978.
- Rubinstein, J., and J.G. Laframboise, Theory of a spherical probe in a collisionless magnetoplasma, *Phys. Fluids* 25, 1174, 1982.
- Rubinstein, J., and J.G. Laframboise, Theory of axially symmetric probes in a collisionless magnetoplasma: aligned spheroids, finite cylinders, and disks, *Phys. Fluids* 26, 3624, 1983.
- Sanmartin, J.R., Theory of a probe in a strong magnetic field, *Phys. Fluids* 13, 103, 1970.
- Self, S.A., and C.H. Shih, Theory and measurements for ion collection by a spherical probe in a collisional plasma, *Phys. Fluids* 11, 1532, 1968.
- Shih, C.H., and E. Levi, Determination of the collision parameters by means of Langmuir probes, *AIAA J.* 9, 2417, 1971.
- Spitzer, L., Jr., Physics of Fully Ionized Gases, Interscience, New York, 1956.
- Strangeby, P.C., The interpretation of plasma probes for fusion experiments. In: Plasma Diagnostics, Vol. 2: Surface Analysis and Interactions, edited by O. Auciello and D.L. Flamm, pp. 157-209, Academic Press, San Diego, 1989.
- Strangeby, P.C., and G.M. McCracken, Plasma boundary phenomena in tokamaks, 1990 (submitted to Nucl. Fusion).
- Stenzel, R.L., Instability of the sheath-plasma resonance, *Phys. Rev. Lett.* 60, 704, 1988.
- Stenzel, R.L., and J.M. Urrutia, Whistler wings from moving electrodes in a magnetized laboratory plasma, *Geophys. Res. Lett.* 16, 361, 1989.
- Szuszczewicz, E.P., and P.Z. Takacs, Magnetosheath effects on cylindrical Langmuir probes, *Phys. Fluids* 22, 2424, 1979.
- Szuszczewicz, E.P., Controlled electron beam experiments in space and supporting laboratory experiments: a review, *J. Atmos. Terrestrial Phys.* 47, 1189, 1985.
- Talbot, L., and Y.S. Chou, Langmuir probe response in the transition regime. In: Proc. 6th Internat. Symposium on Rarefied Gas Dynamics, edited by L. Trilling and H.Y. Wachman, pp. 1723-1737, Academic Press, New York, 1969.
- Tanenbaum, B.S., Plasma Physics, McGraw-Hill, New York, 1967.
- Thompson, W.B., Preliminary investigation of the electrodynamics of a conducting tether. In: Spacecraft Environmental Interactions Technology 1983, edited by C.K. Purvis and C.P. Pike, NASA Conf. Publ. 2359/Rep. AFGL-TR-85-0018, pp. 649-662, Air Force Geophys. Lab., Hanscom Air Force Base, Mass., 1985.

- Thornton, J.A., Comparison of theory and experiment for ion collection by spherical and cylindrical probes in a collisional plasma, AIAA J. 9, 342, 1971.
- Urrutia, J.M., and R.L. Stenzel, Anomalous currents to an electrode in a magnetoplasma, Phys. Rev. Lett. 57, 715, 1986.
- Urrutia, J.M., and R.L. Stenzel, Transport of current by whistler waves, Phys. Rev. Lett. 62, 272, 1989.
- Wasserstrom, E., C.H. Su, and R.F. Probstein, Kinetic theory approach to electrostatic probes, Phys. Fluids 8, 56, 1965.
- Whipple, E.C., Jr., The equilibrium electric potential of a body in the upper atmosphere and in interplanetary space, Ph.D. Thesis, George Washington University/NASA Goddard Space Flight Center, Greenbelt, Maryland, Report No. X-615-65-296, 1965.
- Williamson, P.R., and P.M. Banks, The tethered balloon current generator: A space shuttle tethered subsatellite for plasma studies and power generation, Final Report, NOAA, 1976.
- Winckler, J.R., The application of artificial electron beams to magnetospheric research, Rev. Geophys. Space Phys. 18, 659, 1980.

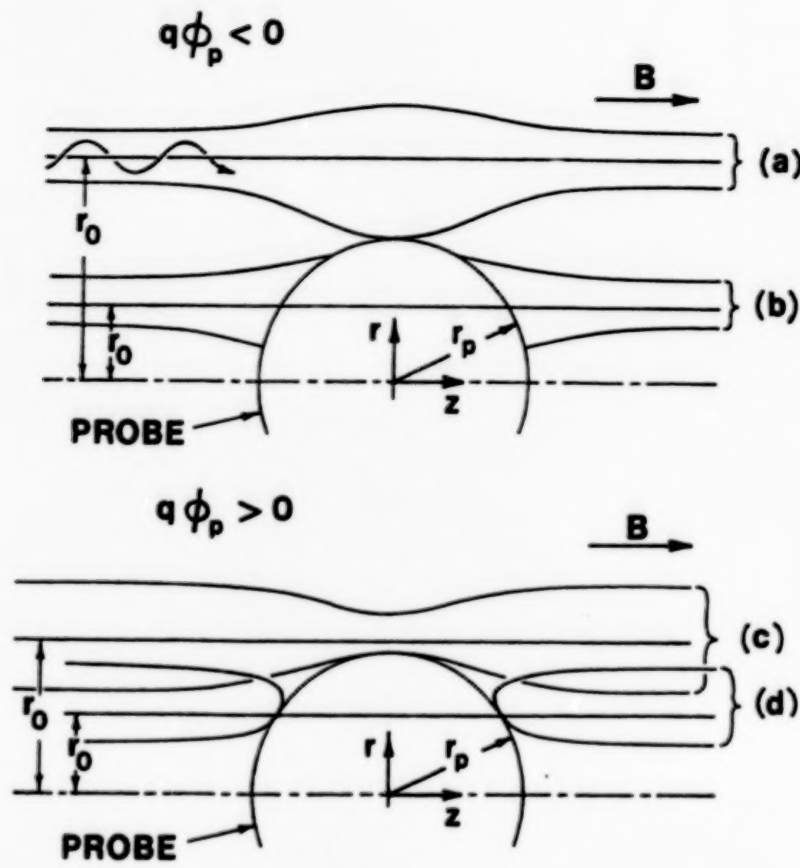


Figure 1. General appearance of "magnetic bottles" for attractive [(a), (b)] and repulsive [(c), (d)] probe potentials, for  $r_0 > r_p$  [(a), (c)] and  $r_0 < r_p$  [(b), (d)], where  $r_p$  is the probe radius and  $r_0$  is defined in Eq. (5). In (a), (c), and (d), the bottles shown just touch the probe. All bottles have rotational symmetry about the  $z$  axis. The bottle shapes are the same for particle orbits encircling or nonencircling the  $z$  axis (Section 2; Rubinstein and Laframboise, 1982, Section IV). Also shown is a typical nonencircling orbit far from the probe; note that if the orbit has nonzero pitch, it does not touch the bottle boundary in general. Reproduced from Figure 6 of Rubinstein and Laframboise (1982).

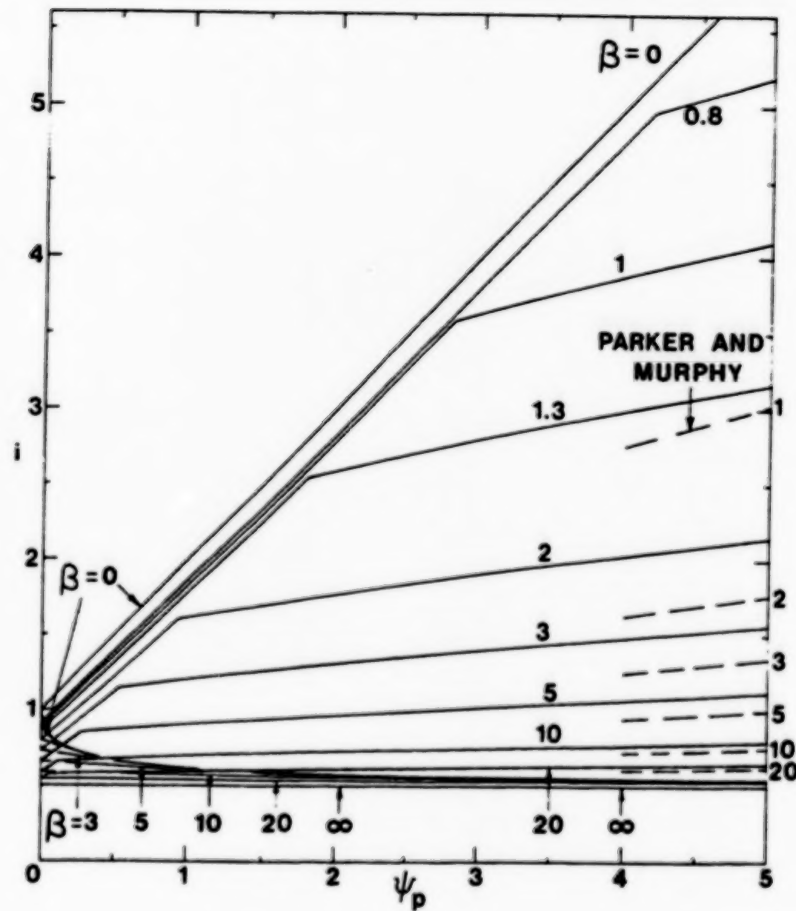


Figure 2. Dimensionless attracted-particle current  $i = I/[4\pi r_p^2 q n_\infty (kT/2\pi m)^{1/2}]$ , versus dimensionless probe potential  $\psi_p = -q\phi_p/kT$ , for various values of dimensionless magnetic-field strength  $\beta = r_p/\bar{a}$ . The increasing and decreasing curves represent least-upper-bound and adiabatic-limit currents, respectively. In the limit  $\beta \rightarrow \infty$ , these currents coincide; otherwise, the question of which curve is closer to the actual current is discussed in Section 2. Note the rapidly increasing disparity between these two sets of curves as  $\psi_p$  increases. The increasing curve for  $\beta = 0$  is the Mott-Smith and Langmuir (1926) orbit-limited-current result. The portions of the increasing curves to the left and right of the "kinks" (discontinuities of slope) in these curves represent "helical" and canonical upper-bound currents (Section 2), respectively. Reproduced from Figure 8 of Rubinstein and Laframboise (1982).

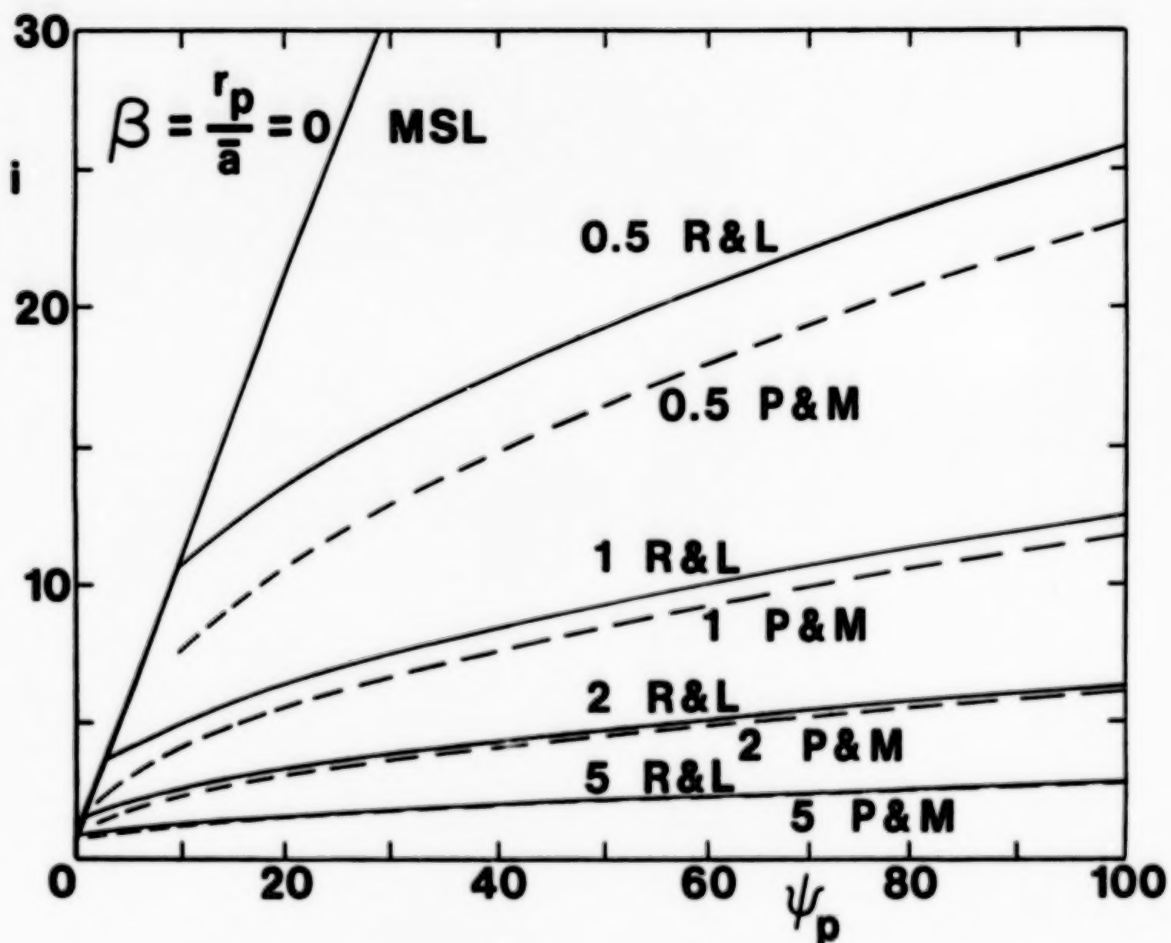


Figure 3. Comparison of the Rubinstein-Laframboise [1982; solid curves; given by our Eqs. (8) - (10)] and Parker-Murphy [1967; dashed curves; given by our Eq. (7)] canonical-upper-bound values for dimensionless attracted-particle current  $i$  as a function of dimensionless probe potential  $\psi_p$ , for various values of the dimensionless magnetic-field strength  $\beta$ . The curve for  $\beta = 0$  is the Mott-Smith and Langmuir (1926) orbit-limited-current result.

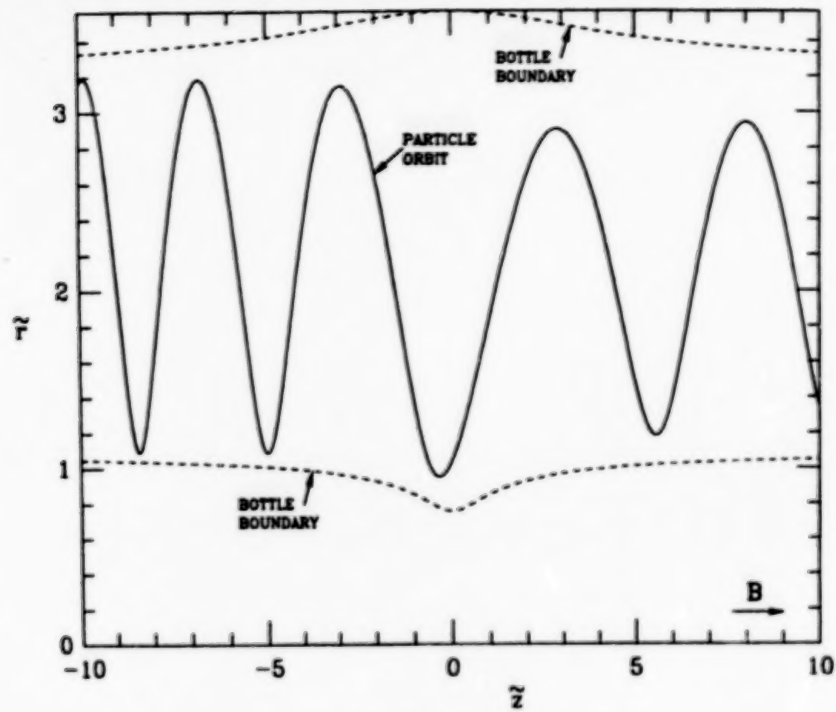


Figure 4(a). Results of L.J. Sonmor (Ph.D. thesis, in preparation), for the trajectory in scaled coordinates [ $\tilde{r} = r(|m\phi_p r_p/qB^2|)^{1/3}$ ,  $\tilde{z} = z(|m\phi_p r_p/qB^2|)^{1/3}$ ] of a charged particle in an attractive Coulomb electric field and uniform magnetic field, given by numerical solution of Eq. (14). Also shown are the boundaries of allowed motion ("magnetic bottle boundaries") for the same particle, implied by conservation of energy and canonical angular momentum. The  $\tilde{z}$  axis (parallel to the magnetic field) has been compressed for purposes of display. The portions of the trajectory which are outside the plot boundary are monotonic progressions in  $\tilde{z}$  from and to infinity. The initial conditions are:  $\tilde{z} = -20$ ,  $d\tilde{z}/d\tau = \sqrt{0.17}$ , scaled radius  $\tilde{r}_g$  of guiding centre =  $\sqrt{4.6}$ , scaled gyroradius =  $\sqrt{2.2}$ , and phase angle = 0.

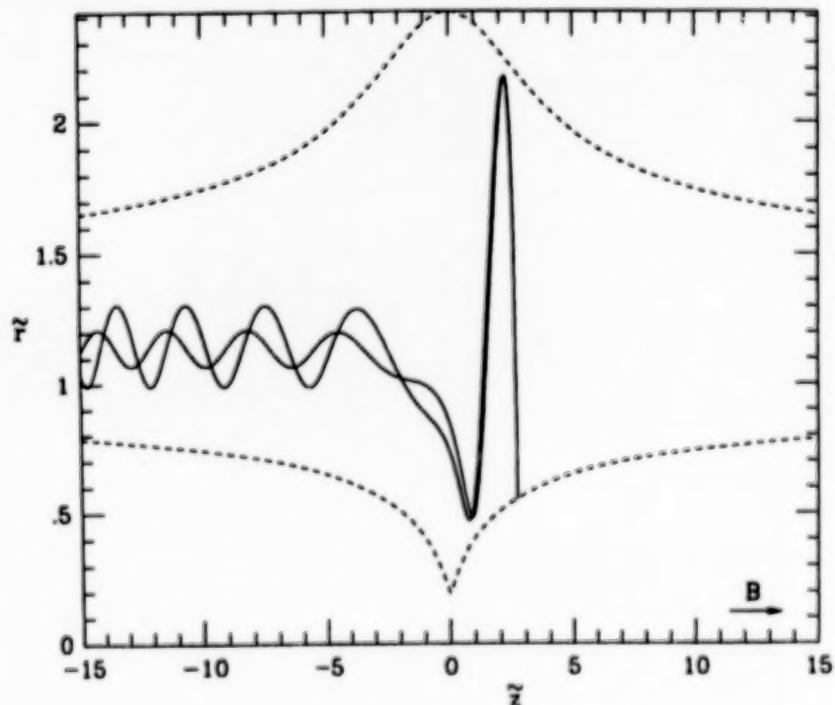


Figure 4(b). Same as Fig. 4(a), except that the initial conditions are:  $\tilde{z} = -20$ ,  $d\tilde{z}/d\tau = \sqrt{0.15}$ ,  $\tilde{r}_g = \sqrt{1.3}$ , scaled gyroradius =  $\sqrt{0.02}$ , and phase angle = 0.

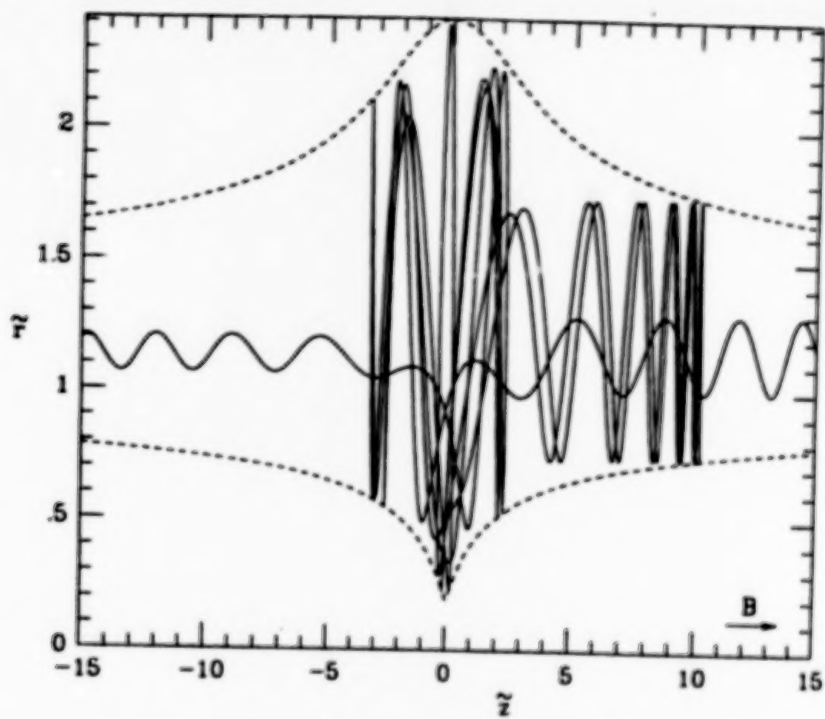


Figure 4(c). Same as Fig. 4(b), except that the initial phase angle is  $7\pi/32$ .

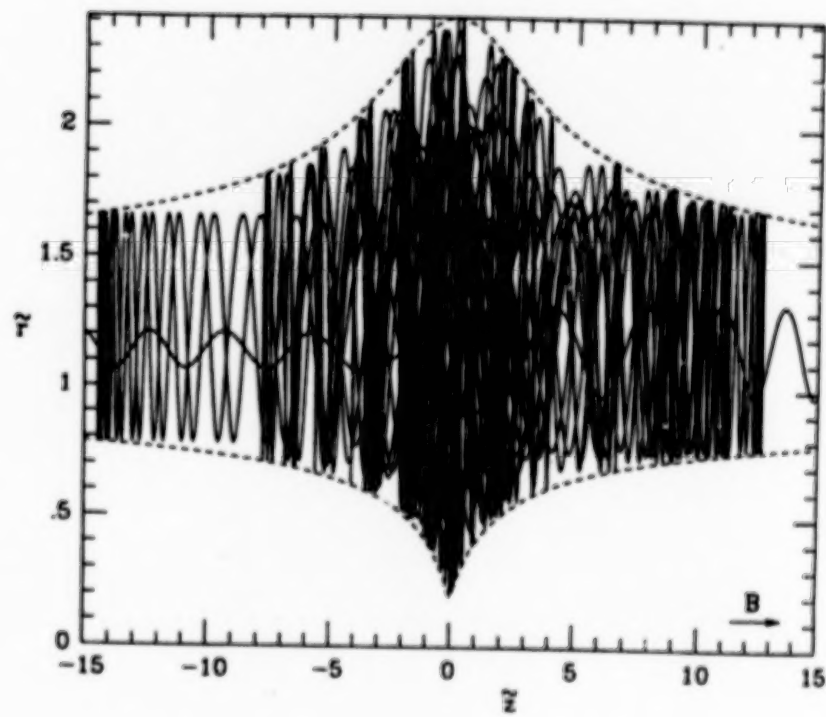


Figure 4(d). Same as Fig. 4(b), except that the initial phase angle is  $11\pi/32$ .

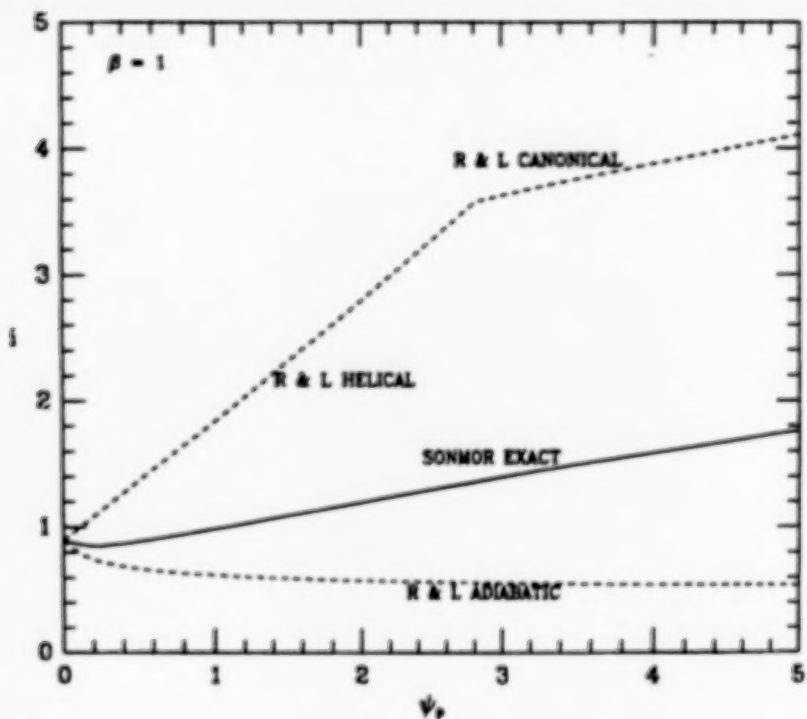


Figure 5(a). Dimensionless attracted-particle current  $i$  versus dimensionless probe potential  $\psi_p$  for a ratio  $\beta$  of probe radius to average ambient attracted-particle gyroradius of 1. Also displayed are the adiabatic-limit currents and the smaller of the helical upper-bound and canonical upper-bound currents, calculated by Rubinstein and Laframboise (1982).

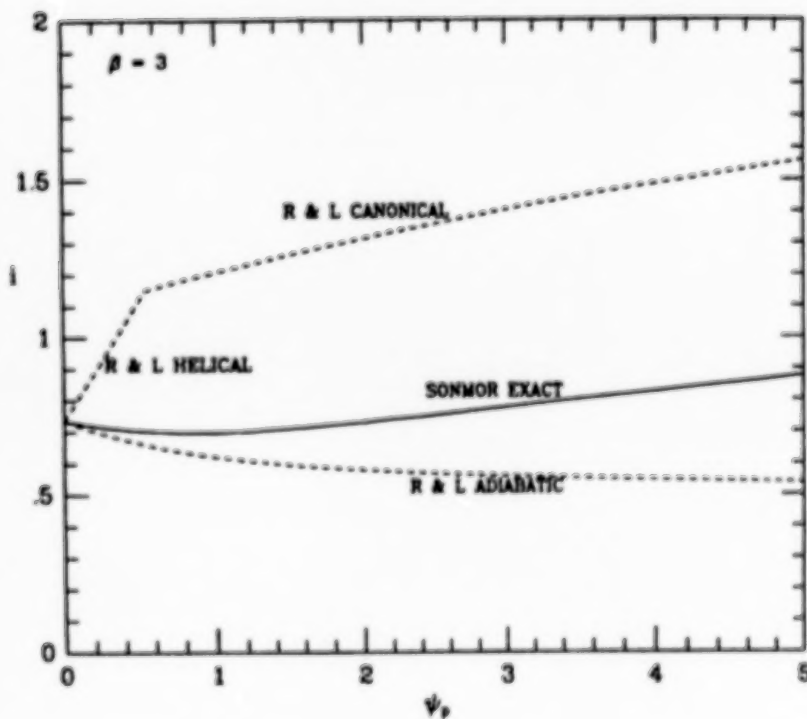


Figure 5(b). Same as Fig. 5(a), except that  $\beta = 3$ .

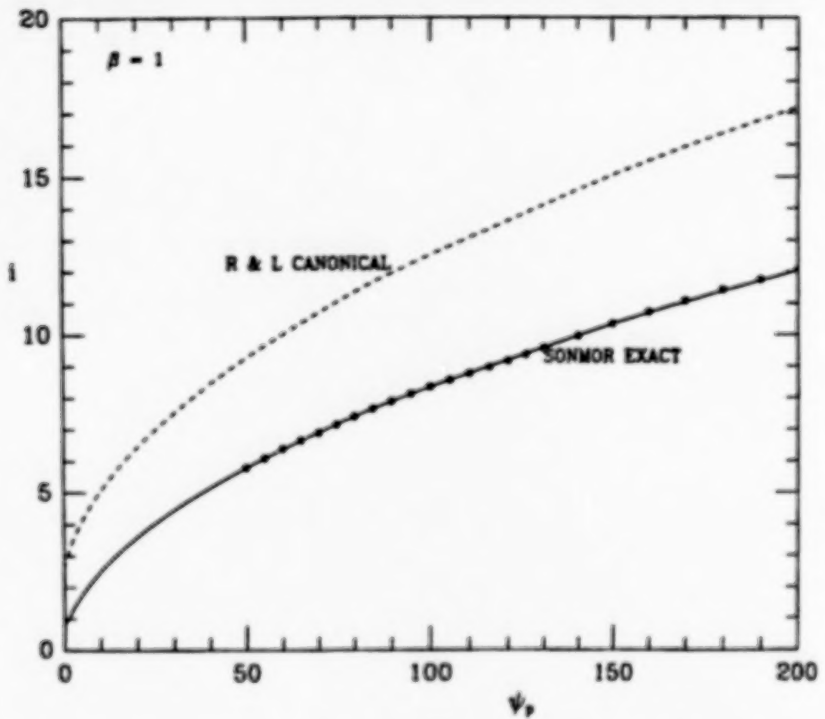


Figure 6(a). Dimensionless attracted-particle current  $i$  versus dimensionless probe potential  $\psi_p$  for a ratio  $\beta$  of probe radius to average ambient attracted-particle gyroradius of 1, plotted for a larger range of probe potentials than in Fig. 5(a). Also displayed is the canonical upper-bound current due to Rubinstein and Laframboise (1982). The minimum in the exact current at  $\psi_p \approx 0.2$ , which was evident in Fig. 5(a), is only barely visible here. Here and in Fig. 6(b), numerical errors in the "exact" results at larger  $\psi_p$  are noticeable on the scale of these graphs, and we have therefore marked actual computed values for larger  $\psi_p$  by open circles, and a curve-fit to them by a solid line.

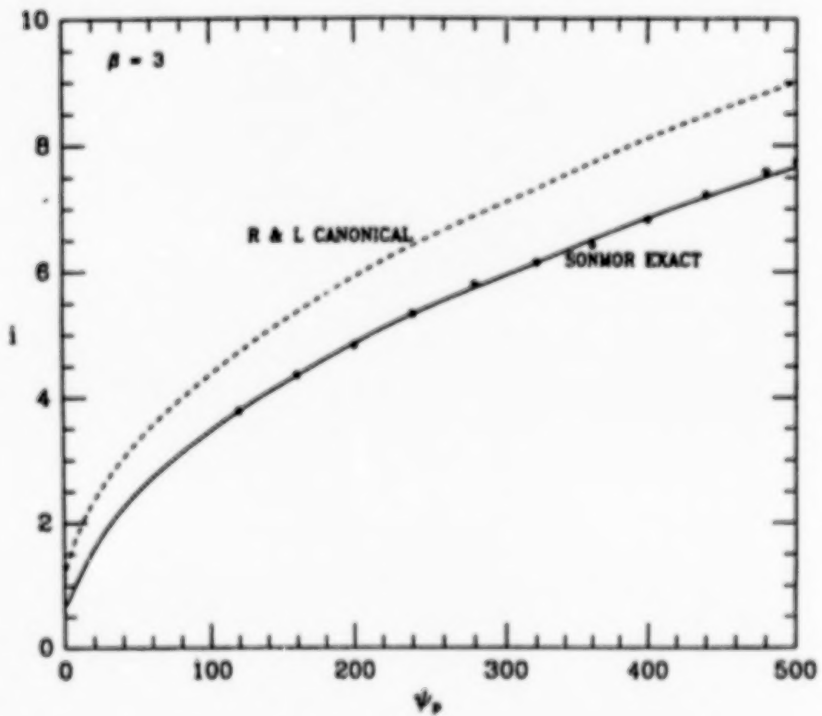


Figure 6(b). Dimensionless attracted-particle current  $i$  versus dimensionless probe potential  $\psi_p$  for a ratio  $\beta$  of probe radius to average ambient attracted-particle gyroradius of 3, plotted for a larger range of probe potentials than in Fig. 5(b). Also displayed is the canonical upper-bound current due to Rubinstein and Laframboise (1982). The minimum in the exact current at  $\psi_p \approx 0.8$ , which was evident in Fig. 5(b), is only barely visible here.

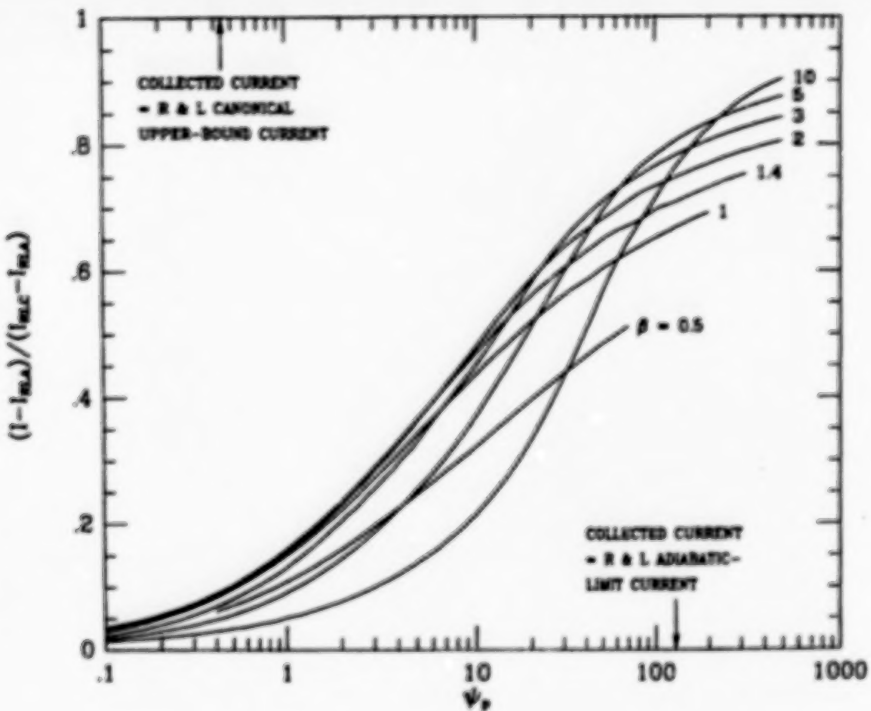


Figure 7. Computed results of L.J. Sosnoff (Ph.D. thesis, in preparation), showing transition from adiabatic-limit current toward canonical upper-bound current as probe potential  $\psi_p$  becomes more attractive, for various ratios  $\beta$  of probe radius to average ambient attracted-particle gyroradius.  $I_{RLA}$  and  $I_{RLC}$  are the adiabatic-limit current and the canonical upper-bound current, respectively, both due to Rubinstein and Laframboise (1982). The canonical upper-bound current is also given by Eqs. (8)–(10). In this Figure, the curves have been smoothed to reduce oscillations caused by numerical errors in individual results.

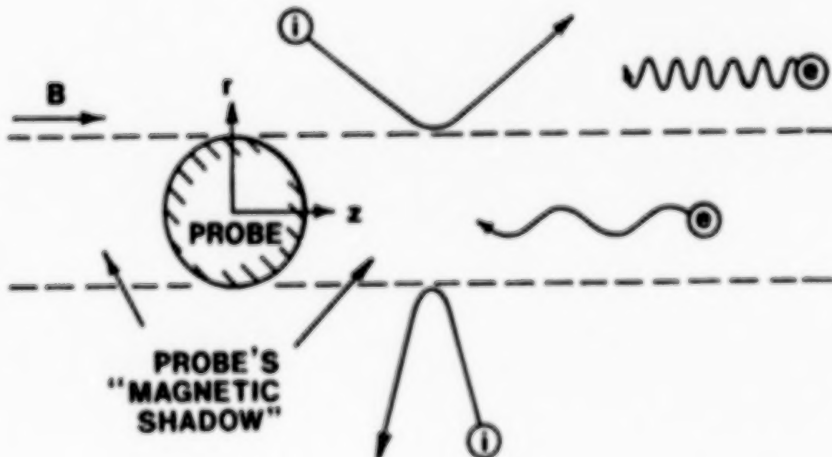


Figure 8. General appearance of representative collisionless ion and electron orbits far from the probe but not beyond the positive-potential disturbance (Sammarria, 1970) which extends along the probe's magnetic shadow. Diagram is schematic only since this disturbance can extend very far in the  $z$  and  $-z$  directions.

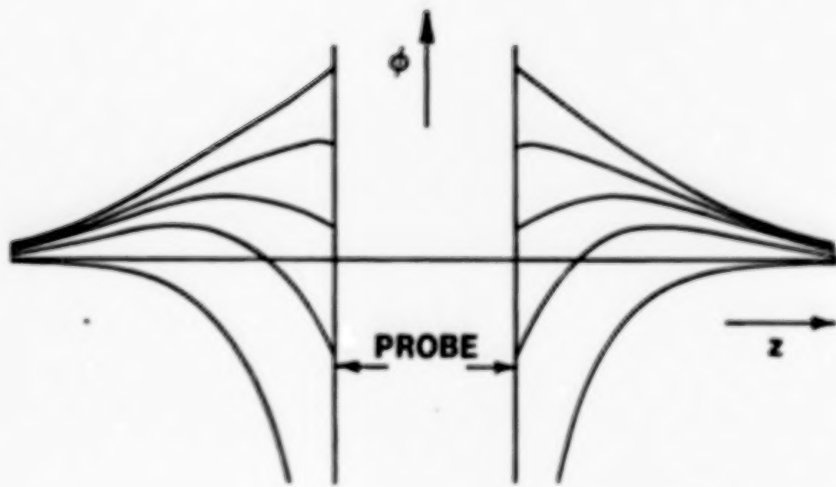


Figure 9. General appearance of potentials as a function of  $z$  for  $r = 0$  under conditions analyzed by Sanmartin (1970) and described in Section 3.

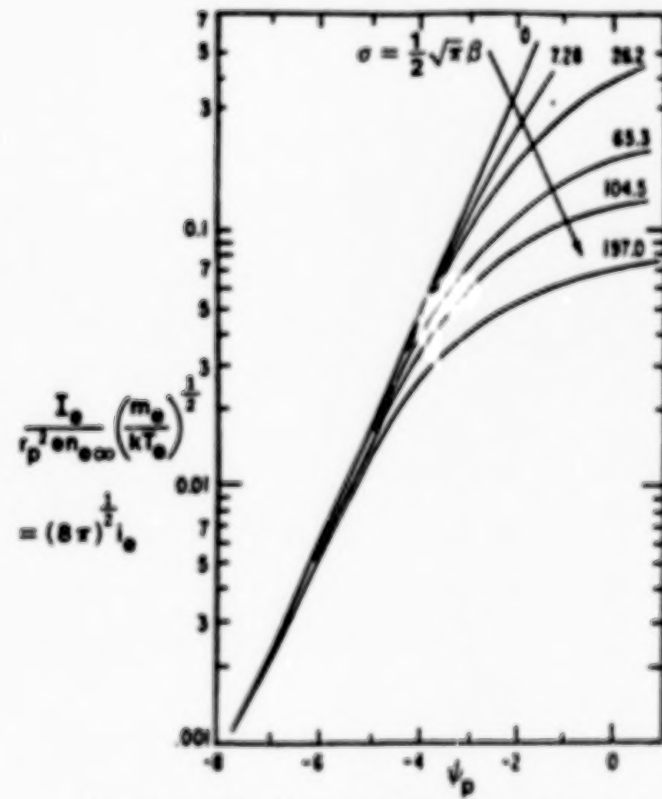


Figure 10. Reproduced from Fig. 1 of Sanmartin (1970), with notation changed, showing his results for electron current collection by a spherical probe in a magnetoplasma for which  $T_1 = T_2$  and containing singly-charged ions. Other assumptions made in Sanmartin's treatment are described in Section 3.

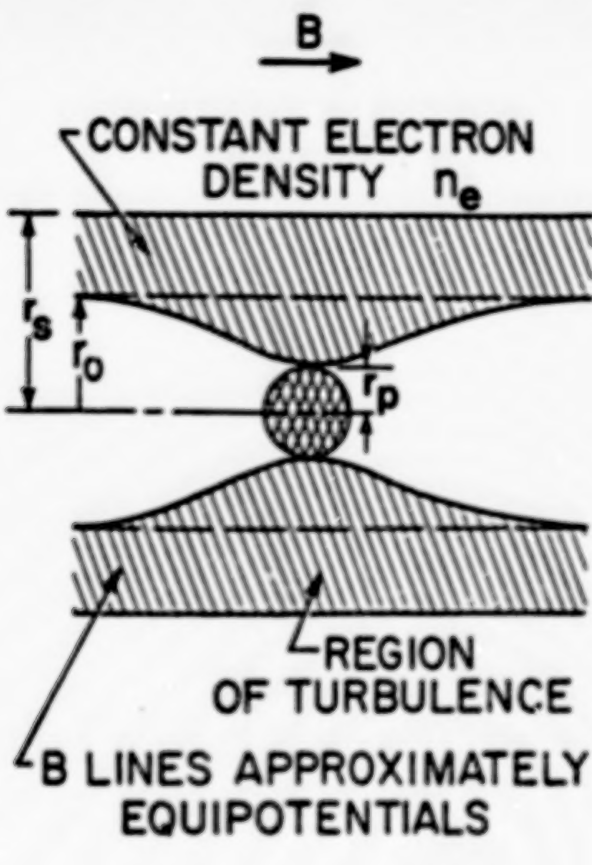


Figure 11. Reproduced from Fig. 2 of Lissner (1969), showing the construction of his constant-density cylindrical space-charge shielding model.  $r_0$  is the critical radius defined by his Eq. 8 (our Eq. 6).

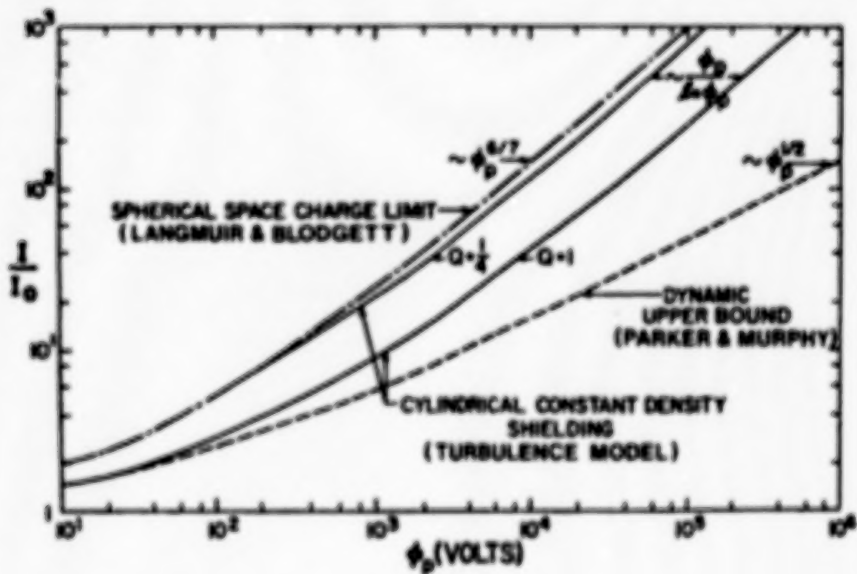


Figure 12. Reproduced from Fig. 3 of Lissner (1970), with some notation changed, showing a comparison of current-versus-probe-voltage predictions from three models discussed by him. Their asymptotic behaviour for large probe voltage  $\phi_p$  is shown. In this Figure,  $I_s$  equals one-half the random current  $I_R$  defined in our Section 2. The dot-dash curve represents the Langmuir-Bloedgett (1921) spherical space-charge-limited current value. For constant potential, this current scales approximately as  $I_s^{4/7}$ . The normalized voltage  $\phi'$  defined following our Eq. (18) is the same as the quantity  $\phi_p$  defined in Lissner's Eq. (8), and has been taken to be 178 volts, which is equivalent to  $B r_p = 0.45 \text{ Gm}$ . A change in the constant  $Q$  displaces the solid curve horizontally by the appropriate factor.

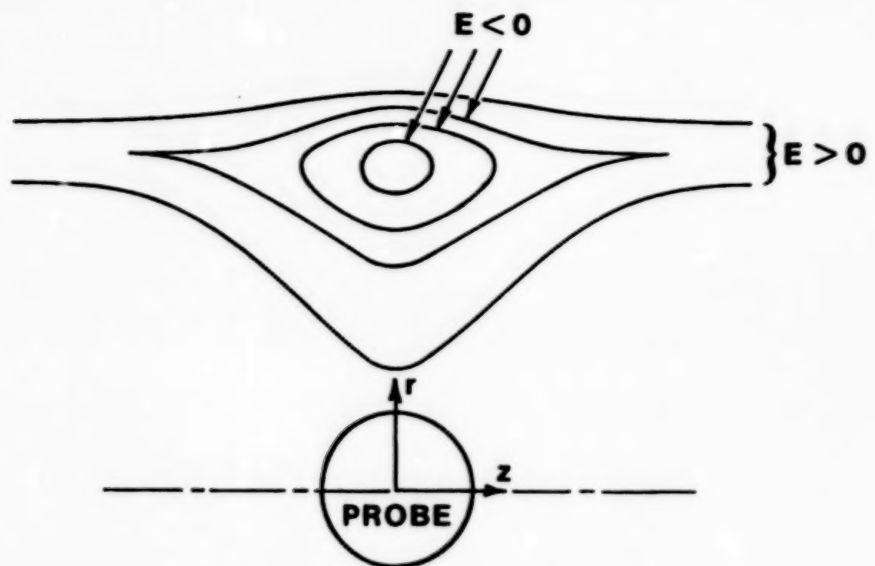


Figure 13. General appearance of open magnetic bottles corresponding to  $E > 0$  and closed ones corresponding to  $E < 0$ , all for the same value of the canonical angular momentum component  $J$  about the  $z$  axis, defined in Eq. (2). Note the "pointedness" of bottles corresponding to slightly negative values of  $E$ .

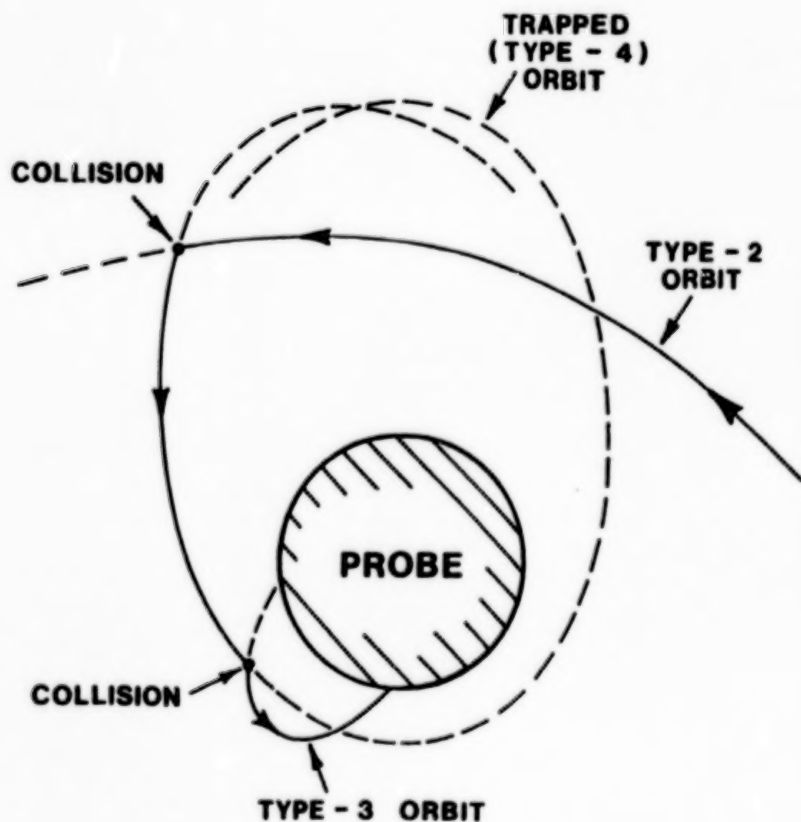


Figure 14. Illustration of how trapped orbits provide an additional current pathway to a probe. Whether trapped orbits exist depends on electric and magnetic fields present; if  $B$  is negligible,  $E$  must vary with  $r$  less steeply than  $r^{-3}$  for trapped orbits to exist (Section 5). The orbit classification shown is that due to Parker (1973, 1975); see preceding paper by E.C. Whipple in these Proceedings. In a magnetic field, the shapes of these orbits can be much more complicated than those shown.

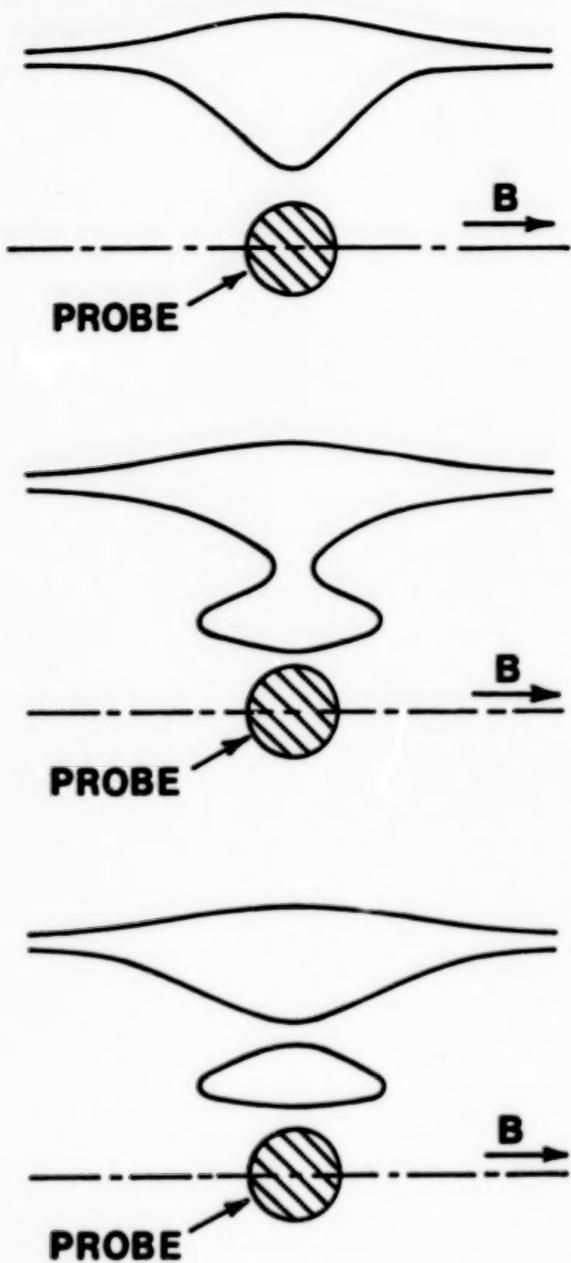


Figure 15. Development of "bulges" and disjoint "bubble" regions in magnetic "bottles", as described in Section 5.

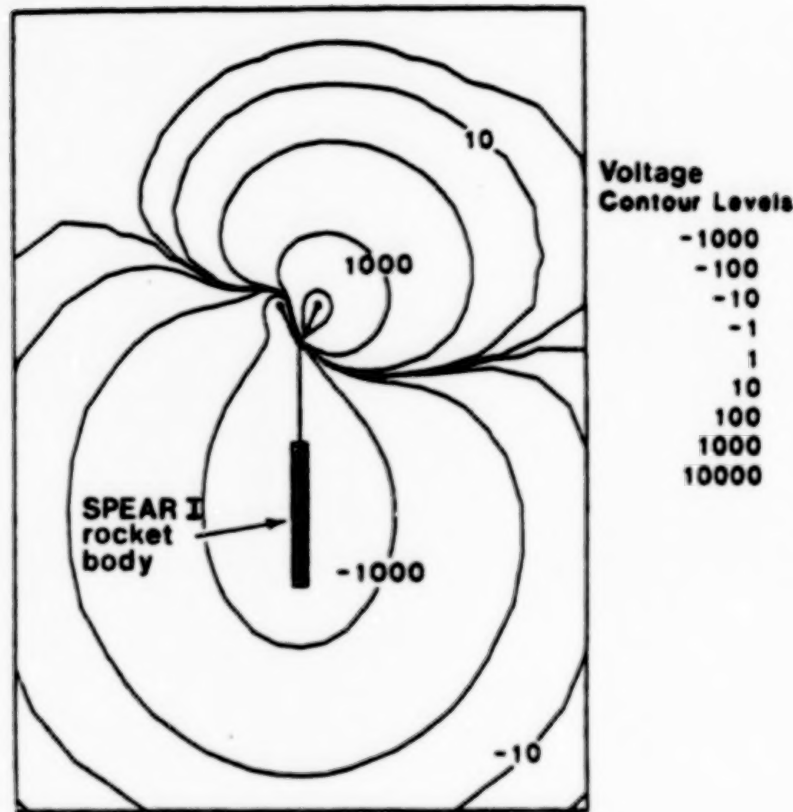


Figure 16(a). Reproduced from Fig. 8a of Katz *et al* (1989), showing SPEAR I potential contours calculated by the NASCAP/LEO simulation program for the case with one sphere biased to 46kV and the spacecraft ground at -6kV.

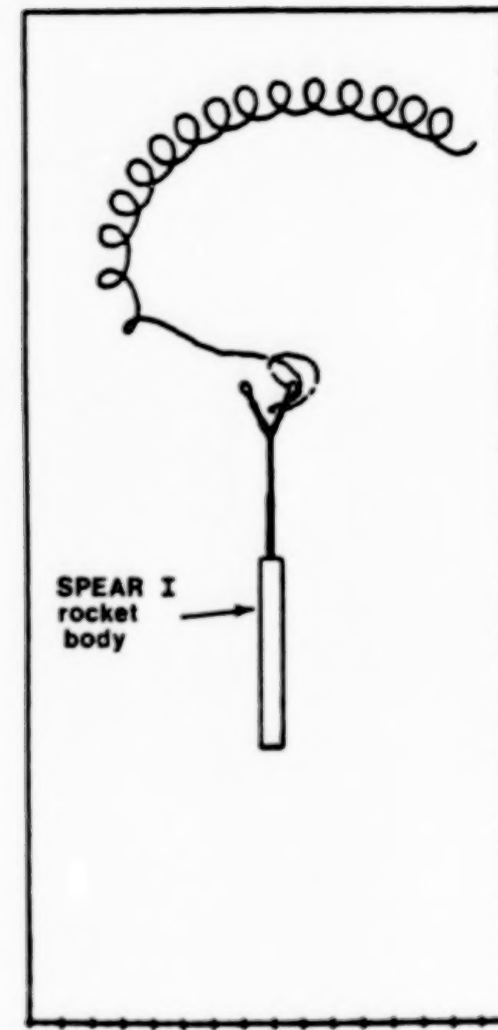


Figure 16(b). Reproduced from Fig. 8b of Katz *et al* (1989), showing the path of an electron in the potential distribution shown in Fig. 16(a). Note that the path is dramatically influenced by the presence of the ion-attracting sheath around the rocket body. Note also the sudden transition from "E  $\times$  B drifting" motion to "accelerated" motion, and subsequent limiting of this motion by angular-momentum effects (Section 6).

ST

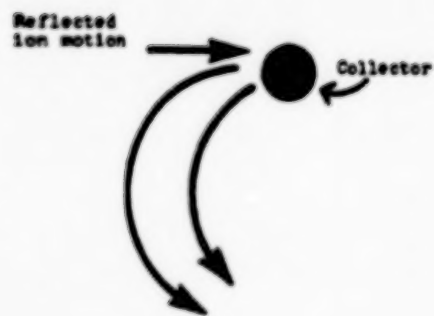
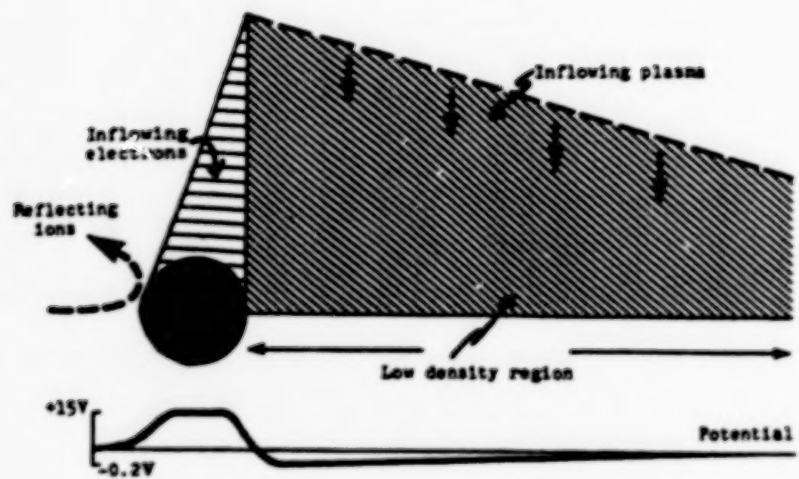


Figure 17. Reproduced from Figure 2 of Thompson (1985), showing the structure of the disturbed region around a large sphere in a drifting magnetoplasma.

# CURRENT COLLECTION IN A FLOWING MAGNETOPLASMA

Nagendra Singh and B.I. Vashi

Department of Electrical and Computer Engineering and

Center for Space Plasma and Aeronomics Research

University of Alabama, Huntsville, AL 35803

**ABSTRACT:** Effects of plasma drift on the current collection by a long conducting cylinder in a magnetized plasma is studied by means of a 2 1/2 dimensional PIC code. It is found that for the drift velocity ( $V_0$ ) perpendicular to the magnetic field  $B_0$ , the electron current collected by a positive cylinder is considerably enhanced depending on the drift velocity. The distributions of plasma and the potential structure around the cylinder for several relative orientations between  $V_0$  and  $B$  are presented along with the comparisons of current with and without the magnetic field. Simulations with the magnetic field in the simulation plane show that the potential structures around the cylinder are two-dimensional double layers with dimension ( $L_\perp$ ) perpendicular to  $B$  much smaller than the dimension ( $L_\parallel$ ) parallel to  $B$ . In fact,  $L_\perp$  is found to be approximately determined by the current limiting radius given by the Parker-Murphy model. However, it is found that the collected currents in the simulations are generally higher than those given by this model.

## 1. INTRODUCTION

The knowledge of current collection by conducting bodies in space plasma is relevant to numerous applications such as the operation of plasma probes, charge neutralization on space vehicles, working of the solar cell arrays and the operation of an

electrodynamic tether. Most theories dealing with this topic are limited to simple geometries and idealized plasma models. For reviews of the theoretical studies, the reader is referred to Whipple and Laframboise and Sonmor in this volume. These reviews show that there is a general lack of theoretical studies on current collection in a magnetized plasma when there is a relative drift between the magnetized plasma and the current collector. The purpose of this paper is to contribute to this area by means of computer simulations using a PIC code.

Our computer model is two dimensional; the axis of the cylinder is perpendicular to the plane of simulation. The magnetic field is oriented along the axis of the cylinder or in the simulation plane in different simulations, which bring out the effects of relative orientation between the magnetic field and the plasma drift on the sheath structure and the current collection properties. For the axial magnetic field, a simple-minded picture with radial electric fields indicates that the  $E \times B$  drift will cause a magnetic insulation stopping any collection of electrons by the positive cylinder. Simulations show that this picture is not valid when there is a relative flow between the plasma and the cylinder; the potential structure is considerably modified so that the flowing electrons are focused onto the cylinder, making possible the collection of a relatively large electron current.

When the magnetic field is in the simulation plane, the potential structure is extended along the magnetic field and its transverse dimension is quite limited and it is found to be given by the current limiting radius calculated by Parker and Murphy [1] in a non-flowing plasma. We find that when the flow is perpendicular to the magnetic field, the electrons intercepted by the extended field-aligned potential structure are partially collected by the cylinder and the current is found to be considerably enhanced over the current predicted by the Parker-Murphy model [1]. However, for the flow parallel to the magnetic field, the current is seen to be limited in a fashion described by the above model. Since in the low earth orbit, the orbital velocity vector is at large oblique angles with respect to the geomagnetic field, a current enhancement is expected.

## 2. SIMULATION TECHNIQUE

The plasma flow past the cylinder is simulated as shown in Figure 1. The hatched area is the end view of the long conducting cylinder of radius  $r_s$ . In the rest frame of the cylinder, plasma flows along the positive  $x$  direction with the velocity  $V_0$ . The flow is facilitated by imposing a dc convection electric field  $E_0$  so that  $V_0 = E_0 \times B/B^2$ . The simulated plasma region is limited to  $r \leq R_{\max}$  (Figure 1). At the initial time  $t = 0$ , the simulation region is a vacuum and the plasma flow for  $t > 0$  is maintained by injecting charged particles at the rim of the simulation box ( $r = R_{\max}$ ) over the angular region  $\pi/2 \leq \theta \leq 3\pi/2$  (Figure 1). The average injection velocity of the charged particles is  $V_0$ . At each time step a predetermined number ( $N_{\text{inj}}$ ) of electron-ion pairs are injected to simulate a desired plasma flux. The plasma particles used in the simulations are like rods parallel to the axis of the cylinder [2]. The injected particles are chosen from Maxwellian

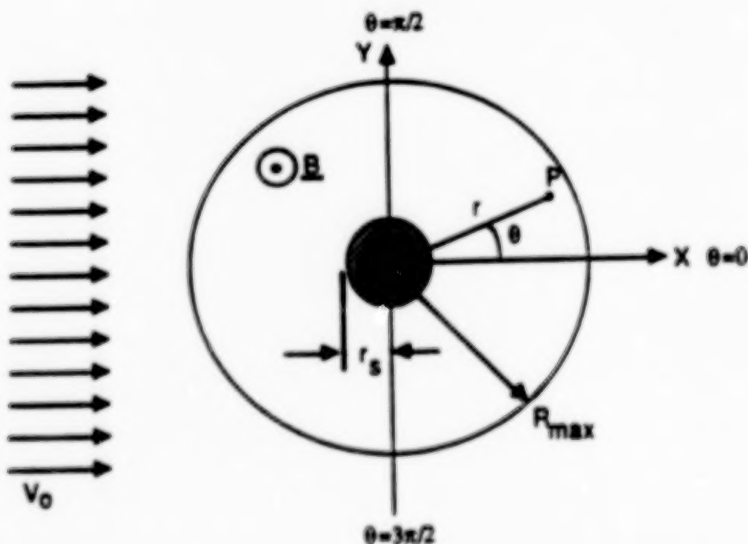


Figure 1. Geometry of the simulation. The conducting cylinder is shown by the hatched region.  $R_{\max}$  gives the radius of the simulation system. Plasma flows across the cylinder with a velocity  $V_0$ . The magnetic field is parallel to the axis of the cylinder.

distributions with electron temperature  $T_e = T_0$  and ion temperature  $T_i = 0$ . The Y coordinates of the particles are chosen according to a uniform probability distribution. The X coordinates are first calculated by  $X = (R_{\max}^2 - Y^2)^{1/2}$  and then further randomized by replacing X by  $X + V\Delta t$  where V is the particle velocity randomly chosen from a Maxwellian distribution and  $\Delta t$  is the time step. Our injection technique is quite similar to that described by Aldrich [6].

The magnitude of charge ( $q_a$ ), per unit length of such computer particles, is obtained by balancing the plasma flux into the simulation region at the injection boundary and the simulated flux due to the injection of the charge particles at each time step of duration  $\Delta t$ , giving

$$|q_a| = 2 R_{\max} e N_0 V_0 \Delta t / N_{\text{inj}} \quad \text{C/m} \quad (1)$$

where  $N_0$  is the ambient plasma density and e is the magnitude of the electron charge. The injection of equal numbers of electrons and ions insures that no net charge is injected into the system.

The temporal and spatial evolutions of the plasma and fields are calculated by the self-consistent solutions of the equations of motions [2] of all the charged particles and the Poisson equation for the electric potential  $\phi$ . It is important to note that in our simulations, the electric field has two contributions as indicated by the following equation

$$\mathbf{E} = \mathbf{E}_0 + \mathbf{E}_1 \quad (2)$$

where  $\mathbf{E}_0$  is the convection field and  $\mathbf{E}_1$  is determined by the space charges and the bias potential on the cylinder. Since  $\mathbf{E}_0$  is uniform in space,  $\nabla \cdot \mathbf{E}_0 = 0$  and the divergence of (2) gives

$$\nabla \cdot \mathbf{E} = \nabla \cdot \mathbf{E}_1 = \rho / \epsilon_0 \quad (3)$$

where  $\rho$  is the electric charge density. Under the electrostatic approximation,  $\mathbf{E}_1 = -\nabla \phi$  and (3) gives the Poisson equation

$$\nabla^2 \phi = -\rho / \epsilon_0 \quad (4)$$

The boundary conditions on the electric potential  $\phi$  are  $\phi(r = r_s, \theta) = \phi_0$  and  $\phi(r = R_{\max}, \theta) = 0$ , where  $\phi_0$  is the bias potential of the cylinder. The particles striking the cylinder and those leaving the system are assumed to be lost. However, the simulation system is maintained quasi-neutral at the 'global' scale. For this purpose, we compare the total numbers of electrons and ions in the entire system at each time step. The deficit charged particles, which are taken from a Maxwellian plasma reservoir are randomly distributed over the entire simulation system according to a uniform probability distribution.

The collected current ( $I$ ) is calculated by counting the electrons and ions striking the cylinder during each time step,

$$I = \sum_{\alpha} q_{\alpha} \delta N_{\alpha} / \Delta t \quad (5)$$

where  $\delta N_{\alpha}$  is their number, and  $q_{\alpha}$  is given by (1). We note that although  $q_{\alpha}$  depends on the numerical factors  $R_{\max}$ ,  $N_{\text{inj}}$  and  $\Delta t$ ; the current  $I$  is found to be independent of them, if  $R_{\max}$  and  $N_{\text{inj}}$  are sufficiently large and  $\Delta t$  is sufficiently small. This was verified by carrying out simulations by varying these parameters.

### 3. NORMALIZATIONS AND DEFINITIONS

We discussed earlier that the charge on a computer particle is given by (1). If  $q_{\alpha}/e = \eta$ , the analogy between the real and computer particles requires that the masses  $m$ , effective temperatures  $T$  and density  $N$  satisfy the relations

$$m_{c\alpha} = \eta m_{r\alpha}, T_{c\alpha} = \eta T_{r\alpha} \text{ and } N_{c\alpha} = N_{r\alpha} / \eta \quad (6)$$

where the subscripts  $r$  and  $c$  refer to the real and computer particles, respectively. It is worth mentioning that the electron and ion Debye lengths and plasma frequencies are invariant under the scaling law described by (6) [4].

The results presented in this paper are based on simulations with the following ionospheric plasma parameters: ambient plasma density  $N_0 = 10^{11} \text{ m}^{-3}$ , electron

temperature  $T_e = 0.2$  eV, plasma debye length  $\lambda_{do} \approx 1$  cm, electron plasma frequency  $\omega_{po} \approx 1.8 \times 10^7$  rad/s, and the magnetic field  $B_0 = 0.3$  G. With the above ambient plasma parameters, the electron thermal current  $J_t = N_0 e V_{te} / \sqrt{2\pi} \approx 1.2$  mA/m<sup>2</sup>, where  $V_{te} = (kT_0/m_e)^{1/2} \approx 192$  km/s.

In order to simplify the equations and to generalize the applicability of their solutions to different situations with varying plasma and current-collector parameters, we use the following normalizations: potential  $\tilde{\phi} = \phi/\phi_n$ ,  $\phi_n = k_B T_e/e$ ; time  $\tilde{t} = t \omega_{po}$ ; velocity  $\tilde{V} = V/V_{te}$  and distance  $\tilde{r} = r/\lambda_{do}$ .

In view of the above normalizations the Poisson equation (4) can be written as

$$\frac{\partial^2 \tilde{\phi}}{\partial \tilde{r}^2} + \frac{1}{\tilde{r}} \frac{\partial \tilde{\phi}}{\partial \tilde{r}} + \frac{1}{\tilde{r}^2} \frac{\partial^2 \tilde{\phi}}{\partial \tilde{\theta}^2} = -\frac{\lambda_{do}^2}{\phi_n} (q n_{ic} - q n_{ec}) \quad (7)$$

where  $q n_{ic}$  and  $q n_{ec}$  are the charge per unit volume associated with the computer ions and electrons, respectively. It is assumed that both types of particles have the same magnitude of charge, i.e.,  $q_e = q_i = q$ , as given by (1). These charge densities ( $q n_{ic}$  and  $q n_{ec}$ ) are determined by calculating the number of computer particles at each grid point by the area sharing method [2] and dividing it by the effective volume of a cell. This volume is given by  $r_j \Delta \theta \Delta r \Delta z$ , where  $r_j$  is the radial distance of a grid point,  $\Delta r$  and  $\Delta \theta$  are the radial and angular grid spacings, respectively and  $\Delta z$  is the length along the axial direction. With these definitions and equation (1), the normalized Poisson equation takes the form

$$\frac{\partial^2 \tilde{\phi}}{\partial \tilde{r}^2} + \frac{1}{\tilde{r}} \frac{\partial \tilde{\phi}}{\partial \tilde{r}} + \frac{1}{\tilde{r}^2} \frac{\partial^2 \tilde{\phi}}{\partial \tilde{\theta}^2} = -2 \tilde{R}_{max} \tilde{V}_o \Delta \tilde{t} (\Delta n_{ic} - \Delta n_{ec}) / \tilde{r}_j \Delta \tilde{r} \Delta \tilde{\theta} N_{inj} \quad (8)$$

where  $\Delta n_{ic}$  and  $\Delta n_{ec}$  are the number of computer ions and electrons shared on a grid point ( $j \Delta r, i \Delta \theta$ ). The above equation is solved by employing FFT in  $\theta$  and triadiagonal method in  $r$ .

The numerical results presented below are based on the following numerical parameters:  $R_{max} = 140 \lambda_{do} \approx 1.4$  m,  $r_s = 10 \lambda_{do} \approx 0.1$  m,  $\Delta \tilde{t} = 0.2$ ,  $\Delta \tilde{r} = 1$ ,  $\Delta \theta = 10^\circ$  and the normalized flow velocity  $\tilde{V}_o = V_o/V_{te}$  is varied. The simulations are carried out with H<sup>+</sup> plasma for which  $m_i/m_e = 1836$ . We note that in our simulation electron

cyclotron period  $\tau_{ce} \approx 18 \omega_{po}^{-1}$  while the ion cyclotron period  $\tau_{ci} \approx (m_i/m_e) \tau_{ce}$ . Thus, for the time scales in the simulations, electrons are magnetized, while ions behave as unmagnetized charged particles.

#### 4. NUMERICAL RESULTS

In the following discussion we first present results for  $B = 0$ , which are later used for the purpose of comparisons with the results for non-zero magnetic fields with different orientations.

##### 4.1 Simulations with $B = 0$

We recall that the simulation begins with no initial plasma in the system. The simulation plasma builds up in the system in response to the injection of particles as described above in Section 2. In the simulation described in this subsection  $\phi_0 = 100$  and  $V_0 = 0.3$ . Figures 2 and 3 show the evolution of the plasma; in Figure 2 the contours of constant density of ions are shown at some selected times. The minimum density contour is  $\bar{n} = 0.1$  and the density interval between the contours is  $\Delta\bar{n} = 0.3$ . The electron density shows nearly the same evolution as the ions. After about  $i = 550$ , a quasi-steady state is reached in the plasma distribution.

The distribution of the computer particles in the  $r-\theta$  plane are shown in Figure 3, each dot in the panels of this figure represents a particle. The left-hand panels show electrons while the right-hand ones show ions. Note the formation of a distinct wake behind the cylinder (also see Figure 2). Another noteworthy feature of Figures 2 and 3 is that a bow structure forms in the ram direction; in this structure the density is generally enhanced. We also see from Figure 3 that ions are not able to reach the cylinder because the kinetic energy of the ions ( $1/2 m_i V_0^2 = 82.6 kT_0$ ) associated with the plasma drift is smaller than the potential energy  $e\phi_0 = 100 kT_0$ , where  $\phi_0$  is the bias voltage on the cylinder. Outside the wake region, the plasma density  $\bar{n} = 1$ , indicating a uniform plasma flow in the ram direction away from the bow structure.

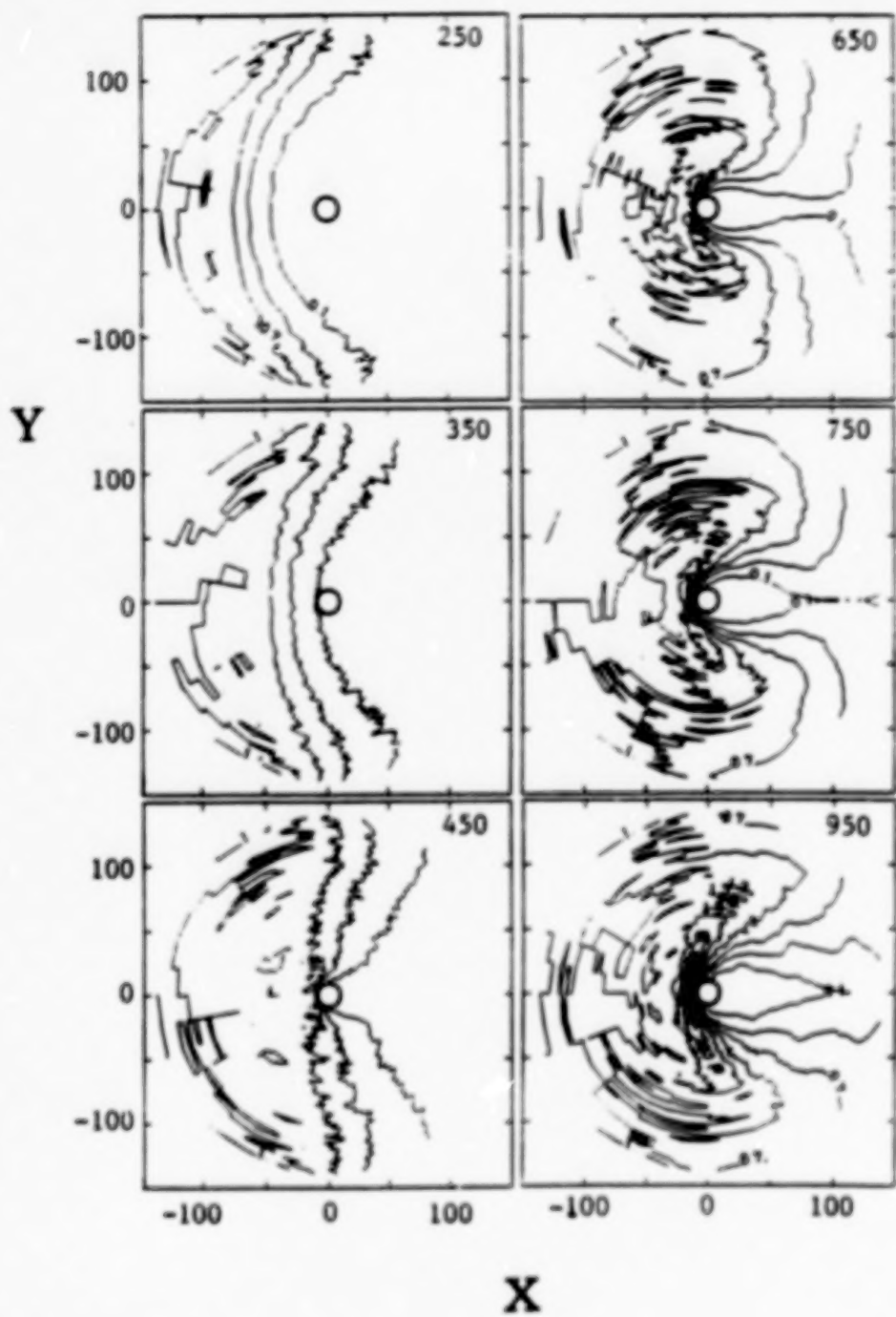


**Figure 2.** Evolution of the plasma inside the simulation region. Contours of constant densities are shown with a contour spacing of  $\Delta \tilde{n}_i \approx 0.3$ . Note that the plasma distribution attains a quasi-steady state after about  $i = 600$ .  $\phi_0 = 100$ .

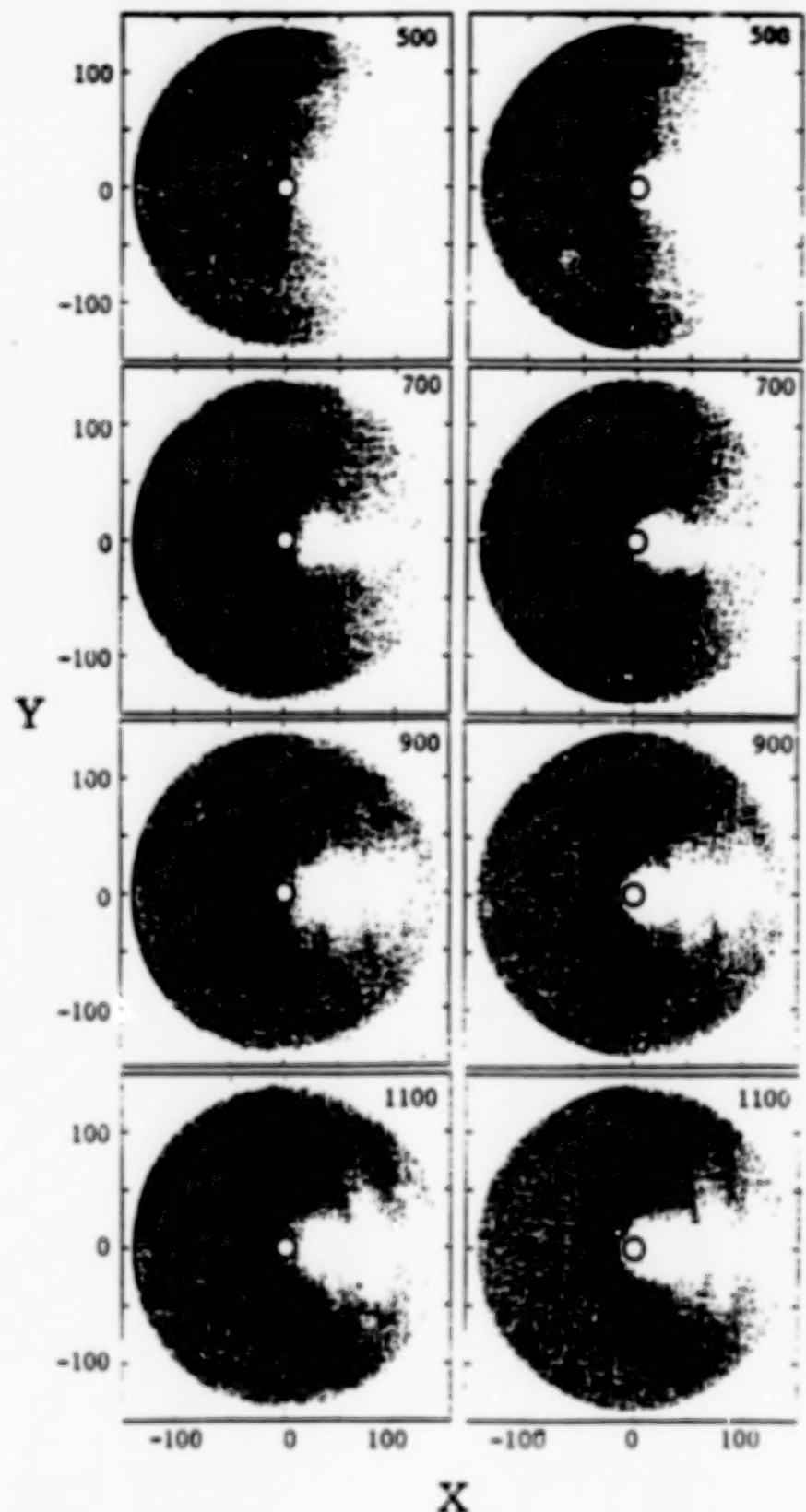


Figure 3. Evolution of plasma is shown by showing the distribution of (a) electrons and (b) ions in the  $r-\theta$  plane. Each dot in this figure represents a computer particle.  $\phi_0 = 100$ ,  $B = 0$ ,  $\hat{V}_0 = 0.3$ .

The evolution of the potential distribution around the cylinder is shown in Figure 4, which gives the equipotential surfaces at some selected times. The contour levels are  $\Delta\tilde{\phi} = 5$  apart. This figure shows that after about  $\tilde{t} = 500$ , the sheath structure reaches a quasi-steady state. In the wake region the potential is generally negative.

In response to the evolution of the plasma and potential around the cylinder, the collected current evolves as shown in Figure 5. The current reaches a quasi-steady state after about  $\tilde{t} = 500$ , in agreement with the evolutions of the density and the plasma potential. After this time, the plasma and the potential are still undergoing some changes, especially in the wake region, but they seem to have negligible effect on the current collection. The time-average current for  $B = 0$  in the quasi-steady state ( $\tilde{t} > 500$ ) is about  $I \approx 18$  mA.

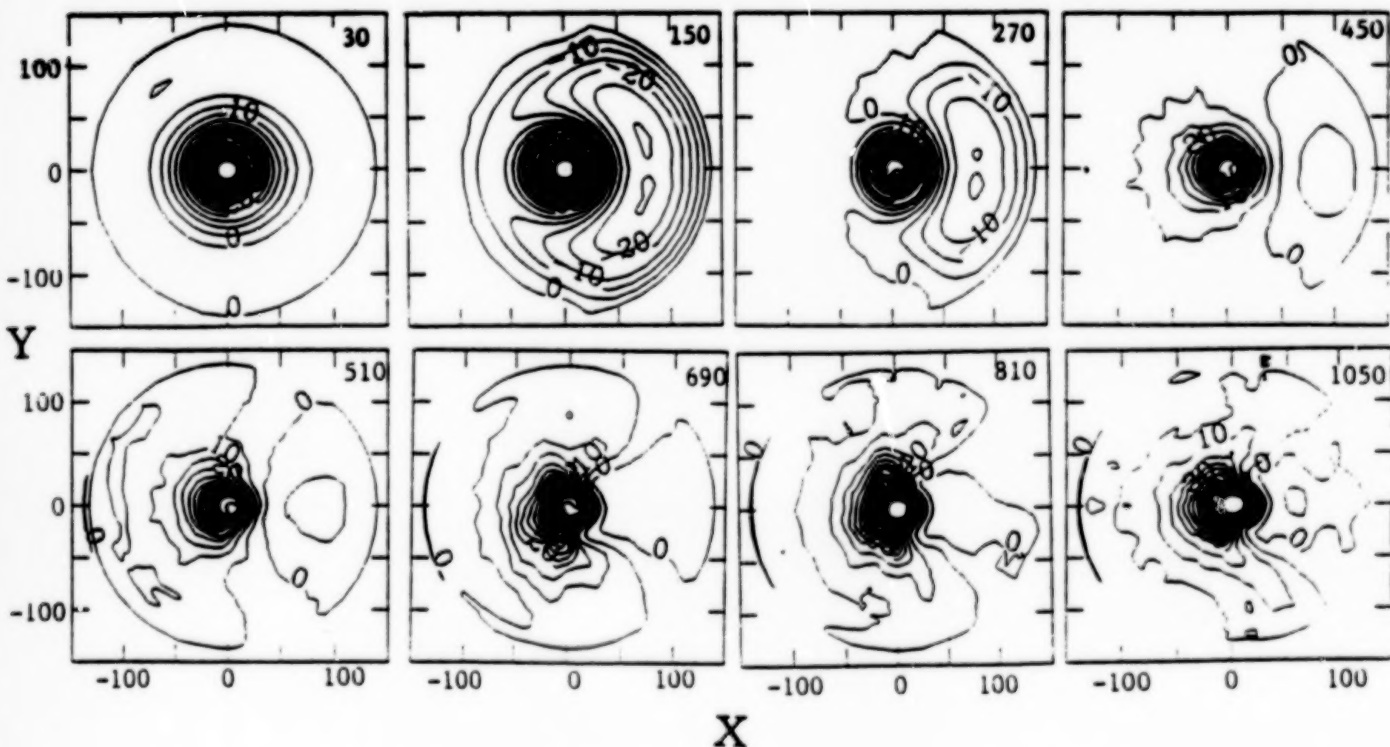


Figure 4. Evolution of the equipotential surfaces around the cylinder. Note that after about  $\tilde{t} = 600$ , the equipotential surfaces attain a quasi-steady state. The equipotential contours are  $\Delta\tilde{\phi} = 5$  apart.  $\tilde{\phi}_0 = 100$ ,  $B = 0$ ,  $\tilde{V}_0 = 0.3$

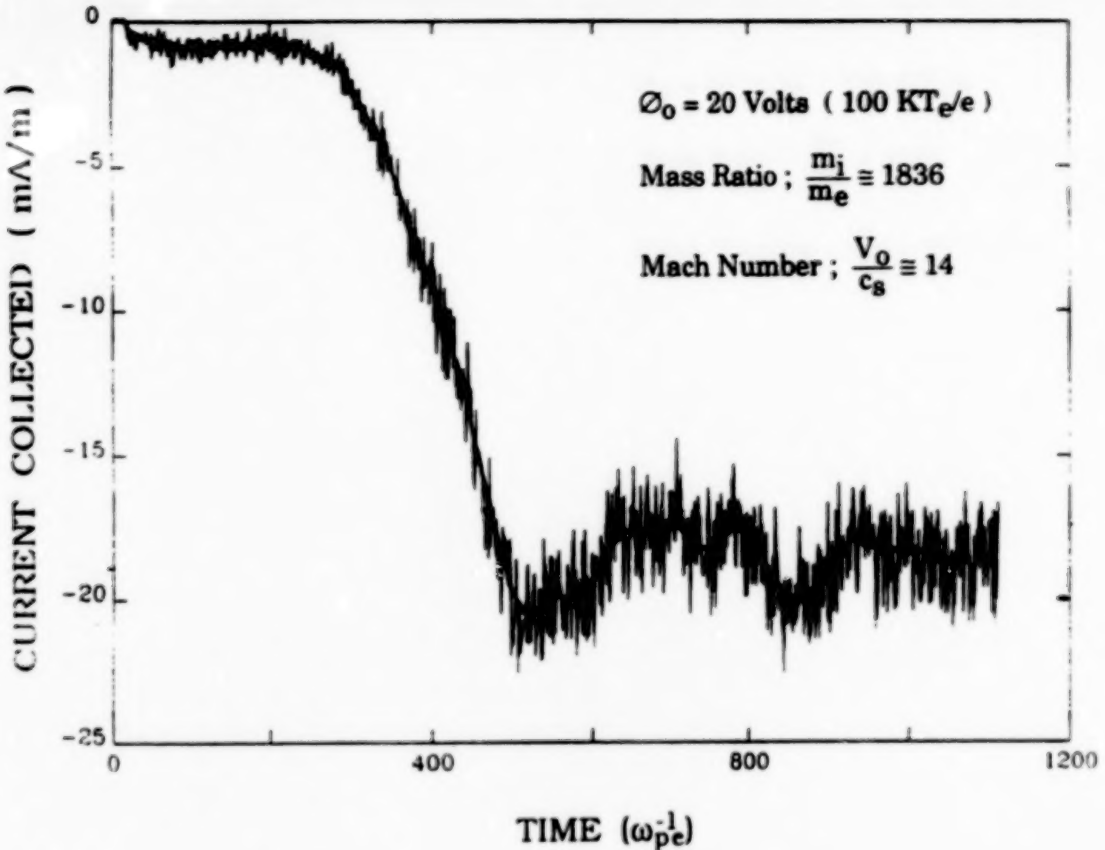


Figure 5. Temporal evolution of the current collected by the cylinder. The thick line curve shows the time average current when fast oscillations are averaged out. Note that the current attains a quasi-steady state when about  $t \geq 600$ .  
 $\tilde{\phi}_0 = 100$ ,  $B = 0$ ,  $\tilde{V}_0 = 0.3$

The simulations with  $B = 0$  were carried out for several bias potentials. Figure 6 shows the V-I characteristics of the cylinder. It is found that  $I \propto \phi_0^{1/2}$ , which is in agreement with the orbit-limited current collected by a cylinder (e.g. see Chen [5]). However, the proportionality constant is found to be given by

$$I \approx 1.8 (e\phi_0/kT_e)^{1/2} \text{ mA/m ,}$$

which is found to be by a factor of two larger than that for  $V_0 = 0$ . It is expected that in the limit  $V_0 = 0$ , the simulations must yield the current as predicted by the orbit-limited current. However, the simulation runs with very small drift velocities take too long to complete and so far we have not carried out such simulations.

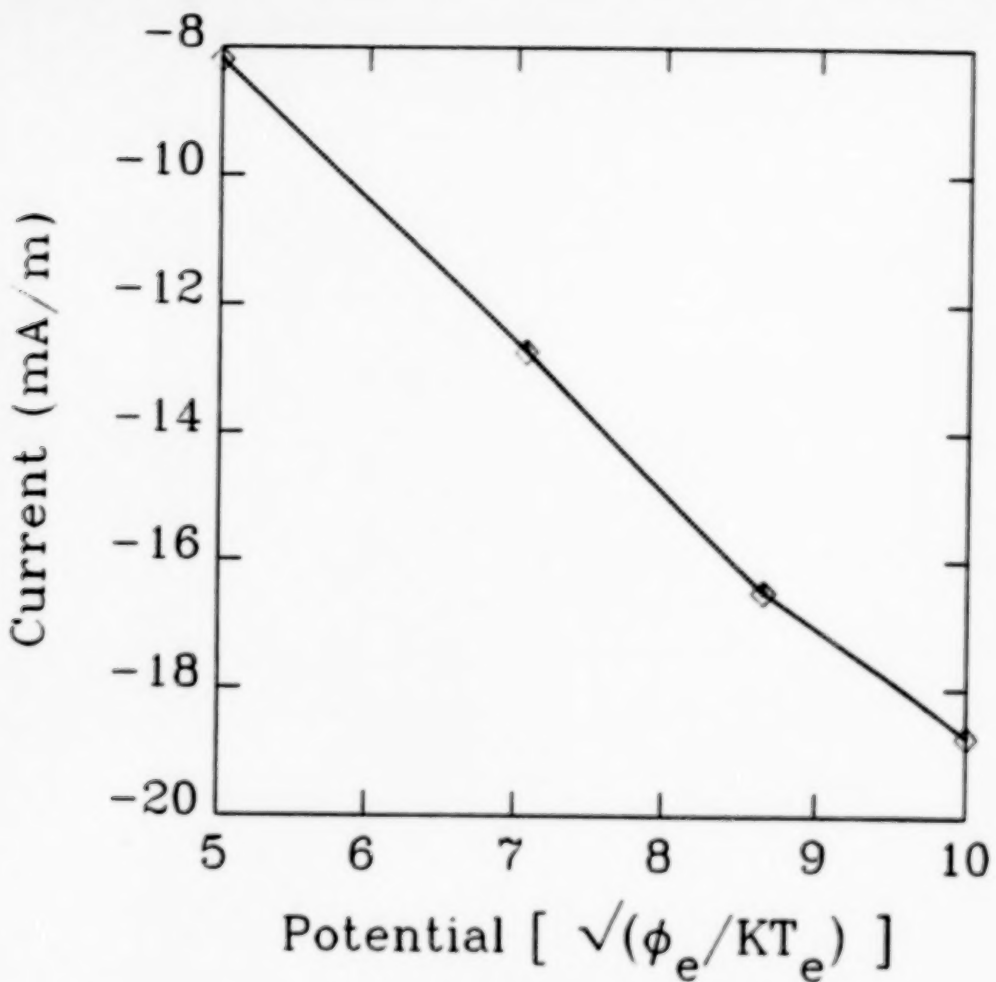
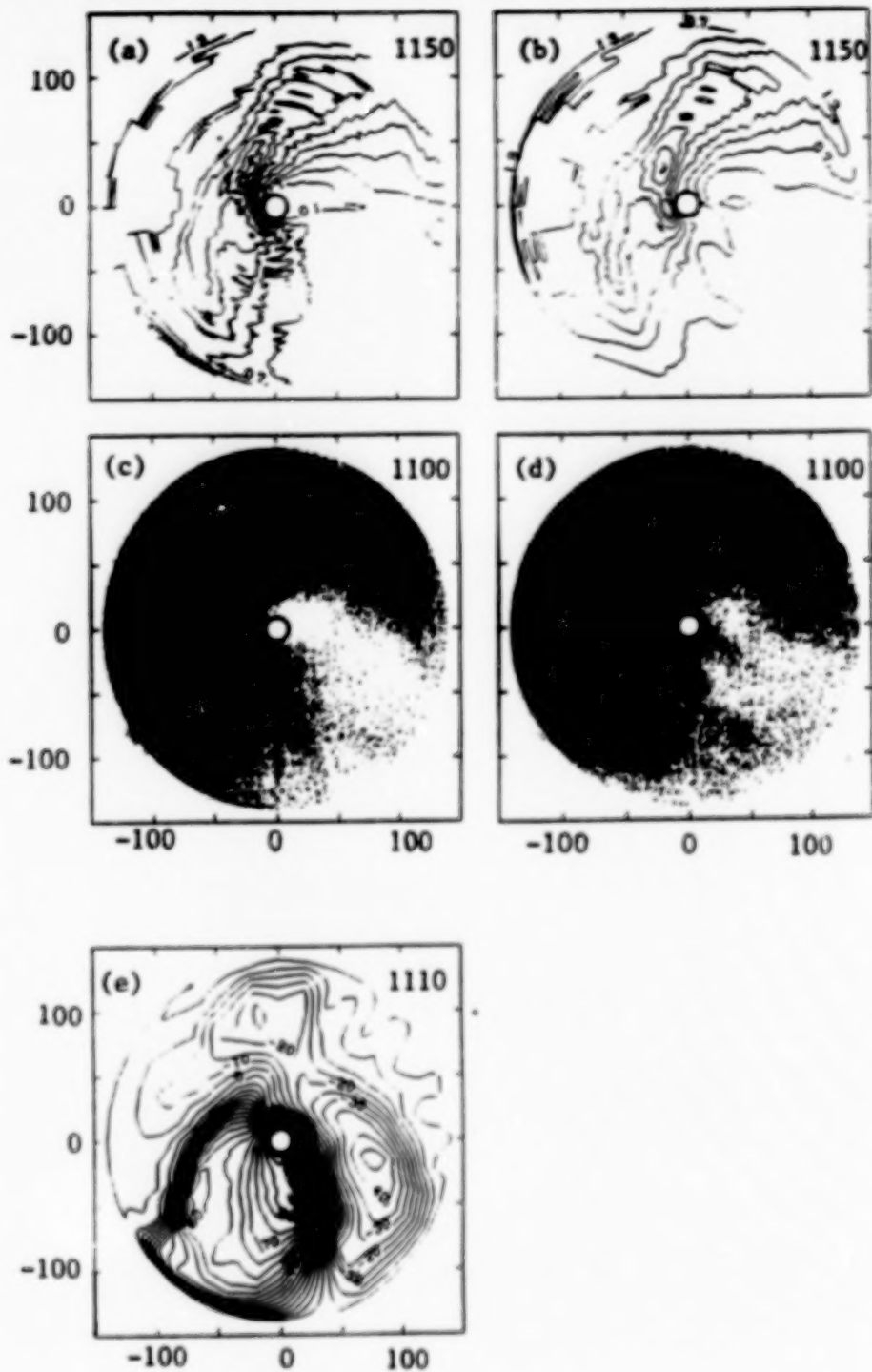


Figure 6. I-V characteristic of the cylinder. Note that the horizontal axis is  $\phi_0^{1/2}$ . The current variation shows the linear relation  $I \propto \phi_0^{1/2}$ .  $\bar{V}_0 = 0.3$ ,  $B = 0$ .

#### 4.2 Simulation with $B = B_z = 0.3$ G and $\tilde{\phi}_0 = 100$

We do not show the temporal evolution of the plasma and potential here, instead we just present here the quasi-steady state distribution of the plasma and potential around the cylinder. The top two panels of Figure 7 show the contours of constant ion and electron densities. The corresponding distributions of the particles in the  $r-\theta$  plane are shown by the two middle panels. The bottom single panel shows the distribution of potential; equipotential surfaces at intervals of  $\Delta\phi = 5$  are shown. It is worth pointing out that the plasma and potential distributions for  $B_z = 0.3$  Gauss is quite different from those for  $B = 0$ . In the former case ( $B_z = 0.3$  Gauss), the equipotentials show a multicell convection pattern [6]. The fan-shaped structure extending below the cylinder is the



**Figure 7.** Quasi-steady state feature of the plasma (a) Ion density distribution, (b) electron density distribution. The contour levels in (a) and (b) are  $\Delta \bar{n} = 0.3$  apart. (c) spatial distribution of ions, (d) spatial distribution of electrons, (e) distribution of potential; equipotential surfaces are  $\Delta \bar{\phi} = 5$  apart.  $\bar{\phi}_0 = 100$ ,  $B = 0$ ,  $\bar{V}_0 = 0.3$ .

consequence of the stagnation of the plasma flow below the cylinder due to the opposition to the flow by the  $E \times B$  drift in the initial radial electric field [6]. The fan-shaped equipotentials cause electrons to circulate around the cylinder due to the  $E \times B$  drift. The electron flow coming from the left is caught in this convection cell and focused on to the cylinder as shown by the crowded equipotentials immediately on the top of the cylinder. This circulation of the flowing electrons facilitates their collection by the cylinder.

The temporal evolution of the current collected by the cylinder with the axial field  $B_z$  is shown in Figure 8. The current is seen to reach a quasi-steady state at about  $t \approx 700$ , after which its average value  $I \approx 14 \text{ mA/m}$ , which is only slightly lower than 18 mA/m for  $B = 0$ . The simulation with the axial magnetic field shows that the magnetic insulation due to  $E \times B$  drift in the initial radial electric field is destroyed due to the considerable modification of the potential distribution caused by the plasma flow [6].

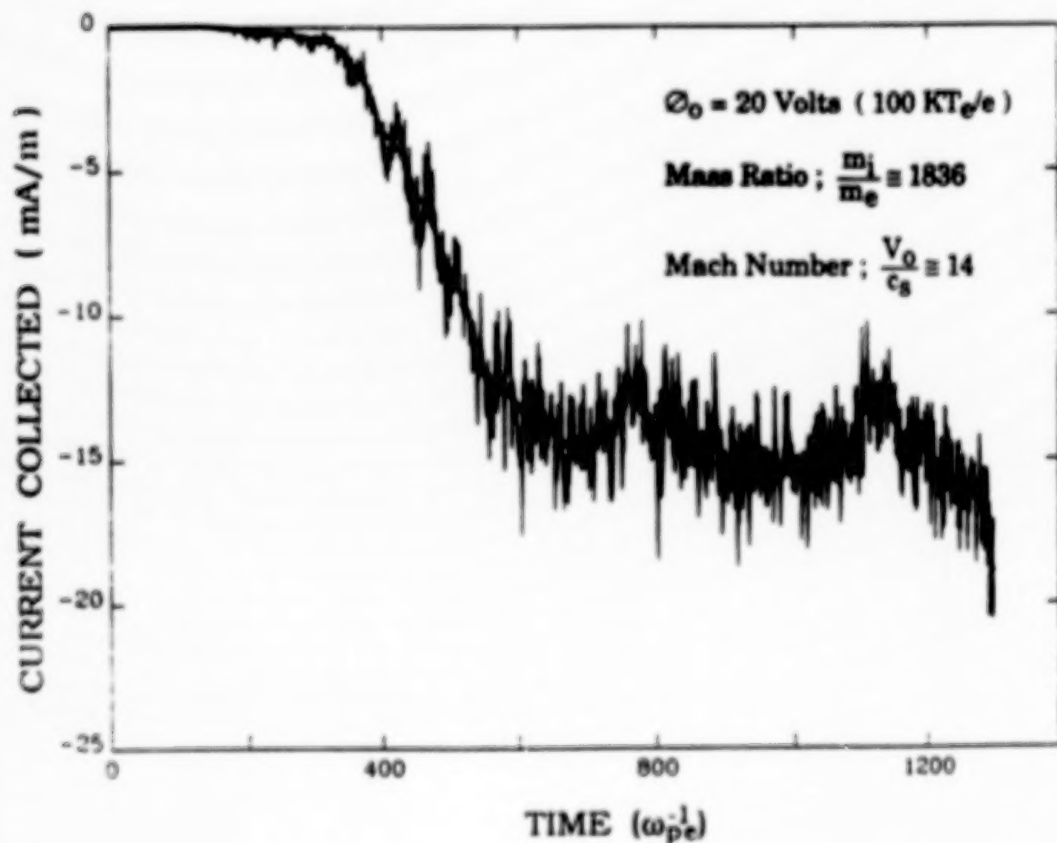


Figure 8. Temporal evolution of the current for  $B_z = 0.3 \text{ G}$ ,  $\phi_0 = 100$  and  $\bar{V}_0 = 0.3$ .

#### 4.3 Simulation with $B = B_y = 0.3$ Gauss, and $\bar{\phi}_0 = 50$

Note that in this case the magnetic field is in the plane of the simulation. This allows us to study the B field-aligned potential structures. The quasi-steady state distributions of the plasma and potentials are shown in Figure 9. The top two panels show the contours of the ion and electron densities. The corresponding distributions of ions and electrons in the  $r-\theta$  plane are shown in the middle panels. The wake structure is clearly seen from these panels. In the ram direction the plasma is generally uniform with the normalized density  $\bar{n} = 1$ . The bottom panels show the equipotential surfaces from simulation with  $\bar{\phi}_0 = 50$  (left) and  $\bar{\phi}_0 = 25$  (right). These bottom panels show that the potential distributions are extended along the magnetic field. When  $\bar{\phi}_0 = 50$ , the potential structure is seen to extend all the way to the boundary of the simulation plasma. In order to examine the effect of the boundary the simulation was repeated by lowering  $\bar{\phi}_0$  to 25 and increasing the size of the system from  $\bar{R}_{\max} = 140$  to 185. The result is shown in the bottom right-hand panel. It is seen that potential structure is now nearly fully accommodated in the simulation region.

It is interesting to examine the size ( $L_\perp$ ) of the potential structure transverse to the magnetic field. Figure 10 shows the radial distribution of the potentials for  $\bar{\phi}_0 = 50$  and 25 in the ram direction ( $\theta = 180^\circ$ ). It is seen that the potential structure becomes narrower with increasing  $\bar{\phi}_0$ . The radial distances at which  $\phi = 0$  for the above bias voltages are given by

$$L_\perp \approx 25 \lambda_d, \bar{\phi}_0 = 25 \quad (9a)$$

$$L_\perp \approx 31 \lambda_d, \bar{\phi}_0 = 50 \quad (9b)$$

Parker and Murphy [1] have considered the collection of electrons by a positive sphere. Using conservation of energy and angular momentum, they have shown that in the case of non-flowing plasma, the electrons which are possibly collected by the sphere, are confined in a cylinder of radius  $r_0$  as shown in Figure 11, where  $r_0$  is given by

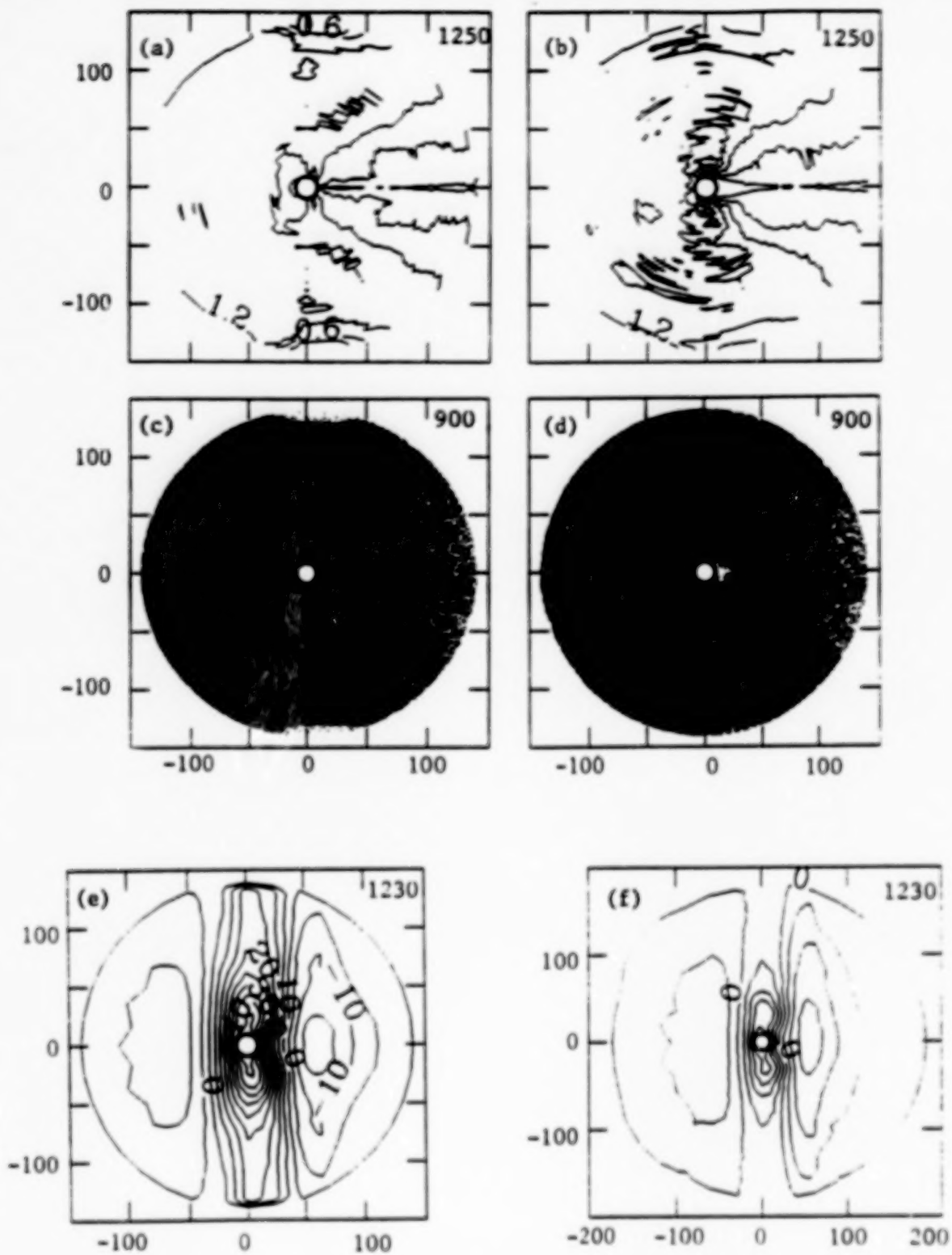


**Figure 9.** Quasi-steady state distributions of (a) electron density, (b) ion density, (c) electrons, (d) ions, (e) potential for  $\tilde{\phi}_0 = 50$ ,  $\tilde{V}_0 = 0.3$ ,  $B = B_y = 0.3$  Gauss, and (f) potential distribution for  $\tilde{\phi}_0 = 25$ ,  $\tilde{V}_0 = 0.3$ ,  $B = B_y = 0.3$  Gauss in a simulation with larger system size.

$$r_0 = [1 + \frac{2\rho_{e\phi}}{a}]^{1/2} a$$

$$\approx \sqrt{2\rho_{e\phi}a}, \quad \rho_{e\phi} \gg a \quad (10)$$

where  $\rho_{e\phi}$  is the electron Larmor radius with the electron energy  $e\phi_0$ . It is interesting to note that the value of  $L_\perp$  estimated above for  $\phi_0 = 25$  and 50 are quite accurately given by (10), with  $a$  as the radius of the cylinder.

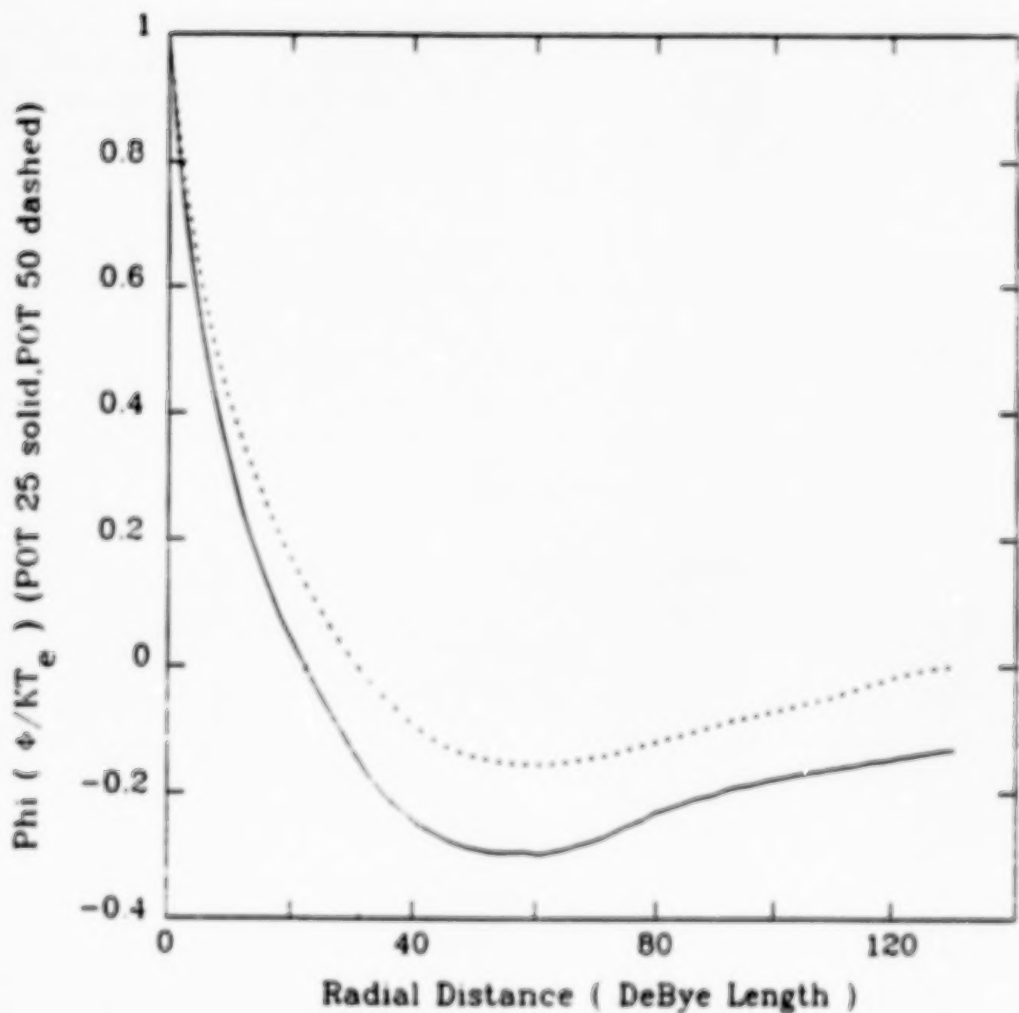


Figure 10 Radial distributions of potential for  $\phi_0 = 50$  and 25 in the ram direction ( $\theta = 180^\circ$ ).  $B = B_y = 0.3$  Gauss.  $\bar{V}_0 = 0.3$ .

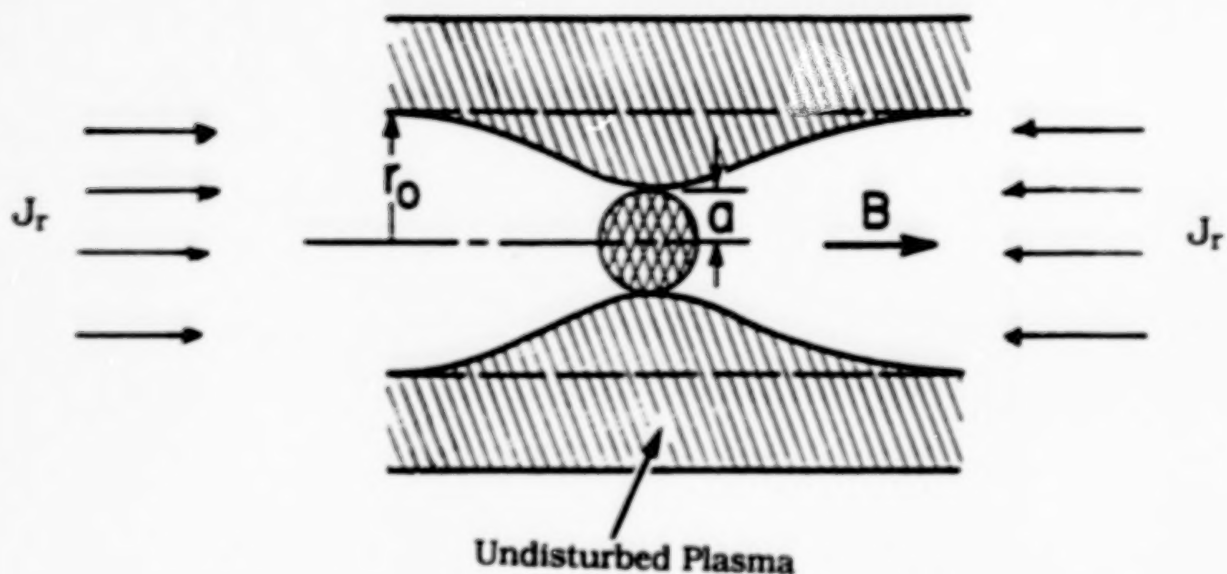


Figure 11 Geometry of the Parker-Murphy model for the current limitation. Electrons contained inside the cylindrical volume of radius  $r_0$  are possibly collected by the electrode at a positive potential.

According to the Parker-Murphy model the current collected by the spherical electrode in a non-drifting plasma is simply the electron flux intercepted by the cylinder of radius  $r_0$  (Figure 11):

$$I_{PM} = 2\pi r_0^2 J_r \quad (11)$$

where  $J_r$  is the electron thermal current given by  $J_r = N_0 e V_{te} / \sqrt{2\pi}$ . In the present situation,  $J_r$  is associated with the thermal motion along the  $y$  direction parallel to  $B_y$ .

We find that for the flow in a direction transverse to the extended potential structure, the current is considerably enhanced. If the current was collected primarily through the two ends of the potential structures (Figures 9e and 9f), the total electron current collected by the cylinder is given by

$$I_{PM} = 2 * 2r_0 J_r \text{ A/m} \quad (12)$$

which is only about 1.2 mA/m for  $\phi_0 = 25$ . Our simulation shows a considerably larger collection of electron current. Figure 12 shows the evolution of the current collected by the

cylinder when  $\phi_0 = 25$ ; in the quasi-steady state the current is about 7.5 mA/m, which is found to be close to the current collected without the ambient magnetic field with the same drift velocity  $\bar{V}_0 = 0.3$  (Figure 6). The excess current ( $\sim 6.3$  mA/m) is interpreted in terms of the interception of the electron flow by the extended potential structure along the magnetic field.

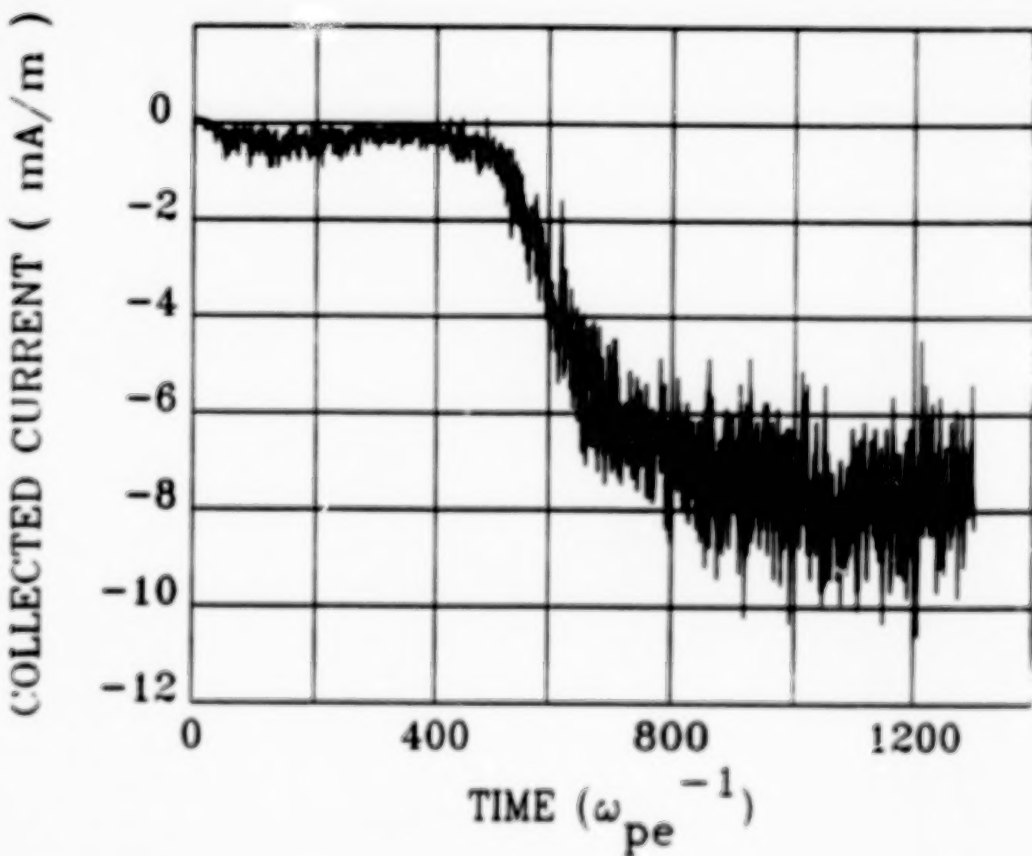


Figure 12 Temporal evolution of the current for  $B = B_y = 0.3$  Gauss,  $\bar{V}_0 = 0.3$ ,  $\phi_0 = 25$ .

#### 4.4 Simulation with $B = a_x B_0$

In order to examine the effects of relative orientation of the drift velocity with respect to the ambient magnetic field  $B_0$  in the simulation plane, we carried out another simulation with  $V_0 \parallel B_0$ . The potential structure for this case in the quasi-steady state is

shown in Figure 13. It is seen that now the potential structure is extended along  $x$ , the direction of the  $B$  field. Its transverse dimension  $L_x$  is again found to be limited according to (10), which gives the current limiting Parker-Murphy radius as a function of the bias voltage  $\phi_0$ . The temporal evolution of the collected current for  $B = \hat{a}_x B_0$  is shown in Figure 14a. For the purpose of comparison, the current with  $B_y$  is plotted in Figure 14b for the same value of  $\phi_0 = 50$ . Note the different vertical scales in Figures 14a and 14b. It is seen that for the flow along  $B$ , the current is significantly reduced compared to the case with flow transverse to  $B$ . As noted earlier, in the later case the interception of the flow by the elongated potential structure enhances the current.

It is instructive to quantitatively compare the current from the Parker-Murphy model with that from the simulation with  $B_x$ . We already saw that the former current is

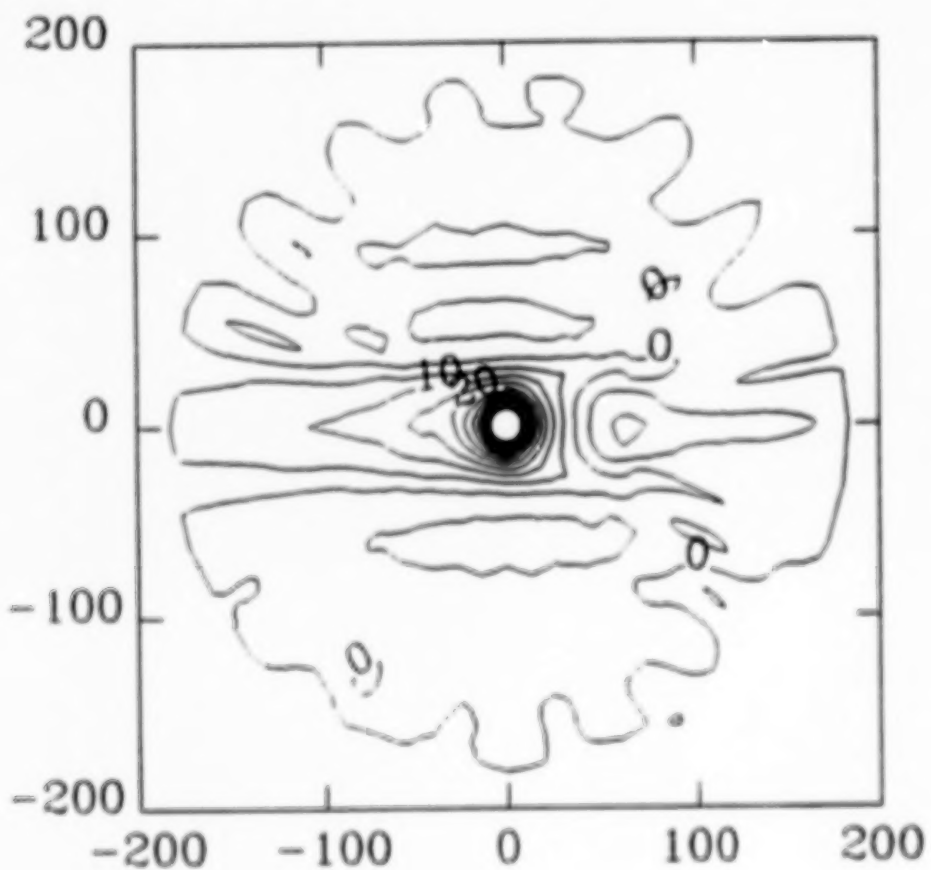


Figure 13     Quasi-steady state potential distribution for  $B = B_x = 0.3$  Gauss,  $\dot{V}_0 = 0.3$ ,  $\bar{\phi}_0 = 50$ .

given by (12). However, a few observations must be made while using this expression in the present case. The flow along the magnetic field makes the potential structure asymmetric with respect to  $x = 0$  because of the formation of the wake behind the cylinder, making the first factor of 2 in (12) inaccurate. The use of this factor will give an overestimate. Furthermore,  $J_r$  in (12) must be replaced by a modified current density due to the plasma flow; for the flow velocity  $V_0 = 0.3 V_{te}$ , this modified current density  $J_e = 1.44 J_r$ . With these considerations, (12) gives  $I_{PM} < 2.2 \text{ mA/m}$ . Figure 14 shows that the time average current is about  $3.5 \text{ mA/m}$ , which is at least 60% larger than the current predicted from the Parker-Murphy model. The enhancement in the current suggests the transport of electrons across the magnetic field line. The exact mechanism for the cross-field electron transport has not been identified from the simulations. However, cross-field diffusion due to the fluctuations in the field need to be examined [7].

## 5. CONCLUSIONS AND DISCUSSION

The main conclusions of this paper are as follows:

- (i) When the relative plasma flow is transverse to the magnetic field, the current collected by a positive electrode can be considerably enhanced depending on the relative drift velocity.
- (ii) For the flow along the magnetic field, the current is limited as predicted by the Parker-Murphy model [1].
- (iii) Simulations with  $B$  in the simulation plane show that the magnetic field-aligned potential structure is like a double layer with dimensions transverse to the magnetic field determined by the limiting radius given by the Parker-Murphy model [1], but it is extended along the field line.
- (iv) Simulation with the axial magnetic field shows that the potential structure represents a multi-cell convection pattern. The fan-shaped cell is seen to focus the electron flow on to the cylinder thus destroying the magnetic insulation effect.

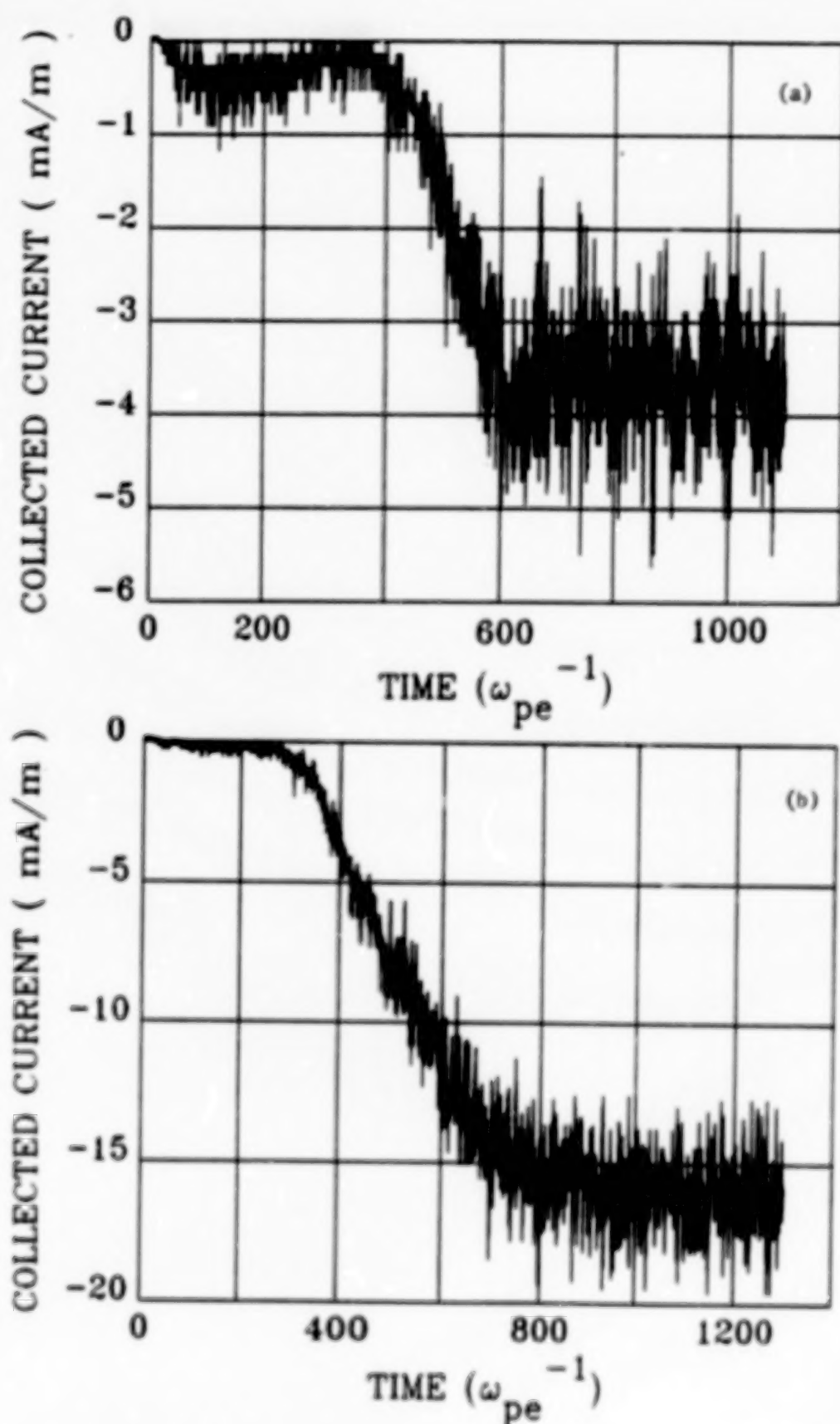


Figure 14 Temporal evolution of the current for (a)  $B = B_x = 0.3$  Gauss,  $\hat{V}_0 = 0.3$ ,  $\hat{\phi}_0 = 50$ . (b)  $B = B_y = 0.3$  Gauss,  $\hat{V}_0 = 0.3$ ,  $\hat{\phi}_0 = 50$ .

(v) In the low earth orbit, the orbital motion is nearly perpendicular to the magnetic field, and the relative flow velocity  $V_0 \approx 8$  km/s, which can considerably enhance the current collection.

\* In a real situation with an arbitrary orientation between  $B_0$  and  $V_0$ , the potential structure will be the combinations of the structures shown in this paper.

Recently Myers et al. [8] have demonstrated that the measured currents in a rocket experiment agree well with the predictions from the Parker-Murphy model [1]. Raitt et. al [this volume] have carried out a similar comparison. Since in the rocket experiments the relative drift velocities are only a few hundred meters per second, the current enhancement due to the relative drift is not expected to be significant.

In our present simulations plasma flows while the electrode is standing. In space the electrode cuts across the magnetic field lines. This raises some question about the dynamical effects. We note that in the simulations starting with an initial vacuum state, the quasi-equilibrium is reached quite quickly in a time of about  $500\omega_{po}^{-1} \approx 30 \mu s$ . In real situations of space the quasi-equilibrium condition are expected to reach in a considerably shorter time. On the other hand, the contact time of a current collector with a magnetic flux tube depends on its sheath size. If we use the sheath size as given by (10) for large electrode voltages, the contact time  $\tau_c$  can be estimated by

$$\tau_c = 2\sqrt{\rho_e \phi^3} / V_0$$

Using typical parameters ( $\phi_0 = 100$  V,  $a = 1$  m,  $B = 0.3$  G and  $V_0 = 8$  km/s) it is found that  $\tau_c \gtrsim 250 \mu s$ . Comparing this time with the sheath establishment time of the order of a few tens of microseconds, it is inferred that the quasi-equilibrium conditions for the potential structure and the current collection as found from the simulations are likely to be maintained for a current collecting electrode in the low earth orbit.

## 6. ACKNOWLEDGEMENT

This work was supported by NASA Grant NAGW-1562. The simulation code was developed under a grant from the CRAY Research Inc.

## REFERENCES

- [1] Parker, L.W. and B.L. Murphy, Potential Buildup of an Electron-Emitting Ionospheric Satellite, *J. Geophy. Res.*, 72, 1631, 1967.
- [2] Morse, R.L., Multidimensional Plasma Simulations by Particle-in-Code Methods, in *Computational Physics*, edited by Alder, Fernbach and Rotinberg, 9, 213, Academic Press, New York, Vol. 9, 213, 1970.
- [3] Aldrich, C.H., Particle Code Simulations Using Injected Particles, in *Space Plasma Simulations*, ed. by M. Ashour-Abdalla and D.A. Dalton, D. Riedel Publ. Comp., Boston, p. 131, 1985.
- [4] Thiemann, H., N. Singh, R.W. Schunk and R. Grard, Numerical Simulation of Spacecraft Charging by Impact-Produced Plasmas During a Cometary Flyby, *J. Geophy. Res.*, 91, 2989, 1986.
- [5] Chen, F.F., *Plasma Diagnostic Techniques*, edited by R.H. Huddlestone and S.L. Leonard, Chapt. 4, Academic Press, New York, 1964.
- [6] Singh, N. and B.I. Vashi, Current Collection by a Long Conducting Cylinder in a Flowing Plasma, AIAA 90-0724, Jan. 8-11, 1990/Reno, Nevada.
- [7] Linson, L.M., Current-Voltage Characteristics of an Electron-Emitting Satellite in the Ionosphere, *J. Geophys. Res.*, 74, 2368, 1969.
- [8] Myers, M.B., W.J. Raith, B.E. Gilchrist, P.M. Banks, T. Neubert, P.R. Williamson and S. Susaki, A Comparison of Current-Voltage Relationships of Collectors in the Earth's Ionosphere with and without Electron Beam Emission, *Geophys. Res. Lett.*, 16, 365, 1989.

# Current Collection in an Anisotropic Plasma

Wei-wei Li

Center for Astrophysics and Space Sciences  
University of California at San Diego, La Jolla, CA 92093

**Abstract.** A general method is given to derive the current-potential relations in anisotropic plasmas. Orbit limit current is assumed. The collector is a conductive sphere or an infinite cylinder. Any distribution which is an arbitrary function of the velocity vector can be considered as a superposition of many mono-energetic beams whose current-potential relations are known. The results for two typical pitch angle distributions are derived and discussed in detail. The general properties of the current potential relations are very similar to that of a Maxwellian plasma except for an effective temperature which varies with the angle between the magnetic field and the charging surface. The conclusions are meaningful to generalized geometries.

## The Introduction

The current collection from incoming particle is a fundamental problem in charging theory. In this paper the current collection in anisotropic plasmas is studied. The analytic expressions for current potential relations which have been used so far are derived from Maxwellian distribution.

Here the basic current potential relation for Maxwellian plasma are repeated briefly. These well known results will be compared to that of anisotropic plasma frequently in rest part of this paper. The orbit limited current to a spherical conductor or cylindrical conductor for repelled particles is (Mott-Smith and Langmuir 1926; Prokopenko and Laframboise 1977,1980;):

$$I = I_o e^{-\beta} \quad (1)$$

For attractive particle, the charging current is:

$$I = I_o(1 + \beta) \quad (2)$$

for a spherical conductor and the following:

$$I = I_o(2/\sqrt{\pi})(\sqrt{\beta} + \frac{1}{2}\sqrt{\pi}e^{\beta} \int_{\sqrt{\beta}}^{\infty} e^{-t^2} dt) \quad (3)$$

for a cylinder.

Charging currents to satellites in anisotropic plasmas have not been discussed systematically. The real distributions of the plasmas at synchronous orbit may be very different from Maxwellian. For example, the pitch angle distributions in the earth magnetic field are very common. In this paper, the current collection in

anisotropic plasmas is studied to see how it would be deviate from that in isotropic plasma.

In order to discuss the variety of distributions, all other conditions are assumed as simple as possible:

- 1) The effect of space charge is neglected. Orbit limited current is assumed.
- 2) The distribution function can be an arbitrary function of the velocity vector but it does not depend on the spacial location. The currents from two distributions are derived in this paper:

a.

$$f(\bar{v}) = N \left( \frac{m}{2\pi k} \right)^{\frac{3}{2}} / T_{\parallel}^{\frac{1}{2}} T_{\perp} e^{-\frac{1}{2} m \frac{v^2}{k T_{\parallel}} - \frac{1}{2} m \frac{v^2}{k T_{\perp}}} \quad (4)$$

$T_{\parallel}$  and  $T_{\perp}$  mean the directions related to the magnetic field.

b. A source cone or a loss cone in a Maxwellian distribution function.

- 3) The probe is a conducting sphere or an infinite cylinder.
- 4) VXB force is neglected. The role played by the magnetic field is only to indicate the direction of the anisotropy.
- 5) Plasma is collisionless.

The above assumptions are reasonable for satellites at the synchronous orbit.

A distribution function of plasma and its current to a charged conductor can be separated and superposed. the plasma are separated into many monoenergetic beams whose charging currents are known. The currents to a sphere conductor  $I_p$  from such a beam are( Mott-Smith and Langmuir 1926 ):

$$I_p = I_o (1 + e\phi/E) = \pi R^2 i (1 + e\phi/E) \quad (5)$$

for attracted particle, the following:

$$I_p = I_o (1 - e\phi/E) = \pi R^2 i (1 - e\phi/E) \quad (6)$$

for repelled particle with  $E > e\phi$ . When  $E < e\phi$ ,  $I_p = 0$

Here

$$\beta = \frac{e\phi}{kT}$$

The "e" is the magnitude of a electron charge.

$e\phi$  is the potential energy at the surface.

k is the Boltzmann's constant.

T is the temperature of the plasma

$I_0$  is the current to a uncharged probe. I and  $I_0$  are define as total current for the sphere and refer to the current per unit length for the cylinder.

$$I_0 = \text{area} \times \sqrt{\frac{kT}{2\pi m}}$$

m is the mass of a ion.

E is the kinetic energy of a particle at infinity.

The i is the current density of the beam.

R is the radius of the sphere.

The equation (4) and (5) simply comes from the energy conservation and the angular momentum conservation.

The basic assumption is that particles which carry maximum angular momentum and still reach the sphere are the grazing particle. This may not be true for attracted particles if the space charge effect is included (Laframboise 1965 Fig 4d). Therefore the condition for equation (4) and (5) is that current be orbit limited.

Similar relations hold for the cylinder:

$$I = I_0 \sqrt{1 + e\phi/E} = 2R i \sqrt{1 + e\phi/E} \quad (7)$$

for attracted particle and the following:

$$I = I_0 \sqrt{1 - e\phi/E} = 2R i \sqrt{1 - e\phi/E} \quad (8)$$

for repelled particles with  $E > e\phi$  when  $E < e\phi$ ,  $I_p = 0$

The assumption and derivation of (7) and (8) is the same as equation (5) and (6). Caution should be observed: If the beam is not perpendicular to the axis of the cylinder, the  $i$  in (7) and (8) is not the current density of the beam but is the component perpendicular to the axis at infinity. Also the  $E$  is not the total kinetic energy of the particle but the kinetic energy in the direction perpendicular to the axis. Integrating of these beam with weight of distribution function leads to the total charging current of incoming plasma. The integral is carried out in the plasma frame. The superposition method will be illustrated in more detail in next section.

### The Result of the Current-potential Relations

It is more convenient to use dimensionless quantities:

$I_0$  : the current to an uncharged conductor

$I/I_0$ : Dimensionless charging current

$\beta$  : Nondimensional potential  $\beta = e\phi/kT_{\perp}$  or  $e\phi/kT$

$k$  : the Boltzmann's constant.

$T$  : the temperature of the plasma

#### The current to a attracting sphere from a two temperature plasma.

The "i" in equation (4) is the current density of the beam at infinity. It is equal to the density times the velocity. Now the density should be replaced by the number of particles in a infinitesimal volume in velocity space  $f(\bar{v})d^3(\bar{v})$ .  $f(\bar{v})$  is the distribution function (4)

The current to the charged sphere is:

$$I = \int \int \int f(\bar{v})V(1 + e\phi/E)d^3(\bar{v})S \quad (9)$$

Here  $S = \pi R^2$

$$d^3(\bar{v}) = V^2 d\phi \sin\theta d\theta dV$$

The angle  $\theta$  and  $\phi$  indicate the directions of particles at infinite.  $\theta$  is the polar angle of the velocity.  $\phi$  is the azimuthal angle of the velocity. All quantities are defined in the plasma frame. The distribution function  $f(\bar{v})$ , the velocity  $V$ , and the kinetic energy  $E$  are the values at infinity(i.e. in the plasma frame). The integral is carried out in the plasma frame.

$$\begin{aligned} I &= Ne\pi R^2 \left( \frac{m}{2\pi k} \right)^{\frac{1}{2}} / T_{\parallel}^{\frac{1}{2}} T_{\perp} \int_0^{\infty} dV \int_0^{2\pi} d\phi \int_0^{\pi} \sin\theta d\theta \\ &\times \left( 1 + \frac{e\phi}{\frac{1}{2}mV^2} \right) V^3 e^{-\frac{1}{2}mV^2 \left( \frac{\sin^2\theta}{kT_{\parallel}} + \frac{\cos^2\theta}{kT_{\perp}} \right)} \end{aligned}$$

Define

$$B = \frac{2 A}{m^2} = Ne R^2 \left( \frac{2\pi}{m} \right)^{\frac{1}{2}} / T_{\parallel}^{\frac{1}{2}} T_{\perp} \quad (10)$$

$$K(\theta) = \frac{\sin^2\theta}{kT_{\parallel}} + \frac{\cos^2\theta}{kT_{\perp}} \quad (11)$$

$$E = \frac{1}{2}mV^2$$

$$I = B \int_0^{\infty} dE \int_0^{\pi} \sin\theta d\theta E (e^{-E K(\theta)} + e\phi e^{-E K(\theta)}) \quad (12)$$

Define  $I_0$  as the current to an uncharged sphere.

$$I_0 = 2\pi R^2 N \sqrt{\frac{kT_{\parallel}}{2\pi m}} \left( 1 + \frac{1}{2} \frac{CD}{\sqrt{|1-C|}} \right) \quad (13)$$

$$\text{Here } C = \frac{T_{\perp}}{T_{\parallel}}$$

$$D = 2 \operatorname{tg}^{-1} \sqrt{C-1} \text{ if } T_{\perp} > T_{\parallel}$$

$$D = \ln \frac{1+\sqrt{1-C}}{1-\sqrt{1-C}} \text{ if } T_{\perp} > T_{\parallel}$$

Define the effective Temperature as:

$$T_f = T_{\perp} \left( \frac{\sqrt{|1-C|}}{CD} + \frac{1}{2} \right) \quad (14)$$

The current to a charged sphere becomes

$$I = I_0 (1 + e\phi/kT_f) \quad (15)$$

The dimensionless current are plotted in Fig. 1 as the function of the dimensionless potential for different values of  $T_{\perp}/T_{\parallel}$  which is the indication of the

anisotropy. The lower curves correspond to lower  $T_{\parallel}$ . The curves are simply straight lines. The different slopes of the curves is calculated by equation (14). The form of current-potential relation is similar to the one of the Maxwellian plasma equation (2). The the relation between the current and the potential is linear. From equation(5), the current potential relation is linear for a beam to a sphere. Therefore the superposition of the beams is also linear. This is clear according to equation(13). The change of the charging current is :

$$\Delta I = I - I_0 = e\phi \int f(\bar{V}) \frac{V}{E} d^3\bar{v}$$

The current to a uncharged probe is:

$$I_0 = \int f(\bar{V}) V d^3\bar{v}$$

$$\Delta I/I = e\phi \frac{\int \frac{V}{E} f(\bar{V}) d^3\bar{v}}{\int f(\bar{V}) V d^3\bar{v}}$$

If we write

$$\Delta I/I = \frac{e\phi}{T_f}$$

The change of the current is proportional to the potential. The quantity  $T_f$  is independent of the potential and has the unit of energy. So we have the definition of  $T_f$ :

$$T_f = \frac{\int f(\bar{V}) V d^3\bar{v}}{\int \frac{1}{2m} V^2 f(\bar{V}) V d^3\bar{v}}$$

If the distribution function is Maxwellian.  $T_f$  identifies with the temperature. In an anisotropic plasma,  $T_f$  is related to the energy in the direction perpendicular to the surface. It is a combination of  $T_{\perp}$  and  $T_{\parallel}$ . Its values lie between  $T_{\perp}$  and  $T_{\parallel}$  and is more close to  $T_{\perp}$  since  $T_{\perp}$  corresponds to two dimensions while  $T_{\parallel}$  only corresponds to one dimension.

### The current to a repelling sphere of two temperature plasma

Starting from equation (12). I changed the lower limit of the integral and the sign before  $e\phi$

$$I = B \int_{e\phi}^{\infty} dEE (e^{-E K(\theta)} - e\phi e^{-E K(\theta)}) \sin\theta d\theta$$

Here B is defined by equation (10)  $K(\theta)$  is defines by equation (11) The charging current is:

$$I = 2\pi R^2 \sqrt{\frac{kT_{\perp}}{2\pi m}} \left( \frac{T_{\perp}}{T_{\parallel}} \right)^{\frac{1}{2}} \int_{-1}^1 dX \frac{e^{-e\phi G X^2}}{(1 - G kT_{\perp} X^2)^2} e^{-\frac{e\phi}{K T_{\perp}}} \quad (16)$$

Here  $G = \frac{1}{kT_1} - \frac{1}{kT_{\parallel}}$ , Define  $\beta = e\phi/kT_1$

$$I/I_0 = e^{-\beta} \frac{C^{\frac{1}{2}}}{1 + \frac{1}{2} \frac{CD}{\sqrt{1-C}}} \times \int_{-1}^1 dX \frac{e^{-e+\beta G X^2}}{(1 - G kT_1 X^2)^2} \quad (17)$$

$I_0$  is the current to an uncharged sphere defined by equation (12)

In Fig.2 the dimensionless current  $I/I_0$  is plotted as the function of dimensionless potential  $e\phi/kT_1$ . Each figure correspond to a different ratio of  $T_1/T_{\parallel}$ . The shapes of the curves are very similar to the exponential form of Maxwellian. The logarithm scale is used for dimensionless current to show this similarity.

#### The current collected by a sphere from a plasma with a loss cone

For repelled particles,

$$I = Ne\pi R^2 \left(\frac{m}{2\pi kT}\right)^{\frac{3}{2}} \int_{\sqrt{\frac{2e\phi}{m}}}^{\infty} dV_r \times e^{-\frac{\frac{1}{2}m V^2}{kT}} \int_0^{2\pi} d\phi \int_{\theta_0}^{\pi-\theta_0} \sin\theta d\theta$$

$\theta_0$  is the angle of loss cone

$$I = I_{om} e^{-\frac{e\phi}{kT}} \cos\theta_0$$

Here  $I_{om}$  is the current to a uncharged sphere in a Maxwellian plasma.

$$I_{om} = I = 4\pi R^2 \sqrt{\frac{kT_1}{2\pi m}}$$

The Current to an uncharged sphere  $I_0$  is

$$I_0 = I_{om} \cos\theta_0$$

$$I/I_0 = e^{-\frac{e\phi}{kT}} \quad (18)$$

For attracted Particles

$$I = Ne\pi R^2 \left(\frac{m}{2\pi kT}\right)^{\frac{3}{2}} \int_0^{\infty} dV_r \ e^{-\frac{\frac{1}{2}m V^2}{kT}} \left(1 + \frac{e\phi}{\frac{1}{2}m V_r^2} V_r^3\right) \int_0^{2\pi} d\phi \int_{\theta_0}^{\pi-\theta_0} \sin\theta d\theta$$

$$I = I_{om} \left(1 + \frac{e\phi}{kT}\right) \cos\theta_0$$

$$I_0 = I_{om} \cos\theta_0$$

$$I/I_0 = 1 + \frac{e\phi}{kT} \quad (19)$$

The  $I - \phi$  relation is exactly the same as Maxwellian plasma. This conclusion can be generalized to any pitch angle distribution if the angle dependence is separated from energy dependence. i.e.  $f(\bar{v}) = f(\theta, \phi) \times f(E)$  This result

supports the condition that the angle preference of a distribution function does not change the  $I - \phi$  relation for a spherical conductor if the energy dependence of the distribution is the same as the Maxwellian distribution.

### The current to a cylinder in a two temperature plasma.

Define the coordinates as shown in Fig. 3. The axis of the cylinder is defined as the Z direction. X axis is in the plane of B field and axis of the cylinder. The magnetic field is parallel to the plane with azimuthal zero. The polar angle of B field is  $\theta_0$ . The azimuthal angle of the velocity is  $\phi$ . The polar angle of the velocity is  $\theta$ .  $\parallel$  and  $\perp$  in The  $V_s$  is the velocity component in the direction of axis of the cylinder.  $V_r$  is the velocity perpendicular to the axis.

$$I = 2NeR\left(\frac{m}{2\pi k}\right)^{\frac{1}{2}}/T_{\parallel}^{\frac{1}{2}}T_{\perp} \int_0^{\infty} dV_s dV_r f_0^{2\pi} d\phi \int_{\sqrt{\frac{2e\phi}{m}}, 0}^{\infty} \sqrt{1 \pm \frac{e\phi}{\frac{1}{2}mV_r^2}} V_r^2$$

$$\times e^{-\frac{1}{2}m\frac{V_r^2}{T_{\parallel}} - \frac{1}{2}m\frac{V_r^2}{T_{\perp}}}$$

in  $\int_{\sqrt{\frac{2e\phi}{m}}, 0}^{\infty}$  use  $\sqrt{\frac{2e\phi}{m}}$  for repelled particles, use 0 for attracted particles.

$$I = 2NeR\sqrt{\frac{2k}{m}}/T_{\parallel}^{\frac{1}{2}}T_{\perp} \sqrt{\frac{2\pi}{m\left(\frac{\cos^2\theta_0}{kT_{\parallel}} + \frac{\sin^2\theta_0}{kT_{\perp}}\right)}} \int_{\pm\sqrt{\frac{2e\phi}{m}}}^{\infty} \sqrt{e\phi \pm E_r} e^{-\frac{E_r}{kT_{\perp}} b} I0(b) dE_r \quad (20)$$

Here  $I0$  is the zero order first kind of Bessel function  $E_r = \frac{1}{2}mV_r^2$

$$b = E_r \sin^2\theta_0 \left(\frac{1}{T_{\parallel}} - \frac{1}{T_{\perp}}\right) \times \left(1 + \frac{\frac{1}{2}\cos^2\theta_0\left(\frac{1}{T_{\parallel}} - \frac{1}{T_{\perp}}\right)}{\frac{\cos^2\theta_0}{T_{\parallel}} + \frac{\sin^2\theta_0}{T_{\perp}}}\right)$$

$$I0 = 2NeR\sqrt{\frac{2}{m}/kT_{\parallel}^{\frac{1}{2}}T_{\perp}} \sqrt{\frac{2\pi}{m\left(\frac{\cos^2\theta_0}{kT_{\parallel}} + \frac{\sin^2\theta_0}{kT_{\perp}}\right)}} \int_0^{\infty} \sqrt{u} e^{-u(1+H)} I0(HU) dU \quad (21)$$

For  $H > 0$ . Here,  $U = E_r/T_{\perp}$   $E_r$  is the kinetic energy perpendicular to the surface of the cylinder.

$$H = 1 + \frac{\sin^2\theta_0(1-C)}{(C-1)\cos^2\theta_0 + \sin^2\theta_0} \quad (22)$$

$$C = \frac{T_{\perp}}{T_{\parallel}}$$

$\theta_0$  is the angle between the B field and the axis of the cylinder

$$I/I0 = \frac{\int_{\frac{2e\phi}{m}, 0}^{\infty} \sqrt{u \pm \beta} \times e^{-u(1+H)} I0(HU) dU}{\int_0^{\infty} \sqrt{u} e^{-u(1+H)} I0(HU) dU} \quad (23)$$

Here

$$\beta = \frac{e\phi}{kT_{\perp}}$$

$$C = \frac{T_{\perp}}{T_{\parallel}}$$

in  $\sqrt{U \pm \beta}$  use + for attracted particles. use - for repelled particles

See Fig.4 and Fig.5 In each figure the curves which change slower with potential correspond to higher  $T_{\parallel}$ . The angle effect is indicated by the H factor in equation(22). When the B field is parallel to the axis of the cylinder, H=0 and the  $I_0(Hu)$  in equation (23) approaches 1. The  $I - \phi$  relation is reduced to the form of Maxwellian plasma. In this situation the velocity parallel to the axis will not be changed by electric field and does not contribute to the charging current at all. Therefore  $T_{\parallel}$  does not appear in equation (23). While  $\theta_0$  decreases from  $90^{\circ}$  to 0, the motion parallel to B contributes less and less to the charging.  $T_{\parallel}$  becomes less important.

#### Current in a Maxwellian plasma within a small source cone

$$I_{\text{attract}}/I_0 = U e^U K_1(U) \quad (24)$$

$$I_{\text{repel}}/I_0 = U e^{-U} K_1(U) \quad (25)$$

Here  $U = e\phi/2T \sin^2\theta_0$ .  $K_1$  is the Third kind Bessel function of order one. If  $\theta_0$  is small current-potential relation behaves like a Maxwellian distribution with a lower temperature. If plasma come from a direction which is almost perpendicular to the surface, The curves behave like a Maxwellian plasma with a higher temperature.

See Fig.6 and Fig.7  $I/I_0$  is plotted as the function of  $e\phi/kT$ . A curves of Maxwellian distribution is plotted in each figure to be compared with source cone. The U factor in equation (25) and (26) shows that  $2T \sin^2\theta_0$  is the effective temperature.  $T_{\text{effect}}$  is less than T when  $\theta_0 < 45^{\circ}$ .  $T_{\text{effect}}$  is greater than T when  $\theta_0 > 45^{\circ}$ . The temperature of a Maxwellian plasma can be understood as the average of these  $T_{\text{effect}}$  over all direction.

I only calculated the  $I - \phi$  relation for a flow from a small solid angle, but the behavior of a wider source cone can be estimated from the result of the small solid angle. If the maximum angle between the axis and a beam within the wide solid angle is  $60^{\circ}$  and the minimum angle is  $30^{\circ}$ . The  $I - \phi$  curve of such a source cone should lie between the two curves corresponding to  $\theta^0 = 30^{\circ}$  and  $\theta^0 = 60^{\circ}$ .

#### The Discussion

### Arbitrary Distribution

There are other distributions such as a double Maxwellian and a monoenergetic beam plus a Maxwellian distribution function, for which charging currents are very easy to be obtained by using superposition. In general the method in this paper applies to any homogeneous distribution function. The only problem left is a mathematical one which refers to integrals of equation (5)-(8) in three dimensional space of canonical momenta. Sometime integrals have to be carried out numerically.

### The similarity to the Maxwellian plasma

The general properties of the current-potential curves of pitch angle distributions are very similar to that of the Maxwellian plasma. The current potential relations of attractive particle for a sphere is exactly linear as shown in Fig.1. For repelled particles the relation are almost exponential for both sphere and cylinder as shown in Fig.2,5 and 7.

### The importance of the effective temperature

While the energy of Maxwellian plasma is indicated by the the temperature, the energy of a pitch angle distribution in the charging problem refers to an effective energy in the direction perpendicular to the charged surface.

### The value of the effective temperature

For a pitch angle distribution defined by equation (1), The value of effective temperature is an average of  $T_{\perp}$  and  $T_{\parallel}$ . If the surface has no angle preference (a conducting sphere)  $T_{effect}$  is defined by equation (9).  $T_{\perp}$  contributes more to the average since  $T_{\perp}$  indicates the kinetic energy in two dimensions while  $T_{\parallel}$  is only related to the motion in one dimension. When the surface is parallel to the B field,  $T_{effect}$  will deviates from the value of equation (9) and move closer to the  $T_{\perp}$ . When the surface is perpendicular to the B field,  $T_{effect}$  will approach  $T_{\parallel}$ .

For the charging of a cylinder from a source cone of a Maxwellian plasma the  $T_{effect}$  equals the temperature of the Maxwellian distribution times an angle factor. The factor is less than 1 when the source cone makes a small angle with the surface. When the source cone is perpendicular to the surface, the  $T_{effect}$  will be greater than T.  $T_{effect}$  can not exceed 2T.

### Current to a uncharged surface element

The current to a uncharged surface has not been studied in section 2. All for-

mula and Figures are shown in terms of dimensionless currents  $I/I_0$ . There is not much physics involved in the calculation of  $I_0$ . It is just the random flux along the normal direction of the surface. Obviously the current varies with the angle between the surface and the preferred direction of the anisotropic distribution disregarding the geometry of the whole satellite. The change of the electron current and ion current due to  $I_0$  will affect the equilibrium potential.

#### The equilibrium potential varies with the orientation of the surface.

The equilibrium potential varies with the angle between the magnetic field and the charging surface. The surface which is parallel to a source cone feel that the plasma has less energy; therefore, it would be charged to a lower equilibrium potential than the surface perpendicular to the source cone. The equilibrium potential depends on the effective temperature. The  $T_f$  of a source cone has a upper limit which is about 2T.

#### The Conclusion

In case of (4) and source cone, the properties of current-potential relation of a conductor in a anisotropic plasma are qualitatively similar to that in Maxwellian since the energy distribution is similar. The difference caused by anisotropy is that a surface tangential to the preferring direction of anisotropy starts charging with a less charging current and reaches a lower equilibrium potential than a surface perpendicular to the preferred direction.

Acknowledgments. This work was supported by NASA grant NGL 05-005-007. I would like to thank E. C. Whipple and J. G. Laframboise for many helpful discussions.

#### References

- Laframboise, J. G. (1966). Theory of spherical and cylindrical Langmuir probes in a collisionless, Maxwellian plasma at rest. University of Toronto, Institute for Aerospace Studies, report 100.
- Mott-smith, H.M., and I. Langmuir, The theory of collector in gaseous discharges, Phys. Rev., 28, 727-763, 1926
- Prokopenko, S.M.L., and J. G. Laframboise, Prediction of large negative shaded-side spacecraft potentials, in Proceedings of the Spacecraft Charging Technology Conference AFGL-TR-77-0051/NASA TMX-73537, edited by C. P. Pike and R. R. Lovell, PP. 369-387, 1977.

Prokopenko, S.M.L., and J. G. Laframboise, High-voltage differential charge of geo-stationary spacecraft, *J. Geophys. Res.*, 85, 4125-4131, 1980

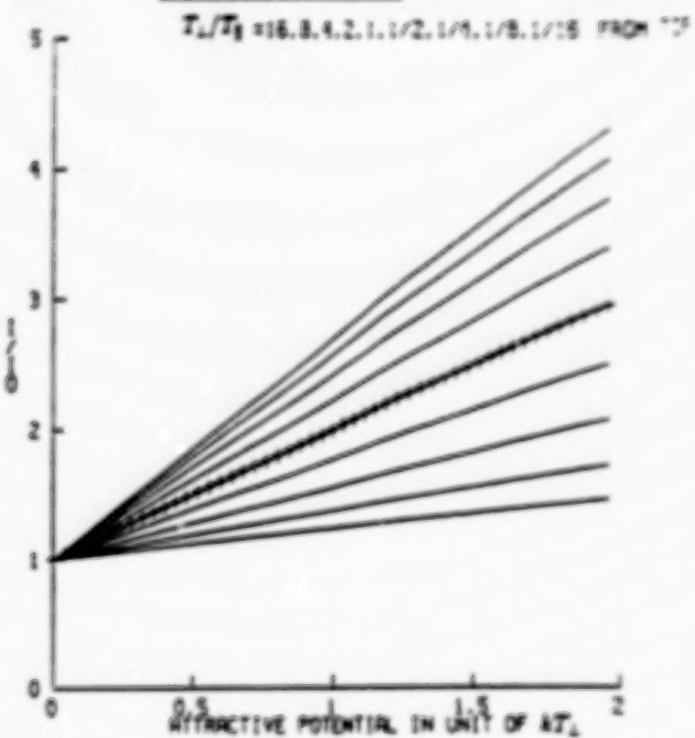


Fig. 1 The current to a sphere from attracted particles of two temperature plasma.

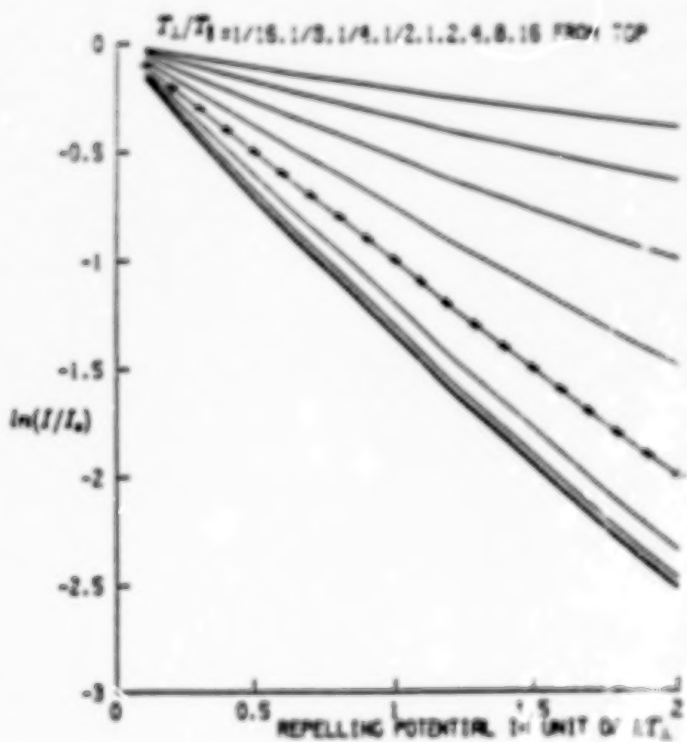


Fig. 2 The current to a sphere from repelled particles of a two temperature plasma.

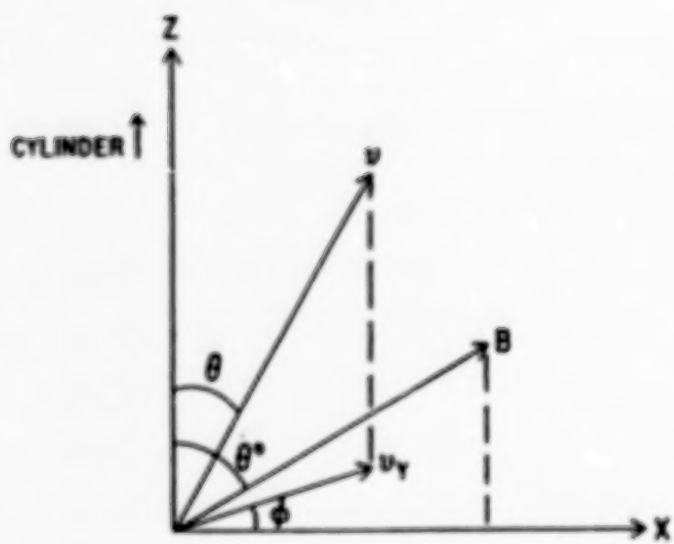


Fig. 3 A cylinder in a spherical coordinate

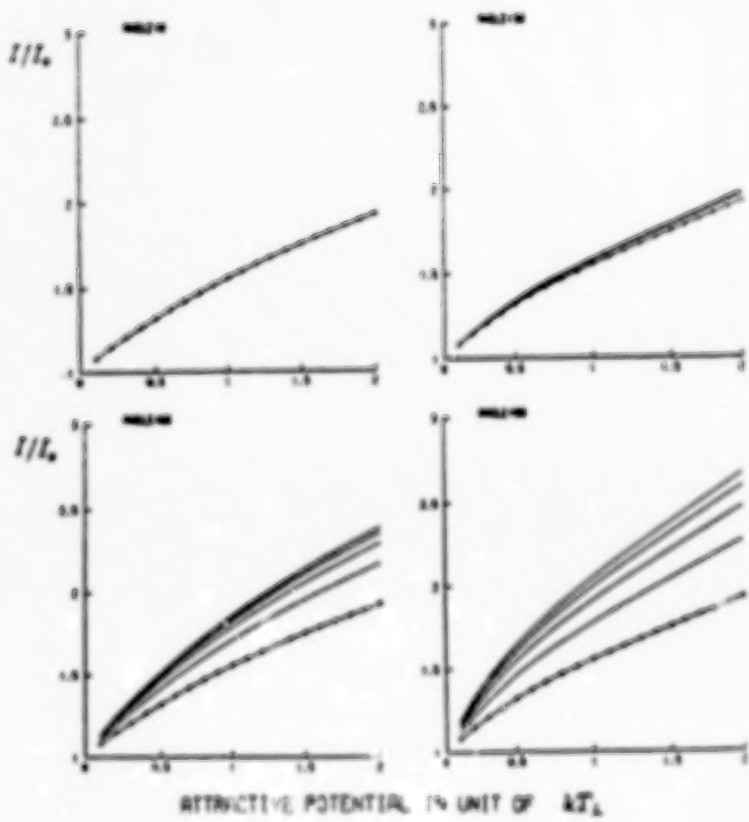


Fig. 4 The current to a cylinder from attracted particles of a two temperature plasma.  $T_{\perp}/T_b = 16, 8, 4, 2, 1$  from top

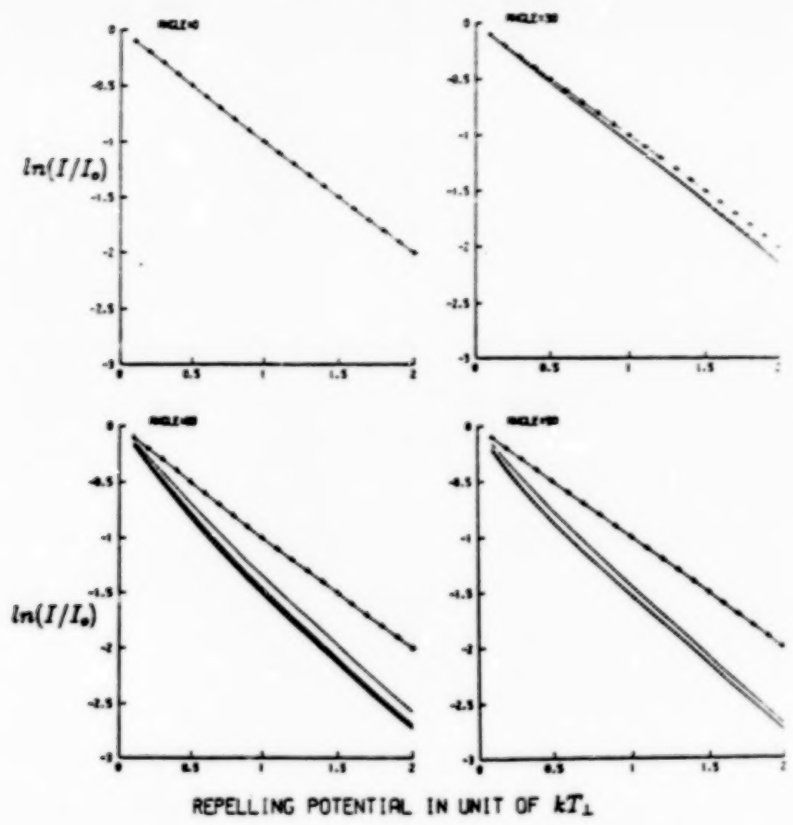


Fig. 5 The current to a cylinder from repelled particle of a two temperature plasma  $T_{\perp}/T_{\parallel} = 1, 2, 4, 8, 16$  from top

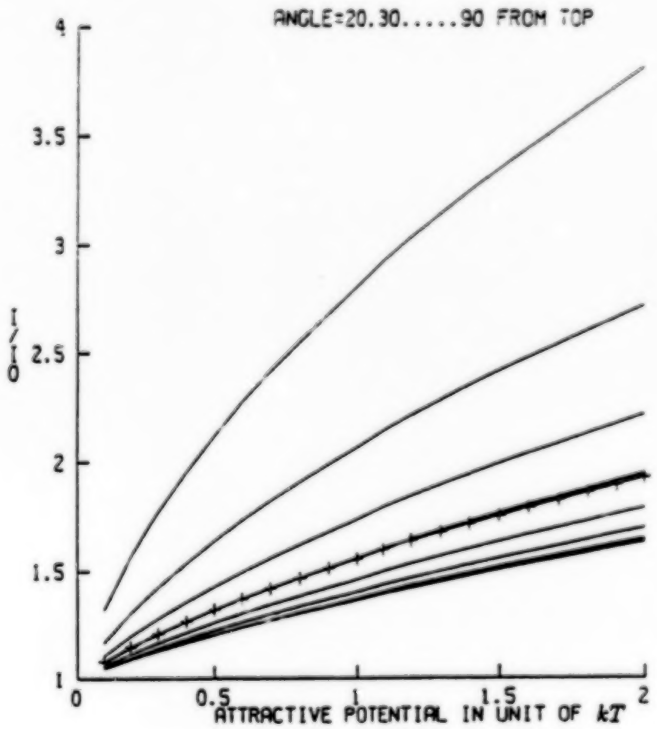
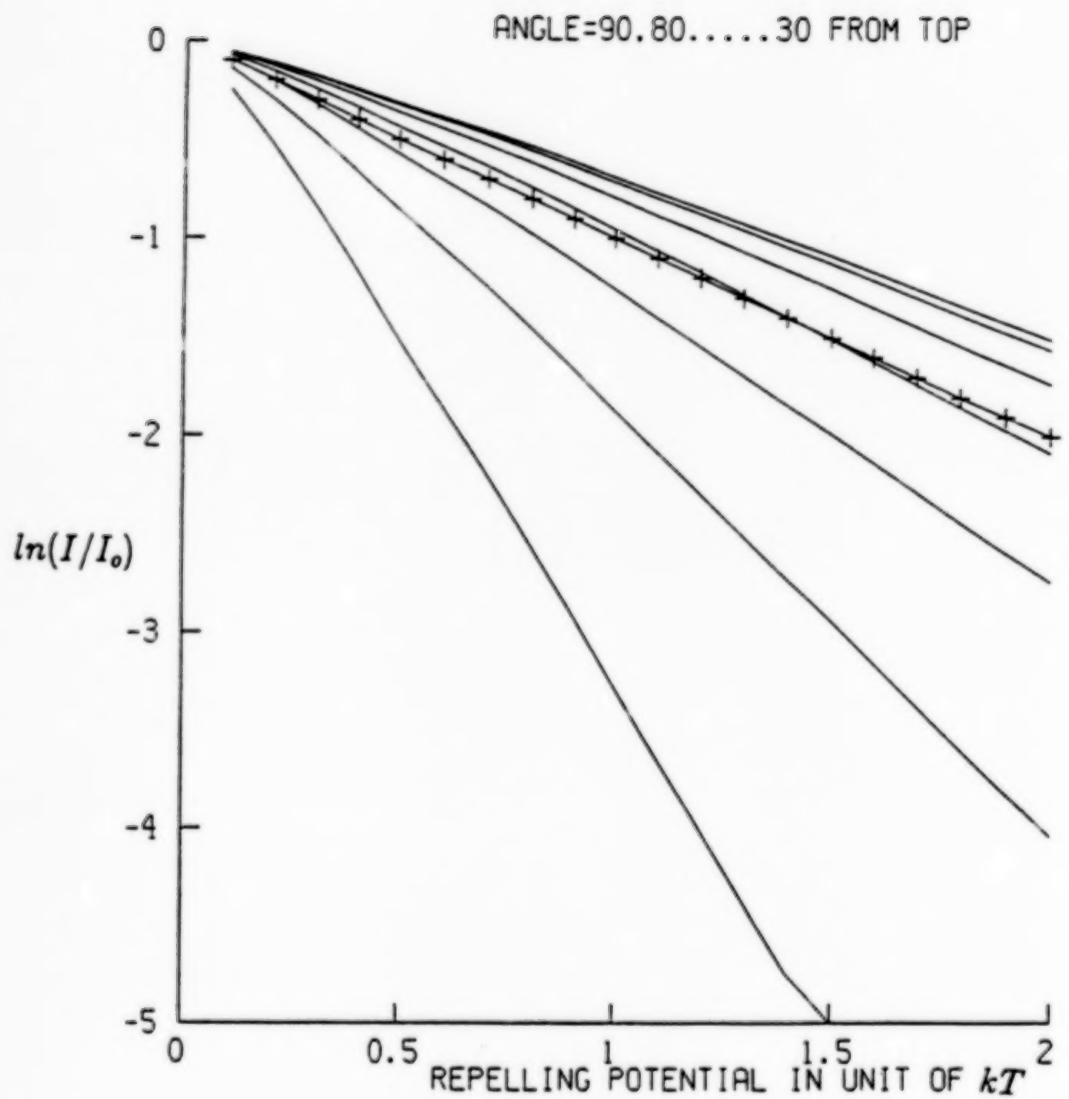


Fig. 6 Current to a cylinder from attracted particles of a Maxwellian plasma within a small source cone



**Fig. 7 Current to a cylinder from repelled particles of a Maxwellian plasma within a small source cone**

# MEASUREMENT REALITIES OF CURRENT COLLECTION IN DYNAMIC SPACE PLASMA ENVIRONMENTS

E. P. Szuszczewicz

Laboratory for Atmospheric and Space Sciences  
Science Applications International Corporation  
McLean, Virginia

## Abstract

Theories which describe currents collected by conducting and non-conducting bodies immersed in plasmas have many of their concepts based upon the fundamentals of sheath-potential distributions and charged-particle behavior in superimposed electric and magnetic fields. Those current-collecting bodies (or electrodes) may be Langmuir probes, electric field detectors, aperture plates on ion mass spectrometers and retarding potential analyzers, or spacecraft and their rigid and tethered appendages. Often the models are incomplete in representing the conditions under which the current-voltage characteristics of the electrode and its system are to be measured. In such cases, the experimenter must carefully take into account magnetic field effects and particle anisotropies, perturbations caused by the current collection process itself and contamination on electrode surfaces, the complexities of non-Maxwellian plasma distributions, and the temporal variability of the local plasma density, temperature, composition and fields. This set of variables is by no means all-inclusive, but it represents a collection of circumstances guaranteed to accompany experiments involving energetic particle beams, plasma discharges, chemical releases, wave injection and various events of controlled and uncontrolled spacecraft charging. This paper attempts to synopsize these diagnostic challenges and frame them within a perspective that focuses on the physics under investigation and the requirements on the parameters to be measured. Examples will include laboratory and spaceborne applications, with specific interest in dynamic and unstable plasma environments.

## 1. Introduction

Electrical currents and associated current-collection characteristics are fundamental manifestations of charged-particle density and energy distribution functions, their collisionality in a host medium and their interactions with electric and magnetic fields. In naturally-occurring space plasmas we have current systems everywhere, from the Sun's photospheric and chromospheric domains, to the Earth's geoplasma region where the magnetosphere and the ionosphere are interactively coupled through the Birkland current system. In man-made systems focused on the interests of plasma physics in general, and space plasmas in particular, we have currents in electrode-type discharges (e.g., hollow-cathode discharges), currents to Langmuir probes, and other charged-particle detectors, and currents to a spacecraft body and tethered satellite configurations.

The current collected by any body immersed in a plasma (e.g., a satellite, an antenna, or a Langmuir probe) is controlled by the size and geometry of the body,

surface materials and levels of surface contamination, body aspect and velocity relative to the plasma and ambient fields, and of course the potential of the body itself.<sup>1-5</sup> On the other hand, the details of the plasma response function are controlled by the electric and magnetic fields and the electron and ion densities, the ion composition, the energy distribution functions and collision frequencies. Our best understood plasma-electrode systems are the simplest ones. Such systems generally involve:

- a) "Perfect" body geometries (i.e., cylinders, spheres and "infinite" planes), with contamination-free perfectly-conducting surfaces that have a unity accommodation coefficient for every impinging charged particle;
- b) Zero velocity of the body relative to the plasma, no magnetic fields, and potentials  $< 25kT_e/e$  or  $< 50$  volts, whichever is less; and
- c) A neutral, quiescent, collisionless, non-drifting, fully-Maxwellian plasma with a single ion constituent.

However, most scientific interests focus on practical systems that at times bear little resemblance to the ideal simple system. A preponderance of investigations involve "imperfect" moving bodies (e.g., a satellite with a multitude of appendages and an admixture of conducting and non-conducting surface materials), high potentials (except for probes and particle detectors), and local sources of surface contamination (e.g., uncontrolled outgassing, or effluents from attitude control jets or an open cycle chemical power system). Plasmas of greatest interest (and concern) are those that are non-Maxwellian, bi-Maxwellian, drifting or otherwise have anomalous energy distributions; and the properties are time-dependent and turbulent with a multi-ion constituency and collisionality characteristics in the transition regime. It is also inevitable that magnetic field effects can not be ignored and the current flow configuration is anisotropic.

These real systems represent a challenge to the theoretical community and to the experimentalist who must develop a diagnostic procedure that can contend with the multiplicity of dynamic plasma properties and apply the procedure in a manner free from unknown parasitic effects. In sections to follow, an attempt is made to identify experimental problem areas, point to existing and/or possible solutions, and illustrate the findings with specific applications to unique geoplasma domains to spaceborne systems and to laboratory-based simulation experiments. Initial emphasis will be on several aspects of basic probe diagnostics, with subsequent treatments addressing measurement demands in naturally-occurring geoplasmas, beam-plasma and vehicle-plasma interactions and in spaceborne environments affected by hollow-cathode discharges. The fundamental issues will then be carried over into discussions of larger-scale systems.

## 2. Fundamental Considerations and Sources of Error

### 2.1 Area effects

One of the oldest, most fundamental, and often overlooked considerations in probe diagnostics is the importance of reference electrode area relative to that of the diagnostic probe.<sup>4</sup> The Langmuir probe, like a tethered satellite, should be the smaller electrode of a two-electrode configuration with the ratio of the two areas approaching a value

which, for all practical purposes, should be considered infinite. When the two electrodes are in electrical contact with a plasma, a current will pass between them which is a function of an applied voltage difference. When the current is plotted as a function of the applied voltage difference, the resulting curve is referred to as the probe's I-V characteristic. Fig. 1 shows a schematic representation of a Langmuir probe circuit as well as a typical characteristic. (In a laboratory situation the reference electrode can, in fact, be the metal container of the plasma volume; while in spaceborne applications the reference electrode is the rocket payload or satellite skin.) The potential of the reference electrode is normally defined as zero, and it is of paramount importance to the measurement technique that this potential remain constant (with respect to the plasma potential) for all values of current. When the area of the reference electrode is sufficiently small its potential will shift, resulting in a net distortion of the probe's I-V characteristic.

From the simple considerations to be introduced here (and adapted from Ref. 4), the uncontrolled potential shift of the reference electrode is a function of the area ratio  $\alpha \equiv A_r/A_p$  and the circuit current  $i$ , where  $A_r$  and  $A_p$  are the reference and probe areas, respectively. The total current collected by the probe system must equal zero, that is,  $i^r = -i^p$ , where  $i^r$  and  $i^p$  are net currents collected from the plasma by the reference electrode and the probe, respectively. This constraint yields the identity given by

$$i_i^r - i_e^r = -i_i^p + i_e^p, \quad (1)$$

where the subscripts  $i$  and  $e$  designate the ion and electron components of the net current. A useful view of area influences can be achieved by assuming that both electrodes are operating at potentials which are less than or equal to the plasma potential and that there are just two charged species—positive ions and negative electrons (the electrodes are therefore ion attracting). Eq. (1) can be written in the form shown in Eq. (2):

$$\alpha = \frac{\exp\chi^p - (m_e/M)^{1/2} I_i(\beta_p, \tau, \chi^p)}{(m_e/M)^{1/2} I_i(\beta_r, \tau, \chi^r) - \exp\chi^r}. \quad (2)$$

In Eq. (2),  $\chi^p$  and  $\chi^r$  are, respectively, the probe and reference-electrode potentials  $\phi_p$  and  $\phi_r$ , measured with respect to the plasma potential  $\phi_0$  and normalized to  $kT_e/e$  [see Eq. (3)], while  $\beta_p$  and  $\beta_r$  are the corresponding radii divided by the electron Debye length  $\lambda_D$  [see Eq. (4)]. (Only spherical and cylindrical geometries will be considered explicitly):

$$\chi^p = e(\phi_p - \phi_0)/kT_e, \quad \chi^r = e(\phi_r - \phi_0)/kT_e, \quad (3)$$

$$\beta_p = R_p/\lambda_D, \quad \beta_r = R_r/\lambda_D. \quad (4)$$

$\tau$  is the ratio of ion-to-electron temperature  $T_i/T_e$ ,  $m_e$  is the electron mass,  $M$  is the charge-normalized ion mass  $M = m_i/Z^2$ , where  $m_i$  and  $Z$  are the ion mass and multiplicity of ionization, and  $I_i$  is the dimensionless ion current [defined by Eq. (5)] which, in the collisionless limit, is available in numerical form in the calculations of Laframboise:<sup>5</sup>

$$j_i = n_e e(kT_e/2\pi M)^{1/2} I_i. \quad (5)$$

In Eqs. (2), (3) and (5) the quantities as yet undefined are the undisturbed electron density  $n_e$ , the magnitude of the charge of an electron  $e$ , the Boltzmann constant  $k$ , and the experimentally-observed ion-current density collected by an electrode  $j_i$ .

There is substantial utility in several computational results associated with Eqs. (1)-(5). The first involves the effect of area ratio on the change in reference electrode potential as a Langmuir probe is swept from its own floating potential to the plasma potential (i.e., over the entire retarding field region where the electron temperature is determined). A sample result, taken from Szuszczewicz<sup>4</sup>, is presented in Fig. 2, where the potential  $\chi_\alpha^r$  of a cylindrical reference electrode is shown as a function of  $\alpha$  for the case  $\beta_r = 10$ . The running parameter is the charge-normalized ion mass expressed in amu and the results for  $\tau=0$  and 1 are presented.  $\chi_\alpha^r$  is the value of the dimensionless potential which the reference electrode must assume in order to satisfy the identity  $i^p = -i^r$  when the probe is at the plasma potential. The total shift in  $\chi^r$  which results when the probe is operated over the entire transition region is given by Eq. (6) for any given set of values ( $\beta_r$ ,  $\tau$ ,  $M$ , and  $\alpha$ ):

$$\Delta\chi^r = \chi_\alpha^r - \chi_f^r. \quad (6)$$

The quantities necessary for calculating  $\Delta\chi^r$  are readily obtained from Fig. 2, where  $\chi_f^r$  can be taken as the value of  $\chi_\alpha^r$  at  $\alpha = 10^4$ . As an illustration, consider the case  $(\beta_r, \tau, M, \alpha) = (10, 0, 16, 100)$ . In this situation  $\Delta\chi^r = \chi_\alpha^r - \chi_f^r = 7.0 + 4.7 = -2.3$ . This corresponds to a voltage shift of -20 V and 0.2 V for  $T_e = 10^5$  and  $10^3$  K, respectively. Such a shift would be unknown to a probe experimenter, and the result would be an I-V characteristic that yielded a value of  $T_e$  approximately 60% higher than that actually present in the plasma.

Results like those in Fig. 2 at  $\alpha = 10^4$  can be used to generate curves which present the dimensionless floating potential  $\chi_f$  as a function of  $M$  for  $\tau = 0$  and 1, and  $\beta \leq 3, = 10, = 100$ . (Here  $\chi_f$  is not superscripted nor is  $\beta$  subscripted, since the results apply to any electrode.) The results of this approach, presented in Fig. 3, show that  $-\chi_f$  increases with increasing  $\beta$  for a given  $(\tau, M)$ . This reflects the reduction in the relative sheath size for increasing values of  $\beta$  and consequently a reduction in the dimensionless ion current to the electrode.

Reflection on results like those shown in Figs. 2 and 3 provides some additional insight. It is first noted that errors in  $T_e$  measurements due to inappropriate values of area ratios can be kept to zero with a value of  $\alpha = 10^4$ . Depending on the circumstances however, that can be relaxed to values of  $\alpha < 10^3$ , and approach even lower limits near  $10^2$  for H<sup>+</sup> plasmas (see Ref. 4 for details).

The results of Fig. 2 can also be used to baseline considerations for two-electrode systems (including, for example, a tethered satellite), where large bias-voltages are applied. If the objective is to have the entire bias voltage applied to the smaller of the two electrodes (i.e., there is no shift in the reference electrode potential), the area ratio  $\alpha$  must be at least 1000, and higher values are likely, depending on the plasma regime and the magnitude of the applied potential.

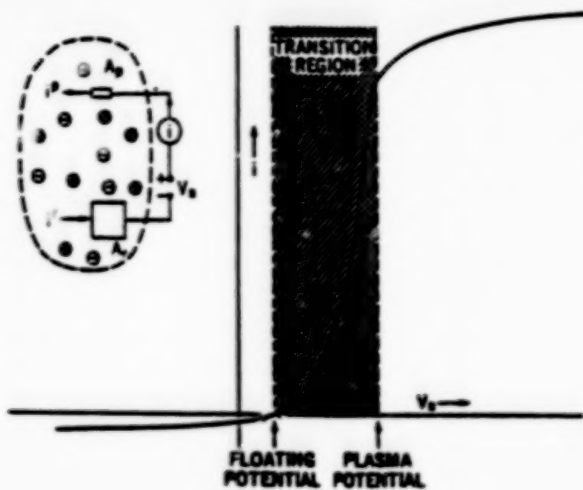


Figure 1. Schematic representation of a Langmuir-probe (or tethered satellite) circuit and a corresponding current-voltage characteristic.

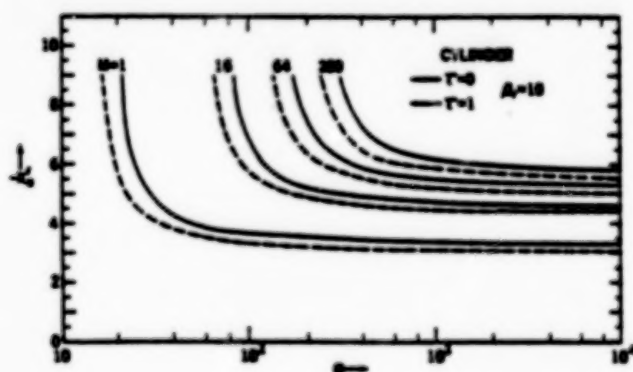


Figure 2. Dimensionless potential  $\chi_r^r$  of a cylindrical reference electrode as a function of  $\alpha (\equiv A_r/A_p)$  for  $\beta_r (\equiv R_r/\lambda_D)$ .  $M$  is the charge-normalized ion mass (in amu),  $\tau = T_i/T_e$ , and the Langmuir probe is assumed to be operating at the plasma potential.

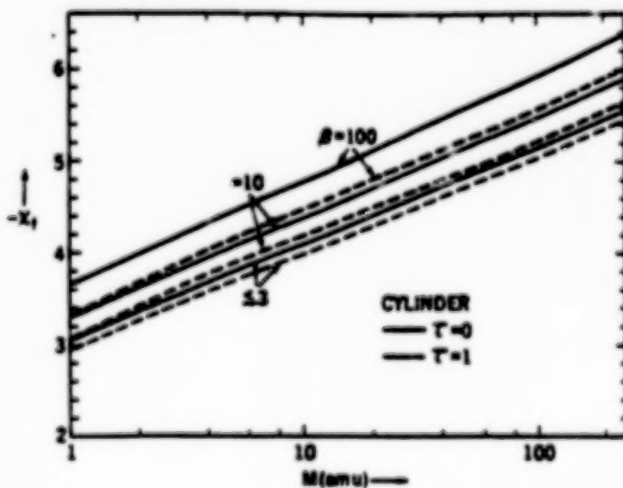


Figure 3. Dimensionless floating potential  $\chi_f$  of a cylindrical body immersed in a collisionless Maxwellian plasma plotted as a function of the charge-normalized ion mass  $M$  (in amu) for ratios of ion-to-electron temperature equal to 0 and 1.  $\beta$  is the ratio of body radius to Debye length.

Important implications for double probe measurements of electric fields can also be extracted from Fig. 3. Such measurements are in effect high impedance determinations of the difference between the floating potentials of two probes. The assumption is that the floating potential tracks the plasma potential. That is indeed the case, but the tracking involves the local (i.e., local to each sensor) values of  $\beta$ ,  $\tau$  and  $M$ . In dynamic and irregular plasma environments, with scale sizes less than the separation distance between the double-probe sensor tips, differences between floating potentials can be mistaken as an electric field when in reality the difference can be simply a manifestation of differences in local densities, ion masses and energy distribution functions. Under such circumstances results of double probe measurements should be the subject of substantial scrutiny.

## 2.2 Contamination Effects

The detrimental effects of surface contamination on active electrodes in plasmas have been known for years.<sup>6-8</sup> Experimental studies have shown that the standard continuous-sweep approach to Langmuir probe measurements can be seriously compromised by temporal variations in the probe's effective work function. When these variations occur during the measurement interval, the current-voltage (I-V) characteristic is distorted, resulting in erroneous determinations of charged-particle densities and energy distribution functions. These effects are reviewed here, following closely the published work of Szuszczewicz and Holmes.<sup>8</sup>

Variations in the probe's surface condition can manifest themselves by hysteresis in the I-V characteristic when the probe is driven with a symmetric sawtooth voltage<sup>9</sup> (and even time function). If the I-V characteristic is not identically reproduced in the positively and negatively sloped portions of the applied sawtooth voltage [upward and downward going arrows in Fig. 4(b), respectively], the familiar hysteresis curve results. This behavior is attributed to the layering of foreign material on the surface of the probe resulting in a variation of the work function.

A model<sup>7</sup> for the surface layering phenomenon is illustrated in Fig. 4(a), which schematically depicts a contaminated probe in a plasma. The mechanisms for the development of the surface layer of contamination are not always easily identified but contributions may come from the deposition of sputtered material from other solids in the system or from the sorption of gases and vapors in the plasma itself. For example, a perfectly cleaned and outgassed probe when immersed in an un-ionized gas immediately begins to absorb and occlude the ambient neutral species.<sup>10</sup> If these species are nonconductive, an insulating layer will develop. This layer is phenomenologically represented by capacitance  $C_c$  and leakage resistance  $R_c$  in Fig. 4(a). When a plasma is part of the environment and a voltage  $V$  is applied to the probe, charged particles will flow to the probe's contaminated surface, charge up the associated capacitance  $C_c$ , and simultaneously alter the absorbate surface layer by bombardment.<sup>11</sup> These conditions and their associated dependence upon the applied probe voltage bring about the hysteresis in the current-voltage characteristic. [It is possible to sweep the probe voltage so slowly that the (I, V) data points come to identical equilibrium values in the up- and downlegs of the sweep.<sup>6</sup> In this case the measurements are still in error but

the investigator does not have the advantage of telltale hysteresis.]

When surface contamination is a problem, conventional Langmuir probes have indicated "hotter" electron distributions than actually present in the ambient medium and hotter distributions than those measured by a "clean" probe. As indicated in the discussion of Fig. 4(a), contamination can also result in an unknown offset voltage  $V_c$  across the layer, contributing to uncertainties in determining the actual voltage imposed on a plasma by fixed-potential electrodes and errors in double-probe measurements of dc electric fields. These problem areas impose genuine constraints upon experimenters and make it necessary to eliminate the contaminating species from the system or circumvent the distortions in measurement by some modification in the experimental technique. The latter approach is not always feasible, making it incumbent upon the experimenter to modify his technique so that it is not susceptible to distortion by contamination.

There are two conventional approaches which attempt to eliminate or circumvent the problem of surface contamination on Langmuir probes. One involves periodic cleaning of the probe surface by ion bombardment or heating of the probe. The second approach reduces the period of the sweep voltage to a value shorter than the time constant  $\tau_c = RC_c$ , where  $R = R_s R_c / (R_s + R_c)$ ,  $C_c$  is the effective contamination capacitance, and  $R_s$  is a simple Ohmic approximation to the sheath impedance [Fig. 4(a)].

The use of a short period for the sweep voltage finds its basic limitation in values of the effective time constant  $\tau_c = RC_c$ . Attempts to sweep the probe voltage much shorter than  $\tau_c$  have met with some success, but the fundamental limitation in  $\tau_c$  can impose unworkably high sweep rates on the probe voltage. High sweep rates can often be handled in laboratory experiments, but difficulties can arise in rocket or satellite applications where data rate constraints are imposed by telemetry. At high sweep speeds and low telemetry rates, resolution of the I-V characteristic is lowered and the accuracy of measurement reduced.

The periodic probe cleaning procedure is of limited use because new contamination layers can develop immediately after the ion bombardment or heating period is ended. In the presence of high sorption rates another cleanup is sometimes necessary within seconds of the preceding cleanup termination. Consider, for example, a neutral gas environment with a 28-amu mean molecular weight at  $10^{-4}$  Torr and a temperature of 300°K. (These parameters are typical of the ionospheric *E*-region at 120 km altitude.) With unity sticking probability for a clean surface and a monolayer defined by approximately  $5 \times 10^{18}$  molecules/m<sup>2</sup>, the first monolayer of contamination develops in 0.13 msec. The next monolayer forms on a timescale of tens of seconds with an equilibrium surface condition resulting after some minutes.<sup>10</sup> This illustration clearly shows that an atomically clean surface can be a very short-lived condition.

To eliminate the aforementioned problems and to improve the reliability and versatility of Langmuir probe measurements, a pulsed plasma probe (acronym, *P<sup>3</sup>*) technique<sup>12</sup> has been developed. The approach employs a pulsed-voltage procedure designed to maintain a single-probe surface condition throughout the collection period of the I-V characteristic; that is, it allows the existence of a contamination layer but

keeps the layer and its associated potential drop at a constant level. Fig. 5(a) shows a continuous symmetric-sawtooth sweep voltage, representing the conventional approach to Langmuir probe operation. Fig. 5(b) shows the approach of the  $P^3$  techniques which employs a discontinuous modulated sweep of pulses following a sawtooth envelope. Between pulses, the sweep returns to a fixed baseline voltage  $V_B$ . A sequence of pulses generates distinct I-V data points for the probe's current-voltage characteristic. (Generally a single I-V characteristic is generated by 150 contiguous pulses.) During the interpulse period when the probe is at a fixed baseline voltage  $V_B$ , the current  $I_B$  collected by the probe can be monitored and used to measure variations in the probe-plasma system, and unfold density fluctuations from the I-V characteristics occurring on a short time frame in comparison to the sweep period.

The pulse sequencing procedure allows the probe to rest at its baseline potential  $V_B$  for a period of time  $\tau_B$ , which is much longer than the pulse width  $\tau_{on}$ . The probe current is always sampled during a subinterval within a sweep pulse, with the subinterval position and sampling duration adjusted so that the plasma is allowed to achieve a steady-state condition and all circuit transients are avoided. With  $\tau_{on}$  much less than both  $\tau_B$  and the time constant of the surface layer  $\tau_c$ , the pulse procedure will maintain the probe's surface condition at a constant level.

In the  $P^3$  technique the sweep time  $\tau_s$  can be as long as an individual experimenter wishes since the I-V characteristic is generated by point data collected within short pulsed-voltage periods  $\tau_{on}$ . The elimination of surface effects by the  $P^3$  technique requires  $\tau_{on} \ll \tau_c$ , whereas in the high sweep-frequency approach it is necessary that  $\tau_s \ll \tau_c$ . Since  $\tau_{on}$  is always much less than  $\tau_s$ , the  $P^3$  approach greatly extends the range over which the time constant effects of  $\tau_c$  can be neglected.  $\tau_{on}$  can be as short as the time required for the plasma to establish itself at a steady-state condition, whereas  $\tau_s$  can never be that short.

This technique has proven invaluable in contaminating and highly-variable plasma environments, the most dramatic manifestation of which occurred in the pulsed-plasma-probe measurements of a reentry plasma<sup>13</sup> and laboratory studies of beam-plasma interactions.<sup>14,15</sup> Contamination problems can also be severe in diffusion-pumped vacuum systems and in spacecraft environments with effluents from attitude control jets, uncontrolled outgassing, or chemical exhaust systems. It is interesting to note that vectored nozzle expulsion of effluents can still result in substantial backflow and the deposition of contaminants on sensitive surfaces. This is illustrated in Fig. 6, which presents the results of a numerical simulation of an open-loop chemical exhaust system mounted on the end of a long, segmented cylindrical payload.<sup>16</sup> The effluent was taken to be 80% water and 20% hydrogen expelled in the +X direction at a rate of 53kg/sec through a supersonic ( $M = 4$ ) 7° nozzle. With the effluent stagnation pressure and temperature at 1000°K and 2 atm, respectively, the resulting steady-state isodensity contours of water in mks units show a  $10^{21}/m^3$  contour some 30 m in front of the nozzle and contours as high as  $10^{15}$  in the backflow engulfing the spacecraft. This is a very high level, guaranteed to cause problems for sensitive surfaces and active plasma detectors.

### 2.3 Magnetic field effects

In the previous sections we have dealt with parasitic effects with potentially disastrous influences on the outcome of an experiment and on the interpretation of results. If one assumes that these effects and other sources of experimental error have been eliminated, the accuracy in one's understanding of the currents collected on a spacecraft surface and the accuracy of the diagnostic technique (probes, RPA's, electrostatic analyzers, etc.) is limited by the theoretical description of the  $I - V - B$  characteristics under the prevailing plasma conditions. Most difficulty is encountered when current collection is in any one of the various transition regions, where we use the term "transition region" to describe any domain between the mathematically convenient limits of collision-free and collision-dominated, thin sheath and thick sheath, and strong field and weak field. These regions are particularly difficult to describe because one must account for detailed charge-particle trajectories that have no convenient closed mathematical form as they traverse the region between the undisturbed plasma volume and the collecting surface. In this section we look at the transition region of magnetic field effects and the associated response of cylindrical Langmuir probe electron-saturation currents. (Under certain constraints, the discussions apply to any cylindrically-shaped current-collecting body.)

Probe response in magnetoplasmas can be grouped into three broad categories defined by the relative magnitudes of the probe radius  $R_p$ , the sheath thickness ( $R_s - R_p$ ), and the Larmor radii for electrons ( $R_L^e$ ) and ions ( $R_L^i$ ). We define these categories as:

$$R_p, (R_s - R_p) \ll R_L^{e,i} \text{ (weak field)}, \quad (7a)$$

$$R_p, (R_s - R_p) \gg R_L^{e,i} \text{ (strong field)}, \quad (7b)$$

and

$$R_p, (R_s - R_p) \approx R_L^{e,i} \text{ (transition field)}, \quad (7c)$$

Each of these categories has its own morphological sub-division established by the independent ratios  $R_L^{e,i}/R_p$  and  $R_L^{e,i}/(R_s - R_p)$ . The first ratio,  $R_L^{e,i}/R_p$ , involves geometrical effects which result in magnetic field shadowing<sup>17</sup> and the associated perturbation of a fully Maxwellian plasma distribution at the sheath edge. A number of authors<sup>3,16-21</sup> have used this ratio to describe magnetic field effects on cylindrical probes and have shown reduced saturation currents when the ratio was small. Miller<sup>20</sup> and Laframboise and Rubinstein,<sup>21</sup> however, infer that magnetic field effects may occur even when  $R_L^{e,i} \gg R_p$  if  $R_L^{e,i} \lesssim (R_s - R_p)$ . It is the latter inequality which is of primary concern in the present discussion.

With the use of sheath-size descriptions developed in Szuszczewicz and Takacs<sup>22</sup> guidelines can be determined for the inequalities (7a) - (7c) by examining the ratio  $R_L^e/(R_s - R_p)$ . This ratio can be written as

$$\frac{R_L^e}{R_s - R_p} = \frac{\omega_p^e / \omega_c^e}{(2.50 - 1.54 \exp[-0.32 R_p / \lambda_D]) (e \varphi_p / k T_e)^{1/2}}, \quad (8)$$

where

$$\omega_p^e = (4\pi Ne^2/m_e)^{1/2} \quad (9)$$

is the electron plasma frequency, and

$$\omega_c^e = eB/m_ec \quad (10)$$

is the electron gyro frequency.

The criteria established in (7), particularly as they apply to the effect of  $R_L^*/(R_s - R_p)$  on electron-saturation currents, can now be expressed as

$$\frac{\omega_p^e/\omega_c^e}{F(e\varphi_p/kT_e)^{1/2}} \begin{cases} \gg 1 & \text{weak magnetosheath}, \\ \ll 1 & \text{strong magnetosheath}, \\ \approx 1 & \text{transition magnetosheath}, \end{cases} \quad (11a)$$

$$(11b)$$

$$(11c)$$

where

$$F = 2.50 - 1.54\exp(-0.32R_p/\lambda_D). \quad (12)$$

These inequalities show that a weak-, transition-, or strong-field classification depends not only on the magnitude of the field but also on plasma parameters of density and temperature, as well as the probe size and applied potential  $\varphi_p$ . Thus, a 0.25 G field could have a similar effect on an ionospheric plasma sheath (typically  $N_e^{max} = 10^6$  cm<sup>-3</sup> and  $T_e = 2000^\circ K$  at  $F$ -region altitudes) as a 30 kG field in a confined hot, dense plasma [ $N_e = 5(10^{15})$  cm<sup>-3</sup>,  $T_e = 1.16(10^7)^\circ K$  (=1 keV)]. Examining these conditions in terms of (11), we find

$$\frac{\omega_p^e/\omega_c^e}{F(e\varphi_p/kT_e)^{1/2}} = 4 \quad (13)$$

in the ionospheric case, and

$$\frac{\omega_p^e/\omega_c^e}{F(e\varphi_p/kT_e)^{1/2}} = 0.95 \quad (14)$$

for the hot, dense plasma. These results assume  $e\varphi_p/kT_e = 10$  as a nominal operational value for the collection of electron-saturation currents by a cylindrical probe of radius  $R_p = 3.8(10^{-2})$  cm. Since Eqs. (13) and (14) are of comparable magnitude, their results show that dramatically different probe-plasma systems can have similar classifications with regard to magnetosheath effects.

This semi-quantitative approach is helpful but far from complete since the anisotropic nature of charged-particle motion makes it necessary to consider the field direction  $\hat{B}$  relative to the probe and sheath axes  $\hat{L}$ . The most complete work done to date in this area is that of Laframboise and Rubinstein<sup>21</sup> who have conducted a theoretical analysis of a cylindrical probe in a collisionless plasma, with the probe operating under

### SURFACE EFFECTS      HYSTERESIS

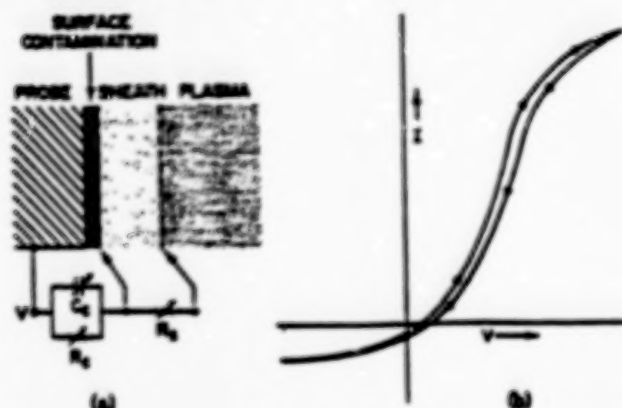


Figure 4. (a) Effective circuit equivalents in phenomenological model for surface contamination. (b) Hysteresis effects in conventional Langmuir probe current-voltage characteristic resulting from layering of surface contaminants.

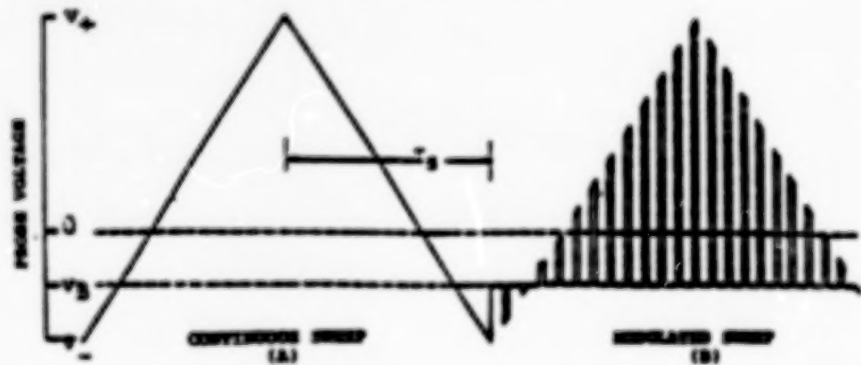
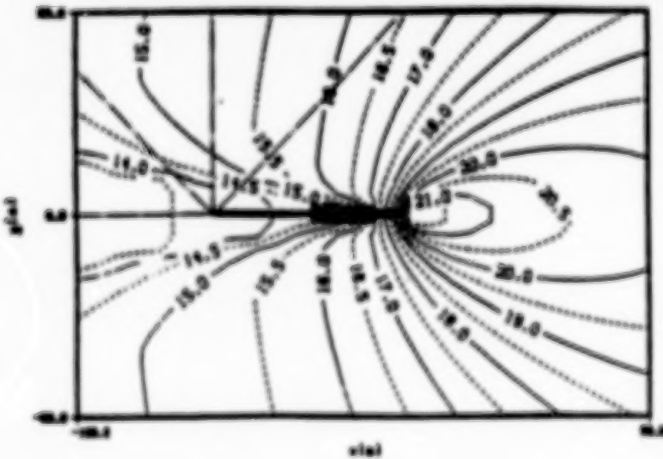


Figure 5. Continuous (conventional Langmuir probe) and pulsed-modulated ( $P^2$  format) sweeps.

### HYDROGEN EFFLUENT DENSITY CONTOURS (FMBL CODE) BOUNDARY LAYER FLOW ONLY AT MACH 4.0 (Log $\text{Nm}^{-2}$ )

$T_e = 1000 \text{ K}$       Mean  $C_p/C_e = 1.37$       Total flow rate =  $13 \text{ kg/sec}$   
 $P_0 = 1 \text{ atm}$       Mean molecular mass =  $2.4 \text{ g}$       Nozzle angle =  $7 \text{ deg}$



thick-sheath conditions at an arbitrary angle  $\theta$  [ $\equiv \cos^{-1}(\vec{L} \cdot \vec{B}/LB)$ ] with respect to a uniform magnetic field. For a probe at plasma potential, their analysis is exact; but in regions of electron saturation currents their theory provides only an upper bound and an adiabatic limit. These limits are approached, respectively, at larger and smaller values of  $R_L^*/L_\varphi$ , where  $L_\varphi$  is defined by Laframboise and Rubinstein as the gradient scale length of sheath potential  $\varphi / |\nabla\varphi|$ . The adiabatic limit corresponds to  $R_L^*/L_\varphi \rightarrow 0$  and can be represented approximately by  $R_L^*/(R_s - R_p) \rightarrow 0$ .

The influences on current-collection due to the direction of the B-field relative to the probe and sheath axes  $\vec{L}$  is illustrated with rocket-borne probe data. The data was collected with a payload spinning at 4 rps and the cylindrical probe radially extended on a boom from the payload skin. The spinning payload moved probe axis from  $0^\circ$  to  $90^\circ$  with respect to the magnetic field twice during each spin period. The probe technique was that of the  $P^3$  described in the previous section, and the baseline voltage level was set in the electron saturation region of the I-V characteristic (i.e.,  $I_B = I_e^{sat}$ ). Two major parameters varied throughout flight. The first was plasma density, making possible correlations with the contributing influences of sheath sizes; and second was the orientation of the probe axis relative to the ambient B-field. An overview of the combined effects of sheath size and magnetic field is presented in Fig. 7, where  $I_B (= I_e^{sat})$  is plotted at values of  $I_B$  at  $\theta = 0^\circ$  ( $+5^\circ$  and  $-0^\circ$ ) and  $\theta = 90^\circ$  ( $\pm 0^\circ$ ). Using the  $I_B(\theta = 90^\circ)$  profile as the more accurate measure of relative density<sup>20</sup> and establishing the conversion  $N_e(\text{cm})^{-3} = 1.25(10^{11})I_B(A)$ , Fig. 7 demonstrates the importance of plasma density (through its control of sheath size) in determining the effect of magnetic fields on electron-current collection by cylindrical Langmuir probes. (The  $N_e/I_B$  proportionality was determined near apogee by conventional analysis<sup>3</sup> of the electron-saturation portion of the current-voltage characteristic, i.e.,  $d(I_e^{sat})^2/d\varphi_p \rightarrow N_e$ . The simultaneous measurement of  $N_e$  and  $I_B$ , made possible with the  $P^3$  technique, yielded the constant. (Sources of error identified with possible plasma depletion,<sup>23</sup> surface contamination,<sup>6</sup> reference electrode area,<sup>4</sup> and convective effects<sup>2</sup> were inconsequential.) In the ionospheric E-region trough (125-170 km), where the plasma density was lowest [ $\approx 6.0(10^3)\text{cm}^{-3}$ ], the percent modulation,  $M \equiv 100 \times [I_B(90^\circ) - I_B(0^\circ)]/I_B(90^\circ) = 75\%$ , was much greater than in the F region ( $Z > 170$  km) where the modulation is only 10%-15%. The difference is attributed to sheath size variation since over the altitude range in this investigation the Earth's magnetic field and associated Larmor radii are approximately constant. [ $R_L$  values are constant only if temperature are constant, a situation which is not generally true over this altitude range where we can expect up to a factor of two difference. But, we can neglect the temperature effect ( $2\times$ ) compared to the density effect ( $100\times$ ).]

The results in Fig. 7 identify a problem area for plasma experimenters who utilize fixed-bias cylindrical probe measurements of electron-saturation currents to determine changes in electron density. Even when the probe is held at a fixed angle with respect to the magnetic field, the spatial or temporal profile of plasma density can be distorted by changing sheath sizes that accompany varying plasma densities. Distorted data can result in misleading interpretations of active physical principles. In Fig. 7, the

$I_B(\theta = 0^\circ)$  curve could lead to erroneous conclusions concerning nighttime E-region depletion mechanisms (130-170 km) or applicability of the electron density gradient at the bottom-side of the F-layer (170-240 km) to the Rayleigh-Taylor instability and the triggering of ionospheric plasma irregularities.

Three cases have been selected from the ionospheric probe data in Fig. 7 to detail the behavior of  $I_B(\theta)$  as a function of plasma density. The results have been normalized to  $I_B(90^\circ)$  and plotted in Fig. 8 as curves A, B, and C. We note that the modulation increases with decreasing  $N_e$ , a parametric dependence not shown in current theories involving thick sheath conditions ( $R_p/\lambda_D \ll 1$ ). Specifically, we find that  $(\omega_p^e/\omega_c^e)/F(e\varphi_p/kT_e)^{1/2} [= R_L^e/(R_s - R_p)]$  equals 2.5, 0.47, and 0.3 for A, B, and C, respectively. In terms of the inequalities in (11), these cases qualify as transiton magnetosheath. We observe that the  $R_L^e/(R_s - R_p) = 2.5$  case has the smallest modulation since it approaches the condition of weak magnetosheath. The data show that the modulation would not be zero as a result of  $R_p/R_L^e \rightarrow 0$  alone. The modulation can be zero only if  $R_p/R_L^e$  and  $(R_s - R_p)/R_L^e$  both go to zero, a combined condition represented by  $R_L^e/(R_s - R_p) \gg 1$  [Eq. 11a] in the thick-sheath limit. The data demonstrate the important coupling of  $B, N_e, T_e, R_p$ , and  $\varphi_p$  in determining the degree to which magnetic fields perturb electron-current collection. One cannot give sole consideration to  $R_p/\lambda_D$  or  $R_p/R_L^e$ , but rather their important interrelationships as described in Eq. (11).

The consequences of these results are substantial in the following context:

- 1) Magnetic field effects on electron current collection characteristics can be dramatic. If strong magnetosheath conditions prevail, the use of a  $B = 0$  model for I-V characteristics could lead to errors in  $N_e$  determination as big a factor as 10;
- 2) There is no  $B \neq 0$  model available to date which describes probe current collection characteristics in the transition-magnetosheath domain. This is the domain often encountered in space plasma diagnostics.
- 3) The transition- and strong-magnetosheath conditions are guaranteed to prevail in analysis of currents flowing to a charged spacecraft emitting a net negative particle beam. For the charging/discharging process to be properly analyzed, the detailed controls of a superimposed magnetic field must be taken into account.

### 3. Measurements in Dynamic Space Plasma Environments

Thus far the treatment of current collection from plasmas has dealt with experimental and theoretical problems in plasma probe diagnostics, with perhaps an unfortunate suggestion that there is substantial difficulty in obtaining accurate information from the attendant current collection characteristics. While experimental and analytical care is warranted, there can be a wealth of valuable data in a properly implemented and analyzed experiment configuration. We attempt in this section to develop this perspective, and choose to treat an area of plasma and space plasma physics that has a focus on plasma instabilities, irregularity distributions and multi-ion constituencies. While instabilities and irregularity distributions tend to be standard fare in dynamic plasma environments, little diagnostic attention has been given to the impact of cases

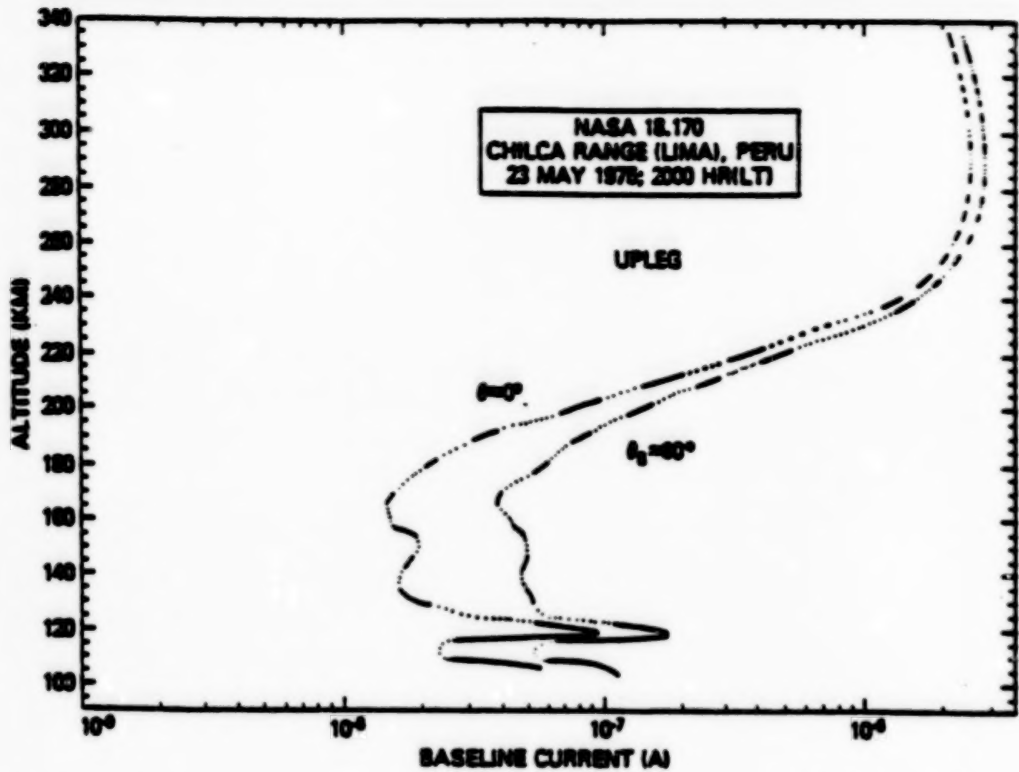


Figure 7. Baseline current  $I_B$  collected when the probe was at  $0^\circ$  ( $+5^\circ$ ) and  $90^\circ$  with respect to the geomagnetic field.

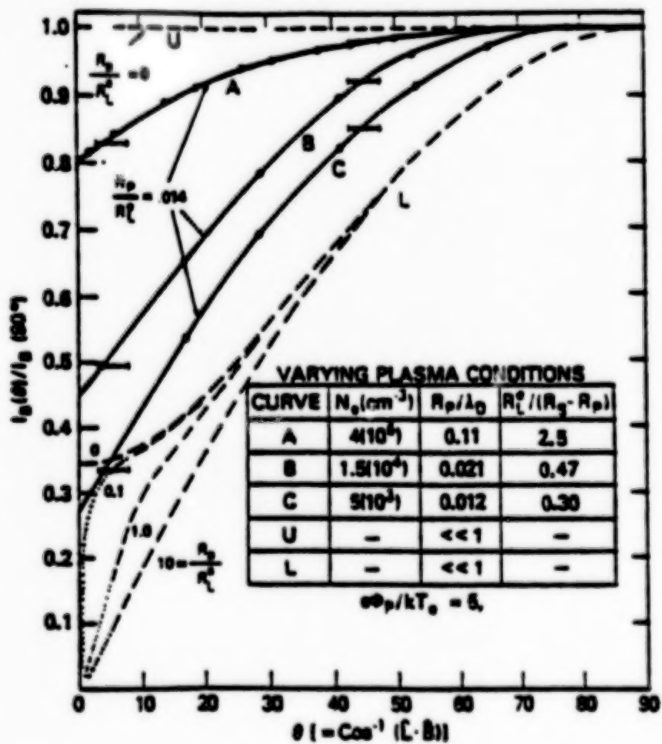


Figure 8. Experimental (curves A, B, and C) and theoretical (curves U and L with parametric dependence on  $R_p/R_L^e$ , U and L define the upper and lower bounds discovered in the text) results showing the effect of magnetic aspects on cylindrical electron-collecting probe current.

which involve a multi-ion population and the associated effects on the growth of the instability process and impact on irregularity scale size distributions. We develop this latter perspective here, using unique features of ion and electron current collection characteristics by Langmuir-type probes. We will do this by focussing on the S3-4 satellite experiment,<sup>24</sup> which was designed to explore the role of multi-ion distributions in instability processes. The treatment presented here follows that in Ref. 24.

The S3-4 experiment employed a pair of pulsed plasma probes ( $P^3$ ), each of which was capable of simultaneous measurements of electron density, temperature and density fluctuation power spectra, regardless of the state of turbulence or the degree of irregularity in the ionospheric plasma medium. Together, the pair of probes also provided mean-ion-mass fluctuation measurements to a maximum Nyquist frequency of 200 Hz.

Subject to the selection of one of eight commandable modes of operation, each of the probes had applied to it some variation of the voltage function illustrated in Fig. 5. The pulse modulated waveform, following the sawtooth envelope, provided the fundamental data set for a "conventional" Langmuir current-voltage characteristic and associated determination of  $N_e$  and  $T_e$  (Chen<sup>3</sup>) at a nominal 3 Hz rate. During the interpulse period, a fixed-voltage  $V_B$  was applied to the probe and associated current measurements provided a running measure of density fluctuations (assuming  $\delta I_B \propto \delta N_e$ ) and a time-dependent data set for power spectral analysis with a Nyquist frequency of 400 Hz in the high data-rate mode.

The probes were routinely operated with  $V_B$  on one probe set for electron-saturation-current collection (defined as the E-probe with  $I_B = I_e(\text{sat}) \equiv E$ ), while the value of  $V_B$  on the second probe was biased for ion saturation current collection (defined as the I-probe with  $I_B = I_i(\text{sat}) \equiv I$ ). The expressions for the currents collected by the two cylindrical probes take the forms

$$E \equiv I_e(\text{sat}) = N_e \sqrt{\frac{kT_e}{2\pi M_e}} A_p e \left\{ \frac{2}{\sqrt{\pi}} \left( 1 + \frac{e\phi_p^e}{kT_e} \right)^{1/2} \right\} \quad (15)$$

(Chen<sup>3</sup>; for thick sheaths), and

$$I \equiv I_i(\text{sat}) = N_i \sqrt{\frac{kT_i}{2\pi M_i}} A_p e \left\{ \frac{2}{\sqrt{\pi}} \left( \frac{|e\phi_p^i|}{kT_i} + \frac{M_i w^2}{2kT_i} \right)^{1/2} \right\} \quad (16)$$

(Hoegy and Wharton,<sup>26</sup> for probe axis perpendicular to the vehicle velocity vector in the ionospheric plasma rest frame). In the above equations,  $A_p$  is the probe area,  $M_{e(i)}$  and  $N_{e(i)}$  are the mass and density of the electron (ion) population,  $T_{e(i)}$  is the associated temperature of an assumed Maxwellian distribution,  $e$  is the fundamental electron charge,  $k$  is Boltzmann's constant,  $w$  is the satellite velocity, and  $\phi_p^{e(i)}$  is the baseline voltage  $V_B$  applied to the  $E(I)$  probe and referenced to the plasma potential ( $\phi_p^{e(i)} = V_B^{e(i)} - V_\infty$ ).

The square of the ratio  $I_e(\text{sat})/I_i(\text{sat})$  can be written as

$$\left(\frac{I_e(\text{sat})}{I_i(\text{sat})}\right)^2 \equiv \left(\frac{E}{I}\right)^2 = \frac{T_e}{T_i} \frac{M_i}{M_e} \left\{ \frac{1 + |e\phi_p^e/kT_e|}{(M_i w^2/2kT_i + |e\phi_p^i/kT_i|)} \right\} \quad (17)$$

with additional manipulation (assuming  $|e\phi_p^e| \gg kT_e$ ) resulting in

$$\left(\frac{I_e(\text{sat})}{I_i(\text{sat})}\right)^2 = \frac{M_i}{M_e} \left| \frac{\phi_p^e}{\phi_p^i} \right|, \quad \frac{1}{2} M_i w^2 \ll e\phi_p^i; \quad (18a)$$

$$\left(\frac{I_e(\text{sat})}{I_i(\text{sat})}\right)^2 = \frac{2 |e\phi_p^e|}{M_e w^2}, \quad \frac{1}{2} M_i w^2 \gg e\phi_p^i; \quad (18b)$$

$$\left(\frac{I_e(\text{sat})}{I_i(\text{sat})}\right)^2 = \frac{M_i}{M_e} \left| \frac{\phi_p^e}{\phi_p^i} \right| \left( 1 + \frac{M_i w^2}{2e\phi_p^i} \right)^{-1}, \quad \frac{1}{2} M_i w^2 \approx e\phi_p^i. \quad (18c)$$

For laboratory and rocket-borne experiments Eq. (18a) would apply, whereas in the S3-4 satellite investigation, Eq. (18c) applies. Eq. (18c) is plotted in Fig. 9 for two sets of bias potentials, ( $|\phi_p^e|, |\phi_p^i|$ ) = (2V, 1V) and (1V, 2V). The results in Fig. 9 show that over limited mass ranges (e.g., 1-4, 4-8, 16-32 amu), variations in  $(I_e/I_i)^2$  can be taken to vary directly with ion mass for constant values of  $\phi_p^e$  and  $\phi_p^i$ .

Bulk processing and plotting of  $P^3/S3 - 4$  data included orbit-by-orbit plots of relative electron density as measured by changes in ion- and electron-saturation currents near the F-region peak. (This is the region for minimum sheaths in ionospheric Langmuir probe operations.) A representative sample of this data collected on orbit 2177 is shown in Fig. 10, where the abscissa coordinates are universal time, altitude, latitude, longitude, magnetic latitude, and L-shell value. The probes magnetic aspect angle is also plotted in the figure.

The left-hand edge in Fig. 10 corresponds to the satellite's ascending node (south-to-north) in the midnight hemisphere near the south magnetic pole. With increasing time (UT) the satellite passed through the nighttime equator, the main trough, over the northern auroral oval and into the dayside ionosphere where vehicle solar cell voltage biased the entire vehicle such that both probes drew approximately equal ion-saturation currents. (It is worthwhile to note that the shifted payload potential was a direct consequence of the area ratio issue discussed in Section 2.1.)

The simultaneous measurements of electron- and ion-saturation currents,  $I_B(E)$  and  $I_B(I)$ , respectively, provide confidence that the observed irregularities involve plasma variations and not just secondary effects (e.g., aspect sensitivities or variations in spacecraft potential).

While data sets like that shown in Fig. 10 provided global maps of large scale ionospheric features, primary investigative objectives were directed at the relationships

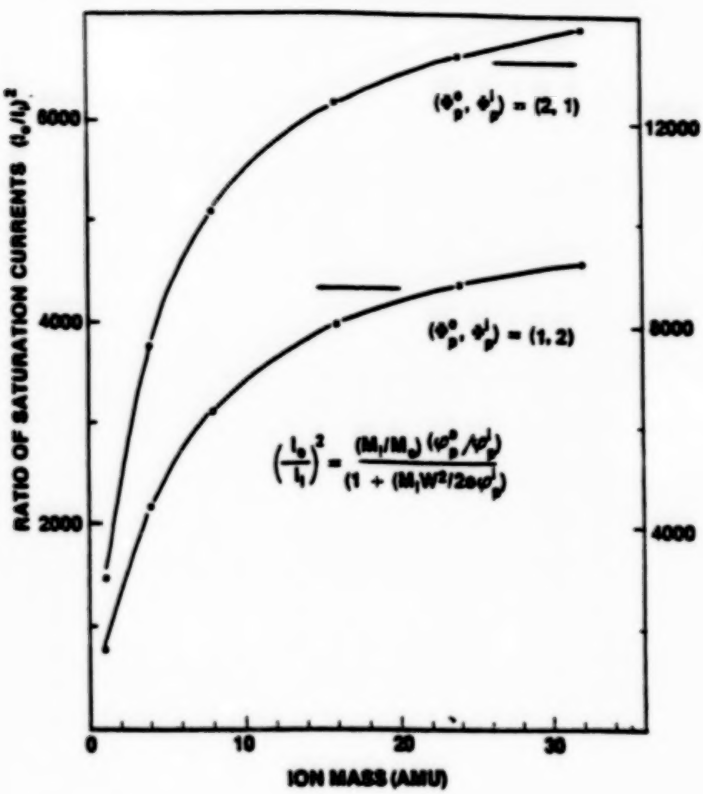


Figure 9. Dependence of the saturation current ratio  $(I_e/I_i)^2$  on ion mass.

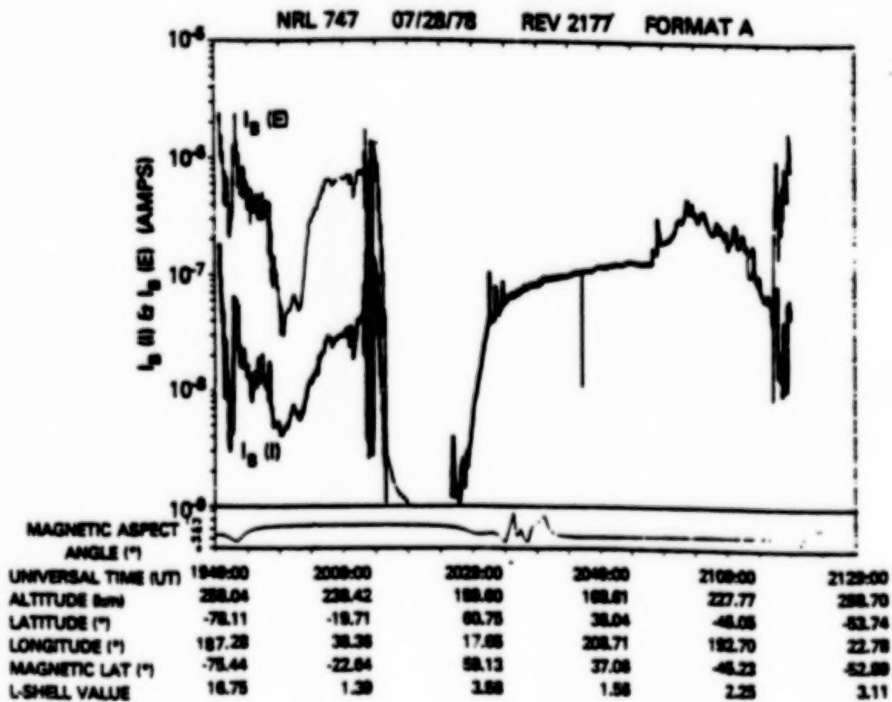


Figure 10. Relative electron density as measured on one complete orbit by the pulsed-plasma-probe experiment on the S3-4 satellite.

between the large scale features and much smaller scale irregularities (tens of meters and less) believed to result from multi-stepped plasma processes. To this end, the fundamental data sets  $I_e(\text{sat})$  and  $(I_e(\text{sat})/I_i(\text{sat}))^2$  were Fast-Fourier analyzed to determine density and ion-mass fluctuation power spectra  $P_N(k)$  and  $P_M(k)$ , respectively, were

$$\left| \frac{\delta I_e}{\bar{I}_e} \right|^2 \equiv \left| \frac{\delta N_e}{\bar{N}_e} \right|^2 \rightarrow P_N(k) \quad (19)$$

and

$$\frac{\delta(I_e/I_i)^2}{(\bar{I}_e/\bar{I}_i)^2} \equiv \frac{\delta M_i}{\bar{M}_i} \rightarrow P_M(k). \quad (20)$$

The analytical relationship between  $\delta N_e/\bar{N}_e$  and  $\delta M_i/\bar{M}_i$  can be simply established for a 2-component ion distribution of masses and densities  $(M_\alpha, M_\beta)$  and  $(N_\alpha, N_\beta)$ , respectively. This is done by using the definitions

$$\bar{M}_i = \frac{M_\alpha N_\alpha + M_\beta N_\beta}{(N_\alpha + N_\beta)}, \quad (21a)$$

$$N_e = N_\alpha + N_\beta, \quad (21b)$$

$$N_\alpha = N_\alpha^0 + N_\alpha^1, \quad (21c)$$

$$N_\beta = N_\beta^0 + N_\beta^1, \quad (21d)$$

$$\delta N_e = \delta N_\alpha + \delta N_\beta = N_\alpha^1 + N_\beta^1; \quad (21e)$$

and a straightforward manipulation to derive

$$\frac{\delta M_i}{\bar{M}_i} = \frac{\delta N_e}{\bar{N}_e} f(\alpha, \beta), \quad (22a)$$

where

$$f(\alpha, \beta) = \left\{ -\frac{\left( \frac{M_\alpha}{M_\beta} \right) - 1}{\left( \frac{M_\alpha}{M_\beta} \right) \left( \frac{N_\alpha^0}{N_\beta^0} \right) + 1} \right\} \left\{ \frac{N_\alpha^1/N_\beta^1 - N_\alpha^0/N_\beta^0}{(N_\alpha^1/N_\beta^1) + 1} \right\}. \quad (22b)$$

It is appropriate to note that the experimental determination of mean-ion-mass fluctuations  $\delta M_i (\rightarrow P_M)$ , through variations in  $[I_e(\text{sat})/I_i(\text{sat})]^2$ , assumes the relative constancy of all potentials. (This includes the spacecraft potential as well as the potentials which each probe presents to the plasma.) The spacecraft potential can vary as a direct result of changes in local plasma density, since the floating potential of a body is dependent upon the ratio of its radius to the local Debye length. For large space vehicles however, floating potential variations caused by even substantial plasma density variations should be small.<sup>4</sup> Another possible source of potential variations involves charging of contamination layers on the vehicle and/or on the probes.<sup>8</sup> From the S3-4 data, variations in  $(I_e/I_i)^2$  associated with charging on contamination layers appear to be a slowly varying function of time with no attendant effects on  $P_M$ . Therefore,

it has been concluded that the spectral dependence of  $P_M$  is indeed representative of variations in mean-ion-mass  $\delta M_i$ .

To experimentally demonstrate  $P_M(k)$  and the associated relationship, with  $P_N(k)$  consider the high-resolution measurements (rev. #2123) of the relative electron density across the nighttime equator (Fig. 11). The peak electron density is approximately  $5 \times (10^5) \text{ cm}^{-3}$  at  $I_B = 3 \times (10^{-6}) \text{ amp}$ . The large scale depletions are seen to extend to two orders of magnitude with widths ranging from 50 to 170 km over a 600 km orbital segment.

$P_N$  and  $P_M$  results are presented in Fig. 12 for a one second interval located by point A in the density profile of Fig. 11. Fitting the results to a power law behavior shows

$$P_N = A_n f^{-2.9} \quad (23a)$$

and

$$P_M = A_m f^{-1.5}. \quad (23b)$$

By assuming that the time (frequency) domain spectral analysis in Fig. 12 can be converted to wavelength through the vehicle velocity ( $7.53 \text{ km s}^{-1}$ ), the experiment shows  $f_N^{-2.9} (\propto k^{-2.9})$  from  $k \approx 2\pi/1\text{km}$  to  $k = 2\pi/20\text{m}$ . This is the first such satellite determination to wavelengths as short as 20m, with the earlier work of McClure and Hanson<sup>26</sup> having defined some of the spectral features of equatorial spread-F down to 70m. (Conversion to the component of  $k$  perpendicular to the geomagnetic field extends the low wavelength end of Fig. 12 down to  $k = 2\pi/6\text{m}$ , the approximate value for O<sup>+</sup> Larmor radius.)

The spectral index for  $P_N$  is approximately 15% steeper than previously reported values<sup>27</sup> for conditions of bottomside spread-F, but well within the distribution of S3-4 spectral indices currently being accumulated and analyzed for conditions identified with the intermediate wavelength domain ( $k = 2\pi/1 \text{ km}$  to  $k = 2\pi/20\text{m}$ ).

The  $P_M \propto f^{-1.5}$  observations are the first of their kind and unique to the  $P^3$ /S3-4 experiment. Currently there are no computational guidelines on the expected behavior, but there is sufficient evidence in laboratory plasma studies to warrant such systematic considerations of ions and their role in the hierarchy of possible mechanisms covering the spectrum of observed ionospheric irregularities. The importance of ions is clear...even from the simple considerations of the Rayleigh-Taylor instability in which a difference in charged-particle drift velocities produces an electric field across a horizontal perturbation. There drift velocities are mass dependent ( $\bar{V}_i \propto M_i(\bar{g} \times \bar{B})/B^2$ ) and vary directly as the mass of the  $i$ th species. Similar mass discriminatory effects play an important role in ambipolar diffusion processes across gradients in plasma density. The process operates more rapidly on lighter ions and can result in "patches" of varying ion mass, with local variations in conductivity and electric fields, and ultimately an ion-dependent interaction in the process of energy dissipation in the large-to-small

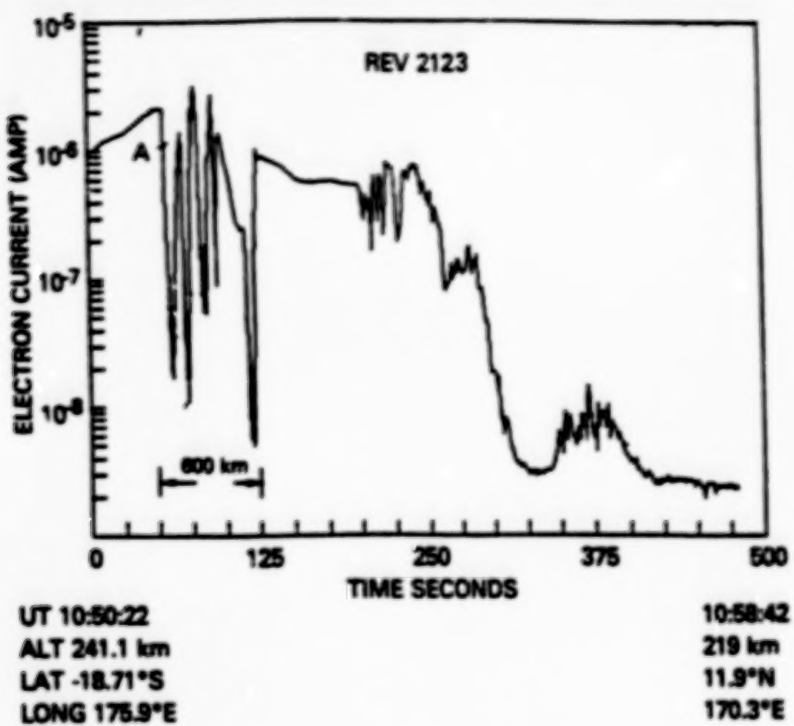


**Figure 11.** An expanded view of relative electron density encountered during the nighttime equatorial crossing on S3-4 rev 2123. The relative electron density is presented by baseline electron saturation current.

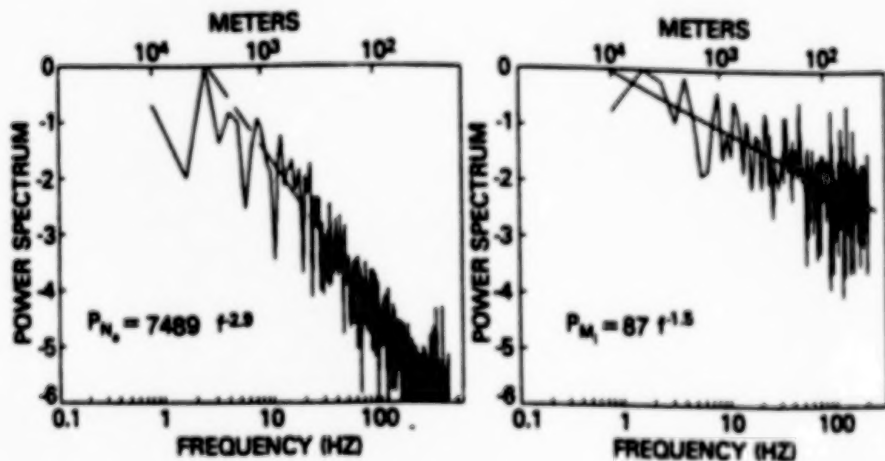


**Figure 12.** Sample illustration of simultaneously determined density fluctuation power spectrum  $P_N$  and mean ion mass fluctuation power spectrum  $P_M$ .

scale irregularity distribution. The  $P_M$  measurement has been designed to test for just that type of interactive mode.  $\delta M_i / \bar{M}_i$  is a fairly complicated function of  $M_\alpha / M_\beta$ ,  $N_\alpha^0 / N_\beta^0$ ,  $N_\alpha^1 / N_\beta^1$  and  $\delta N_e / \bar{N}_e$  itself [see Eq. (22)]; and at this point we can only speculate on the many manifestations that  $P_N$  and  $P_M$  might take for the varied ionospheric conditions encountered in the S3-4 mission. For example, it has been suggested that differences in gradient scale lengths for  $N_e$  and  $M_{\alpha,\beta}$  would result in a more rapid fall off with increasing  $k$  for the quantity with an initially larger gradient scale length. This difference should be a direct observable through the  $P_N$  and  $P_M$  determination. Furthermore, there is the possibility that the simultaneous measurement of  $P_M(k)$  could help differentiate between a  $k^{-2}$  spectrum due to sharp edges and a  $k^{-2}$  spectrum due to gradient-drift or drift-dissipative waves.

#### 4. Currents in Future Space Plasma Experiments

##### 4.1 Tethers, Uncontrolled Potentials and Plasma Contactors

Thus far the treatment has focused on the experimental implementation, collection and analysis of currents to probe systems. We transition now to larger systems like spacecraft and tethers, and note that while bigger systems appear to grow more complex, the issues in many ways remain the same...currents, sheaths and fields. We also note that probes will play important roles in diagnosing the currents and their controls in the larger systems.

We now address several of the larger systems and look not only into sheath currents, and currents collected on spacecraft surfaces, but we look into the effects of large potentials and current closure through the ionosphere. This additional aspect is addressed because many mission concepts advanced in the planning of tethered satellite systems (TSS), beam experiments and Space Station applications are faced with uncertainties in current closure in the ionosphere and the threat of uncontrolled potentials.<sup>28-30</sup> The problem of large and uncontrolled potentials was the subject of a special TSS-1 report that pointed out that tether-system potentials could reach hundreds to thousands of volts depending on the nature of operating anomalies and the tether deployment distance.

A continuing effort has been made to develop techniques with the ability to control these large potentials and maintain spacecraft (and tethered satellites) at or near the local plasma potential. Some success has resulted from improvements in vehicle surface conductivities and expanded areas for ionospheric current collection; but the magnitude of the problem has brought about a focus on the application of high-current on-board charged-particle sources, often referred to as "plasma contactors" or "plasma bridges."<sup>29-33</sup> This was one of the recommendations of the TSS-1 committee on charging.<sup>34</sup> With this result and the call for innovative technologies in space, plasma contactors are now expected to play an additional role in electrodynamic tether applications to power and thrust generation on the Space Station. These applications exploit the stable self-orientation of a long tether (see Fig. 13) along with associated Faraday  $(\vec{V} \times \vec{B}) \cdot \vec{L}$  voltages and  $\vec{I} \times \vec{B}$  Lorentz forces, where  $\vec{V}$ ,  $\vec{L}$  and  $\vec{I}$  are the velocity, length and current in the tether, and  $\vec{B}$  is the geomagnetic field. The current-

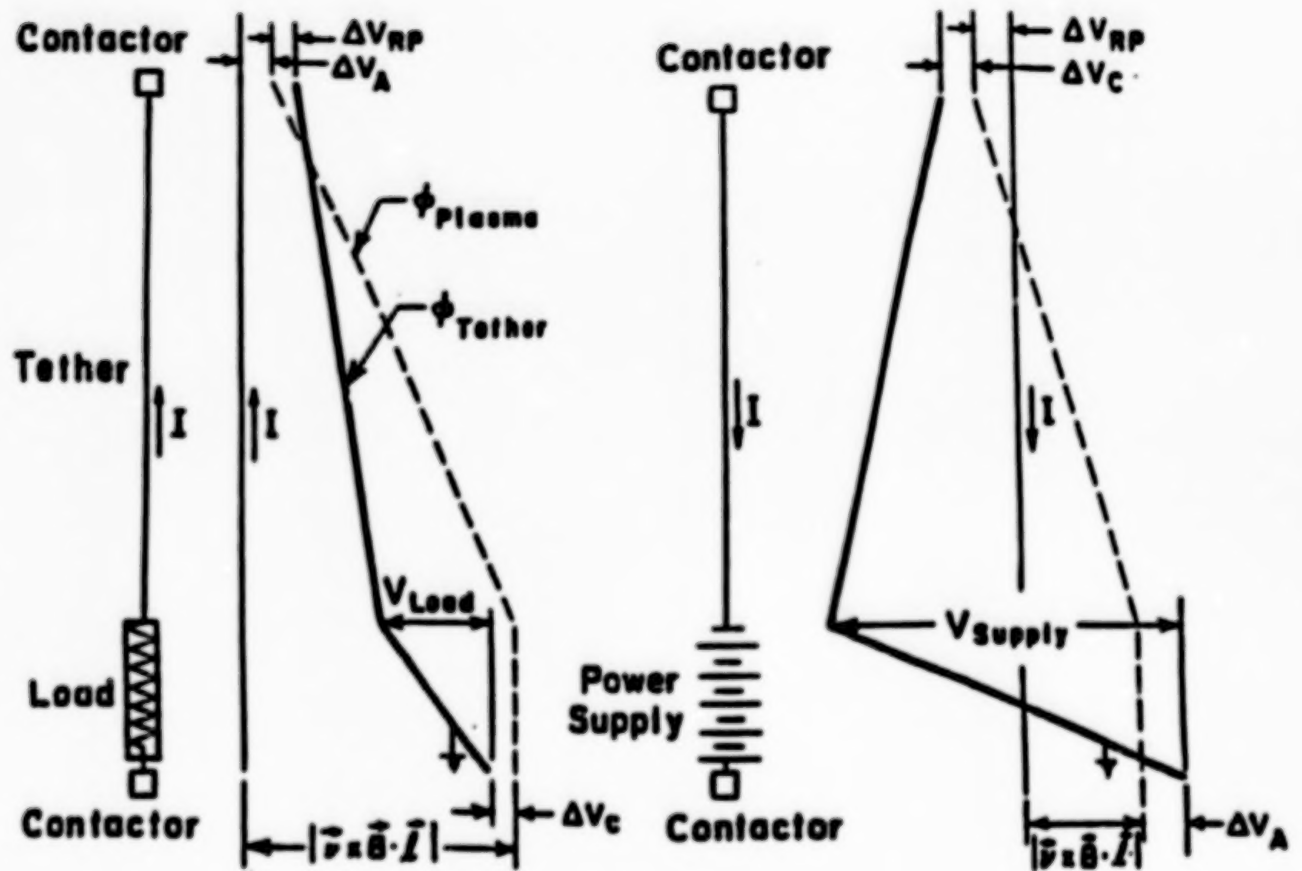


**Figure 13.** A) Potential diagram for tether as a generator, (load at bottom, tether deployed upwards), and B) as a thruster (with power supply at bottom, tether deployed upwards). From Hastings and Martinez-Sanchez.<sup>35</sup>

carrying capabilities of the tether depend on the emf (induced in the generator mode or provided by an on-board power supply in the thruster mode), its impedance and the effectiveness of the ionospheric path to complete the circuit. A 20 km aluminum cable several mm in diameter would have an impedance  $\approx 10 - 50\Omega$ , and in principle could carry a self-induced short-circuit current of 100A [Hastings and Martinez<sup>35</sup>]. However, maximum ionospheric currents ( $n_e^{max} \sim 10^6 cm^{-3}$ ) can only provide  $\sim 10$  ma/m<sup>2</sup>, so to draw even 10A of ionospheric current would require 1000m<sup>2</sup> of collecting surface. In this case, plasma contactors are seen as a solution. Their high density plasma clouds hold promise for enhanced local plasma conductivities, larger effective collecting areas, and reduced threat of uncontrolled potentials. In its final report, the TSS-1 charging committee recommended the inclusion of a hollow-cathode in its mission.<sup>34</sup>

One type of plasma contactor is the hollow-cathode discharge, illustrated schematically in Fig. 14A. Fundamentally, it is a thermionic electron emitter in the presence of a high gas flow, which can produce plasma densities upwards of  $10^{14} cm^{-3}$  near the cathode orifice.<sup>36-38</sup> The expansion characteristics of this plasma (and its associated "contactor" capabilities) are influenced by specific device-design considerations, the ambient plasma itself, and the local geomagnetic field. The ideal contactor should provide large controllable currents of electrons and ions at minimum applied fields in the cathode-anode region. We note, however, that large controllable currents are best carried by electrons, provided they can move freely not only parallel but perpendicular to magnetic fields. The latter condition requires that  $\nu_e > \Omega_e$ , where  $\nu_e$  is the effective electron momentum collision frequency and  $\Omega_e$  is the electron cyclotron frequency. Under normal operating conditions, particle-particle collisions are insufficient and only an "anomalous" collision term through wave-particle interactions can provide the necessary random walk process which can transport electrons perpendicular to  $\vec{B}$  (note  $R_L^e$ , the electron gyroradius, is typically  $\sim 3$  cm in ionospheric applications). Indeed, as a current source between a space platform and the background ionosphere, the HC is potentially replete with current-driven instabilities and associated wave spectra. Candidates include lower-hybrid-drift, ion-acoustic and Buneman instabilities<sup>30,39</sup> to name just a few. But while the bulk current-carrying characteristics of the HCD have been receiving attention, there has been little-to-no effective experimental work focussed on the wave- and wave-particle processes intrinsic to HC operations and to the physics of HC plasma interactions with the local ionospheric plasma and the geomagnetic field. These interactions are critical to device performance and to the perturbations that the device is likely to introduce in its near-space and flux-tube-coupled domains. This "plasma noise" aspect of operations due to unstable plasma modes can have serious implications for a broad range of "in situ" requirements for plasma-particle and wave measurements intended for Space Station, TSS and active particle-beam platforms.

Fig. 14A presents a schematic view of the phenomenological domains of hollow-cathode operation in a space plasma environment. The cathode can be biased in either polarity relative to the spacecraft ground and its outer skin (assumed a conductor in contact with the ambient geoplasma). The skin will itself be of either polarity relative to the local plasma potential, and ionospheric currents will flow across the spacecraft-associated sheath. The magnitude and polarity of skin potential relative

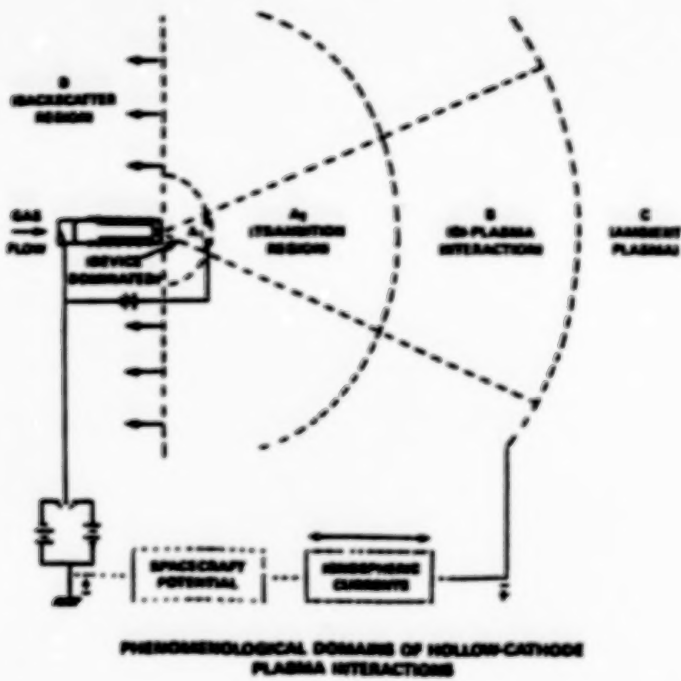


Figure 14A. Current paths and plasma domains in the hollow-cathode circuit coupling the spacecraft with the background ionosphere. (From Sussczewics [1985] and Sussczewics et al. [1988])

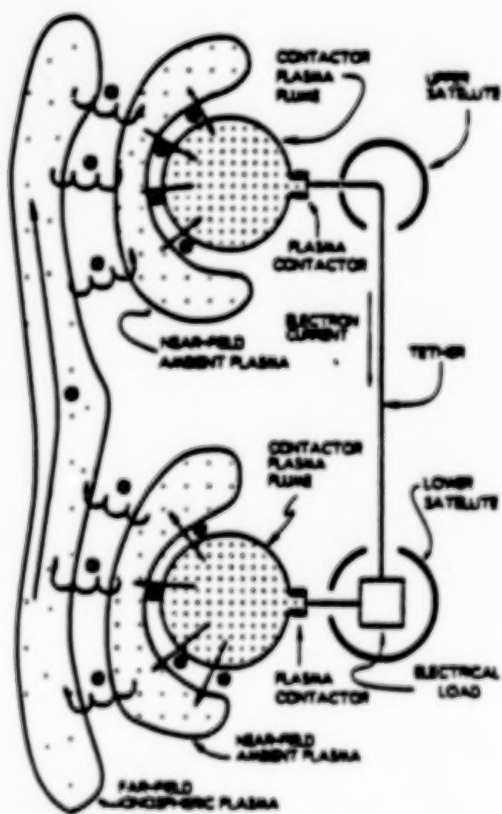


Figure 14B. Conceptualized electrodynamic tether circuit (adapted from Williams and Wilbur<sup>45</sup>; note that the lower plasma contactor is in an electron emitting mode so that the lower contactor can be replaced by an electron gun).

to space will depend on ambient plasma conditions, the spacecraft geometry and configuration, and the operation of on-board experiments (e.g. particle-beam injection). Another current path to the payload (besides that through the spacecraft sheath) is along and through the expanding hollow-cathode plasma. The expansion process, represented phenomenologically by regions A<sub>1</sub>, A<sub>2</sub>, B, and D, governs the current carrying capabilities of the HC. In a tethered configuration analogous to Fig. 13, the ground plane (spacecraft skin) in Fig. 14A and its current path to the ionosphere through its sheath are replaced by another hollow-cathode with its own phenomenological regions designated by A<sub>1</sub>, A<sub>2</sub>, B and D and its current path through the ionosphere. This is illustrated in Fig. 14B.

The plasma production and expansion process begins with neutral gas flow (typically Ar or Xe) into the cathode at pressures typically in the range 1-100 torr. Plasma is created inside the thermionically-electron-emitting cathode and the neutral gas and plasma experience a choked flow as they pass through the cathode's exit orifice (diameter  $\approx 0.030"$ ) into domain A<sub>1</sub>. In this phenomenological model, A<sub>1</sub> is defined as the "Device Dominated Region" because the attendant plasma processes depend on the cathode characteristics and the anode-to-cathode fields. In zero order, the expansion of the neutrals in A<sub>1</sub> is thermal, while that of the charged particles is thermal with increasing drift velocities imparted by the applied field. The domain is collisional, with orifice plasma and neutral densities quoted at  $10^{15}$  and  $10^{17} \text{ cm}^{-3}$ , respectively (J. McCoy, private communication). The field in region A<sub>1</sub> can impart a relative drift velocity between the electrons and ions, with the electrons easily satisfying the Dricer field condition for the onset of collective plasma effects and the Buneman instability.<sup>30,40-42</sup> This instability can turn on and off, heating the electron population and destroying all assumptions of isothermality. This will affect the plasma resistivity and the current delivery capabilities of the device.

Exiting A<sub>1</sub>, the source plasma can diminish to levels near  $10^{12} \text{ cm}^{-3}$  where it begins its exposure to a new electric field configuration resulting from the potential difference between the anode and the ambient plasma (beyond the sheath edge in region C). Region A<sub>2</sub> is dominated by the source plasma, which by current estimates should have a high kinetic  $\beta$ , excluding the ionospheric plasma and the geomagnetic field. A<sub>2</sub> is a transition region in which the source plasma diminishes in dominance over the domain and its kinetic  $\beta$  drops to unity. This is expected to occur over one-to-several meters, depending on prevailing conditions.

The processes in Regions A<sub>1</sub> and A<sub>2</sub> may be considered less complex than those in Region B, where counterstreaming source and ionospheric plasmas and magnetic field effects must be taken into account. In Region B, the magnetic fields control the net electron emission or collection characteristics of the contactor, and it is here that the payload is truly in "contact" with the ionospheric plasma through the HCD. While it is the physics in this region that holds the key to the capabilities of the device to deliver or attract large currents with low-to-moderate anode potentials, the properties of the expanding hollow-cathode plasma in region A<sub>2</sub> and that of the ambient ionosphere in C define the zero-order inputs for the interactions which form the basis of current flow.

The final input control involves the magnitude of the ambient magnetic field and its orientation relative to the cathode axis and the plasma "surfaces" defining Region B.

Since the introduction of the phenomenological model of HC plasma interaction domains by Szuszczewicz,<sup>30</sup> there has been a number of theoretical<sup>43,44</sup> and experimental<sup>45-48</sup> efforts focussed on their existence and controls. Region B, for example, has been referred to by Davis et al.<sup>43</sup> and Williams and Wilbur<sup>45</sup> as a "double sheath" or a "double layer," across which most of the potential between the HC and ambient plasmas is dropped, and where the HC and background plasma counterstream.

The regimes A-D in the hollow-cathode plasma represent only one subelement in the current closure path illustrated in Figs. 14A and B. Other subelements include the ionospheric path itself, and the return current path through the reference electrode (or tethered satellite) sheath. To understand, measure and model the current closure system and to establish the I-V-B characteristic is indeed a challenge. There are some guidelines from laboratory simulation experiments, but while they represent valuable adjuncts to the development of theoretical models and the planning of spaceflight investigations, care must be taken in their interpretation and their extrapolation to direct applications on a space platform. This is not to say that there is not a history of meaningful laboratory simulations of space plasma processes, even when scaling laws did not rigorously apply. We include in this class the reconnection and tether-simulation experiments of Stenzel et al.<sup>49-51</sup> and Urretia and Stenzel<sup>52</sup>, as well as the energetic beam-plasma-discharge studies of Bernstein et al.<sup>53-55</sup>, Szuszczewicz et al.<sup>56-57</sup> and Kellogg et al.<sup>58-59</sup>. In the case of HC simulations there are some special problems however, and we illustrate that with reference to Table 1 where we compare the HC and background plasma properties that are likely to be encountered in space with those that have been encountered in the lab. Several problem areas stand out. If we look first at the ratio of hollow-cathode plasma density  $N_{HC}$  to that of the background plasma  $N_O$  to which it must couple, we see a major discrepancy.... $N_{HC}/N_O = 2.8$  under laboratory conditions compares unfavorably with projected spaceflight applications where we expect  $48 \leq N_{HC}/N_O < 1.9(10)^5$ . Differences between laboratory and spaceflight conditions also include relative thermal energy densities (2.2 in the lab and 7400 in space) and the diamagnetic properties of the plasmas (expressed by  $\beta = 8\pi N_{HC}(kT + K.E.)/B^2 = 0.15$  and 3.7 in the lab and in space, respectively). (The difference in the  $\beta$ -values stems from the directed velocity of the space vehicle relative the background plasma, a value near 8 km/sec on a low-earth-orbiting spacecraft and in the range 0.5-2.0 km/sec on a rocket.)

Other problems involve the laboratory simulation of the background ionospheric plasma, which should be fully-Maxwellian with  $T_e = 0.2$  eV. Instead, we find in the work of Williams and Wilbur<sup>45</sup> a two-component electron distribution (defined by  $T_e^c$  and  $T_e^h$ ) in the background simulator. The temperatures of the cold and hot components ( $T_e^c$  and  $T_e^h$ ) were at 6.5 and 52 eV, respectively, and their relative densities  $N_e^h/N_e^c$  were at a 4% level. With plasma interaction processes critically-dependent on relative energies and densities, and the specifics of the energy distribution functions of the interacting plasmas, it is clear that the laboratory experiments conducted to date must

Table 1

## COMPARISONS OF HOLLOW-CATHODE AND BACKGROUND PLASMA REGIMES

	Lab Simulation [After Williams and Wilbur <sup>59</sup> ]	Typical Space Application
<b>Plasma Densities</b>		
Hollow-Cathode Plasma Density,* $N_{HC}$	$1.9 (10^8) \text{ cm}^{-3}$	$1.9 (10^8) \text{ cm}^{-3}$
Background Plasma Density, $N_o$	$6.8 (10^7) \text{ cm}^{-3}$	$10^3 < N_o \leq 4(10^6) \text{ cm}^{-3}$
Ratio $N_{HC}/N_o$	2.8	$48 \leq N_{HC}/N_o < 1.9(10^5)$
<b>Plasma Electron Energies</b>		
Hollow Cathode Plasma	Multi-Component $T_e^c \sim 4.8 \text{ eV}, T_e^h \sim 45 \text{ eV}$	Multi-Component** $T_e^c \sim 5 \text{ eV}, T_e^h \sim 50 \text{ eV}$
Background Plasma	Multi-Component $T_e^c \sim 6.5 \text{ eV}, T_e^h \sim 52 \text{ eV}$ ( $N_o^h/N_o^c = 4\%$ )	Single-Component Maxwellian $T_e \sim 0.2 \text{ eV}$ ( $N_o^h/N_o^c = 0$ )
<b>Relative Thermal Energy Densities</b>		
$N_{HC}kT_e^c/N_o kT_o^c$	2.2	$7.4 (10^3)$
<b>Hollow-Cathode <math>\beta</math></b>		
$\beta = 8\pi N_{HC}(kT + K.E.)/B^2$	0.15	3.7

\* These values depend on operating parameters and point of measurement. We use here the published values of Williams and Wilbur<sup>59</sup> and assume the same values apply in a spaceborne system.

\*\* We assume the multi-component nature observed in the lab will also apply in space.

be carefully scrutinized before their results are directly extrapolated to spaceborne applications. There is no question however that there is merit in the accumulated results, for Williams and Wilbur<sup>45</sup> and Vannaroni et al.<sup>46</sup> have drawn attention to the non-Maxwellian nature of the hollow-cathode plasma and have helped develop an appreciation for the expansion process and interacting plasma regimes illustrated in Figures 14A. They have established a database that needs to be tested and explored in space.

The relative merits and limitations of individual laboratory experiments notwithstanding, we turn now to the power spectral density measurement of electrostatic waves in the investigation of Szuszczewicz et al.<sup>60</sup> Shown in Fig. 15, these measurements were taken in a 1m x 2m chamber with the hollow-cathode mounted on one end of the system and allowed to expand into vacuum. The experiment was designed to test the original position of Szuszczewicz,<sup>30</sup> that the hollow-cathode plasma was an intrinsically "noisy" device with significant potential for perturbing spaceborne experiments designed to study other plasma phenomena. The experiment was effectively a survey of wave observations with parametric control over hollow-cathode conditions (current, voltage and gas flow) and superimposed magnetic fields. Wave structures were ubiquitous, ranging from intense lower frequency white noise characteristics like that shown in Fig. 15A (levels at volts/meter) to mv/meter levels shown in Fig. 15B. (Note that the high power spectral component at the low frequency end in Fig. 15B is the 120 Hz multiple of the ac power.) In panels C and D we see varying waveforms and spectral indices with and without resonances in the 0.01 - 2.0 Mhz region. The overwhelming conclusion is that hollow-cathode plasmas are replete with wave perturbations driven by current and streaming instabilities, with important effects on energy distribution functions and net current carrying capabilities. Certain modes appear innocuous (e.g. mv/m E-field fluctuations) while others appear to generate large perturbations (e.g. volts/m).

The results of Williams and Wibur,<sup>45</sup> Paterson et al.,<sup>47</sup> Vannaroni et al.,<sup>46</sup> and Szuszczewicz et al.,<sup>60</sup> while limited in the integrity of their capabilities to simulate HC operations in space, provide powerful guidelines for future experiments and establish the clear need for a spaceborne experiment to test and characterize the principles and operations of the hollow-cathode device and develop a detailed understanding of the I-V-B characteristics. These I-V-B characteristics represent the complete system of current closure with all the complications discussed in Sections 1-3. There will be bi-Maxwellian and non-Maxwellian energy distributions, multi-ion constituencies (e.g.,  $Ar^+$  or  $Xe^+$  from the hollow cathode device, and  $O^+$ ,  $NO^+$ ,  $O_2^+$  from the background plasma), and a broad spectrum of turbulence as suggested in the results of Figure 15. There will also be the challenge of properly diagnosing the currents impinging on the tethered satellite. Should there still be large sheaths and potentials there will surely be anomalous energy distributions and anisotropies in the charged particle populations. Some perspectives on these phenomena will be advanced in the next section.

#### 4.2 Beams, Charging and Return Current Measurements

Current closure involving plasmas and man-made systems like probes and satellites

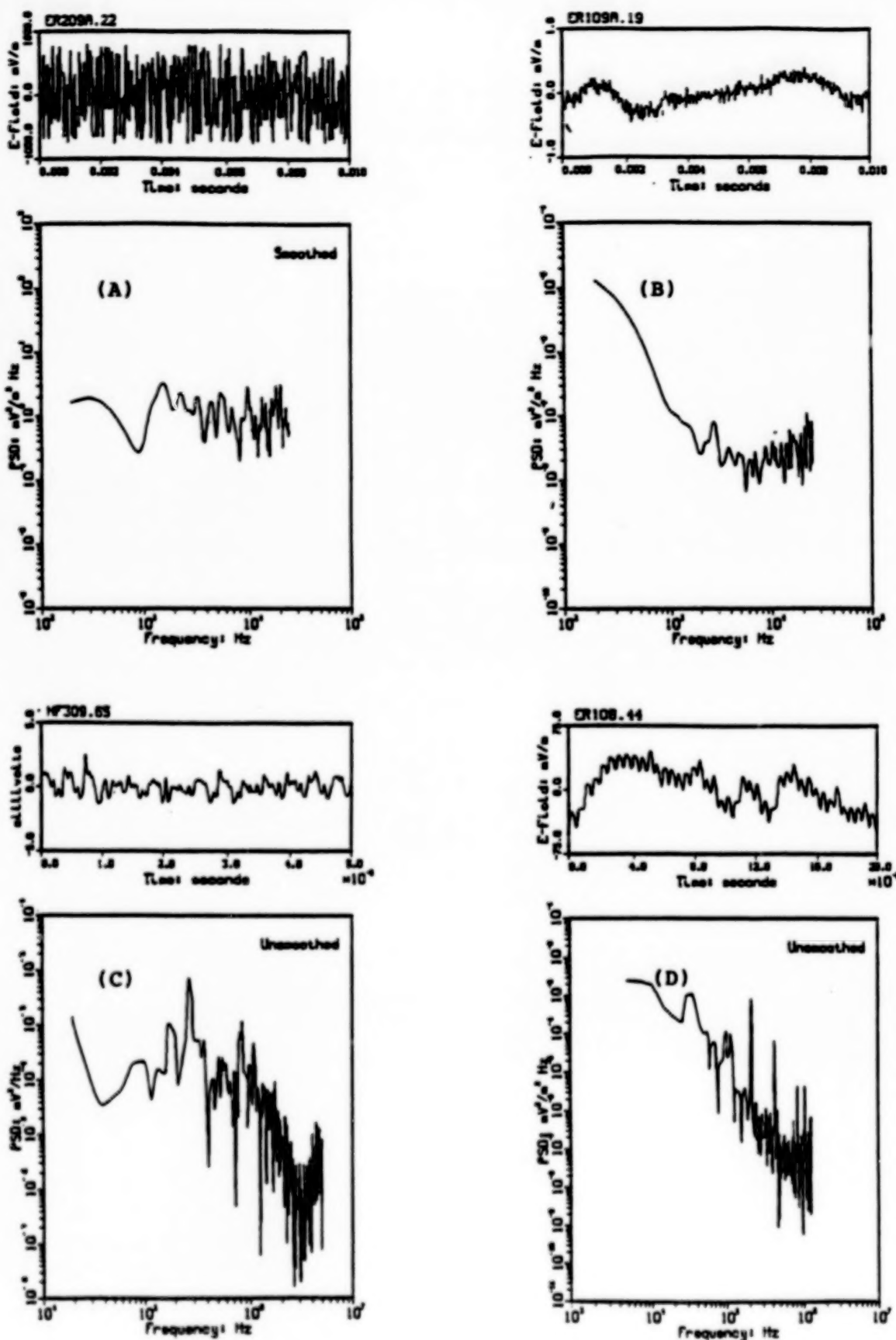


Figure 15. Selected observations of fluctuating electric fields (small upper panel) and associated spectral distributions (larger lower panel) under four different conditions in the laboratory hollow-cathode plasma investigation of Szuszczewicz et al.<sup>60</sup>

ultimately involve current flow across a sheath. This is indeed the case in the illustration of Fig. 14A, and certainly the case in a tethered system in which one end may have current flow dominated (or controlled) by a hollow-cathode-like device, while the other end relies primarily on sheath currents. In general, sheath currents can be small, limited in first order by the thermal currents in the ambient plasma and the size of the sheath. Currents across sheaths however, can be difficult to diagnose, and may in fact be dominated by a complicated set of non-linear effects. This possibility is highest for large potentials and large sheaths, giving rise to the need for a fairly complete understanding of active phenomena within the sheath and an accurate measurement of currents transferred from the plasma and collected at the spacecraft surface.

That a space vehicle can charge is an accepted fact, but accumulated experimental results on charging levels are mixed. In all cases however, the database suggests that the incorporation of mitigation techniques in spacecraft design is a prudent approach to safety and mission success. This is particularly true in high altitude and geosynchronous orbit, and with all particle-beam experiments regardless of ephemerides.

The fundamental issue in spaceborne applications of energetic-particle beams involves current conservation of the charged-particle component of the beam, i.e. the space vehicle can eject an energetic particle beam of  $I_B$  amperes only if the ambient plasma can provide an equal quantity of return current. (The closure path is analogous to that shown in Figure 14A, with current from the hollow-cathode replaced by currents emitted by an energetic charged-particle beam.) If there is no return current, a simple linear analysis suggests that a meter-size spherical body emitting a net 10 mA electron beam would be expected to charge to 9 kV in 0.1 ms. In order to avoid charging to high positive potentials (for a net electron current emission) relative to the ambient plasma, the vehicle must attract an equal quantity of return electron current from sources that include ambient plasma electrons, beam-produced secondaries, and possibly suprathermal electrons created by non-linear interactions. If the spacecraft charges to levels greater than local ionization potentials, additional ion-electron pairs can be created in the vehicle sheath.

An estimate of the return current available to a body of collecting surface  $S$  [ $\text{m}^2$ ] from an ambient thermal plasma of density  $N_e$  and temperature  $T_e$  is given by:

$$I_\infty[\text{mA}] = \left( \frac{n_\infty[\text{cm}^{-3}]}{10^5} \right) \left( \frac{T_e[\text{°K}]}{1600} \right)^{1/2} S[\text{m}^2] \quad (24)$$

For collecting areas of order 1  $\text{m}^2$  and ambient plasma densities less than  $10^6 \text{ cm}^{-3}$ , this return current is less than 10 mA.<sup>61</sup> With ionospheric densities potentially as low as  $10^3 \text{ cm}^{-3}$ , this suggests that a prudent spacecraft design needs to emphasize the importance of total conducting surface area, even for very modest beam currents.

Charging to large vehicle potentials also raises concern with large plasma sheaths and attendant modification of the spacecraft's nearby plasma environment. Estimates for sheath sizes determined previously<sup>62</sup> were found to be adequately represented for

probe-like potentials by

$$(R_{sh} - R_{sc}) = \lambda_D \left[ 2.5 - 1.54 \exp\left(\frac{-0.32R_{sc}}{\lambda_D}\right) \right] \left( \frac{e\Phi_{sc}}{kT_e} \right)^{1/2} \quad (25)$$

where  $R_{sh}$  and  $R_{sc}$  are the radii of the sheath and spacecraft, respectively,  $\lambda_D$  is the electron Debye length, and  $\phi_{sc}$  is the spacecraft potential relative to the ambient plasma. For a spacecraft potential of only 130 volts, the sheath size can approach 7 meters in the low density limit of  $10^3 \text{ cm}^{-3}$ ; and at 1300 volts (and  $10^3 \text{ cm}^{-3}$ ) it approaches 21 meters. The corresponding sheath sizes at  $10^6$  are 21 cm and 70 cm, respectively.

An illustration of the large sheath scenario is presented in Fig. 16. The figure is intended to represent a cylindrical payload with its axis parallel to the ambient magnetic field. Assuming that one can define a discrete sheath edge at a radius  $R_{sh}$  and at a potential of  $-V_{sh}$  with respect to the payload frame, electrons will be attracted from the ambient plasma and undergo an  $E \times B$  driven orbit in passing from the plasma to the satellite surface. In striking the payload surface, there will be a broad range of incident angles, suggesting that skin-mounted detectors intended to determine sheath potential from an energy measurement of impinging particles, must be capable of full pitch angle resolution. It is clear that a detector with acceptance angles only aligned with the radius vector will give inaccurate measurements of sheath potentials and current collected by the spacecraft surface.

Time dependency in sheath size and potential growth is also an important factor. At moderate to low ionospheric densities ( $10^4 - 10^5 \text{ cm}^{-3}$ ) consider for example a cylindrical payload ( $L = 30 \text{ m}$ ,  $d = 3 \text{ m}$ ) oriented with respect to the magnetic field as illustrated in Fig. 16. If at a time defined as  $t = 0$  an electron emitting beam is ejected parallel to  $B$ , the payload would charge to levels in the 1 - 10 kV range within 150  $\mu\text{s}$ . Results of numerical calculations for such a simulation, with a beam-on pulse of 150  $\mu\text{s}$ , are presented in Fig. 17 (adopted from Drobot et al.<sup>63</sup>). Other aspects of the simulation (not detailed here) also show that the entire system would be replete with plasma oscillations, placing very severe constraints on "in situ" diagnostics within the sheath and on skin-mounted particle detectors attempting to resolve the energy of impinging particles and the total potential across the sheath. Such measurements are indeed a necessity if one is to achieve an understanding of the charging/discharging mechanism and beam-plasma current closure in the spacecraft-ionosphere system.

## 5. Comments and Conclusions

In addressing the realities of current collection in dynamic space plasma environments, we have treated theoretical and experimental issues. The overall conclusion points to the fact that there are a substantial number of challenges remaining for some of the more complex and dynamic systems, not the least of which involves energetic beam experiments and long tethered satellite systems. In many cases experimental techniques must be able to diagnose and account for simultaneous variations in electric fields, plasma densities, energy distribution functions and ion mass. Inevitably,

CHANGING PHENOMENOLOGY FOR SPACECRAFT  
WITH NET EMITTED CURRENTS

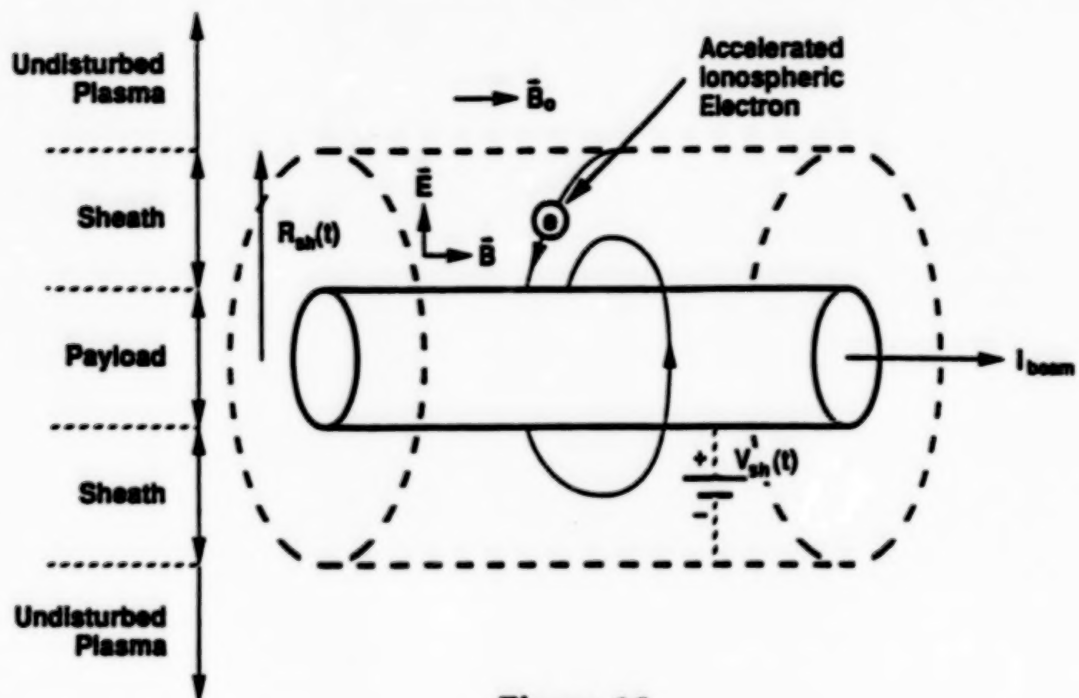


Figure 16

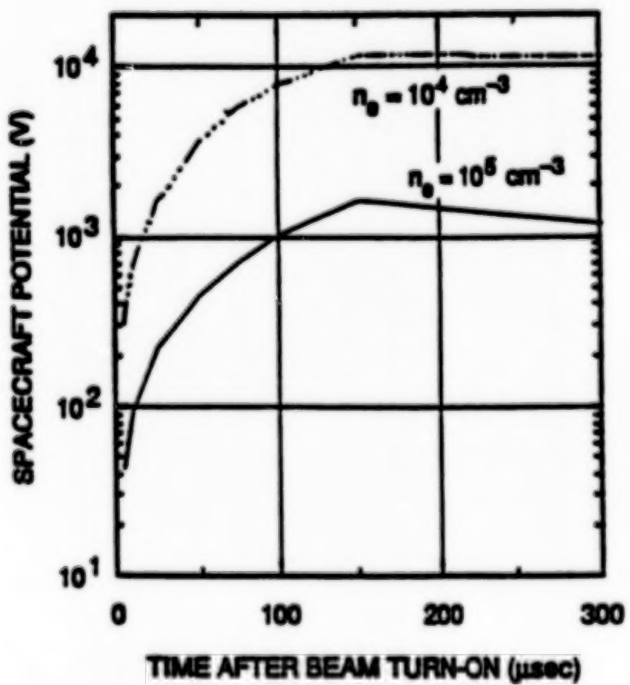


Figure 17. Time-dependent charging profile for a cylindrical payload ( $L,d) = (30\text{m}, 3\text{m}$ ) oriented parallel to the geomagnetic field. The calculations assumed an energetic electron beam ( $I_B = 100 \text{ mA}$  parallel to  $\vec{B}$ ) with turn-on/turn-off at  $t=0/t=150 \mu\text{s}$ , respectively, and background ionospheric density states of  $10^4$  and  $10^5 \text{ cm}^{-3}$ . (Adapted from Drobot et al.<sup>53</sup>)

most diagnostic systems assume that one or more of those variables is constant. In laboratory experiments there are times when this problem can be dealt with by virtue of experiment repeatability. This often is not the case in spaceborne experiments. At best there is some repeatability, but never comparable to that in a laboratory-based experiment. Ultimate success will rely on the development of new measurement techniques and a close synergism in theoretical developments and laboratory-based and spaceborne experiments.

### References

1. Langmuir, I., and H. Mott-Smith, *Phys. Rev.* 28, 727 (1926).
2. Boyd, R.L.F., in *Plasma Diagnostics*, edited by W. Lochte-Holtgreven (North-Holland, Amsterdam, 1968), p. 732.
3. Chen, F.F., in *Plasma Diagnostic Techniques*, edited by R.H. Huddlestone and S.L. Leonard (Academic, New York, 1965), p. 113.
4. Szuszczewicz, E.P., "Area influences and floating potentials in Langmuir probe measurements," *J. Appl. Phys.* 43, 874 (1972).
5. Lafraimboise, J.G., University of Toronto Institute of Aerospace Studies Report No. 100 (1966) (unpublished).
6. Wehner, G., and G. Medicus, *J. Appl. Phys.* 23, 1035 (1952).
7. Hiroa, K., and K. Oyama, *J. Geomagn. Geoelectr.* 24, 415 (1972).
8. Szuszczewicz, E.P., and J.C. Holmes, "Surface contamination of active electrodes in plasmas: Distribution of conventional Langmuir probe measurements," *J. Appl. Phys.* 45, 5134 (1975).
9. Investigators who drive their probes with a ramp voltage function may never be aware that their measurements are distorted by surface effects.
10. See, for example, G.L. Gains, in *Scientific Foundations of Vacuum Techniques*, 2nd ed., edited by S. Dushman and J.M. Lafferty (Wiley, New York, 1966), p. 376; E.W. McDaniel, *Collision Phenomena in Ionized Gases*, (Wiley, New York, 1964), Chap. 13.
11. See, for example, H.F. Winters and P. Sigmund, *J. Appl. Phys.* 45, 4760 (1974).
12. J.C. Holmes and E.P. Szuszczewicz, *Rev. Sci. Instrum.* 46, 592 (1975).
13. Szuszczewicz, E.P., and J.C. Holmes, "Re-entry plasma diagnostics with a pulsed plasma probe," AIAA Paper No. 76-393, *AIAA 9th Fluid and Plasma Dynamics Conference*, July 1976.
14. Szuszczewicz, E.P., "Laboratory simulation of controlled energetic electron-beam-plasma interactions in space," *AIAA J.* 21, 1374 (1983).
15. Szuszczewicz, E.P., "Controlled electron beam experiments in space and supporting laboratory experiments," *J. Atm. Terr. Phys.* 47, 1189 (1985).
16. Grossmann, W., D. Rault, A. Drobot, J. Bukson, J. Mimis and D. Buden, "Non-

- nuclear megawatt pulsed power," *SAIC Rpt. to AFWAL*, February 1988.
- 17. Sanmartin, J.R., *Phys. Fluids* 13, 103 (1970).
  - 18. Brown, I.G., A.B. Compher, and W.B. Kunkel, *Phys. of Fluids* 14, 1377 (1971).
  - 19. Chen, F.F., C. Etievant and D. Mosher, *Phys. Fluids* 11, 811 (1968).
  - 20. Miller, N.J., *J. Geophys. Res.* 77, 2851 (1972).
  - 21. Laframboise, J.G., and J. Rubinstein, *Phys. Fluids* 19, 1900 (1976).
  - 22. Szuszczewicz, E.P. and P.Z. Takacs, *Phys. Fluids* 22, 2424 (1979).
  - 23. Waywouth, F., *J. Appl. Phys.* 37, 4492 (1966).
  - 24. Szuszczewicz, E.P., J.C. Holmes and M. Singh, *Astrophys. and Sp. Science* 86, 235 (1982).
  - 25. Hoegy, W.R. and L.J. Wharton, *J. Appl. Phys.* 44, 5365 (1973).
  - 26. McClure, J.P. and W.B. Hanson, *J. Geophys. Res.* 78, 7431 (1973).
  - 27. Keskinen, M.L., E.P. Szuszczewicz, S.L. Ossakow and J.C. Holmes, *J. Geophys. Res.* 84, 17 (1979).
  - 28. Baracat, W.A. and C.L. Butner, *Tethers in Space Handbook*, Bantam Books (1986).
  - 29. Penzo, P.A., "A survey of tether applications to planetary exploration," NASA/AIAA/PSN, Intl. Conf. on Tethers in Space, (17-19 September 1986).
  - 30. Szuszczewicz, E.P., "Technical issues in the conduct of large space platform experiments in plasma physics and geoplasma sciences," invited paper presented at the NASA/JPL Workshop on "Space Technology Plasma Issues in 2001", September 24-26, 1986 (in the Proceedings, Jet Propulsion Laboratory, Pasadena, California; J. Feynman, H. Garrett, and S. Gabriel, editors, 1986)
  - 31. Krishnan, M., R.G. Jahn, W.F. Von Jashowsky and K.E. Clark, "Physical processes in hollow cathodes," *AIAA J.* 15, 1217 (1977).
  - 32. Lidsky, L.M., S.D. Rothleider, D.J. Rose, S. Yoshikawa, C. Mishelson, and R.J. Machin, Jr., "Highly ionized hollow-cathode discharge," *J. Appl. Phys.* 33, 2490 (1962).
  - 33. Hastings, D.E., "The use of plasma contactors in the ionosphere," *J. Spacecraft and Rockets* (1986).
  - 34. Duncan, B., A. Konradi, J. Raitt, J. R. Winkler, I. Katz, W. Nobles, N. Stone and E. C. Whipple, "Final report of the 'ad hoc' orbiter charging committee for the TSS-1 mission," USRA Publication (Nov. 25, 1985).
  - 35. Hastings, D. E. and M. Martinez-Sanchez, "The use of electrodynamic tethers for generating power and thrust," *Proceedings of the 33rd Annual Meeting of the Am. Astronautical Society*, Boulder, CO (1986).
  - 36. Davis, V.A., I. Katz, M.J. Mandell, and D.E. Parks, "Three-dimensional simulation of the operation of a hollow-cathode electron emitter on the shuttle orbiter,"

NASA/AIAA/PSN, *Intl. Conf. on Tethers in Space* (17-19 September 1986).

37. a) McCoy, J., "Electrodynamic interactions," in Applications of Tethers in Space, *NASA Conf. Publ. 2422*, NASA Scientific and Technical Information Branch (1986).  
b) McCoy, J., "Plasma motor/generator reference for power and propulsion," *NASA/AIAA/PSN Intl. Conf. on Tethers in Space*, Arlington, VA (September 18, 1986).
38. Wilbur, P., "Plasma contactor performance characterization," *NASA Conf. Publ. 2422*, NASA Scientific and Technical Information Branch (1986).
39. Gioulekas, A. and D. E. Hastings, "The role of current driven instabilities in the operation of plasma contactors used with electrodynamic tethers," *J. Propulsion and Power* (1989, in press).
40. Davidson, R.C., N.A. Krall, and R. Shanny, "Electron heating by electron-ion beam instabilities," *Phys. Rev. Lett.* 24, 579 (1970).
41. Papadopoulos, K., "A review of anomalous resistivity for the ionosphere," *Rev. Geophys. and Space Phys.* 15, 113 (1977).
42. Ishihara, O. and A. Hirose, "Non-linear evolution of Buneman instability," *Phys. Fluids* 24, 452 (1981).
43. Davis, V. A., I. Katz, M. J. Mandell and D. E. Parks, "A model of electron collecting plasma contactors," in Tethers in Space Toward Flight, an AIAA Proceedings Publication on the Third Int'l Conf. on Tethers in Space (San Francisco, CA, May 1989), pp. 94-99, Paper # 89-1560-CP.
44. Iess, L., and M. Dobrowolny, "A fluid model of plasma contactors in the ionosphere," in Tethers in Space Toward Flight, an AIAA Proceedings Publication on the Third Int'l Conf. on Tethers in Space (San Francisco, CA, May 1989), pp. 70-76, Paper # 89-1557-CP.
45. Williams, J. D. and P. J. Wilbur, "Ground-based tests of hollow-cathode plasma contactors," in Tethers in Space Toward Flight, an AIAA Proceedings Publication on the Third Int'l Conf. on Tethers in Space (San Francisco, CA, May 1989), pp. 77-87, Paper # 89-1558-CP.
46. Vannaroni, G., C. B. Cosmovici, J. McCoy, C. Bonifazi, M. Dobrowolny, U. Guidoni, L. Iess, L. Scandurra, "Experimental characterization of hollow-cathode plasma sources at Fracatti," in Space Tethers for Science in the Space Station Era, ed. L. Guerriero and I. Bekey, Societa Italiana di Fisica, 14, Bologna, Italy (Conf. Proceedings, Oct. 1987), pp. 254-260, published in 1988.
47. Patterson, M. J. and R. S. Aadland, "Ground-based plasma contactor characterization," in Space Tethers for Science in the Space Station Era, ed. L. Guerriero and I. Bekey, Societa Italiana di Fisica, 14, Bologna, Italy (Conf. Proceedings, Oct. 1987), pp. 261-268, published in 1988.
48. Williams, J. D., P. J. Wilbur and J. M. Manheiser, "Experimental validation of a

- phenomenological model of the plasma contacting process," in Space Tethers for Science in the Space Station Era, ed. L. Guerriero and I. Bekey, Societa Italiana di Fisica, 14, Bologna, Italy (Conf. Proceedings, Oct. 1987), pp. 245-253.
49. Stenzel, R. L., R. Williams, R. Aguero, K. Kitazaki, A. Ling, T. McDonald, and J. Spitzer, *Rev. Sci. Instrum.* 53, 1027 (1982).
  50. Stenzel, R. L., W. Gekelman, and N. Wild, *Phys. Fluids* 26, 1949 (1983).
  51. Stenzel, R. L., W. Gekelman, and N. Wild, *J. Geophys. Res.* 88, 4793 (1983).
  52. Urretia, J. M. and R. L. Stenzel, "Waves and wings from tethers and electrodes in a laboratory plasma," in Tethers in Space, Conference Proceedings (AIAA/NASA/ASI/ESA, 17-19 May 1989), AIAA Publication (1989), p. 63.
  53. Bernstein, W., H. Leinbach, H. Cohen, P. S. Wilson, T. N. Davis, T. Hallinan, B. Baker, J. Martz, R. Zeimke, W. Huber, "Laboratory observations of RF emissions at  $\omega_{pe}$  and  $(N + 1/2)\omega_{pe}$  in electron beam-plasma interactions," *J. Geophys. Res.* 80, 4375 (1975).
  54. Bernstein, W., H. Leinbach, P. Kellogg, S. Monson, T. Hallinan, O. K. Garriott, A. Konradi, J. McCoy, P. Daly, B. Baker and H. R. Anderson, "Electron beam experiments: the beam plasma discharge at low pressures and magnetic field strengths," *Geophys. Res. Lett.* 5, 127 (1978).
  55. Bernstein, W., H. Leinbach, P. J. Kellogg, S. J. Monson and T. Hallinan., "Further laboratory measurements of the beam-plasma-discharge," *J. Geophys. Res.* 84, 7271 (1979).
  56. Szuszczewicz, E. P., K. Papadopoulos, W. Bernstein, C. S. Lin and D. N. Walker, "Threshold criteria for a space-simulation beam-plasma-discharge," *J. Geophys. Res.* 87, 1565 (1982).
  57. Szuszczewicz, E. P., D. N. Walker, H. Leinbach, "Plasma diffusion in a space simulation beam-plasma-discharge," *Geophys. Res. Lett.* 6, 201 (1979).
  58. Kellogg, P. J., H. R. Anderson, W. Bernstein, T. J. Hallinan, R. H. Holzworth, R. J. Jost, H. Leinbach and E. P. Szuszczewicz, "Laboratory simulation of injection of particle beams in the ionosphere," in Artificial Particle Beams in Space Plasma Studies, B. Grandal, ed., Plenum Publishing Co., New York, pp. 289-329 (1982).
  59. Kellogg, P. J. and R. W. Boswell, "Beam-plasma instabilities and the beam-plasma discharge," *Phys. Fluids* 29, 1669 (1986).
  60. Szuszczewicz, E. P., G. Earle, T. Bateman and J. McCoy, "Laboratory studies of electrostatic noise in a hollow-cathode plasma," *Geophys. Res. Lett.* (1989, in preparation).
  61. Linson, L.M. and K. Papadopoulos, "Theoretical Support of the Spacelab Instrument/Experiment Definition of a Theoretical and Experimental Study of Beam-Plasma Physics (TEBPP)," Report No. LAPS 76/SAI-023-081-316-LJ, Science Applications Inc., La Jolla, California (Sept. 1981).
  62. Szuszczewicz, E.P. and P.Z. Takacs, "Magnetosheath Effects on Cylindrical Lang-

- muir Probes," *Phys. of Fluids* **22**, 2424 (1979).
63. Drobot, A., K. Ko, L. Linson, R. Smith and E. P. Szuszczewicz, "Spacecraft Charging," in The Neutral Particle Beam Program: Environmental Effects Analyses Threat Assessment Instrument Design, and Operational Considerations, E. P. Szuszczewicz (ed.) SAIC/MCL-157-361-20-A, **19**, 35 (1987).

Laboratory Experiments on Current Flow Between  
Stationary and Moving Electrodes in Magnetoplasmas

R. L. Stenzel and J. M. Urrutia

Department of Physics  
University of California  
Los Angeles, CA 90024-1547

Laboratory experiments have been performed in order to investigate the basic physics of current flow between tethered electrodes in magnetoplasmas. The present extended abstract summarizes the major findings and points to references for further details. The experiments are performed in an effectively very large laboratory plasma ( $2 \text{ km} \perp \vec{B}$ ,  $5 \text{ km} \parallel \vec{B}$  when scaled in terms of Debye lengths to low Earth orbit conditions) in which not only the nonlinear current collection is addressed but also the propagation and spread of currents, the formation of current wings by moving electrodes, the current closure, and radiation from transmission lines are explored.

The laboratory plasma<sup>1</sup> consists of a pulsed dc discharge ( $1\text{m} \perp \vec{B}$ ,  $2.5\text{m} \parallel \vec{B}_0$ ,  $n_e \leq 10^{12} \text{ cm}^{-3}$ ,  $kT_e \leq 5 \text{ eV}$ ,  $B_0 \leq 100 \text{ G}$ , Ar  $3 \times 10^{-4} \text{ Torr}$ ) whose Maxwellian afterglow provides a quiescent, current-free uniform background plasma. Electrodes consisting of collectors ( $\approx 1 \text{ cm}$  diam) and electron emitters ( $\approx 1 \text{ cm}$  diam, hot cathode) are inserted into the plasma and a pulsed voltage is applied between two floating electrodes via insulated transmission lines. Besides the applied current in the wire the total current density in the plasma is obtained from space and time resolved magnetic probe measurements via Maxwell's law,  $\nabla \times \vec{H} = \vec{J} + \partial \vec{D} / \partial t = \vec{J}_{tot}$ . Langmuir probes yield the plasma parameters  $n_e$ ,  $kT_e$ , and  $\phi_{plasma}$ .

Although current collection on a spacecraft appears to be a dc problem the rapid motion across the magnetic field results in a pulse-like current flow in the stationary plasma. When such pulses are applied to fixed electrodes in the laboratory plasma the current front is found to penetrate as a whistler wave packet along  $\vec{B}_0$ .<sup>2</sup> Whistlers rather than Alfvén waves are excited since the time variation (pulse width or electrode transit time across  $\vec{B}_0$ ) are fast compared with the ion cyclotron period. When a sequence of pulses is applied and the electrodes are moved across  $\vec{B}_0$  the situation of a moving tethered electrode system is modeled.<sup>3</sup> Superposition of wave packets from repeated measurements indicates the formation of a "whistler wing," i.e. an oblique current trail at an angle with respect to  $\vec{B}_0$  determined by both

the wave speed ( $\|\vec{B}_0\|$ ) and the electrode speed ( $v\vec{B}_0$ ). The current wings spread since the radiation sources (electrodes) are finite and the waves can propagate within a ray cone ( $\theta_c = 19^\circ$ ). Most interesting is the fact that the current wings do not depend on the collected/emitted particle speeds, i.e. whistler wings are observed for ion collection, electron collection and fast electron beam emission. Pulsed beams are current and charge neutralized by background electrons.<sup>4</sup> Current closure appears to arise from cross-field wave currents rather than collisional cross-field particle currents (Pedersen currents) or equivalent boundary currents (line tying).

Time-varying currents in stationary transmission lines (or dc currents in moving lines) are observed to induce plasma return currents.<sup>5</sup> These may couple to collective modes (whistlers) or diffuse resistively (eddy currents) depending on the direction (and motion) of the line with respect to the magnetic field  $\vec{B}_0$ . For the standard tether configuration ( $\vec{v} \perp \vec{B} \perp \vec{l}$ ) the entire insulated wire can be expected to radiate a sheet-like whistler wing, not only the conducting end electrodes. Thus, the radiation resistance of the tether system is considerably larger than that of the electrodes alone.

Since it is desirable to conduct the largest possible current through the ambient plasma the question of plasma nonlinearities arises. The laboratory experiments have demonstrated the existence of a disruptive instability<sup>6</sup> which has also been conjectured theoretically.<sup>7</sup> When electrons are extracted from a flux tube in a magnetoplasma its potential rises leading to an acceleration of ions out of the flux tube. The resultant density depression reduces the collected current. At large current densities, the ion dynamics leads to a fluctuating current ( $\delta I/I \sim 100\%$ ) as plasma periodically sloshes back and forth out of the flux tube near the positive electrode. When sufficient neutral gas is supplied ionization takes place near the anode which quenches the ion expulsion, hence current fluctuation. Such contactors formed by self-ionization of excess neutrals appear to occur in space as well.

This work was supported by grants from NSF, NASA and UERG

## REFERENCES

1. R. L. Stenzel and J. M. Urrutia, Currents between tethered electrodes in a magnetized laboratory plasma, UCLA Report PPG 1245 (submitted to *J. Geophys. Res.*), June 1989.
2. J. M. Urrutia and R. L. Stenzel, Transport of current by whistler waves, *Phys. Rev. Lett.* 62, 272 (1989).
3. R. L. Stenzel and J. M. Urrutia, Whistler wings from moving electrodes in a magnetized laboratory plasma, *Geophys. Res. Lett.* 16, 361 (1989).
4. R. L. Stenzel and J. M. Urrutia, Laboratory model of a tethered balloon-electron beam current system, *Geophys. Res. Lett.* 13, 797 (1986).
5. J. M. Urrutia and R. L. Stenzel, Waves and wings from tethers and electrodes in a laboratory plasma, in *Proceedings of Tethers in Space Toward Flight*, Third International Conference on Tethers in Space, San Francisco, CA, pp. 63-69, AIAA, Washington, DC, 1989.
6. J. M. Urrutia and R. L. Stenzel, Anomalous currents to an electrode in a magnetoplasma, *Phys. Rev. Lett.* 57, 715 (1986).
7. W. B. Thompson, Passive current collection, in *Proceedings of Tethers in Space Toward Flight*, Third International Conference on Tethers in Space, San Francisco, CA, pp. 88-93, AIAA, Washington, DC (1989).

## LABORATORY EXPERIMENTS ON PLASMA CONTACTORS

Paul J. Wilbur and John D. Williams  
Department of Mechanical Engineering, Colorado State University  
Fort Collins, CO 80523

**Abstract.** Experimental results describing the operation of hollow cathode plasma contactors collecting and emitting electrons from and to an ambient plasma at current levels of order one ampere are presented. The voltage drops induced between a contactor and an ambient plasma are shown to be a few tens of volts at such current levels. The development of a double sheath and the production of substantial numbers of ions by electrons streaming across it are associated with the electron collection process. The development of a complex potential structure including a high potential hill just downstream of the cathode orifice is shown to characterize a typical contactor emitting electrons.

### Introduction

Objects placed in a space plasma collect and emit charged particles at variable rates and, consequently, they can accumulate net electrical charge. Because the capacitance of a typical spacecraft surface is small, this net charge accumulation can cause the potential of such a surface to change rapidly and dramatically. A space plasma contactor serves to prevent this problem by providing low impedance electrical connections 1) between spacecraft surfaces and space plasma thereby preventing gross spacecraft charging (Purvis and Bartlett, 1980) and 2) between adjacent spacecraft surfaces that are isolated from each other thereby preventing differential charging (Olsen, et al., 1981). A contactor could also serve to establish a firm reference potential (local space plasma potential) for space-based instruments.

Effective spacecraft charging control is realized when the voltage differences associated with gross and differential charging are minimal over the full range of environmental conditions in which the spacecraft could find itself. A hollow cathode appears to be a device that can be used to achieve such control in both positive and negative spacecraft charging environments. The purpose of this paper will be to review the operating principles of a hollow cathode, to describe laboratory experiments conducted to demonstrate how hollow cathodes couple to ambient plasmas and to suggest, based on test results, mechanisms by which a hollow cathode and possibly other discharge plasma devices effect spacecraft charging control.

### Background

#### Hollow Cathode Devices

A review of the desirable characteristics of a plasma contactor (e.g. reliability, simplicity, low expellant and power demands and low coupling impedance) has suggested that a hollow cathode discharge is attractive compared to other contactor alternatives (Wilbur, 1986). Key features of a hollow cathode and the mechanisms by which it produces a discharge are illustrated in Fig. 1. The cathode itself consists of a small diameter (of order 1 cm) refractory metal tube that is electron-beam welded to a refractory metal (typically thoriated tungsten) orifice

plate. Located within and electrically connected to the tube is a low work function insert from which electrons are emitted. An anode, biased positive of the hollow cathode and located immediately downstream of it, collects a fraction of the electrons being drawn through the cathode orifice. The remaining fraction can be drawn into plasma plumes that can contact an ambient plasma and couple adjacent isolated surfaces to prevent charging events.

The hollow cathode discharge is generally initiated by flowing an expellant gas such as xenon through the cathode tube and orifice, applying power to the heater to raise the insert temperature to thermionic emission levels and applying a bias on the anode that can range, depending on insert temperature, from a few hundred to several thousand volts. Once the insert begins to emit electrons the anode voltage drops into the ten volt range. At this point a dense plasma develops within the cathode and a discharge is established between this plasma and the anode through the orifice. A detailed study of a hollow cathode (Siegfried and Wilbur, 1984) has suggested that the following physical processes illustrated in Fig. 1 are active:

1. Primary electrons emitted from the insert surface via a field-enhanced, thermionic emission process are accelerated into the cathode interior plasma through a sheath at the insert surface.
2. These electrons acquire sufficient energy as they pass through the sheath so they can ionize neutral atoms present in the hollow cathode interior through multistep, inelastic collision processes.
3. Both electrons that originate at the insert surface and those resulting from ionization are generally unable to reach the insert surface from the plasma because of the adverse potential gradient at the cathode interior plasma/insert interface. Consequently, they must leave the cathode interior plasma through the orifice at a rate equal to their supply rate.
4. Ions created within the cathode, on the other hand, generally will not go through the orifice because of the adverse potential they see between the cathode interior plasma and the plasma downstream of the orifice. They instead bombard cathode interior surfaces heating them and, in the case of the insert, helping to maintain its temperature at the level needed to sustain electron emission.
5. As ions reach the wall surfaces they recombine and then re-enter the cathode interior plasma as neutral atoms. Neutral atoms must leave the cathode interior through the orifice at their supply rate.
6. As electrons pass through the orifice they are accelerated through a potential difference that gives them the energy needed to ionize some of the neutral atoms that are also passing through the orifice.
7. The ions and electrons downstream of the orifice form the plasma structure needed to facilitate the plasma contacting process. These particles are eventually lost by either going to nearby surfaces (e.g. the anode or cathode) where they can recombine or by being drawn into the plasma downstream of the cathode from where they can flow to the ambient plasma or other spacecraft surfaces.

#### Phenomenological Description of the Contacting Process

The physical phenomena observed in ground-based experiments of hollow cathode plasma contactors exchanging current with a simulated

ambient plasma can be described using axial plasma potential profiles. The generalized plots of Fig. 2 show potential structures measured around contactors collecting and emitting electrons from and to a simulated ambient plasma at current levels of the order of 1 A. As Fig. 2a indicates, a contactor that is positive of an ambient plasma collects electrons through a double sheath and a quasi-neutral collector plume. Most of the potential difference associated with this process develops across the double sheath through which ions and electrons counterflow to conduct the current. While electrons are the principal charge carriers in the process, ions play the critical role of reducing the current-limiting effect of electron space charge.

The small potential dip shown separating the ambient plasma and the collector double sheath in Fig. 2a is interesting although its effect on contactor performance may not be significant. Such dips are frequently observed in plasma contactor tests and they have been observed and modeled by other researchers under somewhat different conditions (Langmuir and Compton, 1931). Their results suggest that this dip occurs (and as a result the electron and ion currents counterflowing through the double-sheath are enhanced) because the ambient plasma Maxwellian electron population have a non-zero temperature and they therefore approach the sheath with non-zero velocities.

When a contactor is biased negative of an ambient space plasma, it emits electrons and the general potential structure shown in Fig. 2b develops. The potential hump immediately adjacent to the emitter double sheath appears to evolve because electrons being drawn from the emitter induce substantial ionization of the neutral atoms which are also flowing through the cathode orifice and have a high density close it. Because electrons ejected from typical ionization events have substantial kinetic energies they tend to escape the ionization zone quickly leaving behind an overabundance of relatively massive, low energy and therefore slow-moving ions (Langmuir, 1929). In the region downstream of the peak where the potential drops, forces develop that decelerate the electrons and accelerate the ions. Further downstream, the potential flattens and a non-Maxwellian plasma composed of relatively low density, nearly monoenergetic electrons and ions which have an unknown energy distribution are observed. The required electron emission current is conducted through this region via a plasma expansion (streaming) process to the surrounding ambient plasma. Measurements have suggested the potential rise across the emitter double sheath may range as high as several tens of volts depending upon the emitter operating conditions. The intermediate double sheath shown in Fig. 2a seems to facilitate accommodation of the streaming and ambient plasmas. In laboratory tests it is believed it may stabilize at a location that is influenced by tank wall interactions.

One should note that it is contactor potential (collector potential in Fig. 2a for electron collection and emitter potential in Fig. 2b for electron emission) that determines contactor efficiency. The variation in this potential with electron collection or emission current and the way in which it can be controlled are, therefore, important.

#### Experimental Apparatus and Procedures

In order to study the plasma contacting process experimentally, the apparatus shown schematically in Figs. 3 and 4 has been constructed.

Physically, this apparatus consists of two hollow cathode devices, one (shown at the right of each figure and labeled "simulator"), which is used to generate a simulated ambient plasma, and the other (shown at the left and labeled "contactor"), which is used to generate a contactor plasma. To conduct experiments, the contactor is biased relative to the simulated ambient plasma to induce current flow between these plasmas. Also shown are the power supplies and instrumentation needed to sustain and measure the characteristics of the plasmas produced. The simulator and contactor hollow cathodes are separated by 2.7 m and are located within a 1.2 m dia. by 5.3 m long vacuum chamber. They both utilize cathodes with 6.4 mm dia. orifice plates and electron emission inserts that were fabricated by rolling 0.013 mm thick tantalum foils to form multi-layer hollow cylinders which were then treated with Chemical R-500.

The orifice in the simulator cathode is 0.38 mm in diameter and its anode is a solid 3.0 cm dia., 0.25 mm thick tantalum plate oriented parallel to the orifice plate and separated from it by a distance that can be varied from 1 to 5 mm. The orifice in the contactor cathode is, on the other hand, 0.76 mm in dia. Its anode is a flat stainless steel plate with a 1 cm dia. tantalum insert having a 5 mm dia. orifice in it (Fig. 1). The anode plate and insert are located ~2 mm downstream of the cathode orifice and the anode and cathode centerlines are colinear. The anode outside diameter was varied during the tests, but the data presented here were all obtained using a 12 cm diameter anode unless noted otherwise.

Typical tests were conducted by heating the contactor and simulator cathodes to temperatures where significant thermionic electron emission could occur (~1300 K), establishing high expellant (xenon) flowrates through them, and biasing their anodes positive using the discharge supplies to initiate cathode-to-anode discharges at each device. Next, the desired contactor and simulator flowrates ( $\dot{m}_{CD}$  and  $\dot{m}_{SD}$ ) and discharge current levels ( $J_{CD}$  and  $J_{SD}$ ) were established; the contactor was biased relative to the simulator using the bias power supply shown in Fig. 3; and voltage, current and probing instrument data were collected. The voltages and currents measured during typical tests are designated by the symbols shown within the circles in Fig. 3; they include the contactor and simulator discharge currents and voltages ( $J_{CD}$ ,  $J_{SD}$ ,  $V_{CD}$  and  $V_{SD}$ ), the bias voltage between the contactor and simulator ( $V_B$ ) and the contactor and simulator electron emission currents ( $J_{CE}$  and  $J_{SE}$ ).

The two switches shown at the contactor and simulator in Fig. 4 are positioned at either the "EE" or "EC" position depending on whether the contactor is biased negative of the simulator and therefore Emitting Electrons (EE) or biased positive and therefore Collecting Electrons (EC). Williams (1988) has shown it is necessary to position these switches properly for each operating mode to assure that intentional limitations imposed on the discharge current levels ( $J_{CD}$  and  $J_{SD}$ ) do not result in unintentional limitations being imposed on the contactor or simulator electron emission currents.

---

\*Chemical R-500 is a double carbonate ( $BaCO_3$ ,  $SrCO_3$ ) low work-function mixture that has been made by J.T. Baker Co. but is no longer produced.

The tank bias switch shown in Fig. 3 was installed so the vacuum tank could be allowed to float relative to the contactor/simulator system or be connected to the simulator. Tests conducted to investigate the effects of changes in the position of this switch on plasma and performance data have suggested that it has no significant effect on a contactor collecting electrons. On the other hand, when the contactor is emitting electrons and the switch is connected to the simulator, most of the electron current is drawn to the tank. When the switch is open and the tank is floating, most of this electron emission current must flow to the simulator. Electron currents emitted with the switch open were, therefore, found to induce higher bias voltages and current flow/plasma density patterns that tended to be concentrated along the tank centerline rather than being distributed uniformly in the tank. This occurred because all of the emitted electrons were being forced into collection at the simulator and this distorted the current flow patterns away from the spherical symmetry that would be expected in space. In order to conduct tests that were considered to be more representative of those expected in space, tests described herein were generally conducted with the tank bias switch connected to the simulator. Any data collected with this switch open will be identified specifically.

The plasma environment produced between the contactor and the simulator was probed using the various instruments shown in Fig. 4. These instruments, the function they serve and the physical volume in which they can be used are:

Emissive Probe - This sensor and the associated circuitry system, which are similar to those used by Aston and Wilbur (1981), yield plasma potential data directly. The sensor can be swept axially downstream from the contactor to the simulator and/or radially along an arc that extends from the tank/contactor centerline out to a radius of ~30 cm. Probe output voltage (i.e. plasma potential) and position are recorded simultaneously on an X-Y recorder to assure well-correlated values of the data.

Langmuir Probe - The sensor used on this probe is a 3.2 mm dia stainless steel sphere that can be moved conveniently into any position occupied by the emissive probe. Probe current/voltage characteristic curves recorded at these positions are analyzed using a two-electron-group model (Beattie, 1975) that is assumed to describe plasmas such as these. This analysis yields the density and temperature of a Maxwellian electron group and the density and energy of a primary (or mono-energetic) electron group. This analysis is aided by inputting plasma potential data determined using the emissive probe at each location where Langmuir probe data are collected. The circuitry together with additional detail about the numerical procedures used to obtain plasma information have been described by Laupa (1986).

Shultz-Phelps Ionization Gauge - This commercially available pressure gauge was modified by removing the glass enclosure around the sensor so perturbations to static pressure measurements that could have been induced by gas flows through the contactor, would be minimized and so its spatial resolution would be improved. The probe was used to measure ambient pressure distributions over the same region swept by the emissive and Langmuir probes. Neutral atom density distributions were computed from these data by applying the

perfect gas state equation and assuming the ambient gas was in equilibrium with the vacuum tank walls at a temperature of 300 K. Because gauge readouts from this device are inaccurate when a plasma is present, the measurements were made only when the cathodes were at operating temperatures and flowrates and the plasma discharges were extinguished.

Retarding Potential Analyzer - The sensor on this instrument was designed so it could be swept through an 18 cm radius arc that passed through the tank centerline and was centered at the contactor cathode orifice. In the course of moving through this arc its aperture remained sighted on the cathode orifice. It was biased so it repelled both electrons and low energy ions and therefore sensed the azimuthal current density profile of high energy ions flowing across the sheath.

### Test Results

When a typical hollow cathode plasma contactor is biased relative to an ambient plasma and the voltage difference between it and the ambient plasma in contact with it (defined as the collector or emitter potential in Fig. 2) is measured as a function of the electron current being emitted, data like those shown in Fig. 5 are obtained. These particular data were obtained at a contactor discharge current ( $J_{CD}$ ) of 0.3 A and an expellant flowrate ( $m_c$ ) of 4.1 standard cubic centimeters per second (sccm) of xenon. Under these conditions the ambient neutral gas pressure ( $P_0$ ) in the vacuum tank was  $5 \times 10^{-6}$  Torr and the contactor discharge voltage ( $V_{CD}$ ) varied over the range from 12 to 20 V as the electron emission current ( $J_{CE}$ ) was varied from +1000 mA to -1000 mA. The contactor potential plotted on the horizontal axis in this figure is the difference between the contactor anode or cathode potential ( $V_B$ ) and the ambient plasma potential ( $V_p$ ) sensed by an emissive probe located ~1 m downstream of the contactor. The data of Fig. 5 show the contactor potential remains near -25 V when substantial electron currents are being emitted (second quadrant) and that it rises to about 50 V for substantial electron collection currents (i.e. for negative emission currents in the fourth quadrant).

The curve in the fourth quadrant of Fig. 5 shows that the magnitude of the electron collection current increases rather suddenly at a potential difference of -40 V where the "transition to ignited mode" operation is identified. This transition is generally observed as contactor bias potential is being increased. Its occurrence is accompanied by the appearance of a bright luminous glow that typically extends several centimeters from the contactor and is frequently somewhat spherical in shape. It is believed that this luminosity is caused by the de-excitation of xenon atoms that have been excited by electrons being drawn (streaming) from the ambient plasma toward the contactor and that ionization is also induced by these electrons.

### Electron Collection

When plasma potentials are measured throughout the region immediately downstream of a contactor collecting electrons, data like those shown in Fig. 6 are obtained. This figure includes both a raised potential map, which shows the structure of the plasma field around the contactor qualitatively and an equipotential contour map from which

quantitative information about the potentials can be obtained. These two plots show the plasma field consists of two relatively uniform potential plasma regions separated by a region of large potential gradient. Since neither magnetic field nor collisionally induced impedances are expected in the region where the potential changes rapidly, this must be a sheath region (Langmuir, 1929), i.e. one in which charged-particle acceleration is occurring.

On the basis of the typical data of Fig. 6 one can propose the model of electron collection suggested by Fig. 7. This model shows a relatively higher density plume of quasi-neutral plasma in the region immediately adjacent to the contactor which is separated from a lower density quasi-neutral ambient plasma by a double-sheath (or double-layer). As the centerline plasma potential profile in this figure suggests electrons from the ambient plasma are drawn toward the contactor plume and ions from this plume are drawn toward the ambient plasma. On the other hand, ions from the ambient plasma and electrons from the contactor plume are both reflected at the sheath. The ion and electron currents that can be drawn through the double-sheath region are limited by the space-charge effects suggested by the net accumulations of positive and negative charge shown, respectively, upstream and downstream of the sheath midpoint in the bottom sketch of Fig. 7.

When plasma properties are measured along the vacuum tank/contactor centerline through a typical double-sheath, data like those shown in Fig. 8 are obtained. These results suggest plasma conditions do vary in a way that is consistent with the model of Fig. 7 (note that the zero voltage for the plots of Figs. 6 and 7 is the ambient plasma potential, while that for Fig. 8a is the simulator cathode potential). Figures 8b and c indicate the plume and ambient plasmas are both composed of primary (mono-energetic) and Maxwellian electron groups. They show the Maxwellian temperature and density and the primary energy and density all remain constant at about 6 eV,  $4 \times 10^7$  cm<sup>-3</sup>, 40 eV and  $3 \times 10^6$  cm<sup>-3</sup> respectively, in the ambient plasma region for this case where ~370 mA of electrons are being collected.

It is noted that the energy of the primary electrons in the ambient plasma (Fig. 8c) is approximately equal to the simulator cathode-to-ambient plasma potential difference. This suggests that these electrons are ones that have been accelerated into the ambient plasma from the simulator hollow cathode and have had few energy-degrading collisions. It is noted that the ratio of primary-to-Maxwellian electrons in the ambient plasma is generally not large (usually less than 10% as in the case of the data of Fig. 8). The data of Fig. 8b show the density of the Maxwellian electrons upstream of the double-sheath drops rapidly with distance from the contactor cathode. The floor symbol drawn on Fig. 8b upstream of the double-sheath location indicates that the Maxwellian density and temperature were not measurable at this location because the primary electron signal to the Langmuir probe overwhelmed the Maxwellian one. The data of Fig. 8c show the primary electron density upstream of the sheath is more than an order of magnitude greater than that downstream. The primary electron density upstream of the sheath is also seen to increase as the distance from the contactor decreases probably because these electrons are being concentrated as they stream radially inward toward the cathode. Finally, it should be noted that the energy of the primary electrons in the region upstream of the sheath (35 to 45 V) is roughly equal to the sheath potential drop

( $V_{SH}$ ). This suggests that primary electrons found in the high density plume are indeed those that have been accelerated across the sheath from the Maxwellian electron group in the ambient plasma. This result also supports the proposed physical model of the electron collection process.

When the retarding potential analyzer (RPA) is used to measure the azimuthal profile of the current density of ions expelled across the double-sheath of a contactor collecting electrons at the conditions listed on Fig. 8, the data of Fig. 9 are obtained. One can integrate these ion emission current density data over a hemispherical surface with the radius of the RPA sweep arc (18 cm) to determine the overall ion emission current flowing from the contactor to the ambient plasma. The result of so doing is 4.2 mA in this case. Applying a simple model describing space-charge-limited electron collection through a spherical double sheath (Wei and Wilbur, 1986) one computes an ion emission current (2 mA) that is approximately one half of the measured value. Considering the uncertainties associated with these measurements and the space-charge-limited model being applied, this is considered to be acceptable agreement.

If the current being collected through the double sheath is space-charge-limited, theory (Langmuir, 1929; Wei and Wilbur, 1986) indicates the ion and electron currents counterflowing through the sheath should be related linearly and should be independent of other conditions such as expellant flowrate and sheath voltage drop. Figure 10 shows this linear variation between ion centerline current density, which is proportional to the total ion emission current, and electron collection current. It is noted, however, that the slope of the line in Fig. 10 corresponds to an ion-to-electron current ratio that is about (1/250). This value is nearly twice the expected theoretical value (1/490--the square root of the electron-to-ion mass ratio). The could be due to geometrical differences between the actual shape of the double sheath and that assumed in the simple theoretical analysis.

When the size and shape of the double sheath and the voltage drop across it are changed dramatically, the ion emission current is unaffected provided the electron collection current is held constant. For example, Fig. 11 shows the changes induced in the equipotential contour maps of a contactor collecting 900 mA of electrons by increasing the xenon flowrate from 2.7 to 11 sccm. The data of Fig. 12 show such flowrate changes induce a substantial change in the sheath voltage drop, but no significant change in the centerline ion emission current density occurred.

Ion Production to Support Electron Collection. The location of the upstream boundary of the double sheath is determined by the rate at which low energy ions are supplied to it. Increasing this supply rate causes the upstream boundary to move downstream and this causes the sheath voltage drop to decrease (Williams, et al., 1987). The means by which the ions are produced in the plume region of a contactor collecting electrons is therefore a matter of interest. Some ions are produced by electrons that are drawn through the hollow cathode orifice and collide with neutral atoms in this region, however, production by this mechanism may be insufficient to induce a low voltage drop. It is believed, in fact, that these ions will sustain a low voltage drop only to an electron collection current level of about 100 mA. Above this electron collection current, test results indicate a new mechanism of

ion production, related to the onset of the ignited mode of operation identified in Fig. 5, becomes important. This transition, which is accompanied by a sudden and dramatic increase in the luminosity of the contactor plume, is believed to occur when the voltage drop across the double sheath is sufficient to induce excitation and ionization of expellant atoms coming through the cathode orifice by the electrons being collected. Evidence that excitation reactions are occurring in the ignited mode is provided by plume luminosity. The fact that increased electron collection current accompanies the transition (Fig. 5) suggests that ion current flow also increases to sustain operation at space-charge-limited conditions. Because increased ion production would be required to sustain this ion current, the electron collection current increase implies increased ionization accompanies the transition.

Additional evidence of substantial ionization in the plume of a contactor collecting electrons in the "ignited mode" is obtained by calculating the streaming electron/atom ionization rate in the contactor plume. This has been accomplished by measuring the neutral density distribution downstream of a hollow cathode using the movable Shultz-Phelps gauge and then computing the ion production induced by electrons streaming from the ambient plasma through this atomic cloud toward the hollow cathode. A rough calculation suggests the resulting ion production is more than sufficient to supply the total ion current required to sustain operation at the space-charge-limited condition for a spherical double-sheath (Williams and Wilbur, 1989).

Effects of Anode Area on Electron Collection. Typical plasma potential data measured downstream of a contactor operating with a 3 cm diameter anode are compared to those measured near a contactor with a 12 cm diameter anode in Fig. 13. The most striking differences between these data are the higher voltage levels, the spreading of the double-sheath and the reduction in the size of the contactor plume when the smaller anode is used. Although the relative position, magnitude and shape of the equipotential contours are different, it is argued that the voltage difference that exists must be sustained because acceleration of counterflowing ion and electron currents is occurring in both cases. Thus, the potential structure associated with both anodes must reflect the essential phenomena associated with a double sheath. The differences between the sheaths shown in Fig. 13 appear to develop because the inner boundary of a double sheath must remain anchored to and therefore have a dimension that is about equal to the associated anode diameter. This constraint on the sheath size at the contactor is reasonable when one recalls that the charge carried by electrons collected into the plume must eventually reach the anode.

A simple double-sheath model (Williams and Wilbur, 1987) can be applied to determine the voltage drop across the near-spherical double sheath associated with the large anode data given in Fig. 13. Although this model is not suited to the irregular shape of the double-sheath associated with the small anode, it is expected that the smaller anode case can be modeled numerically provided the double-sheath phenomena are reflected in the model. It is noted that the potential structure shown for the 3 cm anode is similar to structures reported by Patterson and Aadland (1987) for tests involving electron collection from what appears to have been a rather low ambient density plasma at current levels above

1 A on a contactor that utilized a 24 cm diameter anode. A review of their data together with data obtained by the authors suggests a double sheath takes on an irregular (non-spherical) shape when the current being collected exceeds the ambient plasma random electron current density times the area of a hemispherical double-sheath with a radius that is about equal to that of the contactor anode.

Although double sheaths observed in the laboratory appear to tie themselves to the contactor anode, it is considered possible that a large double sheath that might develop in space could be spherical and not be tied to the outer boundary of an anode. Whether or not this would occur appears to depend on whether or not such a double sheath would be stable (Hastings and Blandino, 1989). In any event it is considered important to utilize an anode that is as large as practicable to realize a high electron collection current capability with a low voltage drop in a space plasma.

#### Electron Emission

The plasma potential field measured downstream of a typical contactor emitting electrons is shown in Fig. 14. The contactor cathode (at the 0,0 location) is at the lowest potential (-14 V) of any point in the maps. Downstream of that point the potential rises to a ridge along which the potential peaks before it drops off and then levels out. The peaked potential structure is particularly noteworthy and was initially unexpected. It is noted that the data in Fig. 14 were collected using an emissive probe and this probe becomes increasing inaccurate as it is moved closer to the cathode. More specifically, it indicates potentials that fall progressively further below the true plasma potentials as it is moved into denser plasmas, i.e. into regions closer to the cathode orifice. This inaccuracy arises because the probe cannot be held at the temperature required to assure adequate electron emission in the plasma environment close to the cathode without burning out. Thus it can be stated that the potentials rise to even higher peak values than those indicated at the crest of the ridge shown in Fig. 14.

Potential profiles measured downstream of a contactor emitting electrons, when the tank is floating relative to the contactor and simulator (tank bias switch in Fig. 3 open), are shown in Fig. 15. The low emission current potential profile (15 mA) is considered to be quite accurate because plasma densities are low close to the cathode in this case and the emissive probe should, therefore, indicate accurately. In this case the potential hill is obvious. At the higher current (250 mA) where plasma density close to the cathode is high, however, the probe error would be expected to be greater, and the potential hill is not very obvious.

Downstream of the potential hill the data of Fig. 15 show a region of relatively uniform plasma potential before the potential rises to the ambient plasma potential. These potential structures should be measured correctly by the emissive probe so they are considered accurate. The complexity of the complete potential structure suggests that electron emission is at least as interesting phenomenologically as electron collection.

Some light can be cast on the mechanisms that could induce the potential profile data shown in Figs. 14 and 15 by considering the simplified schematic and corresponding potential profile shown in

Fig. 16. In the potential environment close to the cathode, electrons from the cathode could be accelerated through the potential gradient at the cathode until they had the kinetic energy needed to excite and ionize neutral atoms that would be present at a high density level near the cathode orifice. At a sufficiently high cathode emission current, the ionization could be sufficient to produce an overabundance of ions that would cause a potential hill to develop near the cathode. This ion overabundance is expected because the electron kinetic energy would typically exceed the ionization energy. Thus the electrons coming from the reaction would tend to leave the region of ionization more rapidly than the ions (Langmuir, 1929). Immediately downstream of the peak potential, the potential drops and forces develop that decelerate the electrons and accelerate the ions in an effort to maintain plasma neutrality. Beyond this region, ions and electrons stream outward and expand to the point where another double sheath can develop to accommodate coupling of the ambient and expansion region plasmas. This sheath, which is typically located 40 to 100 cm downstream of the emitter, exhibits a potential rise of -10 V. It serves as a boundary between the plasma coming from the emitter and the ambient plasma that fills the majority of the vacuum chamber. It is considered possible that it is stabilized by interactions with the vacuum chamber wall. Whether or not this is the case has not been verified, but it is noted that the existence of the sheath is not influenced by switching the tank between contactor cathode to floating potentials. On the other hand, connecting the tank to the simulator anode causes it to disappear.

Additional insight into the phenomenological model associated with Fig. 16 can be obtained by considering plasma property data collected throughout the regions shown. Figure 17 presents data collected at a 750 mA electron emission current with the tank bias switch (Fig. 3) open. The solid plasma potential curve shows data measured using the emissive probe. The dashed line indicates what is expected considering emissive probe errors in the high density plasma at the emitter cathode. While the height of this hill is not known for certain, preliminary RPA probe measurements of ions coming from it into the plasma expansion region suggest it may be a few tens of volts high.

The plasma density, temperature and energy data of Fig. 17, which were collected using a Langmuir probe, show the plasma expansion region contains primary (mono-energetic) electrons but essentially no Maxwellian ones. The energy of the primary electrons suggests they came from the cathode--their energy (15 eV) is about equal to the expansion region plasma potential measured relative to the cathode. The density of these primary electrons drops off rapidly with distance from the cathode to a level below that of the 5 eV Maxwellian electrons in the ambient plasma (middle plot of Fig. 17). A more detailed study of the plasma expansion region (Williams and Wilbur, 1989) has shown that primary electron density decays there as  $1/r^2$ . This suggests in turn that a collisionless, spherical expansion model of the region between -10 and 40 cm is appropriate.

The plasma expansion model of the region between the potential hill and the ambient plasma regions is similar to that used by Davis et al. (1987). Their model differs in that it involves Maxwellian electron expansion in accordance with the barometric equation rather than mono-energetic electron expansion.

Finally, it is noted that the ambient plasma contains mostly Maxwellian electrons with a temperature near 5 eV. The fact that primary electrons there have an energy near the plasma potential associated with the ambient plasma measured relative to the cathode suggests primary electrons come from the cathode and that they produce the ions needed to sustain the ambient plasma.

Acknowledgement. This work has been supported by the NASA Lewis Research Center under Grant NAG3-776.

### Conclusions

Hollow cathode plasma contactors can be used to establish a low potential difference connection between an object attached to the hollow cathode and an ambient plasma under conditions where the object is either positive or negative of the ambient plasma, i.e. electrons are being collected or emitted, respectively. The potential structure and therefore the voltage drop associated with the electron collection process is dominated by the development of a space-charge-limited double sheath. This double sheath maintains a boundary near the outer diameter of the contactor anode. The process of electron collection is more efficient when the contactor is "ignited" and some of the ion current required to sustain the double sheath is created by electrons that are being collected.

The potential structure associated with the electron emission process appears to be dominated by a "potential hill" and a plasma expansion region that develops downstream of the contactor. The potential hill and expansion region appear to facilitate the ion production needed to establish a low impedance plasma bridge between the contactor cathode and the ambient plasma.

A contactor designed to both emit and collect electrons should be connected with its anode attached to the largest conducting surface on the spacecraft. This assures a large effective anode area and efficient electron collection (a low voltage difference between the contactor and the ambient plasma). The size of the anode doesn't appear to influence electron emission process significantly.

### References

- Aston, G. and P.J. Wilbur, Ion Extraction from a Plasma, J. Appl. Phys., V. 52, No. 4, April 1981, pp. 2614-2626.  
Beattie, J.R., Numerical Procedure for Analyzing Langmuir Probe Data, AIAA Journal, V. 13, No. 7, July 1975, pp. 950-952.  
Davis, V., I. Katz, M. Sandell, and D. Parks, Three Dimensional Simulation of the Operation of a Hollow Cathode Electron Emitter on the Shuttle Orbiter, appears in Space Tethers for Science in the Space Station Era, L. Guerriero and I. Bekey, eds., Conference Proceedings, V. 14, Societa Italiana di Fisica, Venice, Oct. 4-8, 1987, pp. 241-244.  
Katz, I. and V.A. Davis, On the Need for Space Tests of Plasma Contactors as Electron Collectors, appears in Space Tethers for Science in the Space Station Era, L. Guerriero and I. Bekey, eds., Conference Proceedings, V. 14, Societa Italiana di Fisica, Venice, Oct. 4-8, 1987, pp. 241-244.

- Hastings D. and J. Blandino, Current Collection to Plasma Contactors in the Ionosphere, AIAA Paper 89-0679, Aerospace Sciences Mtg., Reno, Jan. 1989.
- Langmuir, I., The Interaction of Electron and Positive Ion Space Charges in Cathode Sheaths, Phys. Rev., V. 33, No. 6, June 1929, p. 954-989.
- Langmuir, I and Karl Compton, Electrical Discharges in Gases: Part II - Fundamental Phenomena in Electrical Discharges, Reviews of Modern Physics, v 3., No. 2, April 1931.
- Laupa, T., Thick Sheath Langmuir Probe Trace Analysis, appears in Advanced Electric Propulsion and Space Plasma Contactor Research, P. Wilbur, ed., NASA CR-175119, Jan. 1986, pp. 128-138
- Olsen, R.C., C.E. McIlwain and E.C. Whipple, Observations of Differential Charging Effects on ATS 6, J. Geophys. Res., V. 89, No. A8, 1981, pp. 6809-6819.
- Patterson, M.J. and R.S. Aadland, Ground-Based Plasma Contactor Characterization, appears in Space Tethers for Science in the Space Station Era, L. Guerriero and I. Bekey, eds., Societa Italiana di Fisica, V 14, Venice, Italy, 4-8 Oct. 1987, pp 261-268.
- Purvis, C.K., and R.O. Bartlett, Active Control of Spacecraft Charging, Progress in Astron. Aeron., H.B. Garrett and C.P. Pike, eds., V. 71, 1980, p. 299-317.
- Siegfried, D.E. and P.J. Wilbur, A Model for Mercury Orificed Hollow Cathodes: Theory and Experiment, AIAA Journal, V. 22, 1984, pp. 1405-1412.
- Wei, R., and P.J. Wilbur, Space-charge-limited Current Flow in a Spherical Double Sheath, J. Appl. Phys., V.60, Oct. 1, 1986, pp. 2280-2284.
- Wilbur, P.J., Hollow Cathode Plasma Coupling Study-1986, NASA CR-171985, Dec. 1986.
- Williams, J.D., Electrodynamiic Tether Plasma Contactor Research, appears in Advanced Electric Propulsion and Space Plasma Contactor Research, NASA CR-180862, P.J. Wilbur, ed., Jan. 1987, pp. 1-75.
- Williams, J.D., P.J. Wilbur and J.M. Monheiser, Experimental Validation of a Phenomenological Model of the Plasma Contacting Process, appears in Space Tethers for Science in the Space Station Era, L. Guerriero and I. Bekey, eds., Conference Proceedings, V. 14, Societa Italiana di Fisica, Venice, Oct. 4-8, 1987, pp. 241-244.
- Williams, J.D. "Electrodynamiic Tether Plasma Contactor Research, appears in Space Plasma Contactor Research-1987, P.J. Wilbur, ed., NASA CR-182148, Jan 1988.

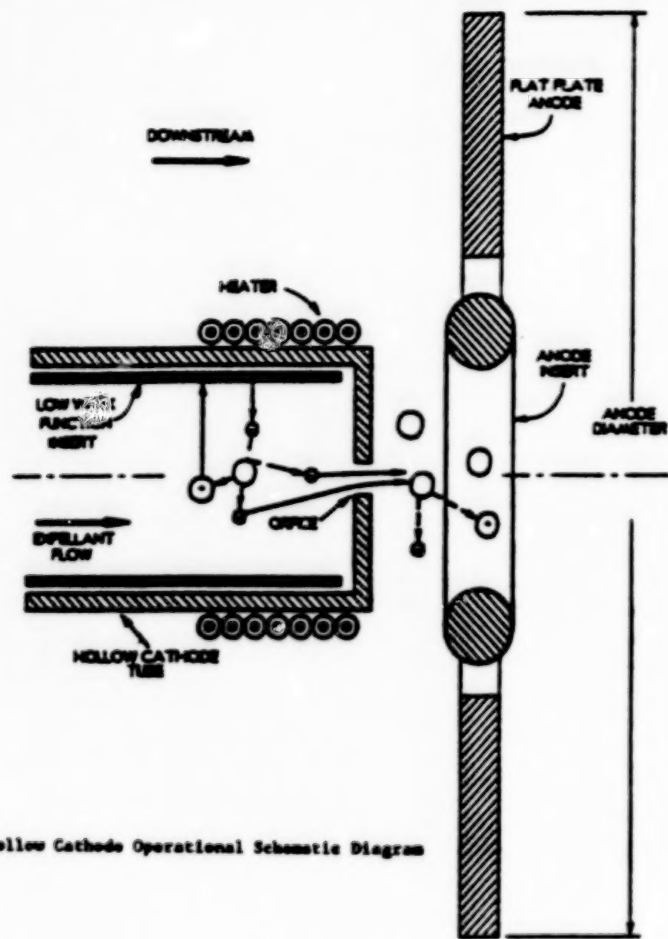


Fig. 1 Hollow Cathode Operational Schematic Diagram

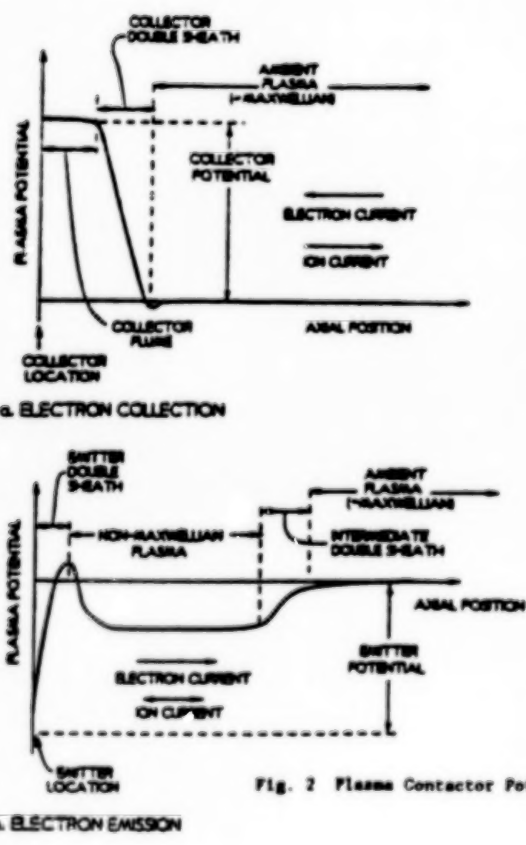


Fig. 2 Plasma Contactor Potential Structure Definitions

b. ELECTRON EMISSION

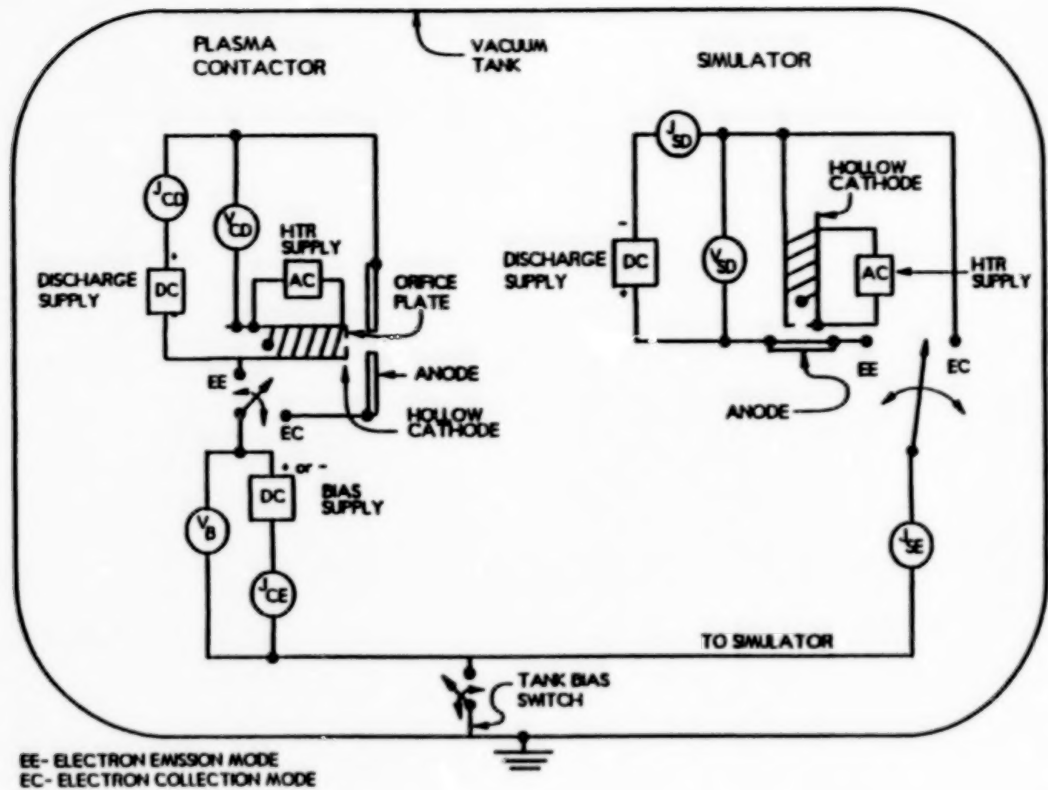


Fig. 3 Test Apparatus Electrical Schematic Diagram

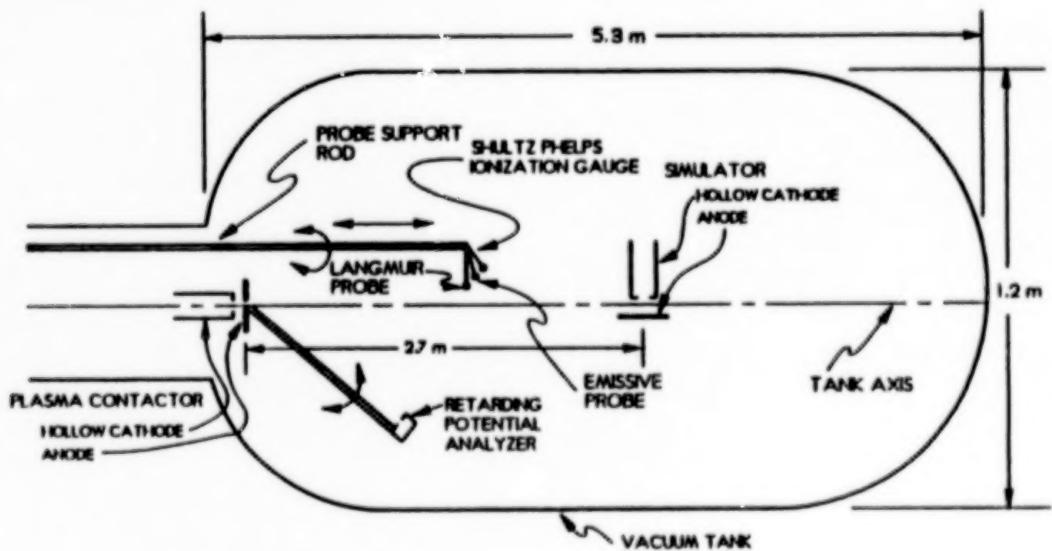


Fig. 4 Mechanical/Instrumentation Schematic Diagram

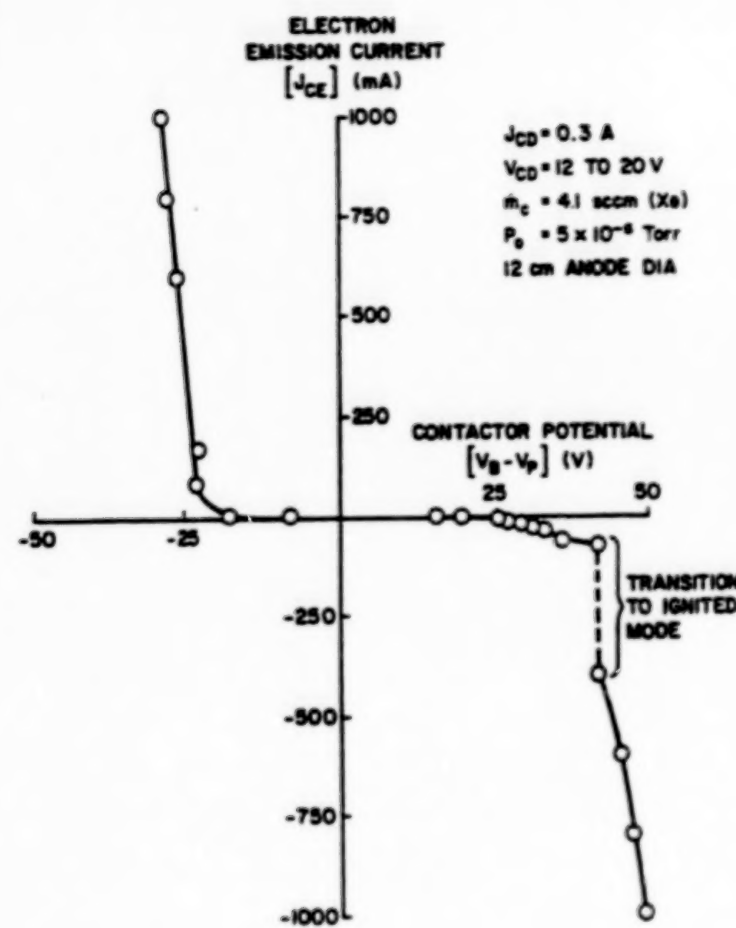
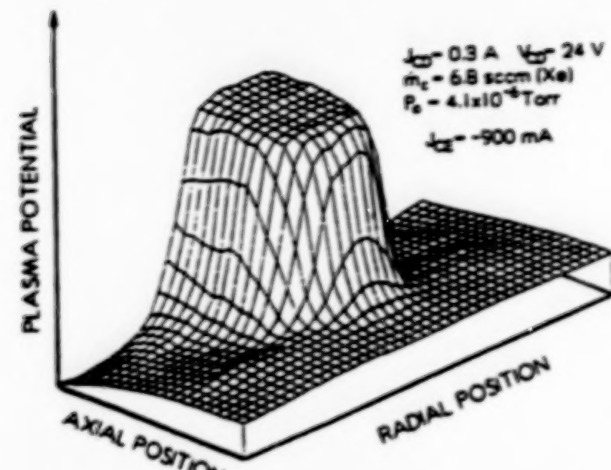
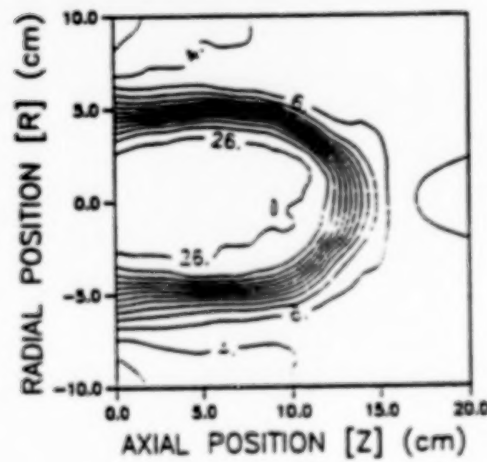


Fig. 5 Typical Plasma Contactor Performance Curve



a. Raised Potential Map



b. Equipotential Contour Map

Fig. 6 Typical Plasma Potential Variation Near a Contactor Collecting Electrons

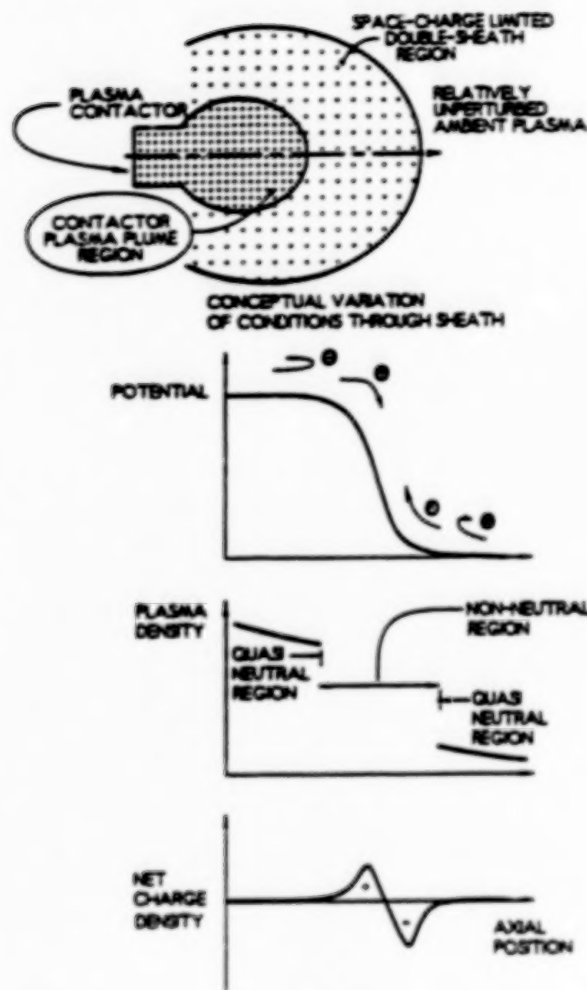


Fig. 7 Conceptual Model of Electron Collection

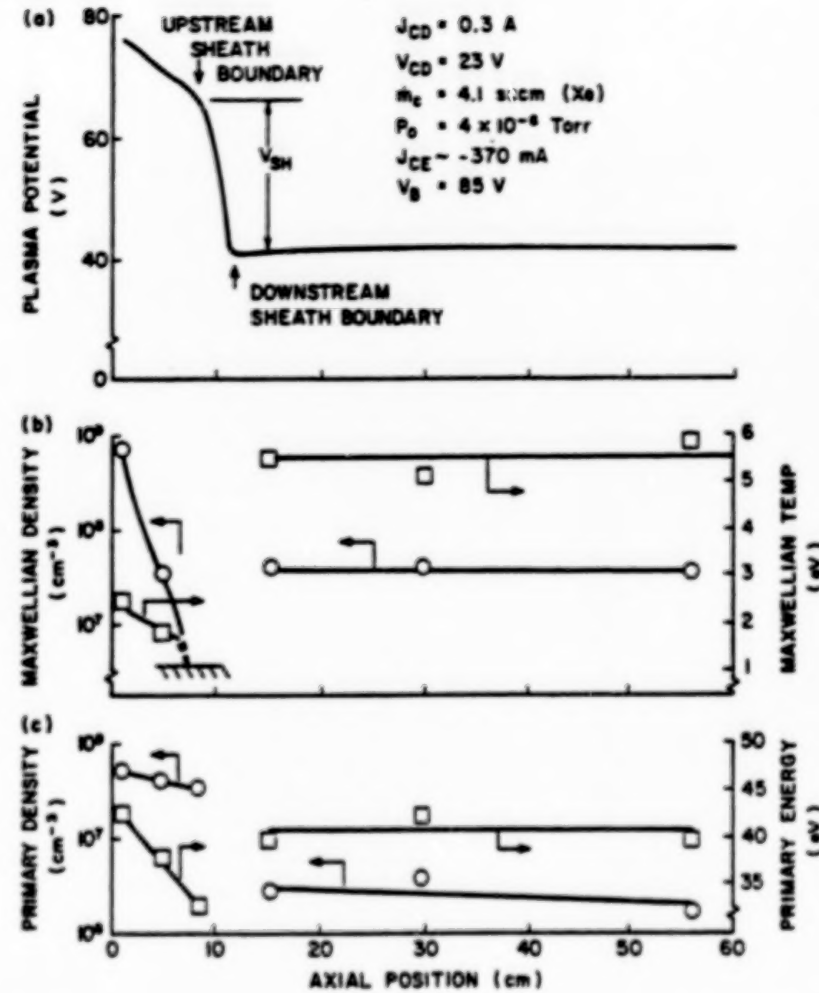


Fig. 8 Typical Centerline Plasma Property Profiles - Electron Collection  
 144

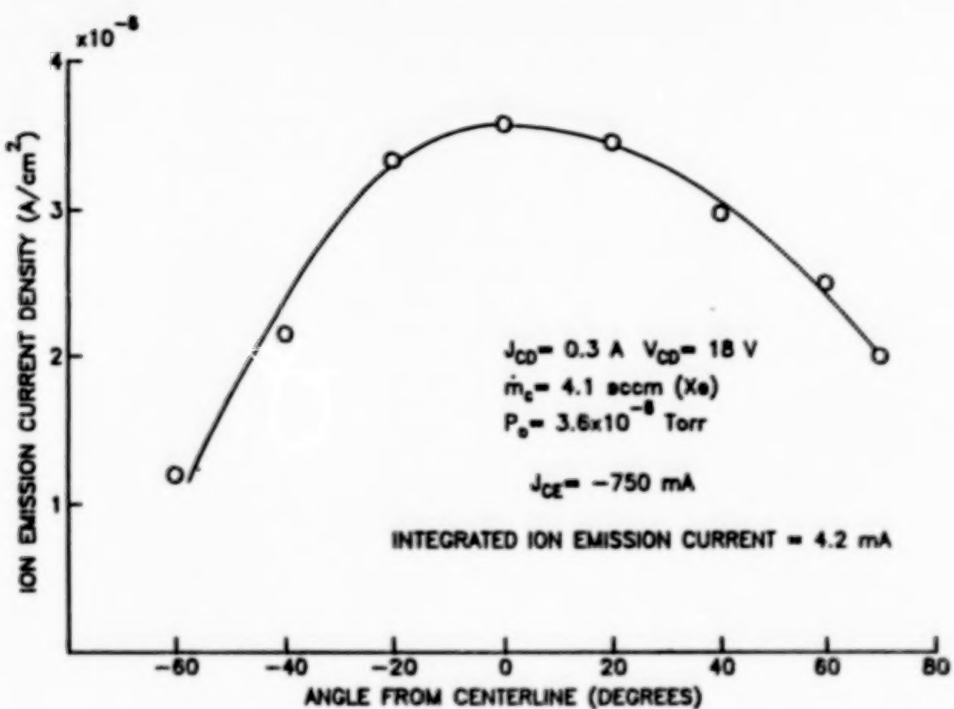


Fig. 9 Azimuthal Variation of Current Density of Ions Emitted from the a Contactor Collecting Electrons

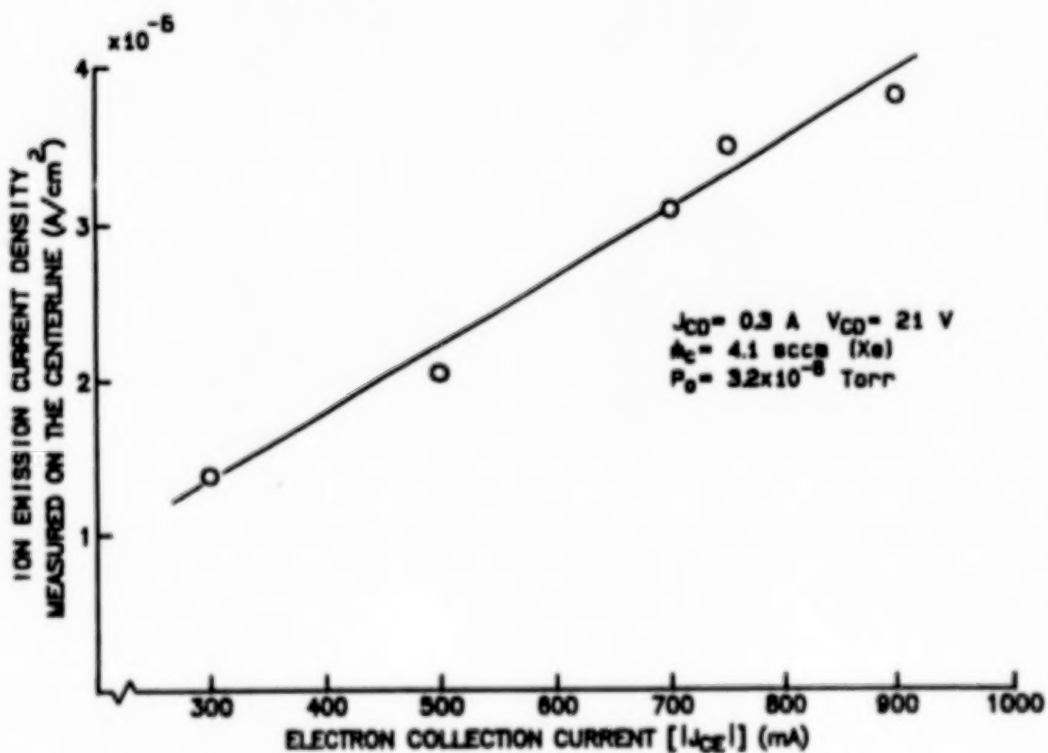


Fig. 10 Measured Correlation of Ion Emission and Electron Collection Currents

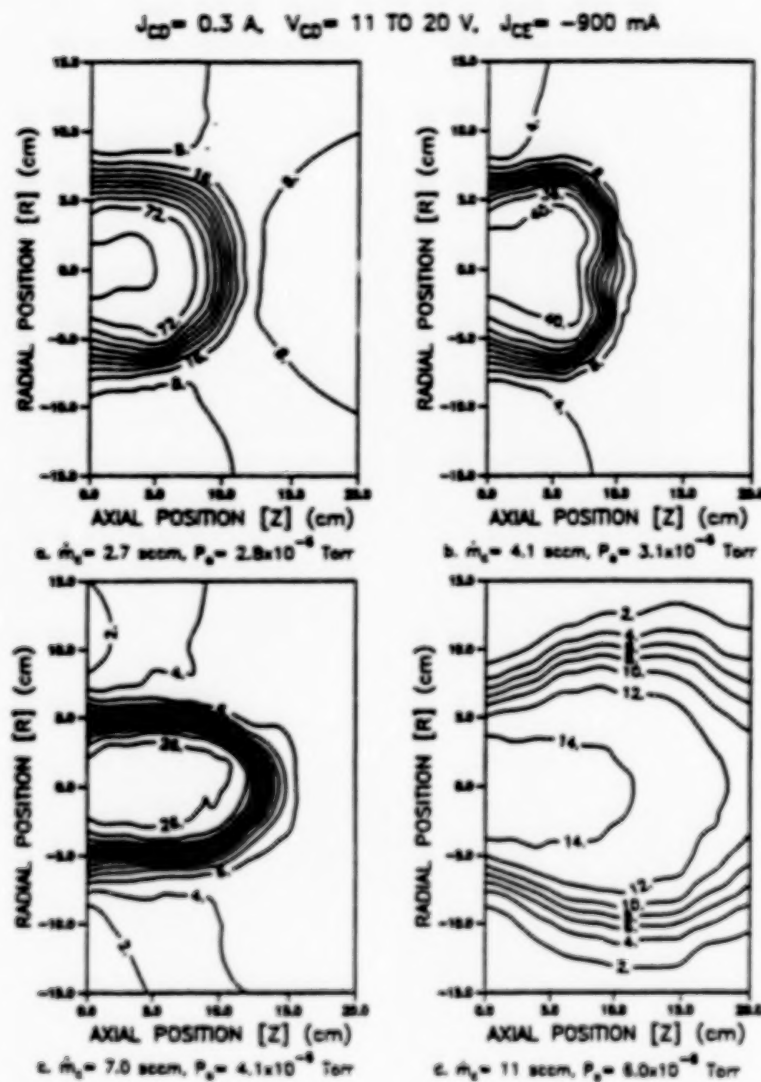


Fig. 11 Effect of Flowrate on Potential Field - Electron Collection

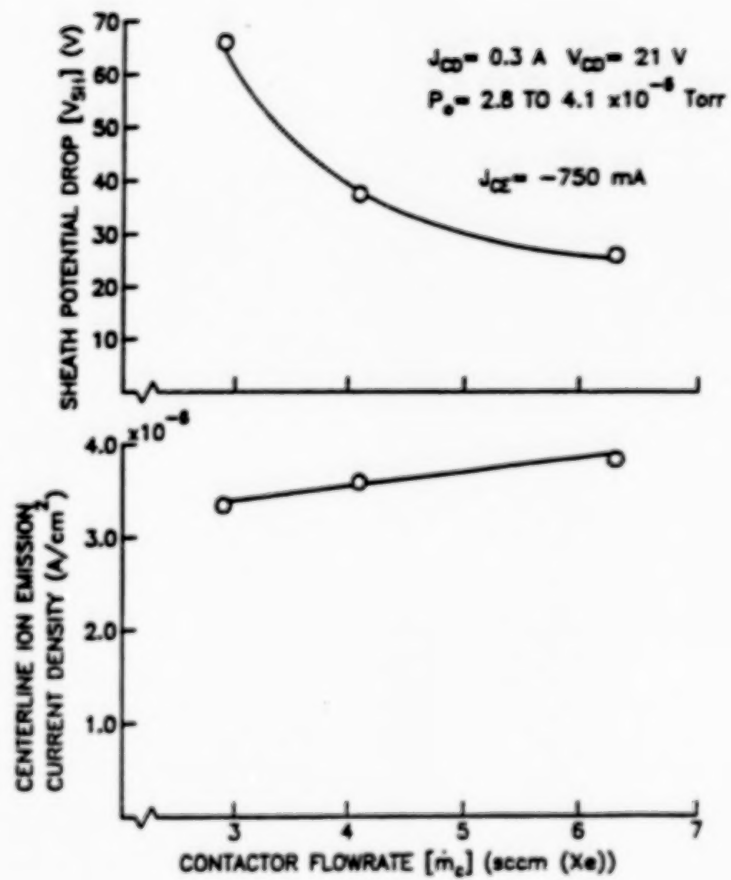


Fig. 12 Effects of Flowrate on Sheath Potential Drop and Ion Emission Current Density - Electron Collection

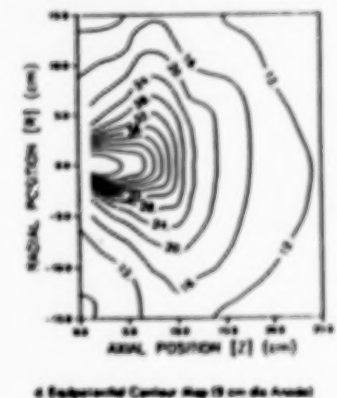
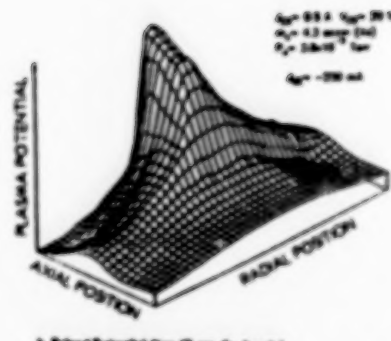
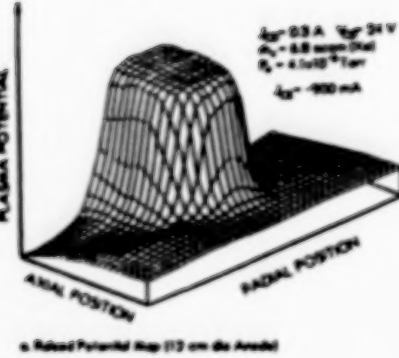
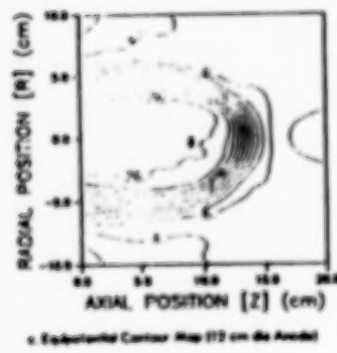
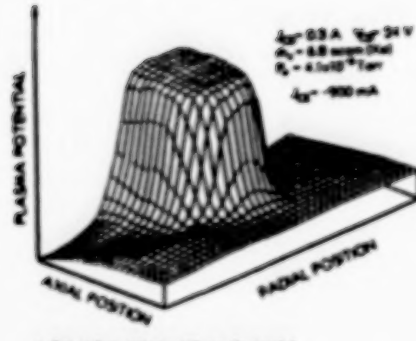


Fig. 13 Effect of Collector Anode Diameter on Potential Field

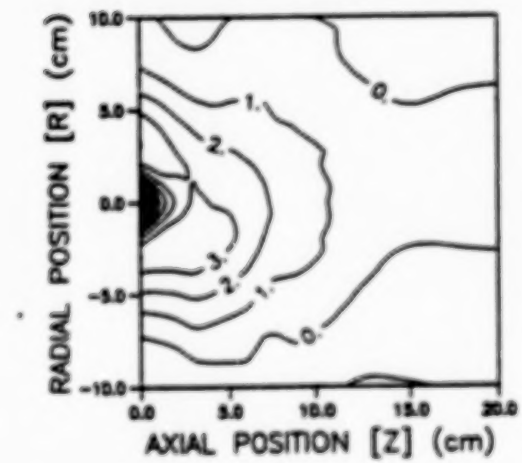
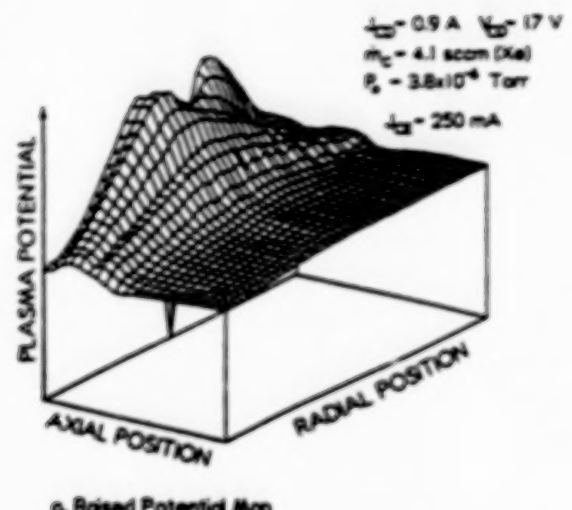


Fig. 14 Typical Plasma Potential Field near a Contactor Emitting Electrons

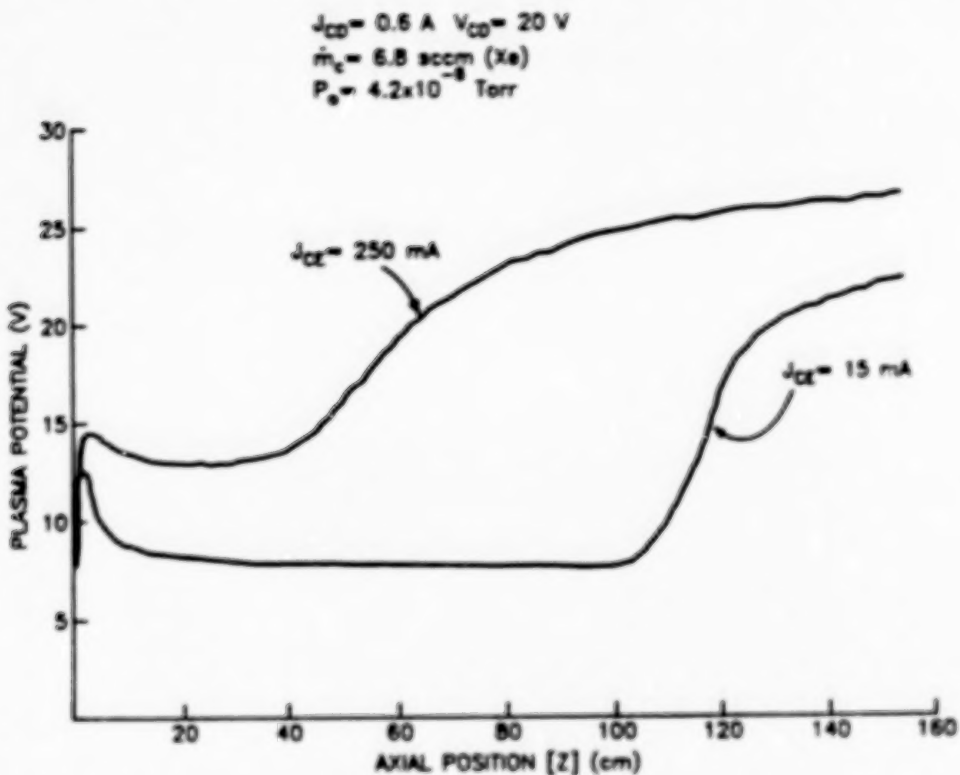


Fig. 15 Effects of Electron Emission Current on Centerline Plasma Potential Profiles

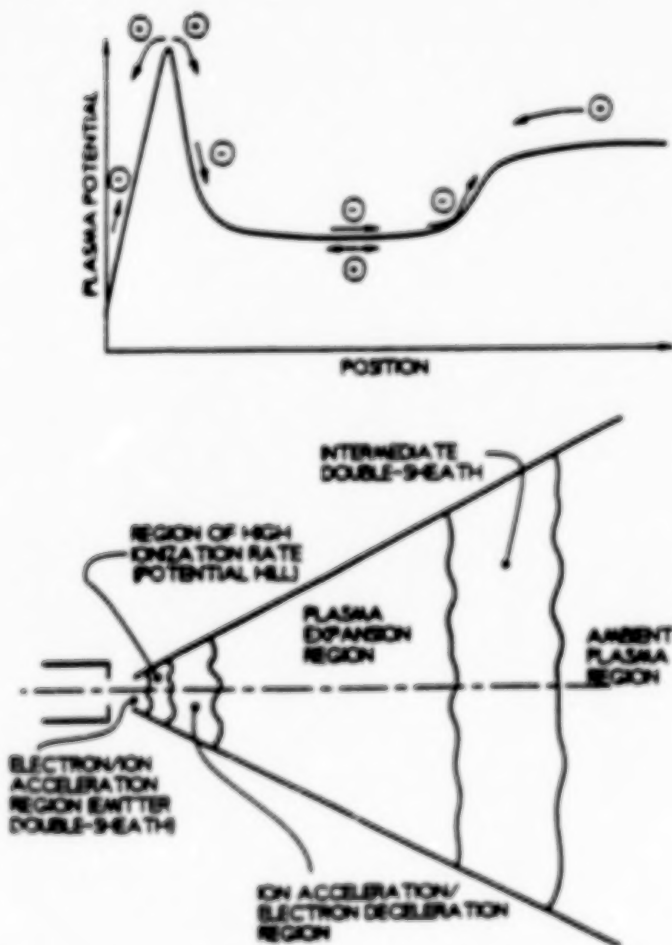


Fig. 16 Simple Physical Model of Electron Emission Process Observed within a Vacuum Chamber

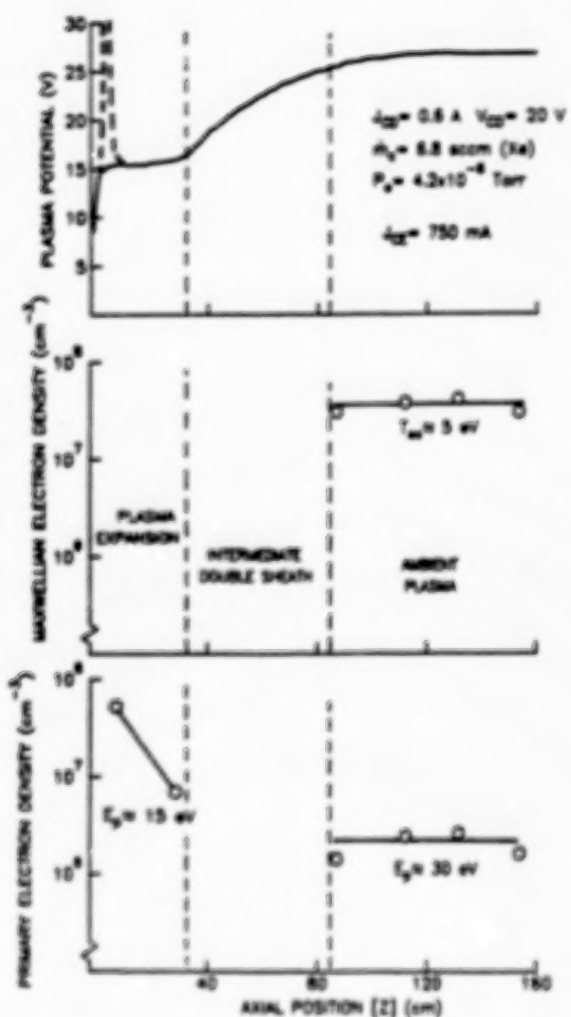


Fig. 17 Typical Plasma Property Profiles - Electron Emission

# Theory of Plasma Contactors in Ground-Based Experiments and Low Earth Orbit

M. J. Gerver\*

Plasma Fusion Center

D. E. Hastings<sup>†</sup> and M. R. Oberhardt<sup>‡</sup>

Dept. of Aeronautics and Astronautics

Massachusetts Institute of Technology

Cambridge MA 02139

## Abstract

Previous theoretical work on plasma contactors as current collectors has fallen into two categories: collisionless double layer theory (describing space charge limited contactor clouds) and collisional quasineutral theory. Ground based experiments at low current are well explained by double layer theory, but this theory does not scale well to power generation by electrodynamic tethers in space, since very high anode potentials are needed to draw a substantial ambient electron current across the magnetic field in the absence of collisions (or effective collisions due to turbulence). Isotropic quasineutral models of contactor clouds, extending over a region where the effective collision frequency  $\nu_e$  exceeds the electron cyclotron frequency  $\omega_{ce}$ , have low anode potentials, but would collect very little ambient electron current, much less than the emitted ion current. A new model is presented, for an anisotropic contactor cloud oriented along the magnetic field, with  $\nu_e < \omega_{ce}$ . The electron motion along the magnetic field is nearly collisionless, forming double layers in that direction, while across the magnetic field the electrons

---

\*Research Scientist

<sup>†</sup>Class of 1956 Career Development Associate Professor of Aeronautics and Astronautics, Member AIAA

<sup>‡</sup>Research Assistant; also at the Air Force Geophysics Laboratory

<sup>§</sup>Copyright ©Daniel Hastings, 1989. All rights reserved.

diffuse collisionally and the potential profile is determined by quasineutrality. Using a simplified expression for  $\nu_e$  due to ion acoustic turbulence, an analytic solution has been found for this model, which should be applicable to current collection in space. The anode potential is low and the collected ambient electron current can be several times the emitted ion current.

## 1 Nomenclature

$B_0$ =ambient magnetic field

$c_s$ =sound speed

$C$ =numerical factor relating electron thermal conductivity to electron transport

$e$ =charge on an electron

$E$ =electric field

$f_i$ =initial ionization fraction of source

$F_\theta$ =azimuthal drag force on electrons

$g$ =focussing factor due to anisotropy

$I_e$ =electron current

$I_i$ =ion current

$I = I_e + I_i$ =total current

$J_e^\infty$ =ambient electron saturation current density

$J_i$ =ion current density

$k_\perp$ =perpendicular wave number

$L$ =length of tether

$m_e$ =electron mass

$m_i$ =ion mass

$n_e$ =electron density

$n_{eo}$ =ambient electron density

$n_{ec}$ =contactor electron density

$n_i$ =ion density

$n_{ic}$ =contactor ion density

$n_{source}$ =source plasma density  
 $n_0$ =neutral density  
 $n_\infty$ =electron density at infinity  
 $n_{critical}$ =neutral density required for ignition  
 $r$ =radial coordinate  
 $r_{anode}$ =anode radius  
 $r_{core}$ =radius at which electrons are collected, for any model  
 $r_{inner}$ =inner radius of double layer  
 $r_{outer}$ =outer radius of double layer  
 $r_{source}$ =source radius  
 $r_1$ =contactor cloud radius in anisotropic model  
 $P_{load}$ =load power  
 $R_t$ =tether resistance  
 $R_{load}$ =load resistance  
 $T_{ec}$ =contactor electron temperature  
 $u_e$ =electron flow velocity  
 $u_i$ =ion flow velocity  
 $v_A$ =Alfven speed  
 $v_d$ =electron azimuthal drift velocity  
 $v_e$ =electron thermal velocity  
 $v_r$ =radial velocity  
 $v_z$ =axial velocity, parallel to the magnetic field  
 $v_0$ =orbital velocity  
 $z$ =axial coordinate  
 $z_0$ =half length of anisotropic contactor cloud  
 $\beta_e$ =ratio of electron pressure to magnetic pressure  
 $\gamma$ =optical depth of source region to electron ionization  
 $\Delta\phi$ =potential drop across double layer

$\eta$ =electrical efficiency of the tether  
 $\kappa$ =cross field electron thermal conductivity  
 $\lambda_D$ =Debye length  
 $\lambda_{D,inner}$ =Debye length at  $r_{inner}$   
 $\lambda_{D,outer}$ =Debye length at  $r_{outer}$   
 $\mu$ =ratio of ion mass to proton mass  $\nu_e$ =effective electron collision frequency  
 $\xi = I/I_i$ =gain  
 $\rho_e$ =electron gyroradius  
 $\sigma$ =electron impact ionization cross-section  
 $\phi$ =potential  
 $\phi_0$ =anode potential  
 $\phi_{total}$ =total tether potential  
 $\omega_{ce}$ =electron cyclotron frequency  
 $\omega_{pe}$ =electron plasma frequency

## 2 Introduction

Plasma contactors are plasma clouds which allow the passage of charge between an electrode and an ambient plasma. They have been proposed for use in power generating devices such as electrodynamic tethers<sup>[1]</sup> because they may substantially reduce the impedance of the electron current collection from the ionosphere and make the emission of electrons much less energetically expensive than using an electron gun. In this paper we will concentrate on plasma contactors used at an anode to collect electrons in the ionosphere or some other ambient plasma. Such a contactor will emit ions, as well as collect electrons. Two figures of merit for such a contactor are its impedance  $\phi_0/I$ , and the gain  $\xi$ , defined as

$$\xi = I/I_i(r_{anode}).$$

The impedance determines the maximum power that can be generated by a tether, since the total tether potential  $\phi_{total}$  is fixed at  $v_e B_0 L$ . If we ignore the ionospheric impedance and the impedance of electron emission, then

$$\phi_{total} = R_{load} I + R_t I + \phi_0(I).$$

The maximum power  $R_{load} I^2$  at fixed  $\phi_{total}$  and  $R_t$  is obtained when  $R_{load} = R_t + d\phi_0/dI \approx R_t + \phi_0/I$ . The power is greatest when the contactor impedance is lowest. The gain is important because it determines the rate at which gas must be used (to produce ions), for a given total current. If the gain is high, less gas is used to collect a given current.

Both the impedance and the gain will depend on the current. In general there is a trade-off: at very low current, both high gain and low impedance are possible, but the power is low. While at high current, high gain can be obtained only at the cost of very high impedance (again resulting in low power). Low impedance and high power are possible only with low gain. To illustrate these trends, we may consider the extreme limits. When the current is equal to the electron saturation current of the ambient plasma over the surface area of the physical anode, then the gain is infinite (since no ions need be emitted to draw this much electron current) and the contactor impedance is zero, but the power (for low earth orbit and practical tether and anode parameters) is at most tens of watts. Arbitrarily large current (and high power) may be obtained by emitting a large ion current, but unless the anode potential is high enough, it will not be possible to collect many electrons across the magnetic field, and the gain will approach unity. A basic goal of contactor research is to determine how large a gain is possible at a given power level. If it turns out that at the power levels of interest for tethers (typically tens of kW) the maximum gain is close to unity, then there is no point in using plasma contactors for current collection; in effect, the best plasma contactor is no better than an ion beam. If, on the other hand, gains at least a few times greater than unity are possible at power levels of interest, then plasma contactors are useful as current collectors for tethers. We will present theoretical results suggesting that this is the case, although the gains are only moderate, in the range of 2 to 10. These theoretical results pertain to a regime (collisionless electron motion along the magnetic field, collisional diffusion across the magnetic field) which we expect to be valid in low earth orbit for high current contactors, but for

which there have been no ground based experiments. Such experiments are very important for confirming the theory, or showing how it must be modified.

In previous work<sup>[2,3]</sup> it has been suggested that the plasma contactor cloud will consist of several different regions. First will be an inner core where the cloud will be isotropic because the two major directions of anisotropy, namely the earth's magnetic field and the direction of motion of the source will be shielded by the dense plasma from the contactor source. There will then be two outer regions where the two directions of anisotropy are manifested. Previously, it has generally been assumed that a substantial current of ambient electrons can be collected only from field lines that pass through the inner core region<sup>[2,4]</sup>. However, we will show in Section 4 that for conditions in low earth orbit it may also be possible to collect a significant electron current from the outer core region, where the anisotropy due to the magnetic field is important.

There has been much debate about the size of the core region from which electrons can be collected. One estimate is obtained by matching the cloud density to the ambient density<sup>[5,6]</sup>

$$n_e(r_{core}) \approx n_{ss}$$

and another by taking magnetic field effects into account<sup>[7]</sup>

$$\nu_e(r_{core}) \approx \omega_{ce}$$

where  $\nu_e$  is the radially dependent electron collision frequency (including effective "collisions" due to turbulence). A third estimate is obtained by requiring regularity of the self-consistent potential<sup>[8]</sup>

$$\frac{\partial \phi}{\partial r} \Big|_{r_{core}} \approx 0$$

and finally a fourth estimate comes by requiring a consistent space charge limited flow inside the core<sup>[9]</sup>

$$m_i n_i u_i^3 |_{r_{core}} \approx m_e n_e u_e^3 |_{r_{core}}$$

These diverse theories give a wide range of current enhancement factors for the plasma cloud.

If we assume a core cloud of radius  $r_{core}$ , then continuity of current gives

$$I = I_i(r_{anode}) + I_e(r_{anode}) = I_i(r_{core}) + I_e(r_{core})$$

and the gain is

$$\xi = \frac{I_e(r_{core})}{I_i(r_{anode})} + \frac{I_e(r_{core}) - I_i(r_{anode})}{I_i(r_{anode})} + 1$$

Plasma contactor clouds enhance or produce electron current flow through two possible paths. First (the first term on the right hand side of the equation), they can serve as virtual anodes through which electrons from far away can be drawn and collected to the real anode at the center of the cloud. Secondly (the second term on the right hand side), the neutral gas associated with the cloud can become ionized, creating electron-ion pairs. The electrons will be collected to the anode, and the ions will be repelled. For use in space with an electrodynamic tether, however, ionization of contactor neutrals is not an efficient use of neutral gas; if this is the only means by which the current is enhanced, then the same neutral gas can be used more efficiently by ionizing it internally in an ion source. Plasma contactors will be useful if they enable the ionosphere to supply electrons. The two sources of electrons in the ionosphere are the ionospheric plasma and the ionospheric neutrals. However the mean free path for ionization of the ionospheric neutral gas is so long (many kilometers) that ionization of this gas on the length scale of the plasma contactor cloud is highly unlikely. For this reason we shall assume that all ionization associated with contactors is ionization of contactor neutral gas. Therefore plasma contactors can be useful with electrodynamic tethers only if they enhance current by collecting ambient electrons from the ionosphere. The collected electron current  $I_e(r_{core})$  will generally be the saturation current times the area of the core cloud  $4\pi r_{core}^2$ , or, if the contactor is only collecting electrons along magnetic field lines running into the core cloud, then  $I_e(r_{core})$  will be the saturation current times  $2\pi r_{core}^2$ . (If, as we consider in Section 4, the core cloud is not spherical but is elongated in the direction of the magnetic field, then  $r_{core}$  is the minor radius, across the magnetic field.) For this reason the size of  $r_{core}$  is crucial to the effectiveness of plasma contactors as electron collectors in space.

In Section 3 a collisionless double layer theory will be derived, along the lines of Wei and Wilbur<sup>[9]</sup>, Amemiya<sup>[10]</sup>, and it will be shown that this theory provides a good quantitative description of ground-based experiments at moderately low currents, but it will not be applicable to space-based contactors except at extremely low current and power. If the electrons are strictly collisionless, then the magnetic field prevents electrons from reaching the anode unless they originate

on field lines that pass close to the anode (which limits the current that can be collected) or the anode potential is high enough to pull electrons across the magnetic field to the anode from some distance away. A necessary condition for this, which depends on the anode radius  $r_{\text{anode}}$ , was found by Parker and Murphy<sup>[11]</sup>. Another constraint on  $r_{\text{anode}}$  is that it must be less than the inner radius of the double layer. We will show that any spherically symmetric double layer with space-charge limited current greater than a very low limit (about 50 mA collected electron current, corresponding to 1 mA emitted ion current, for dayside equatorial low earth orbit, and even lower current for nightside) which satisfies these constraints must have an anode radius that is close to  $r_{\text{core}}$ . Such a plasma contactor would serve no purpose, since it would hardly collect any more ambient electron current than the bare anode. This means that an unmagnetized collisionless space-charge limited double layer model, as analyzed by Wei and Wilbur<sup>[9]</sup>, cannot apply in space, except at very low currents, no matter how great the potential is. If the anode emits a current greater than this, at zero initial velocity (i.e. space-charge limited), and if the electrons are assumed to be collisionless, then the double layer cannot be spherically symmetric, regardless of the potential. Electron collection will be inhibited across the magnetic field, and the collected electron current will be lower than predicted by the Wei-Wilbur theory<sup>[9]</sup> for that anode potential and emitted ion current. Although a theory valid in this regime is not available, we can still obtain an upper limit on the collisionless electron current that can be collected, and a lower limit on the anode potential, for a given ion current, by assuming that the Parker-Murphy condition is marginally satisfied for a double layer obeying the equations of Wei and Wilbur, and ignoring the constraint that the inner radius of such a double layer must occur at a greater radius than  $r_{\text{anode}}$ . We then obtain an upper limit to the power than can be generated by a plasma contactor collecting electrons to a 20 km long tether in space, in the absence of electron collisions. This maximum power is quite low, only a few hundred watts, less than an order of magnitude above the power that can be generated by a tether without a plasma contactor, using a bare anode to collect electrons.

At higher emitted ion current, there will be a region where the electrons cannot go straight to the anode, but where ambient electrons will be trapped, to keep the plasma quasineutral. These electrons will remain trapped for a time long compared to the time it would take for an unmagne-

tized electron to go straight to the anode. If there are effective collisions due to instabilities, some of these trapped electrons may be able to diffuse to the anode, and the collected electron current may be much greater than what would be found in the collisionless model.

In Section 4, we will describe work on a model of the outer core region, in which the motion along the magnetic field is collisionless, forming a double layer, but the motion across the magnetic field is collisional and quasineutral. This model, which is expected to be applicable to contactors in space, suggests that significant current may be collected from this outer core region, with low contactor impedance. Unfortunately there are, to our knowledge, no experiments in this regime, to which the theory can be compared. Conclusions will be presented in Section 5.

### 3 Double-Layer Theory and Implications

#### 3.1 Collisionless Unmagnetized Model

Ground-based experiments in which double layers are seen are well described by a collisionless unmagnetized model, as we will show. A schematic radial potential profile for such a model is shown in Fig. 1. We assume that the potential is monotonic, so there are two components of plasma, an ambient component and a contactor component. The ambient ions and electrons are Maxwellian at positions  $r$  well beyond the double layer, with ion and electron temperatures  $T_{ia}$  and  $T_{ee}$ , and density  $n_{\infty}$ . The contactor plasma has Maxwellian electrons at temperature  $T_{ec}$  and cold ions streaming radially out from a plasma source localized near the anode, with ion current  $I_i$ . The potential drop  $\phi_0$  between the source, at  $r = r_{source}$ , and the ambient plasma at  $r \rightarrow \infty$ , is assumed to be much greater than any of the temperatures, and the radius at which the double layer forms is assumed to be much greater than a Debye length. With these assumptions, the plasma is quasineutral everywhere except inside the double layer, at  $r_{inner} < r < r_{outer}$ . (Here  $r_{outer}$  is the radius, called  $r_{sat}$  in the Introduction, at which the ambient electron saturation current is collected.) Inside the contactor cloud, at  $r < r_{inner}$ , there are no ambient ions, and the density of ambient electrons, which have been accelerated in the double layer, is much less than the density of contactor electrons, so quasineutrality requires  $n_{ee}(r) = n_{ic}(r)$ . The densities of contactor electrons

and ions are related to the potential  $\phi$  (defined relative to  $r \rightarrow \infty$ ) by

$$n_{ic} = n_{source} \exp[(\phi - \phi_0)/T_{ic}] \quad (1)$$

$$n_{ic} = n_{source} (r_{source}/r)^2 [1 + (\phi_0 - \phi)/T_{ic}]^{-1/2} \quad (2)$$

where we have assumed that ions are emerging from the source at the sound speed  $(T_{ic}/m_i)^{1/2}$ , due to acceleration in a Bohm presheath, and we have neglected any ionization or recombination occurring at  $r > r_{source}$ . Setting the right hand sides of Eqs. (1) and (2) equal to each other gives a transcendental equation for  $\phi(r)$ . It is evident that for  $r \gg r_{source}$ ,

$$\phi(r) \approx \phi_0 - 2T_{ic} \ln(r/r_{source}) \quad (3)$$

so the potential only drops a few times  $T_{ic}$  inside the contactor cloud, much less than the total potential drop. The source density  $n_{source}$  is related to the ion current  $I_i$  by

$$I_i = 4\pi r_{source}^2 e n_{source} (T_{ic}/m_i)^{1/2} \quad (4)$$

Outside the double layer, at  $r > r_{outer}$ , the ambient electron density decreases from  $n_\infty$  as  $r$  decreases, because no electrons are emitted from the double layer. We assume that there are no sources of electrons, or collisions, which could fill in the resulting empty region of velocity space. From quasineutrality, the ambient ion density must also decrease as  $r$  decreases (even if the density of contactor ions, accelerated in the double layer, is small compared to the ambient ion density), so the potential must rise by an amount on the order of  $T_{ie}$ . If  $T_{ie}$  is much less than  $T_{ic}$ , then the ambient electron density is not affected by the potential, so it is reduced from  $n_\infty$  by a simple geometric factor

$$n_{ee}(r) = \frac{1}{2} n_\infty [1 + (1 - r_{outer}^2/r^2)^{1/2}] \quad (5)$$

and the potential is given by

$$\phi(r) = T_{ie} \ln(n_\infty/n_{ee}) \quad (6)$$

(This rise in potential going from infinity to  $r_{outer}$  causes the ambient electrons to become supersonic by the time they reach  $r_{outer}$ , so that they satisfy the Bohm sheath condition<sup>[12,13]</sup>. This potential was calculated by Alpert, Gurevich and Pitaevskii<sup>[14]</sup> for the case  $T_{ie} = T_{ic}$ , so we have labeled

this region the "Alpert-Gurevich presheath" in Fig. 1.) The potential drop from  $r_{outer}$  to  $\infty$  is just  $T_{ie}\ln 2$ , much less than the total potential drop. Most of the potential drop must therefore occur in the double layer. Within the double layer,  $r_{inner} < r < r_{outer}$ , the plasma is not quasineutral, and Poisson's equation (for spherical symmetry)

$$\frac{1}{r^2} \frac{d}{dr} r^2 \frac{d\phi}{dr} = 4\pi(n_e - n_i) \quad (7)$$

must be satisfied subject to the boundary conditions that  $\phi$  and  $d\phi/dr$  be continuous at  $r_{inner}$  and  $r_{outer}$ . These four boundary conditions specify a solution to the second order differential equation, and the values of the free parameters  $r_{inner}$  and  $r_{outer}$ . Since most of the drop in potential occurs in the double layer, to a good approximation the boundary conditions are

$$\phi(r_{inner}) = \phi_0 - 2T_{ie}\ln(r_{inner}/r_{source}) \quad (8)$$

$$\phi(r_{outer}) = 0 \quad (9)$$

$$d\phi/dr = 0 \text{ at } r_{inner} \text{ and } r_{outer} \quad (10)$$

If, as we have assumed,  $T_{ie} \ll T_{ee}$ , then the ambient ion density drops much more quickly than the ambient electron density as the potential starts to rise going inward from  $r_{outer}$ , and we can neglect the ambient ion density in Eq. (7). Similarly, since the energy of the contactor ions is greater than  $T_{ee}$  at  $r_{inner}$ , even if only by a logarithmic factor, the contactor electron density drops much more quickly than the contactor ion density in going outward from  $r_{inner}$ , and to rough approximation we can neglect the contactor electron density in the double layer. In the double layer, then, we must solve Poisson's equation, Eq. (7), with

$$n_i = \frac{n_{\infty}}{2} \frac{r_{outer}^2}{r^3} \exp(\phi/T_{ee}) [1 - \operatorname{erf}(\sqrt{\phi/T_{ee}})] \quad (11)$$

$$n_i = n_{source} \frac{r_{source}^2}{r^2} \left( \frac{\phi_0 - \phi(r)}{T_{ee}} \right)^{-1/2} \quad (12)$$

An approximate analytic solution, which provides some physical insight, may be found when the double layer is thin, i.e.  $r_{outer} - r_{inner} \ll r_{inner}$ . Then, in the vicinity of  $r_{inner}$ , for  $\lambda_D \ll r - r_{inner} \ll r_{outer} - r_{inner}$ , the potential approximates a Child-Langmuir sheath, with negligible  $n_i$ ,

$$\phi(r_{inner}) - \phi(r) \approx 3^{4/3} T_{ie} \ln(r_{inner}/r_{source}) \left( \frac{r - r_{inner}}{\lambda_{D,inner}} \right)^{4/3} \quad (13)$$

where

$$\lambda_{D,\text{inner}}^2 = \frac{T_{ee}\ln(r_{\text{inner}}/r_{\text{source}})}{2\pi e^2 n_{\text{source}}} \left(\frac{r_{\text{inner}}}{r_{\text{source}}}\right)^2 \quad (14)$$

is the Debye length at  $r_{\text{inner}}$ . In the vicinity of  $r_{\text{outer}}$ , for  $\lambda_D \ll r_{\text{outer}} - r \ll r_{\text{outer}} - r_{\text{inner}}$ , the potential approximates an inverted Child-Langmuir sheath, with negligible  $n_i$

$$\phi(r) \approx \frac{3^{4/3}}{2} T_{ee} \left( \frac{r_{\text{outer}} - r}{\lambda_{D,\text{outer}}} \right)^{4/3} \quad (15)$$

where

$$\lambda_{D,\text{outer}}^2 = \frac{T_{ee}}{2\pi e^2 n_{\infty}} \quad (16)$$

is the Debye length at  $r_{\text{outer}}$ . The transition from Eq. (13) to Eq. (15) occurs when  $n_e \approx n_i$ , which is to say at the point where the two expressions for  $\phi(r)$ , Eqs. (13) and (15), have second derivatives that are equal in magnitude (but with opposite signs). At this point, the two expressions for  $\phi(r)$  must have the same first derivative. This means that the transition from Eq. (13) to Eq. (15) must occur half way between  $r_{\text{inner}}$  and  $r_{\text{outer}}$ , with  $\phi(r)$  antisymmetric about this point, and the coefficients in front of the two expressions for  $\phi(r)$  must be equal,

$$2T_{ee}\ln(r_{\text{inner}}/r_{\text{source}})\lambda_{D,\text{inner}}^{-4/3} = T_{ee}\lambda_{D,\text{outer}}^{-4/3} \quad (17)$$

Eq. (17) leads immediately to the well known double layer requirement<sup>[7]</sup>

$$I_e/I_i = (m_i/m_e)^{1/2} \quad (18)$$

where  $I_e = 2\pi r_{\text{outer}}^2 J_e^{\infty}$ , and  $J_e^{\infty} = en_{\infty}(2\pi T_{ee}/m_e)^{1/2}$  is the ambient electron saturation current density. In other words, the contactor cloud will expand freely until the ion current density  $I_i/4\pi r^2$  is equal to the ambient electron saturation current times  $(m_e/m_i)^{1/2}$ . If  $T_{ee} \approx T_{ie}$ , then this will occur when the density of the contactor plasma is comparable to the density of the ambient plasma.

From Eqs. (13), (15), and (17), the width of the double layer is related to the potential drop  $\Delta\phi = \phi(r_{\text{inner}}) - \phi(r_{\text{outer}})$  by

$$r_{\text{outer}} - r_{\text{inner}} = \frac{2}{3} \lambda_{D,\text{outer}} \left( \frac{\Delta\phi}{T_{ee}} \right)^{3/4} \quad (19)$$

and these results are valid only if the width given by Eq. (19) is much less than  $r_{\text{inner}}$ . If this condition is not satisfied, then Poisson's equation must be solved numerically, as has been done by Wei and Wilbur<sup>[9]</sup> and by Williams<sup>[15]</sup>, and in this case  $I_e/I_i$  will be smaller than  $(m_i/m_e)^{1/2}$ .

### 3.2 Comparison With Experiment

The model outlined above is in good agreement with the ground-based experiments of Wilbur<sup>[16]</sup>, in those conditions where double layers were seen. In these experiments, the anode had a radius  $r_{\text{anode}} = 6 \text{ cm}$ , but the effective source radius, where most of the ionization occurred, was  $r_{\text{source}} \approx 2 \text{ cm}$ .  $\phi_0$  could vary from 0 to 70V, and the collected electron current could vary from 0 to 1A. (At higher current, the effective collision frequency, due to streaming instabilities, was too high for collisionless double layer theory to be valid.) Neutral gas, xenon, was introduced at the center of the anode at a rate that could vary from 1.8 to 13.7 sccm, which corresponded to a neutral density ranging from  $3 \times 10^{11}$  to  $10^{13} \text{ cm}^{-3}$ , concentrated within  $r_{\text{source}}$  of the origin. For  $\phi_0$  above some critical value, which depended on the neutral density, ambient electrons accelerated in the double layer had enough energy to ionize the gas, and the contactor cloud underwent a transition to an "ignited mode" in which this ionization was the major source of emitted ion current. The electron temperature and density and the plasma potential were measured as functions of position. The ambient ion temperature was much lower than the electron temperatures.

In a typical case, with  $\phi_0 = 37V$ , most of the potential drop, 25V, occurred in a double layer (more or less spherical) located between  $r_{\text{inner}} = 8 \text{ cm}$  and  $r_{\text{outer}} = 11 \text{ cm}$ . The rest of the potential drop occurred between the anode and  $r_{\text{inner}}$ . The potential profile was virtually flat outside  $r_{\text{outer}}$ . The ambient electron temperature was 5.5eV, and the ambient electron density was  $3 \times 10^7 \text{ cm}^{-3}$ . These electrons have a Larmor radius of about 15 cm in the earth's magnetic field, which is greater than  $r_{\text{outer}} - r_{\text{inner}}$ , and once they cross the double layer they have a Larmor radius of about 50 cm, which is greater than  $r_{\text{outer}}^2/2r_{\text{anode}}$ , so the electrons can easily reach the anode according to the Parker-Murphy criterion<sup>[11]</sup>, and the assumption in our model of unmagnetized electrons is valid. The assumption of collisionless electrons was also marginally satisfied if we estimate the effective collision frequency to be  $\nu_e \approx 10^{-3}\omega_{pe}$ . At  $r_{\text{outer}}$  we find  $\nu_e = 3 \times 10^4 \text{ s}^{-1}$ , and the electron mean free path is about 30 cm, greater than the width of the double layer, while at  $r_{\text{inner}}$  we find  $\nu_e = 2 \times 10^6 \text{ s}^{-1}$  and the mean free path of the accelerated ambient electrons is about 1 m, greater than  $r_{\text{inner}}$ . If the effective collision frequency is less than that taken here then the assumption of collisionless electrons is easily satisfied. Note that at densities a few times higher, the electron mean

free path would be comparable to the double layer width, and double layers could not exist. This is in agreement with observations at currents above 1A. There was also a 40eV ambient electron component (the "primary" electrons) of density  $3 \times 10^9 \text{ cm}^{-3}$ . Such a component of electrons was not included in our model, but their effect can be included by using an effective  $T_{ee} \approx 9\text{eV}$  which would give the same electron saturation current as that obtained from the 5.5eV and 40eV components.

The collected electron current, 370mA, was in good agreement with this electron saturation current integrated over the area of the double layer  $2\pi r_{outer}^2$  (not  $4\pi r_{outer}^2$ , since it was a half sphere). The electrons in the contactor cloud had a temperature  $T_{ee} = 2\text{eV}$ , and a density which went from  $8 \times 10^9 \text{ cm}^{-3}$  at  $r_{source}$  down to  $2 \times 10^7 \text{ cm}^{-3}$  at  $r_{inner}$ . This ratio of  $n_e(r_{source})/n_e(r_{inner})$  is close to  $(r_{inner}/r_{source})^2 [(\phi_0 - \phi(r_{inner}))/T_{ee}]^{1/2}$ , the value given by Eq.(2). The emitted ion current  $I_i$  would then be  $2\pi r_{source}^2 n_e(r_{source})(T_{ee}/m_i)^{1/2} = 0.4\text{mA}$ , fairly close to the ion current required by Eq.(17),  $(m_e/m_i)^{1/2} I_e = 0.7\text{mA}$ . The observed width of the double layer,  $r_{outer} - r_{inner} \approx 3\text{cm}$ , is a few times greater than the width of 0.6 cm predicted by Eq.(18), but it is likely that the measured width is smeared out by fluctuations in the position of the double layer. Such fluctuations could be due to some intrinsic property of the double layer that would cause it to oscillate around equilibrium<sup>[17]</sup> instead of asymptotically approaching equilibrium. Such behavior is likely to be associated with non-monotonic potentials<sup>[18]</sup>, a feature that we have not included in our model. The fluctuations could also be caused by a more mundane effect, such as fluctuations in the gas feed. It would be of interest to try to measure such fluctuations and to determine their cause.

### 3.3 Limitations of Wei and Wilbur Model Due to Magnetized Electrons

In Wilbur's ground based experiments<sup>[16]</sup> the Larmor radius of the ambient electrons in the earth's 0.3G magnetic field is about 20cm, much greater than the 3 cm thickness of the double layer, so the magnetic field will not significantly deflect the electrons as they cross the double layer. Once they cross the double layer, they will have a Larmor radius of about 50 cm, and in the 8 cm they have to traverse to get to the anode, they will be deflected by about  $\frac{1}{2}(8)^2/50 = 0.7 \text{ cm}$ , less than the 6 cm radius of the anode, consequently the magnetic field will not inhibit the electrons from getting to the anode<sup>[11]</sup>. Hence our model, which assumed unmagnetized electrons, ought

to be valid. An additional requirement of our model,  $r_{inner} > r_{anode}$ , is also satisfied in Wilbur's experiments.

In space, on the other hand, the ambient electron temperature, at least in the equatorial region, is much less, only about 0.1eV, so the Larmor radius is about 2.5cm, and the density is much less than in the ground based experiments (about  $10^5 \text{ cm}^{-3}$  rather than  $3 \times 10^7 \text{ cm}^{-3}$ ). Therefore, to collect an electron current of several amps from the ambient plasma will require  $r_{outer}$  of tens of meters, much greater than the electron Larmor radius. The electrons can traverse such a distance only if they undergo collisions (or effective collisions due to some kind of instability), or if they can gain enough energy as they cross the double layer to remain, in effect, unmagnetized, until they reach the anode. We have considered the latter possibility, and have found that, even with rather optimistic assumptions, it requires a sheath impedance that is undesirably large, since it would result in most of the tether potential drop occurring in the sheath. We conclude that effective collisions of some kind are needed in a plasma contactor in space, in order to collect a large electron current from the ambient plasma, at a reasonable impedance.

Parker and Murphy<sup>[11]</sup> have shown that, in the absence of collisions, and for  $e\phi_0 \gg T_{ea}$ , a necessary condition which must be satisfied for electrons at  $r_{outer}$  to reach the anode is

$$r_{outer}^2/r_{anode}^3 < 1 + (8e\phi_0/m_e\omega_{ce}^2 r_{anode}^2)^{1/2} \quad (20)$$

Eq. (20) is also a sufficient condition if all of the potential drop occurs in a thin double layer at  $r_{outer}$ . If the double layer is thick, or if a significant part of the potential drop occurs in the quasineutral regions on either side of the double layer, then an even more stringent condition must be satisfied, in order for electrons to reach the anode. Another condition that must be satisfied is  $r_{inner} \geq r_{anode}$ . It turns out that for most parameters of interest this condition and Eq. (20) cannot both be satisfied, for a spherically symmetric space-charge limited collisionless double layer, as described by Wei and Wilbur<sup>[9]</sup> and Amemiya<sup>[10]</sup>. This is true except at very low currents, or for anodes with  $r_{anode}$  almost equal to  $r_{outer}$ . If higher ion currents are emitted from an anode (with  $r_{anode} \ll r_{outer}$ ) with zero initial velocity, and there are no collisions or turbulence allowing electrons to be transported across the magnetic field, then a spherically symmetric double layer cannot develop, no matter how great the potential is. Electron collection will necessarily be inhibited in the direction across the

magnetic field; in this direction the potential profile will not follow the form found by Wei and Wilbur<sup>[9]</sup>, because the collected ambient electron current will not be space-charge limited, but will be limited by magnetic field effects. A theory giving the electron current and potential in this anisotropic collisionless regime regime is not available. However, if we ignore the requirement that  $r_{inner} > r_{anode}$  and assume that only Eq. (20) and the Wei-Wilbur equations must be satisfied, then we can obtain an upper limit for the electron current than can be collected, and a lower limit for the potential, for a given ion current and anode radius.

The electron current  $I_e$  is related to  $r_{outer}$  by

$$I_e = 2\pi r_{outer}^2 J_e^\infty \quad (21)$$

where  $J_e^\infty = en_{ea}(T_{ea}/2\pi m_e)^{1/2}$  is the ambient electron saturation current. We have calculated what the impedance of the double layer will be assuming Eq. (20) is barely satisfied, for  $r_{anode} = 10$  cm. If, as turns out to be true, the resulting impedance is too high to make an efficient plasma contactor, we will know that we should look at plasma contactors in which the electrons undergo collisions (or are subject to turbulence which causes effective collisions) and diffuse into the anode, rather than going into the anode directly.

Using Eq. (21) for  $I_e$ , assuming Eq. (20) is barely satisfied, and using Wei and Wilbur's calculation<sup>[9]</sup> which relates  $r_{outer}/r_{inner}$  uniquely to  $I_e/I_i$ , we can find  $\phi_0$  and  $I_e$  for a given  $I_i$  and electron saturation current  $J_e^\infty$ . Since  $J_e^\infty$  depends only on the properties of the ionosphere in low earth orbit, both  $I_e$  and  $\phi_0$  are determined by  $I_i$ . These values really represent an upper limit for  $I_e$  and lower limit for  $\phi_0$ , since Eq. (20) is only a necessary condition, not a sufficient condition, for collisionless electrons to reach the anode, and since we ignored the requirement that  $r_{inner} > r_{anode}$ . The gain and potential drop are obtained by imposing the Parker-Murphy requirement and the limited source requirement (Eq. (21)) on the Wei and Wilbur results.

In Figure 2 we show the gain  $\xi$  against the ion current for argon and for a range of electron saturation current densities which span the range experienced in an equatorial low earth orbit (LEO). The gain is somewhat less than  $(m_i/m_e)^{1/2} = 272$  for argon, and is weakly dependent on the ion current. We also show the associated potential drop through the double layer, which is really a lower limit on the potential drop. Typical potential drops are in the range of thousands

of volts for ion currents in the milliampere range. In Figures 2 through 4, the curves are dashed in the regime where Eq. (20) cannot be satisfied for a collisionless double layer with space charge limited current except by violating  $r_{inner} \geq r_{anode}$ . Note that the curves are dashed except at the smallest ion currents, showing that a collisionless unmagnetized double layer with space charge limited current is not possible for most parameters of interest in low earth orbit. This conclusion does not depend on  $r_{anode}$ . Making  $r_{anode} < 10$  cm would only make things worse, since, for a fixed ion current,  $r_{inner}$  would shrink faster than  $r_{anode}$ . Making  $r_{anode}$  much greater than 10 cm would allow higher ion and electron currents while satisfying Eq. (20) and  $r_{inner} > r_{anode}$ . However, for  $J_e^\infty \leq 2 \times 10^{-3}$  A/m<sup>2</sup>, this could only be done if  $r_{anode}$  were nearly equal to  $r_{outer}$ , in which case the plasma contactor would serve no purpose. Another way to show that this conclusion does not depend on  $r_{anode}$  is to use Eqs. (19) and (20), with  $\phi_0 \approx \Delta\phi$ ,  $r_{anode} = r_{inner}$ , and  $r_{outer} \approx 2r_{inner}$ . Combining these equations gives us

$$\phi_0 \approx \frac{T_{ee}}{e} \left( \frac{\omega_{pe}}{\omega_{ce}} \right)^4 \quad (22)$$

$$r_{outer} \approx \left( \frac{\omega_{pe}}{\omega_{ce}} \right)^2 \rho_e \quad (23)$$

where  $\omega_{pe}$  is the ambient electron plasma frequency and  $\rho_e$  is the ambient electron gyroradius. Equations (18) and (21) then give

$$I_i < 2\pi \left( \frac{m_e}{m_i} \right)^{1/2} J_e^\infty \left( \frac{\omega_{pe}}{\omega_{ce}} \right)^4 \rho_e^2 \quad (24)$$

as the maximum ion current for which a collisionless unmagnetized double layer with space-charge limited current is possible. This ion current depends only on ambient quantities and  $m_e/m_i$ , not on  $r_{anode}$  or  $\phi_0$ , and is never greater than about 1mA for low earth orbit.

In Figure 3 the total current is shown as a function of the electron saturation current density. The curve obtained for the collisionless double layer (really an upper limit) is shown for a fixed ion current of 10 mA. For comparison, we also show the total current for the isotropic quasineutral model described in Ref. [4], and for the anisotropic contactor model described in Section 4, for a fixed ion current of 1 Amp. This figure compares the realistic range of operation for the three models in typical ambient electron saturation current densities. A significant feature of this figure is that as the source varies by two orders of magnitude from  $2 \times 10^{-4}$  A/m<sup>2</sup> to  $2 \times 10^{-2}$  A/m<sup>2</sup>, the

total current (which is almost all collected electron current) varies by only a factor of 1.5, for the collisionless double layer model. This would seem to invalidate one of the conclusions in Ref. [1] which was that plasma contactors would not be useful on the nightside of an equatorial low earth orbit because the collected current would drop to almost nothing. Here the double layer moves out as the electron pressure drops so that the collected electron current is almost the same. On the other hand, if we took into account the actual requirements for electrons to reach the anode, rather than only using the Parker-Murphy condition, then it is likely that at low saturation current the double layer would be inhibited from moving out so far, and the collected electron current would be more sensitive to saturation current. Except for the upper end of the range of saturation current, the actual electron current that could be collected without collisions is certainly far less than the upper limit shown in Fig. 3. For the anisotropic collisional contactor model, which is more relevant for high current plasma contactors in low earth orbit, Fig. 3 shows that the total current is about 4 times higher, and the collected electron current is about 10 times higher, on the dayside ( $J_e^\infty \approx 2 \times 10^{-3} \text{ A/m}^2$ ) than on the nightside ( $J_e^\infty \approx 2 \times 10^{-4} \text{ A/m}^2$ ).

In Figure 4 the current voltage characteristic is shown for the range of electron saturation current densities. At constant current in the milliampere range the voltage is seen to vary by two or three orders of magnitude for one order of magnitude variation in electron saturation current, for the collisionless double layer. At constant voltage, the current is roughly linear with the electron saturation current. Ampere range currents (which are mainly electrons) require tens of thousands of volts of potential drop, even for the highest value of the electron saturation current. These curves represent an upper limit on the electron current for a given potential, or a lower limit on the potential for a given electron current. For currents greater than about 50 mA, the space charge limited collisionless double layer model on which these curves are based cannot satisfy both Eq. (20) and  $r_{inner} > r_{anode}$ ; the actual potential needed to collect such currents, in the absence of collisions, would be far greater than the lower limits shown in Fig. 4. Curves for the isotropic quasineutral model and anisotropic model discussed in Ref. [4] and Section 1 are shown for comparison.

With the use of these results we can calculate an upper limit for the current that could flow through a tether using a plasma contactor to collect electrons. A circuit diagram for a tether is

Table 1: Load power against efficiency of double layer contactor

$\eta$	$I_i(\text{mA})$	$\xi$	$I(\text{A})$	$P_{\text{load}}(\text{W})$
0.1	7	26	0.18	100
0.3	6	27	0.16	260
0.5	5	35	0.14	380
0.7	2.5	44	0.11	400
0.9	0.8	75	0.06	290

shown in Fig. 1 of Ref. [19]. The total potential drop  $\phi_{\text{total}}$  across the contactor, tether, load, and electron gun (or electron emitting contactor) is fixed by the length  $L$  of the tether, the earth's magnetic field  $B_0 = 0.33 \times 10^{-4} T$ , and the orbital velocity of the spacecraft  $v_o = 8 \text{ km/s}$ . For  $L = 20 \text{ km}$ , we find  $\phi_{\text{total}} = v_o B_0 L = 5333 \text{ V}$ . The potential across the load is  $\phi_{\text{load}} = R_{\text{load}}(I_i + I_e)$ . The potential across the tether is  $R_t(I_i + I_e)$ , where we take the tether impedance  $R_t = 200 \Omega$ . We could include the radiation impedance<sup>[20]</sup> but this is typically only about  $10 \Omega$ , so may be neglected compared to the tether impedance. We also neglect the impedance of the electron gun or electron emitting contactor. If we assume a typical dayside ionosphere with  $J_s^{\infty} = 2 \times 10^{-2} \text{ A/m}^2$ , a good fit to the numerical results in figure 4 is  $\phi_0 = b(I_i + I_e)^{2.08}$  where  $b = 1.8 \times 10^5$ . For a given load  $R_{\text{load}}$ , the current  $I = I_i + I_e$  may be found by solving

$$\phi_{\text{total}} = R_{\text{load}}I + R_tI + bI^{2.08} \quad (25)$$

and we may then find the power across the load  $P_{\text{load}} = R_{\text{load}}I^2$ , and efficiency  $\eta = R_{\text{load}}I/\phi_{\text{total}}$ , as functions of  $R_{\text{load}}$ . (This definition of efficiency neglects the energy needed to produce the ions, but that is justified since this energy, about 50 eV, is much less than the potential drop across the double layer, unless  $\eta \approx 99\%$ .) Table 1 shows  $P_{\text{load}}$  and  $\xi$  as functions of the efficiency  $\eta = R_{\text{load}}I/\phi_{\text{total}}$ .

The maximum power to the load is 400 W, but this occurs when the efficiency is only 70%. As noted in Ref. [1], in order for tethers to be competitive with other power systems in space it is necessary for them to operate at high efficiency, at least 80% or 90%. This is because all of the power has to be made up by periodically boosting the tether but only the load power can be

usefully used. If we desire an efficiency of 85%, then the maximum load power we can obtain is only 320 W. The maximum power will in fact be much less than this, since Eq. (20) is not a sufficient condition for electrons to get across the magnetic field to the anode<sup>[11]</sup>, and is known to be far from sufficient in the regime where  $r_{outer} \gg r_{inner}$ , which is true at the maximum power. Also, the requirement that  $r_{inner} > r_{anode}$  is far from satisfied at the ion current needed for maximum power.

We conclude that it is not possible to design a high power contactor which draws electrons straight across a double layer without collisions. Instead we should consider designs where collisions (or, more realistically, effective collisions due to instabilities of some kind) transport electrons across the magnetic field to the anode.

### 3.4 Conditions for Ignited Plasma

The calculations so far with the double layer model have all been for a totally ionized plasma. For a partially ionized plasma it is possible to include the effect of ionization and to show when the plasma will ignite. If we assume the neutral gas is expanding radially from the source at  $r_{source}$ , and that only a small fraction of it gets ionized, then the neutral density varies with radius as  $n_0(r) = n_0(r_{source})(r_{source}/r)^2$ . We apply conservation of mass from  $r_{source}$  to  $r_{inner}$  to obtain

$$I_e(r) = I_e(r_{inner}) \exp\left(\gamma(\Delta\phi)\left[\frac{r_{source}}{r} - \frac{r_{source}}{r_{inner}}\right]\right) \quad (26)$$

where  $\gamma(\Delta\phi) = n_0(r_{source})r_{source}\sigma$ . Here the electron ionization cross-section  $\sigma$  is to be evaluated at a typical energy for an incoming ambient electron,  $\Delta\phi + T_{ea}$ . From conservation of current we obtain the gain as

$$\xi = 1 + \frac{(\xi(r_{inner}) - 1) \exp(\gamma(1 - \frac{r_{source}}{r_{inner}}))}{1 + (\xi(r_{inner}) - 1)(1 - \exp(\gamma(1 - \frac{r_{source}}{r_{inner}})))} \quad (27)$$

where  $\xi(r_{inner}) = I/I_i(r_{inner})$ . The ion current at the source in terms of the ion current just inside the double layer is

$$\frac{I_i(r_{source})}{I_i(r_{inner})} = 1 + (\xi(r_{inner}) - 1)(1 - \exp(\gamma(1 - \frac{r_{source}}{r_{inner}}))) \quad (28)$$

In order to interpret the calculations in Fig. 2 with ionization present we must interpret the ion current in the abscissa as  $I_i(r_{inner})$ , and the gain as  $\xi(r_{inner})$ . The relationship in terms of the ion

current emitted at the source is given above. It is apparent that there may be no positive solution of the source ion current for a given ion current at the double layer. Physically this will occur when there is so much neutral gas that the mixed gas-plasma flow ignites giving an avalanche of ion current. The ion current and collected electron current will continue to increase, and cannot reach a steady state until the collisionless double layer model is no longer valid. By setting the source ion current to zero we can obtain this critical neutral density for ignition as

$$n_{\text{critical}} = \frac{-\ln(1 - 1/\xi(r_{\text{inner}}))}{(1 - r_{\text{source}}/r_{\text{inner}})} \frac{1}{r_{\text{source}} \sigma} \quad (29)$$

If we relate the source neutral density to the ion flow rate and initial fractional ionization ( $f_i$ ) we obtain ignition for

$$I_i(r_{\text{inner}}) > \frac{4\pi r_{\text{source}}^2 c_s e f_i}{1 - f_i} n_{\text{critical}} \quad (30)$$

Taking  $r_{\text{source}} = 0.1$  m,  $c_s = 4.89 \times 10^3$  m/s,  $\sigma = \sigma_{\text{max}} = 3.21 \times 10^{-20}$  m<sup>-2</sup> (for ionization of argon) and  $f_i = 10^{-4}$  which is typical of hollow cathode devices, we find that the critical ion current is much greater, for a given gain, than the ion currents for which the collisionless double layer model is valid in low earth orbit, shown as solid curves occur in Fig. 2. Hence ignition will never occur in this regime. Ignition might be possible in the regime of higher ion current and lower gain typical of the anisotropic collisional contactor model described in Section 4.

#### 4 Anisotropic Contactor Model

Hastings and Blandino<sup>[4]</sup> considered a model where electrons were transported across the magnetic field by effective collisions due to instabilities, and assumed that such transport could occur only out to a distance  $r_{\text{core}}$  where the effective collision frequency  $\nu_e$  was greater than the electron cyclotron frequency  $\omega_{ce}$ . With that model, they found that the collected ambient electron current for typical parameters in low earth orbit was less than the emitted ion current. Here, we consider the possibility that electrons can be collected from a more distant region where  $\nu_e < \omega_{ce}$ . In that region the contactor cloud will be anisotropic, extending further in a direction along the magnetic field than across the magnetic field. We therefore use cylindrical coordinates  $z$  and  $r$ , where  $r$  now refers only to the distance across the magnetic field, not to the total distance from the anode as it

did in previous sections. We assume that the plasma density in the cloud is still great enough to short out the electric field due to the orbital velocity, so the cloud will be cylindrically symmetric. (At still larger distances from the anode, the effects of the orbital motion induced electric field will become important, and the cylindrical symmetry will be broken.) In this region the electron velocity will be mostly azimuthal, at the drift velocity

$$v_d = \frac{e}{m_e \omega_{ce}} \frac{\partial \phi}{\partial r} - \frac{1}{m_e \omega_{ce}} \frac{\partial T_e}{\partial r} - \frac{T_e}{m_e \omega_{ce} n_e} \frac{\partial n_e}{\partial r} \quad (31)$$

For parameters of interest, this drift velocity is much greater than the radial flow velocity of the emitted ions, which are effectively unmagnetized since we assume that the scale lengths are all much less than an ion Larmor radius. The velocity difference between the electrons and ions will then be nearly in the azimuthal direction. This relative cross-field drift velocity of magnetized electrons and unmagnetized ions can give rise to several instabilities, among them the ion acoustic instability (both  $k_{\perp} \rho_s > 1$  and  $k_{\perp} \rho_s < 1$  varieties), the Buneman instability, the electron cyclotron drift instability (also known as the beam cyclotron instability), the modified two-stream instability, and the lower hybrid drift instability. Which of these instabilities dominates depends on such parameters as  $T_e/T_i$ ,  $v_d/c_s$ ,  $v_d/v_e$ ,  $\beta_s$ ,  $\omega_{pe}/\omega_{ce}$ , and  $v_d/v_A$ . These instabilities will give rise to turbulent azimuthal electric fields, which will exert an azimuthal drag force  $F_\theta = \nu_e m_e v_d$  on the electrons, giving rise to a drift in the  $\mathbf{F} \times \mathbf{B}_0$  (inward radial) direction at velocity

$$v_r = \frac{\nu_e}{\omega_{ce}} v_d \quad (32)$$

We will assume that the potential drop in the plasma cloud is very much greater than the ion temperature  $T_i$ , which is typically only a few eV. Since, as we will show later,  $T_e$  tends to be only a few times less than  $\phi_0$ , this implies that  $T_e/T_i \gg 1$ , except perhaps near the edge of the cloud. Also  $c_s \ll v_d \ll v_e$ . In these circumstances, we expect the  $k_{\perp} \rho_s > 1$  ion acoustic instability to dominate (this is the same as the ion acoustic instability in an unmagnetized plasma). The effective collision frequency  $\nu_e$  for this instability in its nonlinear saturated state scales with density like  $\omega_{pe}$ , and is independent of  $c_s/v_d$  for  $c_s \ll v_d$ , but there is some uncertainty as to its dependence on  $T_e/T_i$  and  $v_d/v_e$ . We will simply assume that

$$\nu_e \approx 10^{-3} \omega_{pe} \quad (33)$$

independent of the other parameters. There is considerable theoretical and experimental evidence that the effective collision frequency due to ion acoustic turbulence is proportional to  $\omega_{pe}$ , and somewhat weaker evidence that the constant of proportionality should be  $10^{-2}$ , as in Eq. (33). This evidence is discussed in Ref. [7]. In addition, we note that particle simulations of saturated ion acoustic turbulence in infinite medium<sup>[21,22,23]</sup> generally give effective collision frequencies of this magnitude, and that experimental observations of collisionless shocks are in agreement with this result<sup>[24]</sup>. In a plasma contactor, the scale lengths are not infinite compared to the wavelengths of the unstable modes, the geometry differs from that of Ref. [24], and Eq. (33) may have to be modified. (Indeed, the requirement that the wavelengths of the dominant unstable modes be small compared to the radial scale length will probably set a lower limit on the ion current for which this model is valid.) A proper determination of  $\nu_e$  would require a 3-D particle simulation of a contactor cloud, and experimental observations in the relevant regime to make sure that the simulation includes all of the relevant physics. Short of that, Eq. (33) is a reasonable guess that should be of help in choosing parameters for more careful theoretical and experimental studies. The method we will use to find analytic expressions for  $\phi(r, z)$  and the collected electron current may also be applied using more realistic expressions for  $\nu_e$ .

The divergence of the radial flux of electrons due to  $\nu_e$  and the radial electric field and temperature and density gradients must be balanced by an inward flux of electrons along the magnetic field, neglecting ionization and recombination:

$$\frac{1}{r} \frac{\partial}{\partial r} r n_e v_r + \frac{\partial}{\partial z} n_e v_z = 0 \quad (34)$$

At high densities, such as those in the experiment of Urrutia and Stenzel<sup>[25]</sup>, with  $\omega_{pe} \gg \omega_{ce}$ , the mean free path of electrons will be short compared to the length of the contactor cloud, and the velocity  $v_z$  along the magnetic field may also be found by balancing the force from the electric field  $e\partial\phi/\partial z$  with the drag force  $m_e v_z v_z$ . In this case Eq. (34) will generally not be separable in  $r$  and  $z$ , and it is necessary to solve a fully two-dimensional partial differential equation. The boundary conditions will be that  $v_r = 0$  and  $\dot{\phi} = 0$  at the same surface, and the flux of electrons across this surface must be equal to the flux of the electron saturation current of the ambient plasma (along the magnetic field) outside the surface. The potential  $\phi(r, z)$  would be quasineutral everywhere.

Since the position of the  $\phi = 0$  surface is not known in advance, this would be a difficult numerical problem. The ambient plasma in low earth orbit has much lower density,  $\omega_{pe} \leq \omega_{ce}$ , and this would also be true in most of a space-based contactor cloud, which, as we will show, would extend along the magnetic field to a distance where the cloud density is comparable to the ambient density. In this case, the electrons will flow freely along the magnetic field, and a different model is needed. If the total potential drop  $\phi_0$  between the anode and the ambient plasma is greater than  $T_{ee}$  and  $T_{ie}$ , then double layers will form at a distance  $z_0$  along the magnetic field in both directions, where

$$J_i = \frac{I_i g(z_0)}{2\pi z_0^2} = \left(\frac{m_e}{m_i}\right)^{1/2} J_e^\infty \quad (35)$$

for thin double layers, just as in the unmagnetized collisionless case (see Eq. (18)). Here  $g(z)$  is a factor to take into account that the ions are focussed by the potential  $\phi(r, z)$  if it is not spherically symmetric. Although the flow of electrons along the magnetic field is nearly collisionless, we will assume that there is enough drag to slow down the incoming electrons slightly, so that they will not escape out the other end, but will become trapped in the cloud. Only a small amount of drag is needed for this if  $\phi_0 \gg T_{ee}$ , and this could be provided by electron-electron streaming instabilities which produce effective collision frequencies of only a small fraction of  $\omega_{pe}$ . Even if all of the electrons are not trapped, making this assumption will not introduce a large error if most of them are trapped. At  $z = \pm z_0$ , the flux of electrons along the field must then satisfy the boundary condition

$$n_e v_z = \mp J_e^\infty / e \quad (36)$$

Because the flow of electrons across the magnetic field is collisional, no double layer exists in the radial direction. For fixed  $|z| < z_0$ ,  $\phi(r, z)$  must decrease smoothly to zero at some  $r_1(z)$ , satisfying quasineutrality all the way. For fixed  $r$ , along a given field line, as long as  $\phi(r, z=0) > T_e(r)$ ,  $\phi(r, z)$  will not go to zero for  $|z| < z_0$ . If  $\phi_0$  is at least a few times greater than  $T_e$ , then  $\phi(r, z=0)$  will be greater than  $T_e$  for all  $r$  not too close to  $r_1(z=0)$ . It follows that  $r_1$  is nearly independent of  $z$ . The contours of  $\phi(r, z)$ , and the flow of ions and electrons, are shown schematically in Fig. 5.

This means that Eq. (34) will be separable in  $r$  and  $z$ . The boundary conditions in  $r$  are

$$\phi(r = r_{anode}, z) = \phi_0 + T_e \ln(n_e(z)/n(z=0)) \quad (37)$$

$$\phi(r = r_1) = 0 \quad (38)$$

$$\frac{\partial \phi}{\partial r} = \frac{1}{e} \frac{\partial T_e}{\partial r} \quad \text{at } r = r_1 \quad (39)$$

The last condition follows from the fact that  $v_r = 0$  outside the contactor cloud, and there is no source or sink of electrons at  $r = r_1$ , hence  $v_r$  must vanish at  $r_1$  just inside the contactor cloud. Eq. (31) (with  $T_s = 0$ ), and Eq. (32) then yield Eq. (39).

#### 4.1 Electron Temperature

Before proceeding with the calculation of the potential profile  $\phi(r)$ , we will briefly consider whether we are justified in assuming that  $\phi_0$  is at least a few times greater than  $T_e$ . The electron temperature profile  $T_e(r)$  is determined by the balance between convection, conduction, and ohmic heating (both perpendicular and parallel to the magnetic field). We neglect ionization and line radiation, which should only be important near the anode, and we neglect heat lost by electrons boiling out along the magnetic field.

$$\frac{-3}{2} v_r \frac{\partial T_e}{\partial r} + \frac{1}{rn_e} \frac{\partial}{\partial r} r \kappa \frac{\partial T_e}{\partial r} + ev_r \frac{\partial \phi}{\partial r} + \frac{J_e^\infty}{n_e z_0} \left( \phi - \frac{T_e}{e} \right) = 0 \quad (40)$$

Here  $\kappa$  is the cross-field thermal conductivity, which is dominated by turbulence just as the drag is. In general

$$\kappa = \frac{C n_e T_e \nu_t}{m_e \omega_{ce}^2} \quad (41)$$

where  $C$  is a constant which depends on the details of the "collisions" causing the heat transport. For electron thermal conductivity across a magnetic field due to Coulomb collisions<sup>[26]</sup>, for example.  $C = 4.7$ .

The boundary conditions are

$$T_e = 0 \quad \text{at } r = r_1 \quad (42)$$

$$\kappa \frac{\partial T_e}{\partial r} = \frac{Q}{4\pi r_{anode} z_0} - n_e v_r T_e \quad \text{at } r = r_{anode} \quad (43)$$

where  $Q$  is the heat flux going into the anode. This is generally greater than the convective heat flux into the anode (the second term on the right hand side), because  $\langle v_s^2 \rangle$  for a half-maxwellian is

greater than  $\langle v_x^2 \rangle / \langle v_z \rangle$ . So  $\partial T_e / \partial r > 0$  at  $r_{\text{anode}}$ . Because  $T_e = 0$  at  $r = r_1$ ,  $\partial T_e / \partial r$  must change sign between  $r_{\text{anode}}$  and  $r_1$ , and we can estimate that the second term in Eq. (40) is of order  $-\kappa T_e / n_e r_1^2$ . Using Eqs. (31), (32), and (41) we find

$$v_r = \frac{\kappa}{n_e T_e C} \left( e \frac{\partial \phi}{\partial r} - \frac{\partial T_e}{\partial r} \right) \quad (44)$$

Then the first term in Eq. (40) is of order  $\pm \kappa e \phi / C n_e r_1^2$ , and the third term is of order  $\pm \kappa e^2 \phi^2 / C n_e T_e r_1^2$ . From Eqs. (34) and (36) the fourth term in Eq. (40) is comparable to (and has the same sign as) the third term.

If  $C \leq 1$ , it follows that the second and/or the first term must balance the third and fourth terms, so  $T_e$  is of order  $e\phi$ . If  $C \gg 1$ , then the second term alone must balance the third and fourth terms, and  $T_e \approx e\phi/C^{1/2} \ll e\phi$ . Our assumption that  $T_e$  is at least a few times less than  $\phi$  is thus valid if  $C$  is somewhat greater than one. This is true for Coulomb collisions; whether it is true for ion acoustic turbulence is an open question that is beyond the scope of this paper. If  $\kappa$  is dominated by an energetic tail of the electron distribution, perhaps electrons collected from the ambient plasma which have not yet thermalized, then  $C \gg 1$ .

## 4.2 Potential Profile and Cloud Radius

To find  $\phi(r)$ , we first integrate Eq. (34) over  $z$  from  $-z_0$  to  $+z_0$ , and use Eq. (36) to eliminate  $v_z$

$$\int_{-z_0}^{+z_0} dz \frac{1}{r} \frac{\partial}{\partial r} r n_e v_r = 2 J_i^\infty \quad (45)$$

(It may seem counter intuitive that finding the electron current should require an integration over  $z$ , since no electrons are collected across field lines at the boundary of the cloud at  $r = r_1$ , only along field lines at the boundary at  $z = \pm z_0$ . The purpose of the  $z$  integration is simply to show that the dominant contribution to the cross-field electron transport comes from small  $z$ , so that  $v_r$  may be evaluated at  $z = 0$  when the radial integration is done.) To obtain an expression for  $n_e$ , which appears explicitly in Eq. (45) and also implicitly through the dependence of  $v_r$  on  $\omega_{pe}$ , we use quasineutrality

$$n_e = n_i = (4\pi)^{-1} I_i m_i^{1/2} e^{-3/2} (r^2 + z^2)^{-1} g(r, z) (\phi_0 - \phi)^{-1/2} \quad (46)$$

The expression for  $n_i$  in Eq. (46) comes from the fact that the ions are unmagnetized, and expanding spherically from the anode. The factor  $g(r, z)$  takes into account the focussing of the ions by  $\phi(r, z)$  which is not spherically symmetric. Using Eq. (32) for  $v_r$ , Eq. (33) for  $v_z$ , Eq. (46) for  $n_i$ , taking  $B_0 = 0.3G$ , defining the ion atomic weight  $\mu = m_i/m_p$ , and expressing  $I_i$  in amps,  $J_i^{\infty}$  in amps/m<sup>2</sup>, and  $\phi$  and  $\phi_0$  in volts, Eq. (45) becomes

$$\int_{-r_0}^{+\infty} dz \frac{1}{r} \frac{\partial}{\partial r} \left[ r(\phi_0 - \phi)^{-3/4} (r^2 + z^2)^{-3/2} g(r, z) \frac{\partial \phi}{\partial r} \right] = -12 I_i^{-3/2} \mu^{-3/4} J_i^{\infty} \quad (47)$$

Because  $(\phi_0 - \phi)$  and  $\partial \phi / \partial r$  are fairly independent of  $z$ , and the integrand is most strongly weighted near  $z = 0$ , we replace  $\phi$  and  $\partial \phi / \partial r$  by their values at  $z = 0$ , so they can be taken out of the integral. Similarly, we can set  $g(r, z) \approx 1$ , because self-consistently there cannot be a strong focussing effect for  $z < r$  where most of the contribution to the integral is. We then do the integration over  $z$

$$\frac{\partial}{\partial r} \left[ \frac{1}{r} (\phi_0 - \phi)^{-3/4} \frac{\partial \phi}{\partial r} \right] = -12 r I_i^{-3/2} \mu^{-3/4} J_i^{\infty} \quad (48)$$

We integrate Eq. (48) over  $r$ , using the boundary condition Eq. (39) to obtain the integration constant

$$\frac{1}{r} (\phi_0 - \phi)^{-3/4} \frac{\partial \phi}{\partial r} = 6 I_i^{-3/2} \mu^{-3/4} J_i^{\infty} (r_1^2 - r^2) \quad (49)$$

where

$$r_1^2 = r_1^2 + \frac{1}{6} r_1^{-1} \phi_0^{-3/4} e^{-1} \frac{\partial T_e}{\partial r} I_i^{-3/2} \mu^{3/4} (J_i^{\infty})^{-1} \quad (50)$$

We integrate over  $r$  again, using Eq. (37) at  $z = 0$  to obtain the integration constant

$$(\phi_0 - \phi)^{1/4} = 0.5 I_i^{-3/2} \mu^{-3/4} J_i^{\infty} (2r_1^2 r^2 - r^4) \quad (51)$$

Finally we use Eq. (38) in Eq. (51) to obtain an equation for  $r_1$

$$\phi_0^{1/4} = 0.5 I_i^{-3/2} \mu^{-3/4} J_i^{\infty} \left[ r_1^4 + \frac{1}{3} r_1 \phi_0^{-3/4} e^{-1} \frac{\partial T_e}{\partial r} I_i^{-3/2} \mu^{3/4} (J_i^{\infty})^{-1} \right] \quad (52)$$

If, as we have been assuming,  $T_e \ll e\phi_0$ , then the second term in brackets may be neglected, and

$$r_1 = 1.2 \phi_0^{1/16} I_i^{3/8} \mu^{3/16} (J_i^{\infty})^{-1/4} \quad (53)$$

Note that  $r_1$  has an extremely weak dependence on  $\phi_0$ . For almost any reasonable  $\phi_0$ , say  $10V < \phi_0 < 1000V$ , for argon, and for  $J_e^\infty = 2 \text{ mA/m}^2$ , which is between the typical dayside and nightside values,

$$r_1 \approx 15 I_i^{3/8} \quad (54)$$

and

$$I_e = 2\pi r_1^2 J_e^\infty \approx 2 I_i^{3/4} \quad (55)$$

In general the total current  $I = I_i + I_e$  is

$$I = I_i + 8(J_e^\infty)^{1/2} I_i^{3/4} \mu^{3/8} \phi_0^{1/8} \quad (56)$$

A substantial ambient electron current can be collected for values of  $\phi_0$  and total current that are of interest for tethers. For 1 A of argon at  $J_e^\infty = 2 \text{ mA/m}^2$ , for example, we get a gain  $I/I_i = 3$ , while for 0.5 A of xenon, at a typical dayside electron saturation current  $J_e^\infty = 20 \text{ mA/m}^2$ , we obtain  $I/I_i = 12$ . These gains, although not as large as the gains that were found with a completely collisionless double layer model, can still make a significant contribution to operation of tethers for power generation. These electron currents are much greater than the electron currents found in the quasineutral model of Ref. [4]; the physical reason for this is that electrons are transported across the magnetic field from much greater radius, where  $v_e \ll \omega_{ce}$ .

In Fig. 3, the total current is shown for a fixed ion current of 1 A, as a function of electron saturation current, using Eq. (56), and is compared to the total current for the isotropic quasineutral model discussed in Section 4, and for the collisionless double layer model using an ion current of 0.01 A. Note that the current from Eq. (56) is much more sensitive to the electron saturation current than in the case of the collisionless double layer model. The reason is that the anisotropic contactor cloud, unlike the collisionless double layer cloud, cannot easily expand to larger radius to make up for a decrease in the ambient electron density. In Fig. 4, the current voltage characteristic is shown, from Eq. (56), for  $J_e^\infty = 2 \text{ mA/m}^2$ , and compared to the results from the isotropic quasineutral model, and from the collisionless double layer model for a range of electron saturation currents. For realistic potentials, less than 1000V, the current from Eq. (56) is at least an order of magnitude greater than for the collisionless double layer model.

Table 2: Load power against efficiency of anisotropic contactor

$\eta$	$I_i(A)$	$\xi$	$I(A)$	$P_{load}(kW)$
0.1	1	4.99	4.99	2.64
0.3	1	4.83	4.83	7.65
0.5	1	4.6	4.6	12.1
0.7	1	4.22	4.22	15.4
0.9	1	2.32	2.32	10.6

Table 3: Load power against efficiency of emitting an ion beam

$\eta$	$I_i(A)$	$\xi$	$I(A)$	$P_{load}(kW)$
0.1	22.64	1	22.64	12.1
0.3	17.56	1	17.56	28.1
0.5	12.48	1	12.48	33.3
0.7	7.4	1	7.4	27.7
0.9	2.3	1	2.3	11.2

Table 2 shows the load power  $P_{load}$  against efficiency, using the same ambient plasma and tether parameters as in Table 1, but using Eq. (56) to relate  $I$  and  $\phi_0$ . In this case, the maximum power obtained at  $\approx 80\%$  efficiency is 12kW, much higher than in Table 1. Of course in a comparison with the collisionless double layer results the energetic cost of producing more ion current must be compared to the cost of the high potential associated with the space charge limited double layer.

Finally in Table 3 we show the power to the load for a quasineutral model which just emits an ion beam, or a double layer model with ionization, so that a large current flows for very low potential drop ( $\Delta\phi \approx 0$ ,  $\xi = 1$ ). At 90% efficiency this configuration, which makes no use of the ambient plasma, can generate only slightly higher power than the anisotropic contactor, and requires substantially higher emitted ion current. This shows that the anisotropic contactor could make a significant contribution to the operation of tethers for power generation.

Table 4: Contactor models and the regimes where they are valid

Model	Limits of validity	Applicable situations	Where discussed
Bare ion source	$I_i > I_e$	$I_i > 1\text{A}$ in nightside LEO	Table 3
Bare anode	$I_i < I_e$ $r_{\text{outer}} < 2r_{\text{anode}}$	Very low $I_i$ , large $r_{\text{anode}}$ , e.g. $I_i < 10\mu\text{A}$ , $r_{\text{anode}} = 1\text{m}$ , LEO	Briefly in Sec. 2
Collisionless unmagnetised double layer	$r_{\text{outer}} > 2r_{\text{anode}}$ , $r_{\text{anode}} < r_{\text{inner}}$ , $r_{\text{outer}}^2/r_{\text{anode}} < (e\phi_0/m_e)^{1/2}\omega_{ce}^{-1}$ , $r_{\text{outer}}^2/r_{\text{anode}} < (e\phi_0/m_e)^{1/2}\nu_e^{-1}$	$1\mu\text{A} < I_i < 1\text{mA}$ in dayside LEO, ground-based experiments[19] with $I_i < 1\text{A}$	Sec. 3
Low collisionality magnetized	$r_{\text{outer}} > 2r_{\text{anode}}$ , $r_{\text{outer}}^2/r_{\text{anode}} > (e\phi_0/m_e)^{1/2}\omega_{ce}^{-1}$ $\nu_e < \omega_{ce}$ , $k_{\perp}r_1 < 1$	$1\text{mA} < I_i < 100\text{mA}$ ? in dayside LEO	Not discussed
Anisotropic (magnetised collisional)	$\nu_e < \omega_{ce}$ at $r_1$ , $\rho_e < r_1$ , $k_{\perp}r_1 > 1$ , $r_{\text{anode}} < r_1$ , $I_i < I_e$	$I_i = 1\text{A}$ in dayside LEO	Sec. 4
Isotropic (unmagnetised collisional)	$\nu_e > \omega_{ce}$ at $r_1$ , $\nu_e/\nu_e < r_1$ , $k_{\perp}r_1 > 1$ , $I_i < I_e$	M marginally in experiment of Urrutia & Stensel[25], never in LEO	Briefly in Sec. 4, similar model in Ref.[4]

## 5 Conclusions

We have examined several models for electron collection by plasma contactors. The range of validity of the different models, and the situations where they are applicable, are summarized in Table 4.

The ground based experiments at currents below 1 A appear to be well described by a double layer model which treats the electrons as collisionless and unmagnetized. In those experiments, the double layer forms approximately at the radius where the plasma emitted from the contactor reaches the ambient plasma density. This radius is less than or comparable to both the electron Larmor radius, and the mean free path of the electrons, based on a model for effective collisions due to instabilities. In high power space applications, where the plasma cloud must have a radius of tens of meters, and the ambient electron Larmor radius is only a few cm, neither of these conditions applies. Still neglecting collisions, but taking into account the finite electron Larmor radius, we

find that ambient electrons can get across the double layer and reach the anode only if the Parker-Murphy condition<sup>[11]</sup> is satisfied (and even that is not a sufficient condition). For  $r_{anode} \ll r_{outer}$  and ion current greater than the right hand side of Eq. (24) (about 1 mA for dayside low earth orbit, even lower for nightside), the Parker-Murphy condition cannot be satisfied for a spherically symmetric double layer with space charge limited current, since the  $r_{inner}$  determined by Wei and Wilbur<sup>[9]</sup> would be less than  $r_{anode}$ , for any potential and  $r_{outer}$  satisfying the Parker-Murphy condition. This means that such collisionless double layers are not possible in space except at very low ion currents. This conclusion follows from the mass ratio and the magnetic field, electron density and temperature found in low earth orbit (since the right hand side of Eq. (24) depends only on these parameters), and does not depend on any assumption made about the potential or the size of the anode, other than  $r_{anode} \ll r_{outer}$ . (Collisionless double layers with higher ion currents are possible if  $r_{anode}$  is made big enough so that the bare anode could collect almost as much electron current as the contactor cloud, but the contactor cloud would then serve no purpose.) At higher ion currents and small anodes, if we assume the electrons are still collisionless, the collected electron current will not be space charge limited, as assumed by Wei and Wilbur, but will be limited to a lower value by the magnetic field. Neglecting the requirement that  $r_{inner} > r_{anode}$ , and considering only the Parker-Murphy condition, we found an upper limit to the collisionless electron current that could be collected, and a lower limit to the potential, as a function of ion current. We found that such a large potential is needed across the double layer in order to draw a reasonably large electron current that the available load power for a 20km long tether is never greater than 400 W. The maximum power is surely far less than this, since this figure was found for a configuration with  $r_{inner} \ll r_{outer}$ , and the Parker-Murphy condition is known to be far from sufficient in that limit; also,  $r_{inner} > r_{anode}$  was known to be far from satisfied at the maximum power. The collisionless double layer model should be valid in space for emitted ion current sufficiently low ( $I_i < 1$  mA for dayside low earth orbit, much lower for nightside) that a double layer can form with  $\phi_0 < 5$  kV (the total tether voltage) allowing electrons to get across the magnetic field to the anode, and satisfying  $r_{inner} > r_{anode}$ . There is a further requirement for validity: the electrons must not be deflected from the anode by effective collisions, due to instabilities, as they are traversing the contactor. But

this requirement is easily satisfied in space, where the ambient  $\omega_{pe}$  is not too much greater than  $\omega_{ce}$ .

Since a plasma contactor described by the collisionless double layer model cannot generate anything close to the desired power, we must use much higher emitted ion currents. Although the transition from the collisionless double layer model to the collisional quasineutral model is not completely understood, we expect at sufficiently high ion current that there will be instabilities strong enough to produce a high effective electron collision frequency in the contactor cloud. Such a contactor can be described by a collisional quasineutral fluid model, in which electrons can flow across the magnetic field within a radius  $r_{core}$  of the anode. If  $r_{core}$  is defined conservatively as the radius within which the effective electron collision frequency, due to ion acoustic and Buneman instabilities, exceeds the electron cyclotron frequency<sup>[4]</sup>, then we find that the contactor has a very low impedance, but draws very little electron current because  $r_{core}$  is rather small. The total contactor current is hardly enhanced at all above the ion current that it is emitting. Even for those cases of higher  $T_e$  where a modest gain in current occurs, that gain is due almost entirely to ionization of neutral gas emitted by the contactor, not to collection of electrons from the ambient plasma. In this case, the gas would probably be used more efficiently if it were ionized internally, in an ion source, rather than externally, where much of it can be lost.

If we include the anisotropic part of the contactor cloud where the effective electron collision frequency is less than the electron cyclotron frequency, then electrons can be collected out to a much larger radius, and an electron current a few times greater than the ion current can be drawn from the ambient plasma, even at fairly low potentials. In contrast to the upper limits derived for the collisionless double layer model, and to the quasineutral model based on the more conservative definition of  $r_{core}$ , the electron current has a significant dependence on the electron saturation current of the ambient plasma in this case, and is substantially higher, for a given ion current, on the dayside than on the nightside in equatorial low earth orbit. Analytic expressions for the potential profile and collected electron current can be obtained when the electron motion along the magnetic field is fairly collisionless, so that a double layer forms in that direction, but the electrons flow collisionally across the magnetic field. This is the regime that is relevant to high

current plasma contactors in low earth orbit. Although the model which is solved analytically in Section 4 made the simple approximation that the effective electron collision frequency, due only to ion acoustic turbulence, is equal to  $10^{-2}\omega_{pe}$ , independent of  $T_e$  and the electric field, the same method should be applicable using more realistic expressions for the effective collision frequency. Another approximation made in our analysis of this model is that there is sufficient electron thermal conductivity across the magnetic field to keep  $T_e$  much lower than  $\phi_0$  in the contactor cloud. The validity of this approximation must be examined using realistic turbulence models. If this approximation is at least marginally valid, then our results should be qualitatively correct.

One important conclusion of our analysis is that most of the present ground based experiments have limited relevance to space applications of plasma contactors, since they operate in a regime where the magnetic field and effective collisions are not important, or only marginally important. This is true of space-based contactors only at very low current and power levels. An exception is the experiment of Urrutia and Stenzel<sup>[25]</sup>, which examined a plasma in which the electron Larmor radius was small compared to the scale of the potential, and anomalous transport of electrons across the magnetic field was important. Indeed, they found that the anode collected an electron current a few times greater than the saturation current of the flux tube that intersected the anode, even when the effective collision frequency was less than the electron cyclotron frequency. Urrutia and Stenzel attributed their cross field electron transport to ion acoustic instabilities that were excited by the azimuthal  $E \times B$  drift of the electrons relative to the unmagnetized ions, which gave rise to azimuthal wave electric fields which cause radial  $E \times B$  drifts. In this respect the experiment was similar to the anisotropic contactor cloud model considered in Section 4. However, this experiment differed in one important respect from the regime, appropriate to low earth orbit, that was considered in Section 4. In the experiment, the density was about  $2 \times 10^{11} \text{ cm}^{-3}$  and  $\omega_{pe}/\omega_{ce} \approx 50$ , much higher than in low earth orbit, and as a result the anomalous parallel resistivity, due to Buneman and ion acoustic instabilities excited by the relative electron and ion flow velocity along the field, was high. The electrons did not flow freely along the magnetic field, but diffused along the field like a collisional fluid, so there were no double layers along the field. It would be

desirable to do ground-based experiments in the regime where the electrons flow freely along the magnetic field but collisionally across the magnetic field, since this is applicable to high power plasma contactors in low earth orbit, and to compare the measured  $\phi(r, z)$  and collected current to the expressions calculated in Section 4, or to similar expressions found with more realistic models for  $\nu_e$ .

Another interesting feature seen by Urrutia and Stenzel is that the enhanced electron current was not continuous in time but occurred in periodic bursts, as the instabilities periodically grew up, saturated, and decayed. This behavior is probably due to the positive bias instability, which has been widely observed in configurations of this sort<sup>[17]</sup>. It is not known whether similar behavior would occur in the regime of free electron flow along the magnetic field and collisional flow across the magnetic field, appropriate for low earth orbit. Theoretical and experimental studies are needed to answer this question, which could have important implications for power systems based on electrodynamic tethers in space.

## References

- [1] M. Martinez-Sanchez and D. E. Hastings. A systems study of a 100 kW tether. *J. of Astronautical Sciences*, 35:75-98, 1987.
- [2] D. E. Hastings and N. A. Gatsonis. Plasma contactors for use with electrodynamic tethers for power generation. *Acta Astronautica*, 17:827-836, 1988.
- [3] E. P. Szuszczewicz. Technical issues in the conduct of large space platform experiments in plasma physics and geoplasma sciences. In *Space Technology Plasma Issues in 2001*, Jet Propulsion Laboratory 86-49, California Institute of Technology, Pasadena, California, 1986.
- [4] D. E. Hastings and J. Blandino. Bounds on current collection by plasma clouds from the ionosphere. *Journal of Geophysical Research*, 94:2737-2744, 1989.
- [5] D. Parks, M. J. Mandell, and I. Katz. Fluid model of plasma outside a hollow cathode neutralizer. *Journal of Spacecraft and Rockets*, 19:354-357, 1982.
- [6] D. Parks and I. Katz. Theory of plasma contactors for electrodynamic tethered satellite systems. *Journal of Spacecraft and Rockets*, 24:245-249, 1987.
- [7] D. E. Hastings. Theory of plasma contactors used in the ionosphere. *Journal of Spacecraft and Rockets*, 24:250-256, 1987.
- [8] M. Dobrowolny and L. Iess. Model of the interaction of a hollow cathode with the ionosphere. In *Second International Conference on Tethers in Space*, American Institute of Aeronautics and Astronautics, 1988.
- [9] R. Wei and P. Wilbur. Space charge limited current flow in a spherical double sheath. *Journal of Applied Physics*, 60:2280-2284, 1986.
- [10] H. Amemiya. Space charge limited current between coaxial cylinders and concentric spheres. *Scientific Papers of the Institute of Physical and Chemical Research*, 63:1-6, 1969.

- [11] L. W. Parker and B. L. Murphy. Potential buildup of an electron emitting ionospheric satellite. *J. Geophys. Res.*, 72:1631, 1967.
- [12] Lewi Tonks and Irving Langmuir. A general theory of the plasma of an arc. *Physical Review* 34:876, 1929.
- [13] David Bohm. Minimum ion kinetic energy for a stable sheath. In *The Characteristics of Electrical Discharges in Magnetic Fields* (A. Guthrie and R. K. Wakerling, eds.), McGraw-Hill, 1949.
- [14] Ya. L. Al'pert, A. V. Gurevich, and L. P. Pitaevskii. *Space Physics with Artificial Satellites*. Consultants Bureau, 1965.
- [15] J. D. Williams. private communication.
- [16] P. Wilbur and T. Laupa. Plasma contactor design for electrodynamic tether applications. *Advances in Space Research*, 8:221-224, 1988.
- [17] M. A. Raadu and M. B. Silevitch. On the negative resistance of double layers. *J. Plasma Phys.*, 30:249-254, 1983, and references therein.
- [18] K. Y. Kim. Theory of nonmonotonic double layers. *Phys. Fluids*, 30:3686-3694, 1987.
- [19] J. D. Williams and P. J. Wilbur. Plasma contacting- an enabling technology. *27th Aerospace Science Meeting*, January 9-12, 1989, Reno, Nevada, AIAA-89-0677.
- [20] D. E. Hastings and J. Wang. The radiation impedance of a electrodynamic tether with end connectors. *Geophysical Research Letters*, 14:519-522, 1987.
- [21] D. Biskamp and R. Chodura. Computer simulation of anomalous dc resistivity *Phys. Rev. Lett.*, 27:1553-1556, 1971.
- [22] M. Z. Caponi and R. C. Davidson. Influence of ion-resonance broadening on the anomalous heating and momentum transfer in a current-carrying plasma. *Phys. Rev. Lett.*, 31:86, 1973.
- [23] J. A. Wesson and A. Sykes. Theory of ion-sound resistivity. *Phys. Rev. Lett.*, 31:449, 1973.

- [24] P. C. Liiver and N. A. Krall. Self-consistent approach to anomalous resistivity applied to theta pinch experiment. *Phys. Fluids*, 16:1953-1963, 1973.
- [25] R. L. Stenzel and J. M. Urrutia. Laboratory model of a tethered balloon-electron beam current system. *Geophysical Research Letters*, 13:797-800, 1986. J. M. Urrutia and R. L. Stenzel. Anomalous currents to an electrode in a magnetoplasma. *Phys. Rev. Lett.* 57:715, 1986.
- [26] David L. Book. NRL Plasma Formulary. Naval Research Laboratory, 1980.

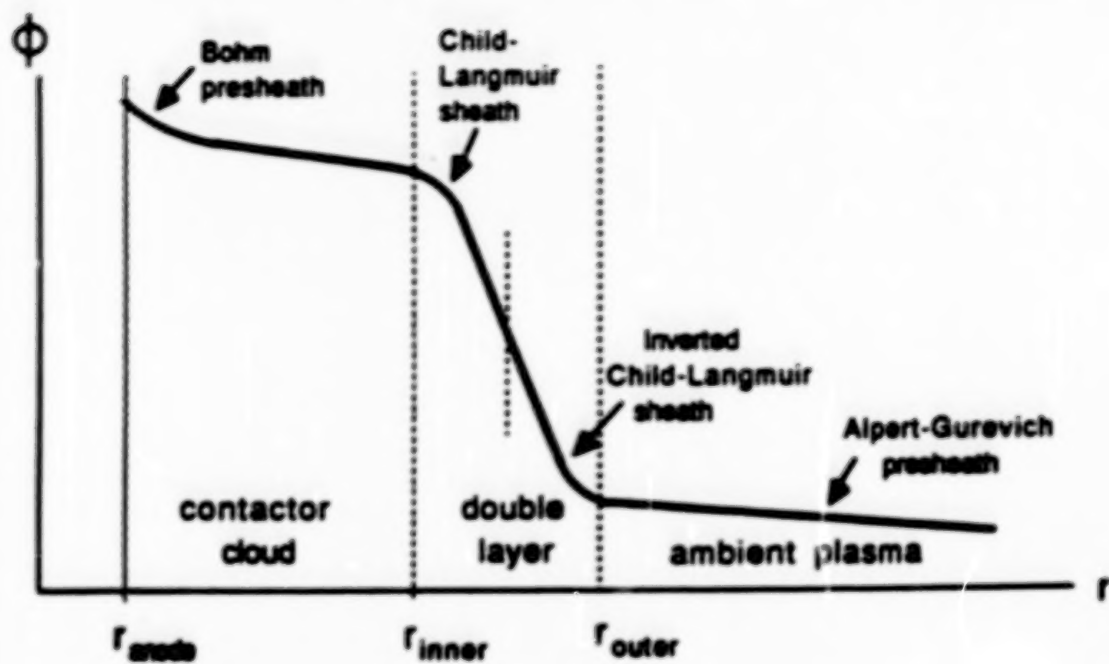


Figure 1 Schematic radial potential profile for collisionless unmagnetized double layer. The Bohm presheath is described in Ref. [12] and [13], and the Alpert-Gurevich presheath in Ref. [14].

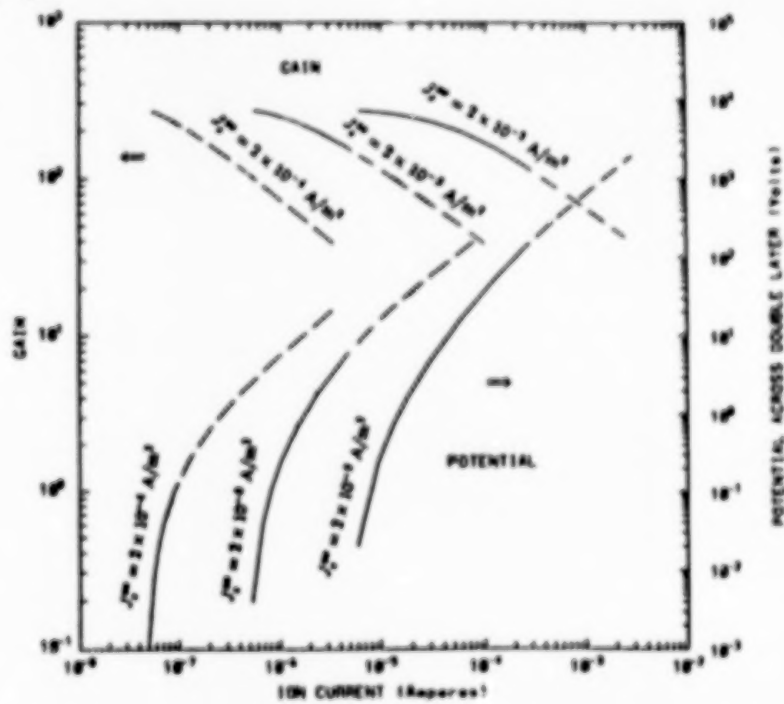


Figure 2 Gain and lower limit on potential drop, as functions of the emitted argon ion current and the electron saturation current, for collisionless double layer with space charge limited current, marginally satisfying the Parker-Murphy condition with a 10 cm anode radius, using Eq. (20) and Eq. (21), and Fig. 5 of Ref. [9].

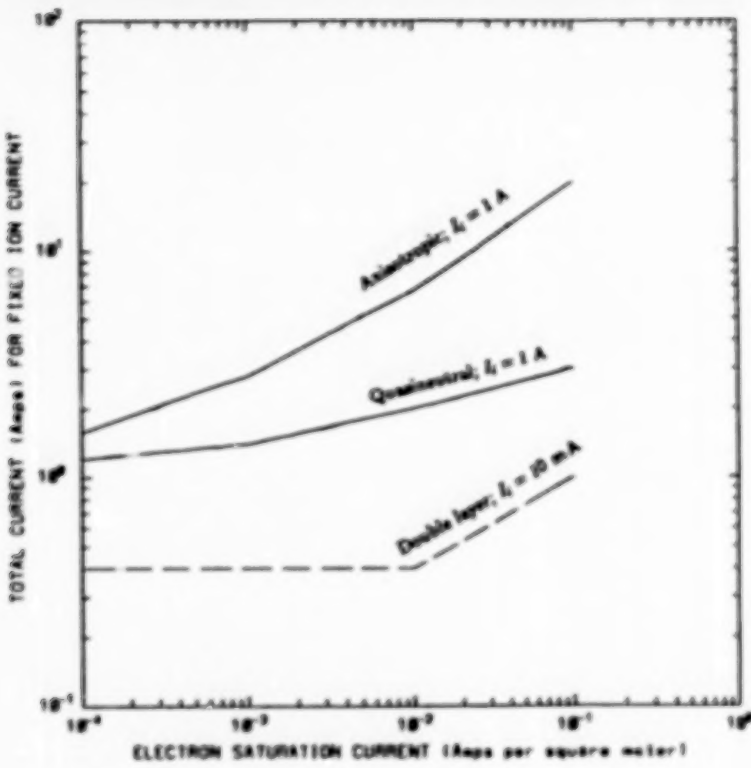


Figure 3 Total collected current vs. electron saturation current with the emitted ion current held constant, for the collisionless double layer model (upper limit), the isotropic quasineutral model<sup>[4]</sup> and the anisotropic contactor model.

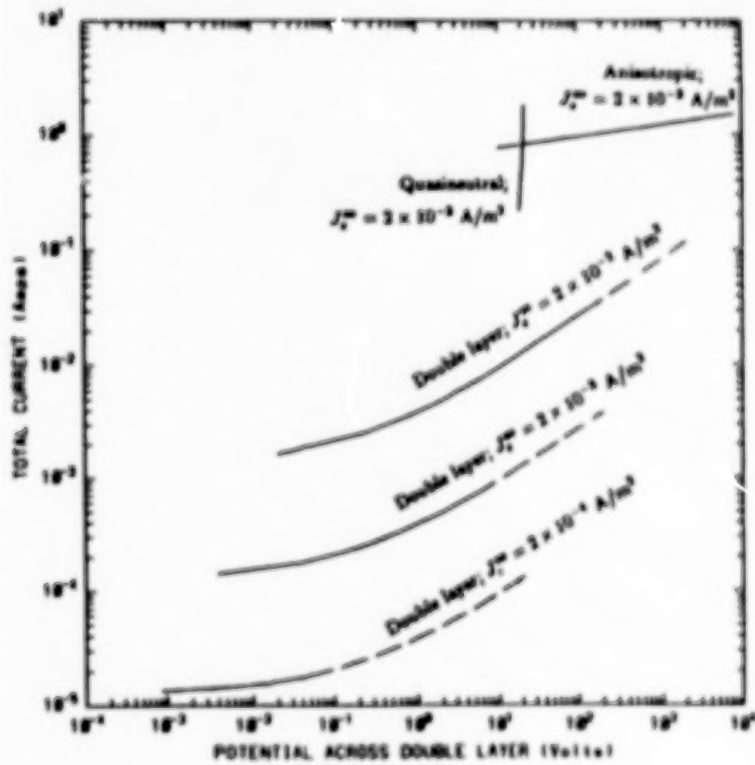


Figure 4 Total current vs. potential drop for the collisionless double layer model, the isotropic quasineutral model<sup>[4]</sup> and the anisotropic contactor model.

### Anisotropic Contactor Model

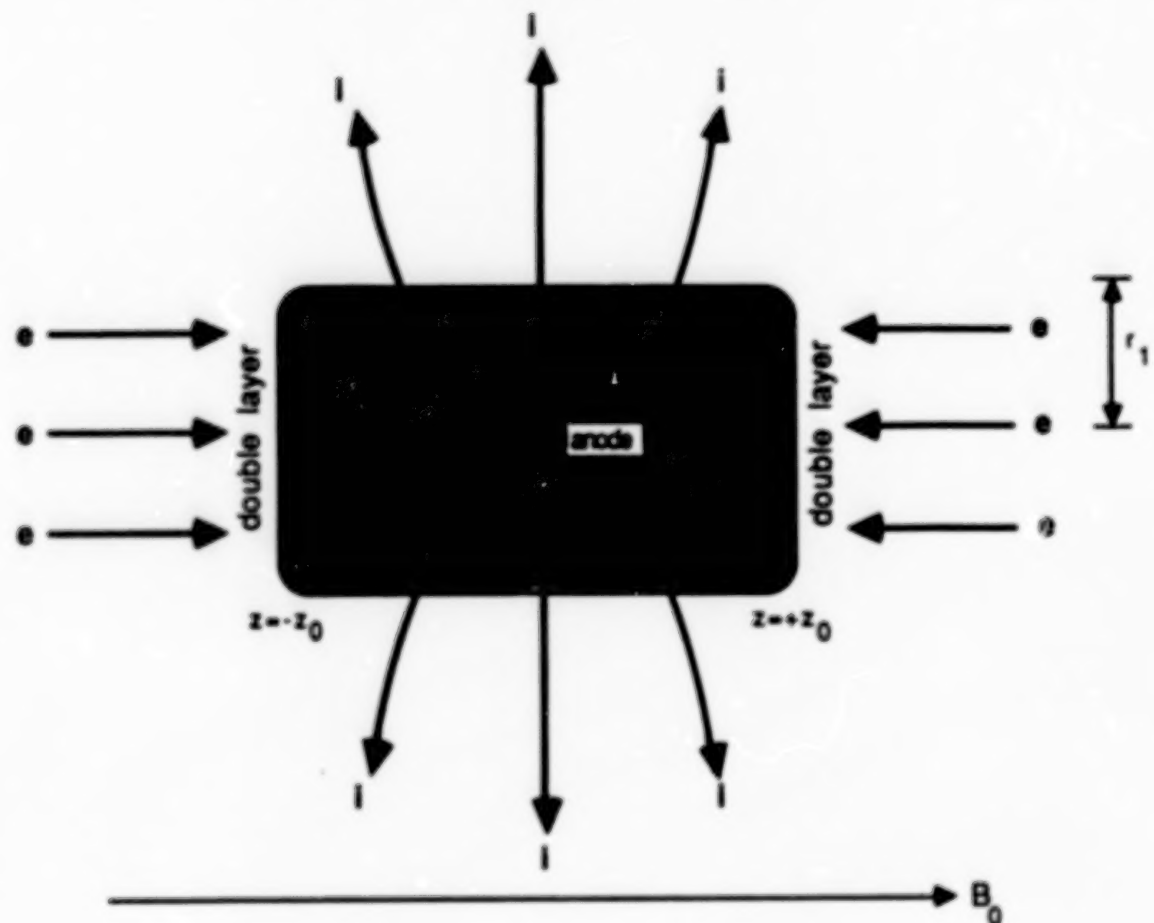


Figure 5 Schematic picture of the anisotropic contactor model, showing equipotential contours and the flow of ions and electrons.

PHYSICAL PROCESSES ASSOCIATED WITH CURRENT COLLECTION  
BY PLASMA CONTACTORS

Ira Katz and V. A. Davis

S-CUBED, A Division of Maxwell Laboratories, Inc.  
P. O. Box 1620, La Jolla, California 92038

**Abstract.** Recent flight data confirms laboratory observations that the release of neutral gas increases plasma sheath currents. Plasma contactors are devices which release a partially ionized gas in order to enhance the current flow between a spacecraft and the space plasma. Ionization of the expellant gas and the formation of a double layer between the anode plasma and the space plasma are the dominant physical processes. A theory is presented of the interaction between the contactor plasma and the background plasma. The conditions for formation of a double layer between the two plasmas are derived. Double layer formation is shown to be a consequence of the nonlinear response of the plasmas to changes in potential. Numerical calculations based upon this model are compared with laboratory measurements of current collection by hollow cathode-based plasma contactors.

#### Introduction

Plasma double layers were first reported by Langmuir in 1929. The boundary between two different plasmas frequently takes the form of a double layer. In the laboratory, ionization near an anode forms a localized, dense plasma. The boundary between this anode plasma and any background plasma is visually sharp. The potential drops rapidly at the boundary. Such a localized potential drop requires layers of both positive and negative charge; hence, the term "double layer." Double layers have also been observed in the auroral zone ionosphere (Block, 1978).

Extensive investigations, both theoretical and experimental, have uncovered many properties of the particle distributions and potential structures in double layers (Block, 1978). Most of the theoretical work has focused on the transition region between two semi-infinite half spaces filled with collisionless, Maxwellian plasmas. While some authors have employed the full particle distribution function to describe the plasma charge density (Schamel and Bujarbarua, 1983), most, starting with Langmuir (1929), recognized that, for unmagnetized plasmas, the essential features of the charge density can be modeled in a much simpler fashion (Andrews and Allen, 1971). The theory presented below uses that equilibrium plasmas shield small potential perturbations linearly, while for high potentials,

the shielding decreases. These features are correctly represented in most descriptions of the plasma charge density. This approach is analogous with Van der Waals' theory of simple fluids in which inclusion of approximate expressions for both excluded volume and long range attractive forces are sufficient to describe the first order liquid-gas phase transition.

While previous studies have concentrated on the planar double layer stability conditions, the theory presented here applies more naturally to the case of one plasma expanding spherically into a uniform background plasma. An anode plasma, which was the first system identified as having a double layer by Langmuir (1929), is an example of a spherically expanding plasma. Anode plasmas have been previously been modeled in terms of a spherical double diode (Wei and Wilbur, 1986). The analysis below includes both electrons and ions from both the anode and background plasmas. The advantage for our analysis of the spherically expanding case is the additional parameter,  $r_{DL}$ , the radius at which the double layer occurs. The theory below identifies under what conditions a double layer will form and the radius at which it will be located. Only at that radius can a double layer exist and satisfy Poisson's equation.

#### Planar Double Layers

The equilibrium state of a collisionless, unmagnetized plasma can be described by the Vlasov equation and Poisson's equation,

$$\nabla^2 \Phi = - \frac{\rho}{\epsilon_0} \quad (1)$$

$$\rho(\mathbf{x}) = e \iiint f_i(\mathbf{x}, \mathbf{v}) d\mathbf{v} - \iiint f_e(\mathbf{x}, \mathbf{v}) d\mathbf{v} ,$$

where  $\Phi$  is the potential,  $\rho$  is the charge density, and  $f_i$ ,  $f_e$  the ion and electron distribution functions. The potential is with respect to the unperturbed plasma at a great distance.

In a neutral plasma at equilibrium, small perturbations in potential give rise to Debye shielding. However, as the potential increases, the attracted species is accelerated and the effective shielding decreases. A variety of approximations to this shielding function have been introduced by various authors. The theory presented below is insensitive to the particular functional form of the charge density with respect to potential. Following Andrews and Allen (1971), the charge density is represented by a function of potential. The particular form chosen here,

$$\frac{\rho(\phi)}{\epsilon_0} = - \frac{\phi}{\lambda_D^2 \left( 1 + \sqrt{4\pi \frac{|\phi|^3}{\theta}} \right)}, \quad (2)$$

has been previously used by the authors to successfully calculate ionospheric currents to high-voltage spacecraft (Katz et al., 1981; Mandell and Katz, 1982; Katz et al., 1989). This charge density function, as shown in Figure 1, is highly nonlinear. In the limit of potentials small with respect to the plasma temperature, this expression reduces to Debye shielding.

$$\frac{\rho(\phi)}{\epsilon_0} \equiv - \frac{\phi}{\lambda_D^2}, \quad \phi \rightarrow 0 \quad (3)$$

For large potentials, the charge density approaches the one-sided thermal flux of the attracted species divided by the particle velocity.

$$\rho(\phi) \equiv - \frac{j_{th}}{v}, \quad \phi \rightarrow \infty \quad (4)$$

For two plasmas of equal temperatures and densities, but with reference potentials  $\Delta\phi/2$  and  $-\Delta\phi/2$ , the combined charge density is

$$\rho(\phi) = - \frac{(\phi + \Delta\phi/2)}{1 + \sqrt{4\pi |\phi + \Delta\phi/2|^3}} - \frac{(\phi - \Delta\phi/2)}{1 + \sqrt{4\pi |\phi - \Delta\phi/2|^3}} \quad (5)$$

where  $\lambda_D$ ,  $\theta$  and  $\epsilon_0$  are taken to be unity. Figure 2 shows Equation (5) graphed for four values of  $\Delta\phi$ , the difference between the reference potentials. For small  $\Delta\phi$ , the charge density has only one zero. The bulk of the plasma will have potential  $\phi=0$ ; the potential differences are dropped across sheaths at the boundaries. As  $\Delta\phi$  increases, the slope of the charge density at  $\phi=0$  goes through zero, and two other roots appear. When all three roots are present, the central root is not stable; it corresponds to negative shielding of potential fluctuations. In the limit of very large  $\Delta\phi$ , the two stable roots approach the two reference potentials.

Integrating Poisson's equation using Equation (5) with large  $\Delta\phi$  leads to a double layer as shown in Figure 3. The plasma is quasi-neutral,

$$\nabla^2 \phi = -\rho \equiv 0 , \quad (6)$$

everywhere but within the double layer. Plasmas whose Debye lengths are small compared with the scale size for potential changes are typically described assuming quasi-neutrality. Quasi-neutrality implies that the potential everywhere is at or near a root of the charge equation. However, regardless of the Debye length, for the boundary potentials in Figure 3 there exists no solution that is quasi-neutral everywhere. A region of large charge density must exist to support the transition between the potentials corresponding to the two roots of Equation (5).

The bifurcation of the charge equation occurs at the critical value of the separation of potentials,

$$\Delta\phi_{\text{critical}} \approx 1.430 ,$$

below which a double layer does not exist. The critical value of potential is numerically just the separation between the minimum and maximum in the charge density expression, Equation (2), since the expression has odd symmetry around the origin. Thus any similar expression for charge density will result in about the same critical value of the potential separation. The stable roots of the charge equation showing the bifurcation are graphed in Figure 4. Andrews and Allen (1971) previously described planar double layers in terms of the integration of Poisson's equation from one stable root to the other stable root. What has been introduced here is a critical value below which there is only a single root, and above which there are multiple roots and, therefore, double layers.

#### Source Plasma Expansion Into A Background Plasma

Early laboratory observations of double layers were of those that form the boundary of the glowing hemisphere of intense ionization surrounding an anode. Most analyses assumed planar geometry for simplicity. In this section, it is shown how examining the roots of the charge density expression for a spherically expanding plasma and a uniform background plasma can be used to calculate the radius of the double layer. The introduction of the radial dependence,  $r$ , in the charge density expression leads to a unique solution for the double layer radius.

A source at radius,  $r_s$ , is assumed to generate an ion current,  $I_i$ , which falls through a potential,  $\phi_s$ , as it leaves the anode region. Near the anode, the ions are neutralized by Maxwellian electrons. The ambient

plasma,  $\rho_a(\phi)$ , is represented by Equation (2).

$$\rho(r, \phi) = \rho_s^i(r, \phi) + \rho_s^e(\phi) + \rho_a(\phi) \quad (7)$$

$$\rho_s^i(r, \phi) = \frac{I_i}{4\pi r^2 v_i} = \frac{I_i}{4\pi r^2 \sqrt{\frac{2E_0}{m_i} + \frac{2e(\phi_s - \phi)}{m_i}}} \quad (8)$$

$$\rho_s^e(\phi) = \frac{e^{(\phi - \phi_s)} - e^{-\phi_s}}{1 - e^{-\phi_s}} \times (-\rho_s^i(r_s, \phi_s) - \rho_a(\phi_s)) \quad (9)$$

These particular analytical expressions reflect the spherical expansion of the ions and that the effect of the source plasma vanishes at very large radius. The ions have initial energy  $E_0$ , and mass  $m_i$ . The expression for the source electrons is chosen so that the net charge density vanishes at the source potential at the source radius and also vanishes at zero potential at infinite radius.

The dependence of the charge density on potential for three different radii is shown in Figure 5. The parameters chosen are

$$\begin{aligned} r_s &= 1, \\ \phi_s &= 20, \\ \rho_s^i(r_s, \phi_s) &= 100, \\ \frac{2E_0}{m_i} &= 5. \end{aligned}$$

At small radii, the source plasma dominates and the charge density equation has a single root at a potential very close to the source potential. Far from the source, the background plasma dominates and the charge density equation has a single root very close to the background plasma reference potential. For a limited range of radii, the charge density equation has three roots. The high potential root is associated with the source plasma; the low potential root is associated with the background plasma. The middle root corresponds to negative shielding and is thus physically unstable. Figure 6 shows the roots as a function of the radius. The two physically realizable branches never intersect. Within the transition between the two branches, the plasma must be nonneutral. The thickness of the nonneutral region can easily be estimated from spherical diode theory (Wei and Wilbur, 1986). For plasmas in which the density changes on a scale-length long compared with the Debye length, the nonneutral region will be short compared with the scale length of the density changes. Since the electric fields in the quasi-neutral region are

small, the nonneutral region will contain an equal amount of positive and negative charge,

$$\int_{r_1}^{r_2} \rho(r) 4\pi r^2 dr \equiv 0 , \quad (10)$$

where  $r_1$  and  $r_2$  are the radial boundaries of the double layer. Rigorously, a determination of the location of the double layer requires solving Poisson's equation from the first root,  $\phi_1$ , to the second root,  $\phi_2$ . An approximate location can be obtained by neglecting the spherical terms in the divergence. Using that the magnitude of the electric field is small in the quasi-neutral regions, Poisson's equation can be multiplied by the electric field and integrated by parts to obtain

$$\int_{\phi_1}^{\phi_2} \rho(r_{DL}, \phi) d\phi = 0 . \quad (11)$$

Equation (11) locates the double layer at the radius,  $r_{DL}$ , where the charge density curve has equal areas of positive and negative charge between the two physical roots. This approximate integration of Poisson's equation was previously presented by Andrews and Allen (1971) as a constraint on the charge density in planar double layers. Here, it is used to locate the double layer.

As seen in the planar case, the multiple roots and the double layer exist only for a potential difference greater than a critical value. When the source potential is less than the critical value, the charge density equation has only a single root, and therefore a quasi-neutral solution exists for all radii. For this case, as shown in Figure 7, there is no double layer.

Numerically, the approximate radius found from Equation (11) is typically within a few percent of that found by solving Poisson's equation. That this potential construct corresponds to the physical double layer is illustrated by Figure 8. The solid curve is calculated by solving Poisson's equation using the charge density given by Equation (7) with additional ionization of the background gas, the circles are laboratory measurements of the potential of an anode plasma double layer by Wilbur and Williams (private communication).

### Conclusions

Inclusion of the most basic nonlinear features in the charge density expression leads to a description of plasma

double layers in terms of roots of that expression. The theory is similar to Van der Waals' description of a fluid, with the double layer corresponding to the liquid-gas phase transition. The theory locates the double layer in agreement with observation.

Much of the analysis presented depends on heuristic expressions for the plasma charge density. They are the weakest part of the arguments presented. The forms are, with the exception of the source ions, similar to those normally used for modeling plasmas in planar geometry. They are clearly restricted to double layers whose thickness is small compared with their radius of curvature. The use of semi-infinite half-plane formulations makes sense if the scattering lengths, whether through collisions or turbulence, are large compared with the double layer thickness and small compared with the system dimensions. Further research is required to develop a more rigorous theory. In particular, extension to a magneto plasma is required to understand ionospheric double layers.

Acknowledgements. The authors have benefitted from discussions with Dr. Paul Wilbur and Mr. John Williams of Colorado State University and with several of their colleagues at S-CUBED, including Dr. Gary Jongeward, Dr. Donald Parks, and Dr. Eduardo Waisman.

This work was funded by NASA/Lewis Research Center under contract NAS3-23881.

#### References

- Andrews, J. G. and J. E. Allen, Proc. Roy. Soc. Lond., **A 320**, 459, 1971.  
Block, L. P., Astrophys. Space Sci., **55**, 59, 1978.  
For a review of double layers, see Ref. 2.  
Katz, I., M. J. Mandell, G. W. Schnuelle, D. E. Parks, and P. Steen, J. Spacecraft, **18**, 79, 1981.  
Katz, I., G. A. Jongeward, V. A. Davis, M. J. Mandell, R. A. Kuharski, J. R. Lilley, Jr., W. J. Raitt, D. L. Cooke, R. B. Torbert, G. Larson, and D. Rau, J. Geophys. Res., **94**, 1450, 1989.  
Langmuir, I., Phys. Rev., **33**, 954, 1929.  
Mandell, M. J. and I. Katz, IEEE Trans. Nucl. Sci., **NS-30**, 4307, 1983.  
Schamel, H. and S. Bujarbarua, Phys. Fluids, **26** (1), 190, 1983.  
Wei, R. and P. J. Wilbur, J. Appl. Phys., **60**, 2280, 1986.  
Wilbur, P. J. and J. D. Williams (private communication).

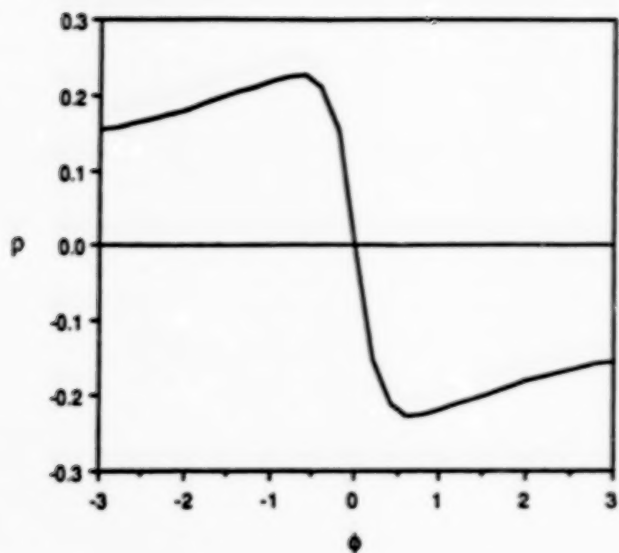


Figure 1. Charge density as a function of potential from Equation (2).

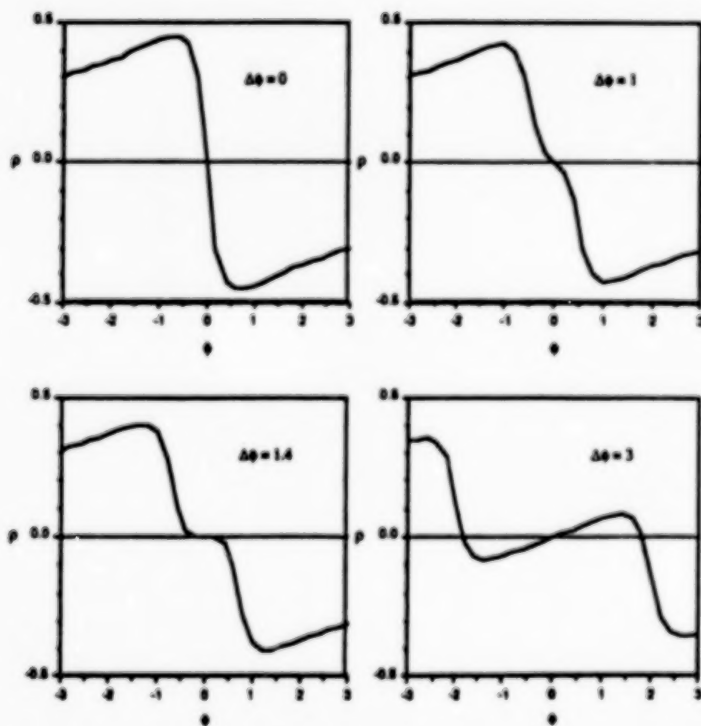
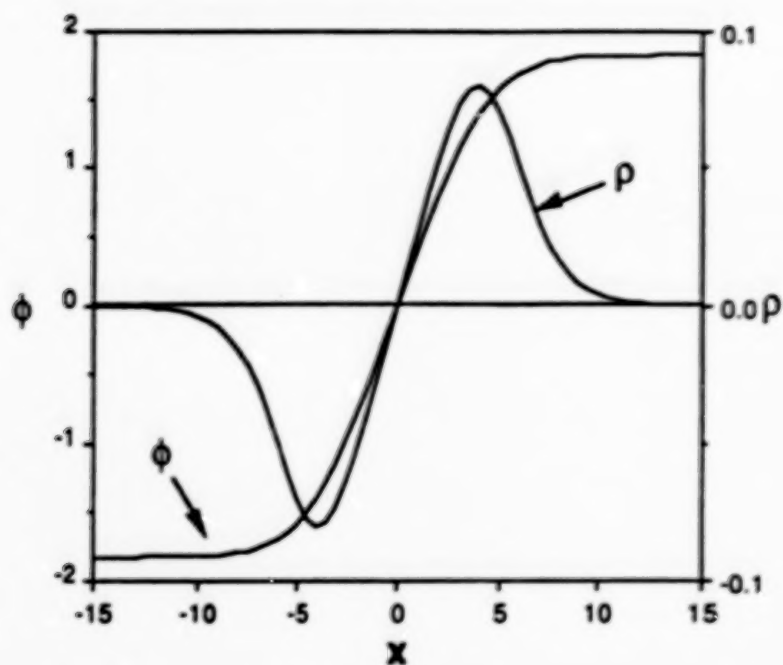
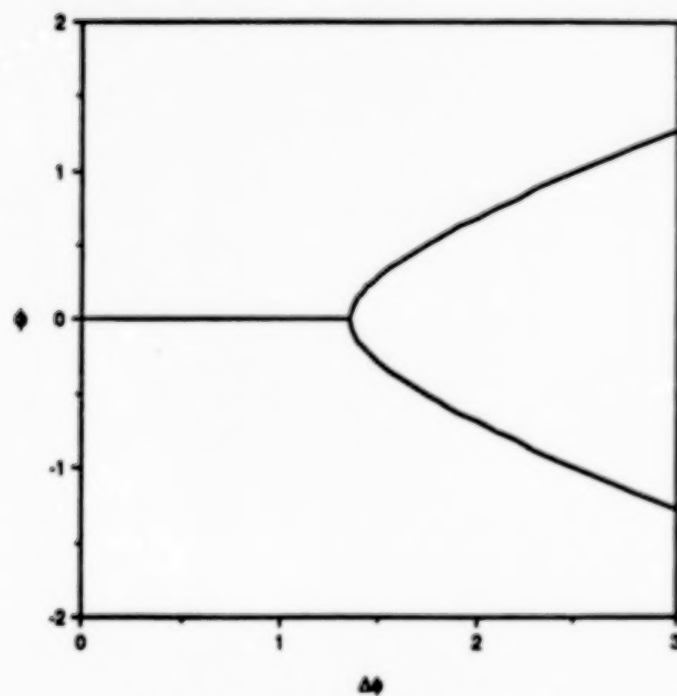


Figure 2. The charge density a function of potential for various differences in the reference potential. The curve for  $\Delta\phi = 0$  is just twice that in Figure 1.



**Figure 3.** Solution of Poisson's equation with the charge density specified by Equation (5) for  $\Delta\phi = 4$ . The charge density as a function of position is also graphed and shows the expected double layer structure.



**Figure 4.** The roots of the charge density expression, Equation (5), plotted as a function of the difference in reference potentials,  $\Delta\phi$ .

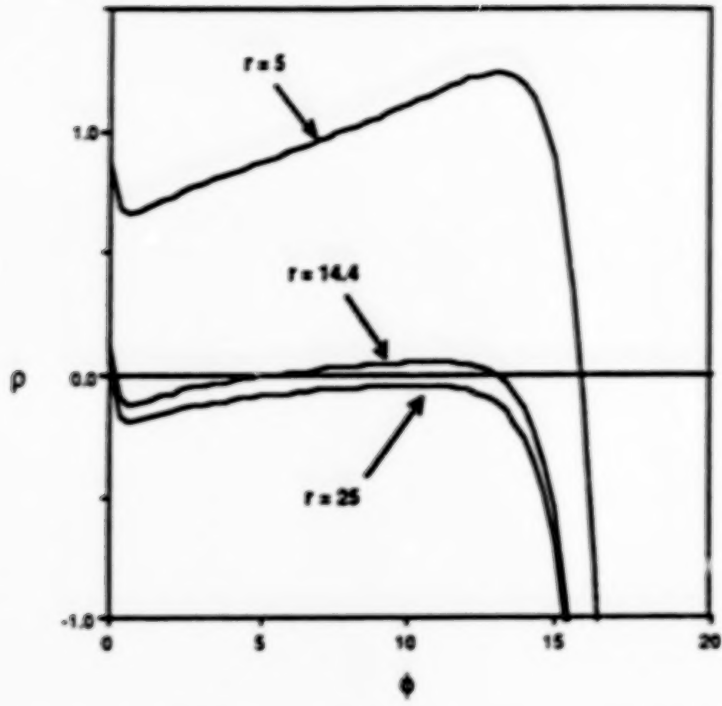


Figure 5. Charge density as function of potential for three radii. The density has a single root for  $r = 5$  and  $r = 25$ , and has three roots for  $r = 14.4$

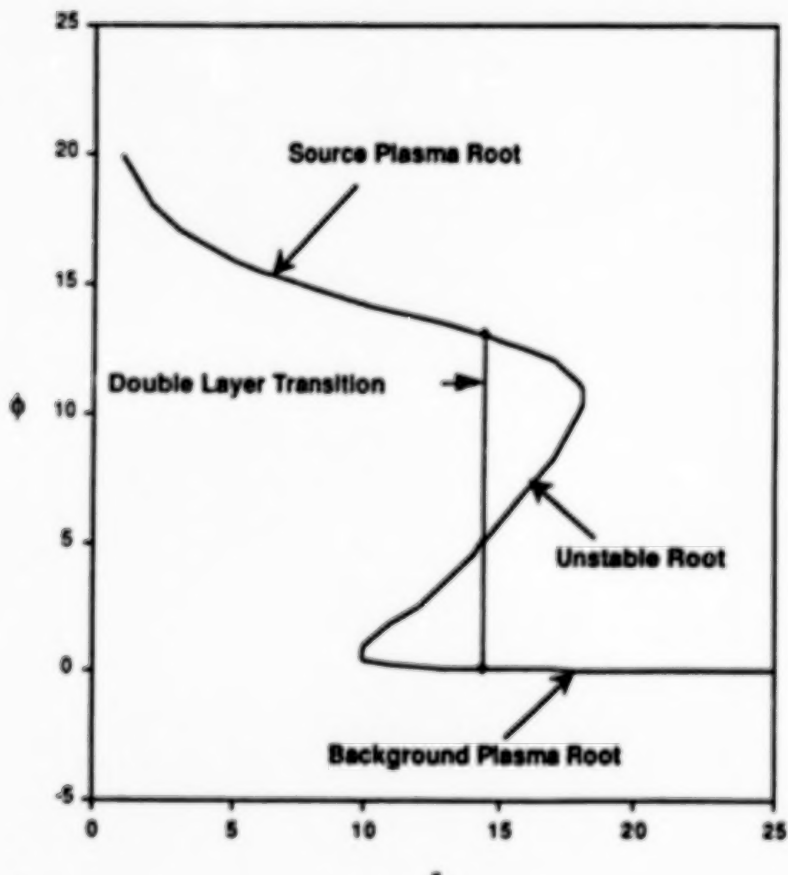


Figure 6. Roots of the charge equation for the spherical expansion of one plasma into a uniform background plasma. The double layer transition is located using Equation (11).

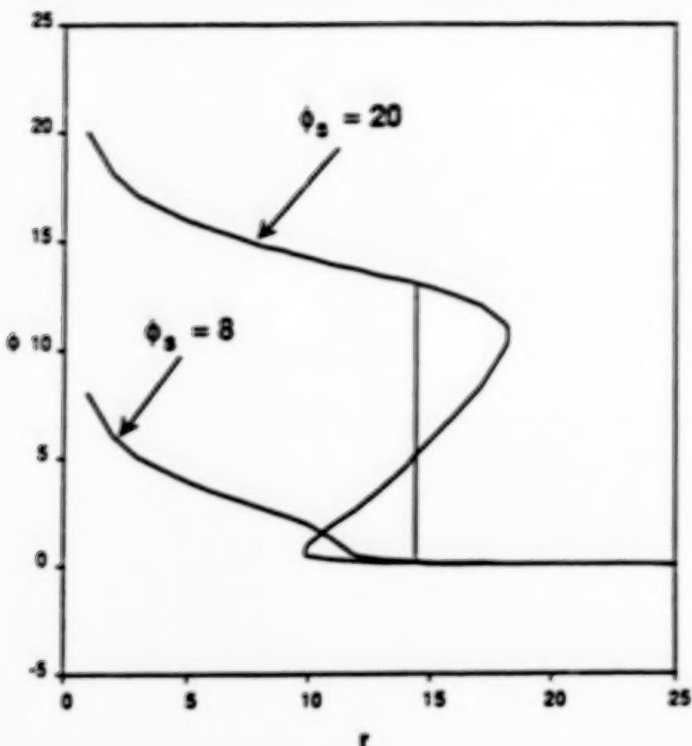


Figure 7. Roots of the charge equation for two different cases of the spherical expansion of a plasma into a uniform background plasma. The upper curve is the same as Figure 6,  $\phi_{\text{source}} = 20$ , and has a double layer. The lower curve is for  $\phi_{\text{source}} = 8$  and doesn't have a double layer transition.

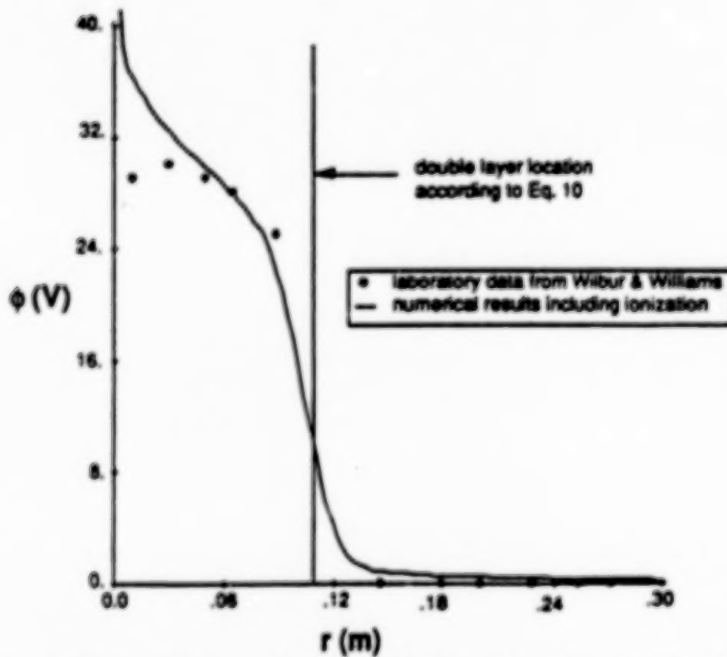


Figure 8. Comparison of numerical results with data for a hollow cathode plasma contactor operating as an electron collector. The location of the double layer according to Equation (11) is seen to agree with both the observation and the numerical, self-consistent solution of Poisson's equation including ionization of the neutral gas.

## Double Layers in Contactor Plasmas

David L. Cooke  
Air Force Geophysics Laboratory  
Hanscom AFB MA, 01731

The concept of using a hollow cathode to establish a low impedance contact between a spacecraft and the ambient plasma continues to gain in popularity, and is often then referred to as a plasma contactor. A growing number of studies indicate that large contact currents can be supported with small potential difference between the contactor and the ambient plasma. Results will be presented from a simple one-dimensional spherical model that obtains potentials from the solution of Poisson's equation, and particle densities from a turning point formalism that includes particle angular momentum. The neglect of collisions and magnetic field limits the realism, however the results illustrate the effect of double layers that can form at the interface between contactor and ambient plasmas, when there is any voltage differential between the contactor and the ambient. The I-V characteristic of this model shows the usual space charge depend collection when the contactor flux is lower than some threshold; independence of I from variation in V when the flux is slightly greater than that threshold, and (numerical ?) instability for excessive flux suggesting the possibility of "negative resistance". Even if a real I-V characteristic does not exhibit negative resistance, flat spots or high resistance regions, may still be troublesome (or useful) to the total circuit.

# **Current Collection by High Voltage Anodes in near Ionospheric Conditions**

**J. A. Antoniades, R. G. Greaves, D. A. Boyd and R. Ellis**

**University of Maryland**

**College Park, MD.**

## **Introduction**

In the absence of neutral gas breakdown in the vicinity of an orbital or suborbital vehicle the spacecraft charging potential of the vehicle is primarily determined by the current collection from the ambient plasma as well as the energetic particle flux incident on it. In the presence of a low pressure neutral background and a weak magnetic field the current collection behavior can be strongly modified due to electrical discharges in the vicinity of a high voltage electrode. These discharges usually produce large amounts of plasma in the surrounding region of the electrode, which overwhelms the ambient plasma environment resulting in highly modified current collection and large scale high current glow discharges. In situations where the system size is larger than the local Parker-Murphy radius, [1] the neutral pressure required for the breakdown is usually far below the pressure at the Paschen minimum.

For positively charged conductors the main cause for the discharges is electron trapping in magnetic bottles formed in the vicinity of the anode by the combination of the anode's electric field and the ambient axial magnetic field. The magnetic bottle boundaries have been discussed in the work of Rubinstein and Laframboise. [2] The existence of these bottles has been verified experimentally by Greaves et al. [3] Trapping of electrons can lead to the initiation of ionization cascades resulting in breakdown. The breakdown criteria for this type of discharge have been treated analytically in a theory by Kunhardt et al. [4]

We have experimentally identified three distinct regimes with large differences in current collection in the presence of neutrals and weak magnetic fields. In magnetic field/anode voltage space the three regions are separated by very sharp transition boundaries. We performed a series of laboratory experiments to study the dependence of the region boundaries on several parameters, such as the ambient neutral density, plasma density, magnetic field strength, applied anode voltage, voltage pulselwidth, chamber material, chamber size and anode radius.

The three observed regimes are:

- Classical magnetic field limited collection
- Stable medium current toroidal discharge
- Large scale, high current space glow discharge

There is as much as several orders of magnitude of difference in the amount of collected current upon any boundary crossing, particularly if one enters the space glow regime. We measured some of the properties of the plasma generated by the breakdown that is present in regimes II and III in the

vicinity of the anode including the sheath modified electrostatic potential, I-V characteristics at high voltage as well as the local plasma density.

## Experiments and Diagnostics

The low neutral pressure discharges were initially observed during the Space Power Experiments Aboard Rockets (SPEAR I) vacuum chamber tests at the University of Maryland and NASA Plum Brook station by Antoniades et al.[5, 7, 9] They were then reproduced and studied in more detail at the University of Maryland SPIE chamber by Alport et al. [6]

Figure 1 shows a schematic diagram of the Maryland SPIE chamber where the majority of the experiments were conducted. SPIE is a cylindrical vacuum chamber 1.8 m diameter, 5 m long constructed entirely of non-magnetic stainless steel. The chamber can be evacuated to  $5 \times 10^{-7}$  Torr with a combination of a turbomolecular and a cryogenic pump. A multi-dipole plasma source is capable of filling the chamber with cold plasmas of varying ion species, but mainly with argon and nitrogen. The plasma density in the main chamber can be varied between  $10^8 - 10^{13} \text{ m}^{-3}$ . Typical plasma electron temperatures are in the range of 1 - 3 eV.

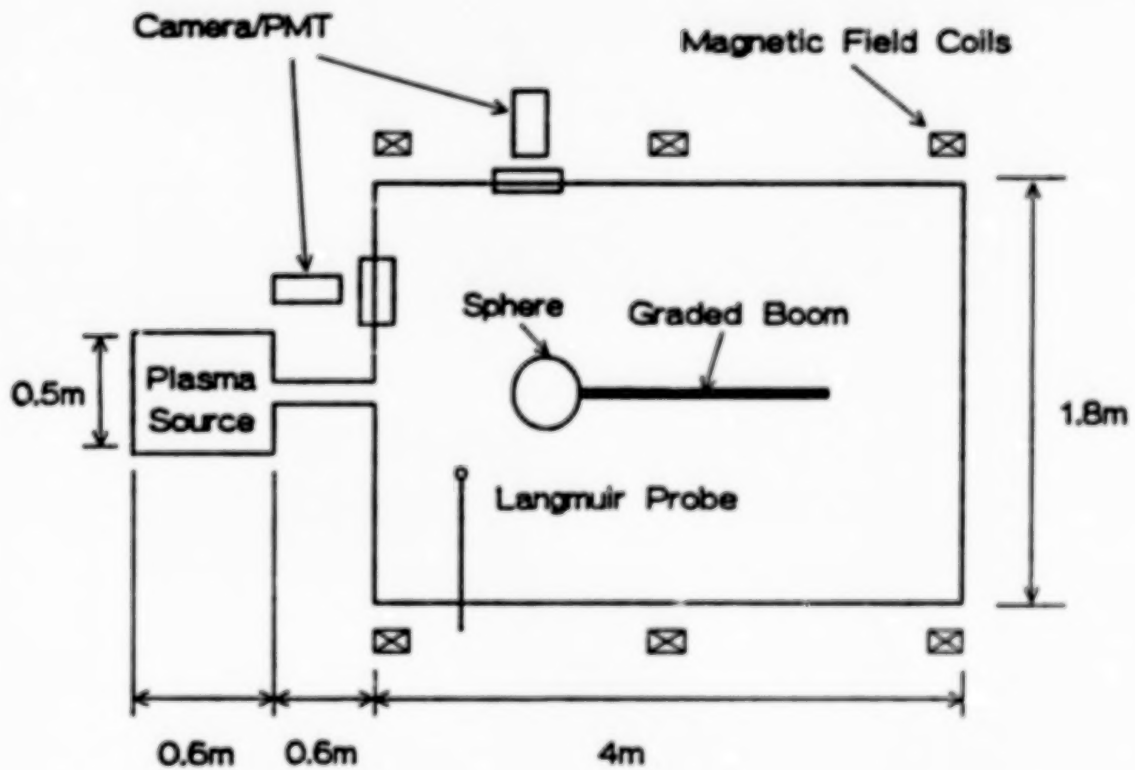


Figure 1 : Schematic diagram of the SPIE chamber (Only the axial magnetic field coils are shown).

Two sets of magnetic field coils surround the chamber. One set can apply transverse magnetic fields but is primarily used to cancel the earth's

magnetic field inside the chamber while the other allows the application of an axial magnetic field in the range of .1-36 Gauss. The anodes consisted of several high voltage spheres ranging in radius from 1 - 10 cm.

The NASA Plum Brook B-2 chamber is a 13 m diameter 20 m long cylindrical vacuum chamber. The chamber can be pumped to  $1 \times 10^{-6}$  Torr with 12, 36" diffusion pumps. It was also filled with plasma to densities comparable to the peak plasma density in the LEO environment (up to  $5 \times 10^6$   $\text{cm}^{-3}$ ). Only one sphere was present for the mockup tests instead of the two spheres that were actually flown in the SPEAR I Mission.[7] A capacitive discharge system was used to apply the high voltage pulses to the sphere. When a low impedance glow discharge was initiated the pulse RC decay time was 4 msec with a maximum output current ~ 11 Amps. When no discharge was present the pulse decay time was 1 sec. Figure 2 shows a schematic diagram of the capacitive discharge pulse circuit.

Several diagnostics were utilized during the experiments. Single electric probes with an assortment of tips were used to measure the electron density and temperature. Hot filament emissive probes were used to

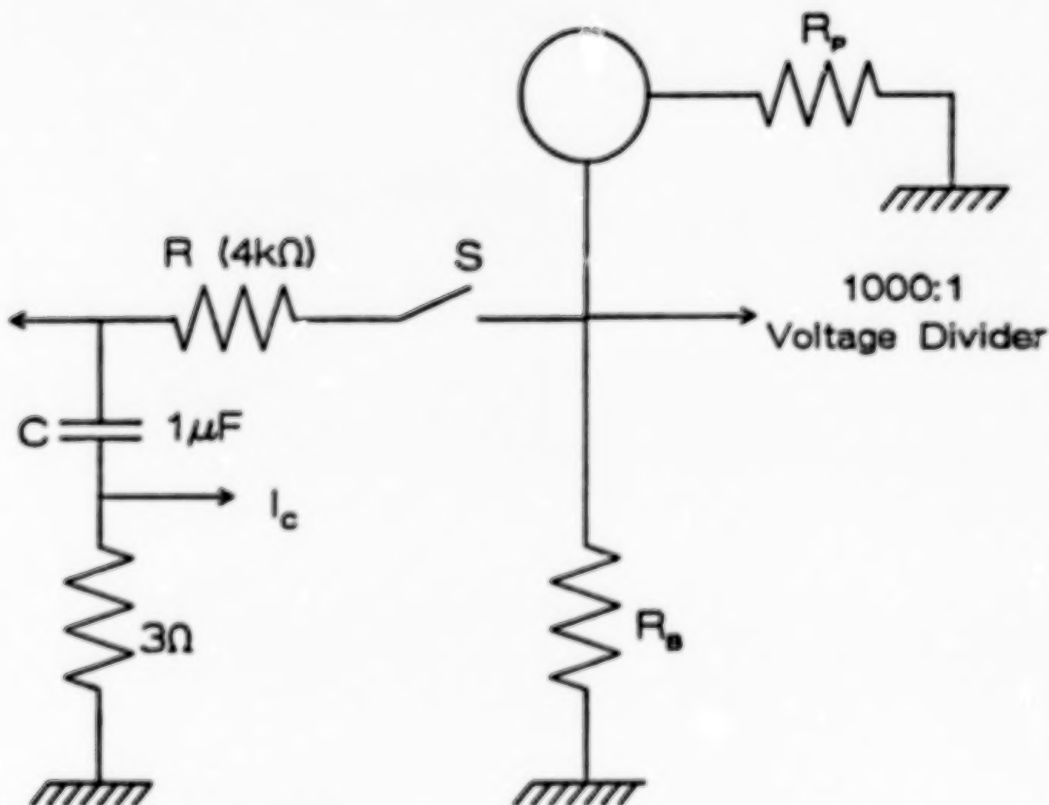


*Figure 2. Schematic diagram of the capacitive discharge circuit for the current collection experiments. When the plasma impedance  $R_p$  is large (no breakdown) the RC decay time constant is 1 sec, but when breakdown occurs the RC time drops to 4 msec.*

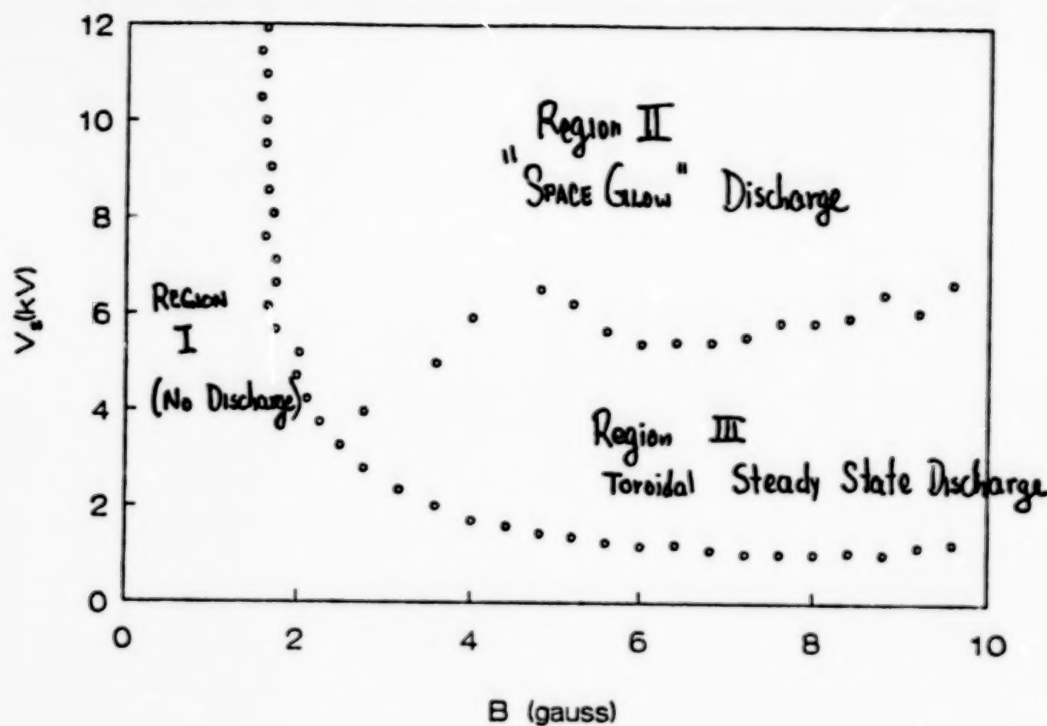
measure the plasma potential inside the discharge itself. The time-dependent evolution of the wavelength-integrated visible light emission from the discharge was measured with cooled photomultiplier tubes. An ion energy analyzer measured the ion spectra for the ballistic ions ejected from the discharge. A set of isolated metallic plates near the outside wall was used to measure the time-resolved wall current distribution during all phases of the discharge. Video and photographic equipment, 35 mm and a video cameras were used to photograph the discharges. The main power system was monitored by a resistive voltage divider measuring the applied voltage and a two current shunts to measure the current collected by the sphere and the specially shielded graded support boom.

## Results

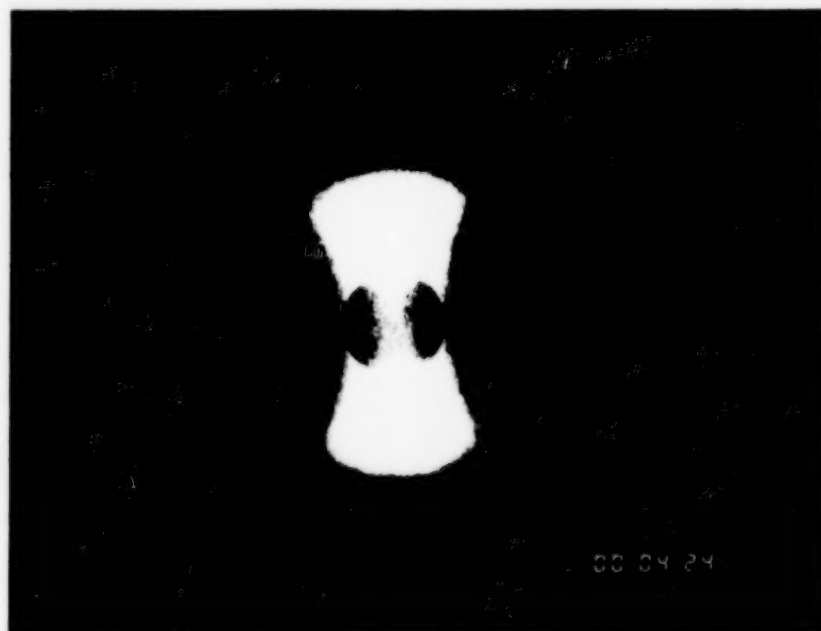
Figure 3 shows a typical breakdown region diagram in Anode Voltage/Magnetic field space. Region I differs from the other two in that there is no self-sustaining discharge in the anode vicinity. Regions II and III are distinctly different because the system collection characteristics are dominated by the plasma resulting from breakdown of the ambient neutral gas. Region II is the "Space Glow" regime where very large currents were drawn by the anode limited seemingly by the current capability of our pulse discharge system. Region III is the "Torus" regime where the anode is surrounded by a steady state toroidal discharge as shown in figure 4. The current drawn by the anode in region III lies between the currents in regions I and II. The location of the boundaries separating the discharge regions is a function of the ambient neutral pressure, electron trapping efficiency, anode size and ambient plasma density. The region boundaries represent very sharp transitions in collected current and optical emission in the vicinity of the anode. They are also very sharply dependent on magnetic field, so that B field changes of < 0.1 Gauss can result in a boundary crossing.

Figure 5 shows a typical set of time resolved diagnostic traces for a space glow formation. The top trace shows the visible light intensity, the center trace shows the current collected by the anode and the bottom trace shows the anode voltage. The light emission from the cascade initiation in the vicinity of the anode starts several hundred microseconds before any noticeable effects are observed in the anode current or voltage. The light intensity initially rises exponentially but when the cascades develop further it rises faster than a simple exponential. The drop in the anode voltage and the apparent current saturation in this figure are due to a current limiting series resistor in the driving circuit to prevent catastrophic arcs from occurring.

Figure 6 shows the dependence of the discharge formation time when the axial magnetic field is varied. The background neutral pressure is  $2 \times 10^{-5}$  Torr. This figure demonstrates the sharpness of the dependence of the breakdown threshold on magnetic field since it shows that a field change of 0.05 Gauss can reduce the time for discharge initiation from practically infinity to less than 1 msec.



*Figure 3. Discharge region diagram in Magnetic field vs Anode voltage space for neutral pressure is  $2 \times 10^{-5}$  Torr and no ambient plasma injection.*



*Figure 4. Photograph of the plasma filled torus that is generated by the trapped electrons.*

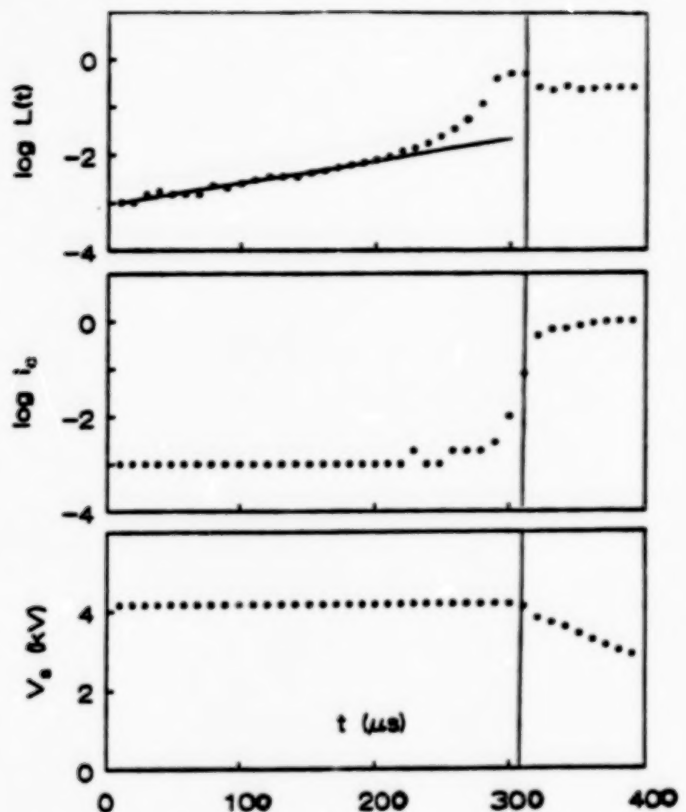


*Figure 5. Waveforms for the wavelength-integrated optical light emission, anode current and anode voltage. The low level light emission starts well before any detectable effects are observed in the other diagnostics.*

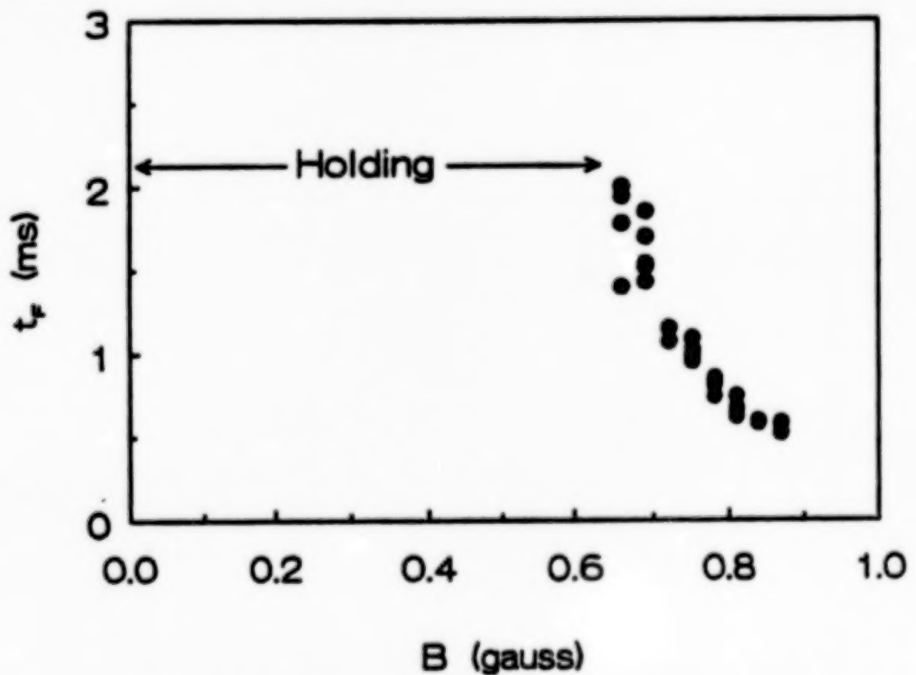


*Figure 6. Discharge formation time vs axial magnetic field. For magnetic fields below the critical value no self-sustaining discharge is formed even when a DC high voltage is applied to the anode.*

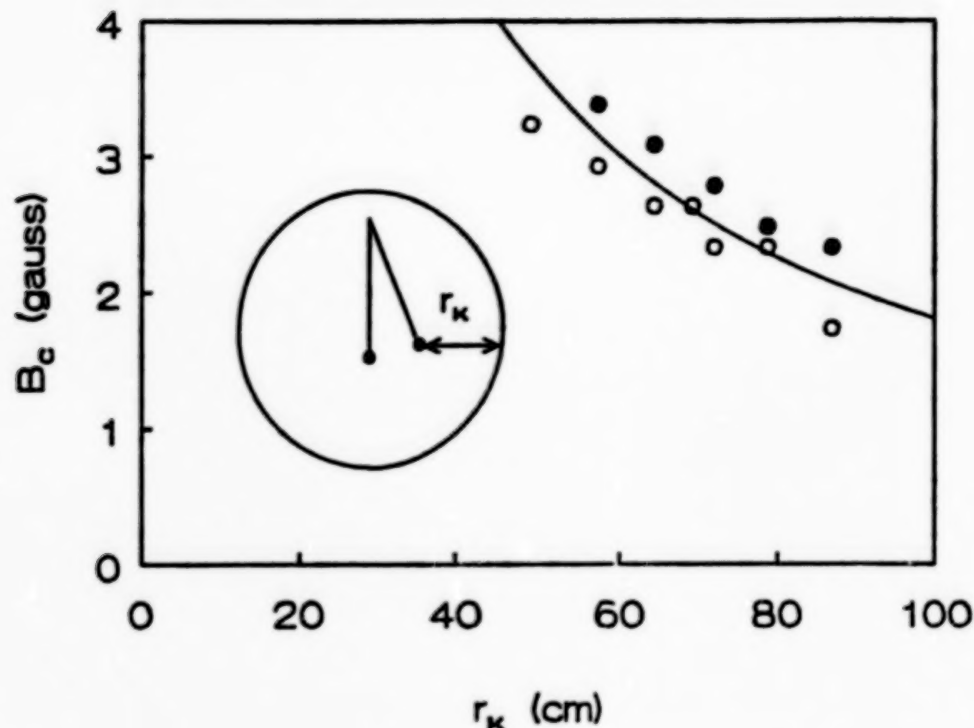


Figure 7. The critical magnetic field for discharge initiation is shown as a function of the chamber size. The neutral pressure is  $2 \times 10^{-5}$  Torr.

When an ambient plasma is introduced into the chamber the discharge formation time decreases sharply with increasing plasma density. In addition the magnetic field threshold for a discharge to occur is also reduced compared to the case without an ambient plasma.

The proximity of the walls plays a major role in the breakdown initiation and discharge gain. Figure 7 shows the critical magnetic field, that is the value of magnetic field below which no breakdown is observed, as a function of the anode to cathode radius. In these experiments this is accomplished by swinging the anode closer to the chamber wall. The critical field increases with decreasing radius, which is consistent with the trapping picture since higher magnetic fields are required to reduce the size of the magnetic bottles to fit into the smaller chamber.

Figure 8 shows the axial dependence of the currents perpendicular to the magnetic field in a region III discharge. The vertical axis represents the ratio of the current at an some axial position divided by the current at  $z=0$ , which is in the midplane of the anode and perpendicular to the magnetic field. The two curves in the figure correspond to magnetic field values of 5 Gauss and 15 Gauss. As the magnetic field increases the wall current distribution becomes more strongly peaked at the midplane. The optical and probe measurements indicate that the torus plasma density is peaked at the midplane and since the ions are unmagnetized, they are ejected radially

outwards resulting at a higher ion flux and secondary electron flux at the wall at the midplane and thus a peaked wall current profile.

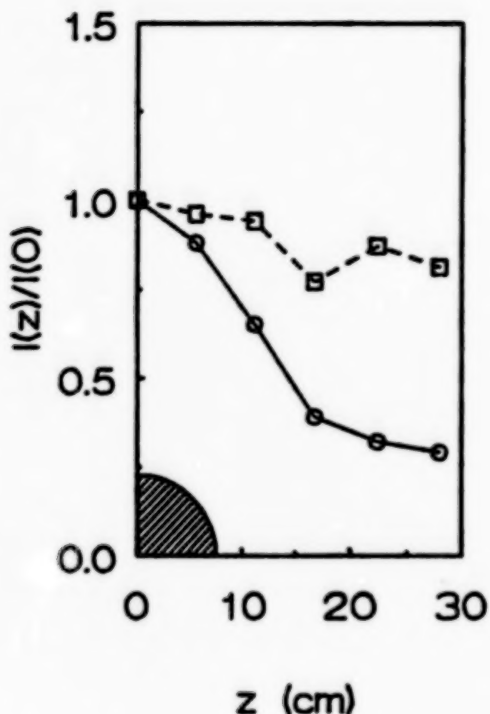


Figure 8. Wall current distribution for 5 and 15 Gauss applied axial magnetic field. The wall current is the sum of the incident ion current and the secondary electron current.

The shape of the potential sheath around the anode during a steady state torus regime discharge was measured using an emissive electric probe. The potential vs radius for 5 and 15 Gauss axial field shown in figure 9. It is important to notice that the sheath radius decreases with increasing magnetic field and a large flat potential region separates the sheath from the chamber wall. It is also apparent that there are small local potential wells near the edges of the sheath signaling the possible existence of thin double layers.

Figures 10 and 11 show the collected current dependence on pressure and anode voltage for discharges in the torus regime. For pressures below  $1 \times 10^{-5}$  Torr the collected current is directly proportional to the ambient neutral pressure, but as the pressure increases the dependence becomes exponential and eventually the current increases dramatically when the pressure increases to initiate a space glow discharge. The current-voltage characteristics are much more complicated with the slope of the I-V curve

changing significantly as a function of voltage even exhibiting hysteresis and negative resistance regions especially when a background plasma is present.[8]

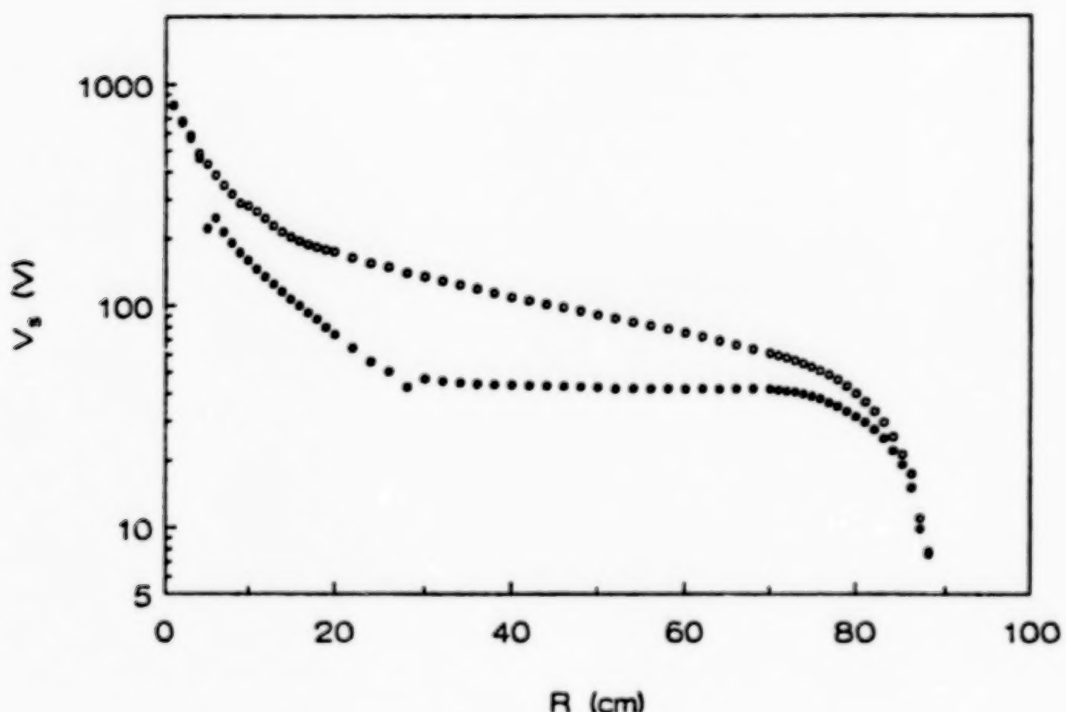


Figure 9. The radial potential distribution for a 7.5 cm diameter anode in the presence of the region III torus measured with an emissive electric probe. The curves correspond to magnetic fields of 5 and 15 Gauss.

## Discussion

The increase in current collection in the presence of a neutral background is due to electron trapping in the region surrounding the anode in the presence of a magnetic field. Electrons are trapped by a combination of  $E \times B$  trapping and electrostatic trapping. The  $E \times B$  trapping is due to the electric field of the anode crossed with the ambient magnetic field. The electrostatic trapping is due to the axial variation of the electrostatic potential of the charged anode. As the calculations of Rubinstein and Laframboise [2] show, the electrons are trapped in magnetic bottles and they can only be collected only when they are scattered into a bottle that comes in contact with the anode surface. Electron scattering can result from collisions with the background neutrals or sheath turbulence [9]. The magnetic bottles have scale lengths of the order of the Parker-Murphy radius so in order for breakdown to

occur the chamber radius must be larger than the P-M radius since trapping is destroyed if a magnetic bottle comes in contact with the chamber wall. This is the reason for the increase in critical magnetic field for a decrease in chamber radius. Thus even though the mean free path for electron-neutral collisions in this regime is very much longer than the anode-cathode distance, the effective path length of a collected electron can exceed the mean free path for collisions. Long path trajectories give rise to very high gain ionization cascades, thus driving the system to a glow discharge mode even at the extremely low neutral pressures far below the Paschen breakdown curve.

The ions generated by ionization cascades are unmagnetized in low values of magnetic field and are accelerated by the anode potential hill and ballistically ejected in the radial direction. When these ions impact the chamber wall they release secondary electrons that enter the discharge and produce more ionization cascades leading to high current breakdown when the ionization rate exceeds the electron detrapping rate. It also theoretically shown by Kunhardt [4] that this type of breakdown is also possible if the secondary emission from a wall is replaced by the thermal electron current collected through a sheath when the entire system is surrounded by a large plasma as is the case in the ionosphere.

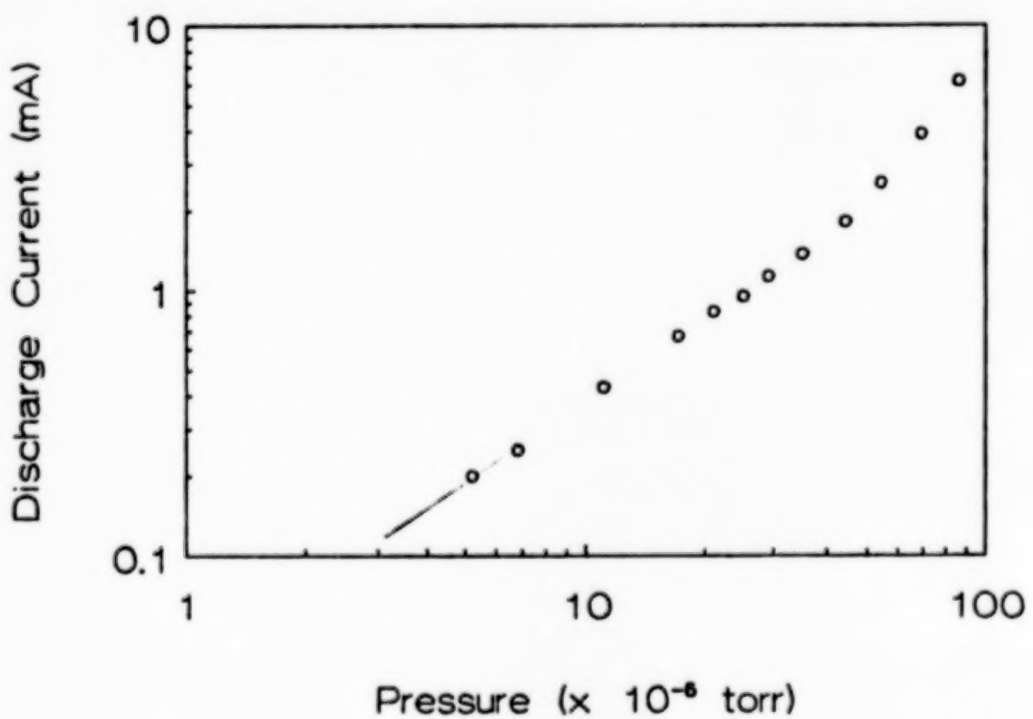


*Figure 10. Anode current collection for a constant magnetic field as a function of the ambient neutral pressure. Further pressure increase above  $1 \times 10^{-4}$  Torr results in a high current glow discharge.*

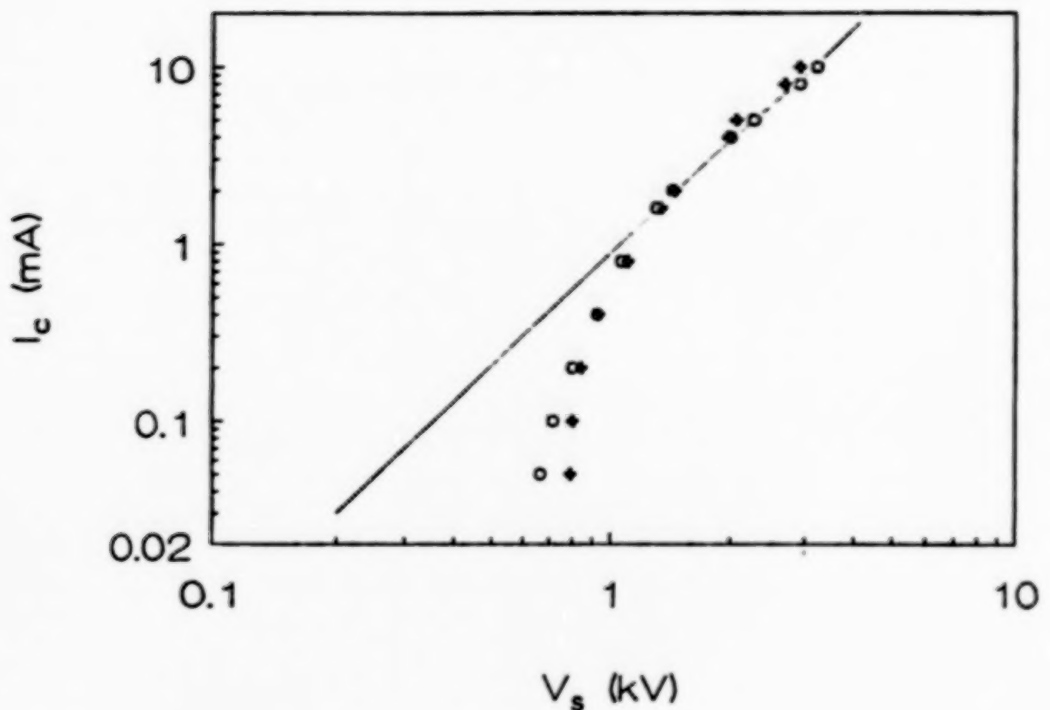


Figure 11. Anode current vs applied voltage for fixed magnetic field and ambient neutral pressure.

## Conclusions

In the presence of a low pressure neutral background in the vicinity of an anode charged to voltages as low as several hundred volts highly enhanced current collection due to large scale diffuse breakdown is possible in a weakly magnetized system. The neutral gas pressure required for breakdown initiation is usually far below the value of the Paschen curve and corresponds to pressures identified as "high vacuum". Even though for many space applications discharges are undesirable, there are situations such as a spacecraft "grounding" or electromagnetic tethers where high collection currents are necessary. These discharges which are diffuse in nature offer possible alternatives to hollow cathodes, hot filaments or charged particle guns for those types of applications that require sustained high current collection.

This Research was supported by the Strategic Defense Initiative Office of Innovative Science and Technology through the Office of Naval Research.

## References

- [1] L. W. Parker and B. L. Murphy, "Potential Buildup on an electron-emitting satellite", *Journal of Geophysical Research*, Vol. 72, 1967, pp. 1631-1636.
- [2] J. Rubinstein and J. G. Laframboise, *Phys. Fluids* 25, 1982, pp. 1174-1182.
- [3] R. G. Greaves, D. A. Boyd, J. A. Antoniades and R. F. Ellis, "Steady-State Toroidal Plasma around a Spherical Anode in a Magnetic Field", *Phys. Rev. Lett* 64, #8, 1990, pp. 886-889
- [4] E. E. Kunhardt, S. Lederman, E. Levi, G. Schaefer, W. C. Nunnally, W. E. Dillon and C. V. Smith, "Electrical Breakdown of the Insulation Properties of the Space Environment", *Proceedings of the XIII International Symposium on Discharges and Electrical Insulation in Vacuum*, Paris, 1988, pp. 247-249
- [5] J. A. Antoniades, M. J. Alport, D. A. Boyd and R. F. Ellis, "Vacuum Chamber Ground Testing of the SPEAR I Exposed High Voltage Components", *IEEE Transactions on Electrical Insulation*, to be published, June 1990
- [6] M. J. Alport, J. A. Antoniades, D. A. Boyd, R. G. Greaves and R. F. Ellis, "Electrical Breakdown at Low Pressure in a Weak Magnetic Field", *Journal of Geophysical Research*, to be published, Spring 1990
- [7] D. B. Allred et al., "The SPEAR I Experiment, High Voltage Effects on Space Charging in the Ionosphere", *IEEE Transactions on Nuclear Science*, Vol. 35, 1988, pp. 1386-1393
- [8] J. A. Antoniades, R. G. Greaves, D. A. Boyd and R. F. Ellis, "Current Collection in Near Ionospheric Conditions in the Presence of Neutrals", *Reprint from the 28th Aerospace Sciences AIAA Meeting*, Reno, 1990, #90-0632
- [9] P. Palmadesso, *Private Communication*.

SPEAR-1, AN EXPERIMENT TO MEASURE CURRENT COLLECTION IN THE  
IONOSPHERE BY HIGH VOLTAGE BIASED CONDUCTORS

W. John Raitt, Neil B. Myers, Jon A. Roberts, and D. C. Thompson

Center for Atmospheric and Space Science, Utah State University,  
Logan, Utah 84322-4405

**Abstract.** An experiment will be described in which a high electrical potential difference, up to 45 kV, was applied between deployed conducting spheres and a sounding rocket in the ionosphere. Measurements were made of the applied voltage and the resulting currents for each of 24 applications of different high potentials. In addition, diagnostic measurements of optical emissions in the vicinity of the spheres, energetic particle flow to the sounding rocket, DC electric field and wave data were made. The ambient plasma and neutral environments were measured by a Langmuir probe and a cold cathode neutral ionization gauge, respectively.

In this presentation, the payload will be described and examples of the measured current and voltage characteristics will be presented. The characteristics of the measured currents will be discussed in terms of the diagnostic measurements and the in-situ measurements of the vehicle environment.

In general, it was found that the currents observed were at a level typical of magnetically limited currents from the ionospheric plasma for potentials less than 12 kV, and slightly higher for larger potentials. However, due to the failure to expose the plasma contactor, the vehicle sheath modified the sphere sheaths and made comparisons with the analytic models of Langmuir-Blodgett and Parker-Murphy less meaningful. Examples of localized enhancements of ambient gas density resulting from the operation of the attitude control system thrusters (cold nitrogen) were obtained. Current measurements and optical data indicated localized discharges due to enhanced gas density reduced the vehicle-ionosphere impedance.

#### Background

A vehicle in space will attain an electrical potential with respect to the background environment in order to balance the ion and electron fluxes to the vehicle which differ greatly when the vehicle is at the background plasma potential. The causes for the difference in fluxes may include the larger thermal velocity of electrons compared to ions, secondary electron emission from the vehicle due to ion impact, photoemission of electrons due to sunlight, and any active emission of either electrons or ions. Much of the literature has been concerned with environmentally induced charging of geosynchronous satellites which can attain potentials of tens of kilovolts with respect to the background plasma. Recently, interest in the charging of vehicles in the lower ionosphere has increased because of the planned use of large space vehicles with high power requirements (such as the space station) at low Earth orbit (LEO) altitudes. Numerous electron beam experiments have been performed in the lower ionosphere to study the processes that occur when exposing high potentials to the space environment [Winckler, 1980; Szuszczewicz, 1985]. It was found that electron beam emission

complicated the interpretation of these processes and could change the current collection characteristics of the beam-emitting vehicle [Myers et al., GRL, 1989].

The Space Power Experiments Aboard Rockets (SPEAR) program was initiated to provide guidelines in designing high voltage (HV) systems that utilize the near vacuum of the space environment as insulation at LEO altitudes. The development of these guidelines requires better understanding of the physics of the HV interaction with LEO environment. The SPEAR program has involved a theoretical modelling group, a ground-based laboratory group, and a flight experiments group to study HV interaction with plasmas.

#### Science Objectives

The science objectives of the SPEAR-1 experiment were to; 1) study the altitude dependence of the current-voltage characteristics of a metallic conductor exposed to the space environment when biassed up to tens of kilovolts, 2) study the interaction of high voltage biassed conductors within each other's charge sheaths, 3) make diagnostic measurements to aid the development of theoretical models to predict the current collection by conductors biassed to high voltages in the ionosphere, 4) study the effectiveness of a plasma contactor in grounding the power platform to the ambient ionosphere, and 5) obtain this data in a timely fashion to be useful in the SPEAR-2 program.

#### Principle of Experiment

The SPEAR-1 experiment included two spherical conductors separated from the upper portion of the rocket body by a fiberglass boom and biassed to potentials as large as 45 kV. Spherical conductors were employed to enable a comparison of current collection from a space plasma with analytic models [Langmuir and Blodgett, 1924; Parker and Murphy, 1967; and Linson, 1969]. The upper portion of the boom utilized a grading ring structure to ensure a uniform potential drop from the spheres to the main portion of the boom that was maintained at the rocket body potential. The grading rings also reduce the possibility of surface flashover on the boom by hiding triple points from the ambient ionospheric plasma. A plasma contactor was located on the lower portion of the rocket body to clamp the main vehicle potential near the plasma potential. The potential between the rocket and the spheres was measured and the current collected by the spheres was determined. A low light level television (LLLTV) camera and three photometers were used to measure light emission accompanying the current collection of the spheres. Figure 1 shows the general configuration of the payload and the location of the instruments. A series of bias operations was performed to study the altitude dependence of the HV interaction. An attitude control system (ACS) stabilized the rocket body with the spheres in three different orientations relative to the geomagnetic field, allowing magnetic effects of the HV interaction to be studied.

#### Payload Arrangement

The two spheres were made from aluminum plated with gold over nickel. The diameter of the spheres was 0.2 m. The grading rings were

shallow, saucer shaped rings made of aluminum with nickel plating. The grading rings were separated by resistors between adjacent rings. The rings were oriented to prevent electrons accelerated to the spheres from striking the boom. The total resistance of the grading rings to sphere 1 was  $1.1 \text{ M}\Omega$ , and to sphere 2 was  $980 \text{ k}\Omega$ . The difference was due to the slightly different lengths of the two grading ring booms necessary to accommodate the spheres and booms in their folded, pre-deployment configuration.

A LLLTV camera with a wide angle lens was located to view both spheres and their charge sheaths to an area extending about 5 m from either side of the spheres. One of the guiding rods for nosecone deployment blocked the view of sphere 2 during most of the flight although portions of the charge sheath were not obstructed. Figure 2 shows the location of the LLLTV (and some of the other instruments) with respect to the spheres.

Three photometers were oriented to view the region between the spheres with a field-of-view of  $5^\circ$  half-maximum full-width. The photometers measured wavelengths of 476.5 nm, 441.5 nm, and 391.4 nm, which correspond to emissions from  $\text{Ar}^+$ ,  $\text{O}^+$ , and  $\text{N}_2^+$  respectively.  $\text{Ar}^+$  was chosen because the plasma contactor released argon gas.

A cold cathode ionization gauge provided measurements of neutral pressure in the range of  $10^{-3}$  to  $10^{-7}$  torr. The neutral pressure gauge was located in the upper portion of the rocket, placing it as far as possible from the plasma contactor, and as close as possible to the HV spheres.

The high voltages were applied to the spheres using  $2.5\text{-}\mu\text{F}$  capacitors charged to voltages between 6 kV and 45 kV. Different potentials were applied to the two spheres, and at times a potential was applied to only sphere 1. Fixed resistors were connected to the capacitors in parallel to the rocket ground to ensure that the capacitors completely discharged within about five seconds. The equivalent circuit diagram for sphere 1 is shown in Figure 3. All of the known resistances were the same for sphere 2 except that of the grading ring resistance.

A cylindrical Langmuir probe was deployed radially from the rocket body with a total collection area of about  $0.001 \text{ m}^2$  to measure the ambient plasma density. The probe voltage was swept from +5 V to -1 V and back again over a period of one second, which repeated every 2.3 seconds.

Electrostatic waves were measured by two single-axis antennas deployed radially 1 m from the rocket. Very low frequency (VLF) waves were monitored from 20 Hz to 30 kHz with varying bandwidths up to 20 kHz. High frequency (HF) waves were measured with a 200-kHz bandwidth up to 10 MHz.

Four imaging ion and electron detectors monitored particle fluxes in the energy ranges of 2 eV to 5 keV and 10 eV to 30 keV with several view directions and a 32 ms spectral resolution. The higher energy bandwidths were about 11% of the energy channel while the lower energy bandwidths were about 20%.

A hollow cathode plasma contactor was intended to clamp the vehicle potential to between -100 and -150 V during voltage bias operations. The plasma contactor was located at the bottom of the rocket body to minimize contamination of the sphere environment.

### Flight Operations

SPEAR-1 was launched at 20:45 EST on December 13, 1987 from the NASA Wallops Flight Facility, Virginia. The vehicle reached an apogee of 369 km at 351 seconds mission elapsed time (MET). The ACS was used to place the spheres into three orientations with respect to the geomagnetic field as shown in Figure 4. The first orientation was such that the plane described by the v-shaped booms deploying the spheres was nearly perpendicular to the geomagnetic field. In the second orientation the plane of the v-shaped booms of the spheres was parallel to the geomagnetic field. In the third orientation the sphere 1 boom was parallel to the geomagnetic field. Twenty four voltage bias operations were performed between 192 seconds and 622 seconds as shown in Figure 5. The altitude of the rocket is shown versus MET. The bias operations are shown with the voltage bias of sphere 1 above the trajectory and that of sphere 2 below the trajectory. The three orientations of the spheres with respect to the geomagnetic field are also shown.

### Measurements

#### Atmospheric Parameters

A comparison of the neutral pressure measured during the experiment with that predicted by the MSIS-86 model [Hedin, 1987] is shown in Figure 6. Pressure in torr is shown versus MET in seconds. The difference between the measurements and the model is attributed to outgassing from the instrument initially, and outgassing of the fiberglass boom (located very near the instrument) and the rocket body. Since the mean free path is large, we can assume that the pressure at the spheres due to outgassing decreased by the inverse square of the distance to the spheres. This yields pressures at the spheres in agreement with the MSIS model results.

The electron density derived from the Langmuir probe during the experiment is shown in Figure 7. Altitude is shown versus measured electron density (squares) and electron density predicted by the IRI model [Rawer et al., 1981] (triangles). The electrons in the ionosphere are more dynamic than the neutrals, and as a result the IRI model results are not in good agreement with the measurements. No density measurements were obtained during the discharges. The plasma density was measured to be lower during downleg, since the Langmuir probe was in the vehicle wake during the downleg portion of the flight. The electron temperature was also derived from the Langmuir probe data and is shown in Figure 8. Altitude is shown versus the measurement of temperature (squares) and the electron temperature prediction from the IRI model (triangles).

#### Current-Voltage

Raw Measurements. The currents measured directly during voltage bias operations were the current down the grading ring boom,  $I(b)$ , and the total current to the capacitor,  $I(t)$ , as seen in Figure 3. The plasma current to the sphere is obtained by subtracting  $I(b)$  and the current through the  $700\text{ k}\Omega$  resistor from  $I(t)$ . The measurements of

$I(t)$  and  $I(b)$  and the resulting derived plasma current are shown in Figure 9 for one of the voltage bias operations. The individual currents are shown versus increasing potential. The potential was the measured potential of the capacitor, which would equal the potential of the sphere with respect to the background ionosphere if the plasma contactor had been able to clamp the rocket body to the ionospheric potential. Unfortunately, the cover on the plasma contactor failed to deploy preventing the plasma contactor from being exposed to space. This allowed the rocket body to charge to several kilovolts negative during voltage bias operations. Time increased with decreasing potential since the bias operations applied the full potential to the spheres that subsequently decayed to zero voltage. There were no large current spikes in the measurements, indicating that no discharges occurred between the plasma and the spheres in space.

Numerous discharges were observed during pre-flight vacuum chamber tests. This can be seen in Figure 10, which shows  $I(t)$ ,  $I(b)$ , and the potential on the sphere versus time during the vacuum chamber tests. The discharges can be seen as the large current spikes of  $I(t)$  that resulted in the sharp decreases in the measured potential. The contrasting results demonstrate the difference between an experiment in a vacuum chamber and in space.

Plasma Currents. A series of voltage bias operations is shown in Figure 11. Plasma current is shown versus the capacitor potential for three different altitudes. The measurements for sphere 1 are shown on the left, and the measurements for sphere 2 are shown on the right. The sheath resistance has been calculated using the capacitor potential and the plasma current as shown in the figure, ranging from  $900\text{ k}\Omega$  to  $5.9\text{ M}\Omega$ . These calculations are larger than the actual sheath resistance since the actual sphere potential can be several kilovolts less than the capacitor potential. The data obtained at 257 km show three enhancements to current collected by the spheres. The LLLTV images showed brief bursts of light around the grading rings after the initial glow had disappeared. The presumed cause of the current enhancements was the outgassing of the grading rings since this was the first bias operation. An interesting curve of the i-v characteristic is seen in the sphere 2 data obtained at 303 km (panel e). The sphere current increased as the potential decreased from 5 kV to near zero. This is thought to be due to the impingement of the rocket body ion sheath on the electron sheath of the sphere. Initially the potential on sphere 1 was 36 kV and the potential of the rocket body was several kilovolts negative. The rocket body must develop a very large ion sheath to attract ions from the plasma [Katz et al., 1989]. This large ion sheath would partially envelope the electron sheath of the spheres, decreasing the current collection by the spheres. As the potential on the capacitor decayed, the rocket body ion sheath decreased in size, reducing the interaction of the charge sheaths and allowing an increased current to the spheres.

The rocket body potential could be inferred at times from the particle detector data. Two sweeps of the particle detector data obtained at 361 km are shown in Figure 12. The data of the top panel show a peak at about 6 kV with a width from 4 to 9 kV. The rocket body potential is interpreted to be between 4 and 9 kV. The large number of lower energy electrons are due to ionization in the sheath. The data in the lower panel were obtained almost a second later and the rocket body potential has decreased to between 1 and 5 kV. The actual sphere

potential with respect to the ionosphere can be calculated using the rocket body potential measured during each sweep and is shown in Figure 13 for the data obtained at 361 km. There is a large uncertainty in the rocket body potential obtained in this fashion and not all of the particle detector sweeps were as simple to interpret as the ones shown in Figure 12, complicating the usefulness of this procedure.

Three bias operations that applied the maximum potential (45 kV) to sphere 1 exhibited a current enhancement at the largest potential on the sphere. An example of this is shown in Figure 13 for the data obtained at 361 km, which shows plasma current versus capacitor potential and the corresponding predictions of the Langmuir-Blodgett (dashed line) and Parker-Murphy (solid line) models. The LLLTV images showed a diffuse glow around the grading rings which moved toward the connection point of the two graded booms. This is possibly a volume discharge at potentials greater than 40 kV for the geometry of the experiment.

Since the electron density remained fairly constant over the altitude range of the voltage bias operations, no definite trend was seen in the calculated sheath resistance over the altitude range of the experiment. There was a dependence on the orientation of the spheres with respect to the geomagnetic field. The sheath resistances were between 100 k $\Omega$  and 250 k $\Omega$  lower in the V-plane parallel orientation compared to the V-plane perpendicular. This is about 15% of the total sheath resistance, however there were only three discharges for comparison in the parallel case.

Considerable ACS activity occurred during two voltage bias operations because of attitude changes of the rocket body just prior to the bias operations. The ACS thruster firings resulted in temporary enhancements to the current collected by the spheres. Figure 14 shows the capacitor voltage and plasma current versus time for a bias operation without ACS activity at 285 km (left) and with ACS activity at 235 km (right). The current enhancements are seen as the spikes in the plasma current (up to 0.15 A) in the lower right panel. The current enhancements had very little affect on the capacitor potential since the charge required to produce these spikes was small compared to the charge stored in the capacitor. Figure 15 shows the plasma current and ACS nozzle firings versus time for the operations at 352 km (top two panels) and at 235 km (lower two panels). There is a strong correlation between the ACS nozzle firings and the enhanced current spikes. The misalignments of some of the current spikes with the ACS nozzle firings can be explained by the slower sample rate of the ACS data.

The ACS operations from the rocket body may effectively neutralize the rocket body potential, functioning as a plasma contactor [B.E. Gilchrist et al., Observations of electron collection enhancement using neutral gas thruster jets on an isolated charged vehicle in the ionosphere, in press, *J. Geophys. Res.*, 1989; N.B. Myers et al., Vehicle charging effects during electron beam emission from the CHARGE-2 experiment, in press, *J. Space Rockets*, 1989]. Under these circumstances the rocket sheath impedance (Figure 3) becomes short circuited by the ionization in the thruster jet, thereby reducing the total series impedance in the capacitor discharge circuit. Thus, the capacitor potential may represent the sphere-to-ionosphere potential during the portions of the voltage bias operations with ACS firings, allowing a comparison of the current collection with analytic current-

voltage models. This has been done in Figure 16. The top panel shows the plasma current to the sphere during ACS firings versus potential compared with the Langmuir-Blodgett (dashed line) and the Parker-Murphy (solid line) models at 353 km. The middle panel shows the data obtained at 235 km with the same format. The lower panel shows the collected current during ACS firings normalized to the Parker-Murphy model for all cases of ACS firings during voltage bias operations. The data agree well with the Parker-Murphy model at potentials less than 12 kV. This is in agreement with the CHARGE-2 results for the current collection of a 1-kV conductor in the ionosphere [Myers et al., 1989]. Above 12 kV The collected current exceeds that of the Parker-Murphy model but is still substantially less than that of the Langmuir-Blodgett model.

#### Optical Data

LLLTV. The view from the LLLTV camera is represented in Figure 17. The camera was located at the top of the payload looking forward at the deployed spheres. Three guiding rods for the nosecone deployment are in the field-of-view of the camera. One of the guiding rods partially obstructs sphere 2 and a portion of its grading ring boom. The wire that connects the HV capacitors with the spheres is visible connecting the main payload with the two grading ring booms. The time tag of the video is usually seen as a blur in the lower right corner of the reproduction of the single freeze-frame images.

A typical image during a voltage bias operation is shown in Figure 18. A 7-kV potential was applied to sphere 1 and a 21-kV potential was applied to sphere 2. A glow surrounding the spheres and extending down the grading ring booms is evident in the image, although the guiding rod partially obstructs the glow of sphere 2. The airglow layer is also seen in the image. The glow during voltage biassing was always seen around both the spheres and their guiding rods whenever it was visible. Relative intensity measurements from the digitized images show that the glow is about the same brightness as the airglow.

Figure 19 shows an image during the same voltage bias operation just after a vehicle maneuver and coincident with an ACS thruster firing from the rocket body. The thruster firing must have resulted in a localized generation of light caused by impact ionization of the released neutral gas by the charged particles accelerated by the rocket potential. The light generated in the thruster cloud can be seen reflected from two of the guiding rods, the main boom, and its wire. The light must have been fairly localized since a sharp shadow was produced on one side of the wire and can be seen where the wire crosses the main boom.

The image shown in Figure 20 indicates a possible volume discharge as evidenced by the large glow that can be seen at the connection point of the two grading ring booms. The airglow layer is seen extending partially through that region. A 43-kV potential was applied to sphere 1, while no potential was applied to sphere 2. This type of glow was only seen for the three single-sphere bias operations of bias voltages greater than 40 kV. The diffuse glow was seen in the video images to move along the grading rings toward the connection point of the booms.

Photometer. No correlation of light measurements with voltage bias operations was seen in any of the photometer channels. The field-of-view of the photometers was the region between the spheres, whereas the

largest light emission occurred in the volume surrounding the grading ring booms. All three photometers showed increased light measurements when the airglow layer passed through their field-of-view.

#### Summary and Conclusions

The SPEAR-1 payload successfully applied up to 45 kV to two spherical conductors in the ionosphere. Negligible volume discharge effects occurred when the HV interacted with the LEO environment, in the geometrical configuration used. The rocket body potential was probably near ambient plasma potential during ACS thruster firings. During those times it was determined that the sphere current collection was magnetically limited and in agreement with the Parker-Murphy model for potentials less than 12 kV. The collected current exceeded the Parker-Murphy model for potentials above 12 kV. The net space load placed on the power supply was well represented by a linear resistance of 500-1000 k $\Omega$  for the geometry of the SPEAR-1 payload. Negative potentials of up to 10 kV on the rocket body resulted in no adverse effects resulting from transient surface discharges. Transient discharge currents were triggered by release of neutral gas from the rocket body during voltage bias operations. The SPEAR-1 payload demonstrated the feasibility of using high energy, high voltage capacitors on a space vehicle.

Acknowledgements. The SPEAR-1 rocket flight was funded by the Defense Nuclear Agency under grant DNA001-87-C-0015.

#### References

- Hedin, A. E., MSIS-86 Thermospheric model, *J. Geophys. Res.*, 92, 4649, 1987.  
Langmuir, I. and K. Blodgett, Current limited by space charge flow between concentric spheres, *Phys. Rev.*, 24, 49, 1924.  
Linson, L. M., Current-voltage characteristics of an electron-emitting satellite in the ionosphere, *J. Geophys. Res.*, 74, 2368, 1969.  
Myers, N. B., W. J. Raitt, B. E. Gilchrist, P. M. Banks, T. Neubert, P. R. Williamson, and S. Sasaki, A comparison of current-voltage relationships of collectors in the Earth's ionosphere with and without electron beam emission, *Geophys. Res. Lett.*, 16, 365, 1989.  
Parker, L. W. and B. L. Murphy, Potential buildup on an electron-emitting ionospheric satellite, *J. Geophys. Res.*, 72, 1631, 1967.  
Rawer, K., S. Ramakrishnan, D. Bilitza, International reference ionosphere 1978, URSI Brussels and World Data Center, Report UAG-82, Boulder, 1981.  
Szuszczewicz, E. P., Controlled electron beam experiments in space and supporting laboratory experiments: a review, *Journal of Atmospheric and Terrestrial Physics*, 47, 1189, 1985.  
Winckler, J. R., The application of artificial electron beams to magnetospheric research, *Reviews of Geophysics and Space Physics*, 18, 659, 1980.

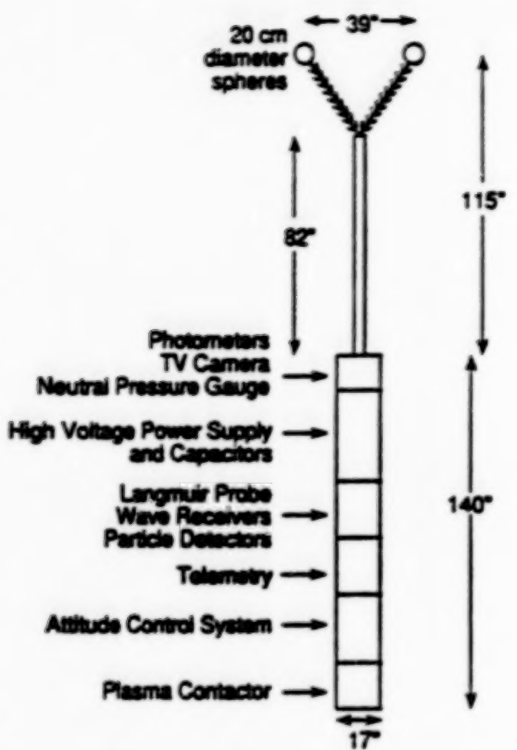


Fig. 1. Schematic diagram of the payload configuration of the SPEAR-1 experiment.

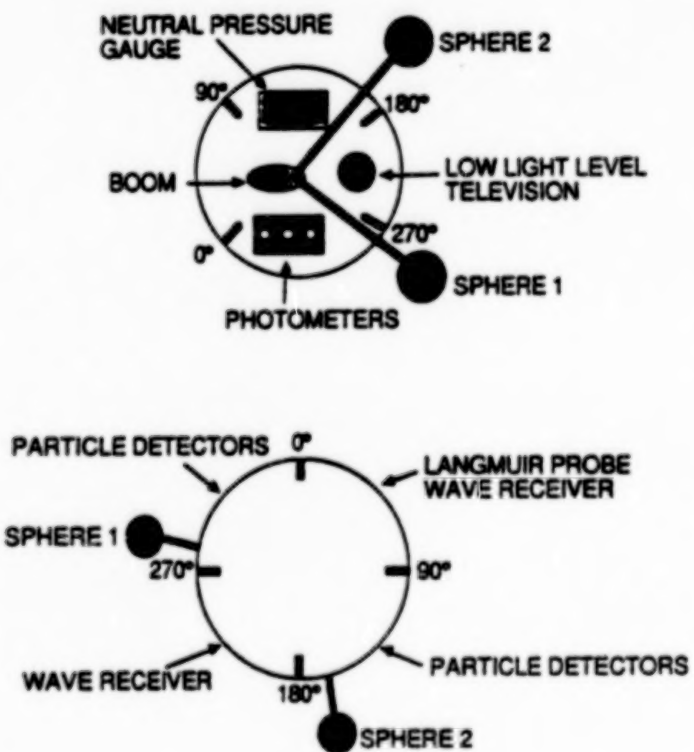


Fig. 2. Schematic diagram of the cross-section of the SPEAR-1 payload. Top panel shows view from the top of the rocket while the lower panel shows the view from the bottom of the rocket.

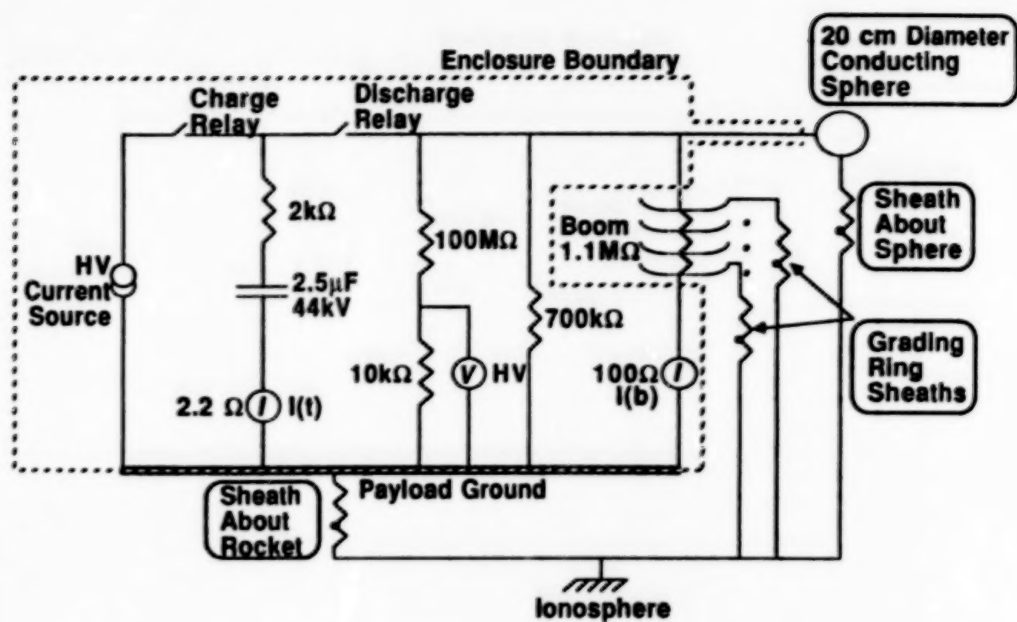
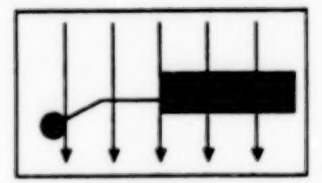
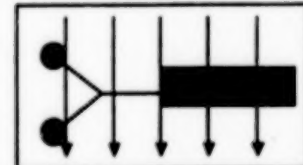


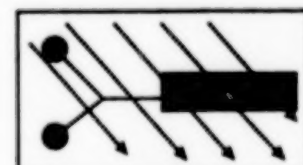
Fig. 3. Equivalent electrical circuit diagram for sphere 1.



V-PLANE PERPENDICULAR



V-PLANE PARALLEL



SPHERE 1 BOOM PARALLEL

Fig. 4. Schematic representation of the three vehicle orientations with respect to the Earth's magnetic field represented by arrows.

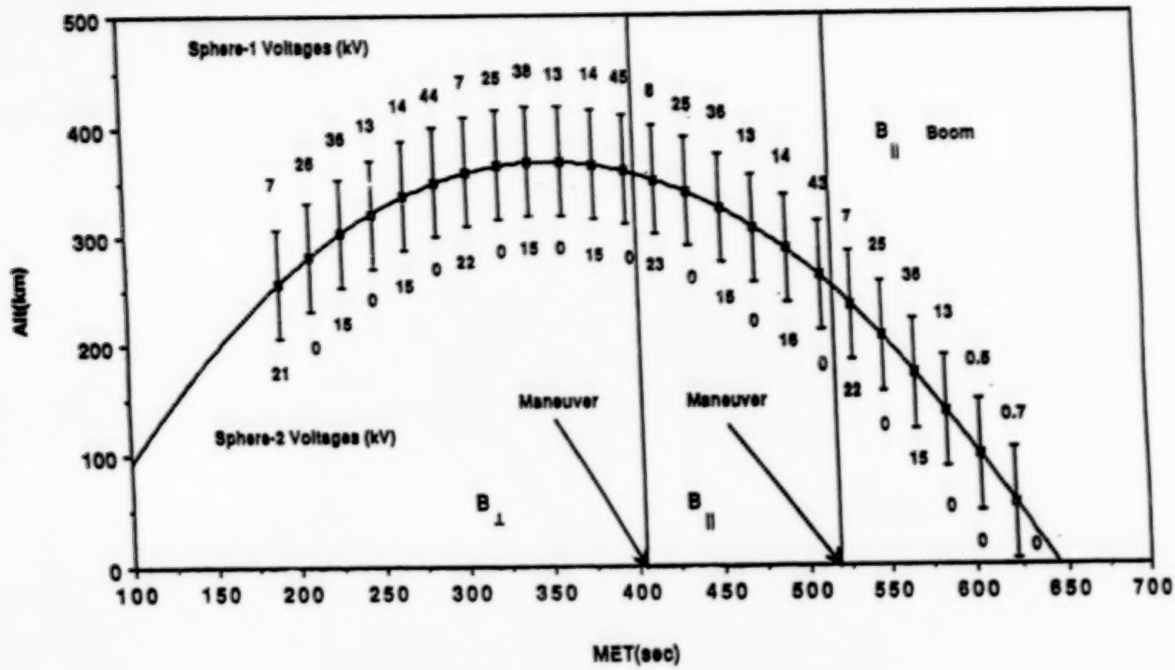


Fig. 5. Trajectory of the SPEAR-1 payload with the voltage bias operations included. The maximum potentials are given for sphere 1 (above the trajectory) and sphere 2 (below the trajectory). The two maneuvers accomplished by the ACS to achieve the three orientations are also shown.

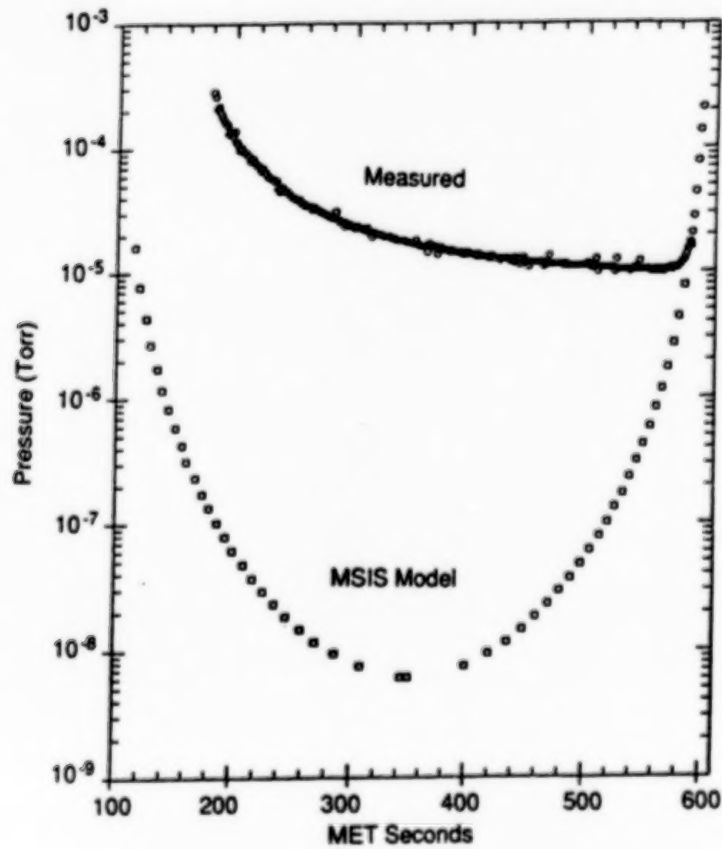


Fig. 6. Comparison of the neutral pressure measured during the experiment and calculated using the MSIS-86 model.

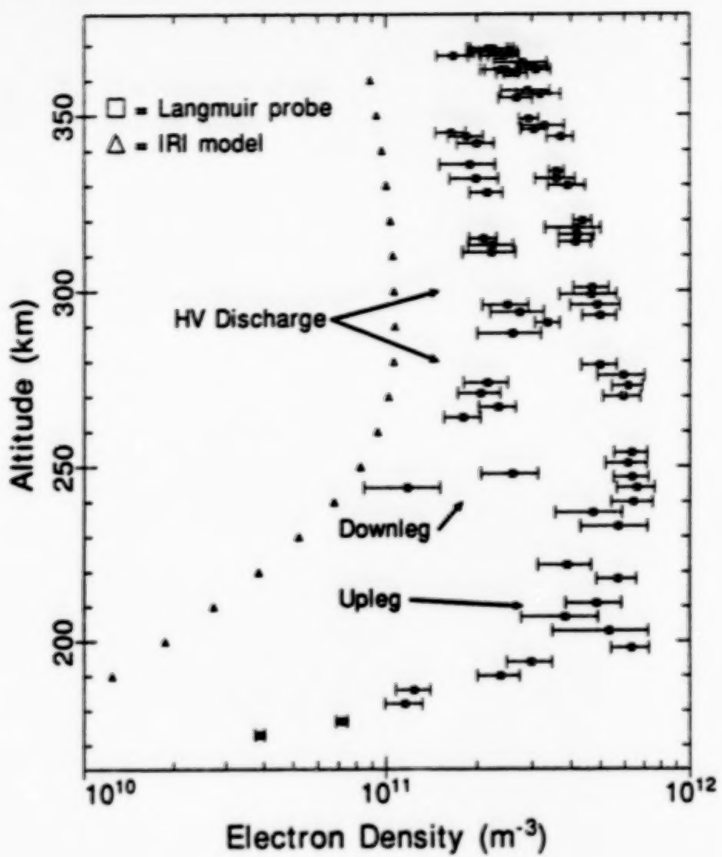


Fig. 7. Comparison of the electron density measured during the experiment and calculated using the IRI model.

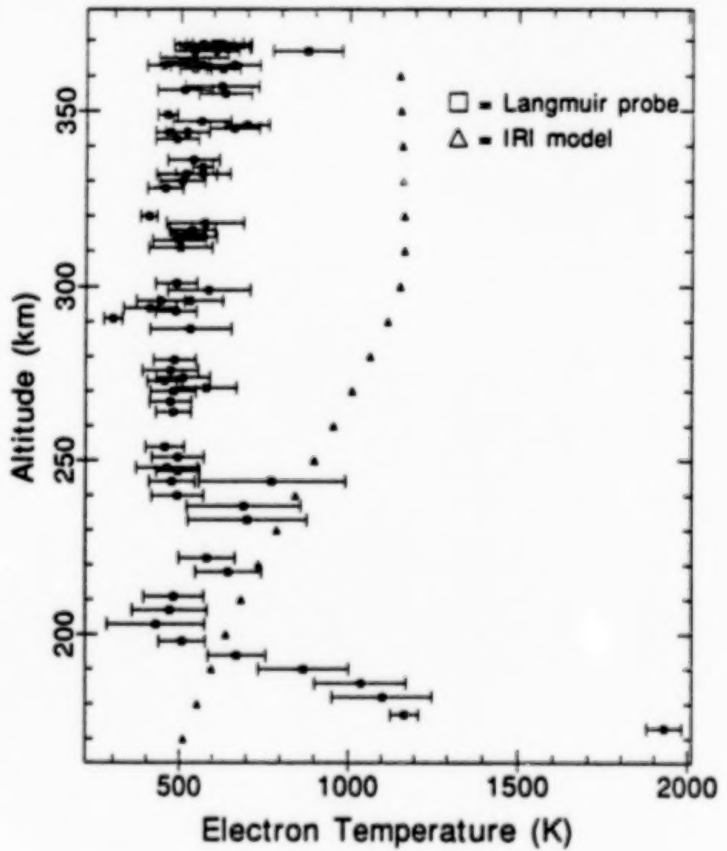


Fig. 8. Comparison of the electron temperature measured during the experiment and calculated using the IRI model.

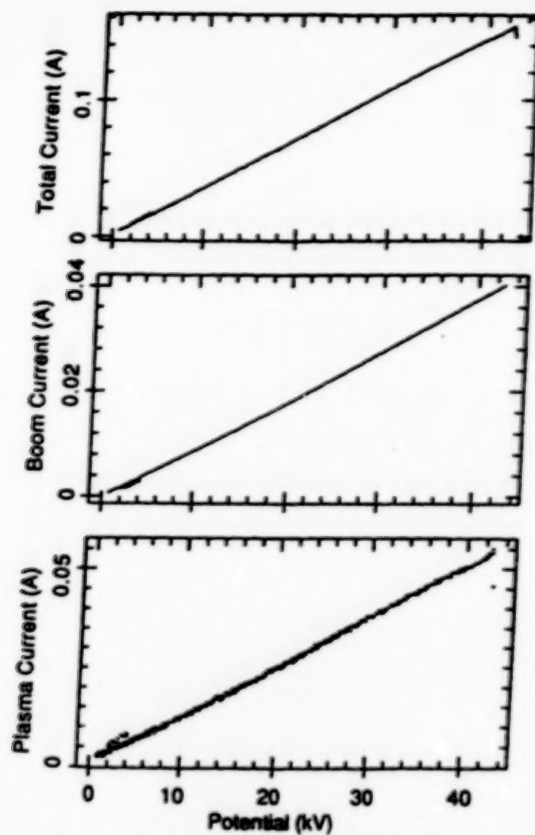


Fig. 9. The measured boom and total current, and the derived plasma current to the sphere versus the potential applied to sphere 1.

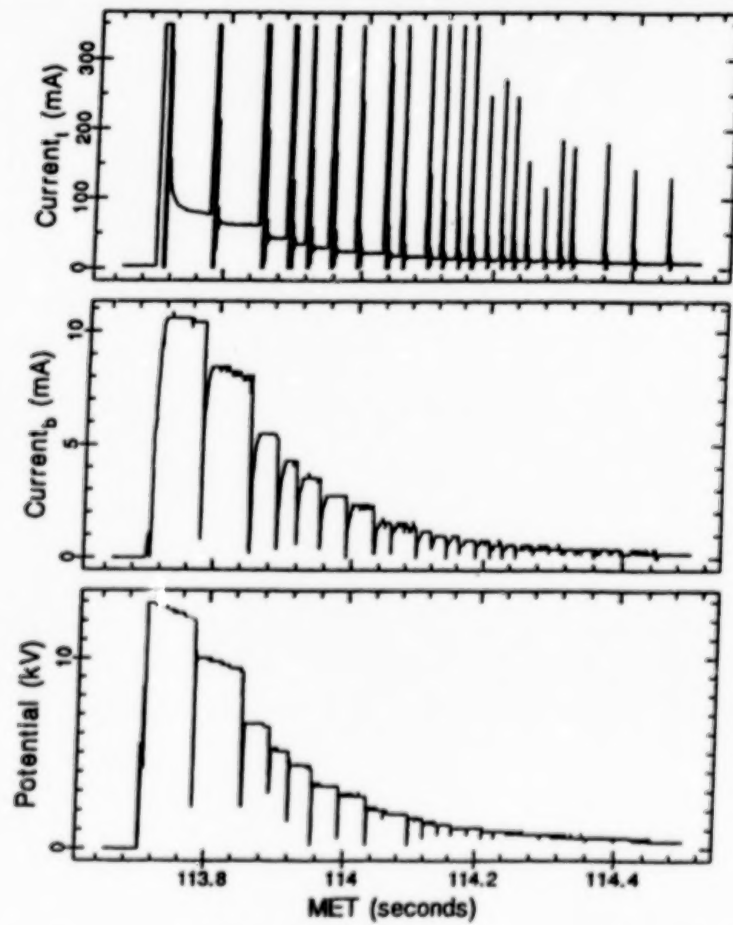


Fig. 10. The measured boom and total current, and the potential on sphere 1 versus time during the vacuum plasma chamber tests.

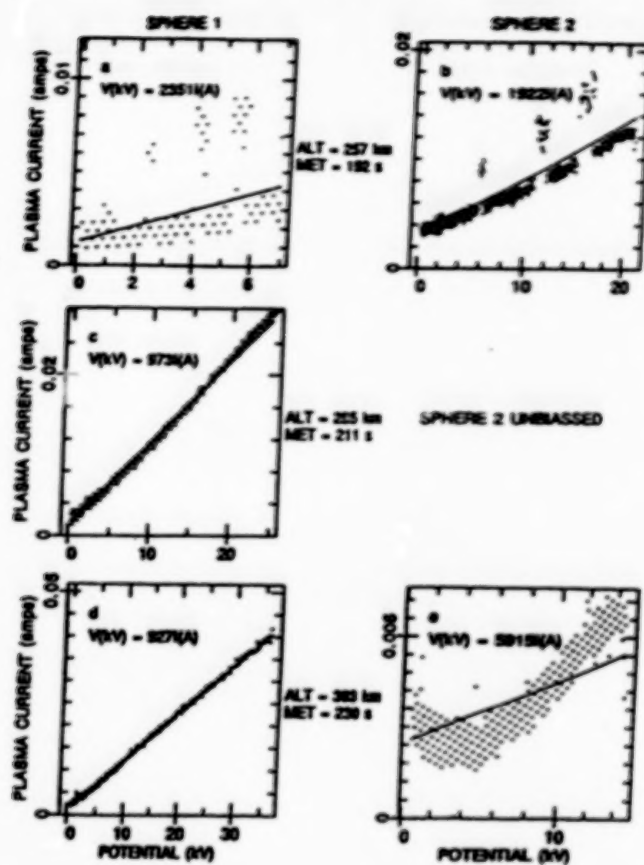


Fig. 11. Plasma current versus voltage for both spheres during the first three voltage bias operations of the experiment.

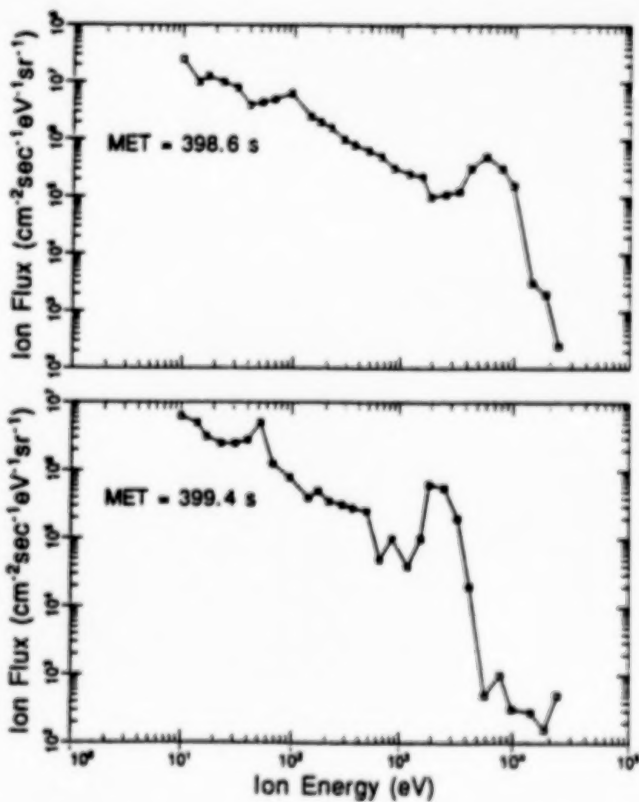


Fig. 12. The ion flux data versus energy for two sweeps of the particle detector during one voltage bias operation at 361 km.

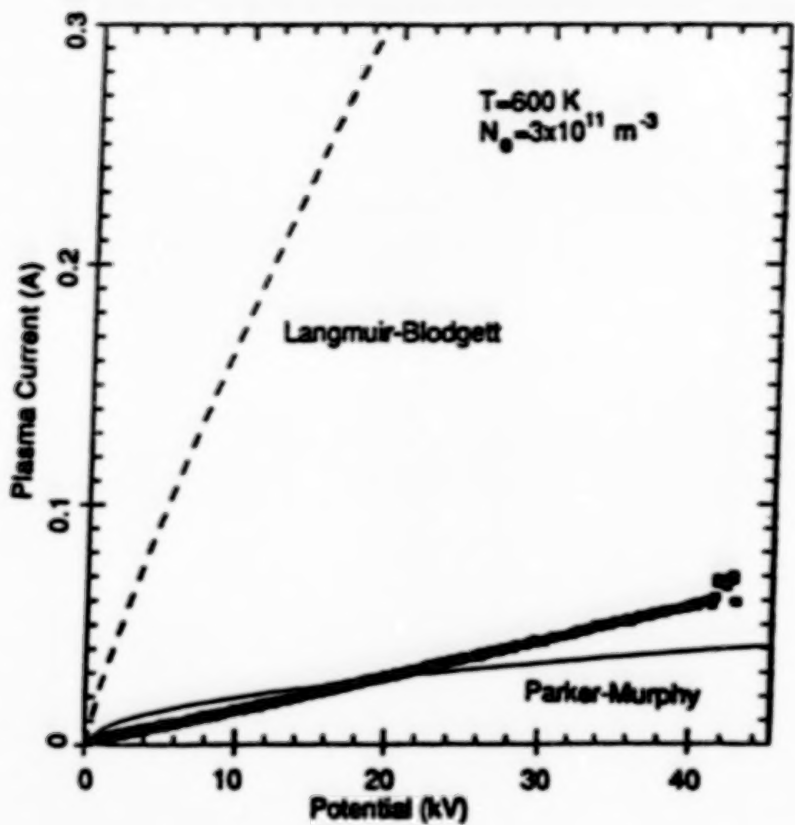


Fig. 13. The plasma current versus potential of sphere 1 at 361 km. The Langmuir-Blodgett and Parker-Murphy models are shown for reference.

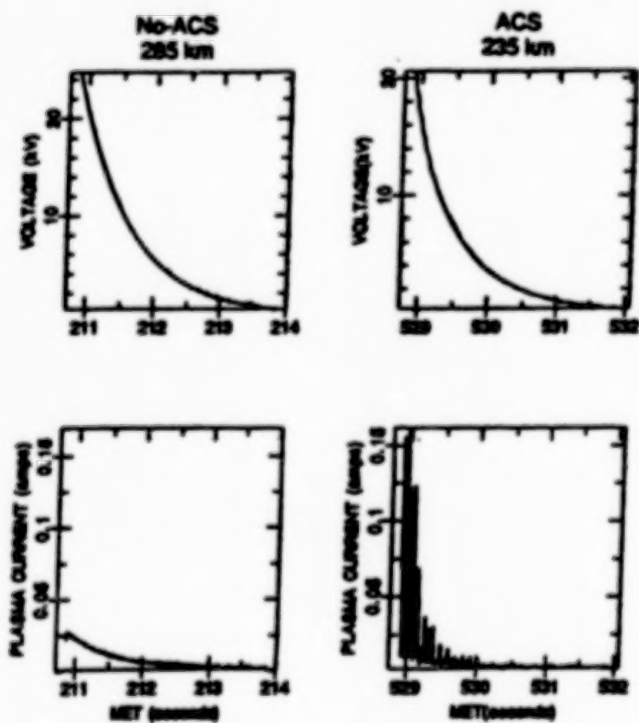


Fig. 14. The voltage (top panels) and plasma current (bottom panels) for voltage bias operations without ACS activity at 285 km (left panels) and during ACS activity at 235 km (right panels).

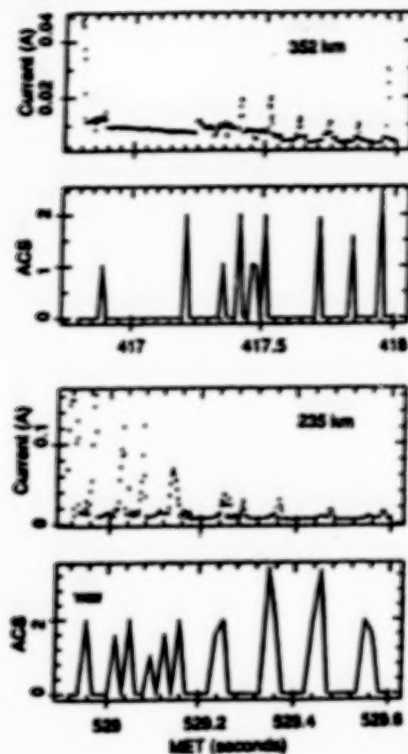


Fig. 15. Enhancement of plasma current correlated with ACS nozzle firings at 352 km (top two panels) and 235 km (bottom two panels).

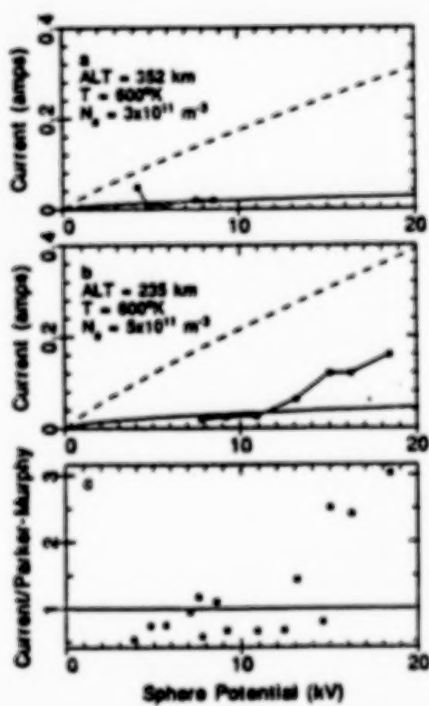


Fig. 16. Plasma current to the sphere versus sphere-to-ionosphere potential (top two panels) measured when ACS activity reduced the rocket body potential. The lower panel shows the sphere current normalized to the Parker-Murphy model versus sphere potential for all operations when the ACS reduced the rocket body potential. The numbers next to data points indicate the bias operation number where different from the top two panels.

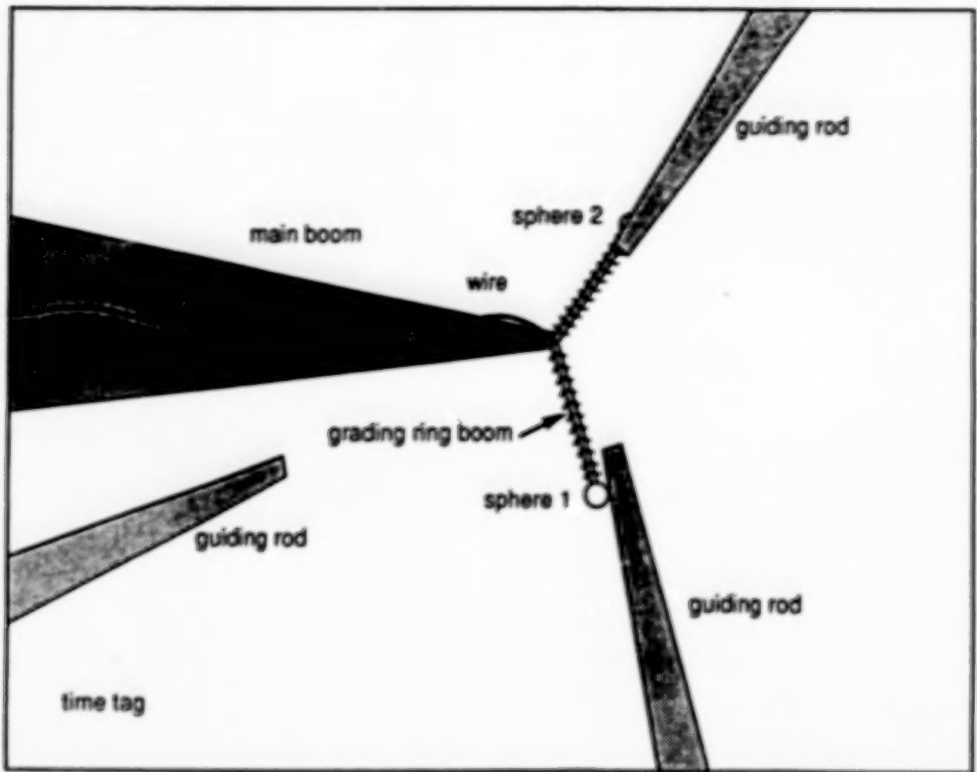


Fig. 17. Schematic representation of the view from the LLLTV camera.

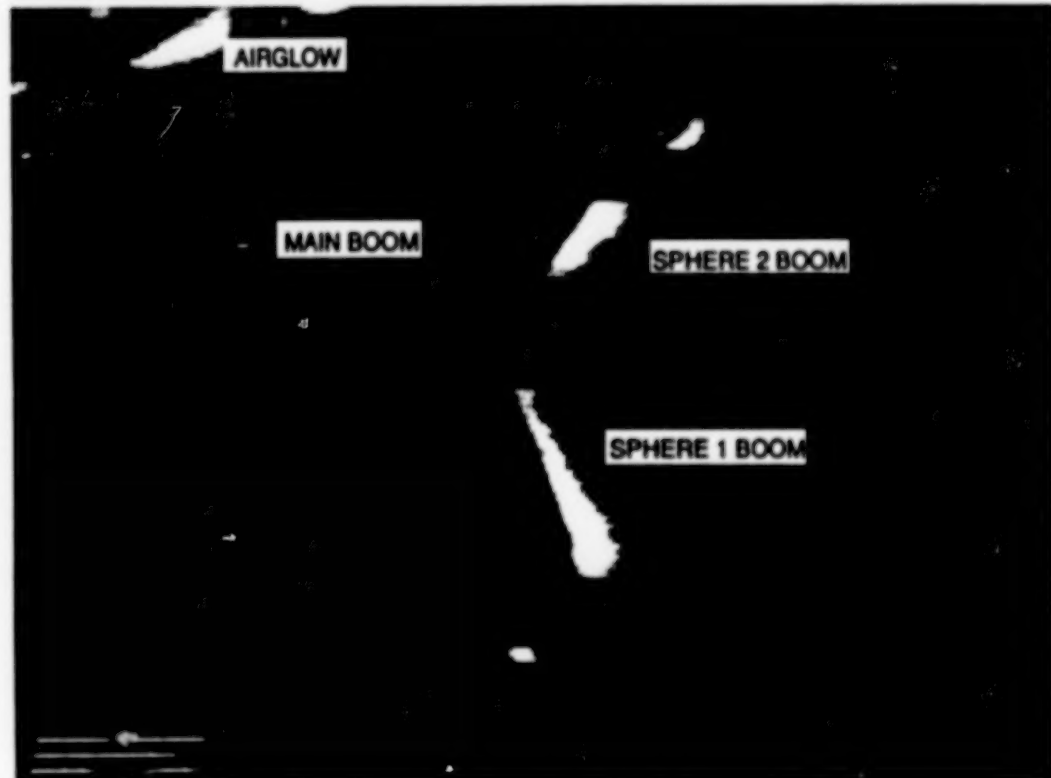


Fig. 18. Image from the LLLTV during a typical voltage bias operation at 235 km. Maximum voltages of 7 kV for sphere 1 and 21 kV for sphere 2 were applied.

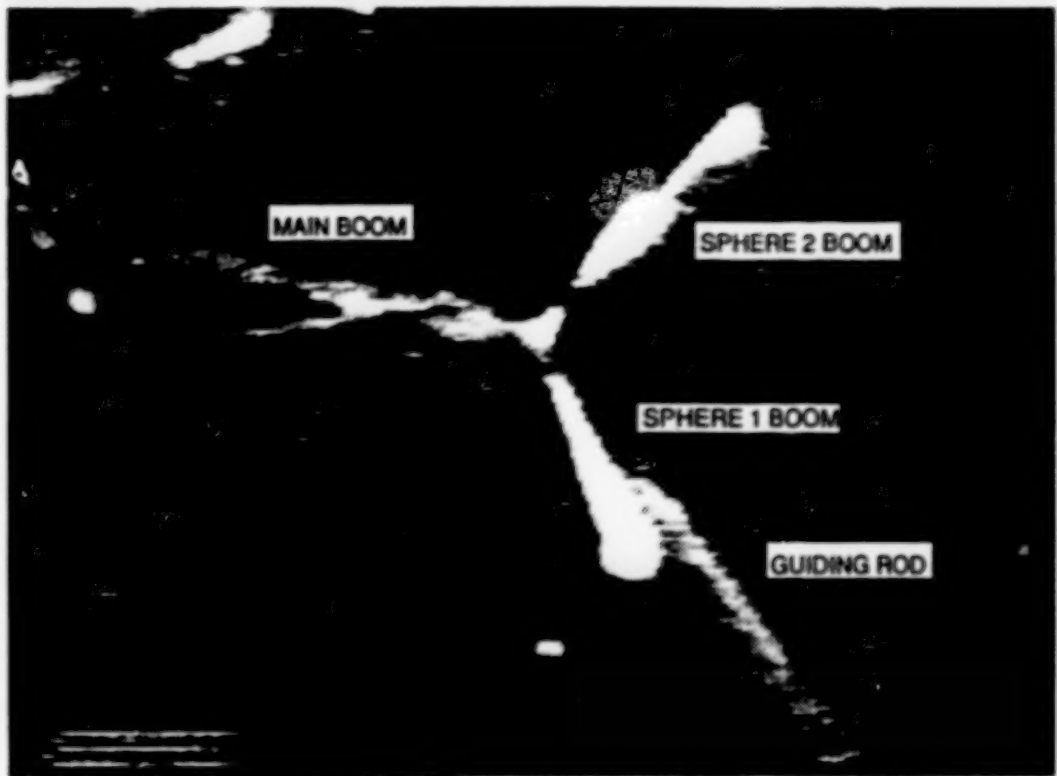


Fig. 19. Image from the LLLTV for the same voltage bias operation as Figure 18 just after an ACS gas release.

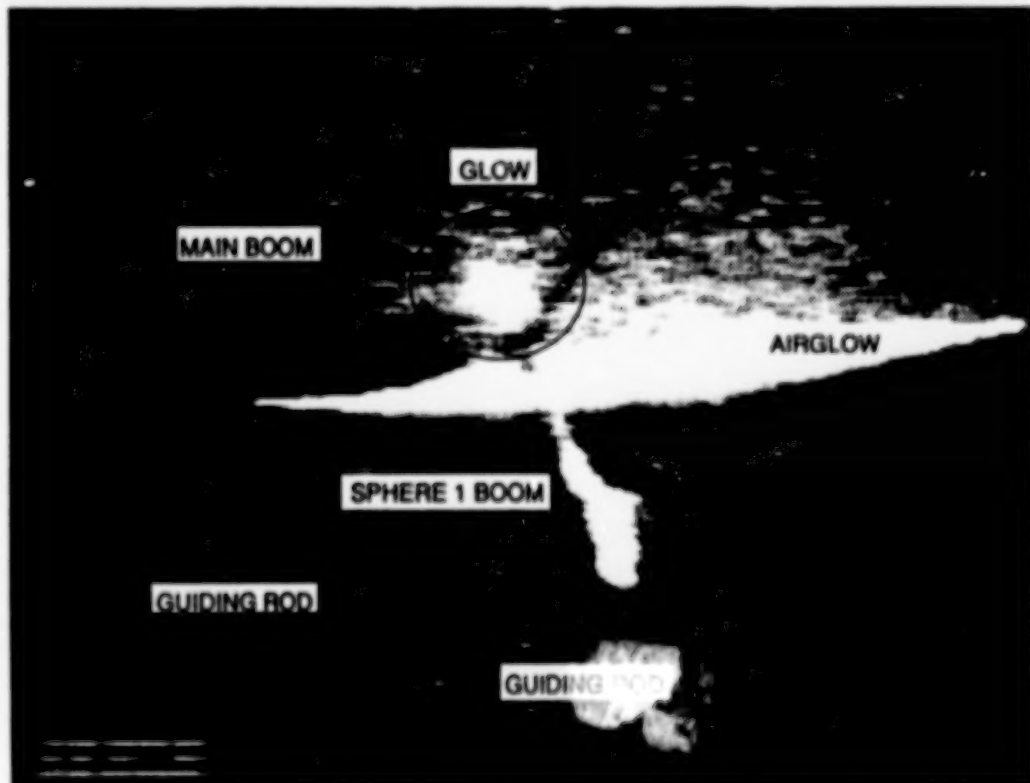


Fig. 20. Image from the LLLTV for a sphere 1 potential of 43 kV at 263 km.

CURRENT COLLECTION BY A SPHERICAL HIGH VOLTAGE PROBE:  
ELECTRON TRAPPING AND COLLECTIVE PROCESSES

P.J. Palmadesso (Plasma Physics Division, Naval Research Laboratory,  
Washington DC 20375

We summarize the results of theoretical studies of the interaction of an uninsulated, spherical, high voltage (10's of KV positive) probe with the ionospheric environment. The focus of this effort was the phenomenon of electron trapping and its implications for breakdown processes (collisional regime) and the current-voltage relationship governing current collection (collisionless regime) in space-based pulsed power systems with high voltage components exposed to space, e.g., the SPEAR I experiment.

In a force field consisting of an attractive radial electric field and a uniform magnetic field, the electric field provides a potential well in which electrons can be bound if they have insufficient energy to escape and cannot be captured by the spherical probe (by virtue of angular momentum conservation and/or the effects of the magnetic field). Electrons entering such a well from infinity may become trapped if they lose energy as a result of some scattering process acting within the well, such as inelastic collisions with neutral atoms or wave-particle interactions due to plasma collective effects. Alternatively, trapped electrons may be created within the well as a result of ionizing collisions between neutrals and other electrons. Trapped secondaries may be accelerated and then ionize other neutrals, raising the possibility of an avalanche.

In the opposite limiting case, when the neutral density is low and/or electric field fluctuations due to collective effects are strong enough so that trapped electron lifetimes fall below the ionization time, breakdown is inhibited, but the electron trapping phenomena persists if plasma scattering due to collective effects is significant within the sheath. In the absence of scattering all the electrons at any point  $r$  within the sheath have kinetic energy  $e\Phi(r) + k_B T_{ai}$ , where  $k_B T_{ai}$  is the initial thermal energy of the  $i^{\text{th}}$  electron, regardless of the path they followed to reach  $r$ . In the case of a multi-kilovolt body in the relatively cold ionospheric plasma  $k_B T_{ai}$  is negligible, so that the electrons occupy a thin spherical shell of radius  $v_s = [2e\Phi(r)/m_e]^{1/2}$  and thickness  $v_a \ll v_s$  in velocity space. Electric field fluctuations generated by instability of this shell distribution, convection of pre-sheath instabilities, etc., are likely to result in velocity space diffusion which would move electrons down the very steep gradients on the inner and outer surfaces of the shell. Electrons moving inward in  $v$ -space are energetically trapped if they lose more energy than their initial thermal energy ( $k_B T_a \sim .1$  eV in the ionosphere). We assume that trapped electrons diffuse toward the sphere and are eventually captured, and calculate current-voltage curves for various levels of turbulent diffusion. Our results indicate that the sheath structure and the current-voltage relation of a charged sphere configured as in the originally planned SPEAR I experiment (with an operating plasma contacter) would be substantially modified by the combined action of trapped electrons and plasma instabilities.

This work was supported by the Defense Nuclear Agency under the SPEAR Theory Project.

## OBSERVATIONS OF THERMAL ION INFLUXES ABOUT THE SPACE SHUTTLE

J. M. Grebowsky

NASA/Goddard Space Flight Center, Planetary Atmospheres Branch,  
Code 614, Greenbelt, Maryland 20771

A. Schaefer

Marquette University, Physics Department  
Milwaukee, WI 53233

Abstract. Ion mass spectrometer measurements made, as part of the University of Iowa's Plasma Diagnostic Package, on the STS-3 and Spacelab 2 Space Shuttle missions sampled a variety of ion composition and collected ion current responses to gas emissions from the vehicle. The only other shuttle ion measurements were made by an AFGL quadrupole spectrometer flown on STS-4. Gas emissions change the distribution of the incoming plasma through scattering and charge transfer processes. A background flux of contaminant ion species (mostly relating to water) always exists in the near vicinity of the shuttle with a magnitude which is dependent on the look direction of the spectrometer but which varies differently with changes in the angle of attack than that of the ambient ions. There is a near shuttle wake cavity in the contaminant ion distributions which has a different spatial configuration than the wake of the ambient ions. Although water dumps produce the most persistent ion perturbations, the sources for ion current modification were best delineated from measurements made when only one or two of the Reaction Control System thrusters fired for a relatively long duration. Contaminant ion perturbations associated with such firings were observed to persist for the order of a second after the cessation of the firings. The dense thruster plumes are efficient collisional, charge exchange barriers to the passage of ambient ions. Collected ion current perturbations were more evident for firings of the rear verniers, whose plumes scatter off projecting surfaces, than for the nose thrusters. The effect of the Vernier firings was found to depend not only on the location and attitude of the spectrometer with respect to the shuttle and thruster plume direction, but also on the orientation of the local magnetic field with respect to the shuttle velocity.

### Background

Several space shuttle missions carried experiments to measure the concentrations and thermal properties of the low energy plasma in the near vicinity of the vehicle. These observations have shown that the thermal ion distributions and the ambient ion influxes to collectors in the vicinity of the spacecraft are affected by gases emitted from the spacecraft. The exact manner in which the incoming ion fluxes are modulated depend upon the properties of the gas releases (such as their composition, source locations and durations), the attitude of the moving

spacecraft, the local magnetic field direction and of course the location of the ion current detector with respect to the shuttle and payloads. In this paper features of this interaction between incoming ion fluxes and the shuttle's "contaminant" neutral gas environment will be highlighted by using ion mass spectrometer measurements taken in the immediate vicinity of the space shuttle. These measurements serve as a means of tracing the dynamics of plasma perturbations in the vicinity of large space vehicles as well as providing a background for predicting consequences in the vicinity of even larger gas emitting space structures such as the space station.

### Ion Spectrometer Experiments

Ion composition measurements were made by ion mass spectrometers on three space shuttle missions. An ion-neutral quadrupole mass spectrometer was flown by the Ionospheric Disturbances and Modification Branch of the Air Force Geophysics Laboratory on the STS-4 mission in June-July 1982. A Bennett RF ion mass spectrometer supplied from Goddard Space Flight Center was flown as part of the University of Iowa's Plasma Diagnostic Package (PDP) within the NASA Office of Space Science-1 (OSS-1) payload on the STS-3 flight in May 1982 and was then refloated as part of the Spacelab 2 (SL-2) payload on the STS-51F mission in July-August 1985.

The ion mode of the ion-neutral spectrometer as described by Narcisi et al. (1983) provided high temporal and good mass resolution of ion species from within the near vicinity of the shuttle's open payload bay. The Bennett ion mass spectrometer although more limited in temporal and mass resolution was flown for a longer period of time under a more varied complement of positions- particularly on the SL-2 mission where a concentrated period of Shuttle operations was focused on Plasma Diagnostic Package (PDP) science objectives with planned attitude changes, remote manipulator system (RMS) movement of the PDP and even a brief PDP free flight away from the shuttle. In this paper only observations made while the instruments were secured within the open cargo bay or on the RMS will be considered. The general range of altitudes of the shuttle orbits on these three missions fell between approximately 240 and 320 kilometers, i.e. within the F2 region of the ionosphere.

One characteristic of these ion spectrometers is the directionality of their field of view and the resultant dependence of the collected ion flux on the average direction and magnitude of the incident ion velocity with respect to the spectrometer orifice as well as on the incident ion concentrations. The angle of attack response of the PDP spectrometer followed that shown in Figure 1 for the same type of instrument that was flown on Atmosphere Explorers C and E. This dependence on angle of attack plays a significant role in studies from the shuttle since ion measurements are most frequently made when shuttle operations and attitudes are dedicated to other experiments resulting in other than an optimum ram pointing configuration for the spectrometer. Further, as will be seen, ions may be flowing relative to the shuttle from a direction different from that of ram. Hence one must be aware of the

orientation of the spectrometers with respect to the vehicle's coordinate system. The ion spectrometer look directions are indicated in Figure 2 for the 3 shuttle missions when the experiments were anchored in the bay. On STS-3 (OSS-1) the PDP was secured within the bay on the rear pallet with its ion spectrometer facing directly toward the port side of the bay; on STS-4 the spectrometer (as described by Narcisi et al., 1983) looked over the starboard side wing but was pitched up by 12°; and on SL-2 the PDP again was on the rear pallet this time with the spectrometer looking forward. Because of complexities in the spectrometer response due to off ram angles it is not feasible to routinely convert the measured ion currents into number densities, so only raw measured currents of the ion species are used to explore the vehicle environment.

It is to be noted also that the Bennett ion mass spectrometer flown on the shuttle missions cycled through 4 sensitivity level mass scans. These levels were produced by the application of a sequence of 4 retarding potentials on a grid positioned in front of the current collector to eliminate ion species which have not been resonantly accelerated in the RF mass selecting portion of the instrument. This is described more fully in the paper by Grebowsky et al. (1987). The choice of the step or level of the data to be studied is made based on whether high mass resolution or high sensitivity is sought - the mass resolution increases with decreasing sensitivity. In the subsequent plots of these measurements the sensitivity level will be cited on the plot without further elaboration. For reference: Level 1 corresponds to the least sensitive mode with sensitivity increasing to a maximum on Level 4.

#### Quiescent Ion Environment Near the Shuttle

The most notable feature of the near-shuttle thermal ion environment is the persistence throughout the duration of all the flights of ion species that are not ambient in origin - most prominently the species  $H_2O^+$  with lower influxes of  $H_3O^+$ . Figure 3 shows observations made during the STS-4 mission when the ion-neutral spectrometer orifice pointed nearly into the ram direction. A relative influx of water ions was detected that was consistently about two orders of magnitude below that of the incoming ambient  $O^+$  ion fluxes. It was noted by Narcisi et al. (1983) that earlier in this mission, background levels of the water ions were of the order of 10% indicating a significant falloff with mission elapsed time.

The SL-2 ion spectrometer observations in the ram direction detected a similar relative background of incoming water ion currents. One of the better examples of this was obtained on a PDP dedicated operation in which the shuttle flew perpendicular to its X axis (i.e., the tail-nose line) rolling about this axis, while the PDP extended on the RMS away from the shuttle was synchronously twisted to maintain a fixed orientation of the PDP to the oncoming ambient plasma velocity. A few of these twist sequences maintained an ion spectrometer look direction into ram. These measurements made during the second day of the mission are depicted in Figure 3. On the ram side of the shuttle where ambient

ions have unimpeded access to the spectrometer, the measured water ion currents were of the order of two magnitudes below that of the ambients. The other prominent ion displayed,  $\text{NO}^+$ , is common to the bottomside of the F-layer and in this instance may not be a contaminant ion. A further survey of the SL data showed a tendency for a decrease of the fractional occurrence of water ion with time through the mission, but even at the end of a week's observations the contaminant fluxes were still between two and three orders of magnitude of those of the ambient  $\text{O}^+$  ions.

These observations demonstrate the general presence of a relatively stable influx of ions around the shuttle which decreases with mission duration but never disappears. The source of the water ions is accepted to be a water bearing gas cloud traveling with the shuttle which charge exchanges with the ambient  $\text{O}^+$ . If the water molecule concentration in the cloud is dense enough the production of  $\text{H}_3\text{O}^+$  will also become very prominent due to charge transfer reactions between the neutral and ionized water molecules as described by Narcisi (1983) and Narcisi et al. (1983). The existence of such a cloud has been directly detected by neutral spectrometers flown on several missions (e.g., Carignan and Miller, 1983; Narcisi et al., 1983; Wulf and von Zahn, 1986). These water related ion-neutral reactions are rapid enough to lead to prominent depletions of local ambient plasma concentrations around space vehicles (e.g., Mendillo, 1981). It is difficult without a mother-daughter type of experiment from the space shuttle to determine quantitatively the magnitude by which the incoming ram flux of ambient ions is significantly reduced in passing through the quiescent gas cloud. The occurrence of only a relatively small fractional percentage of incident water ion fluxes under nominal conditions appears to argue against a significant depletion of the fluxes impinging upon the vehicle although Hunton and Calo (1985) have demonstrated that the ion-neutral collision rates may be rapid enough to produce a change in the incoming ambient  $\text{O}^+$  velocity distribution function. Disturbed conditions however, as will be shown, do exist under which the incoming ion fluxes are notably perturbed. The observed decrease of the average water ion influx with mission elapsed time is anticipated due to the degassing of the spacecraft. The STS-4 mission apparently had the largest contaminant fluxes initially due to the fact that it was launched following a severe rainstorm which damped the spacecraft tiles.

Ion spectrometer measurements on the STS-3 mission could not be used to evaluate the average ram influx toward the shuttle because the spectrometer never had the ideal low angle of attack configuration. However its position on the rear pallet within the bay provided a unique perspective for exploring ion fluxes generated or scattered low within the bay. Figure 5 shows the ion measurements made during part of one STS-3 orbit while the PDP was stowed in the bay. This type of profile was repeatedly seen on this mission because of the persistence employment of the same shuttle attitude configuration which was a nose-to-sun attitude with a shuttle roll period twice the orbital period. Within the bay the spectrometer was facing directly toward the side of the shuttle which would effectively shadow part or all of the incoming ion fluxes to the spectrometer. The only ions with unimpeded access to

the spectrometer are those incident from the port side from the topside of the bay. The ion currents collected in this bay configuration did not increase with decreasing spectrometer angle of attack but maximized when the incoming ion flow was from behind the spectrometer (negative azimuth angles in the figure correspond to shuttle motion in the starboard direction). All the ion species currents tended to track the variation of the shuttle's pitch angle with the maximum currents seen when the bay (and not the spectrometer orifice) was facing most directly into the shuttle velocity direction. In this situation the relative percentage of water ion current to that of the ambient ions, which is the order of 10%, cannot be compared to the previously discussed examples of unobstructed incoming ion fluxes. The buildup of the ion distributions seen in the bay on the STS-3 mission instead occur in association with the measured neutral gas pressure buildup in the bay that is observed as the bay faces more directly into the shuttle velocity direction (Shawhan et al., 1984).

The STS-3 measurements seen in Figure 5 also demonstrate that in addition to water related contaminant ion species occurring in the vicinity of the shuttle, ions such as  $\text{NO}^+$  and  $\text{O}_2^+$  also have a local production source. These ions can readily be produced by charge exchange reactions of ambient  $\text{O}^+$  ions with neutral molecules of oxygen and nitrogen which are enhanced in concentration at the shuttle (Wulf and von Zahn, 1986). It is to be noted also that an analysis of the position of mass peaks in the sweep spectra of the instrument in this STS-3 example indicates that ions are formed or scattered by collisions within the plasma sheath of the -10 volt potential that exists on a guard ring surrounding the entrance aperture of the instrument. Hence the observations are consistent with the presence of not only water species ions but also molecular oxygen and nitric oxide ions of near shuttle origin as part of the usual shuttle background generated ion population. This was also noted from measurements of the spherical retarding potential analyzer flown on the same mission (Raitt et al., 1984 and Siskind et al., 1984). Previously Grebowsky et al. (1983) noted evidence of  $\text{CO}_2^+$  ions also, but a further analysis of the spectrometer response indicated that an instrument harmonic of  $\text{O}^+$  occurs at the same telemetry mass location and may have dominated over the background presence of carbon dioxide ions.

#### Directional Dependence of Shuttle Ion Influxes

The shuttle ion measurements taken with the instruments pointing in different directions with respect to the vehicle's velocity show distinctly different responses between ambient and contaminant ion species. Narcisi et al. (1983) showed that observations made with the STS-4 spectrometer off ram did not detect the same relative ambient/contaminant ion current influxes as were discussed previously for near ram conditions. At pointing angles from ram between 30 and  $40^\circ$  for example they noted comparable current magnitudes for both the dominant and ambient ions. It was noted that the collected number fluxes of the water ions varied less with changes in angle of attack than did the ambient  $\text{O}^+$  - an indication that the  $\text{H}_2\text{O}^+$  ions had higher thermal velocities than the ambient plasma.

The angle of attack variation of the Bennett spectrometer (as shown in Figure 1) is not as predominantly affected by the thermal velocity of the incoming ions as is the quadrupole spectrometer, the field of view of the former is  $180^\circ$  compared to the latter's  $30^\circ$ . The angle of attack sensitivity of the Bennett device for supersonic incident ion flows is more dependent on the average component of the incident velocity perpendicular to the longitudinal axis of the cylindrical spectrometer compared to the rf resonant velocity along the tube axis. Nevertheless the relative current ratio of the contaminant and ambient ions measured with the Bennett rf spectrometer was observed to vary significantly with the angle of attack of the instrument from the shuttle ram direction. This is seen for example in Figure 6 which presents SL measurements during a period when the shuttle was flipping tail-over-nose nose along its orbital path as depicted in the inset. The  $O^+$  current increased with a decreasing angle between the shuttle velocity and the outward normal to the spectrometer orifice (which points forward in the bay) until the instrument was shadowed from the incoming ambient plasma by the front of the shuttle. The ion species  $NO^+$  followed a similar trend insofar as its current peaked coincidentally with that of the ambient  $O^+$ , but its overall current variation did not parallel that of the oxygen. This was particularly evident when the bay initially emerged from the shuttle wake and turned directly into the ram direction. This behavior supports the conclusion previously arrived at from the in-bay STS-3 observations that there is a contaminant  $NO^+$  source in addition to an ambient influx of the same ion species. The other contaminant ion detected on the orbit depicted in Figure 6, the water ion species, shows a definite maximum occurring before the ambient  $O^+$  influx into the spectrometer maximized. This water ion behavior is consistent with a direction of motion different from that of the ambient ionospheric plasma.

The different behavior of the water and oxygen ions with varying instrument angle of attack is a common feature of the shuttle environment. Its explanation lays apparently in the presence of the ambient magnetic field. Water ions formed by the charge exchange between ambient  $O^+$  ions with water molecules in the cloud moving with the shuttle have the shuttle velocity at the moment of their origin. The Lorentz force exerted on these ions due to the presence of the earth's magnetic field causes them to gyrate about the local magnetic field line rather than moving along with the shuttle. Those contaminant ions produced upstream of the shuttle can be subsequently intercepted by the vehicle since these pick-up ions in the shuttle frame of reference will have an average flow velocity corresponding to their guiding center velocity perpendicular to  $B$ . This will in general result in their incidence on the shuttle obliquely from the ram direction as depicted schematically in Figure 7. The effect will be to produce a wake configuration behind the shuttle that is different for contaminant and ambient ions. A similar situation may prevail for other contaminant molecules such as  $NO^+$  although the dynamics will differ due to differing masses and velocities at their origin.

Eccles (1988) has provided further evidence for the existence of differing wake configurations for ambient and contaminant ions by doing

an extensive model calculation of the contaminant ion distributions incident upon the shuttle. This study applied a model neutral cloud which charge exchanged with ambient oxygen ions to produce water ions whose trajectories were electrodynamically modelled in the shuttle frame of reference. The calculation also included a simple model of the payload bay configuration to approximate important shadowing effects. Figure 8 shows the result of one such set of this model's calculations for conditions characteristic of a particular sequence of three SL-2 shuttle orbits. The ion mass spectrometer measurements made from within the bay show distinct differences between the ambient and contaminant ion variations with changing attitude. Using a very approximate angle of attack and energy dependence for the spectrometer, the study of Eccles modeled the variations in the relative ion currents that should be collected by the spectrometer. The model produced water ion current variations that have a wake boundary offset from that of  $O^+$  ions which is similar to the observations. Although the calculation, not surprisingly due to the complexity of both the instrument response and spacecraft environment, does not reproduce all aspects of the measurements it does convincingly demonstrate that the contaminant water ions form an ion source that flows on the average toward the shuttle not from the ram direction but from a direction normal to the local magnetic field. Enhanced temperatures of the water ions also are required to explain the measured relative amplitudes of the current variations.

#### Water Dump Effects

Excess water generated on the shuttle has to be released periodically. This is done predominantly by a water relief vent near the forward bulkhead on the port side of the vehicle. The dump durations last for the greater part of an hour and release water amounts typically in the range of 50 to 100 kg. The Flash Evaporator System is another method used to release water, but will not be considered here since it has less of an impact on the overall thermal ion distributions detected by the spectrometer than does a water dump. A further discussion of details of these operations and their effect on the spacecraft environment can be found in the study of Pickett et al. (1983).

Since the quiescent ion environment about the shuttle consists predominantly of ion species that relate to charge transfer processes with neutral water molecules, it is anticipated that water dumps will significantly perturb the thermal ion influxes in the vicinity of the spacecraft. One example of a dump on the STS-3 mission is presented in Figure 9. In this example the water was released throughout the night until shortly after dawn along the orbit. The effect of the dump was only dramatically evident near sunrise when the collected water ion currents within the bay had magnitudes comparable to those of the ambient  $O^+$  ions. That this is an effect of the dump is clearly established by the abrupt drop of the water ion current at the moment of termination of the dump. An effect on the ambient ions is not clearly evident from the measurements on this one orbit. However, if it is compared to measurements made predawn on the preceding shuttle orbit which had the same attitude configuration and which was previously

considered in Figure 5, it appears that the prominent predawn maximum in the  $O^+$  current is reduced in magnitude during the dump. The choppy nature of the predawn currents in Figure 9 is the result of the periodic firing of an electron gun experiment during this time resulting in the periodic positive charging of the PDP and its spectrometer that repelled incoming positive ions. One anticipates on the basis of the earlier discussion that the introduction of more water molecules to the cloud about the shuttle would lead to a reduction of the incoming ionospheric oxygen ion fluxes due to scattering and charge transfer reactions. Another pervasive effect of the cloud of water emitted is also apparent in the appearance of quantities of  $H_3O^+$  ion currents that are comparable to those of  $H_2O^+$  - the 18AMU ions associated with the water dump depicted in Figure 9 occurred coincidentally with nearly identical currents of 19 AMU ions, the latter of which then fell below the sensitivity threshold of the instrument after the cessation of the dump.

Another example of a water dump effect is seen in Figure 10 which shows ion spectrometer measurements made from within the payload bay on the SL-2 mission. In this instance the water ion currents during the dump were almost an order of magnitude greater than those of  $O^+$  when the spectrometer was clearly within the geometrical wake of the shuttle. A calculation of the direction of influx of water ions in the shuttle frame of reference perpendicular to the magnetic field showed that they have a flow direction into the spectrometer. Hence the large differences in the two species currents can be explained not only as an enhancement in water ion production but also by differing ambient, contaminant ion wake configurations. The perturbation by the water release ceased abruptly after the dusk terminator was crossed and the attitude of the shuttle was such that the spectrometer orifice was pointed directly into the spacecraft ram direction. The effects of the water dump on the ambient ion influx is not clearly evident in this example since the spectrometer turned away from the ram direction at the onset of the dump and then rapidly turned into ram near the cessation. Hence no fixed attitude frame was available to compare before and after effects - the previous and following orbits could not be used because the attitude configurations were different.

The extra water added to the shuttle environment by the dumps does have a significant impact on the ion fluxes and composition in the near vicinity of the shuttle. However the contaminant ions still appear to have the same trajectories as those produced under quiescent conditions so that ambient and contaminant ion wake configurations can be similarly offset from one another in either environment. This is demonstrated in the last water dump example to be considered which is shown in Figure 11. The onset of the dump was associated with an abrupt increase in the water ion currents but as noted above it is difficult from one orbit to determine in detail changes brought about by the water release. The water ion currents dropped off out of step with the ambient  $O^+$  currents as the bay turned into the shuttle's wake. This is characteristic of the behavior in the quiescent state. Indeed this orbit is the central orbit of the sequence of 3 plotted in Figure 8. The preceding and following orbits were characterized by nearly identical shuttle

attitudes so the effects of the water dump can be singled out to be a factor of 2-3 reduction in observed  $O^+$  currents produced by collisions within the water cloud that occurs in association with a definitely observed enhancement of water ion currents during the entire dump period except in the deep wake of the shuttle. However the extra water added around the shuttle had no pronounced effect on the location of the contaminant ion or ambient ion wake boundaries.

### Thruster Effects

The Reaction Control System (RCS) shuttle engine firings in orbit have been noted to have an impact on many shuttle plasma measurements (e.g., Pickett et al., 1983). Unlike the water dumps however, which occur for prolonged periods of time, the thrusters (particularly the attitude tweaking verniers) typically fire for fractions of a second and release directed beams of effluents with velocities of the order of a few km/s in different directions from the shuttle depending on the particular thrusters being fired. Because sequences of different combinations of multiple thruster firings of varying durations are typically executed it is not a straightforward task to sort out the details of how an individual thruster firing affects the ion fluxes in the vicinity of the shuttle. However the thrusters do have a more prominent impact on the local ionization than the water dumps. Even though they are short in duration compared to the water releases they release gases at a rate of the order of 5000 kg/hr from the primary engines and 150 kg/hr from the verniers. These rates are large in comparison to the release rates of 50-100kg/hr and 10 kg/hr that are typical of water dumps and flash evaporator releases respectively.

The effects of the RCS firings on the thermal ion distributions are multifaceted. For example reductions in the ambient  $O^+$  number fluxes in the vicinity of the shuttle analogous to the effects of the previously discussed water dumps are sometimes observed simultaneously with impulsive enhancements in the measured currents of contaminant ion species such as  $H_2O^+$  (and/or)  $NO^+$ . Figure 12 shows such an example from SL-2 data. Figure 13 on the other hand shows an example from STS-4 where depletions of the  $O^+$  currents are observed with corresponding reductions in the  $H_2O^+$  currents during thruster firings (from Narcisi et al., 1983). There are also times when the measurements detect ambient ion current enhancements above their quiescent levels such as those labeled in the earlier discussed Figure 9 and times when no noticeable effect is detectable in the ion measurements during thruster firings. In order to isolate the causes of some of these effects, a comprehensive analysis of SL-2 ion spectrometer measurements was made restricting attention to only vernier engine firings in which one or at most 2 of the verniers fired simultaneously. The firing events were further restricted to those with duration greater than 1 second. The latter criterium was established because the ion spectrometer took 2.4 seconds to sweep through all ion masses and it was desired to insure that there was a high probability that at least one of the ion species associated with a thruster perturbation was sampled by the instrument during the firing.

Figure 14 depicts the locations of the 3 vernier thrusters on the port side of the shuttle. There is a symmetric trio on the starboard side the names of which correspond to the port side nomenclature with the L's replaced by R's. One of the significant features of their locations is the positioning of the rear verniers near prominent projections of the shuttle in contrast to the the shuttle topology near the two forward verniers, F5L and F5R. Due to the expansion of the exhaust plumes, the rearward thrusters will be partially scattered off shuttle surfaces but the forward ones will not. This has been noted by Wulf and von Zahn (1986) to account for the detection of neutral molecule concentration enhancements in the bay during rear thruster firings and the absence of such effects with the firing of the thrusters on the nose. Isolating attention to the verniers rather than all RCS thrusters considerably simplifies the number of thrusters to keep track of - i.e., only 6 verniers compared to 38 main thrusters.

The combustion within a thrust chamber results in the formation of ions as well as the predominantly neutral hot thrust gases and it is possible that such ions could produce an enhancement in contaminant ion number fluxes near the shuttle in association with the firings. Since water, nitric oxide and molecular hydrogen are produced in the nitrogen tetroxide - monomethyl hydrazine reaction similar ion species could appear in measurable concentrations. However the predominant constituents of the thruster jet are neutral molecules of high concentration that enhance, albeit in a complex geometrical fashion, the cloud of gases moving with the shuttle. These neutral effluents will, through collisional reactions with the ambient plasma, result in the production of contaminant ion species. This is clearly seen by taking a model of the molecular concentration variations in a steady state vernier exhaust plume and computing the mean free path distribution for an ambient  $O^+$  ion moving through it. The results of such a computation (depicted in Figure 15) demonstrate that the thruster plumes in the near vicinity of the spacecraft are essentially opaque to the passage of ambient ions which through charge exchange will yield their charge to the neutral thruster jet effluents.

Considering all ion spectrometer observations made while the PDP was secured in the SL-2 bay, a search was made for all individual and paired firings of the verniers. The appended Table lists the number of occurrences of each set of Vernier firings, the number and percentage of firings which caused observable ion perturbations, and the average duration of the firings ignoring the few extremely long ones. Enhancements in ion species currents were the dominant effects observed. The number of events for which depletions in one or more species currents were the result of the firings were infrequent and are listed in parentheses in the Table. The forward verniers although not impacting any prominent scattering surfaces were still at times detectable in the ion measurements taken from within the shuttle payload bay. On the other hand there is evidence that the scattering of the plumes off spacecraft surfaces has a significant impact on the thermal ion distributions - there were significantly more detections of perturbations by the rear thruster firings - particularly for the downward thrusters which skirt past the wings.

The observations at first look seem consistent with the detection of ionization that is produced in the combustion and streams out with the neutral products. For example Figure 16 shows a continuous time segment of SL-2 measurements when the PDP was held out over the port side and the spectrometer was facing rearward and the two opposing rear downward thrusters fired. All contaminant ions anticipated - i.e., 18, 19, 28 and 30 AMU species- were enhanced in current magnitude in association with the firing compared to conditions in the following cycle of sensitivity sweeps when the thrusters were off. However the 1 and 16 AMU ions are ambient in origin and are not from the thruster chamber and yet their collected currents are enhanced relative to the quiescent conditions existing on the sweeps before and after the thruster sequence. This is evidence that the neutral effluents of the thrusters are modifying the ambient ion distributions and perhaps through charge exchange are responsible for the contaminant ions observed rather than ions produced in the thrust reaction. The measured effect lasts approximately for the duration of the firing and appears to endure after the firing ceases - the latter behavior may not be a persistence of the effect however since there was a lack of total synchronization of the PDP data record time and that of the spacecraft clock on this mission. This resulted in unresolvable varying time differences between the recorded thruster firing times and the times of PDP measurements of as much as a few seconds (personal communication, R. L. Brechwald, U. Iowa, 1988).

Evidence that charge exchange between ambients and thruster plume neutral molecules plays a significant role in contaminant ion production was found in several instances in which the observed ion perturbation duration was the order of a second longer than the duration of the thruster firing. Although absolute times of thruster firings and instrument sampling times might be offset, shuttle time intervals given for the thruster firings can validly be compared to intervals of time determined from the ion spectrometer mass sweep scans which are set by internal oscillators. One such example of the persistence of the observed ion effect beyond the duration of the thruster firing is depicted in Figure 17. This again is an example of SL-2 ion measurements taken with the PDP on the extended RMS arm. The thruster perturbations of the ions are in evidence by the obvious difference in the amplitudes and ion species of the ion peaks near the time of the firing from those detected for the same sensitivity levels on the cycle of sweeps before and after the firing. The peaks labeled H correspond to instrument harmonics of 18 AMU ions - these will vary in amplitude in step with the 18 AMU influx occurring at the same time and can be used to denote the presence of the water ions. Such harmonics are natural to the RF response of this type of instrument. The observations in the figure show that the enhanced ionization resulting from the thrusters lasts for over a second longer than the duration of the firings. Since the thruster cutoff times are extremely rapid these observations cannot be accounted for by thruster chamber produced ions.

Finally, it is inherent to the thruster effects that they are dependent upon the ambient magnetic field direction with respect to the moving vehicle. Figure 18 gives an example of measurements during 2

segments of the same orbit during which the same two rear vernier thrusters fired for similar times and during similar sensitivity level scans of the spectrometer - in one instance ion perturbations were definitely detected from within the bay, but in the other nothing was measured above the instrument sensitivity. Comparing the spacecraft velocity vector directions in X,Y,Z body axis coordinate that are listed in the figure shows that the shuttle's attitude with respect to its velocity was identical in both instances. However the magnetic field direction angles in the same coordinate system were distinctly different. Indeed calculating the pickup ion guiding center velocity for the two segments reveals that the thruster related ions were not measured when the pickup velocity was large and directed predominantly into the belly of the spacecraft - i.e., the contaminant ions were shadowed strongly by the shuttle and prevented from encountering the spectrometer within the bay. When the thruster ion effect was detected the corresponding pickup ion flow velocity was relatively low in magnitude and its dominant spatial direction was not toward the belly - hence contaminant ions could more readily have paths that take them to the spectrometer than in the previously discussed instance. Hence just as for the quiescent state and water dump ion contaminant distributions, some of the thruster effects are consistent with charge exchange production and interactions with the shuttle that are characterized by a plasma wake configuration different from that of the ambient ions.

#### Comment

The thermal ion environment of large gas emitting bodies like the shuttle and the space station is always characterized by the presence of ions not of ambient origin. These ions are due predominantly to charge exchange interactions between the ambient ionospheric positive ions and the extended gas cloud moving with the vehicle. After the initial period of degassing of the spacecraft the effects on the ion currents collected near the vehicle are relatively small under quiescent conditions. However for impulsive gas releases such as thruster firings or water releases there are pronounced perturbations in the incoming number fluxes and energy distribution of the thermal ions that need to be fully modeled in order to determine the ramifications for current collecting devices.

#### References

- Carignan, G. R., and E. R. Miller, Mass spectrometer, in STS-2,3,4, Induced Environment Contamination Monitor (IECM), Summary Report, edited by E. R. Miller, NASA TM-82524, 1983.
- Eccles, J. V., The electrodynamics of plasma within the outgas cloud of the Space Shuttle orbiter, Ph.D. Dissertation, Center for Atmospheric and Space Sciences, Utah State University, 1988.
- Grebowsky, J. M., M. W. Pharo III, H. A. Taylor, Jr., and I. J. Eberstein, Measured thermal environment of STS-3, paper presented at the Shuttle Environment and Operations Meeting, Am. Inst. of Aeronaut. and Astronautics, Washington, D.C., October 31, 1983.

- Grebowsky, J. M., H. A. Taylor, Jr., M. W. Pharo, and N. Reese, Thermal ion complexities observed within the Spacelab 2 bay, Planet. Space Sci., 35, 1463, 1987.
- Grebowsky, J. M., H. A. Taylor, Jr., M. W. Pharo, III and N. Reese, Thermal ion perturbations observed in the vicinity of the Space Shuttle, Planet. Space Sci., 35, 501, 1987.
- Hunton, D. E., and J. M. Calo, Low energy ions in the shuttle environment evidence for strong ambient-contaminant interactions, Planet. Space Sci., 33, 945, 1985.
- Mendillo, Michael, The effect of rocket launches on the ionosphere, Advances in Space Res., 1, 275, 1981.
- Murphy, G. R., S. D. Shawhan, and J. S. Pickett, Perturbations in the plasma environment induced by the orbiter's maneuvering thrusters, Am. Inst. of Aeronaut. and Astronautics, paper 83-2599, 1983.
- Narcisi, R. E., Trzcinski, G. Frederico, L. Wydyka and D. Delorey, The gaseous and plasma environment around space shuttle, paper presented at the Shuttle Environment and Operations Meeting, Am. Inst. of Aeronaut. and Astronautics, Washington, D.C., November 2, 1983.
- Narcisi, R. E., Quantitative determination of the outgassing water vapor concentrations surrounding space vehicles from ion mass spectrometer measurements, Adv. Space Res., 2, 283, 1983.
- Pickett, J. S., G. B. Murphy, W. S. Kurth, C. K. Goertz and S. D. Shawhan, Effects of chemical releases by the STS 3 orbiter on the ionosphere, J. Geophys. Res., 90, 3487, 1985.
- Raitt, W. J., D. E. Siskind, P. M. Banks, and P. R. Williamson, Measurements of the thermal plasma environment of the space shuttle, Planet. Space Sci., 32, 457, 1984.
- Shawhan, S. D., G. B. Murphy, and J. S. Pickett, Plasma Diagnostics Package initial assessment of the shuttle orbiter plasma environment, J. Spacecraft, 21, 387, 1984.
- Siskind, D. E., W. J. Raitt, P. M. Banks, and P. R. Williamson, Interactions between the orbiting space shuttle and the ionosphere, Planet. Space Sci., 32, 881, 1984.
- Smith, S. D., Improvements in rocket engine nozzle and high altitude plume computations, presented as paper 83-1547 at the AIAA Thermophysics Conference, Montreal, Canada, June 1983.
- Wulf, E. and U. von Zahn, The shuttle environment effects of thruster firings on gas density and composition in the payload bay, J. Geophys. Res., 91, 3270, 1986.

TABLE1-2 VERNIER PAIR FIRINGS  
Longer Than 1 Second

<u>PAIR</u>	<u>FIRINGS</u>	<u>ION EFFECT (DROP)</u>	<u>% SEEN</u>	<u>AVERAGE DURATION (SEC.)</u>
F5L	7	0	0	1.6
F5R	3	0	0	1.3
F5R,F5L	46	19(3)	41	1.7
F5R,R5R	22	13(2)	59	2.0
F5R,L5L	13	8	62	1.9
L5L,L5D	13	13(4)	100	1.7
R5R,R5D	9	9(2)	100	1.6
L5D,R5D	118	100(7)	85	3.5

246

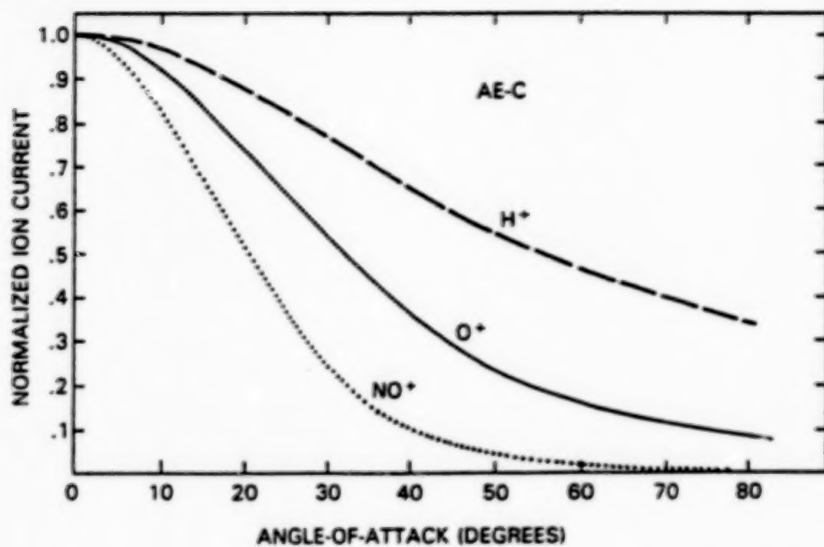


Figure 1. The variation of the collected ion current as a function of angle of attack empirically determined for the Atmosphere Explorer C Bennett RF ion mass spectrometer is plotted for measured ion species.

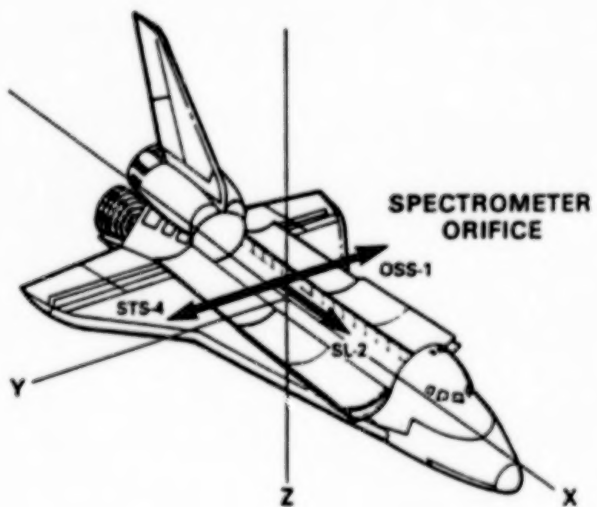


Figure 2. The arrows indicate the directions in which the Bennett RF ion mass spectrometer (on SL-2 and OSS-1 missions) and the ion-neutral quadrupole spectrometer (on STS-4) orifices faced when secured within the shuttle bay.

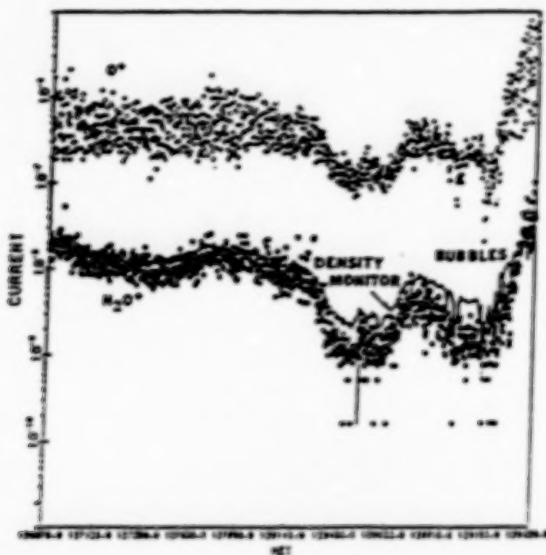


Figure 3. STS-4 ion measurements for a period of time beginning on orbit 24 when the spectrometer was facing into the ram direction show a characteristic H<sub>2</sub>O<sup>+</sup>/O<sup>+</sup> ratio of about 2 %. This plot is taken from Narcisi et al. (1983). MET refers to mission elapsed time.

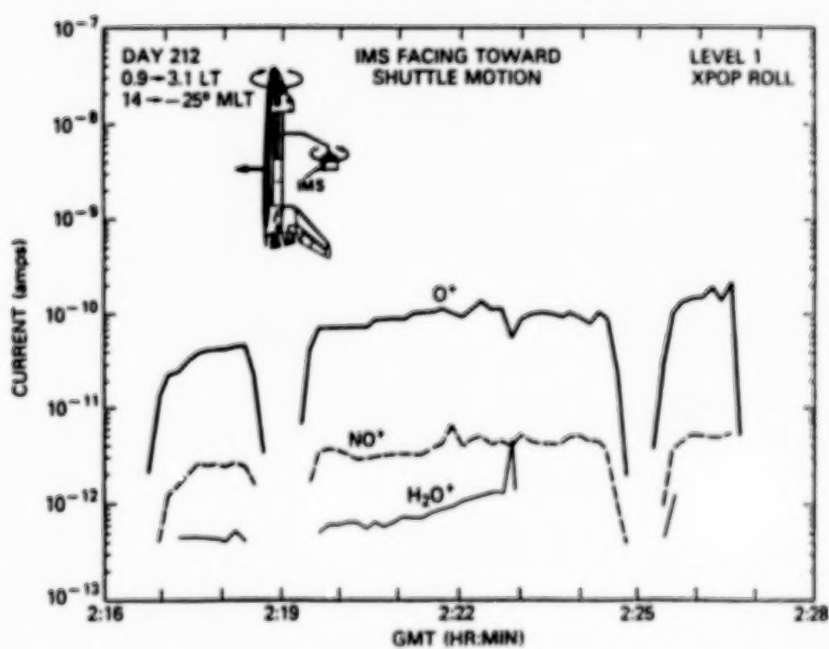


Figure 4. SL-2 measurements of ion composition taken during several X Perpendicular-to-Orbital plane rolls in which the ion spectrometer orifice was maintained in the shuttle ram direction.

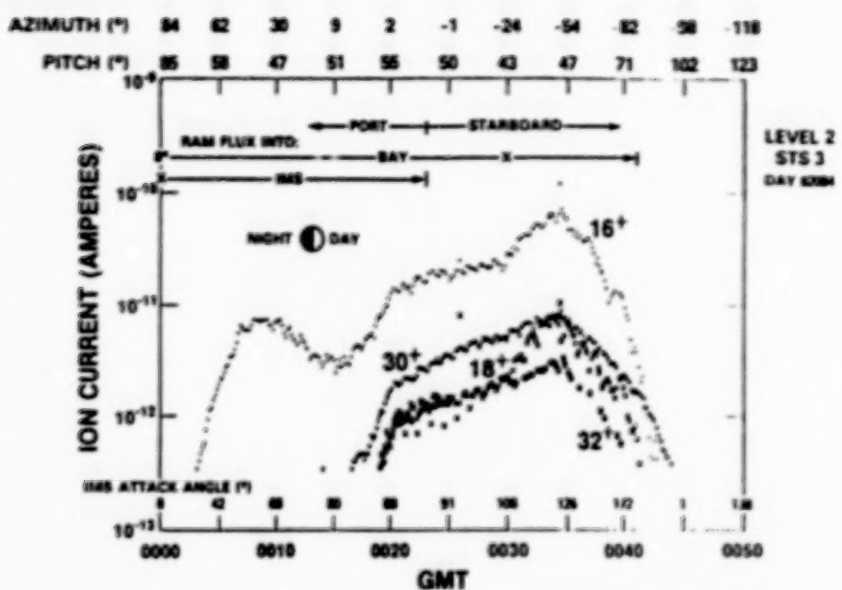


Figure 5. An example of ion composition measurements in the bay on STS-3. The pitch refers to the angle between the spacecraft velocity and the outward normal to the Bay (i.e., the  $-Z$  axis); azimuth is the velocity angle projected into the X-Y plane from the X axis; and the IMS angle refers to the angle the velocity makes with the outward normal to the orifice.

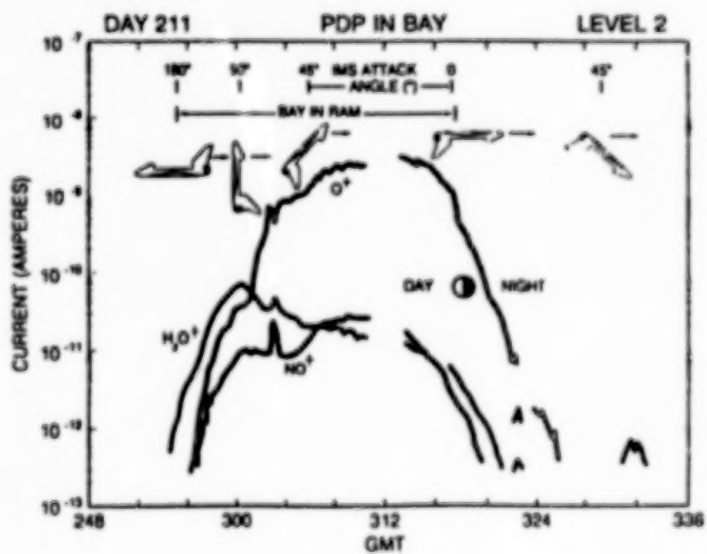


Figure 6. Spacelab 2 observations made from within the payload bay when the spacecraft was flipping end-over-end along the orbit.

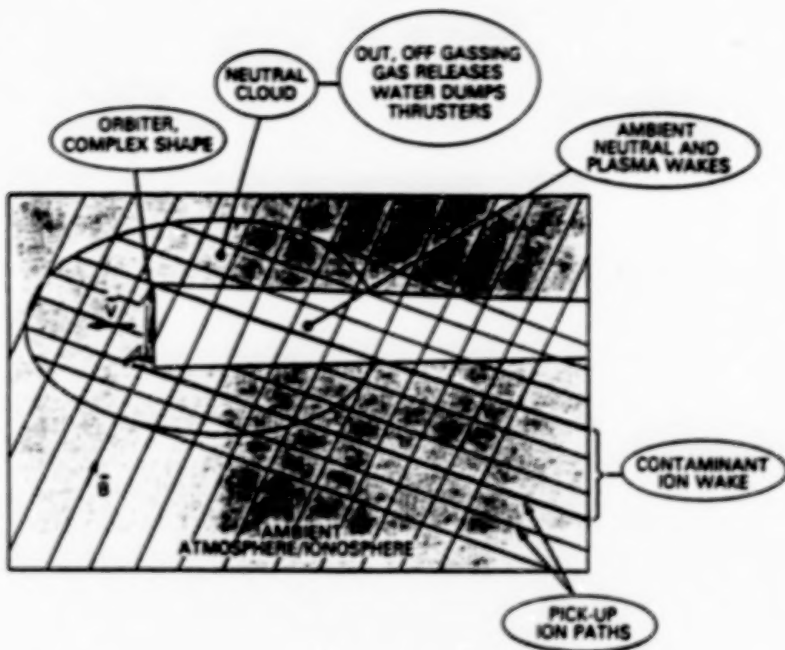


Figure 7. A schematic model of the average environment about the shuttle. Water ions formed by charge exchange follow guiding center paths perpendicular to  $B$  that are oblique, in the shuttle frame of reference, to the streamlines of ambient ions. This results in a contaminant ion influx and resultant depleted plasma wake behind the shuttle that differs from the corresponding ambient ion behavior.

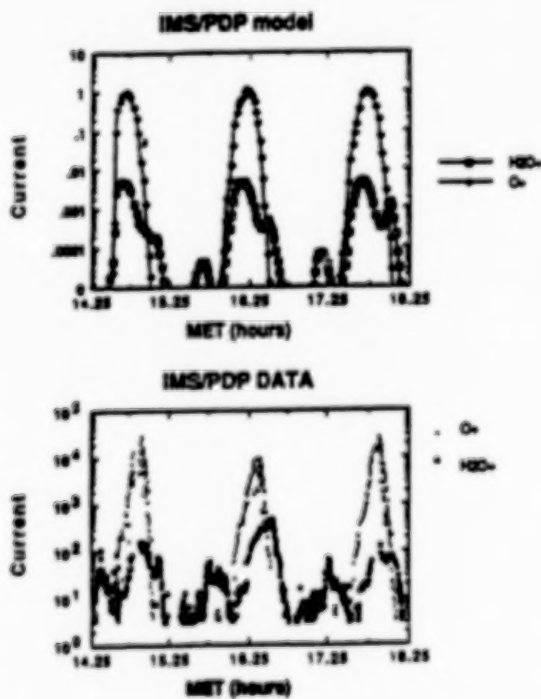


Figure 8. SL-2 ion measurements made within the wake on three consecutive orbits showing differing contaminant and ambient ion behavior are shown on the bottom. Model calculations of currents to be expected for these orbits shown at the top reproduce the differing wake behaviors. This figure is from Eccles (1988).

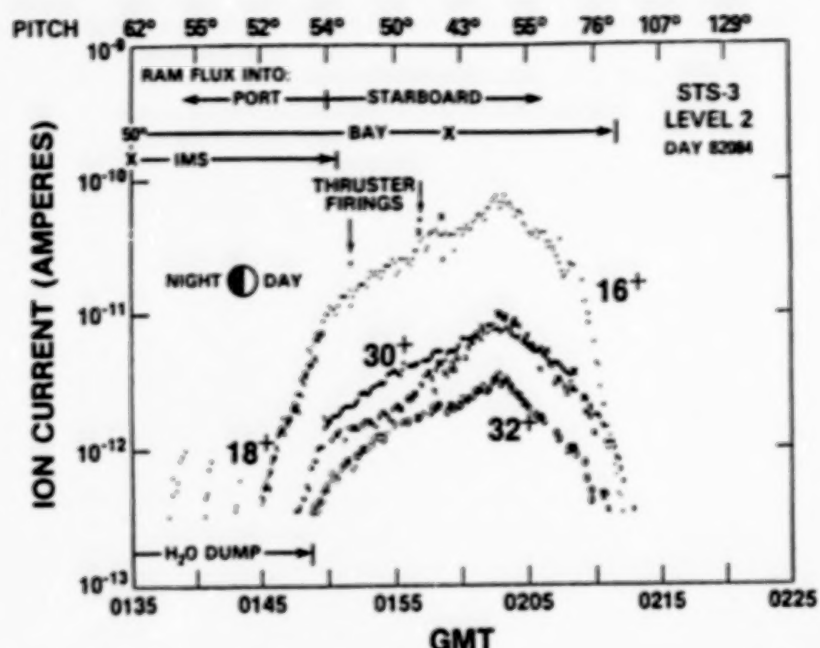


Figure 9. Ion spectrometer measurements taken within the bay of STS-3 during and after a water dump. The regions delineated at the top of the figure denote the direction of motion of ambient ions as viewed from the shuttle. The crosses on the lines indicate the points where the outward normal to the bay and spectrometer orifice were closest to the ram direction and the vertical bars indicate when the angles were  $90^\circ$ . This orbit followed that described in Figure 5 on which no water dump took place.

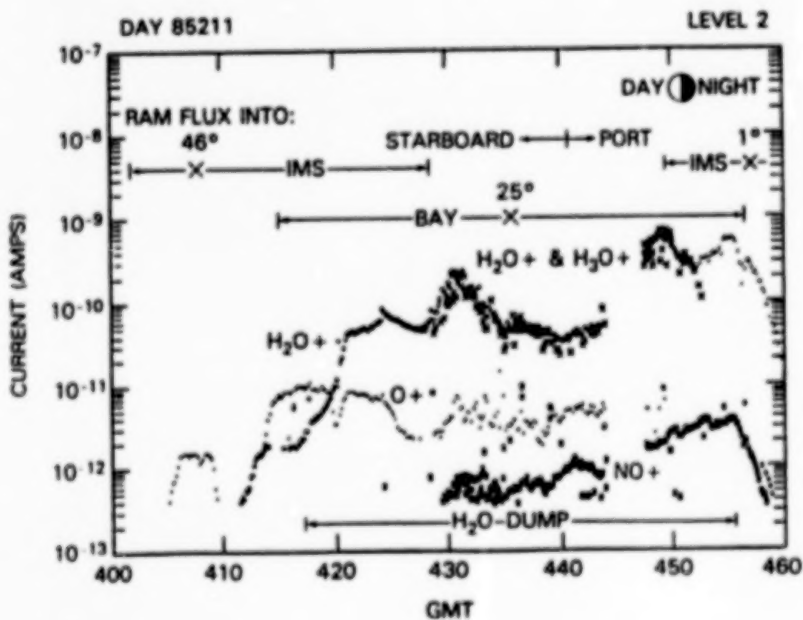


Figure 10. Ion measurements from within the shuttle bay on SL-2 during a water dump show an extreme case where water related ion currents dominate the ambient ion species currents by a factor of 10.

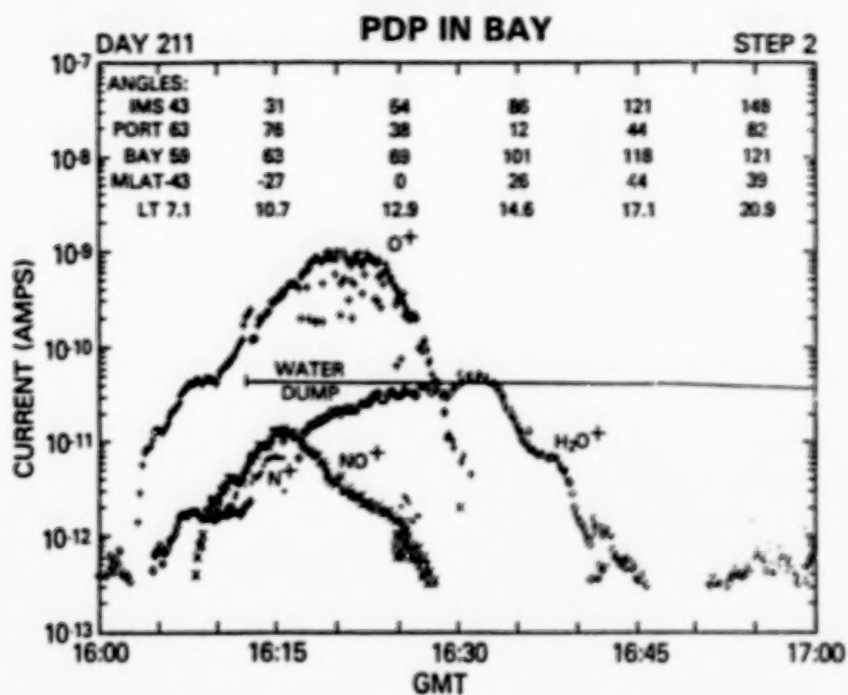


Figure 11. Another SL-2 in-bay example of the effects of a water dump. The crossings of the ambient and contaminant ion wakes still occur at different times. The water dump does not fill in the ion wake. This is the second orbit of the sequence plotted in Figure 8 (bottom).

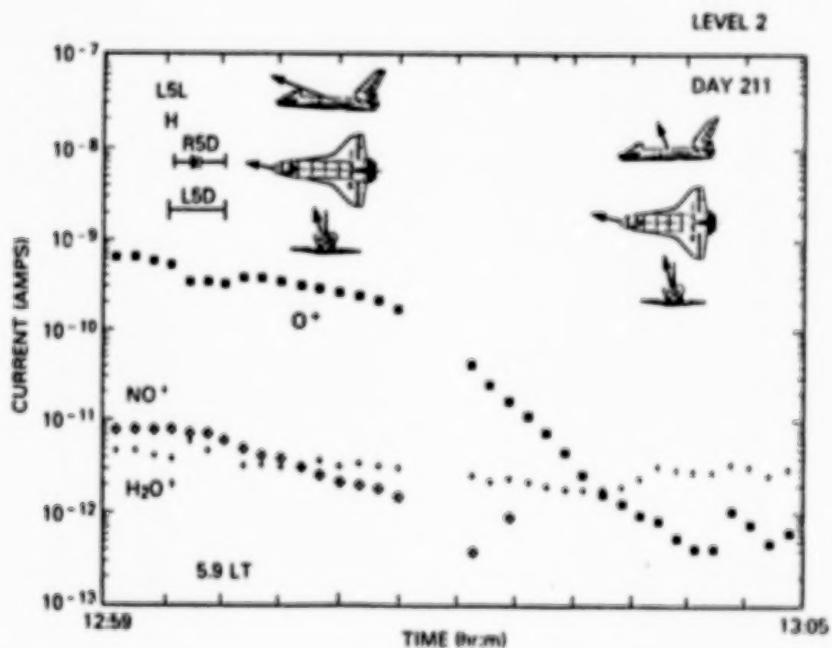


Figure 12. A SL-2 set of measurements from within the bay when a decrease in the ambient ions is detected during thruster firings while the water ion currents are enhanced. Note that the ion spectrometer is directed into the spacecraft direction of motion

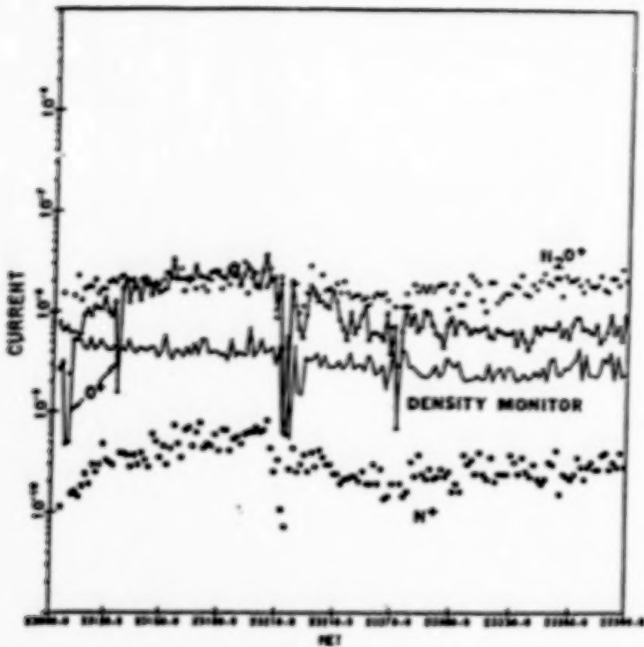


Figure 13. An example of large momentary decreases in  $O^+$  currents incident on the STS-4 spectrometer during thruster firings were detected on orbit 5 along with simultaneous decreases in the water ion currents. This figure is from Narcisi et al. (1983).

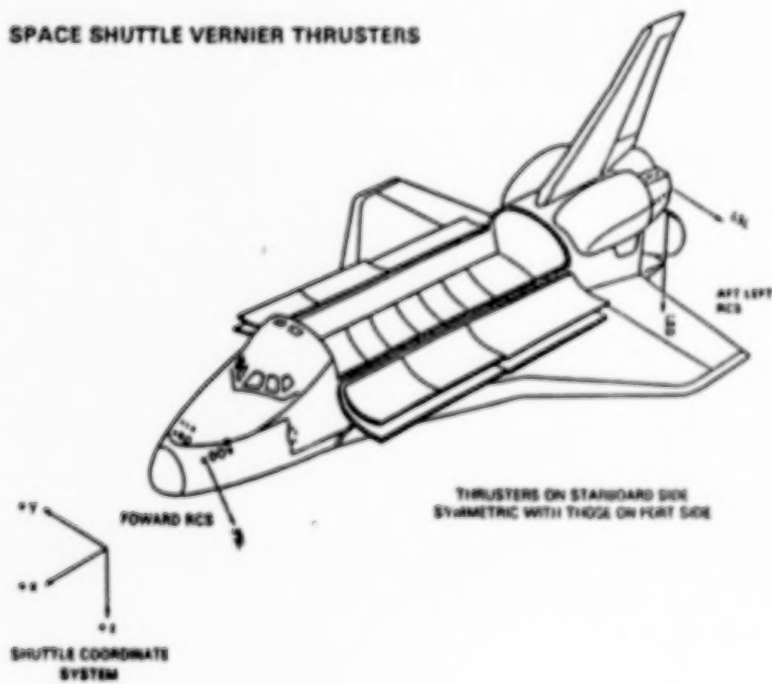


Figure 14. There are 6 vernier thrusters on the shuttle. The three on the port (left) side (F5L, L5L, L5D) are delineated while a similar set (F5R, R5R, R5D) are located symmetrically on the starboard (right) side of the vehicle.

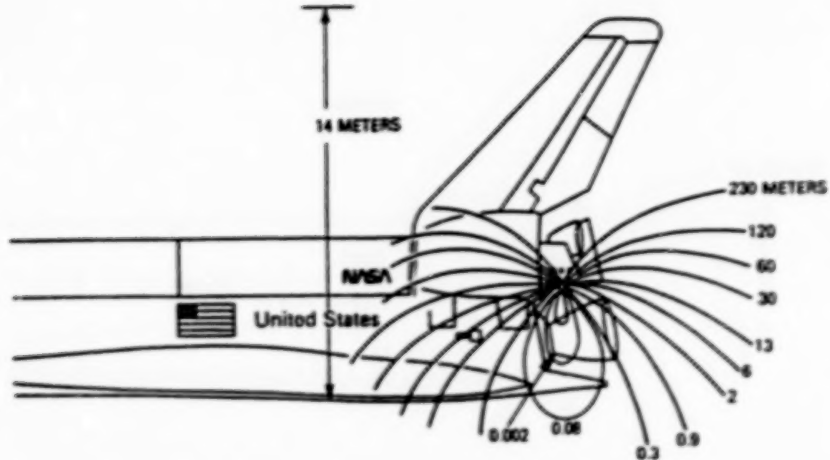


Figure 15. The RCS plume concentration configuration computed by Smith (1983) with the ramp code was simply scaled to the vernier effluent rate and then used to compute the mean free path of ambient  $O^+$  ions moving through it. The thruster plume is depicted as directed downward in the figure - the exact orientation of course is dependent upon which thruster is considered. The angles in the parentheses at the top rate are the angles of the shuttle's velocity in the spacecraft X, Y, Z coordinate system.

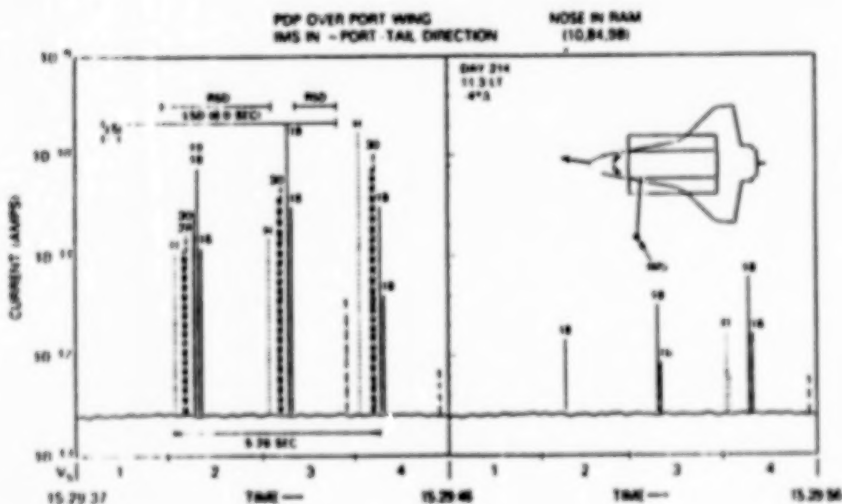


Figure 16. An example from SL-2 of the detection of ion perturbations from a pair of rear firing thrusters. The PDP was on the RMS as shown with the IMS directed tailward and away from the port side. The masses are swept on each cycle from low to high AMU's with each sensitivity level mass scan duration of approximately 2.4 seconds. The current peak variations seen in the background measurements after the firing demonstrate the sensitivity level increases of the instrument from step 1 to 4. The dotted H curves refer to harmonics of the 18 and/or 16 AMU species produced by the RF resonance in the instrument. These vary in amplitude with the fundamental current.

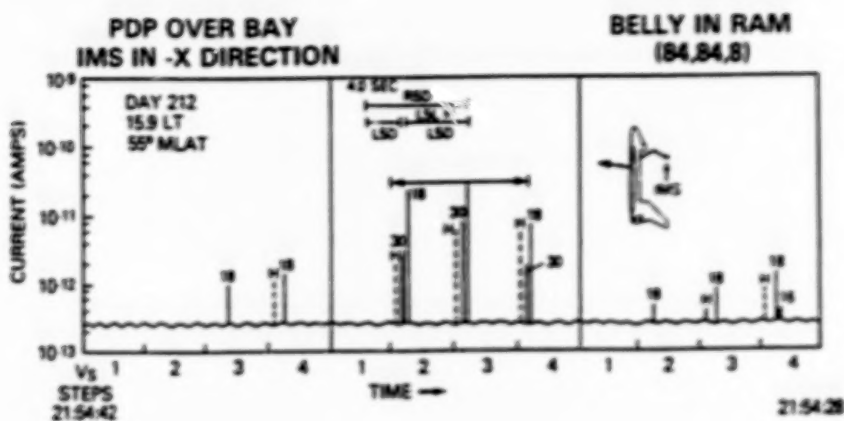


Figure 17. A SL-2 example of thruster ion perturbation duration exceeding the duration of the firing. The time of the observed perturbation is obtained from the known sweep cycle periods of the instrument.

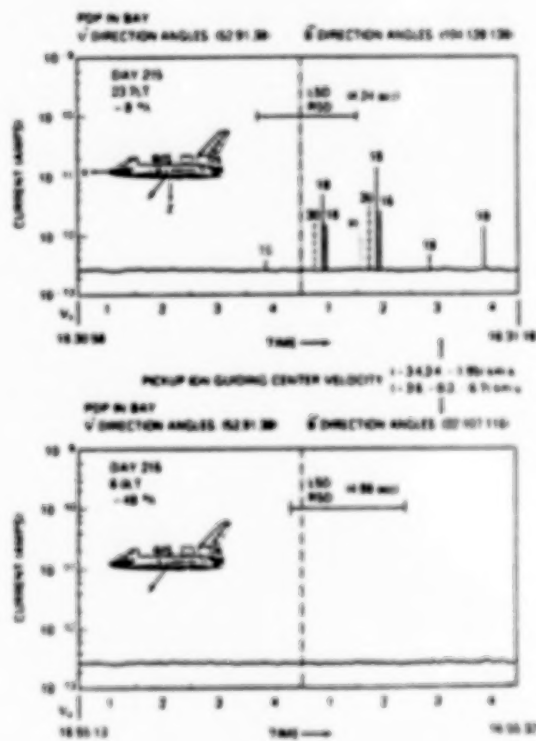


Figure 18. Two sequences of similar SL-2 thruster firings at the same shuttle attitude on the same orbit have different consequences at the ion spectrometer location within the bay. The differences in the magnetic field orientation with respect to the shuttle will produce distinctly different pick-up ion trajectories that could explain the differences.

# INTERACTION OF A NEUTRAL CLOUD MOVING THROUGH A MAGNETIZED PLASMA

C. K. Goertz and G. Lu

Department of Physics and Astronomy, University of Iowa, Iowa City

**Abstract.** Current collection by outgassing probes in motion relative to a magnetized plasma may be significantly affected by plasma processes that cause electron heating and cross field transport. Simulations of a neutral gas cloud moving across a static magnetic field are discussed. We treat a low- $\beta$  plasma and use a 2 - 1/2 D electrostatic code linked with our Plasma and Neutral Interaction Code (PANIC). Our study emphasizes the understanding of the interface between the neutral gas cloud and the surrounding plasma where electrons are heated and can diffuse across field lines. When ionization or charge exchange collisions occur a sheath-like structure is formed at the surface of the neutral gas. In that region the crossfield component of the electric field causes the electron to  $\vec{E} \times \vec{B}$  drift with a velocity of the order of the neutral gas velocity times the square root of the ion to electron mass ratio. In addition a diamagnetic drift of the electron occurs due to the number density and temperature inhomogeneity in the front. These drift currents excite the lower-hybrid waves with the wave k-vectors almost perpendicular to the neutral flow and magnetic field again resulting in electron heating. The thermal electron current is significantly enhanced due to this heating.

## 1. Introduction

It is well known that a neutral gas moving across a magnetic field relative to a plasma causes plasma heating [Machida and Goertz, 1988] and if the relative speed exceeds the Critical Ionization Velocity (CIV)  $V_c$  the neutral gas can be rapidly ionized. [see e.g. Brenning, 1981]. This anomalously rapid ionization phenomenon was first discussed by Alfvén [1954] who postulated that CIV occurs when the kinetic energy of the neutral particles ( $m_n V_c^2 / 2$ ) exceeds the ionization energy ( $e\phi_{ion}$ ) of the neutrals. Although CIV is not directly relevant to current collection in space the microscopic process that leads to electron heating is because it enhances the electron current that can be collected. Turbulence may also allow for rapid transport across magnetic field lines.

The electron heating proceeds in two steps. First the neutrals give energy to ions and then the ions energize the electrons. The energy transfer from neutrals to ions involves the charging of a neutral either by charge exchange or ionization; the transfer of energy from ions to electrons involves the excitation of plasma waves by the moving ions and their subsequent damping by electrons [Raadu, 1978; Galeev, 1981; Abe, 1984; Abe and Machida, 1985; Papdopoulos 1985; Machida and Goertz, 1987]. There is also a more direct way for energizing the electrons. This process occurs in the leading edge of the neutral gas as it moves through the plasma and works in the following manner. If a moving neutral is charged by photoionization, impact ionization or charge exchange the newly created ion will continue to move across the magnetic field with the neutral particle's speed. The plasma electrons are tied to the magnetic field and remain at rest. Thus a charge separation occurs at the edge of the neutral cloud and an electric field pointing into the neutral cloud develops. This electric field causes a secondary electron drift along the front of the neutral gas cloud. Ions are very massive and will not drift in response to this spatially limited field. The electron drift speed can be large and destabilize lower hybrid electrostatic waves by the modified two-stream instability which in turn heat the electrons. Thus intense waves should exist in this front. If the electron energy becomes large enough impact ionization by the energetic electrons creates new ion-electron pairs thus providing a positive feedback process. Whereas the waves and electron heating inside the neutral cloud has been studied extensively before very little theoretical work has been done on the structure and dynamics of the front. In this paper we report the results of a 2 - 1/2 D electrostatic code linked with our Plasma and Neutral Interaction Code (PANIC, see Machida and Goertz, 1987) which focuses on the understanding of this front.

Plasma turbulence inside a neutral gas moving through a magnetized plasma may affect current collection by outgassing probes in two ways. The increased electron temperature increases the thermal electron current. In addition, turbulence can cause enhanced diffusive transport of electrons across magnetic field lines and thus lead to an increased effective collecting area of a probe. This enhanced diffusion has been discussed by Sudan (1983, a, b) and has been verified by simulations (Machida and Goertz, 1988).

## 2. The Charge Separation

Consider a moving neutral at the interface between a neutral cloud and a plasma that is charged (either by a UV photon or an energetic electron or by charge exchange with a stationary ion). Electrons are trapped by the magnetic field pointing out of the plane of figure 1. The ion moves into the plasma at the speed of the neutral. A charge separation evolves and a potential jump occurs at the plasma - neutral gas interface. Clearly the potential will not greatly exceed a value necessary to reflect the ion. Thus

$$e\phi \sim m_e V_n^2 / 2 \quad (1)$$

The distance,  $D$ , over which a finite electric field exists is difficult to estimate. It is clearly smaller than an ion-gyroradius and larger than an electron - gyroradius. An exact theory for  $D$  is difficult because the charge separation may be effected by the pre-existing background plasma outside the neutral cloud. For example plasma ions moving to the left in figure 1 can be accelerated through the potential and plasma electrons could be trapped within the front. It seems reasonable to assume that  $D$  is of the order of the hybrid gyroradius

$$D = \sqrt{R_e R_i} \quad (2)$$

where the newly created particle's gyroradius is

$$R_j = \frac{V_n}{q_j B_0} m_j \quad ; \quad j = e, i \quad (3)$$

Thus the electric field  $E = \phi/D$  will cause all electrons within the front to drift (upwards in figure 1) at a speed

$$V_D = \frac{E}{B_0} = \frac{V_n}{2} \sqrt{\frac{m_i}{m_e}} \quad (4)$$

The drift energy of these electrons is

$$K = \frac{m_e}{2} V_D^2 = \frac{1}{4} \left[ \frac{m_e V_n^2}{2} \right] \quad (5)$$

If a probe would be inserted into this front one would expect an enhanced electron current because  $K$  can be larger than the electron thermal energy. However, it is not clear that the estimate of  $D$  given above is correct.

Because the electron drift speed is large only inside this charge separation front one expects an electron pressure enhancement there. In that case one must consider the electron density gradient drift:

$$V_g = \frac{1}{n_e B_0} \nabla(n_e T_e) \quad (6)$$

Using the scale length D to represent the pressure gradient by  $n_e T_e / D$  we find that

$$\frac{V_g}{V_D} = \frac{m_e}{m_i} \frac{V_e}{V_n} \quad (7)$$

where  $V_e$  is the electron thermal velocity. If the electrons will be thermalized with  $V_e = \sqrt{m_i/m_e} V_n$  we find that  $V_g/V_D = O(\sqrt{m_e/m_i})$ . Thus one may presume that the diamagnetic drift is unimportant. However, the plasma waves excited depend on the magnitude of this drift even when it is small.

Using a local approximation for electrostatic waves propagating in a plane the dispersion relation is given by

$$1 + \left( \frac{\omega_{pi}}{kV_i} \right)^2 (1 + \zeta_i Z(\zeta_i)) + \left( \frac{\omega_{pe}}{kV_e} \right)^2 (1 + I_0(b)e^{-b}(1 - \frac{\omega_2}{\omega_1})\zeta_e Z(\zeta_e)) = 0$$

$$\zeta_i = \omega / \sqrt{2kV_i}$$

$$\zeta_e = (\omega - k_\perp V_D) / \sqrt{2k_\parallel V_e} \quad (8)$$

$$b = (k_\perp V_e / \Omega_e)^2$$

$$\omega_1 = \omega - k_\perp V_D$$

$$\omega_2 = k_\perp V_g$$

[Gladd, 1976].

For  $|\omega_2/\omega_1| = 0$  waves are excited by the modified two-stream instability with

$$\omega_r \sim (\sqrt{3}/2)\omega_{LH}$$

$$\gamma_{max} \sim \omega_{LH}/2 \quad (9)$$

The waves propagate not exactly perpendicular to  $B_0$  but grow most rapidly for

$$k_{\parallel}/k \sim \sqrt{m_e/m_i} \quad (10)$$

Because of this they have an electric field component along the magnetic field which causes electron Landau damping and hence electron heating.

On the other hand, if  $|\omega_2/\omega_1|$  is not very much smaller than 1 the lower - hybrid drift instability is generated with:

$$\omega_r \sim \omega_{LH}$$

$$\gamma_{max} \sim \omega_{LH}$$

This mode propagating exactly perpendicular to  $B_0$  (i.e.  $k_{\parallel}/k = 0$ ) would not suffer electron Landau damping and hence not lead to parallel electron heating. It may, however, give rise to an enhanced effective collision frequency which allows electrons to move across B and along the background electric field and hence to gain energy (Machida and Goertz, 1988).

Figure 2 shows an exact solution of the dispersion relation (8) for parameters relevant to the simulation runs described later ( $m_i/m_e = 100$ ). If the gradient drift velocity had been neglected the growth rate would approach zero for  $k_{\parallel}/k \rightarrow 0$ . The waves with  $k_{\parallel}/k \geq 0.1$  are due to the modified two stream instability and for  $k_{\parallel}/k \leq 0.1$  they are mainly due to the lower hybrid drift instability. This linear theory does, of course, not predict the non-linearly saturated wave spectrum and is thus not capable of making predictions about the electron temperature in the neutral gas cloud and its front. One may, for example, expect that as the modified two-stream instability excited by  $V_D$  saturates by electron trapping and heating. The pressure gradient drift  $V_g$  grows and the wave energy shifts to smaller values of  $k_{\parallel}/k$  reducing the electron heating efficiency in the front. Clearly, only a numerical simulation will allow us to investigate this.

### 3. Simulation

The electrostatic PIC simulation code used for this work has been described in a previous paper (Machida and Goertz, 1987). It has been used to investigate the CIV process in homogeneous gas

clouds (Machida and Goertz, 1987) and in finite size clouds with special emphasis on the ionization front by Machida et al. (1988). We have also used it to investigate the anomalous heating of electrons that occurs when an electric field is applied perpendicular to a magnetic field (Machida and Goertz, 1988). In that work the relative drift between plasma and neutrals was below the critical velocity. It is most closely related to the work reported here. In this work, however, we deal with a finite size cloud whereas in Machida and Goertz (1988) the neutral gas density was assumed to be homogeneous. In this paper we include the following collisional processes as in Machida and Goertz (1988):

- a. Elastic electron-neutral and ion-neutral collisions (collision frequency  $\nu_{ee}$ ,  $\nu_{ie}$ )
- b. Inelastic electron-neutral collisions. In these collisions the electrons lose a certain amount of energy to the excitation of neutrals. The collision frequency is  $\nu_e^*$  and the threshold energy is  $E^*$ . In each collision the electron loses an energy equal to  $E^*$ .
- c. Charge exchange collisions between ions and neutrals occur at a collision frequency  $\nu_{chz}$ .
- d. Electron ionizing collisions  $\nu_{ion}$  occur only if the electron energy is above the ionization threshold energy  $e\phi_{ion}$ . Since the relative drift between plasma and neutrals is smaller than the critical velocity  $v_c$  few ionizing collisions occur.

The values used in the simulation for these parameters are given in Table 1. Since resistive heating is proportional to  $V_D^2$  and the collisional cooling is proportional to  $E^*$  these values would indicate that without wave heating the electrons would rapidly cool inside the neutral cloud. And, indeed, when we run our code without the Poisson solver (i.e. no self-consistently generated waves present) the electrons inside the neutral gas cool as expected (data not shown).

The relative drift  $\vec{V}_D$ , between plasma and neutrals is implemented by applying a constant electric field  $\vec{E}_o = \vec{B}_o \times \vec{V}_D$  to the simulation. The perturbation field  $\vec{E}'$  of the waves and in the charge separation front is calculated self-consistently from Poisson's equation.

We have used two shapes for the neutral gas cloud. In the first set of runs we have used a neutral gas slab as shown in Figure 3a. This shape is unrealistic but allows for easier comparison

with theory. In the second set of runs we have used a circular gas cloud as shown in Figure 3b. A control run was also made with no collisions included (all  $\nu$  were set equal to zero) which corresponds to a zero neutral gas density. The diagnostics include calculations of density, electrostatic fields  $\vec{E}'$  and potentials  $\Phi'$ , electron and ion temperatures, phase space plots and a calculation of the thermal electron flux penetrating a certain small area in the simulation region. In addition we can determine the frequency and wave-number spectra of the electric field fluctuations. A detailed description of all our results using the full set of diagnostics will be published elsewhere.

#### 4. Results

In this paper we are mainly interested in the electron heating that occurs due to collisions and wave-particle interactions. In Machida and Goertz (1988) we found that after a few  $100 \omega_{pe}^{-1}$  the electron temperature saturated at a value given by

$$kT_e = \eta m_e V_D^2 / 2$$

The value of  $\eta$  varied from 0.2 to 0.7 depending on whether lower hybrid wave heating was allowed to occur in the simulation or not. At the shuttle orbit altitudes  $m_e V_D^2 / 2$  may be as large as 3 eV. Thus this heating could be quite significant. It is the purpose of this work to find out whether the value of  $\eta$  is significantly affected by using a finite size cloud.

##### 4.1. Control Run

A control run was made with all collision frequencies set to zero. This run shows the effects of inherent numerical heating and noise in the code. Figure 4a shows the evolution of  $T_e$  with time. Little numerical heating occurred. The temperature increased only by 5%. The electrostatic field frequency spectrum is shown in figures 4b and 4c at different times during the run. The noise level is reasonably small. A small enhancement near the lower and upper hybrid frequency can be seen. The electrostatic potential contours are shown in Figure 4d. No large potentials occur. This run together with the collisional run without the Poisson solver implemented which displayed electron

cooling suggests that any electron heating observed in the subsequent runs is due to wave-particle interactions.

#### 4.2. Neutral Gas Slab Model

Figure 5a shows the evolution of the electron thermal energy (drift energy is subtracted) averaged over the volume occupied by the neutral clouds. In this run the magnetic field is perpendicular to the plane ( $\vec{B} = B_o \hat{z}$ ). Heating in the cloud is quite obvious. The electron temperature saturates at  $kT_e = \eta m_i V_D^2 / 2$  with  $\eta = 1.1$ . Figure 5b and 5c show the electrostatic field spectra at different times. These spectra were obtained in the center of the simulation region (indicated by a cross in Figure 3a). The low frequency peak is at the lower hybrid frequency. The high frequency noise is centered around the upper hybrid frequency. Figure 5d shows equipotential contours. Comparing this with Figure 4d reveals that large electric fields in the direction of the plasma motion (from right to left) are produced as expected and discussed in Section 2. The total potential drop between the leading and trailing edge of the cloud indicated by the dashed lines is about  $10kT_{e0}$  or  $0.8 mV_D^2$ .

In Figure 5 the magnetic field was assumed to be perpendicular to the simulation plane  $\vec{B} = B_o \hat{z}$ . Since lower hybrid waves created by the modified two stream instability have a finite  $k_{\parallel}$  they cannot be excited in this configuration. (See also discussion in Machida and Goertz, 1986.) Thus the electron heating must be mainly due to enhanced resistive heating (enhanced effective collision frequency) and heating by waves driven by the gradient drift instability with  $k_{\parallel} = 0$ . In addition in this run the secondary  $\vec{E} \times \vec{B}$  drift due to the charge separation field is in the plane of the simulation (in the  $-\hat{y}$  direction). Elastic scattering of electrons may transform part of that drift energy into thermal energy.

To allow for the presence of lower hybrid waves driven by the ion beams created by charge exchange we have made another run in which the magnetic field was in the plane of the simulation ( $\vec{B} = B_{oy} \hat{y}$ ). The applied electric field is given by  $\vec{E}_o = \vec{B} \times \vec{V}_D$  where  $\vec{V}_D = -V_D \hat{z}$ . In this case lower hybrid waves driven by the ion beams can be generated. Figure 6 shows the same diagnostics as before.

Surprisingly the electron temperature increase is slightly smaller ( $\eta \rightarrow 1.0$ ) but the fluctuation power spectrum more intense than in the previous case. In this case the gradient drift instability cannot be excited because it must propagate in the  $y - z$  plane and our two-dimensional simulation has  $k_z$  (equal to  $k_{\perp}$  in this case) equal to zero.

#### 4.3. Circular Gas Cloud Model

One may expect that lower hybrid waves could not be excited if the neutral gas cloud is smaller than the wavelength of the excited waves. In the previous case the cloud is infinite in the  $\hat{y}$  direction (periodic boundary conditions in  $\hat{y}$ ). In the circular cloud model the cloud is of finite size. One may also suspect that heated electrons will escape from the cloud and be replaced by cold electrons from the surrounding plasma. Thus we expected that the electron temperature increase would not be as large in this case as in the slab model case.

Figure 7 shows that this is, indeed, the case. Figure 7 shows the results for  $\vec{B} = B_{oy}\hat{y}$ . We see that the charge separation field is only slightly affected by the cloud's finite size. The temperature increase is not as rapid as before but the temperature has not saturated by the end of the run and it is not clear that the final saturated  $T_e$  will be different from the previous case. When a normal magnetic field ( $B_{ox} \gg B_{oy}$ ) is added the escape of electrons from the cloud is reduced and the temperature increase is faster, almost comparable to the slab model case (data not shown). We have not analyzed this case in detail and plan to report on more detailed diagnostics in a future paper.

#### 4.4. Electron Thermal Current

As a first step towards understanding how these results affect the current that can be collected from a probe placed inside a neutral cloud penetrated by a magnetized plasma flow we have calculated the number of electrons hitting a flat plate placed inside the neutral cloud between  $t = 0$  and  $t$  divided by the time  $t$  as a function of time  $t$ . We have used two orientations for the plate. In the first case the plate is placed parallel to the plasma flow. The plate's normal is in the  $\hat{y}$  direction. In this case electrons streaming parallel to the magnetic field  $B_{oy}$  are intercepted by the plate. The plate is 5

grid spaces wide. In the second case the plate is placed perpendicular to the flow with its normal pointing in the  $\hat{z}$  direction (see Figure 7c). In this case the plate intercepts electrons which have a velocity component perpendicular to the magnetic field.

The results are shown in Figure 8a for the perpendicular orientation and in Figure 8b for the parallel orientation. Five curves are shown in each case. The solid line is the control run and shows a low almost constant electron flux, the dashed lines are for the slab model and the dotted lines are for the circular cloud model. The double dashed line is for  $\vec{B} = B_{ox}\hat{z}$ . The large dots are also for  $\vec{B} = B_{ox}\hat{z}$ . The singly dashed line and the small dots are for  $\vec{B} = B_{oy}\hat{y}$ . The increase of the electron flux due to the neutral gas driven heating processes is quite obvious for the slab model. The fact that the integrated currents evolve different for the two different orientations of the plate indicates that the electron heating is anisotropic. The current collected inside a circular cloud is not vastly different from the control run which we attribute to escape of electrons from the cloud. These results are, of course, quite preliminary and require more detailed diagnostics. The difference between the slab and circular model cases may also be affected by the fact that in the circular cloud model the center of the cloud where the plate was placed was positively charged and thus may have contained low density electron beams.

### 5. Discussion

As expected the leading edge of a neutral cloud becomes positively charged and an electric field pointing in the direction of the plasma flow occurs. The total potential drop across the neutral cloud can reach values several times  $m_i V_D^2 / 2e$ . This charge separation electric field causes a rapid  $\vec{E} \times \vec{B}$  drift of the electrons. This drift appears to be fast enough to destabilize the modified two stream instability which can cause strong electron heating. We have found previously that this source for wave generation is more important than the more direct source of ion beams created by charge exchange or ionization (Machida et al., 1988). We also find that the gradient drift instability is important.

We have not found that the waves are suppressed in a small neutral cloud even if the cloud

is smaller than the wavelength of the most unstable waves (roughly the hybrid gyroradius  $R_H = \sqrt{R_i R_e}$ ). The escape of hot electrons from the neutral cloud does slow the heating rate but is not such an efficient cooling mechanism that the heating is suppressed. The heating of electrons does appear to be anisotropic.

Due to the heating of electrons the thermal electron flux is enhanced which should allow for enhanced current collection. This result must, however, be considered as tentative because we have not yet included the charging of a probe to the floating potential. In that case we expect the particle orbits to be significantly different and the current collected may differ considerably from the values indicated by our preliminary results. The position of a probe relative to the edge of the cloud may also be an important factor which we have not studied. We also intend to investigate in a later work the effects of a bias voltage on a probe placed inside the neutral cloud.

This work is also incomplete in the following sense. Whereas these simulations can be used to illustrate the basic physical principles they cannot make quantitative predictions to be used for applications to current collection in space. This is due to computational limitations. For example the mass ratio  $m_i/m_e = 100$  is totally unrealistic. The simulation region is only a few hundred Debye lengths wide which is much smaller than any real outgassing cloud. The collision frequencies are artificially high. If we were to reduce  $\nu/\omega_{pe}$  to realistic values the run time would have to be several orders of magnitude larger. These shortcomings are, of course, not unique to our simulation. They will plague simulations for a long time to come. This does not, however, mean that simulations are useless. Their value lies in their ability to isolate physical processes, assess their relative importance and derive scaling laws from a comparison with analytic theory. We have not yet accomplished this for the runs described here.

Acknowledgements. The authors would like to thank T. Whelan for his help with code modifications. This work was in part supported by NASA Grant NSG-7632, NSF Grant ATM-8411311, and the Lockheed Company.

## Parameters

	Control Run	Neutral Cloud	Comments
$m_i/m_e$	100	100	
$v_D/v_{eo}$	0.24	0.24	initial ion thermal velocity $v_{eo}$
$\omega_{pe}/\Omega_e$	1	1	
$\nu_{ee}/\omega_{pe}$	0	0.02	electron-neutral elastic collision
$\nu_{ie}/\omega_{pe}$	0	0.02	ion-neutral elastic collision
$\nu_e^*/\omega_{pe}$	0	0.02	electron-neutral inelastic collision
$E^*/kT_{eo}$	1.8	1.8	threshold energy for inelastic collis
$\nu_{cha}/\omega_{pe}$	0	0.04	charge exchange
$\nu_{ion}/\omega_{pe}$	0	0.04	ionization
$e\phi_{ion}/kT_{eo}$	7.3	7.3	ionization energy

## References

- Abe, T., Theory of the critical ionization velocity phenomenon, Planet. Space Sci., **32**, 903-906, 1984.
- Abe, T., and S. Machida, Production of high-energy electrons caused by counterstreaming ion beams in an external magnetic field, Phys. Fluids, **28**, 1178-1185, 1985.
- Alfvén, H., On the origin of the solar system, Oxford University Press, New York, 1954.
- Brenning, N., Experiments on the critical ionization velocity interaction in weak magnetic field, Plasma Phys., **23**, 967 -, 1978.
- Galeev, A. A., Proceedings of the International Schools and Workshop on Plasma Astrophysics, Varennna, Eur. Space Agency Spec. Publ., SP-161, 77-82, 1981.
- Gladd, N. T., The lower hybrid drift instability and the modified two stream instability in high density theta pinch environments, Plasma Phys., **18**, 27-40, 1976.
- Machida S. and C. K. Goertz, Computer simulation of the Farley-Buneman instability and anomalous electron heating in the auroral ionosphere, J. Geophys. Res., **93**, 9993-10,000, 1988.
- Machida, S., and C. K. Goertz, A simulation study of the critical ionization velocity process, J. Geophys. Res., **91**, 11965-11976, 1986.
- Machida, S., and C. K. Goertz, The electromagnetic effect on the critical ionization velocity process, J. Geophys. Res., **93**, 11,495-11,506, 1988.
- Machida, S., C. K. Goertz and G. Lu, Simulation study of the ionizing front in the critical ionization velocity phenomenon, J. Geomag. Geoelectr., **40**, 1205-1219, 1980.
- Papadopoulos, K., On the physics of the critical ionization velocity phenomena, in Advances in Space Plasma Physics, edited by B. Buti, p33-58, World Scientific Publication Company, Singapore, 1985.
- Raadu, M. A., The role of electrostatic instabilities in the critical ionization velocity mechanism, Astrophys. Space Sci., **55**, 125-138, 1978.

Sudan, R. N., Nonlinear theory of type I irregularities in the equatorial electrojet, Geophys. Res. Lett., 10, 983, 1983a.

Sudan, R. N., Unified theory of type I and type II irregularities in the equatorial electrojet, J. Geophys. Res., 88, 4853, 1983a.

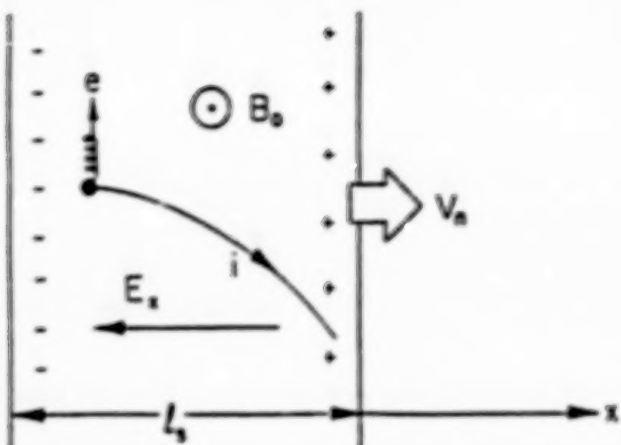


Figure 1. Schematic illustration of the charge separation front. Note that this figure is in the rest frame of the plasma. The neutral gas moves to the right.

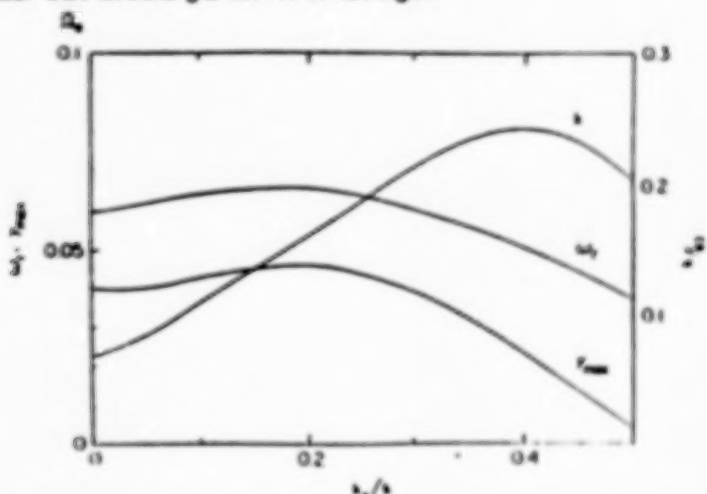


Figure 2. The maximum linear growth rate  $\gamma_{\max}$ , corresponding to the real wave frequency  $\omega_r$ , and wave number  $k$  plotted as a function of  $k_y/k$ .

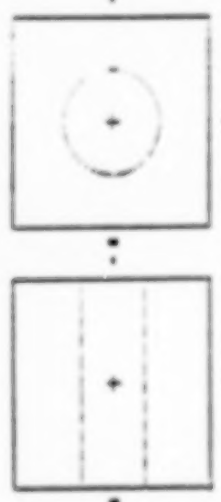


Figure 3. The geometry of the simulations for the slab model (a) and circular cloud model (b). The magnetic field can have either a  $\hat{y}$  or  $\hat{z}$  component or both. The plasma drifts from right to left in both cases.

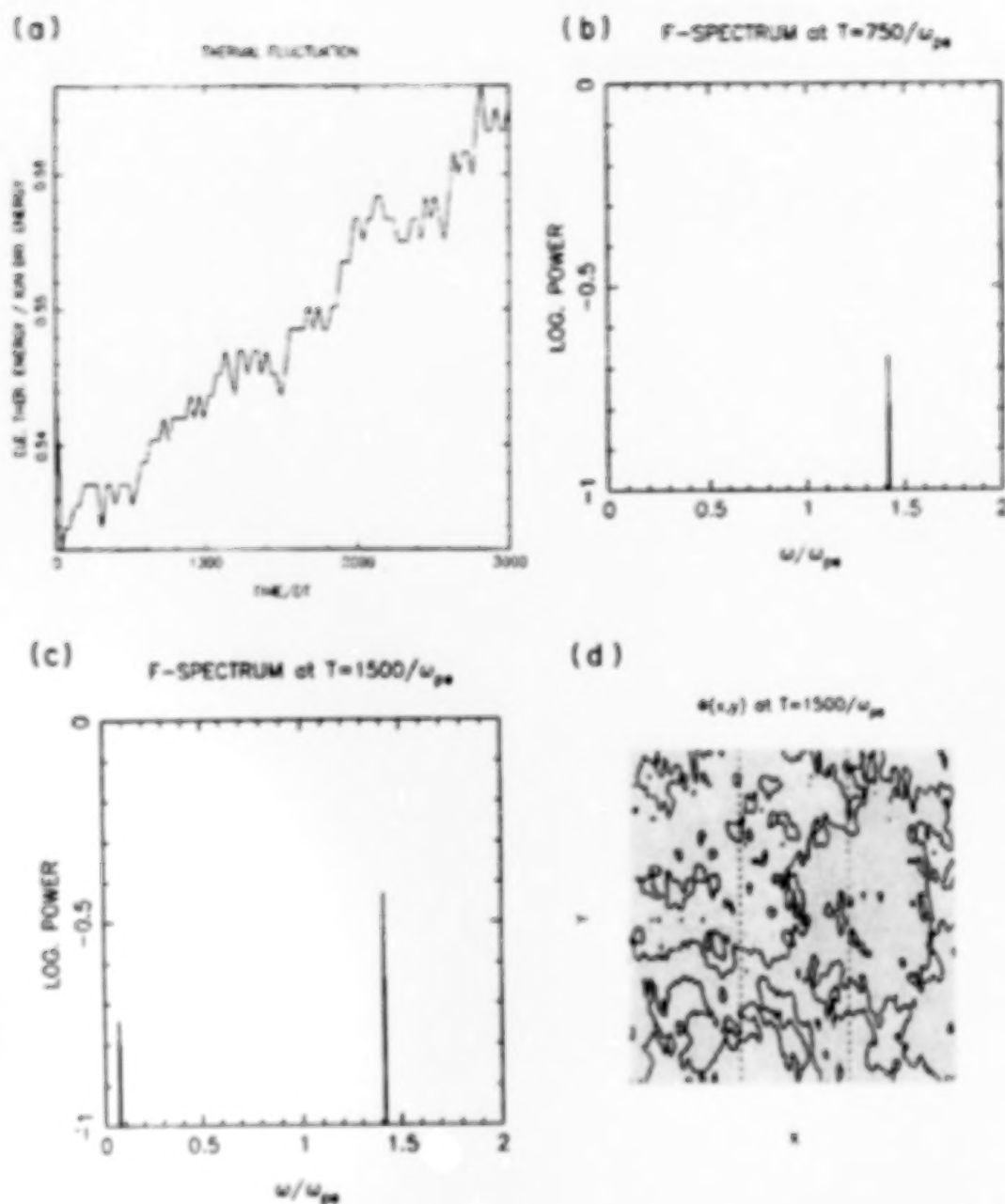
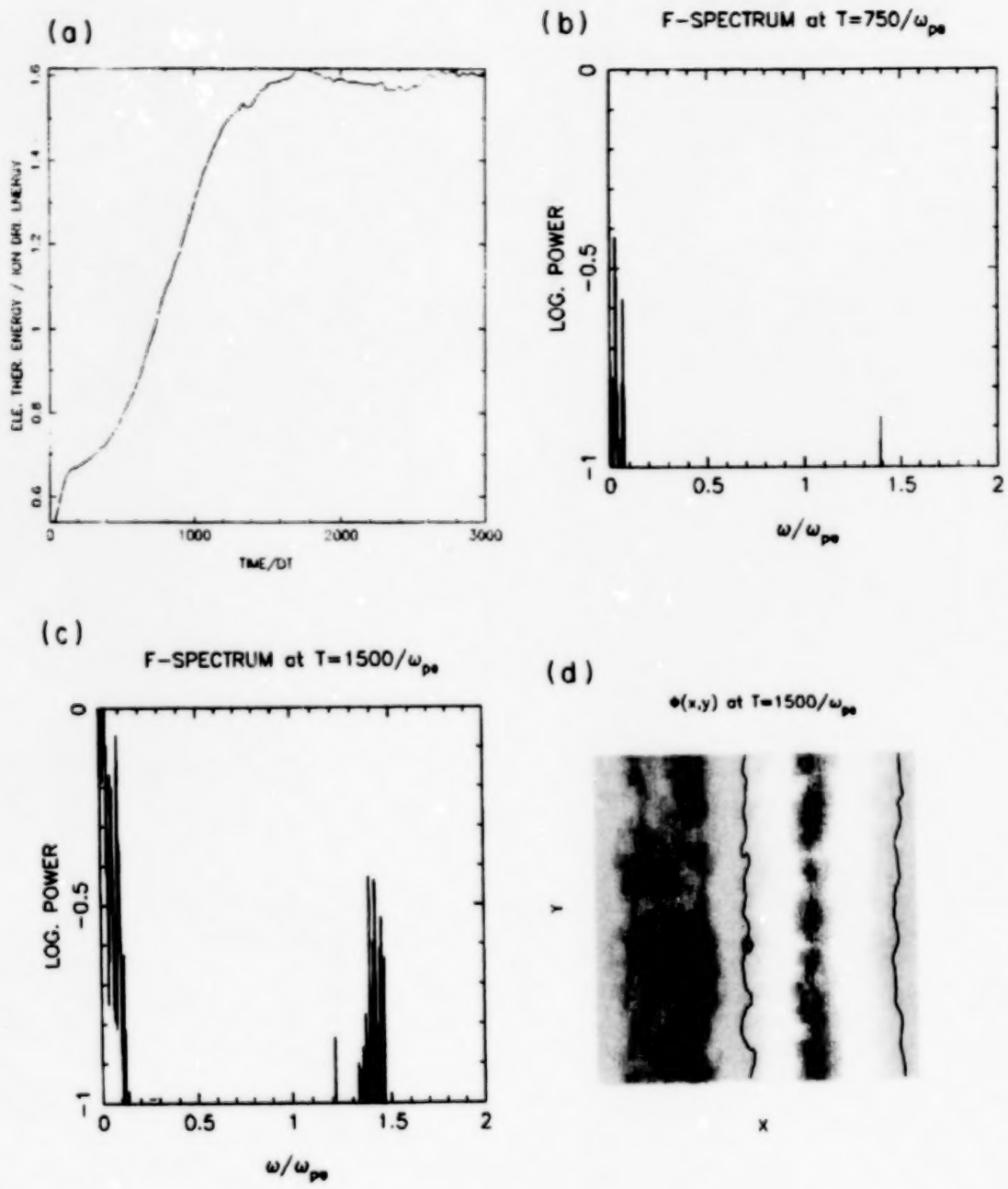


Figure 4. The time evolution of the total electron thermal energy ( $\frac{1}{2}kT_e$ ) normalized to the ion drift energy ( $m_i V_D^2/2$ ) (a). The power spectra at  $t = 750\omega_{pe}^{-1}$  (b) and  $t = 1500\omega_{pe}^{-1}$  (c) taken in the center of the simulation region. The equipotential contours (d) in units of  $kT_{ee}/e$  where  $T_{ee}$  is the initial electron temperature.



[ -8.0, 8.0 ]

Figure 5. Same as Figure 4 for the slab model. The magnetic field is  $\vec{B} = B_{os}\hat{z}$ .

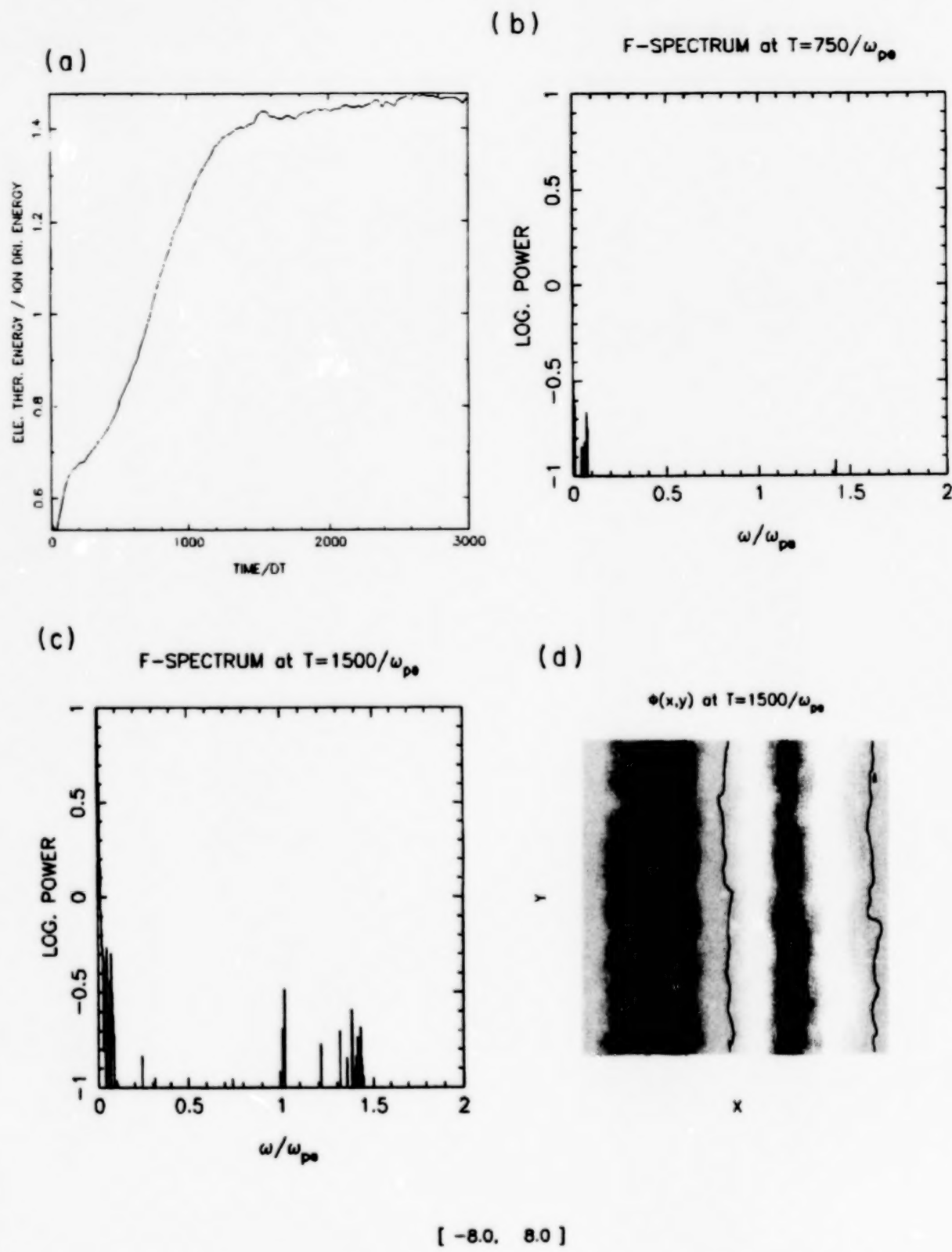


Figure 6. Same as Figure 5 except that in this case  $\vec{B} = B_{oy}\hat{y}$ .

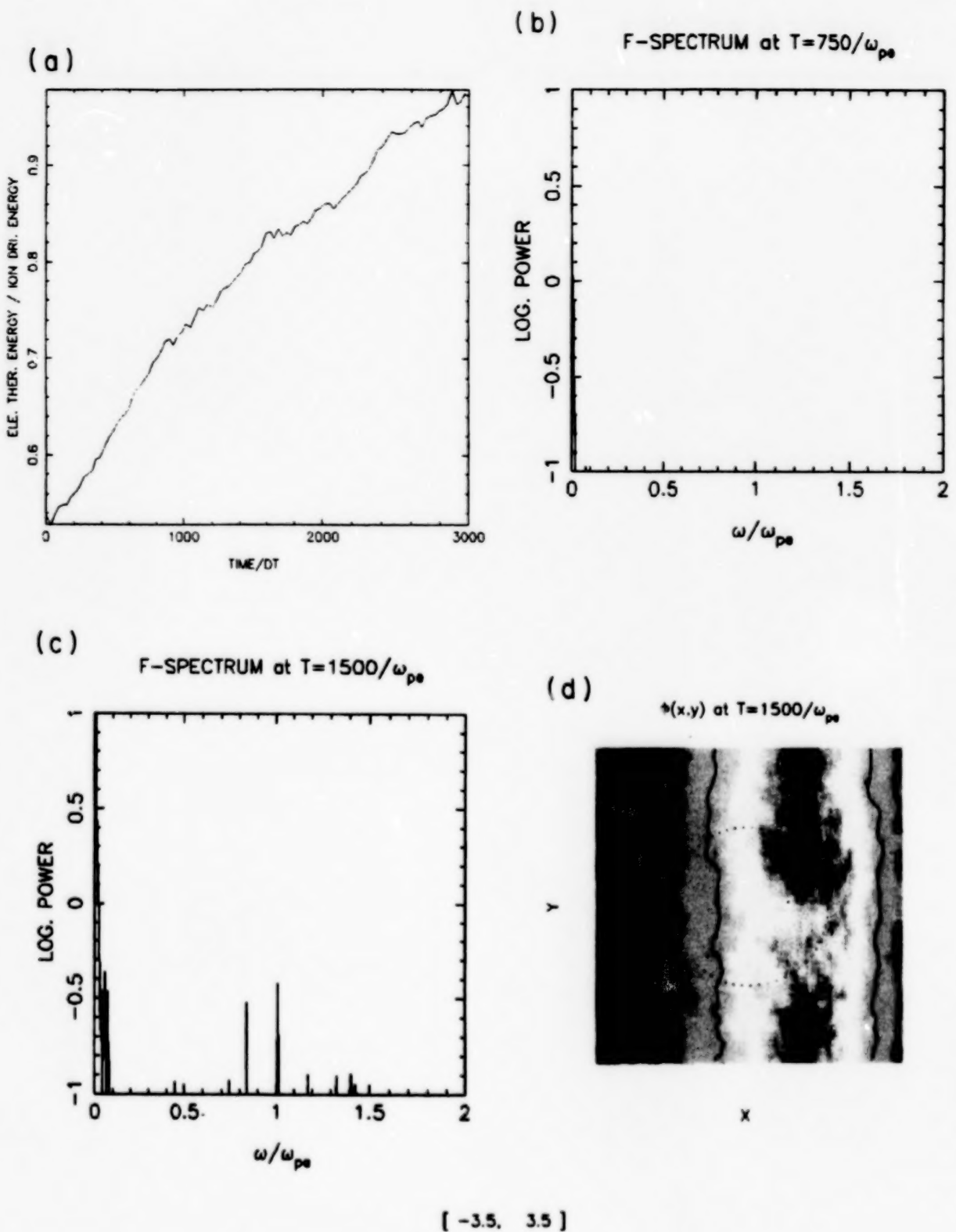


Figure 7. Same as Figure 6 for the circular cloud model.

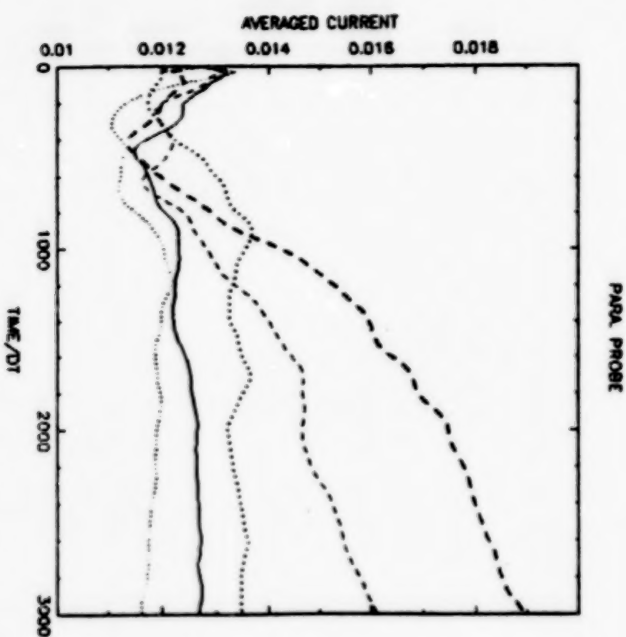


Figure 8a.

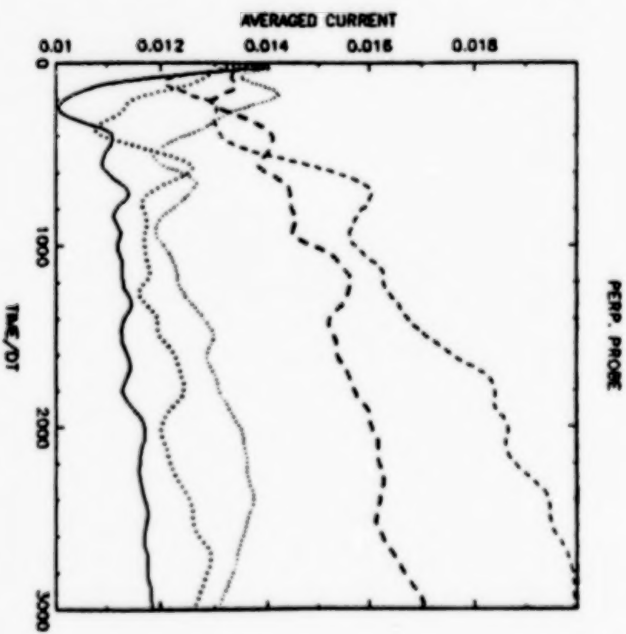


Figure 8b.

Figure 8.

- (a) The rate of electrons absorbed by a flat plate oriented parallel to the flow (plate normal parallel to  $\hat{y}$ ).
- (b) The rate of electrons absorbed by a flat plate oriented perpendicular to the flow (normal parallel to  $\hat{z}$ ). The solid line is from the control run (figure 4); the dashed lines are from the slab (figures 5 and 6) and the dotted lines from the circular cloud (figure 7).

# CURRENT LIMITING MECHANISMS IN ELECTRON AND ION BEAM EXPERIMENTS

R. C. Olsen

Department of Physics, Naval Postgraduate School  
Monterey, California 93943-5000

**Abstract.** The emission and collection of current from satellites or rockets in the ionosphere is a process which, at equilibrium, requires a balance between inward and outward currents. In most active experiments in the ionosphere and magnetosphere, the emitted current exceeds the integrated thermal current by one or more orders of magnitude. The system response is typically for the emitted current to be limited by processes such as differential charging of insulating surfaces, interactions between an emitted beam and the local plasma, and interactions between the beam and local neutral gas. These current limiting mechanisms have been illustrated for 20 years in sounding rocket and satellite experiments, which are reviewed here. Detailed presentations of the SCATHA electron and ion gun experiments are used to demonstrate the general range of observed phenomena.

## INTRODUCTION

The problem of exchanging large currents between a satellite and the environment is a basic one for objectives such as experiments in generating artificial aurora, operation of electrodynamic tethers, beam weapons, and active charge control. Experimental evidence accumulated over the past 20 years indicates that there may be fundamental limits on the amount of current which can be coupled to the ambient plasma, and that this current level is comparable to the thermal current which can be extracted from the ambient plasma.

The free space capacitance of a sounding rocket or satellite is quite low — typically a few hundred picofarads. Hence, currents in the mA range are sufficient to induce potentials in the kV range in milliseconds. Consequently, experiments in charge emission, such as electron beam experiments, require collection of a balancing current which is comparable to the emitted current. The thermal electron flux in the ionosphere is  $J = e n \sqrt{kT_e/m_e} \sim 2 \times 10^{-4} \text{ A/m}^2$ . For a collecting area of  $10 \text{ m}^2$ , currents in the mA range are possible. An attractive potential of a few volts allows for a roughly linear increase in the collected current ( $J \propto (1+e\phi/kT)$ ), ignoring magnetic field effects and most sheath effects. Basic theory on such processes is addressed elsewhere in these proceedings. In principle, the potential will increase until the collected current balances the emitted current. If this potential is less than the accelerating potential for the beam, the beam escapes. It is obviously possible for this condition to be violated, if the beam energy is too low for the emitted current. (This was illustrated in ISEE-1 electron gun experiments in the magnetosphere and solar wind [Lebreton, 1983].)

The objective of this paper is to show that in general, potentials ( $q\phi$ ) which are much greater than the thermal energy ( $kT$ ) of the ambient plasma are not a normal solution to the current balance equation. Limiting mechanisms such as differential charging or beam-plasma interactions typically prevent the effective coupling of current from a satellite to the ambient plasma. The one caveat is that there not be a substantial neutral gas background. When neutral gas is present, nearly infinite current becomes possible.

## ELECTRON BEAM EXPERIMENTS

Electron beam experiments have been conducted from sounding rockets, satellites, and the space shuttle orbiter. These experiments provide a range of environments and beam current values which span orders of magnitude in parameter space. The historical data set is considered here, with detailed presentation of recently analyzed SCATHA experiments.

### SOUNDING ROCKETS

Sounding rocket experiments with electron beams have been conducted since the late 1960's, primarily with the objective of generating artificial aurora. The early experiments were conducted in the face of skepticism that kiloVolt beams could be emitted. The reasons for the skepticism were the prediction of problems with current balance (charging), and prediction that such beams would be unstable, and be disrupted by beam-plasma interactions, like the two-stream instability.

The assurance of an adequate collection of return current can be addressed by deploying a large collecting surface. For this purpose, a large inflation-deployed electron collection screen was developed and fabricated for the first US rocket-borne electron accelerator experiment. This artificial aurora experiment was launched on an Aerobee 350 from Wallops Island in January, 1969. The experiment consisted of ten electron guns capable of up to 490 mA at 9.5 keV. The rocket payload included an aluminized mylar disk, 26 m in diameter, with an inflatable hub and rim and four inflatable spokes. The collector is illustrated in Figure 1. The deployment was apparently incomplete, due to a malfunction in a pressure regulator. Nevertheless, the technique was at least partially successful. This experiment indicated that a substantial fraction of the beam current could be successfully emitted. This was shown by optical observation of artificial auroras generated by the beam at  $\frac{1}{2}$ A at 4.9 and 8.7 KeV, at 200 km altitude. The success eased concerns about current collection, and such extra-ordinary efforts were abandoned with most subsequent sounding rocket experiments [Hess et al, 1971].

In the ECHO series of sounding rocket experiments, electron guns with energies of 40 kV and current levels of 100 mA and above have been used to study magnetospheric plasma phenomena. Beginning with ECHO I, it was found that sufficient beam electrons propagated down to the atmosphere to generate an artificial aurora. The ECHO results were interpreted as showing that tens to hundreds of millamps could be coupled to the ambient plasma [Winckler, 1974; 1976]. Interactions between the beam and ambient plasma were indicated by radio waves emissions particularly at the electron cyclotron frequency ( $f_{ce}$ ) and harmonics. It was concluded that the beam did not lose significant power to the waves. The early ECHO experiments thereby eased concerns about the importance of beam instabilities [Cartwright and Kellogg, 1987].

The Norwegian-American experiment POLAR 5 utilized a 0.1 A, 10 keV electron beam. A "mother-daughter" pair of payloads was utilized. Diagnostics indicated charging to about 1 kV, suggesting that much of the .1 A beam escaped. Hence, sufficient return current was available at the 200 km altitude where POLAR 5 was operated to balance the beam current. It was suggested that the neutralization current was partially due to local beam-plasma interactions. The environment was unusual in that the experiment was conducted in a region with naturally occurring auroral precipitation. [Grandal et al, 1980; Jacobsen and Maynard, 1980]

The MAIMIK experiment in November 10, 1985 used an electron gun with energies of 1-3.2 kV and currents of 20-800 mA. These experiments resulted in some observations indicating that the vehicle charged to near or above beam energy, limiting the emitted current. Significant charging occurred at currents of 80 mA and above, apparently partly as a result of a low ambient plasma density ( $\sim 10^4 \text{ cm}^{-3}$ ). It appears that a virtual cathode formed outside the beam aperture, and only 1-10% of the beam escaped. The escaping electrons were accelerated to 110-120% of the beam energy [Maehlum et al, 1987; 1988].

A Soviet experiment, G-60-S, was launched in 1981, to an apogee of 1500 km ( $L = 2.0-2.4$ ). The unusually high apogee allowed measurements at relatively low ambient neutral and electron densities ( $n_e \approx 10^4 - 10^5/\text{cm}^3$ ). Only the MAIMIK experiments were conducted at comparably low plasma densities. Floating probe measurements indicated that, above 400 km altitude ( $n < 10^5/\text{cm}^{-3}$ ), the 0.5 A gun charged the vehicle to near gun energy during experiments at 1, 2 and 3 kV. Experiments at 4 kV and 5 kV caused the vehicle to charge to +6 kV and +7 kV, respectively. The 'over-charging' occurred as the gun current exceeded  $\sim 0.25$  A. At lower currents, the vehicle potential was linearly related to gun current [Managadze et al, 1988].

The Soviet-French ARAKS experiment was one of the most ambitious experiments of the mid-1970's. ARAKS payloads were launched, on 26 January and 15 February 1975 from Kerguelen Island ( $L \sim 3.68$ ) to  $\sim 200$  km altitude. The 0.5 A guns operated at 15 keV and 27 keV. The guns were neutralized utilizing cesium hollow cathodes capable of 10 A plasma flux. The cathodes were apparently effective, and the electron beams apparently escaped. Vehicle potentials of a few hundred volts were inferred [Cambou et al, 1978; 1980]. VLF waves were observed, again indicating beam-plasma interactions. In particular, strong signals were observed at twice the electron gyrofrequency and at the plasma frequency. [Lavergnat et al, 1980; Dechambre et al, 1980]

These sounding rocket experiments indicate a dichotomy in results. Early experiments were interpreted as being successful in coupling currents of several hundred millamps to the ambient, with relatively low potentials resulting. Later experiments, at higher altitudes and with better diagnostics, have been interpreted as resulting in charging of the vehicle to potentials comparable to or greater than the beam energy. These latter experiments indicate fundamental limitations on the amount of current which can be collected by a body in a plasma. The dichotomy in results may be due to differences in ambient plasma density, variations in the ionization of neutral background gas, or better instruments giving more accurate results.

## SPACE SHUTTLE ORBITER

The Space Experiments with Particle Accelerator (SEPAC) was flown on the space shuttle orbiter Spacelab I payload. The Japanese-American payload was designed to generate artificial aurora using a high power electron beam. It apparently failed in this function, due to shuttle charging, and interactions between the beam and the ambient plasma and neutral gas. The charging problem was more severe than found previously on sounding rockets because of the surprisingly small conducting surface area (only the engine bells are conducting), a higher altitude (and hence lower electron density), and substantial wake effects. In particular, when the engine bells are in the wake (airplane mode flight), very little return current is available for such experiments. Interactions between the beam and local environment limited the emitted current, but may also represent a fundamental limitation in current collection [Sasaki et al, 1985, 1987; Reasoner et al, 1984; Katz et al, 1986, Marshall et al, 1988].

The electron data from these operations bear a startling similarity to SCATHA data which will be described below, and are presented here for comparison purposes. Figure 2 shows the electron flux as a function of energy during one pair of experiments. In these experiments, an argon MPD arcjet was used to generate a pulse of dense plasma, which balanced the emitted 0.3 A, 5 keV beam for  $\sim 10$  milliseconds. The beam pulse was 5 seconds long. During the operation of the arcjet, the shuttle orbiter potential remains near plasma potential. Once the plasma generated by the MPD pulse dissipates, the vehicle charges to a potential which is estimated to be 1 kV. This inference is made by identification of the peak in the flux at 1 keV.

Converting the data to distribution function (Figure 3) shows that there is substantial plasma above and below the beam energy which must have been generated in the region of the shuttle. Even below 1 keV, there is a background plasma which apparently results from the beam operation, independent of beam neutralization. This spectrum has been interpreted as the result of space charge oscillations in the beam [Katz et al, 1986], but could be due to interactions with the neutral gas in the shuttle bay. The feature which those experiments share with the high altitude SCATHA data, presented below, is the apparent scattering of the beam, and the production of electrons at energies substantially above the beam energy.

A second (French) payload also carried on SPACELAB I was dubbed PICPAB. This lower power electron gun (10 mA, 8 kV) was designed to study wave generation. Diagnostics were inconclusive, but appear to indicate the beam operations resulted in low potentials, and hence the beam escaped. This current level is consistent with the amount of thermal electron current which is available. [Beghin et al, 1984].

## SATELLITES

The ATS-5 filament neutralizer was used as an electron emitter at microampere current levels at geosynchronous orbit. ATS-5 electron emitting operations succeeded in reducing the magnitude of the negative eclipse charging potentials on the satellite. However, the spacecraft was rarely discharged

completely. This was the result of differential charging on the satellite surface limiting the emitted current [Olsen, 1985]. This is in contrast to ISEE-1 results. ISEE-1 is effectively a conducting body. Currents of 10's of microamperes were emitted, resulting in potentials up to the beam energy ( $\sim 50$  eV) [Lebreton, 1983].

### SCATHA ELECTRON GUN RESULTS

The nature of the complex problems which can occur when utilizing an electron gun in space are indicated by the SCATHA results. Complex collective plasma effects occur, as well as charging effects which depend on satellite geometry and structure. SCATHA experiments were conducted with an electron gun at current levels ranging from  $1 \mu\text{A}$  to  $13 \text{ mA}$ , and energies from  $50 \text{ eV}$  to  $3 \text{ keV}$ . These experiments showed that even with high energy beams differential charging or other plasma processes prevented beam emission.

#### DIFFERENTIAL CHARGING AS A CURRENT LIMITING MECHANISM

Data from eclipse experiments conducted with the SCATHA electron gun show how differential charging can limit electron emission. Figure 4 shows the satellite potential as a function of time for an eclipse period where the satellite charged initially to  $\sim -8 \text{ kV}$ . In principle, this potential is due to an integrated thermal electron flux in the  $1-10 \mu\text{A}$  range. Even without the balancing effect of secondary electron production and the ambient ion current, it is clear that  $10 \mu\text{A}$  beam current should be sufficient to discharge the satellite. The beam current and beam voltage are stepped through sequences which cover  $10 \mu\text{A}$ ,  $100 \mu\text{A}$  and  $1 \text{ mA}$ , at  $50 \text{ V}$  and  $150 \text{ V}$  accelerating potential. The satellite potential is inferred from measurements of the ion spectrum in two detectors [Olsen, 1985]. The result is that the beam electrons result in a decrease in the magnitude of the potential, but not a complete discharge of the satellite.

This is most clearly illustrated by the  $100 \mu\text{A}$ ,  $150 \text{ V}$  segment at  $\sim 0739$ . The potential shows a decrease to  $|\Phi| < 1 \text{ kV}$ , then recharges to an equilibrium potential of  $\sim -1.5 \text{ kV}$ . This curve shape, characteristic of a charging capacitor with  $\tau \sim 1$  minute, was frequently seen in the ATS-5 experiments, and indicated that the insulating solar array cover slides were charging to a potential a few hundred volts more negative than the mainframe. Equilibrium is attained when the escaping beam current has been reduced by 2 orders of magnitude. Increasing the beam current to  $1 \text{ mA}$  resulted in no increase in the escaping current. These data indicate that coupling even a low current to the ambient plasma can be difficult, due to charging phenomena. Some shuttle data also show indications of tile charging during electron beam experiments [Beghin et al, 1984].

The problems encountered in discharging a negatively charged satellite are generally unique to geosynchronous orbit. A more general class of problems became apparent during experiments in daylight and eclipse for non-charging environments. Experiments conducted when SCATHA was near plasma potential (typically a few volts positive) showed evidence of beam-plasma interactions, and a similarity to SPACELAB 1/SEPAC data which suggests the results may be quite general.

## WAVE PARTICLE INTERACTIONS AS A LIMITING MECHANISM

Data from a sequence of operations on July 20, 1979 (Day 201) are presented. The example chosen here illustrates an experiment in the plasma sheet, near local midnight. July 20 was a disturbed day geomagnetically;  $\Sigma K_p = 24 =$ ,  $K_p = 2+$  for 3–6 UT. The satellite is in the plasma sheet at 0600 UT, 0130 LT,  $7.4 R_E$ ,  $17^\circ \lambda_m$ ,  $L = 8.8$ . The plasma sheet electrons can be characterized with a density of  $0.7 \text{ cm}^{-3}$ , and temperature of 8.6 keV.

The data from this operation are summarized in spectrogram format in Figure 5. In a spectrogram, the instrument count rate (or particle flux) is plotted as a function of time (horizontal axis) and energy (vertical axis), with high fluxes encoded with dark gray or black, and low or zero fluxes encoded as white. The plotted value is the biased log,  $1000x \log_{10} (\text{count rate} + 10)$ . Hence, zero counts gives a biased log of 1000,  $10^5$  counts gives a biased log of 5000. Data from the two high energy detectors are shown here, with the electron data on top. The energy axis starts at zero in the middle of the figure, and increases upwards for electrons, and downwards for ions. The horizontal line plotted along the center is the pitch angle of the measured particles, which is generally near  $90^\circ$  at this time. Two electron gun operation periods occur during this one hour time segment (0600–0700 UT). During the first segment, the gun is turned on, and high electron fluxes are found up to 70–80 eV for the entire period. This is contrary to expectations that the peak would occur at 50 eV, as might be expected for a satellite charged to +50 V. During the second operation visible in the figure, the satellite apparently did not initially charge to the beam energy, and high fluxes of electrons are found only up to a few tens of eV. There is then a subtle change in the keV electron fluxes (a decrease) and the satellite potential apparently rises to near 50 V, and intense electron fluxes are found up to 70–80 eV. Data from the first operation are discussed next.

The electron count rate is shown for beam on conditions at 0614 UT in Figure 6. The features described in the spectrogram are apparent here. The flux peaks at 50,000 counts/sec, or a differential energy flux of  $\sim 10^8 \text{ electrons/cm}^2 \cdot \text{ster}$  at 50–70 eV. There is not a sharp boundary at the expected potential (50V), but rather at 140% of the beam energy, 70 eV. As with the SEPAC experiment (Figure 2), there is a substantial flux above the beam energy. Further information can be obtained by converting count rate to phase space density.

The 0 – 150 eV electron data are shown as a distribution function in Figure 7. In this format (log-linear axes) Maxwellian (e.g., thermalized) distributions will appear as straight lines. When the gun is off (0609 UT), the boundary between spacecraft generated photo electrons and ambient plasma at 10 to 15 eV suggests a satellite potential of +10 to +15 V. When the gun is switched on, a different equilibrium is quickly established. SCATHA charges to near beam energy (50 eV), and enhanced fluxes appear both above and below 50 eV. There is not, however, a peak at 50 eV, as would be expected if the mono-energetic beam electrons returned to the satellite; nor is there a peak which could be attributed to cool ( $T \sim 1 \text{ eV}$ ) ambient electrons which have fallen through a 50 eV potential drop. Instead, there is a local minimum at 52 eV, and a peak above 50 eV, or at least a plateau from 55 to 75 eV. Liouville's theorem requires that if the distribution functions are shifted in energy by the change in spacecraft potential ( $\sim 35\text{V}$ ) that they shall overlap. They do so above about 80 eV, for the unperturbed magnetospheric plasma. It is

clear from this comparison, however, that the 55 to 75 eV data represent a 'new' population, and do not simply represent a charging effect. The density in the 55 to 75 eV portion of the distribution function is about  $1 \text{ cm}^{-3}$ . This is comparable to the ambient density. The 20–45 eV electron data show a density of  $124 \text{ cm}^{-3}$ , and temperature of 6.3 eV. These latter values are appropriate for the local photo-electron cloud, heated to about twice the normal temperature.

Experiments later on this day produced similar results. Figure 8 shows electron distribution functions for  $10 \mu\text{A}$  and  $100 \mu\text{A}$  beam settings for operations near local dusk. The presence of a higher balancing electron flux prevents SCATHA from charging to +50 V at  $10 \mu\text{A}$ , as in the latter portion of the data set shown in Figure 5 (~ 0635–0645). When the current is increased to  $100 \mu\text{A}$ , the data resemble those shown in Figure 7, with a peak above 50 eV.

Observations of electron distribution functions which are symptomatic of heating suggest the need to consider the plasma wave data. Such data are available for the long electric antenna (100 m tip-to-tip) and a magnetic search coil, located 2 meters from the satellite. Data are available continuously from 8 narrowband channels which cover the 400 Hz – 100 KHz frequency range for the electric antenna, and in 4 channels from 400 Hz to 3 kHz for the magnetic antenna. Wideband data covering the range from a few hundred Hertz to 3 or 6 kHz are available for portions of each day. This latter frequency range typically includes the electron gyrofrequency, but not the plasma frequency [Koons and Cohen, 1982].

Observations associated with the second example of SCATHA electron gun experiments on 20 July 1979 (Figure 8) showed evidence of strong signals at the electron cyclotron frequency. Figure 9 shows the plasma wave data for the 4 low frequency channels of the Aerospace Corp plasma wave receiver (SC1). Data are taken from the 100 meter tip-to-tip electric field antenna, and the search coil magnetometer. The latter has proven to be sensitive to electrostatic emissions. It is apparent that substantial wave power is present. The magnetic antenna is located 2 meters from the satellite, and is therefore extremely sensitive to signals generated at the satellite. Major effects are apparent in all 4 of the magnetic channels, and a less obvious response in the electric channels. The magnetic channel saturates at 2.3 kHz for the magnetic receiver during the  $10 \mu\text{A}$  beam operation. No response is seen in the electric channels at 10 kHz and above. There is a current dependence to the amplitude. Much lower amplitudes are seen in the magnetic antenna at  $100 \mu\text{A}$  than at  $10 \mu\text{A}$  beam current.

Figures 10 and 11 show the frequency spectra obtained from the wideband receiver before and during these experiments. The data presented here have not been widely disseminated, and are shown in some detail. The SC-1 receiver cycles between the electric and magnetic antenna every 16 seconds. The narrowband data shown in summary form in Figure 9 are expanded in Figures 10 and 11, on the same time scales as the wideband data. At this time, the wideband frequency range being plotted is 0–4 kHz, with a rolloff due to the transmission bandwidth at 3 kHz. In these displays, intense signals are plotted as black, low signals as white. The wideband receiver response is governed by an automatic gain control (AGC) which is generally driven by the most intense, monochromatic signal in the frequency range.

Figure 10 shows two aspects of the gun off data which are pertinent to the gun experiments. The wideband plot given in Figure 10a shows the existence of broad frequency range signals (0 - 2 kHz) in the electric channel which are erratic in their intensity. The narrow band channels at 400 Hz (Figure 10c) and 1.3 kHz (Figure 10b) reflect the impulsive behavior of this broad spectrum. There are interference lines in the magnetic channel at 700 Hz and 2100 Hz which are due to a tuning fork in another experiment. These lines are commonly observed in the absence of strong electro-magnetic signals.

Figure 10d shows naturally occurring electron cyclotron waves appearing intermittently, at a frequency of about 2.5 kHz. The response of the magnetic loop antenna to these electrostatic waves is not understood, but is a consistent feature of the flight instrument. Both the 3.0 kHz (Figure 10e) and 2.3 kHz (not shown) narrowband channels respond to these intense signals, as is most obvious around 82244 seconds [Koons and Edgar, 1985].

When the electron gun is switched on, a strong signal is generated at about 2.3 kHz. This is the intense signal revealed by the summary plot (Figure 9), and is the thin horizontal line in Figure 11a. The previously seen electrostatic background remains visible, and variations in the background signal are apparent in the wideband data, and the narrowband electric channels (Figure 11b, c). The magnetic loop antenna is almost saturated, though the broadness of the peak in Figure 11a is more a result of the data processing than the instrument response. These signals are very close to the electron cyclotron frequency, and we have concluded that they are most likely electron cyclotron waves. This is reinforced by Figure 11d, which shows an overlap between the naturally occurring waves found in Figure 10d with the gun generated signal.

The data illustrated in Figure 11a are typical of the period. There is a fluctuation in the frequency with spin which is not apparent in these plots. This is associated with the amplitude variation which is visible in Figure 9 in the 3 kHz magnetic channel. Study of this aspect of the data showed that it was associated with fluctuations in the solar array current with spin. Fluctuations in the solar cell currents induced changes in the local magnetic field which were 1-10 nT (1-10% of the ambient field) at the satellite surface. This places the interaction region near the beam aperture. It is tempting at this point to infer that the observed signal is scattering the beam, and heating the local electron distribution.

There is a current dependence to the induced signal, which is as might be expected. During the period illustrated in Figure 11a and 11d, the gun is set at 10  $\mu$ A, 50 eV. At 82948 seconds, the gun current is increased to 100  $\mu$ A. The signal at 2.5 kHz disappears, and the electric and magnetic spectra resume their unperturbed forms (Figure 11d, 11f) when the current is decreased to 10  $\mu$ A at 82996 seconds, the intense signal resumes. This period corresponds to the particle data shown in Figure 8. An unfortunate aspect of this correspondence is the absence of artificially stimulated electron cyclotron waves during the 100  $\mu$ A operation which results in heated electrons above 50 eV. The intense signals at 2.5-2.6 kHz are anticorrelated to the 50-70 eV peak! It may be that signals not apparent in the wideband data are responsible for the 50-70 eV electron distributions. One likely possibility would be electron plasma oscillations, or upper hybrid waves. Such waves would be well out of the wideband frequency range. There is a 10 dB increase in the 100 kHz electric

channel during both of the 100  $\mu$ A beam current operations ( $\sim$  2303, 2322 UT). There are spikes in the 10 kHz data which rise 20–30 dB above background at these times, also. These would be appropriate for plasma oscillations in plasmas with densities of 100 cm $^{-3}$  and 1 cm $^{-3}$ , respectively. This aspect of the data is presently being studied. The electron cyclotron waves may still be responsible for the enhanced temperatures in the 0–50 eV electrons [Olsen et al, 1989].

It appears that when experiments with the electron gun exceeded the amount of current available from the ambient plasma, wave particle interactions occurred which caused the beam to scatter. Electron cyclotron waves may be the causal factor. Similar wave features were reported for the Japanese JIKIKEN (EXOS-B) satellite, with some emission stimulated at the local electron gyrofrequency by a 200 eV, 0.25–1.0 mA beam. The more common features in the JIKIEN data were signals at twice the electron gyrofrequency, and the upper hybrid resonance frequency. [Kawashima et al, 1981; 1982]

This scattering of the beam in energy is similar to the SEPAC behavior described previously. This similarity suggests that this class of limiting mechanisms is much broader than previously suspected.

## ION BEAM EXPERIMENTS

Current limiting mechanisms appear to be less severe for ion beams. The historical record primarily indicates success in propagating ion beams away from satellites and rockets.

### ARCS

The Argon Release Controlled Studies (ARCS) sounding rockets used a modified form of the ion engine originally used on ECHO 1 for electron beam neutralization. Currents of  $\sim$  100 mA of Ar $^+$  were generated at energies from 20–40 eV (ARCS-1) to  $\sim$  200 eV (ARCS-3). ARCS-1 was launched on 27 January 1980. The bulk of the beam apparently escaped. It appears that the payload charged to a potential more negative than -5V. Electrons were observed to be accelerated toward the beam emitting payload during ion beam operations. This effect was ascribed to the creation of an electric field parallel to the geomagnetic field. There also appear to have been substantial electron heating, apparently due to wave turbulence associated with beam operations.

ARCS-3 was launched on 10 February 1985 to an apogee of 406 km. This experiment showed that the injection of particles parallel or perpendicular to the geomagnetic field consistently resulted in the appearance of a population of ions at low energy ( $\sim$  15 eV) and at 90° pitch angle. These ions apparently are scattered out of the beam. Still, the bulk of the beam apparently propagated well away from the rocket, with potentials limited to  $\sim$  -100 V. These experiments indicate that sounding rockets are able to draw neutralizing currents to the beam and rocket via complex processes which accelerate and thermalize the ambient plasma [Kaufmann et al, 1985; 1989; Moore et al, 1982].

### PORCUPINE

The Porcupine experiments conducted by the West Germans utilized a xenon ion engine design previously utilized by the Soviet Union for their METEOR

satellites. Porcupine rockets F3 and F4 were launched in March, 1979 from the European Space Research Range to study the auroral ionosphere. The Xenon ion beam was injected perpendicular to the ambient magnetic field into the collisionless ionospheric plasma at altitudes ranging from 190 to 450 km. These experiments showed that the beam propagated nearly undistorted across the plasma. The beam was not current neutralized [Häusler et al, 1986].

#### ATS-4

An ion engine is a device which combines an ion beam with a charge and current balancing electron source. There is generally little net current. The first major ion engine flight experiment was ATS-4, launched on August 10, 1968. ATS-4 was intended to be a geosynchronous satellite but the booster failed to achieve a second burn. ATS-4 remained attached to its Centaur Stage booster, and remained in a low parking orbit. In spite of this failure, a number of successful ion engine tests were run. Two ion thruster systems were on board, and a spacecraft potential monitor that employed one of the gravity gradient booms as a Langmuir probe. The boom was deployed prior to the last of five ion engine test periods on ATS-4. The large ram ion currents available from the relatively dense ambient plasma precluded the achievement of appreciable neutralizer emission current except for a few brief periods (altitude 218 to 760 km, density  $10^{10}/m^3$ , ambient pressure  $10^{-9}$ - $10^{-6}$  Torr, current 330  $\mu$ A, spacecraft potential -132 V) [Hunter et al, 1969].

#### ATS-5

ATS-5 carried a cesium contact ion engine and filament neutralizer. The ATS-5 ion engine is shown in Figure 12. ATS-5 was launched into synchronous orbit on August 12, 1969 and stationed at 105° W longitude. Again, there was a launch failure. ATS-5 was to be gravity gradient stabilized, but ended up spinning at 100 rpm. The ion engine worked well in spite of the spin problem. Coupling potentials of less than 50 V resulted from engine operation. Induced charging experiments (no neutralization) with the ion beam in sunlight resulted in induced charging to near the beam energy. Figure 13 shows the ion count rate during one of the brief experiments. These experiments indicated the effectiveness of neutral beam emission and at least some success in emitting a non-neutral beam [Olsen, 1985].

#### ATS-6

ATS-6 carried twin cesium thrusters designed to test ion engine technology and their usefulness for stationkeeping on the three-axis-stabilized satellite. It was launched in 1974. ATS-6 engine operations were successful, and had the beneficial side effects of discharging the mainframe and all differentially charged surfaces. The plasma bridge neutralizer alone could also discharge large negative potentials in sunlight or eclipse. A 92 hour operation of the ion engine at 160 mA, 3 kV was successfully conducted [Olsen, 1985].

#### SFL

A soviet sounding rocket program dubbed an automatic ionosphere space-flight laboratory (SFL), had launches in November, 1969 and August, 1970. These experiments made use of an ion engine using surface ionization of cesium on

tungsten. The maximum value of the ion beam current was 100 mA and the effective accelerating voltage was about 2400 V. The rocket body reached -1700 V potential. The thickness of the space charge layer surrounding the SFL was inferred to be 7 m [Gavrilov, 1973].

### SERT II

SERT-II (Space Electric Rocket Test II), carrying dual 15 cm diameter mercury electron bombardment ion thrusters, was launched on February 3, 1970 into a polar, sun-synchronous orbit at 1000 km altitude. The SERT II thrusters accelerated 0.25 A of Hg ions through a 3 kV potential. Hollow cathode, plasma bridge neutralizers were used. The Agena second stage was retained as part of the orbiting system [Byers, 1970].

Emissive probes flown on the SERT-II spacecraft in conjunction with the prime ion thruster experiment allowed an investigation of the interaction between the spacecraft, the ion thruster, and the ambient space plasma. One thruster operated for 5-months and the other operated for 3-months. Both thrusters failed due to sudden shorts between the high voltage grids. It was determined that the cause was sputtering of grid surfaces. They demonstrated thrust, and an absence of harmful interactions with the vehicle [Kerslake et al, 1971].

The mean SERT-II spacecraft equilibrium potential with the engine off was -6 to -8 V. This relatively high negative potential was due to the presence of exposed solar array interconnections at high positive potentials (36 Volts). With the engines on, it was possible to control the potential difference between the spacecraft and the space plasma, using the neutralizer bias. For positive bias voltages, the spacecraft was driven more negative, by an amount equal to the change in bias voltage (Figure 14). The beam to neutralizer potential remained constant (tens of volts), and the current collected by the exposed interconnects was not a factor. This was particularly true where the interconnects remained below plasma potential. When the neutralizer was biased negative with respect to the satellite, the body could be driven positive. The neutralizer to beam potential increased rapidly, and the neutralizer current increased until the device current limited. This could be explained as an increase in electron collection by the satellite [Jones et al, 1970].

### SCATHA

The SCATHA satellite carried a small ion gun, capable of xenon ion currents of 300  $\mu$ A, 1 mA, and 2 mA, at energies of 1 keV and 2 keV (nominal). The AFGL experiment had electron emitting filaments for beam neutralization. The SCATHA experiments indicate again the range of behavior which can be found in space, particularly the effects of collective plasma processes. Data are shown from 2 days. Day 200.

Data from operations on 19 July, 1979 (Day 200), are presented first to illustrate two modes of operation of the ion gun in sunlight. The first example of ion emission begins shortly after 2140 UT. The satellite was located in the plasmashell near local dusk (1954–2042 LT) between L = 7.6 and 8.0 at an altitude of 7.5  $R_E$  and a magnetic latitude of 6 degrees.

The particle data for this day are summarized in spectrogram format in Figure 15. In a spectrogram, instrument count rate (or particle flux) is plotted as a function of time on the horizontal axis and energy on the vertical axis. The flux magnitude is depicted using a gray scale, with high fluxes appearing a dark gray or black and low or zero fluxes showing up as light gray to white. This figure displays data from the two high-energy detectors, with the electron data on top. The energy axis is zero in the middle of the figure and increases upwards for the electrons and downwards for the ions. The lower horizontal line plot in the center is the pitch angle of the measured particles. The pitch angle is the angle between the particle's velocity vector and the magnetic field line. The upper horizontal line plot is the detector head angle. Note the plasma injection at 2149 UT, recognized by the abrupt increase in particle flux over a wide energy range. Injections are the sudden appearance of hot plasma and occur at least daily, more frequently during periods of high magnetic activity, with variable spectra [McIlwain and Whipple, 1986]. The peak in the differential electron flux (count rate) is in the 1 to 10 KeV range, typical for the plasma sheet. The upper bound on the electron flux ( $\sim$ 10 KeV) is the result of magnetospheric convection processes and is termed the Alfvén boundary. It must exceed a critical energy of 15 to 20 KeV for negative charging to occur. The high energy ion flux extends up to 80 KeV.

Unneutralized ion gun operation at 1 kV and a current setting of 1 mA begins at 2141 UT and terminates at 2301 UT. This results in satellite charging, as seen in the spectrogram as a black band representing high ion fluxes. The high fluxes are due to ambient low energy ions being accelerated into the spacecraft at the spacecraft potential energy. There are two periods of trickle mode operation (no accelerating voltage) at 2200–2203 UT and 2227–2232 UT, which correspond to the times in the spectrogram where the black ion flux band is absent. This suggests a spacecraft potential magnitude of less than 10 Volts. Analysis of the data ultimately determined that the average sunlight floating potential for this period ( $\sim$  +5V) was reduced to  $\sim$  +1V by the trickle mode operation, with a net ion current of 20–50  $\mu$ A emitted [Werner, 1988].

When the ion gun is activated at 2141 UT, the satellite is driven to a potential between 600 and 800 volts negative, which is significantly less than the beam energy. This is indicated in the spectrogram by a black band representing high ion fluxes. The ion flux peak is due to the ambient low energy ions being accelerated into the spacecraft at the spacecraft potential energy. Potentials of less than about  $\pm$ 10 Volts are difficult to determine using this method, as seen by the complete absence of any ion charging peak during the two trickle mode operations. The spacecraft potential is most accurately determined by converting flux (count rate) to the particle distribution functions. The peak at about 700 eV in the ion distribution function of Figure 16, taken at 22:10:44 UT, is interpreted to be at the spacecraft potential. Representative energy channel widths are shown using bars on the data points. Note that the energy channels overlap. An alternate potential estimate can be obtained by comparing the potential of one electric field probe to the satellite potential.

Figure 17a is a plot of the potential difference measured by the SC10 electric field experiment. A modulation at the spin period is immediately obvious. There is a turn on transient, indicating the spacecraft momentarily charges to a negative potential corresponding to the magnitude of the beam voltage. The spacecraft potential then rises (becomes less negative). This behavior is seen each time the

gun is switched on and is counter-intuitive as the beam current, plotted in Figure 17b, actually increases during the transient. Note that the beam current is measured at the beam power supply and the net beam current, which stays constant, is measured at spacecraft common.

Figure 18 shows the SC10 data at higher resolution for a period after the turn on transient. It shows the potential, with points plotted every two seconds, as measured by SC10 between 2210 UT and 2215 UT (approximately five spin periods). Also plotted in this figure is the spacecraft potential as determined by the charging peaks for the HI and LO ion detectors. Energy channel widths are shown for representative SC9 data points. The excellent agreement between the SC9 and SC10 values suggest that the SC10 experiment provides a valid measurement of the spacecraft potential during ion-emission induced charging events in sunlight. Both measurements indicate a spacecraft potential less than the beam energy. Since sufficient ion current is available to charge SCATHA to the beam energy (1 kV), there must again be a limiting factor.

Figure 19 shows a distribution function taken during ion gun operation at 22:06:28 UT. The significant feature of this figure is the second peak at an energy greater than the spacecraft potential and near the ion gun energy. This secondary peak appears to be the 1 KeV beam ions scattered into the UCSD detector. It may indicate that periodically, significant fluxes of beam ions are being returned to the satellite. The significance of this becomes more apparent after a second set of experiments is considered.

#### Day 47 High Voltage, HI and LO Current

Observations for 16 February, 1979 (Day 47), are presented to illustrate the effects of ion gun operation on the spacecraft in a different plasma environment using similar (Day 200) beam parameters. During initial operations of the ion gun an experimental low current mode was used. In this mode, the main discharge went out and only the keeper operated. This resulted in a beam at 1 kV and 25–50  $\mu$ A. Unfortunately, the SC10 booms had not yet been deployed so electric field data are not available. These experiments were conducted in the plasmasheet at local dawn near an altitude of  $5.5 R_E$  between  $L = 5.7$  and  $6.5$ . Only the results of the charging analysis are presented.

In Figure 20, the energy of the peak in the distribution function, which is close to the spacecraft potential, is plotted versus time. The turn on transient at 1449 UT again seems to show the satellite charging to near the beam energy. The potential then stabilizes near –500 Volts after one minute. This is 200 volts more positive than the Day 200 operations. Ion gun telemetry for the same period, again shows the beam current increasing during the transient. After half a minute the beam steadies at a current value near 1.05 milliamp. Note that the beam current is 50% lower than the Day 200 experiments.

At 1451 UT, the gun drops into the low current mode and a –10 to –20 Volt potential is seen for a beam current of 20–30  $\mu$ A. As on Day 200 net currents in the 10 to 100 microamps range result in relatively small ( $\Phi_{s/c} < 50V$ ) potentials. It is apparent that 1 mA should have been sufficient to drive the vehicle to near the beam potential.

Analysis of data from other experiment periods showed that the beam rarely caused the vehicle to approach beam voltage. Increasing the beam energy from 1 to 2 kV, at 1 mA, did decrease the vehicle potential (e.g., from -900 to -1800 V on day 293, in eclipse). By contrast, varying the beam current had the opposite effect. On day 293, in eclipse, experiments at 1 kV beam energy showed that at 0.3 mA, the nominal potential was -900 V. Increasing the current to 1 mA caused the potential to rise to -800 V.

The most likely reason for this peculiar behavior is that the ion beam is space charge limited [Stannard et al, 1986]. This process is illustrated in Figure 21. Much of the beam is scattered, with some ions returning to the spacecraft at 1 keV, as seen in Figure 19. The referenced analysis was based upon simple space-charge limited diode theory and brings the predicted satellite voltages in rough agreement with experiment. Net ion beam currents of 50–60  $\mu$ A were predicted to escape the near-satellite region. The reason for this behavior is the relatively small exit aperture of the SPIBS. A larger diameter beam would have been able to emit a larger net current – at least until the satellite reached beam energy.

These results, combined with reports from sounding rockets, suggest a principle similar to that indicated by the electron gun experiments. At low current levels, where sufficient ambient plasma exists to counter space charge effects and to balance the emitted current, the beams propagate freely. As the ambient density decreases, space charge limiting develops. If a neutral plasma is emitted in conjunction with the beam, the beam escapes. This is illustrated by successful ion engine experiments, and SCATHA experiments where both charge carriers were emitted.

## NEUTRAL GAS

The one caveat to the principle of current limiting is that the experiment be conducted in the absence of neutral gas. The injection of a plasma or a neutral gas will neutralize a charged particle beam. The mechanisms which are important are those which result in substantial ionization of the neutral gas cloud. This may be due to the beam itself, the return (collected) electron flux, or perhaps even secondary electron emission from the vehicle surface. Under some conditions, it is believed that as the ionization process proceeds, electrostatic waves are set up, which increase the ionization rate, instigating a Beam–Plasma Discharge (BPD) [Getty and Smullin, 1963].

Neutral gas releases were tried on ECHO 1. No direct evidence of effective vehicle neutralization was obtained. Indeed, the ECHO I results have been traditionally interpreted with the thought that the rocket body provided adequate return current collection. The ECHO IV experiment again considered the effect of a neutral gas release. The 40 kV, 80 mA beam was fired through an N<sub>2</sub> plume. The N<sub>2</sub> densities were obtained by means of a photometer calibrated at 3914 Å. The return current was enhanced by the neutral N<sub>2</sub> and enhanced glow was found when the beam went through the N<sub>2</sub> cloud [Israelson and Winckler, 1979].

This technique was also used in the SEPAC experiments with a beam energy of 2.9 keV and current of 200 mA. The neutral gas plume (NGP) emitted  $10^{23}$  molecules of nitrogen (N<sub>2</sub>) in a 100 ms pulse. The gas release resulted in a neutral gas pressure increase in the shuttle bay, from  $10^{-6}$  Torr to  $2 - 3 \times 10^{-6}$  Torr. This

technique was apparently successful, neutralizing the beam and allowing it to escape [Marshall et al, 1988]. One curious aspect of these experiments was that the 9 keV, 10 mA PICPAB beam did not result in substantial ionization of the emitted neutrals. This may be related to the relatively low shuttle potentials induced by PICPAB ( $\sim +10$ ) [Burch, 1986]. There is substantial disagreement in the literature over occurrence of BPD in the SEPAC experiments [Watermann et al, 1988]

Possible occurrences of BPD during sounding rocket experiments are described by J. R. Winckler. The BPD conditions are that:

$$I = C V^{1.5} / B^{0.7} PL \quad (1)$$

where  $V$  is the accelerating voltage,  $B$  the magnetic field,  $P$  the pressure and  $L$  the scale length of the experiment. Since the beam permeance is generally of the form  $I \propto V^{1.5}$ , it is clear that beam permeance determines the occurrence. Winckler [1982] concludes that BPD has been observed.

## SUMMARY

Analysis of existing flight data on charged particle emission indicates a general difficulty in emitting substantial current. In general, it appears that the emitted current is limited to the thermal current, or the thermal current amplified by an attractive potential which is not much larger than the plasma temperature (e.g.,  $e\phi/kT \sim 1$ ). Besides current limiting, space charge limiting processes restrict the ability to emit charged particle beams. Coupling of large current to the ambient plasma requires a balancing cold plasma source which may be artificial (e.g., a gas discharge), or may be supplied by the local neutral gas environment.

## ACKNOWLEDGEMENTS

The work presented here was largely supported by NASA/Lewis Research Center while the author was at the University of Alabama in Huntsville. The ion gun analysis was completed at NPS, and was largely the work of LT Paul Werner. This work, and the analysis of the wave data, were supported by the Naval Postgraduate School and NASA/LeRC. Dr. Harry Koons and Dr. Jim Roeder at Aerospace Corporation have graciously provided the SC-1 plasma wave data. The principle investigator for the UCSD particle detector was Sherman DeForest. The principal investigator for the SC10 electric field experiment was Dr. Tom Aggson of NASA/GSFC. Mr. Herb Cohen was the principal investigator for the AFGL electron and ion gun experiments. Dr. Jill Marshall of Southwest Research Institute provided the SEPAC distribution functions.

## REFERENCES

- Beghin, C., J. P. Lebreton, B. N. Maehlum, J. Troim, P. Ingsoy, and J. L. Michau, Phenomena induced by charged particle beams, *Science*, 225, 188-191, 13 July 1984.
- Burch, J. L., Space plasma physics results from Spacelab-1, *J. Space. Rockets*, 23, 331-335, 1986.
- Byers, D. C., and J. F. Staggs, SERT-II thruster system ground testing, *J. Space. Rockets*, 7, 7-14, 1970.
- Cambou, F., J. Lavergnat, V. V. Migulin, A. I. Morozov, B. E. Paton, R. Pellat, A. Kh. Pyatsi, H. Rème, R. Z. Sagdeev, W. R. Sheldon, I. A. Zhulin, ARAKS - Controlled or puzzling experiment?, *Nature*, 271, 723-726, 23 February 1978.
- Cambou, F., V. S. Dokoukine, J. Kavergnat, R. Pellat, H. Reme, A. Saint-Marc, R. Z. Sagdeev, I. A. Zhulin, General description of the ARAKS experiments, *Ann. Geophys.*, 36, 271-283, 1980.
- Cartwright, D. G., and P. J. Kellogg, Observations of radiation from an electron beam artificially injected into the ionosphere, *J. Geophys. Res.*, 79, 1439-1457, 1974.
- Dechambre, M., J. Lavergnat, R. Pellat, Waves observed by the ARAKS experiments: the VLF Range, *Ann. Geophys.*, 36, 351-356, 1980.
- Gavrilov, F. V., A. S. Myasnikov, G. G. Zhadan, G. S. Orlova, and M. V. Strokin, Some results of flight tests of an ion-engine model using surface ionization of cesium on tungsten, *Kosmicheskie Issledovaniya*, Vol. 11, No. 1, pp. 140-144, January-February 1973.
- Getty, W. D., and L. D. Smullin, Beam-plasma discharge: buildup of oscillations, *J. of Applied Physics*, 34, 3421-3429, 1963.
- Grandal, B., J. A. Holtet, J. Troim, B. Maehlum, and B. Pran, Observations of waves artificially stimulated by an electron beam inside a region with auroral stimulation, *Planet. Space Sci.*, 28, 1131-1145, 1980.
- Häusler, B., R. A. Treumann, O. H. Bauer, G. Haerendel, R. Bush, C. W. Carlson, B. Theile, M. C. Kelley, M. C., V. S. Dokukin, and Yu-Ya. Ruzhin, Observations of the artificially injected porcupine xenon ion beam in the ionosphere, *J. Geophys. Res.*, 91, 287-303, 1986.
- Hess, W. N., M. C. Trichel, T. N. Davis, W. C. Beggs, G. E. Kraft, E., Stassinopoulos, and E. J. Maier, Artificial aurora experiment and principle results, *J. of Geophys. Res.*, 76, 6067-6081, 1971.
- Hunter, R. E., R. O. Bartlett, R. M. Worlock, and E. L. James, Cesium contact Ion microthruster experiment aboard Applications Technology Satellite (ATS-IV), *J. Space. Rockets*, 6, 968-970, 1969.
- Israelson, G. A., and J. R. Winckler, Effect of a neutral N<sub>2</sub> cloud on the electrical charging of an electron beam-emitting rocket in the ionosphere: ECHO IV, *J. Geophys. Res.*, 84, 1442-1452, 1979.
- Jacobsen, T. A. and N. C. Maynard, POLAR 5 - An electron accelerator experiment within an aurora. 3. Evidence for significant spacecraft charging by an electron accelerator at ionospheric altitudes, *Planet Space Sci.*, 28, 291-307, 1980.
- Jones, S. G., J. V. Staskus, and D. C. Byers, Preliminary Results of SERT-II Spacecraft Potential Measurements Using Hot Wire Emission Probe, NASA TM X-2083 1970.

- Katz, I., G. A. Johneward, D. E. Parks, D. L. Reasoner and C. K. Purvis, Energy broadening due to spacecharge oscillations in high current electron beams, *Geophys. Res. Lett.*, **13**, 64, 1986.
- Kauffman, R. L., D. N. Walker, J. C. Holmes, C. J. Pollock, R. L. Arnoldy, L. J. Cahill, and P. M. Kintner, Heavy ion beam-ionosphere interactions: Charging and neutralizing the payload, *J. Geophys. Res.*, **94**, 453-471, 1989.
- Kauffmann, R. L., R. L. Arnoldy, T. E. Moore, P. M. Kintner, L. J. Cahill, Jr., and D. N. Walker, Heavy ion beam-ionosphere interactions: Electron acceleration, *J. Geophys. Res.*, **90**, 9595-9614, 1985.
- Kawashima, N., and the JIKIKEN (EXOS-B) CBE Project Team, Wave Excitation in Electron Beam Experiment on Japanese Satellite "JIKIKEN (Exos-B)", in Artificial Particle Beams in Space Plasma Studies, edited by Bjorn Grandal, Plenum Press, NY, 101-110, 1982.
- Kawashima, N., A. Ushikoshi, Y. Murasato, A. Morioka, H. Oya, M. Ejiri, S. Miyatake, and H. Matsumoto, Beam-plasma interaction experiment in the magnetosphere by emitting an electron beam from satellite JIKIKEN (EXOS B), *J. Geomag. Geoelect.*, **33**, 145-159, 1981.
- Kerslake, W. R., R. G. Goldman, and W. C. Nieberding, SERT-II Mission, thruster performance, and in-flight thrust measurements, *J. Space. Rockets*, **8**, 213-224, 1971.
- Koons, H. C. and B. C. Edgar, Observations of VLF emissions at the electron gyrofrequency, *J. Geophys. Res.*, **90**, 10961-10967, 1985.
- Koons, H. C., and H. A. Cohen, Plasma Waves and Electrical Discharges Stimulated by Beam Operations on a High Altitude Satellite, in Artificial Particle Beams in Space Plasma Studies, edited by Bjorn Grandal, Plenum Press, New York, 111-120, 1982.
- Lavergnat, J., M. Dechambre, R. Pellat, Yu. V. Kushnerevsky, S. A. Pullinet, Waves observed by the ARAKS experiments: Generalities, *Ann. Geophys.*, **36**, 323-332, 1980.
- Lebreton, J.-P., Active control of the potential of ISEE-1 by an electron gun, Proceedings of the 17th ESLAB symposium on Spacecraft/Plasma interactions and their influence on field and particle measurements, Noordwijk, The Netherlands, 13-17 Sept 1983, ESA Sp-198, 191-197, 1983
- Maehlum, B. N., J. Troim, N. C. Maynard, W. F. Denig, M. Friedrich, K. M. Torkar, Studies of the electrical charging of the tethered electron accelerator mother-daughter rocket Maimik, *Geophys. Res. Lett.*, **15**, 725-728, 1988.
- Maehlum, B. N., W. F. Denig, A. A. Egeland, M. Friedrich, T. Hansen, G. K. Holmgreen, K. Maseide, N. C. Maynard, B. T. Narheim, K. Svenes, K. Torkar, J. Troim, J. D. Winningham, Maimik - A high current electron beam experiment on a sounding rocket from Andoya Rocket range, Proceedings of the 8th ESA Symposium on European Rocket and Balloon Programmes and Related Research, Sunne, Sweden, 17-23 May 1987, ESA Sp-270.
- Managadze, G. G., V. M. Balebanov, A. A. Burchudladze, T. I. Gagua, N. A. Leonov, S. B. Lyakhov, A. A. Martinson, A. D. Mayorov, W. K. Riedler, M. F. Friedrich, K. M. Torkar, A. N. Laliashvili Z. Klos, and Z. Zbyszynski, Potential observations of an electron-emitting rocket payload and other related plasma measurements, *Planet. Space. Sci.*, **36**, 399-410, 1988.
- Marshall, J. A., C. S. Lin, J. L. Burch, T. Obayashi, and C. Beghin, Spacelab I experiments on interactions of an energetic electron beam with neutral gas, *J. Space. Rockets*, **25**, 361-367, 1988.
- McIlwain, C. E., and E. C. Whipple, The dynamic behavior of plasmas observed near geosynchronous orbit, *IEEE Trans. Plasma Sci.*, **PS-14**, 874-890, 1986.

- Moore, T. E., R. L. Arnoldy, R. L. Kaufmann, L. J. Cahill, Jr., P. M. Kintner, and D. N. Walker, Anomalous auroral electron distribution due to an artificial ion beam in the ionosphere, *J. Geophys. Res.*, 87, 7569-7579, 1982.
- Olsen, R. C., Experiments in charge control of geosynchronous orbit - ATS5 and ATS6, *J. Space. Rockets*, 22, 254-264, 1985.
- Olsen, R. C., D. R. Lowery, J. L. Roeder, Plasma wave observations during electron beam experiments at high altitudes, *J. Geophys. Res.*, in press, 1989.
- Reasoner, D. L., J. L. Burch and T. Obayashi, Analysis of electron spectra produced by SEPAC electron beams on Spacelab-1 - Evidence for strong beam plasma interactions, *EOS*, 65, 1042, 1984.
- Sasaki, S., N. Kawashima, K. Kuriki, M. Yanagisawa, and T. Obayashi, Vehicle charging observed in SEPAC Spacelab-1 experiment, *J. Space. Rockets*, 23, 194-199, 1985.
- Sasaki, S., N. Kawashima, K. Kuriki, M. Yanagisawa, T. Obayashi, W. T. Roberts, D. L. Reasoner, R. R. Williamson, P. M. Banks, W. W. L. Taylor, K. Akai, and J. L. Burch, Neutralization of beam-emitting spacecraft by plasma injection, *J. Space. Rockets*, 24, 227-231, 1987.
- Stannard, P. R., I. Katz, N. Mandell, J. Cassidy, D. Parks, M. Rotenberg, P. Steen, Analysis of the charging of the SCATHA (P78-2) satellite, NASA CR-165348, S-Cubed, 1981.
- Watermann, J., K. Wilhelm, K. M. Torkar, and W. Riedler, Space Shuttle Charging or beam-plasma discharge: What can electron spectrometer observations contribute to solving the question?, *J. Geophys. Res.*, 93, 4134-4140, 1988.
- Werner, P., Ion Gun Operations at High Altitudes, M.S. Thesis, Naval Postgraduate School, 1988.
- Winckler, J. R., An investigation of wave particle interactions and particle dynamics using electron beams injection from sounding rockets, *Space Sci. Rev.*, 15, 751-780, 1974.
- Winckler, J. R., A Summary of Recent Results under the ECHO Program for the Study of the Magnetosphere by Artificial Electron Beams, *Cosmic Physics Technical Report 168*, University of Minnesota, 1 September, 1976.
- Winckler, J. R., The use of artificial electron beams as probes of the distant magnetosphere, in *Artificial Particle Beam in Space Plasma Studies*, ed. B. Grandal, pp. 3-33, Plenum Press, New York, NY, 1982.

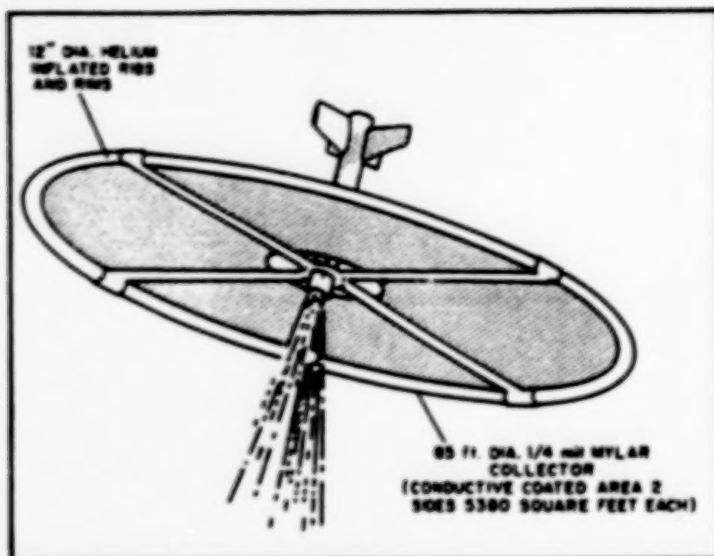


Figure 1. Collector screen in the deployed configuration [Hess et al, 1971]

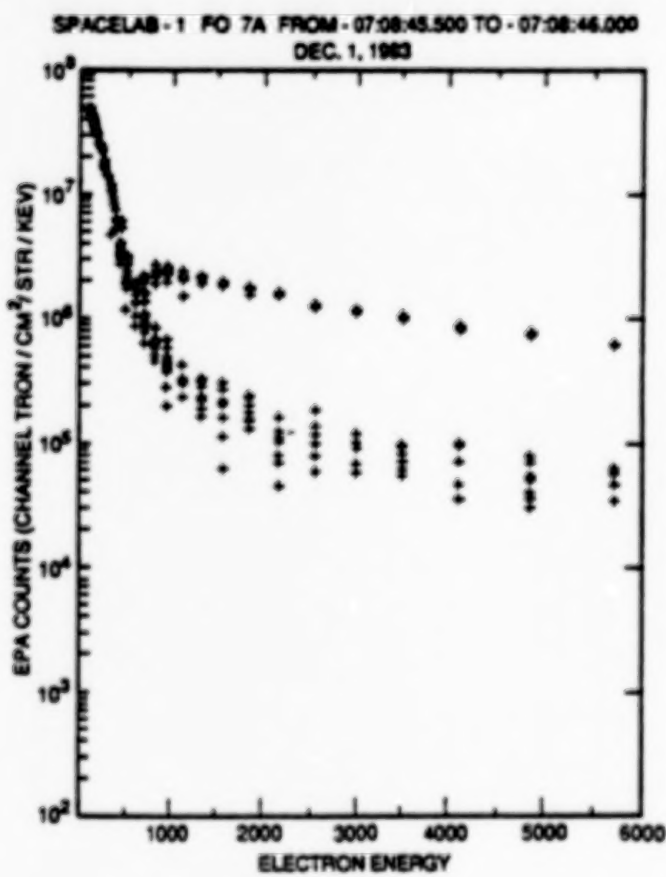


Figure 2. SPACELAB-1/SEPAC electron differential energy flux during electron gun firing. Lower curve(s) are from energy sweeps immediately after the MPD arcjet fires; upper curves follow in time as the shuttle orbiter charges.

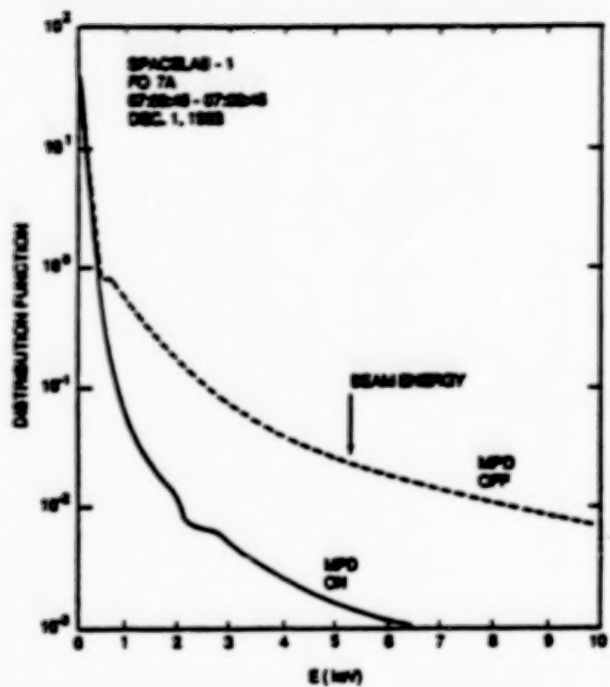


Figure 3. SPACELAB-1/SEPAC electron distribution functions calculated from the data presented in Figure 2.

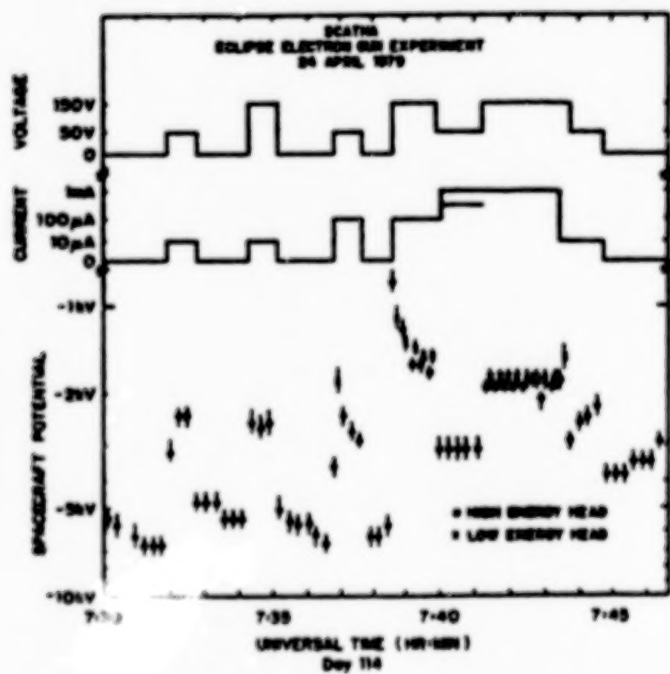


Figure 4. SCATHA (P78-2) potential profile during eclipse gun operations on 24 April 1979 (Day 114). Electron gun parameters are given in the top two plots. Spacecraft potential is estimated from the UCSD ion spectrometers.

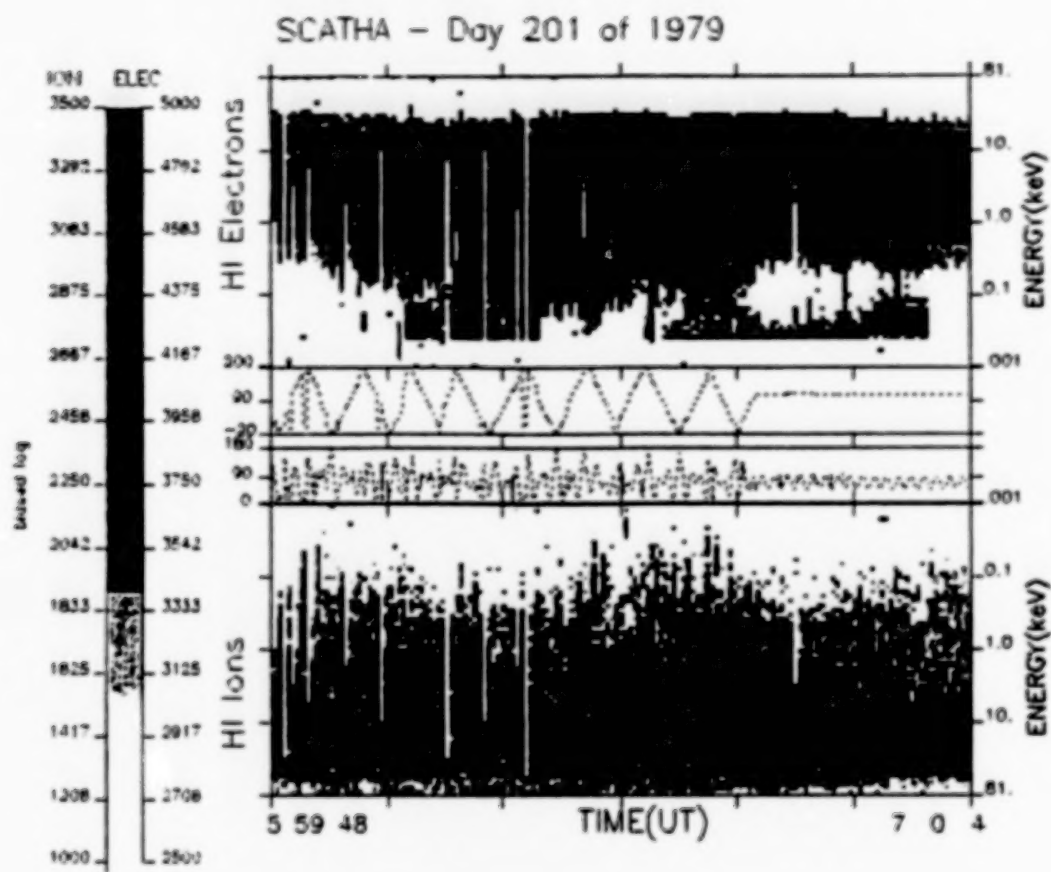


Figure 5. SCATHA (P-78-2) electrostatic analyzer data from 20 July 1979 (Day 201) during daylight electron beam experiments.

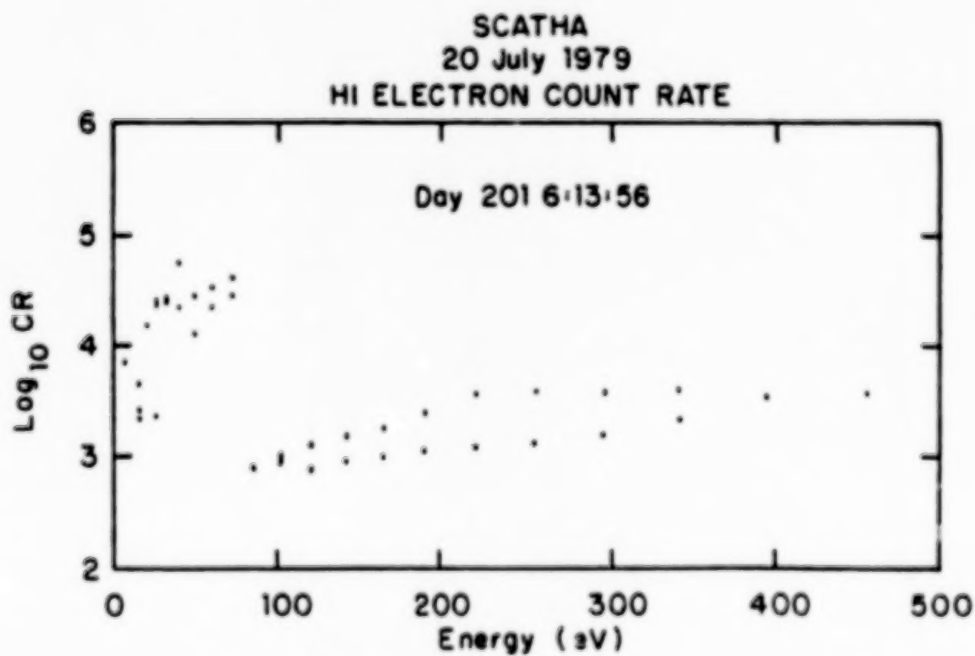


Figure 6. SCATHA electron data during electron beam experiments. Two successive energy sweeps are shown (~ 20 seconds/sweep). For the beam on at 50 eV, 10  $\mu$ A.

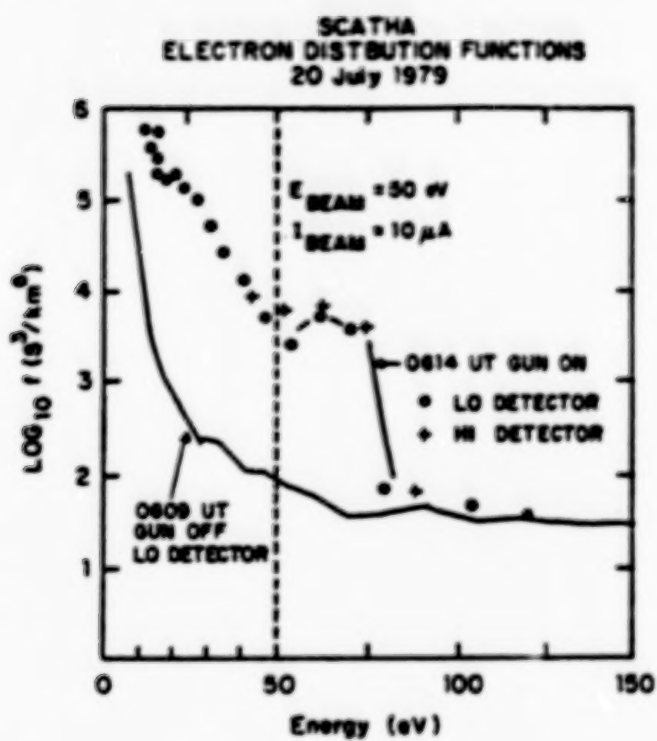


Figure 7. SCATHA electron data from Figure 6, converted to distribution functions, and compared to gun off data (lower curve).

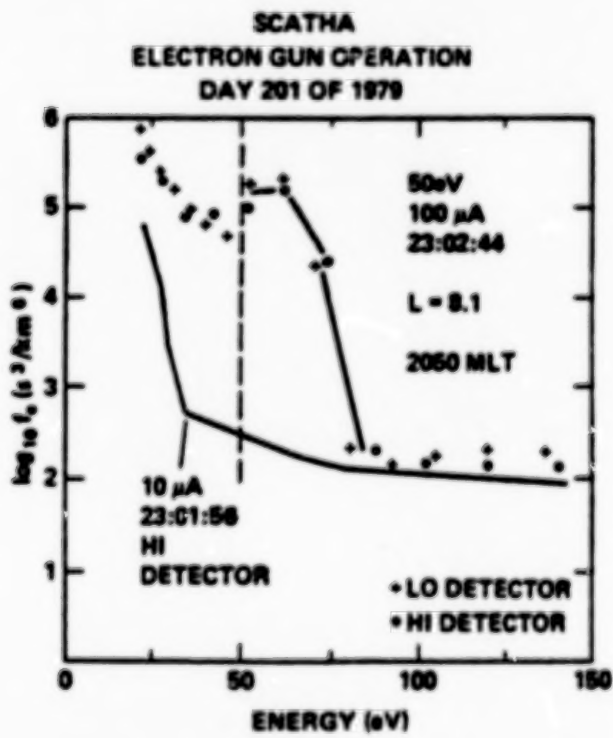


Figure 8. SCATHA electron data, presented as distributions functions (phase space density) for electron beam operations at 50 eV, 10  $\mu$ A and 100  $\mu$ A.

SCATHA - PLASMA WAVE DATA  
20 JULY 1979

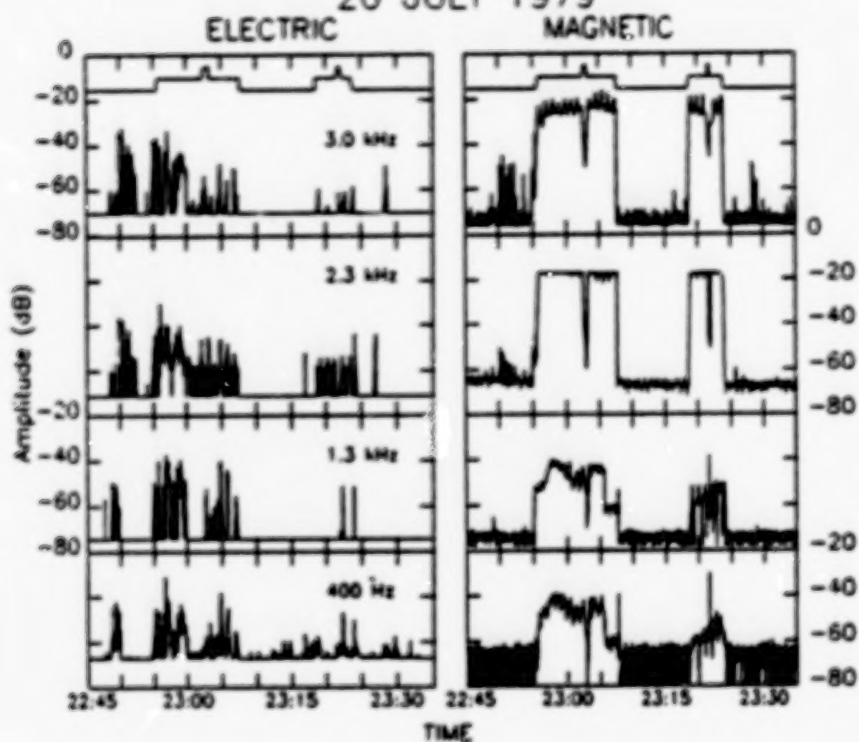


Figure 9. SCATHA plasma wave data during electron beam experiments. The 50 eV beam is set at 0, 10  $\mu$ A and 100  $\mu$ A as indicated by the horizontal line in the 3.0 kHz electric and magnetic channel boxes.

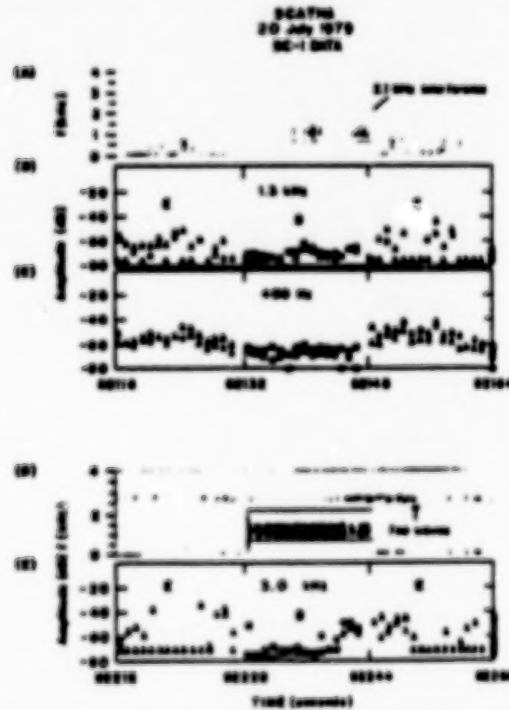


Figure 10. SCATHA plasma wave data for electron gun off conditions. The wideband receiver was in its 0-3 kHz mode. Selected channels of the narrowband receiver are plotted below the wideband data.

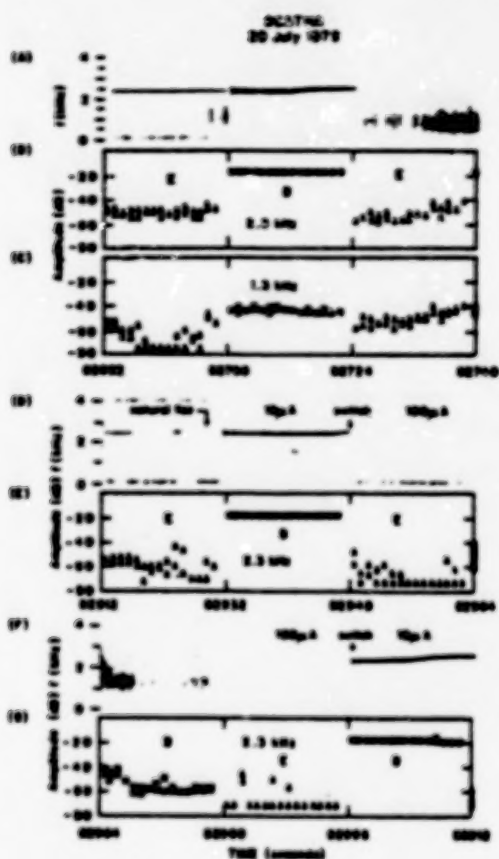


Figure 11. SCATHA plasma wave data for electron gun on conditions.

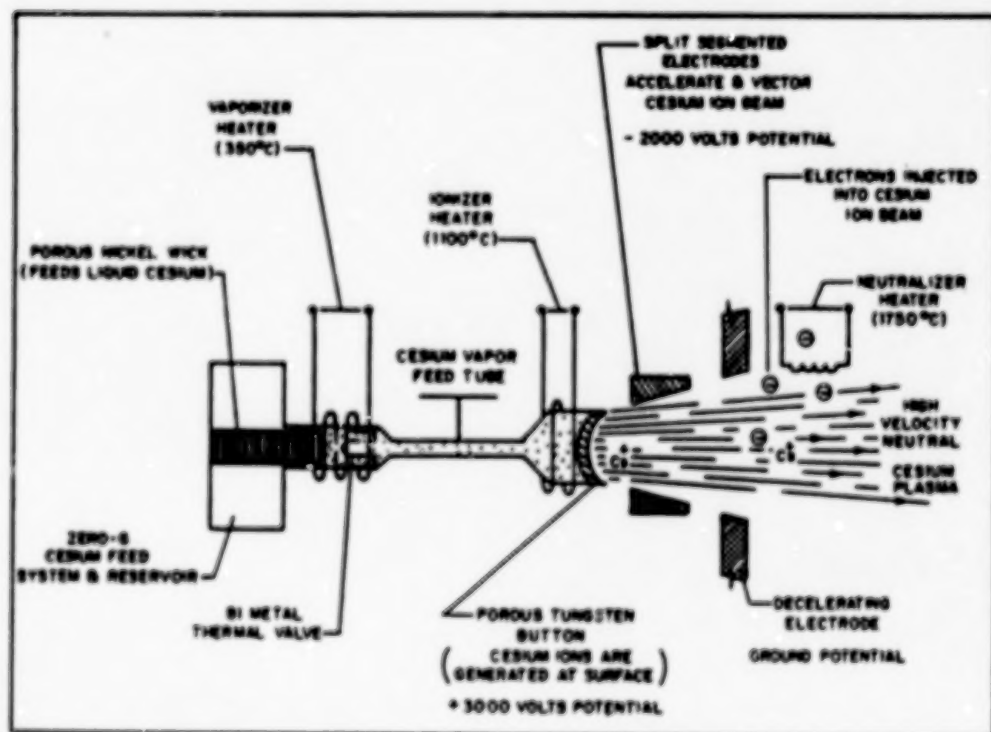


Figure 12. ATS-5 ion thruster.

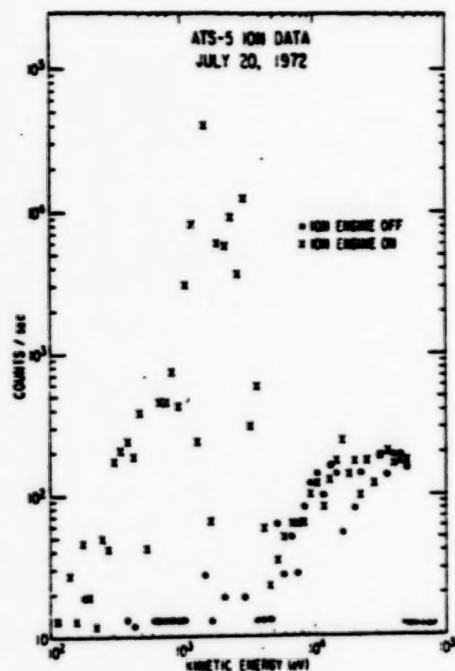


Figure 13. ATS-5 ion flux for ion thruster non-neutral beam experiments. Two consecutive 20 second scans are plotted. When the engine is on, there is a peak in the flux from 1-3 keV indicating a negative potential of -1 to -3 kV. The spacecraft potential is presumably varying on a time scale which is comparable to the energy step period ( $\sim 0.23$  seconds).

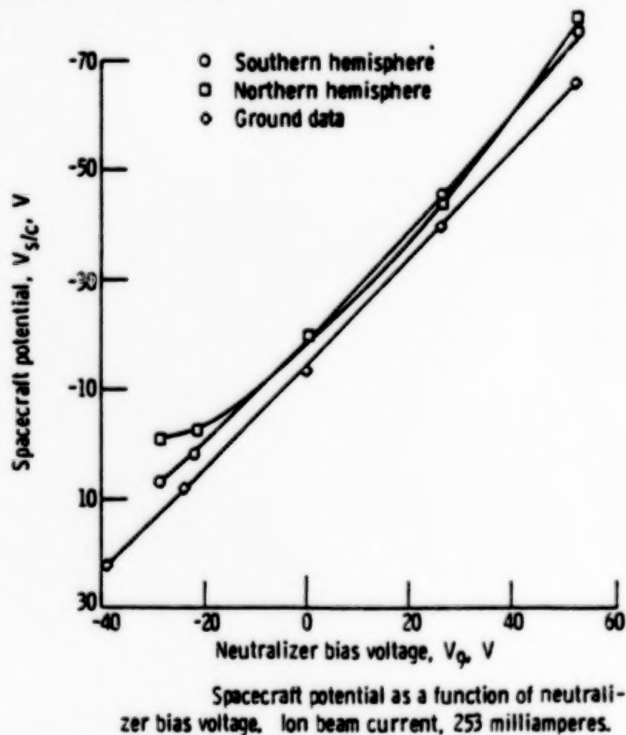


Figure 14. SERT II spacecraft potential measurements during neutralizer bias experiments. Ion beam current is 253 mA [Jones et al, 1970].

SCATHA - Day 200 of 1979

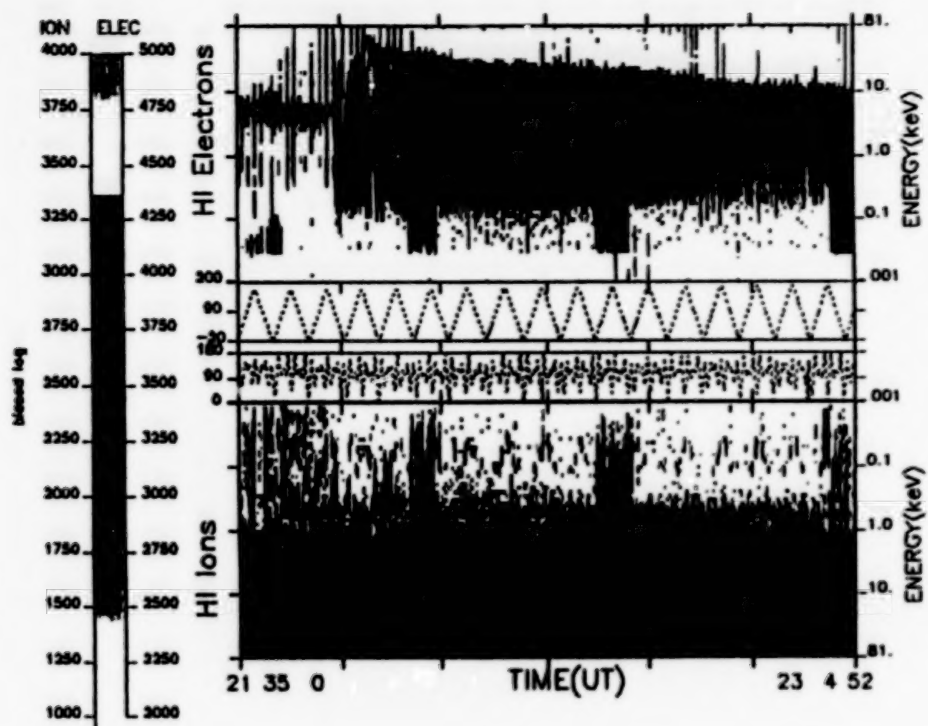


Figure 15. SCATHA electrostatic analyzer data for ion gun experiments on 19 July 1979. The gun is operated at 1 kV,  $\sim 1$  mA.

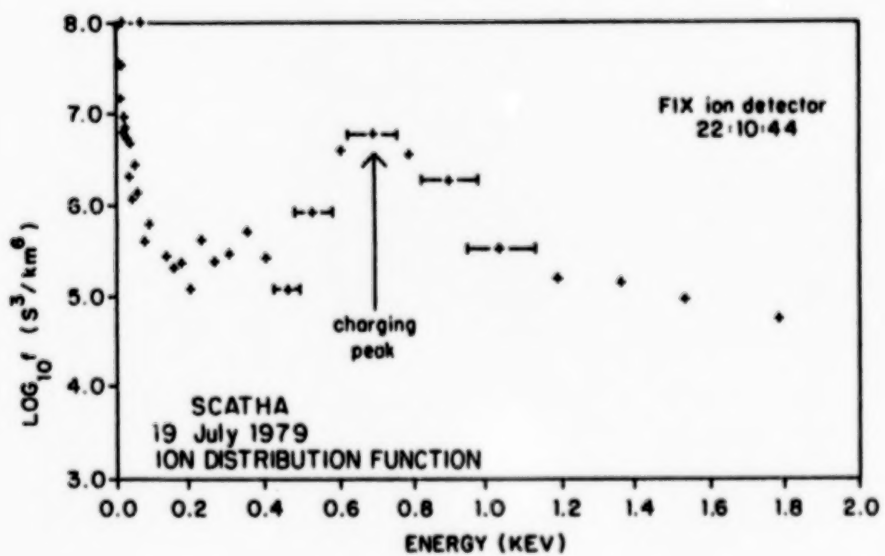


Figure 16. SCATHA ion distribution function, 19 July 1979.

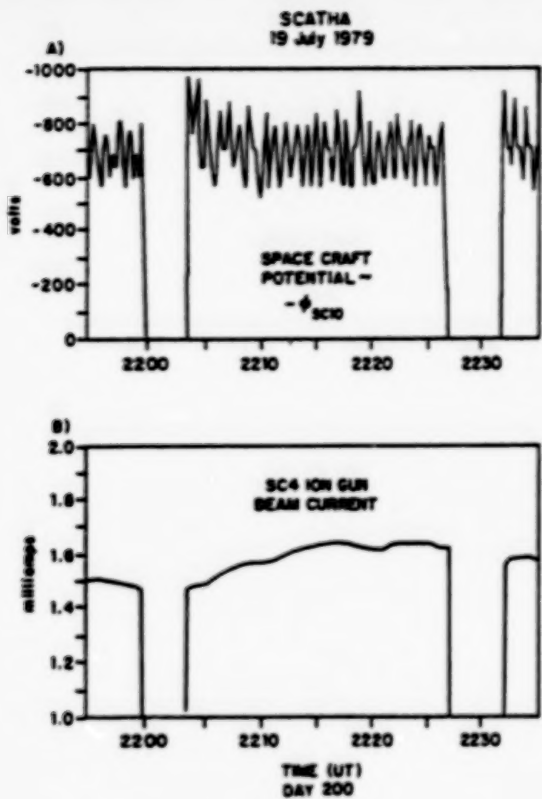


Figure 17. a. Spacecraft potential estimate using the SC10 electric field data. The floating potential of one 50-m antenna segment is plotted.  
 b. Ion gun beam current for 19 July 1979 (Day 200).

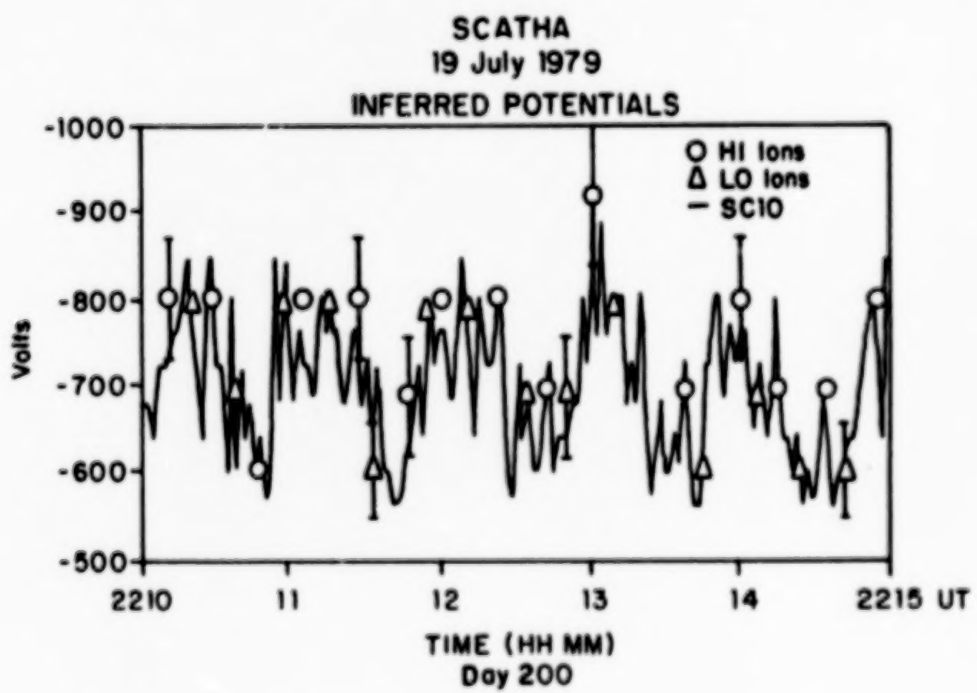


Figure 18. SCATHA SC10 and SC9 potential measurements for a subset of the period shown in Figure 17.

SCATHA  
19 July 1979  
ION DISTRIBUTION FUNCTION

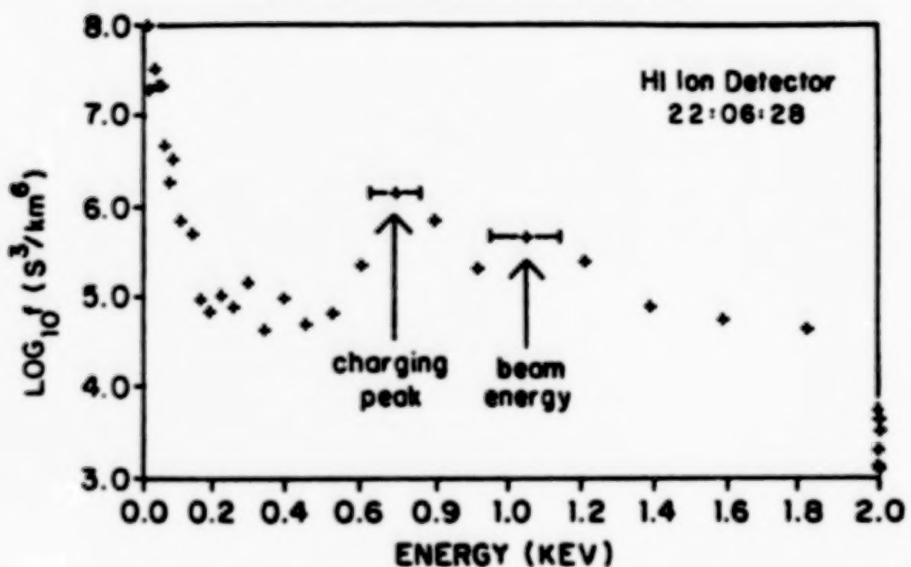


Figure 19. SCATHA ion distribution function, as in Figure 16. There are two relative maxima. The spacecraft potential is associated with the 700 eV peak, returning beam ions with the 1 keV peak.

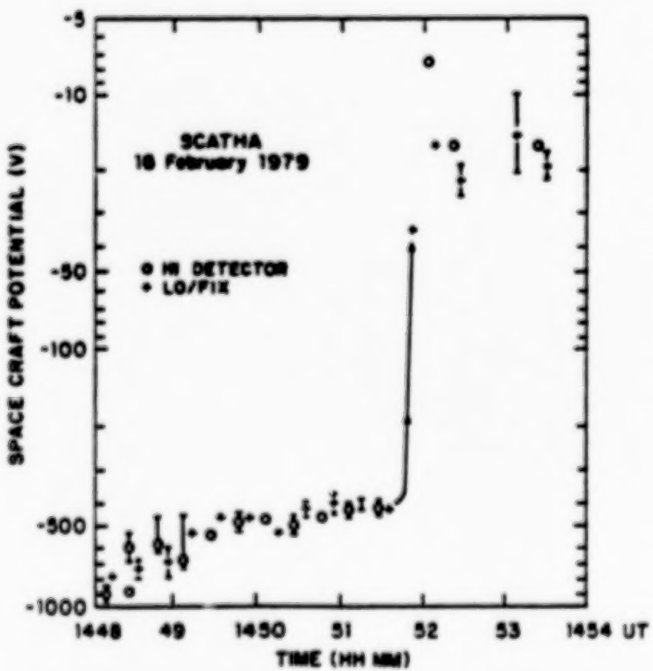


Figure 20. SCATHA potentials, for ion gun operation on 16 February 1979 (Day 47), inferred from the peak in the electrostatic analyzer ion data.

### Space Charge Limiting—Ions Virtual Anode Effect

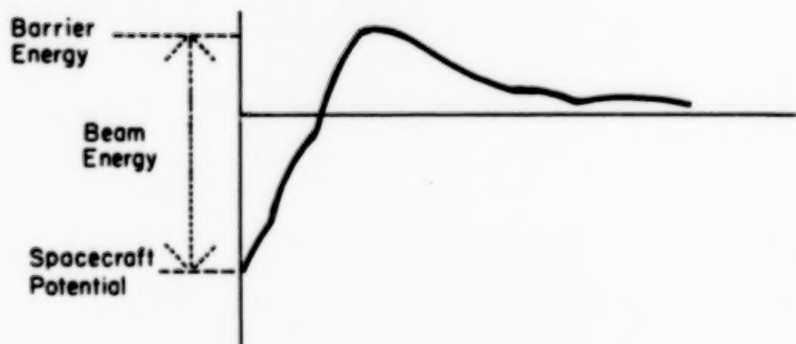
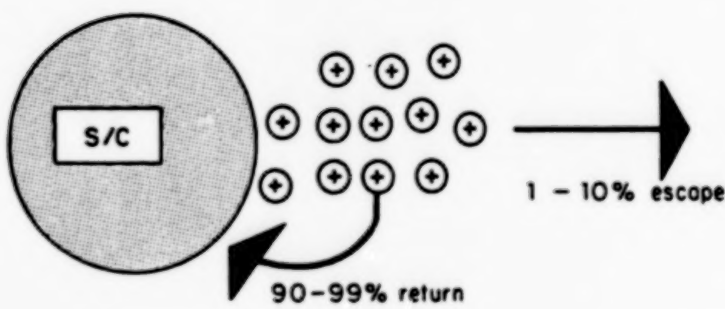


Figure 21. Cartoon illustration of the virtual anode effect in current limiting the ion beam.

# EFFECTS OF NEUTRAL GAS RELEASE ON CURRENT COLLECTION DURING THE CHARGE-2 ROCKET EXPERIMENT

B.E. Gilchrist, P.M. Banks, T. Neubert, P.R. Williamson

STAR Laboratory, Stanford University, Stanford CA, 94305-4055

N.B. Myers, W. J. Raitt

Utah State University, Logan, UT, 84322-4055

S. Sasaki

Institute of Space and Astronautical Science  
4-6-1 Komaba, Maguro, Tokyo, Japan

**Abstract.** Observations of current collection enhancements due to cold nitrogen gas control jet emissions from a highly charged rocket payload in the ionosphere are reported. These observations were made during the second cooperative high altitude rocket gun experiment (CHARGE-2) which was an electrically tethered mother/daughter payload system. Gilchrist et. al (1989), provides a detailed summary of the observations. The current collection enhancement was observed at the daughter payload located 100 to 400 m away from the mother which was firing an energetic electron beam. We interpret these results in terms of an electrical discharge forming in close proximity to the daughter during the short periods of gas emission. The results indicate that it is possible to enhance the electron current collection capability of positively charged vehicles by means of deliberate neutral gas releases into an otherwise undisturbed space plasma. These results can also be compared with recent laboratory observations of hollow cathode plasma contactors operating in the "ignited" mode.

Experimental observations of current collection enhancements due to cold nitrogen gas control jet emissions from a highly charged, isolated daughter payload in the nighttime ionosphere have been made. These observations were derived from the second cooperative high altitude rocket gun experiment (CHARGE-2) which was an electrically tethered mother-daughter payload system. The rocket flew from White Sands Missile Range (WSMR) in December, 1985. The rocket achieved an altitude of 261 km and carried a 1 keV electron beam emitting up to 48 mA of current (Myers, et al., 1989a). The mother payload, carried the electron beam source, while the daughter acted as a remote current collection and observation platform and reached a distance of 426 m away from the main payload. Gas emissions at the daughter were due to periodic thruster jet firings to maintain separation velocity between the two payloads.

The effect of the gas enhanced current collection can best be shown by comparison with collection results without gas emissions. This is shown in Figure 1 where the altitude dependence of the normalized tether current (equal to current collected at the daughter payload) is plotted. The normalization factor is beam current which, in steady state, is assumed to be equal to the total return current to the two payloads. Both the case of gas and no-gas emissions are shown. As can be seen substantial enhancement to the no-gas current collection at the daughter are indicated. Near apogee, enhanced collection levels approach unity.

For the no-gas case, with identical collection processes at the two payloads, the normalized tether current would be 0.29 which is equal to the ratio of daughter to daughter plus mother current collection areas. This condition is only achieved near apogee. Therefore, other preferential processes near the main payload must be operative at lower altitudes (Myers, et al., 1989b).

Without the gas emission, substantial vehicle charging was observed for beam emissions exceeding thermal collection current limits (~3-5 mA) of the payload system. In those cases, the mother payload achieved charging levels of 400 to 600 V, or approximately 50% of beam energy. Because of the low resistance electrical connection to the daughter payload, it also charged to near the same potential. During the collection enhancement, charging was observed to drop below 10% of beam energy. On one occasion, when a 450 V power supply was connected in series between the two payloads through the tether (raising the daughter potential relative to the mother), the mother potential was actually observed to be driven negative during electron beam emission.

The enhancement is interpreted here in terms of an electrical discharge forming in close proximity to the daughter vehicle during the short periods of gas emission. The discharge resulted from accelerated ionospheric electrons, attracted to the charged payload, ionizing a fraction of the neutral gas plume around the daughter payload. This description is similar to models describing recent laboratory observations of hollow cathode plasma contactors operating in the "ignited" mode (Davis, et al., 1989; Williams, et al., 1987). The explanation for the altitude dependence indicated in Figure 1, is in part due to the same preferential processes near mother payload indicated for the no-gas case. Also, it is likely that the discharge around the daughter payload is dependent on the background electron density.

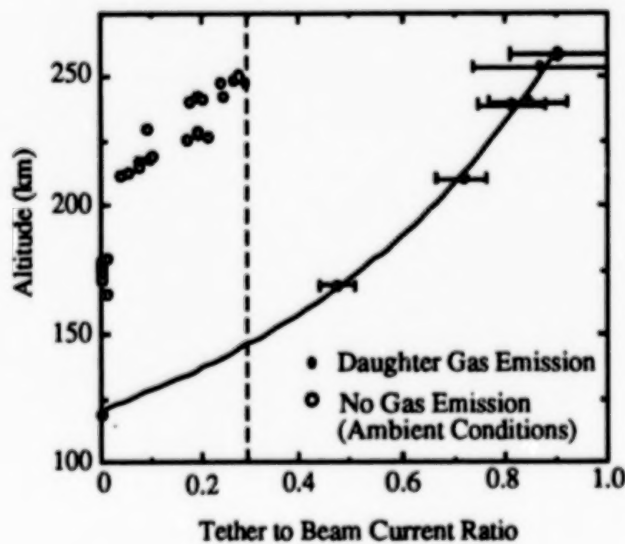


Figure 1 - Plot of tether to beam current ratio versus altitude with and without daughter gas emissions. The ratio of daughter to total (daughter plus mother) current collection areas, 0.29, is identified by the dashed line.

**Acknowledgements.** This work was supported under grant NAGW - 1566 from NASA and the Air Force Geophysics Laboratory.

### References

- Davis, V. A., I. Katz, M. J. Mandell and D. E. Parks, A model of electron collecting plasma contactors, AIAA/NASA/ASI/ESA 3rd International Conference on Tethers in Space - Toward Flight, San Francisco, 17-19 May 1989.
- Gilchrist, B. E., P. M. Banks, T. Neubert, P. R. Williamson, N. B. Myers, W. J. Raitt and S. Sasaki, Electron collection enhancement arising from neutral gas jets on a charged vehicle in the ionosphere, *JGR, in-press*, 1989.
- Myers, N. B., W. J. Raitt, A. B. White, P. M. Banks, B. E. Gilchrist and S. Sasaki, Vehicle charging effects during electron beam emission from the CHARGE-2 experiment, *J. Spacecraft and Rockets, in-press*, 1989a.
- Myers, N. B., W. J. Raitt, B. E. Gilchrist, P. M. Banks, T. Neubert, P. R. Williamson and S. Sasaki, A comparison of current-voltage relationships of collectors in the earth's ionosphere with and without electron beam emission, *GRL, 16, 5*, 365 - 368, 1989b.
- Williams, J. D., P. J. Wilbur and J. M. Monheiser, Experimental validation of a phenomenological model of the plasma contacting process, PSN/NASA/ESA 2nd Annual Conference on Tethers in Space, Venice, Italy, 4-8 October 1987.

# EFFECTS OF NEUTRAL GAS RELEASES ON ELECTRON BEAM INJECTION FROM ELECTRICALLY TETHERED SPACECRAFT

R. M. Winglee

Department of Astrophysical, Planetary and Atmospheric Sciences  
University of Colorado, Boulder, CO 80309-0391

**Abstract.** The presence of high neutral densities at low altitudes and/or during thruster firings is known to modify the spacecraft potential during active electron beam injection. Two-dimensional (three velocity) particle simulations are used to investigate the ionization processes including the neutral density required, the modification of the spacecraft potential, beam profile and spatial distribution of the return current into the spacecraft. Three processes are identified (i) beam-induced ionization, (ii) vehicle-induced ionization and (iii) beam plasma discharge. Only in the first two cases does the beam propagate away with little distortion.

## Introduction

During active injection of electron beams from spacecraft in low earth orbit, the presence of high neutral densities at low altitudes and/or during thruster firings, can modify the spacecraft charging, beam propagation and induced wave emissions (e.g., Gurnett et al., 1988; Gilchrist et al., 1989; Winckler et al., 1989). The presence of such neutrals is important because they can be partially ionized, providing enhanced plasma and thereby enhanced return currents and better neutralization of the spacecraft charge. The ionization can be produced by a variety of processes (e.g. Linson, 1982; Winglee, 1989), including (i) beam-induced ionization where the beam produces the ionization directly, (ii) vehicle-induced ionization where the spacecraft is at sufficiently high potentials to accelerate the return current electrons to ionizing energies, and (iii) beam-plasma discharge where there is rf breakdown of the neutrals via electrons accelerated by high frequency electric fields associated with a beam plasma instability.

Observations of the change in the spacecraft potential associated with thruster firings during the recent CHARGE 2 mission were reported by Gilchrist et al. (1989). In this experiment, a detachable payload (hereafter daughter) was ejected from the main beam-emitting payload (hereafter mother). The daughter was electrically connected to the mother through a conducting tether wire, the aim being to generate controlled VLF emissions. Thruster firings from both the mother and daughter were seen to reduce the spacecraft potential, with the current collected by the daughter increasing during daughter thruster firings while decreasing during mother thruster firings; the spacecraft potential was smallest for mother thruster firings.

The purpose of this paper is to investigate the effects of ionization of neutrals during thruster firings under similar conditions to CHARGE 2 with the aim of identifying (i) the dominant processes responsible for the ionization, (ii) required neutral density around the mother or daughter to prevent strong charging, (iii) the spatial distribution of the currents into the spacecraft and (iv) the changes in the beam properties as the neutral density is increased.

### Simulation Model

In order to investigate the ionization of the neutrals and the change in the spacecraft potential self-consistently with the dynamics of the beam-plasma interaction, two-dimensional (three velocity) relativistic electromagnetic particle simulations with collisional processes included were used (cf. Winglee, 1989). A schematic of the simulation model is shown in Figure 1. The mother and daughter payloads are indicated by the black rectangles and are of equal size of dimensions  $4\Delta \times 16\Delta$ , with the system size being  $512\Delta \times 128\Delta$ , where  $\Delta$  is a plasma Debye length (i.e.,  $v_{T_e}/\omega_{pe}$ ) which is of the order of 10 cm in the present case. The two payloads are assumed to be electrically connected with their potentials being kept equal. The beam is injected at 45 degrees to the ambient magnetic field (which is in the  $x$  direction) with a parallel velocity 10 times the ambient electron thermal velocity (i.e.,  $v_{se} = 10v_{Te}$ ) and a beam width of  $2\Delta$ . This beam width is the minimum beam width that can be easily simulated and represents some initial expansion of the beam within the first few tens of centimeters, due to the opening or cone angle of the gun and/or to beam-plasma interactions. As a result of the large beam width assumed in the simulations, the beam density relative to the ambient density is assumed to be 4 with the total beam current being similar to the maximum beam current emitted during CHARGE 2, i.e. about 100 mA. The ratio of the electron cyclotron frequency  $\Omega_e/\omega_{pe}$  is taken to be 2, similar to the plasma conditions during CHARGE 2. These parameters are also similar to those used in previous simulations by Winglee and Pritchett (1988) and Winglee (1989).

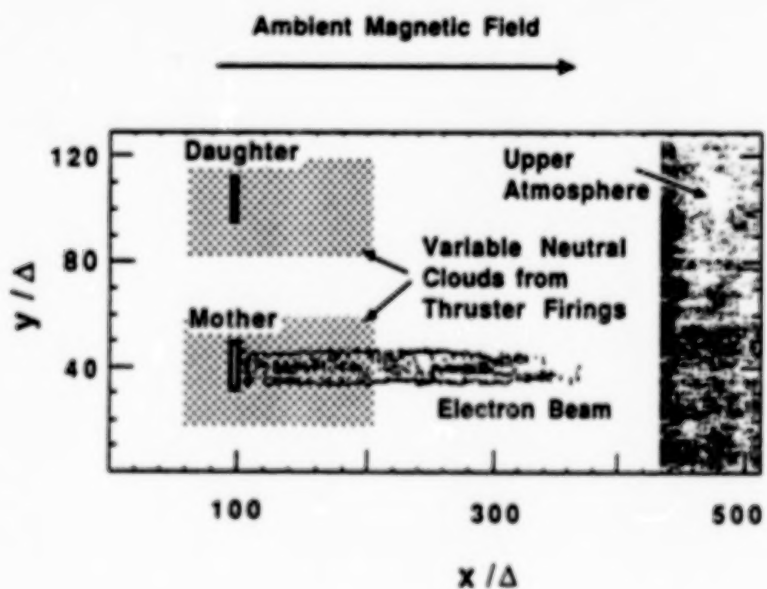


Figure 1. Schematic diagram of the simulation model.

The effects of neutrals and their ionization are incorporated into the simulations as follows. A region of neutrals with a given density is specified on the simulation grid. These neutrals (assumed to be molecular nitrogen) can be placed around the mother or daughter. A dense neutral region is also placed at near the right hand boundary representing the lower ionosphere. The ionization cross-section as given by Banks and Kockarts (1973) has the feature that it increases rapidly once the electron energy is above a few tens of eV, reaching a maximum at about 100 eV and then decreasing approximately inversely proportional to  $v$ . For numerical simplicity, the rise in cross-section at low energies is approximated by a sharp cutoff at 100 eV (i.e.,  $v \approx 3.3v_{Te}$ ). This

cutoff excludes collisional processes by nonaccelerated ambient plasma electrons which are assumed to be in equilibrium with the ambient neutrals. This cutoff has the effect of underestimating the number of low energy electrons produced by ionizing processes. This approximation is not restrictive since these low energy electrons have a large scattering cross-section which reduces their mobility and hence their contributions to any return currents.

All electrons with higher energies above 100 eV are then binned in levels of speeds relative to  $3\sqrt{v_{T_e}}$ , with the cross-section decreasing inversely with bin number. The required number of (primary) electrons determined from the collision cross-section is then chosen randomly from each bin. The velocity of the primary is reduced by about a third and a secondary electron and ion are added to the system with the secondary electron having a velocity one third of the initial velocity of the primary with a differential scattering cross-section as given by Mott and Massey (1965).

#### Beam Injection into Collisionless Plasma

In the absence of any neutrals, the mother and daughter payloads are subject to strong charging and the beam is strongly distorted by the formation of a stagnation region or virtual cathode (cf. Winglee and Pritchett, 1988). The charging of the spacecraft is illustrated in Figure 2 which shows the time histories of (a) the spacecraft potential and (b) the relative current collected by the mother and daughter payloads. The  $v_x - z$  phase space of the beam electrons at five different times during the simulation are shown in Figure 3.

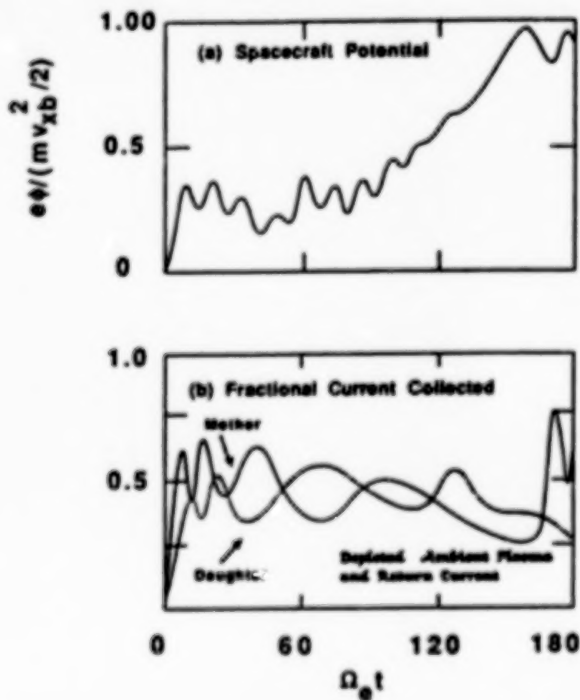


Figure 2. Time histories of (a) the spacecraft potential and (b) the relative current collected by the mother and daughter payloads for injection into a collisionless plasma. At late time the local plasma density becomes depleted, leading to a decrease in the ambient plasma return current collected, particularly by the daughter, and the charging of the spacecraft up to the parallel beam energy.

At early times before the ambient plasma has had sufficient time to respond (i.e.,  $\Omega_E t \leq 30$ ), the return current is much smaller than the emitted beam current so that the spacecraft rapidly

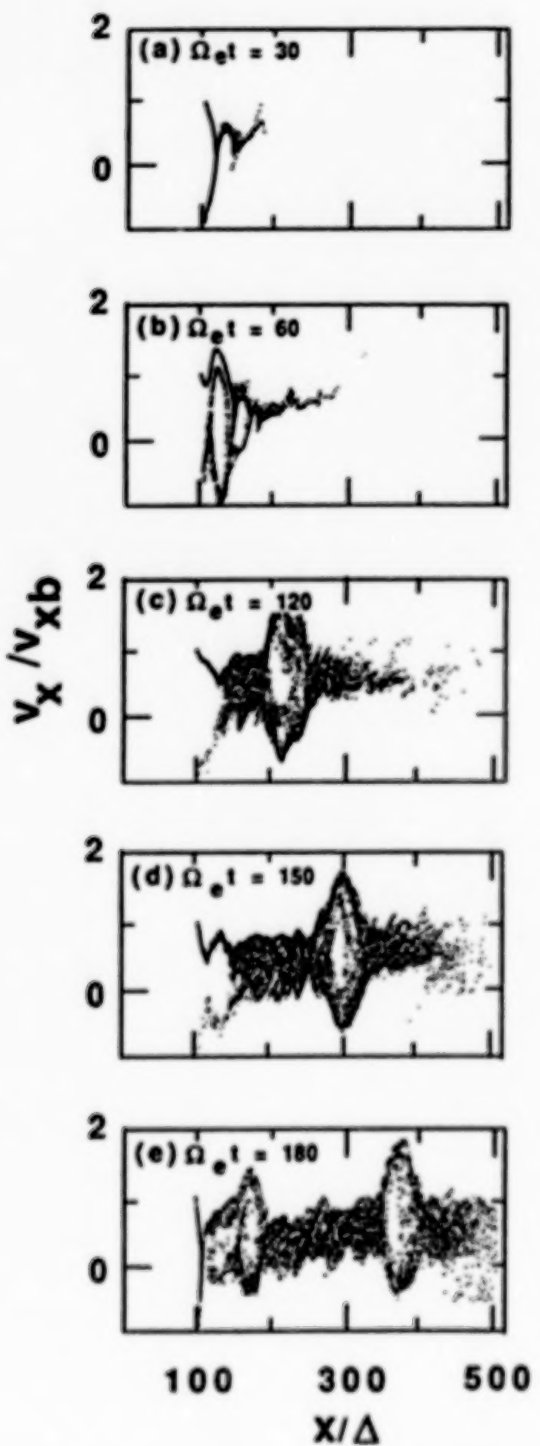


Figure 3. The  $v_x - x$  phase space of the beam electrons for five times during the simulation shown in Figure 2. Stagnation regions or virtual cathodes, close in to the spacecraft, are present at both early and late times.

charge up to about 0.3 of the parallel beam energy. At this stage most of the return current into the spacecraft is collected by the mother (Figure 2b) and consists of beam electrons reflected (i.e.,  $v < 0$ ) by the formation of a stagnation region (Figure 3a). At intermediate times (i.e.,  $30 \leq \Omega_e t \leq 120$ ), the plasma is able to respond to the beam injection and supply a return current to match the beam current, with mother and daughter collecting comparable amounts of current and with little change in the spacecraft potential. The beam phases spaces in Figures 3b and c show that while the bulk of the beam is able to propagate away from the spacecraft, their average energy is reduced by more than 33% and they are dispersed in velocity and coordinate space.

Due to the inflow of plasma into the spacecraft, the plasma becomes locally depleted. As a result, the plasma return current decreases at later times (i.e.,  $\Omega_e t \geq 120$ ) and the spacecraft potential increases until it approaches the parallel beam energy. At this stage, the mother collects most of the return current which again comprises of primarily beam electrons reflected within a stagnation region (Figures 3e).

#### Beam-Induced Ionization

If neutrals are injected into the beam region (e.g. during a thruster firing), enhanced return currents can be produced by beam-induced ionization, leading to a reduction in the spacecraft charging and beam distortion. The effects of this enhanced return current is illustrated in Figures 4 and 5 which show the same quantities as in Figures 2 and 3 except that a neutral cloud has been included about the mother with a density  $5 \times 10^{11} \text{ cm}^{-3}$  (and collision frequency  $\nu_n = 0.01\Omega_e$ ), a width in  $y$  of  $46\Delta$  and extending  $50\Delta$  behind the spacecraft and  $100\Delta$  forward of the spacecraft. This neutral density is about the minimum required to prevent the spacecraft from charging to the beam parallel energy, with the collision period (i.e.,  $1/\nu_n$ ) being comparable to the the spacecraft charging time in the collisionless case (cf. Winglee, 1989). .

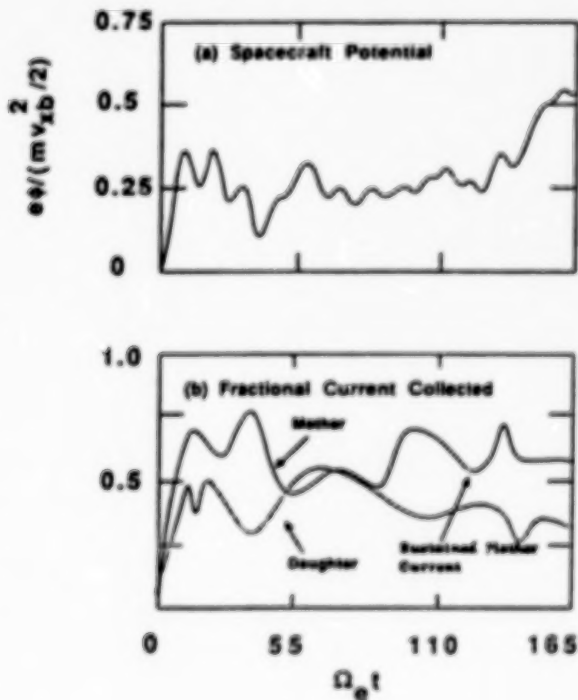


Figure 4. As in Figure 2 except that a neutral cloud around the mother payload has been added. The spacecraft potential on average is reduced by one half to one third and the return current becomes localized to the mother.

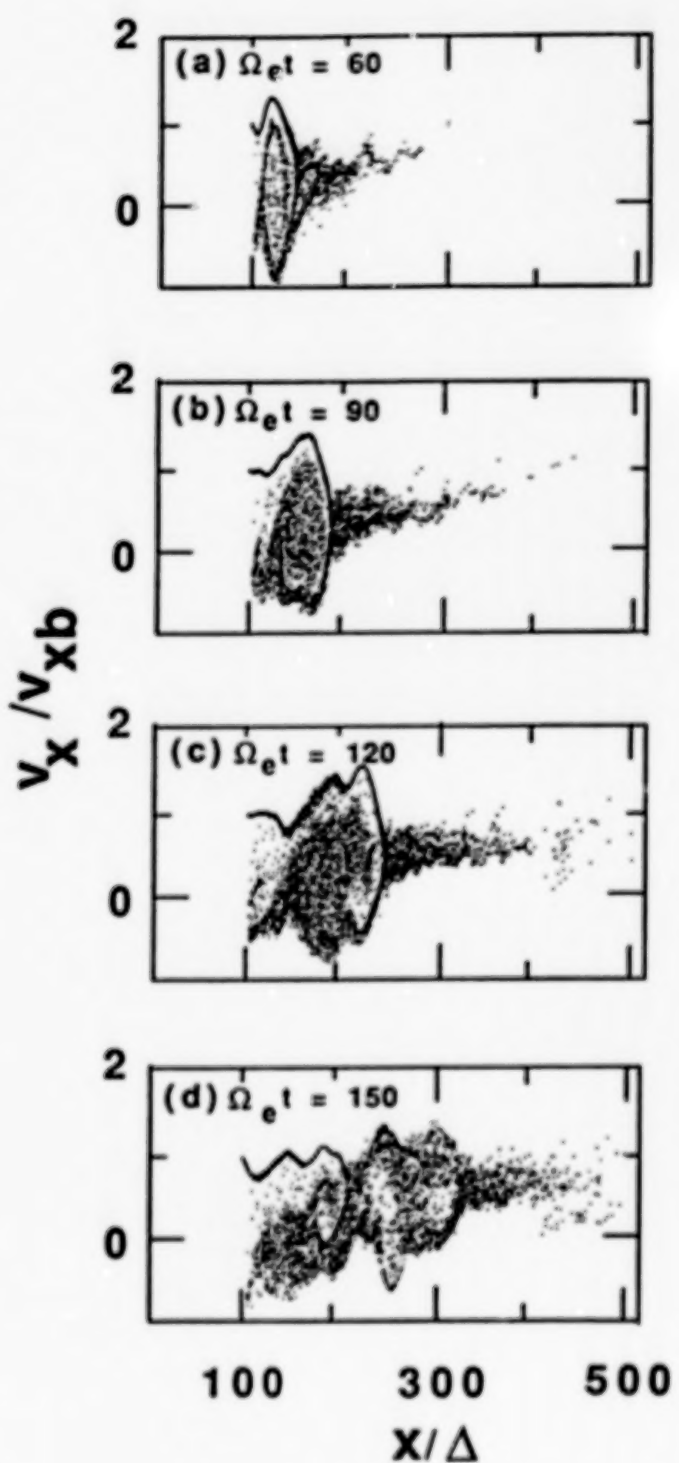


Figure 5. The parallel beam phase space for four times during the simulation shown in Figure 4. Due to the enhanced return current associated with the ionization of the neutrals, the beam is able to propagate outwards with little distortion until it reaches the neutral cloud boundary at  $x/\Delta = 200$ .

The introduction of the neutrals around the mother has the following effects:

- (i) The ionization is predominantly due to direct ionization by the beam particles. As a result, the return current becomes localized to the near vicinity of the beam region. This effect is seen in Figure 4b where the mother on average collects the bulk of the return current into the spacecraft.
- (ii) The average spacecraft potential as seen in Figure 4a is reduced by about one third to one-half of that for the collisionless case in Figure 2a (larger reductions are produced if higher neutral densities are assumed).
- (iii) A well defined beam is seen in the phase spaces in Figure 5 to propagate outward with little distortion until it reaches the neutral cloud boundary at  $z/\Delta = 200$  where strong beam distortion again occurs. This beam distortion is due to the fact that the plasma outside the neutral cloud cannot support the beam current as in the collisionless case and large ambipolar electric fields develop which decelerate the beam electrons and accelerates the ions outwards.

The change in potential and localization of the return current to the mother are consistent with the observations for mother-thruster firings during CHARGE 2.

### Beam Plasma Discharge

In the previous example, the presence of high density neutrals in the beam region allows the enhancement of the return current which is able to neutralize the spacecraft charge and allow the beam to propagate with little distortion. Any instabilities in the beam appear relatively weak and there is no rf breakdown of the neutrals by high frequency instabilities associated with the beam plasma interaction. In other words, the above interaction does not represent beam plasma discharge (BPD). This lack of BPD appears to be due to the beam width being narrow compared with a plasma Debye length which restricts the number of modes than can go unstable in the beam region.

However, wider beams are not subject to this restriction and BPD can be excited. As an example, Figures 6 and 7 show the spacecraft potential and parallel beam phase space for the same parameters as in Figures 4 and 5 except that the beam is twice as wide and the neutral density has been increased by a factor of 2 to compensate for the increased charging rate. It is seen in Figure 6 that the spacecraft potential averaged over the duration of the simulation for the wider beam is about twice as high as that for the narrow beam. Superimposed on the overall increase in spacecraft potential are enhanced high frequency oscillations associated with the growth of instabilities made possible by the increased beam width.

These enhanced high frequency oscillations which have a frequency near the ambient plasma frequency are associated with the beam-plasma interaction and can lead to beam distortion. This is seen in Figure 7 where there is enhanced short-scale turbulence in the beam phase space (particularly at late time as in Figures 7c and 7d). As a result of this turbulence there is trapping of electrons (as evidenced by the vortices in the phase spaces) leading to local beam plasma discharge and dispersion of the beam electrons in velocity space. This beam dispersion or distortion occurs closer in toward the spacecraft for the wide beam case (e.g. compare Figures 5d and 7d).

## Spacecraft Potential with BPD

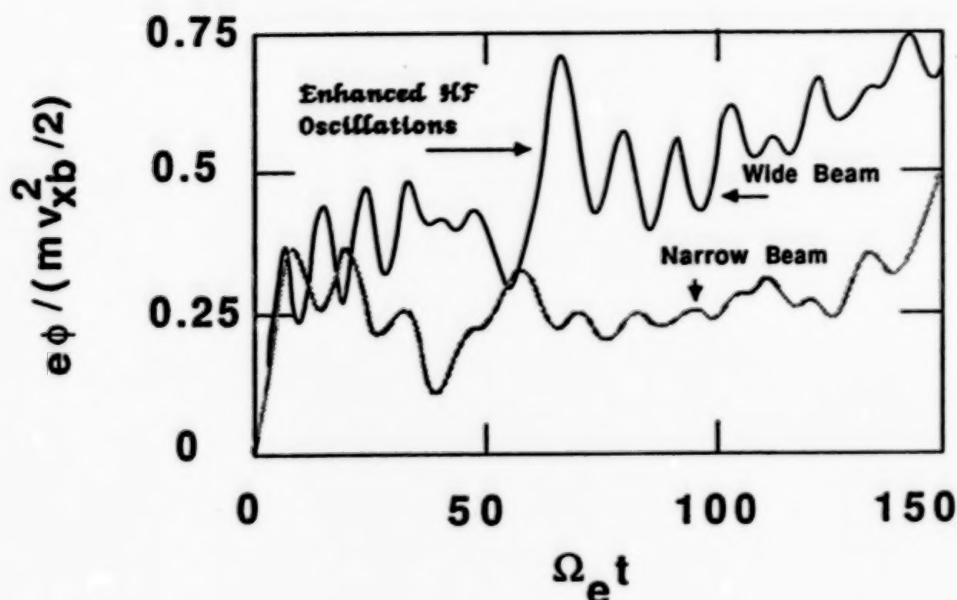


Figure 6. The spacecraft potential for injection of beams with widths of  $2\Delta$  (denoted narrow) and  $4\Delta$  (denoted wide). The neutral density for the wide beam case is twice as large as the wide beam case in order to compensate for the higher charging rate. The potential for the wide beam case is on average twice as high and subject to large-amplitude high-frequency oscillations which can produce local beam plasma discharge.

### Vehicle-Induced Ionization

During certain thruster firings, neutrals need not enter the beam region. In the present application, this occurs during thruster firings from the daughter. The ionization in this case is produced by return current electrons being accelerated by the spacecraft potential to energies greater than a few tens of volts. This vehicle-induced ionization tends to be less efficient than the beam-induced ionization because the highest energy return current electrons are those close in to the spacecraft and moving toward it so that their chance of multiple ionizing collisions before impacting on the spacecraft is small. As a result, higher neutral densities are required to produce the same change in spacecraft potential.

The effects of vehicle-induced ionization on the spacecraft potential is illustrated in Figure 8 which shows the time history of the spacecraft potential for the same size neutral cloud as in the previous cases except that it is centered around the daughter rather than the mother. It is seen that, for the lowest neutral density, the spacecraft charges up to the beam energy whereas, for beam-induced ionization, this density was sufficient to prevent strong spacecraft charging; neutral densities nearly eight times higher are required before the spacecraft potential can be maintained at levels significantly smaller than the beam energy.

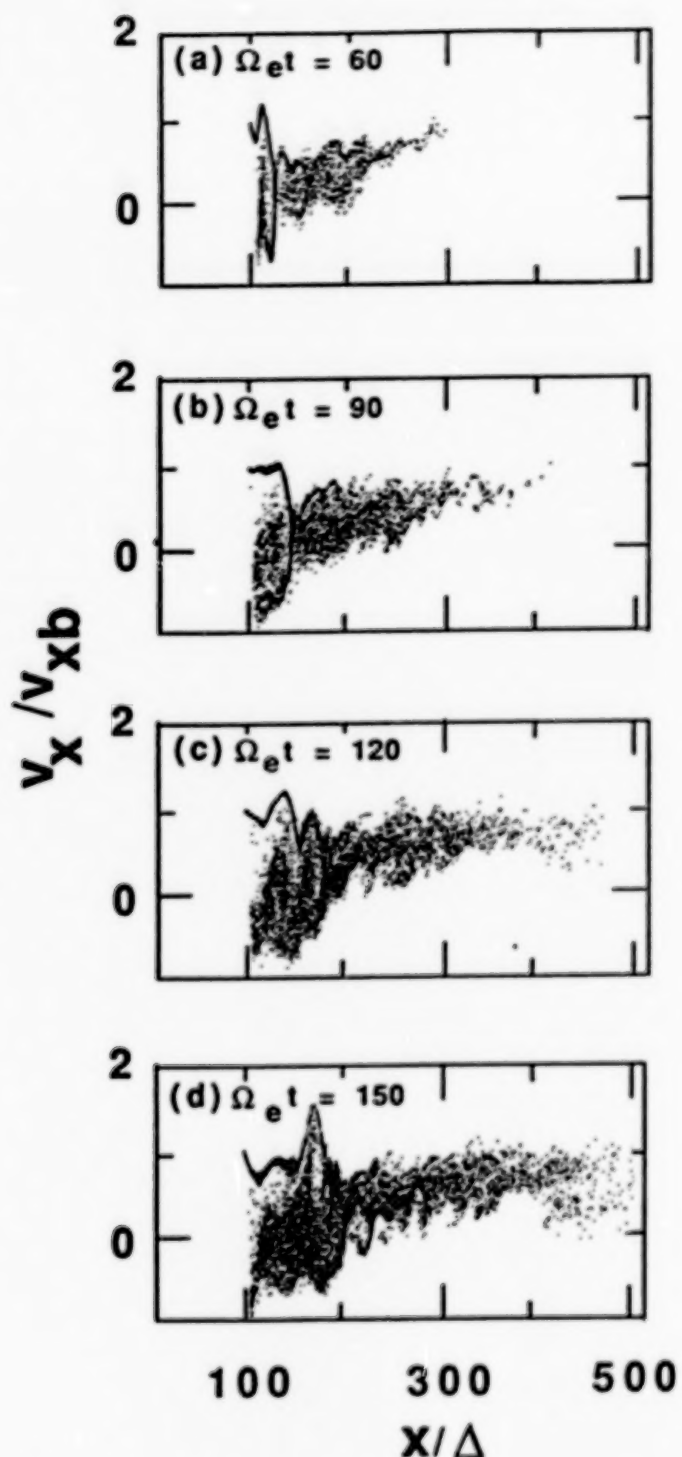


Figure 7. The  $v_x - x$  phase space corresponding the wide beam case in Figure 6. The enhanced high frequency oscillations seen in the spacecraft potential appear as short scale vortices in the phase space, which cause the beam to become dispersed in velocity space, and beam plasma discharge can occur in association with these vortices.

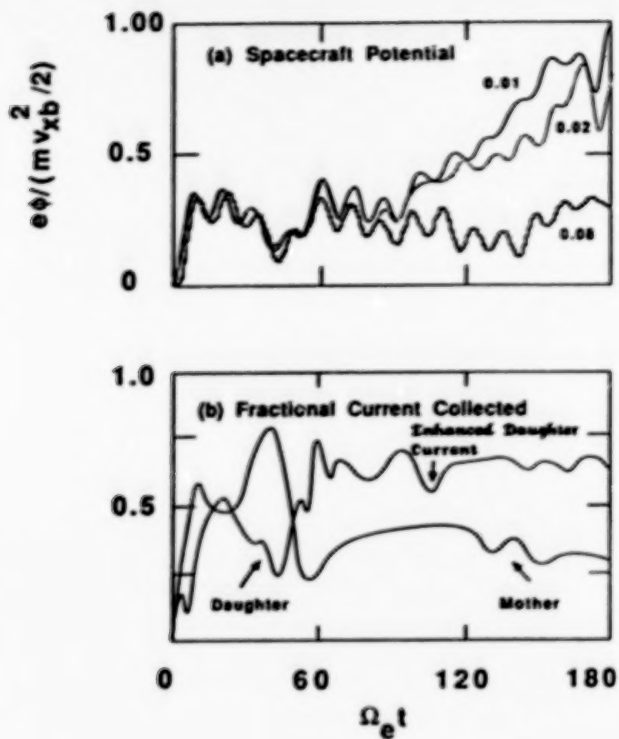


Figure 8. As in Figure 4 except that the neutrals are around the daughter payload instead of the mother. Three different neutral densities are considered with their collision frequency  $\nu_n$  corresponding to  $0.01\Omega_e$ ,  $0.02\Omega_e$ , and  $0.08\Omega_e$ . The lowest neutral density indicated is the same as in Figure 4 which was sufficient to reduce the spacecraft potential to average levels much smaller than the parallel beam energy. Due to the lower efficiency of vehicle-induced ionization, neutral densities nearly 8 times higher are required to produce the same change in potential.

The enhancement of the return current appears as an increase in the current collected by the daughter and a decrease in that collected by the mother (Figure 8a). Both the change in spacecraft potential and the relative amount of current collected by the mother and daughter payloads are consistent with the observations from CHARGE 2 during daughter-thruster firings (Gilchrist et al., 1982). In particular while thruster firings from the daughter were observed to reduce the spacecraft potential, the minimum potential was still higher than that during mother thruster firings. This higher potential arises from the requirement that it be sufficiently high to accelerate electrons to ionizing energies and the efficiency for vehicle-induced ionization associated with daughter-thruster firings is smaller than beam-induced ionization associated with mother-thruster firings.

The evolution of the beam phase space during beam injection at the highest neutral density in Figure 8 is shown in Figure 9. Similar to the case of beam-induced ionization the beam is able to propagate into the plasma with little distortion until a distance along the magnetic field equivalent to the end of the neutral cloud (i.e.,  $x/\Delta \approx 200$ ). At this point the ambient plasma is unable to support the beam current as in the collisionless case and large ambipolar electric fields develop which decelerates the beam electrons and accelerates ambient plasma ions outwards.

### Summary

In summary, the effects of neutral gas releases on active beam injection has been studied through two-dimensional electromagnetic simulations with collisional processes included. Neutrals

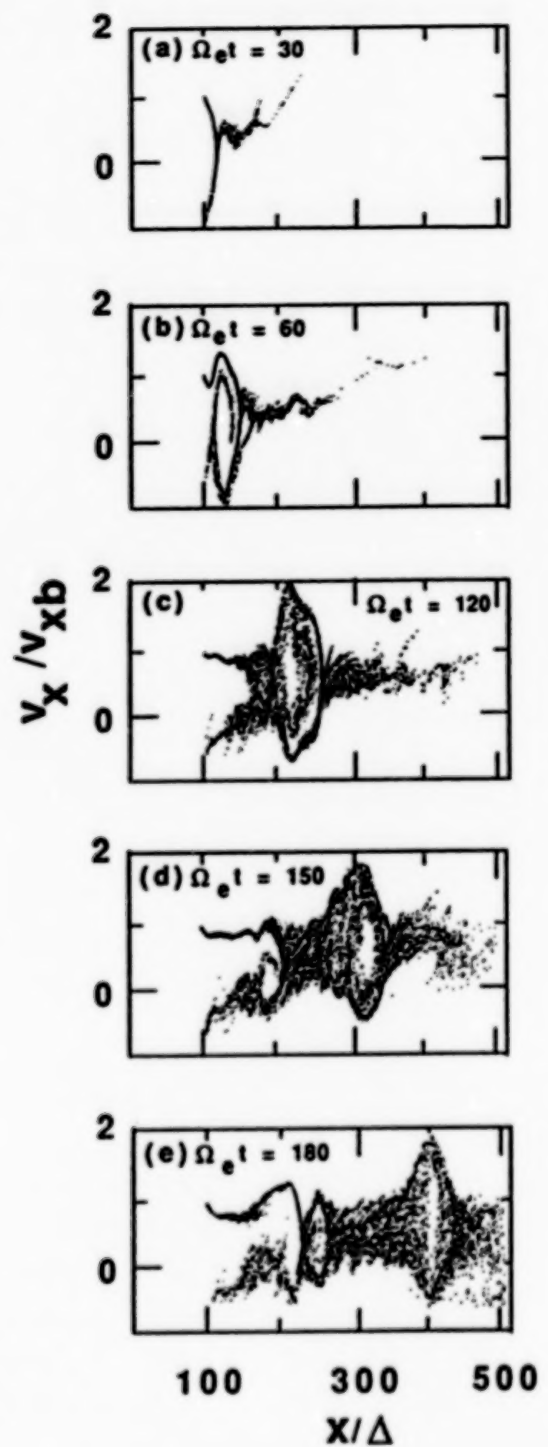


Figure 9. The beam phase space for the high neutral density case in Figure 8.

are important since their partial ionization can increase the local plasma density and provide enhanced return currents to the spacecraft, thereby reducing the amount of spacecraft charging and associated distortion of the beam. It has been shown that the ionization can be produced by (i) direct beam-induced ionization, (ii) vehicle induced ionization and (iii) beam-plasma discharge.

In the cases where beam-induced or vehicle-induced ionization are providing the return current into the spacecraft, the beam is able to propagate away from the spacecraft with little distortion until it reaches the neutral cloud boundary at which point strong ambipolar electric fields develop, causing beam distortion. Vehicle-induced ionization, however, requires high densities to produce the same drop in potential but it has the advantage that the physics of the actual beam-plasma interaction is not modified by the presence of a collisional plasma in the beam region. This latter effect could be important for active experiments where the electron beam is used to investigate beam-plasma interactions and/or to produce controlled wave generation.

Another advantage of using vehicle-induced ionization to neutralize the spacecraft charge is that beam-plasma discharge will not be excited. BPD tends to be excited when there are neutrals in the beam region and the beam is unstable to wave modes which can trap electrons in the beam region and produce enhanced ionization. This trapping tends to preferentially occur for wide beams associated with injection by guns with a large opening angle and/or injection into weak magnetic fields where the beam can expand through the beam-plasma interaction.

**Acknowledgements.** This work was supported by NASA's Ionospheric Physics, Solar Terrestrial Theory and Solar Heliospheric Programs under grants, NAGW-1587, NAGW-91 and NSG-7827 and National Science Foundation grant ATM 87-19371 to the University of Colorado.

#### References

- Gilchrist, B. E., P. M. Banks, T. Neubert, P. R. Williamson, N. B. Myers, W. J. Raith, and S. Sasaki, Observations of electron collection enhancement using neutral gas thruster jets on an isolated charged vehicle in the ionosphere, *J. Geophys. Res.*, submitted, 1989.
- Gurnett, D. A., W. S. Kurth, J. T. Steinberg, and S. D. Shawhan, Plasma wave turbulence around the shuttle: Results from the Spacelab-2 Flight, *Geophys. Res. Lett.*, **15**, 760, 1988.
- Linson, L. M., Charge Neutralization as studied experimentally and theoretically, in *Artificial Particle Beams in Space Plasma Studies*, edited by B. Grandal, p. 573, Plenum Press, New York, 1982.
- Winckler, J. R., and 12 others, Echo 7: An electron beam experiment in the magnetosphere, *EOS*, **70**, 657, 1989.
- Winglee, R. M., Electron beam injection during active experiments 2. Collisional effects, *J. Geophys. Res.*, submitted, 1989.
- Winglee, R. M., and P. L. Pritchett, Comparative study of cross-field and field-aligned electron beams in active experiments, *J. Geophys. Res.*, **93**, 5823, 1988.

PRESSURE AND CURRENT BALANCE CONDITIONS DURING  
ELECTRON BEAM INJECTIONS FROM SPACECRAFT

K. S. Hwang

Department of Mechanical Engineering  
and Center for Space Plasma and Aeronomics Research  
and  
N. Singh

Department of Electrical and Computer Engineering  
and Center for Space Plasma and Aeronomics Research  
The University of Alabama in Huntsville  
Huntsville, Alabama 35899

**Abstract.** Electrostatic charging level of a conducting surface in response to injections of electron beams into space plasma is investigated by means of one-dimensional Vlasov code. Injections of Maxwellian beams into a vacuum shows that the surface can charge up to an electric potential  $\phi_s > W_b$ , where  $W_b$  is the average electron beam energy. Since Maxwellian beams have extended tails with electrons having energies  $> W_b$ , it is difficult to quantify the charging level in terms of the energies of the injected electrons. In order to quantitatively understand the charging in excess of  $W_b$ , simulations were carried out for water-bag types of beam with velocity distribution functions described by  $f(V) = A$  for  $V_{\min} \leq V \leq V_{\max}$  and  $f(V) = 0$  otherwise, where  $A$  is a constant making the normalized beam density unity. It is found that  $V_{\max}$  does not directly determine the charging level. The pressure distribution in the electron sheath determines the electric field distribution near the surface. The electric field in turn determines the electrostatic potential of the vehicle. The pressure distribution is determined by the beam parameters such as the average beam velocity and the velocity spread of the beam.

### Introduction

Electron beam injections from spacecrafts now constitute a major activity in space research. Already there are several experiments involving rockets ranging in altitude from about 100 kilometers to about 1500 km (e.g., see Review by Winckler (1980). During the STS-3 and Spacelab-2 missions of the shuttle, electron beam injections were carried out. These space experiments have revealed that in response to the injection a host of plasma processes are driven (Sasaki et al., 1986; Inan et al., 1984; and Shawhan et al., 1984). Low-altitude rocket experiments have shown that normally the rocket potential  $\phi_s$ , in response to the injection is considerably smaller than the injected electron beam energy  $W_b$  (Winckler, 1980). This is attributed to the effective neutralization of the charges on the vehicle by the return current from the ambient ionospheric plasma. At a low

ionospheric altitude, where neutral densities are significantly high ( $-10^8 \text{ cm}^{-3}$ ), beam-plasma discharge provides an additional means for charge neutralization. On the other hand, high-altitude experiments have demonstrated that the vehicle can charge to potentials  $\phi_s > W_b/e$ , where  $e$  is the electronic charge (Managdze, 1983). The electron beam injections from the shuttle showed that when the current-collecting part of the shuttle was in the wake and an electron beam was injected, the vehicle charged to potentials  $\phi_s \geq W_b/e$  (Sasaki et al., 1986).

Motivated by the experiments, there are now several numerical simulations on the electron beam injection. Parks et al. (1975) used a hydrodynamic approach to study the reflection of monoenergetic electron beam injected from a planar body into vacuum and showed that the reflection time  $t_r \sim 2\omega_{pb}^{-1}$ , where  $\omega_{pb}$  is the electron-plasma frequency associated with the beam density  $n_b$ . Recently Pritchett and Winglee (1987), Okuda et al., (1987) and Okuda and Kan (1987) have used particle-in-cell code to investigate the dynamics of the injected beams. Winglee and Pritchett (1987) carried out simulations using particle codes emphasizing the temporal features of the injected electrons into an ambient plasma with density  $n_a \ll n_b$ . Singh and Hwang (1988) carried out simulations using Vlasov codes and dealt with the questions of the charging level of the vehicle when the ratio  $n_a/n_b$  is varied. They showed that when  $n_a/n_b \gg 1$ , the return current from the background plasma neutralizes the charge on the vehicle and the time-average vehicle potential and  $\phi_{av} \sim kT_e/e$  where  $k$  is the Boltzmann constant and  $T_e$  is electron temperature. On the other hand, when  $n_b > n_a$ , the plasma is not able to neutralize the charge and  $\phi_{av}$  can appreciably exceed the average beam energy. In this case, the electric potential distribution near the vehicle is like a thin sheath. In the intermediate case, when the vehicle potential lies in the range  $kT_e/e \leq \phi_{av} \leq W_b/e$ , the beam penetrates into the plasma but much slower than the beam velocity. The propagation speed depends on the velocity of a triple-charge-layer structure which forms near the propagating beam head.

Despite several simulations, it is not clearly understood why vehicles charge to potentials  $\phi_s > W_b/e$  (Managdze, 1983; and Machlem, 1988) when the ambient plasma is not able to effectively neutralize the positive charge on the vehicle. We have investigated this issue and we find that the electric field in the electron sheath near the vehicle is determined by the pressure balance. Since the pressure distribution does not only depend on the average beam velocity, but also on the beam temperature, density and self-consistent evolution of the plasma distribution in the electron sheath, it is difficult to predict analytically the dependence of the vehicle potential on the injected-beam parameters. Simulations of the injection of electron beams with water-bag types of velocity distribution functions with a sharp cut-off into a vacuum show that the charging level exceeds  $(m/2e)V_{max}^2$ , where  $V_{max}$  is the maximum velocity above which there are no electrons. This is in contrast

to the suggestion of Grard and Tunaley (1971), who assumed that for water-bag distributions of photoelectrons emitted from the surface, the surface potential  $\phi_s = 1/2 (m/e) V_{max}^2$ .

The rest of the paper is organized as follows. The numerical technique is described in section 2. In section 3, we have discussed the injection of Maxwellian and water-bag types of electron beams into both vacuum and ambient plasma. The paper is concluded in section 4.

### Numerical Model

We model the electron beam injection by one-dimensional Vlasov simulations, in which the electron beam from a conducting surface at  $X = 0$  is injected into a plasma of extent  $0 < X \leq L$  as shown in Figure 1. The dynamics of the plasma particles and the self-consistent electric fields are determined by solving the coupled Vlasov and the Poisson equations. The positive charge at  $X = 0$ , resulting from the injection of the electron beam from this surface, is included in determining the electric fields. Any charge particles striking the surface is assumed to be lost, but their charges are added to the surface charges on the body. The surface electric field  $E_x(x = 0)$  is determined by the net surface charge density. The plasma particles which exit the boundary at  $X = L$  are reflected back into the system, simulating a uniform plasma. When the beam electrons begin to reach the surface at  $X = L$ , the simulation is stopped. At  $X = L$ , we use the Dirichlet boundary condition  $\phi(X = L) = 0$ , which is found to be good as long as the perturbations created by the electron beams do not reach this boundary.

In the simulations described here we use  $L = 10^3 l_d$ , where  $l_d$  is the Debye length with a reference plasma density  $n_0$  and temperature  $T_0$ . We have used the electron to ion mass ratio for  $H^+$ . The numerical grids in  $X$  and  $V_x$  space are as follows:  $\Delta X = l_d$ ,  $\Delta V_x$  for electrons is  $0.25 V_t$ , and for ions  $0.05 V_t$ , where  $V_t$  is the electron thermal velocity with the temperature  $T_0$ . The time step to advance the solutions is  $\Delta t = 0.1 \omega_{pe}$ , where  $\omega_{pe}$  is the electron-plasma frequency with the density  $n_0$ . Further details about the simulation technique can be found in the work of Singh and Schunk (1984).

We have used the following normalizations: distance  $\hat{X} = X/l_d$ , velocity  $\hat{V} = V/V_t$ , time  $\hat{t} = t\omega_{pe}$ , current density  $\hat{J} = J/J_t$ ,  $J_t = e n_0 V_t$ , density  $\hat{n} = n/n_0$ , potential  $\hat{\phi} = e\phi/T_0$ , electric field  $\hat{E} = E/E_0$ ,  $E_0 = T_0/e l_d$ . In the case of electron beam injection into a vacuum,  $n_0$  and  $T_0$  refer to the injected beam. When the beam injection occurs into an ambient plasma  $n_0$  and  $T_0$  refer to the ambient plasma.

### Numerical Results

We begin this section with the discussion on the injection of electron beams into a vacuum. Such an exercise throws a great deal of light on the causes for the vehicle charging considerably

in excess of  $W_b/e$ , where  $W_b$  is the average electron beam energy,  $W_b = 1/2m_e V_b^2$ . The results on the injection into an ambient plasma is described in the following section.

### Injection Into Vacuum

Maxwellian Beams. The temporal evolution of the spacecraft potential for several velocities of Maxwellian beams are shown in Figure 2, in which  $V_b$  is the beam velocity normalized to its thermal velocity  $V_t$ . During the early stage ( $t \leq 3\omega_{pb}^{-1}$ ) the potential increases at a fast rate and then it settles down at a quasi-steady value depending on the average beam velocity. It is seen that the quasi-steady value of  $\phi_s$  slowly increases. This is attributed to the fast electrons in the tail of the Maxwellian beam which continually escapes. The analytical calculation of Grard and Tunaley (1971) show an infinitely large potential when the ambient plasma is completely absent. The vehicle potential saturates at a time approximately given by

$$t_s = 3\omega_{pb}^{-1} \quad (1)$$

This time is somewhat longer than the beam reversal time  $t_r = 2\omega_{pb}^{-1}$  calculated by Parks et al (1975), using a hydrodynamic treatment for the beam propagation. However, it should be noted that the  $t_r$  is the time when the beam velocity  $V_b \rightarrow 0$  in the retarding potential distribution which  $t_s$  is the time when the reflected beam electrons reach the surface at  $x = 0$  and effectively neutralize the further increase in the positive charge on it.

Figure 2 shows that the surface vehicle potential  $\phi_s$  increases with the average beam velocity  $V_b$ . The dependence of  $\phi_s$  on  $V_b$  at  $t = 3\omega_{pb}^{-1}$  is plotted in Figure 3, which also shows the plot of  $W_b$  versus  $V_b$ . Comparing the two curves in this figure we find that  $\phi_s \gg W_b$ . Intuitively it can be argued that in a Maxwellian beam with a finite temperature there are electrons at velocities  $V > V_b$  and therefore  $\phi_s$  attains a value for which such fast electrons are also confined by the developing electric fields. But in a Maxwellian distribution there is no unique maximum velocity which can uniquely determine the maximum possible value of the surface potential  $\phi_s$ .

Water-Bag Beams. In order to quantitatively understand the dependence of  $\phi_s$  on the energy of the injected electrons, we carried out simulations with water-bag type of distribution functions defined by

$$f_b(\hat{v}) = \begin{cases} A & \hat{v}_{\min} \leq v \leq \hat{v}_{\max} \\ 0 & \text{otherwise} \end{cases} \quad (2)$$

where  $A$  is chosen so that the beam density is unity, namely,

$$A = \frac{1}{\hat{v}_{\max} - \hat{v}_{\min}} \quad (3)$$

The water-bag distribution functions have the attractive property that they have a sharp cut-off at  $V = V_{\max}$  with no electrons at  $V > V_{\max}$ . Thus, simulations with such distributions can possibly show the dependence of  $\phi_s$  on the maximum electron energy in the beam, which is not a well-defined quantity for a Maxwellian beam.

The solid curves in Figure 4 show the temporal evolution of the surface potential  $\phi_s$  for two water-bag beams with the same average beam velocity  $V_b = 6$ , but  $V_{\max}$  and  $V_{\min}$  for the two beams are different. Beam #1 has  $V_{\max} = 12$  and  $V_{\min} = 0$ , while for beam #2  $V_{\max} = 7$  and  $V_{\min} = 5$ . Beam #1 is warm while beam #2 is relatively cold. For beam #1,  $\phi_s = 170$  while for beam #2  $\phi_s = 75$ . These values far exceed the charging level determined by the maximum kinetic energies of the electrons in the two beams. These energies are

$$\hat{W}_{\max} = \frac{1}{2} \hat{V}_{\max}^2 = 72, \quad \text{beam } \#1 \quad (4)$$

$$\hat{W}_{\max} = 24.5, \quad \text{beam } \#2 \quad (5)$$

Grard and Tunaley (1971) have carried out analytical calculations on the charging of a plane surface in response to photoelectron emissions. They have considered a water-bag distribution for the emitted electrons. They have suggested that the charging level is determined by the maximum electron energy in the velocity distribution function. Our simulations show that this is not true as the surface charges to a potential greatly in excess of  $W_{\max}$  (Figure 4). This authors used continuity and energy conservation equations

$$nV = n_0 V_0 \quad (6)$$

$$\frac{1}{2} mV^2 - e\phi = \frac{1}{2} mV_0^2 - e\phi_0 \quad (7)$$

and the Poisson equation to show that the surface electric field is given by

$$E_s^2 = \frac{2mN_s}{e_0} \int_0^\infty V^2 f_s(V) dV \quad (8)$$

where  $f_s(V)$  is the distribution function on the surface and  $N_s$  is the electron density there. In equations (6) and (7)  $n$  and  $V$  are the density and velocity where electric potential is  $\phi$  and similarly  $n_s$  and  $V_s$  are the density and velocity where  $\phi = \phi_s$ .

We now compare these analytic results with our results obtained from the numerical simulations. In our normalized units equation (8) can be written as

$$\hat{E}_s^2 = 2\hat{N}_s \int_0^\infty \hat{V}^2 f_s(\hat{V}) d\hat{V} \quad (9)$$

where  $f_s(\hat{V})$  is one-sided distribution function and it is normalized to take into account both outgoing and incoming particles. We note that the integral in (9) is the effective electron temperature near the surface, if the average drift velocity is zero.

Figures 5a and 5b show the electron velocity distribution functions near the surface for beam #1 and #2 respectively. The effective electron temperature associated with the distribution functions is given by

$$\hat{T}_{eff} = \int_{-\infty}^{\infty} (\hat{V} - \hat{u})^2 f(\hat{V}) d\hat{V} / \int_{-\infty}^{\infty} f(\hat{V}) d\hat{V} \quad (10)$$

where  $\hat{u}$  is the average drift velocity associated with the distributions. We find that near the surface for both the beams  $T_{eff}$  is about 25 (see Figure 7), and the electron density  $\hat{N}_s = 2$  (see Figure 6). Substituting these values in (9), we obtain  $\hat{E}_s = 10$ , which is remarkably close to the electric fields obtained in the numerical simulations as shown in Figure 4 by the dotted curves. We find that despite this fair agreement on the surface electric fields obtained by theory and simulations, the surface potentials ( $\phi_s$ ) obtained from simulations greatly exceed those predicted by the theory (Grard and Tunaley, 1971). We now show that this difference is caused primarily by the pressure distribution in the electron sheath near the surface. We find that (7) is not valid throughout the electron sheath because it does not include the thermal energy.

The spatial distributions of density  $\hat{N}(X)$ , effective temperature  $T_{eff}(X)$  and electric field  $\hat{E}(X)$  in the simulations for beam #1 and #2 are shown in Figures 6, 7 and 8, respectively. Using these distributions we now examine the relative contributions of the terms in the momentum balance equation,

$$\hat{u} \frac{\partial \hat{u}}{\partial \hat{x}} = -\hat{E} - \frac{1}{N} \frac{\partial \hat{P}}{\partial \hat{x}} \quad (11)$$

where  $\hat{u}$  is the average drift velocity and  $\hat{P}$  is the pressure given by

$$\hat{P} = \hat{N} \hat{T}, \quad (12)$$

If  $\hat{i} = 0$ , the electric field distribution is given by

$$\hat{E} = - \frac{1}{N} \frac{\partial \hat{P}}{\partial \hat{x}} \quad (13)$$

In Figure 8, the solid and dashed curves show the numerically obtained spatial distributions of  $E$  for the two beams. The curve with the triangles is the electric field obtained from (13) for the beam #1. The pressure in (13) is obtained by the density and temperature shown in Figures 6 and 7, respectively. It is seen from Figure 8 that the electric field is quite accurately determined by the pressure force. This shows that the kinetic term  $u \partial u / \partial x$  is negligibly small in the momentum equation. This is expected from the nature of the distribution function in Figure 5a for beam #1.

The curve with circles (o-o) gives the plot of  $N^{-1} \partial \hat{P} / \partial \hat{x}$  for beam #2. It is seen that it slightly underestimates the electric field shown by the dashed curve. This is accounted by the fact that for the beam #2 the distribution function has distinct peaks (Figure 5b), which is not described well by an effective temperature.

The comparison of the electric fields directly obtained from the simulations with those derived from the pressure force clearly shows that it is the pressure force in the electron sheath which determines the electric field distribution and hence the surface potential of the vehicle. Comparing the electric field curves for the beam #1 and #2 in Figure 8, we see that the beam with the large  $V_{max}$  has relatively large electric fields extending to much greater distances than the beam with the smaller  $V_{max}$ . Thus, there is a dependence of charging on  $V_{max}$ , but it is not directly determined by the maximum electron energy  $1/2 m_e V_{max}^2$ . The dependence is determined by the pressure distribution in the electron sheath. It is difficult to predict the pressure distribution because of the highly non-linear nature of the problem.

#### Effects of Ambient Plasma on Charging

The ambient plasma reduces the charging level by providing a return electron current, which partly neutralizes the positive charge on the surface. Figures 9a and 9b show the temporal

evolution of the surface potential for a Maxwellian beam with beam velocity  $V_b = 6$  injected into ambient plasmas with densities  $n_a = 0.1 n_b$  and  $0.2 n_b$ . The beam and ambient plasma temperatures are assumed to be the same. The effect of the ambient plasma on the surface potential is found to be twofold; it causes oscillations in the surface potential and the time average value of  $\phi_s$  decreases with increasing ambient plasma density. Without any ambient plasma, the surface potential attained a quasi-steady value of about  $\phi_s = 70$  (see Figure 3). For  $n_a/n_b = 0.1$  and  $0.2$ , its time-average values reduce to  $50$  and  $45$ , respectively. However, it is important to note that for such small ambient plasma densities, the charging level exceeds considerably the average beam energy  $W_b = 18$ , and the beam does not propagate into the plasma.

The oscillations seen in Figure 9 in the surface potential are found to have time periods determined by the ambient plasma frequency. For example, the time periods seen in Figures 9a and 9b are  $\tau = 20 \omega_{pe}$  and  $14 \omega_{pe}$ , respectively, and they are given  $2\pi \sqrt{(n_a/n_b)} \omega_{pe}$ .

We have found that for sufficiently small beam densities when  $\phi_{sa} \leq W_b$ , the beam begins to penetrate into the plasma (Singh and Hwang, 1988). However, the propagation speed critically depends on the time-average surface potential  $\phi_{sa}$ . When  $\phi_s - (kT/e) \ll W_b$  for  $n_a \gg n_b$ , the beam propagates into the plasma with the injection velocity Singh and Hwang (1988). As  $\phi_s$  increases with decreasing value of the relative ambient plasma density ( $n_a/n_b$ ), the propagation velocity decreases. For surface potentials in the range  $(kT/e) \ll \phi_s \leq W_b$ , Singh and Hwang (1988) found that the beam head penetrates into the plasma with well-defined laminar potential structure near the beam head. The velocity of the potential structure is determined by the nonlinear plasma processes through which it evolves.

### Conclusion

We have investigated in this paper the charging level of a conducting surface when an electron beam is injected from it. Injections into both vacuum and ambient plasma are considered. When a Maxwellian beam is injected into vacuum it is found that the surface charges to a potential much greater than the average beam energy. The dependence of the charging in excess of the average beam energy is investigated by considering beams with water-bag types of velocity distribution functions with distinct maximum velocity  $V_{max}$  such that no electron velocities  $V > V_{max}$ . It is found that the electric field distribution in the electron sheath near the surface is determined by the pressure distribution. Thus, the surface potential is determined not only by the  $V_{max}$ , but by all the beam parameters such as the density  $n_b$ , average beam velocity and the velocity spread of the beam. The parameters determine the pressure distribution in the electron sheath. Since the effective temperature and the density

distributions in the sheath evolve self-consistently through the nonlinear dynamics of the electrons, it is difficult to predict the charging level.

In our one-dimensional model, we have not included return currents coming from directions other than that for the beam injection. For the omnidirectional return current, the surface potential will in general tend to be smaller than that for the one-dimensional case. However, space experiments have shown that vehicles do charge to potentials comparable to, or in excess of, the average electron beam energy (Sasaki, et al. 1986, Managdz, 1983, Machlem, 1988). Therefore, the physical processes seen in the one-dimensional simulations are relevant to space experiments.

Acknowledgement. This work was performed under NASA Contract NAS8-37107.

#### References

- Grard, R. J. L. and J. K. E. Tunaley, Photoelectron sheath near a planar probe in interplanetary space, J. Geophysical Res., 75, 2498, 1971.
- Inan, U. S., M. Pon, P. M. Banks, P. R. Williamson, W. J. Raitt and S. D. Shawhan, Modulated beam injection from the space shuttle during magnetic conjunctions of STS-3 with the DE-1 satellite, Radio Sci., 19, 487, 1984.
- Managadze, G. G., Plasma processes in the region of electron beam injection from a high altitude payload, Active Experiments in Space Symposium at Alpach, 24-28 May 1983, Eur. Space Agency Spec. Publ., ESA SP-195, 161, 1983.
- Okuda, H., and J. R. Kan, Injection of an electron beam into a plasma and spacecraft charging, Phys. Fluids, 30, 209, 1987.
- Okuda, H. R. Horton, M. Ono, and M. Ashour-Abdalla, Propagation of a nonrelativistic electron beam in a plasma in a magnetic field, Phys. Fluids, 30, 200, 1987.
- Parks, D. E., A. R. Wilson, and I. Katz, Monode plasma sheath dynamics T-NS 75, Dec., IEEE Trans. Nucl. Sci., 2368, 1975.
- Prichett, P. L., and R. M. Winglee, Plasma environment during particle beam injection into space plasmas, 1, Electron beams, J. Geophys. Res., 92, 7673, 1987.
- Sasaki, S. N. Kawashima, K. Kuriki, M. Yanagisawa, and T. Obayashi, Vehicle charging observed in SEPAC Space Lab-1 experiment, J. Spacecr. Rockets, 23 129, 1986.
- Shawhan, S. D., G. B. Murphy, P. M. Banks, P. R. Williamson and W. J. Raitt, Wave emissions from dc and modulated electron beams on STS-3, Radio Sci., 19, 471, 1984.
- Singh, N. and R. W. Schunk, Plasma response to the injection of an electron beam, Plasma Phys. Controlled Fusion, 26, 859, 1984.
- Winckler, J. d R., The application of artificial electron beams to magnetospheric research, Rev. Geophys., 18, 659, 1980.
- Winglee, R. M., and P. L. Prichett, Charging effects during the injection of dense electron beams, J. Geophys. Res., 92, 6114, 1987.

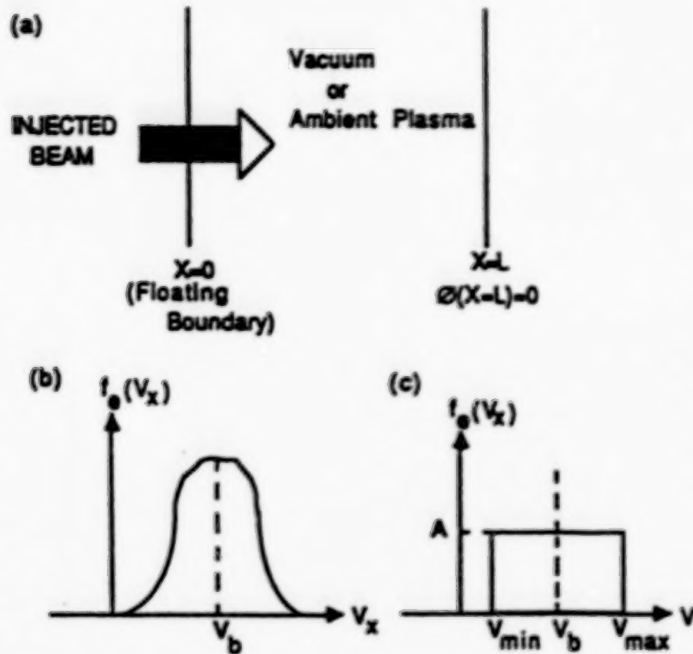


Figure 1. (a) Simulation scheme: the electron beam is injected at the boundary  $x = 0$ . The region  $0 \leq x \leq L$  is either vacuum or it contains an ambient plasma with density  $n_e$  and temperature  $T_e$ . The injected beams may have velocity distribution functions as shown in (b) Maxwellian distribution or in (c) water-bag distribution. The average beam velocity is  $v_b$ . At the right hand boundary the electric potential  $\phi(x=L) = 0$  while the left hand boundary ( $x = 0$ ) is kept floating.

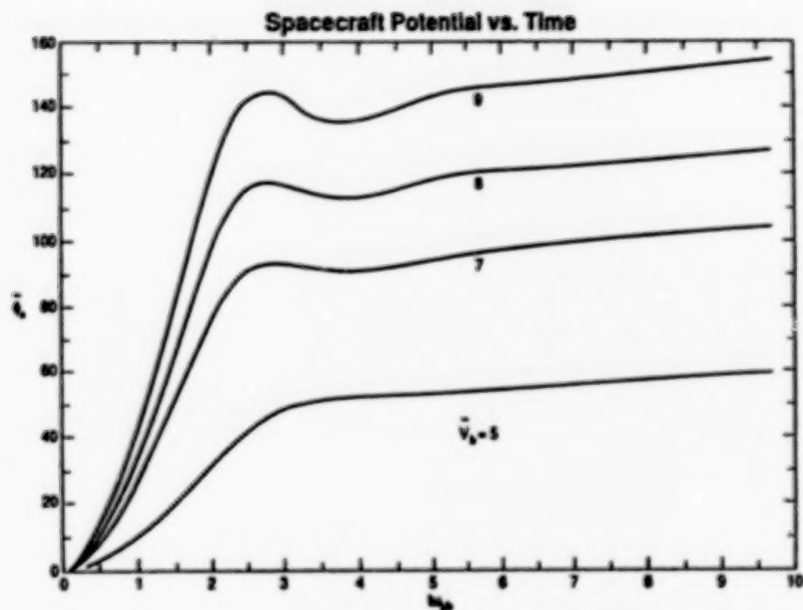


Figure 2. Temporal evolution of the surface potential  $\phi$ , for Maxwellian beams with different beam velocities ( $v_b$ ), which are normalized to the beam thermal velocity.

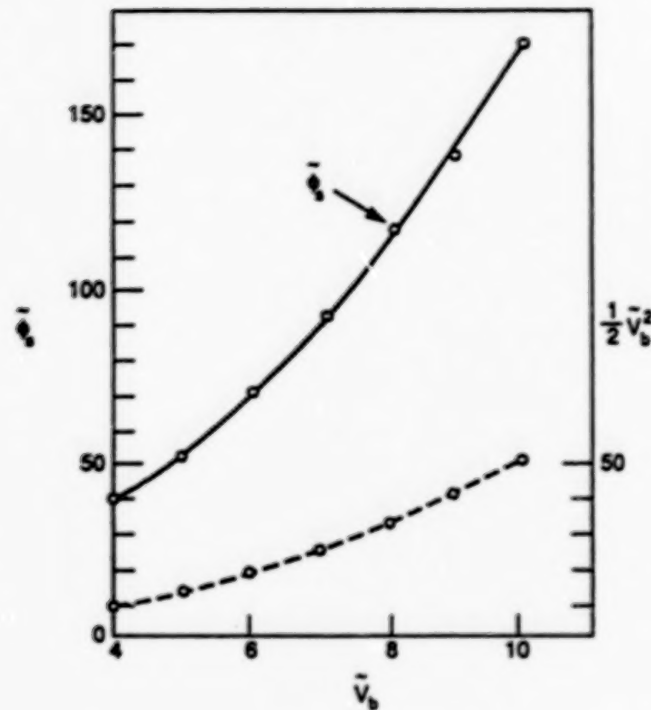


Figure 3. Surface potential  $\hat{\phi}_s$  as a function of beam velocity  $\hat{V}_b$  for the beams injected into vacuum. Normalized beam energy ( $1/2 \hat{V}_b^2$ ) as a function of  $V_b$  is also shown.

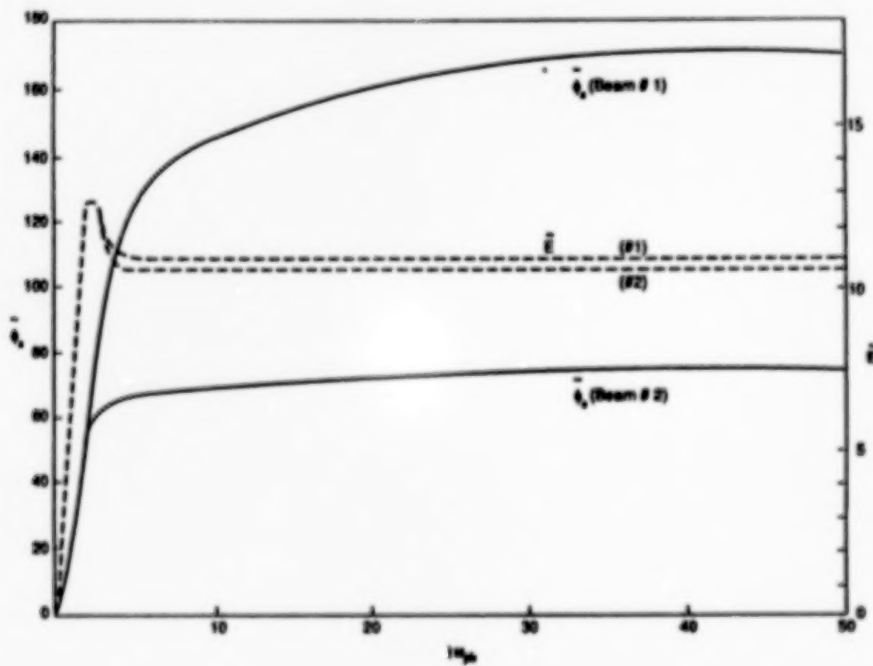
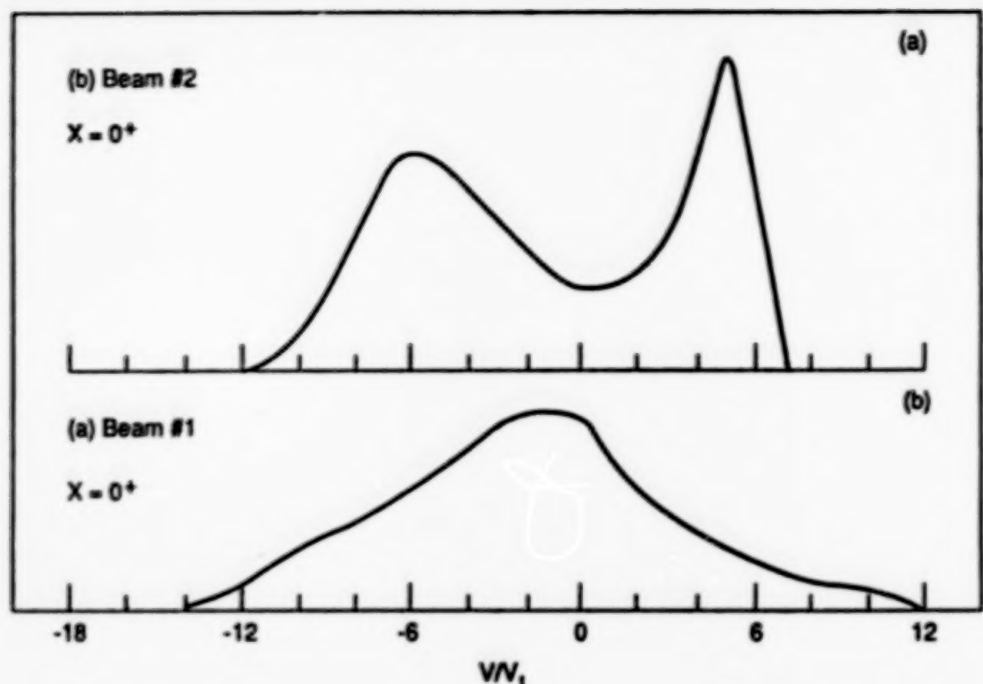
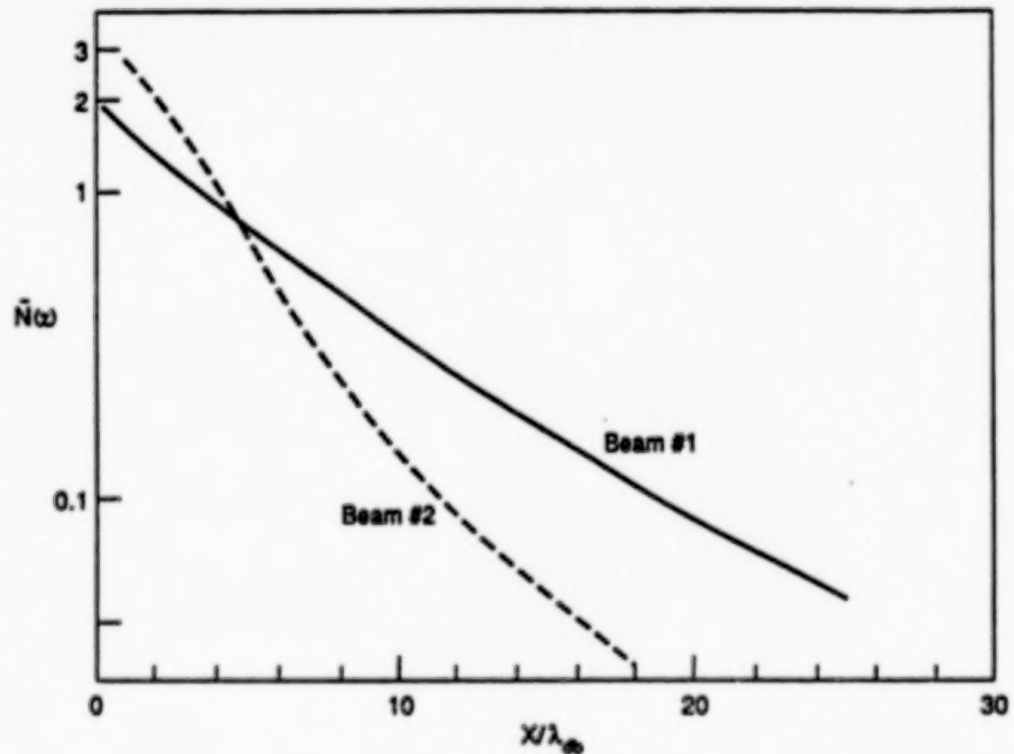


Figure 4. Temporal evolutions of surface potential  $\phi_s$  and electric field  $E$ , are shown for water-bag beams #1 and #2. For both the beams  $V_b = 6$ ; for beam #1  $\hat{V}_{\min} = 0$ ,  $\hat{V}_{\max} = 12$  and for beam #2,  $\hat{V}_{\min} = 5$ ,  $\hat{V}_{\max} = 7$ .



**Figure 5.** Electron velocity distribution functions near the surface  $X = 0^+$  at  $t_{w,p,b} = 50$ . (a) beam #1, (b) beam #2. It is worth mentioning that the distribution functions shown are not exactly at  $x = 0$ , but they are at  $x = 0^+$  as they are averaged over 2 grid spaces in front of the surface at  $x = 0$ . The distributions show that the injected water-bag beams have been modified by the intense electric fields near the surface.



**Figure 6.** Density distribution in the electron sheath for the water-bag beams #1 and #2.

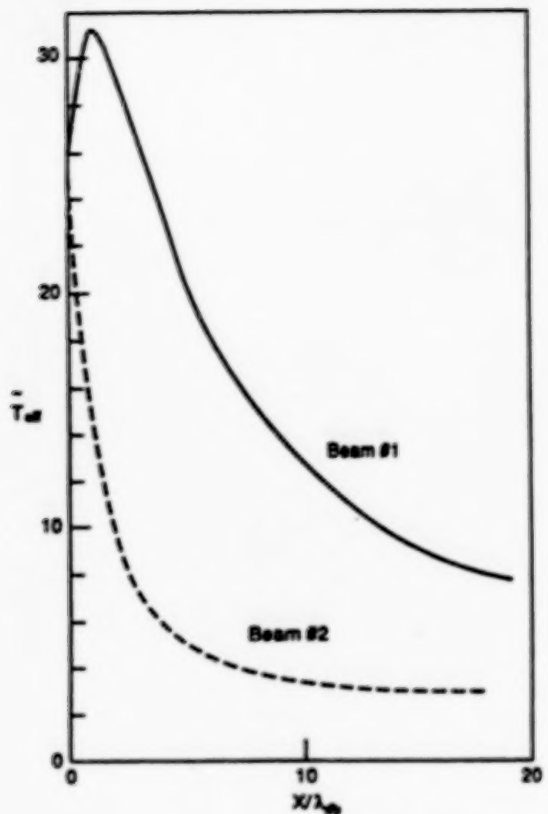


Figure 7. Effective temperature distributions for the beam #1 and #2 in the electron sheath.

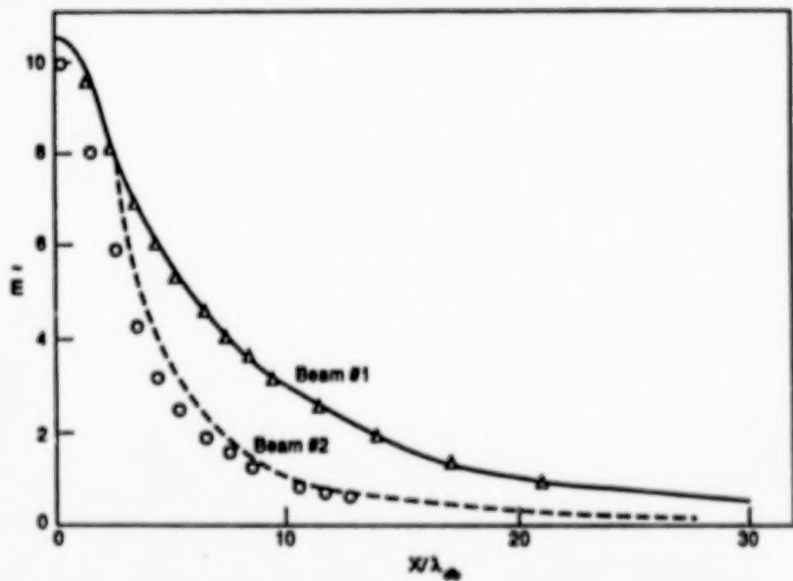
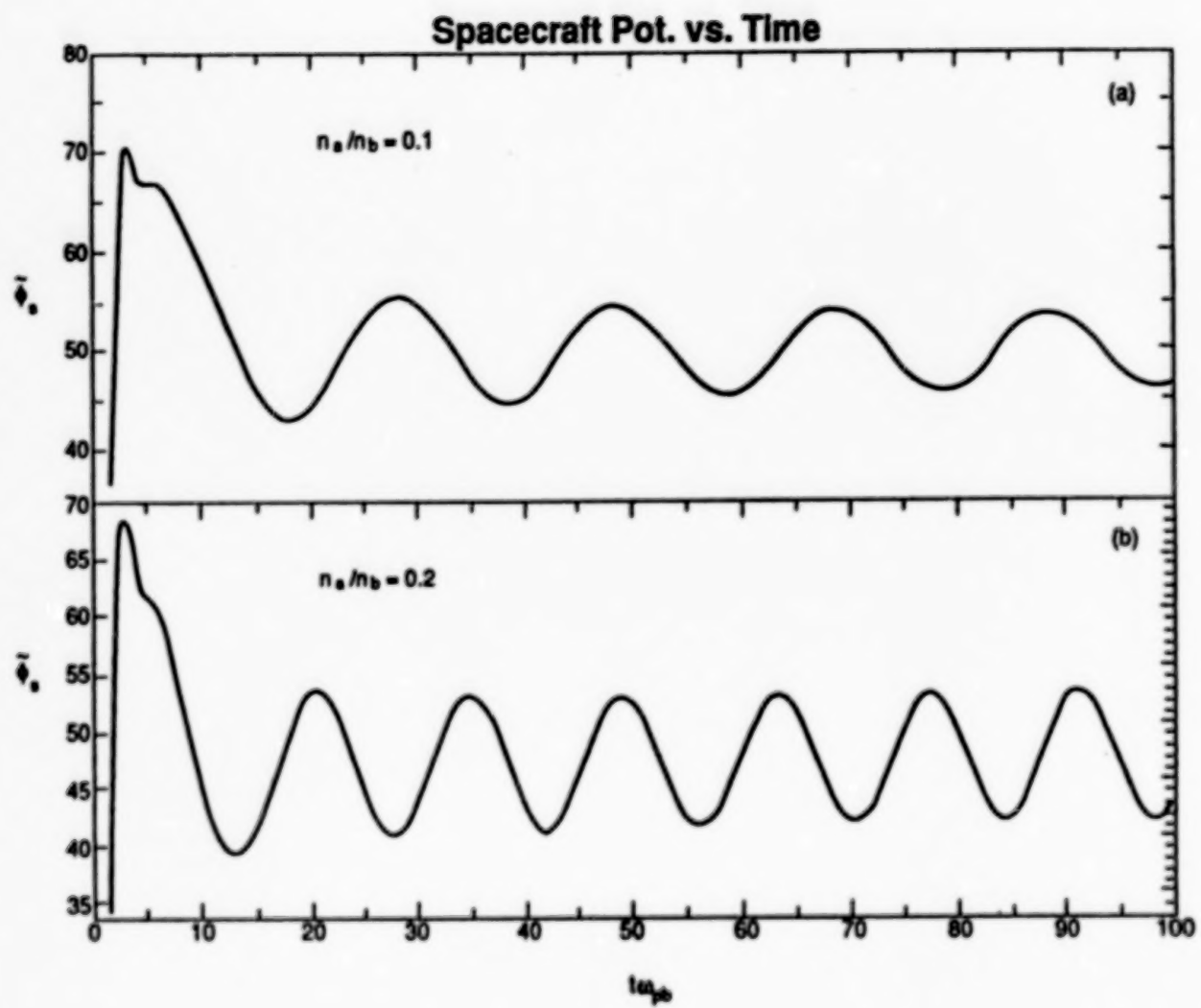


Figure 8. Electric field distributions. Beam #1: solid curve gives  $E$  from numerical simulations and the triangles give the  $E$  field from pressure balance. Beam #2: broken curve gives  $E$  from simulation while the circles give  $E$  field from pressure balance.



**Figure 9.** Temporal evolution of surface potential  $\Phi_s$ , when Maxwellian beams are injected into ambient plasmas:  
 (a) ambient plasma density  $n_a = 0.1 n_b$ , (b)  $n_a = 0.2 n_b$ ;  
 beam velocity  $V_b = 6$ .

## NASCAP/LEO CALCULATIONS OF CURRENT COLLECTION

M. J. Mandell, I. Katz, V. A. Davis, R. A. Kuharski

S-CUBED, A Division of Maxwell Laboratories, Inc.  
P. O. Box 1620, La Jolla, California 92038

**Abstract.** NASCAP/LEO is a 3-dimensional computer code for calculating the interaction of a high-voltage spacecraft with the cold dense plasma found in Low Earth Orbit. Although based on a cubic grid structure, NASCAP/LEO accepts object definition input from standard CAD programs so that a model may be correctly proportioned and important features resolved. The potential around the model is calculated by solving the finite element formulation of Poisson's equation with an analytic space charge function.

Five previously published NASCAP/LEO calculations for three ground test experiments and two space flight experiments are presented. The three ground test experiments are a large simulated panel, a simulated pinhole, and a 2-slit experiment with overlapping sheaths. The two space flight experiments are a solar panel biased up to 1000 volts, and a rocket-mounted sphere biased up to 46 kilovolts. In all cases, we find good agreement between calculation and measurement.

### Introduction

This report is an expanded version of a poster presentation made at the "Workshop on Current Collection from Space Plasmas," Huntsville, Alabama, April 24-25, 1989. The objective of this document is to summarize the capabilities and the physical and numerical basis of the NASCAP/LEO computer code. NASCAP/LEO is capable of calculating the potential and sheath structure around a geometrically and electrically complex spacecraft immersed in a plasma, and the plasma currents collected by the surfaces of such an object.

We present here five previously published case studies of NASCAP/LEO simulations of experiments studying interactions of charged surfaces with a plasma representative of Low Earth Orbit. Three of the experiments were performed under ground test conditions, and two were for actual space flights. As the first four cases were done with an older version of NASCAP/LEO that required that objects be made of cubes, these objects were redefined and a few calculations performed to illustrate NASCAP/LEO's present capabilities. All the new calculations agreed with the previously published results.

NASCAP/LEO features the ability to accept a general geometrical description of the spacecraft or test object. The spacecraft is defined as a finite element surface model using a standard CAD finite element generator such as Patran<sup>(a)</sup> or EMRC<sup>(b)</sup> Display-II. An interface code reads the "neutral file" output by the finite element generator and places the object in a cubic grid. Variable surface resolution is naturally achieved in the finite element generator; locally enhanced spatial resolution is available via directive to the interface code. The object may be defined with correct angles and proportions independent of the cubic grid resolution.

NASCAP/LEO is designed to calculate space potentials in the regime where the applied voltages are large compared to the plasma temperature, and the Debye length is comparable to, or less than, the code resolution. A local space charge formulation takes account of plasma screening and acceleration and convergence of charged particles such that the Langmuir-Blodgett result will be reproduced for a spherical sheath. Currents flowing from the sheath to the object are calculated taking into account ram-wake and magnetic field effects.

NASCAP/LEO also has specialized modules to calculate spacecraft floating potentials, surface charging, mean potential of a solar array surface, parasitic power loss of a solar-voltaic power system, and hydrodynamic ion flow about a spacecraft.

#### Physical and Numerical Basis of NASCAP/LEO

NASCAP/LEO is a 3-dimensional computer code that can calculate self-consistently electrostatic potentials surrounding a charged object, plasma currents incident on object surfaces, and object surface potentials for plasma conditions appropriate to low earth orbit.

The electrostatic potential,  $\phi$ , about the object is determined by solving Poisson's equation

$$-\nabla^2\phi = \rho/\epsilon_0 \quad (1)$$

subject to fixed potential or fixed electric field boundary conditions at object surfaces. (These boundary conditions may be set by the user, or by other modules of NASCAP/LEO.) The space charge,  $\rho$ , appearing in Poisson's equation is approximated as a nonlinear analytic function of the plasma properties and the local potential and electric field. The function used is

---

(a) Patran is a trademark of PDA Engineering, Costa Mesa, CA.  
(b) Engineering Mechanics Research Corporation, Troy, MI.

$$\rho(\phi, E)/\epsilon_0 = -(\phi/\lambda^2) \times [1+C(\phi, E)\phi] \times [1+(4\pi)^{1/2}|\phi/\theta|^{3/2}]^{-1} \quad (2)$$

where the first factor represents linear screening with Debye length  $\lambda$ , the second represents increase in density due to trajectory convergence (where the convergence factor  $C(\phi, E)$  is a function of local field and potential calculated to give the correct answer for a Langmuir-Blodgett spherical sheath), and the third represents decrease in density due to particle acceleration, with  $\theta$  being the plasma temperature [eV]. An algorithm is included to account for ram-wake effects in the neutral particle approximation.

NASCAP/LEO solves the variational form of Poisson's equation

$$\delta \int d^3r \left[ (\epsilon_0/2) |\nabla \phi|^2 + p\phi \right] = 0 \quad (3)$$

using the finite element method and a conjugate gradient technique for sparse linear equations. After each solution of the linear equations, the nonlinear space charge is linearized about the current solution, and the new equations solved. This process is continued until the solution is deemed sufficiently near a fixed point.

The finite element method works well for this problem because most of space is filled with trilinear "empty" elements. "Stiffness matrices" for those elements containing surfaces are constructed numerically. The potential solver allows "nested outer grids" in order to include a large volume of space, and "subdivided inner grids" to achieve locally enhanced resolution where needed.

NASCAP/LEO calculates currents to a charged object using the "sharp sheath edge" approximation. The "sharp sheath edge" is a specified equipotential surface (usually  $\pm 0.1n$ ). Macroparticles representing ion and/or electron currents are generated for each element of sheath area, taking ram-wake effects into account. These macroparticles are tracked in the electric fields resulting from the Poisson solution, and user-specified magnetic fields, to determine where (or whether) they strike the object.

Potentials of insulating surfaces are calculated to achieve current balance among the incident (sheath and thermal) ions and electrons, and the secondary electrons. For insulators near high positive voltage surfaces, we use an electric field boundary condition which represents

equilibrium between incident electrons and transport of secondary electrons along the surface. This boundary condition is given by

$$E_{\text{on}} = [4 \langle E \rangle Y \nabla \cdot \mathbf{E}_0]^{1/2} \quad (4)$$

where  $\langle E \rangle$  is the mean energy of secondary electrons and  $Y$  is the secondary yield for primary electrons with energy equal to the surface potential.

A solar array surface is an important example of a complex surface that is a mosaic of dielectric (coverslips) and conductor (interconnects). Because of the obvious importance of solar arrays on spacecraft, we have developed an algorithm, based on equation (4), to calculate self-consistently the mean potential and mean electric field for a periodic surface. This algorithm, which takes advantage of the periodic structure of solar arrays, is discussed further in section 6 below.

#### Example 1: Simulated Solar Panel (1980) (Katz et al., 1981)

The first NASCAP/LEO paper ever published reported simulation of measurements by McCoy and Konradi (1979) of current collection by a 10-meter long "panel" exposed to an argon plasma in the large vacuum chamber at Johnson Space Center. The "panel" was actually a conducting strip mounted on a plastic frame. The strip could be held at fixed constant potential or could maintain a linear potential gradient along its length.

Figure 1 shows the NASCAP/LEO model of the panel. This model was constructed using EMRC Display-II. Note the variable resolution across the width of the panel, giving good resolution of the metal-plastic interface. Variable resolution is also used lengthwise near the ends. Figure 2 shows the same panel with linear bias (in ten steps) from zero to -4,800 volts.

Figure 3 shows the plasma potentials around the panel for the bias shown in figure 2. The plasma conditions used in the calculation were plasma density  $n = 1.3 \times 10^6 \text{ cm}^{-3}$ , and plasma temperature  $\theta = 2.3 \text{ eV}$ . The sheath shape is in agreement with what was visually observed. The primary grid unit is 0.333 meters. Note the locally enhanced resolution used near the panel surface.

The calculation also gives the current density on the panel surface, which is strongly enhanced at the high voltage end. The total current collected was 26 milliamperes, which compares well with a measurement of "slightly under" 20 milliamperes when the panel was biased from zero to -4,000 volts.

Example 2: Simulated Pinhole (1983) (Mandell and Katz, 1983)

It is well accepted that a small, positively biased conducting surface can collect current out of proportion to its size if surrounded by dielectric material. This is because secondary electron emission facilitates the spread of high positive voltage from the conductor onto the surrounding insulator. NASCAP/LEO models this phenomenon by requiring current balance between the incident electron current and the divergence of the current carried by the secondary electron layer. As the latter is proportional to the incident electron current and a strong function of the normal electric field at the surface, the potential at the dielectric surface is determined by imposing the boundary condition of a small (but nonzero) outward pointing electric field, whose value is given by equation (4).

Experiments performed by Gabriel et al. (1983) made an excellent test of the treatment of this phenomenon by NASCAP/LEO. The experiment fixture was kapton-covered except for a circular region of diameter either 1.27 cm or 0.64 cm. The experimenters measured the potentials in the plasma along the "pinhole" axis. For the smaller pinhole, the collected current was measured.

Figure 4 shows the surface potentials on the NASCAP/LEO model of the fixture with the larger pinhole. The model was constructed using EMRC Display-II, and has good resolution in the region surrounding the pinhole. (A similar model was constructed for the smaller pinhole.) The pinhole was biased to +458 volts in a plasma with  $n = 5.8 \times 10^4 \text{ cm}^{-3}$ ,  $\theta = 4 \text{ eV}$ . The spread of high potential onto the insulator is clearly seen.

Figure 5 shows the potentials in space above the pinhole for the same case. The NASCAP/LEO results are compared with experiment in figure 6, which is taken from the original paper (Mandell and Katz, 1983).

For the smaller pinhole, the experimenters measured a collected current of  $4 \mu\text{A}$  when the pinhole was biased to 458 volts in a plasma with  $n = 2.5 \times 10^4 \text{ cm}^{-3}$ ,  $\theta = 5.3 \text{ eV}$ . This value approaches the orbit-limited value of  $4.2 \mu\text{A}$ , and is far in excess of the planar current estimate of  $0.05 \mu\text{A}$ . The collection of orbit-limited current is consistent with a zero electric field boundary condition on the dielectric. The NASCAP/LEO calculated current is  $2.4 \mu\text{A}$ .

Example 3: Overlapping Sheaths (1987) (Davis et al., 1988)

A related experiment was performed by Carruth. (1987). Rather than the pinhole geometry, Carruth measured collected current and plasma potential for the more complex geometry of two parallel slits. Carruth used relatively low voltages

so as to avoid "snapover". (At higher voltages, a sharp increase in current, indicating snapover, was observed.)

Figure 7 shows the NASCAP/LEO model of Carruth's experiment with biases of 128 and 328 volts on the slits. Once again, this model was constructed using EMRC Display-II. Though it is not apparent from the figure, the model was constructed such that the current collected by the central 4.2 cm of each slit could be calculated, the same quantity measured in the experiment. Figure 8 shows a sheath contour plot for plasma conditions  $n = 2 \times 10^6 \text{ cm}^{-3}$ ,  $\theta = 2 \text{ eV}$ . (The primary grid spacing used for this calculation was 1.429 cm.) The figure shows that the sheaths of the two slits do indeed overlap. The calculated potentials agree well with the experimental measurements.

Figure 9 [taken from the original paper (Davis et al., 1988)] shows the current collected by each of the two slits when one is held at 100 volts and the potential of the other is varied. Agreement between experiment and calculation is excellent.

Example 4: PIX-II Flight Experiment (1983)  
(Mandell et al., 1986)

PIX-II (Grier, 1985) was an orbital experiment designed to measure the interaction of a high-voltage (up to 11,000 volts) solar array with the plasma environment. The instrumentation consisted of a 2,000  $\text{cm}^2$  passive solar array whose interconnects could be biased relative to the rocket ground, a Langmuir probe, and a hot-wire neutralizer. The results showed that current collection was enhanced by the "snapover" effect at positive biases over a few hundred volts, and that arcing occurred at negative biases as low as 250 volts.

In modeling the PIX-II experiment, it rapidly became apparent that it was not possible to resolve in detail a surface consisting of 2 cm x 2 cm solar cells with 0.1 cm interconnects. Strategies such as lumping the many interconnects together into a few surface zones gave a grossly inadequate representation of the surface. Therefore, taking into account that a solar array surface is a periodic structure, an analytic representation of this surface was developed. The physical content of this solar array surface model is that a dielectric in a cold plasma can achieve current balance either (1) at negative potential such that ion and electron currents balance, or (2) at small, positive electric field (given by equation (4)), provided that the resulting potential is high enough to produce secondary electron yield greater than unity. When the coverslips are in the latter condition due to the presence of high-voltage interconnects, the coverslip potential profile must be such that the positive (electron-attracting) mean electric field

must be approximately canceled by the spatially periodic components. These ideas lead to a formulation that calculates the mean potential of the surface self-consistently with the mean electric field returned from NASCAP/LEO's Poisson solver. Its parameters include the cell size, interconnect size, and coverslip material properties. (Mathematical details may be found in Mandell et al., 1986.) Thus NASCAP/LEO is capable of predicting the "snapover" (or partial snapover) of the coverslips in response to high positive interconnect potentials, without explicitly resolving the coverslips and interconnects.

Figure 10 shows the NASCAP/LEO model of PIX-II, constructed using EMRC Display-II. This model is not based directly on the PIX-II rocket, but rather on the original NASCAP/LEO model of PIX-II. It differs from the original model in that the rocket is round rather than square, and that the change in resolution approaching the experiment takes place smoothly rather than suddenly.

Figure 11 shows the surface potentials on the experiment with the interconnects biased to 1,000 volts. Most of the solar cells were calculated to have mean potential in the range of 700-850 volts. For this case, the rocket structure ground was taken to be at -4 volts, and the interconnects comprised 5 percent of the cell area. Thus, we infer a mean coverslip potential of about 150-300 volts below the interconnect potential.

Figure 12 shows the current collected by the solar array as a function of bias voltage. (This figure is taken from the original publication.) The calculated values are in general agreement with the measurements. The calculation exhibits a sharper snapover at lower potential than was measured because calculations were done in a manner which tends to favor the bistable snapped-over state, while the experiment was done by continuously increasing the bias which tends to suppress the snapover.

**Example 5: SPEAR I Rocket Experiment (1987)  
(Katz et al., 1989)**

The SPEAR (Space Power Experiments Aboard Rockets) program has as its objective the development of technology for efficient design of very high voltage and current systems to operate in the space environment. The SPEAR I experiment consisted of two boom-mounted probes that could be biased up to 46 kilovolts positive relative to the rocket body. It was intended that the rocket body would maintain good contact with the ambient plasma via a hollow cathode plasma contactor. However, the contactor was defeated by a mechanical malfunction, so that the rocket body became negatively charged, and the experiment was far less

symmetric than planned. NASCAP/LEO proved the utility of a general 3-dimensional modeling capability to understand the results of this nonsymmetric flight experiment.

Figure 13 shows the NASCAP/LEO model of SPEAR I with a 46 kilovolt bias on one sphere and the rocket body at its floating potential of -8 kilovolts. The model was constructed using Patran. Figure 14 is a sheath contour plot showing the asymmetric sheath formed by SPEAR I under the above bias conditions. The plasma conditions for this calculation were  $n = 1 \times 10^5 \text{ cm}^{-3}$  and  $\theta = 0.1 \text{ eV}$ . The primary grid unit is 0.3 meters, and the resolution in the region of the spheres is 7.5 centimeters.

Because the sheath is not symmetric about the sphere, theoretical results about the role of magnetic field in limiting currents to spheres cannot be directly applied. Figure 15 shows the trajectory of an electron in a potential similar to that shown. The electron  $\mathbf{E} \times \mathbf{B}$  drifts around the surface of the sheath until (unlike the symmetric case) it enters a high electric field region and is collected. Figure 16 shows the NASCAP/LEO calculated electron current to the sphere and the secondary-electron-enhanced ion current to the rocket as a function of rocket potential. As the potential goes negative, the electron current first increases due to loss of symmetry, then decreases due to the ion-collecting sheath engulfing the electron-collecting sheath. Figure 17 shows the excellent agreement between the measured current and the NASCAP/LEO calculation.

While NASCAP/LEO takes account of the effect of magnetic fields on particle trajectories and thus collected currents, it ignores the effect of magnetic fields on the space charge and potential structure. For comparison, the POLAR code was run for the one case above to achieve self-consistent space-charge, potential, and current solutions in the presence of the magnetic field. The differences found were fairly insignificant.

#### Summary

NASCAP/LEO is a 3-dimensional computer code capable of calculating sheath structure, surface potentials, and current collection for a high-voltage object in a plasma. The ability to accept object definition input from standard CAD programs allows spacecraft or test object models to be correctly proportioned with important features adequately resolved. The cubic grid structure and the analytic space charge representation, together with phenomenological models for other relevant physical phenomena (such as snapover), permit realistic calculations to be performed in modest amounts of computer time.

We have highlighted in this report five previously published NASCAP/LEO calculations. These examples show that it is practical to perform calculations for nonsymmetric, 3-dimensional, realistic problems. They also verify that NASCAP/LEO results stand the test of direct comparison with measurement for both ground test and space flight conditions.

Acknowledgements. This work has been supported by NASA/Lewis Research Center under contract NAS3-23881.

#### References

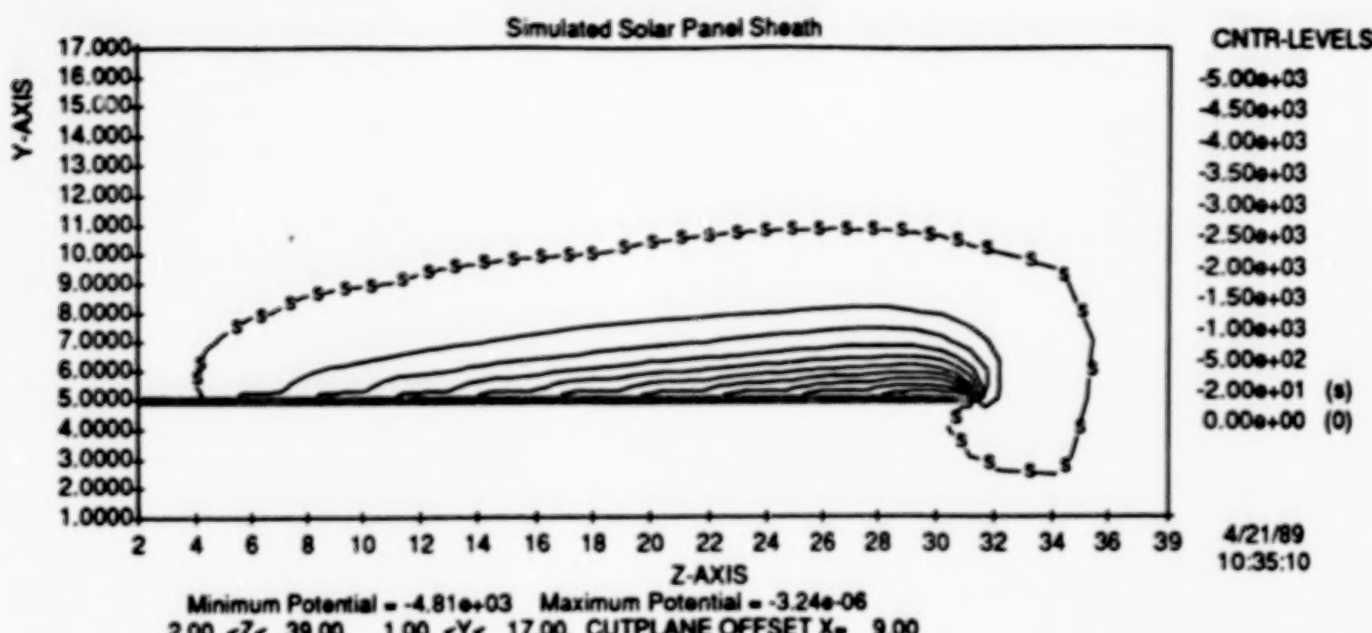
- Katz, I., M. J. Mandell, G. W. Schnuelle, D. E. Parks, and P. G. Steen, Plasma collection by high-voltage spacecraft in low earth orbit, J. Spacecraft, 18, 79, 1981.
- McCoy, J. E. and A. Konradi, Sheath effects observed on a 10 meter high voltage panel in simulated low earth orbit, Spacecraft Charging Technology-1978, NASA CP-2071, 341, 1979.
- Mandell, M. J. and I. Katz, Potentials in a plasma over a biased pinhole, IEEE Trans. Nucl. Sci., NS-30, 4307, 1983.
- Gabriel, S. B., C. E. Garner and S. Kitamura, Experimental measurements of the plasma sheath around pinhole defects in a simulated high-voltage solar array, AIAA Paper No. 83-0311, AIAA 21st Aerospace Sciences Meeting, Reno, NV, January 10-13, 1983.
- Davis, V. A., M. J. Mandell and I. Katz, Electron collection by multiple objects within a single sheath, J. Spacecraft, 25, 94, 1988.
- Carruth, M. R., Jr., Plasma electron collection through biased slits in a dielectric, J. Spacecraft, 24, 79, 1987.
- Mandell, M. J., I. Katz, G. A. Jongeward, and J. C. Roche, Computer simulation of plasma electron collection by PIX-II, J. Spacecraft, 23, 512, 1986.
- Grier, N. T., Plasma Interaction Experiment II: laboratory and flight results, in proceedings of Spacecraft Environment Interactions Technology Conference, Colorado Springs, CO, October 4-6, 1983, NASA CP-2359, 333, 1985).
- Katz, I., G. A. Jongeward, V. A. Davis, M. J. Mandell, R. A. Kuharski, J. R. Lilley, Jr., W. J. Raith, D. L. Cooke, R. B. Torbert, G. Larson, and D. Rau, Structure of the bipolar plasma sheath generated by SPEAR I, J. Geophys. Res., 94, 1450, 1989.



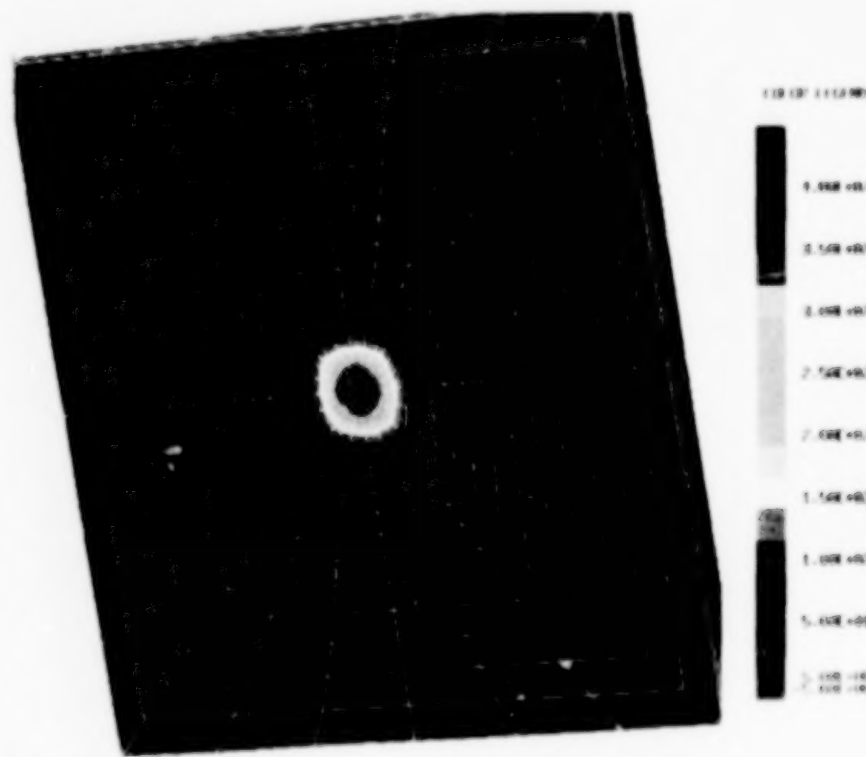
Figure 1 NASCAP/LEO model of a 10-meter simulated solar panel, consisting of a conductive strip mounted on a plastic frame.



Figure 2 The simulated solar panel (mounted on a plastic frame) is shown with a uniform (in ten steps) potential gradient from zero to -4,800 volts.



**Figure 3** NASCAP/LEO results for the plasma sheath around the simulated solar panel. (Note that the dark blue region consists of potentials from -4,800 volts to -100 volts.)



**Figure 4** NASCAP/LEO model of the experimental fixture with a 1.27 cm diameter pinhole biased to 458 volts, showing surface potentials. Note the spread of high voltage onto the surrounding insulation.

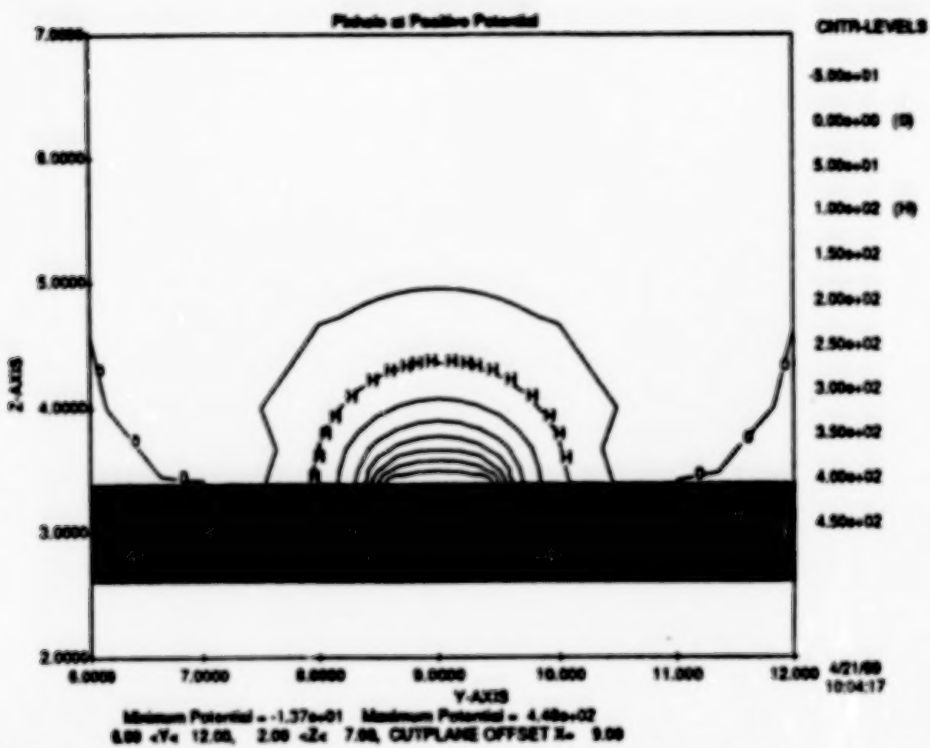


Figure 5 NASCAP/LEO results for potentials in the plasma above the simulated pinhole.

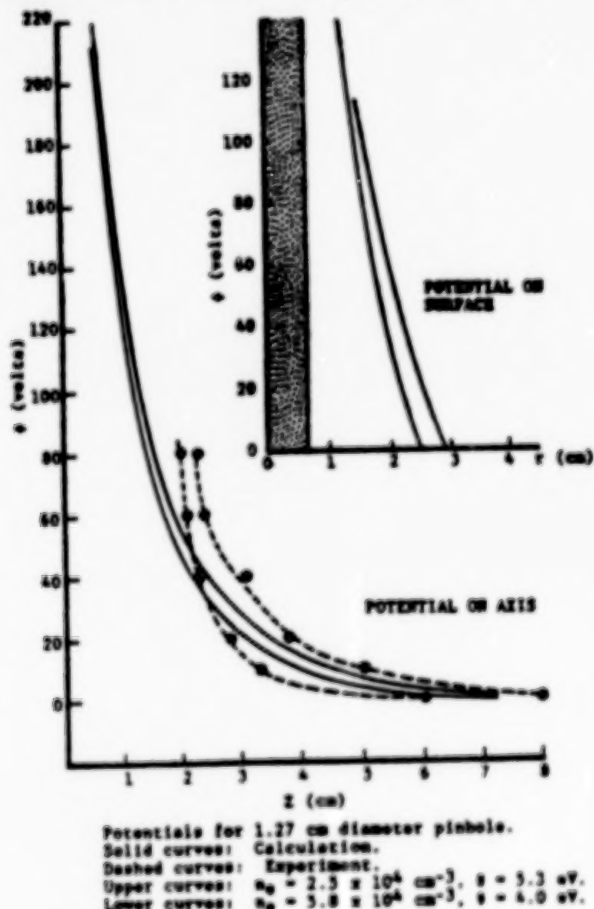
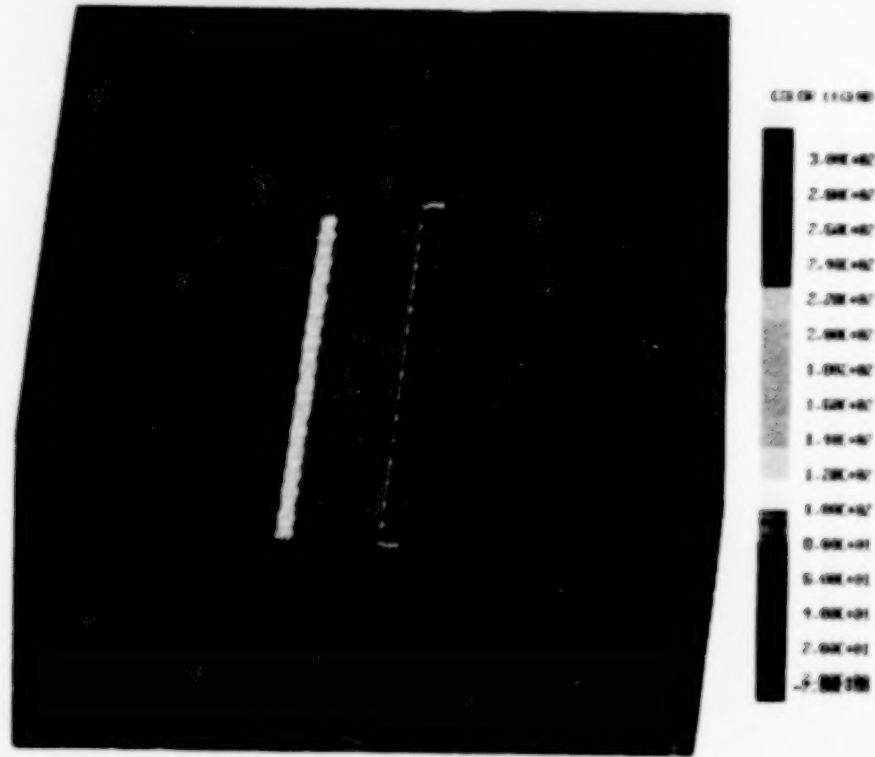
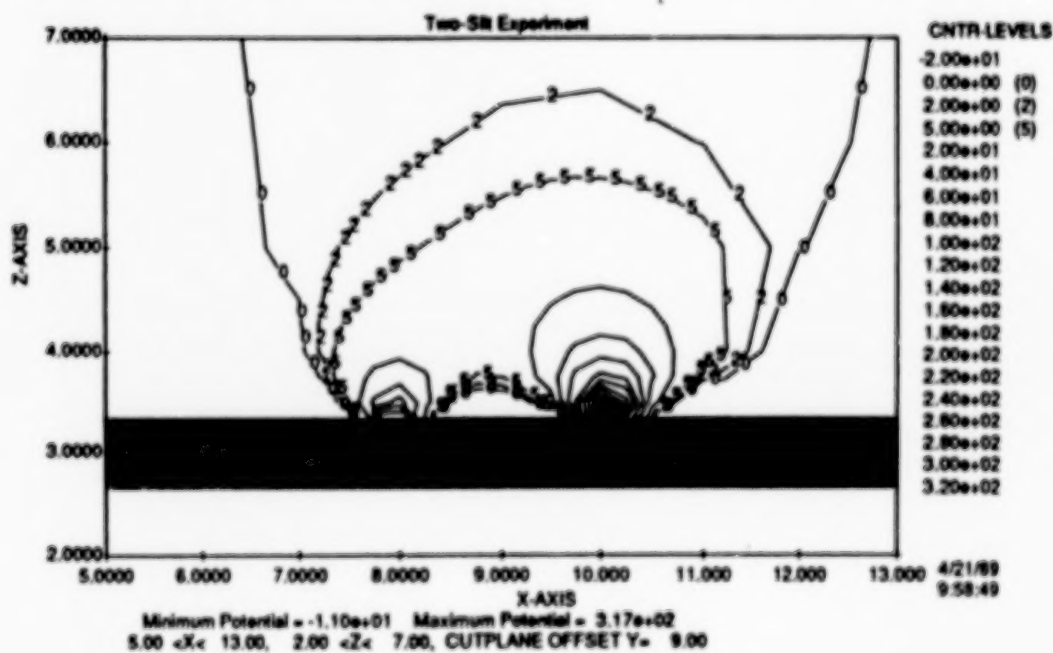


Figure 6 Comparison of measured and calculated potentials along the pinhole axis.



**Figure 7** NASCAP/LEO model of the 2-slit experiment, showing surface potentials for the two slits biased at 128 volts and 328 volts.



**Figure 8** Sheath contour plot showing overlapping sheaths for the bias condition of figure 7. (Note that the bright red region consists of potentials from 20 to 328 volts.)

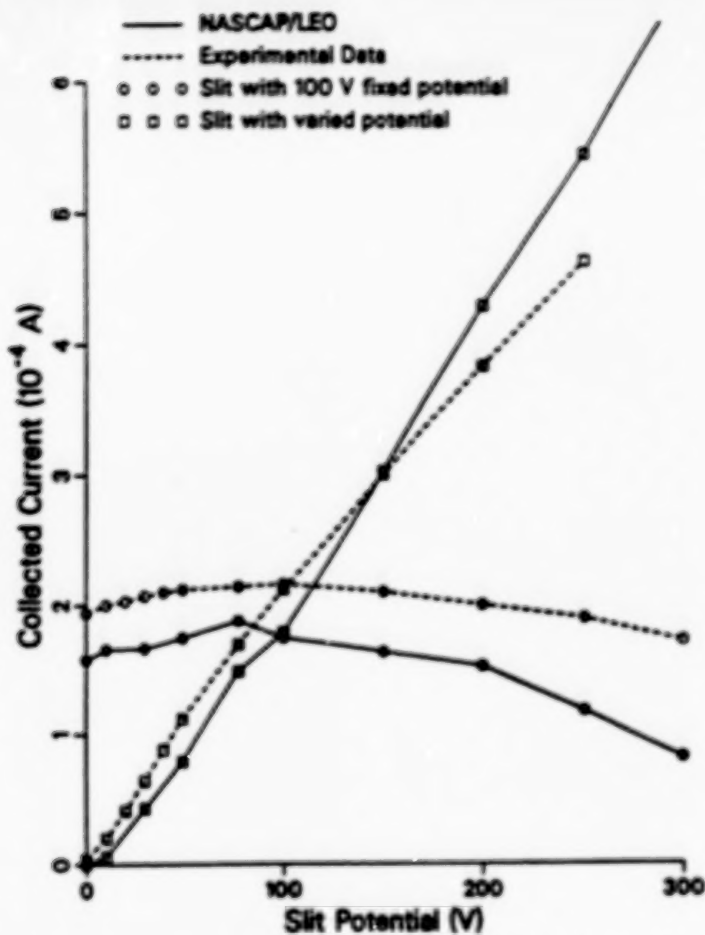


Figure 9 Collected current for two slits with one slit fixed at 100 volts and the second at variable potential.

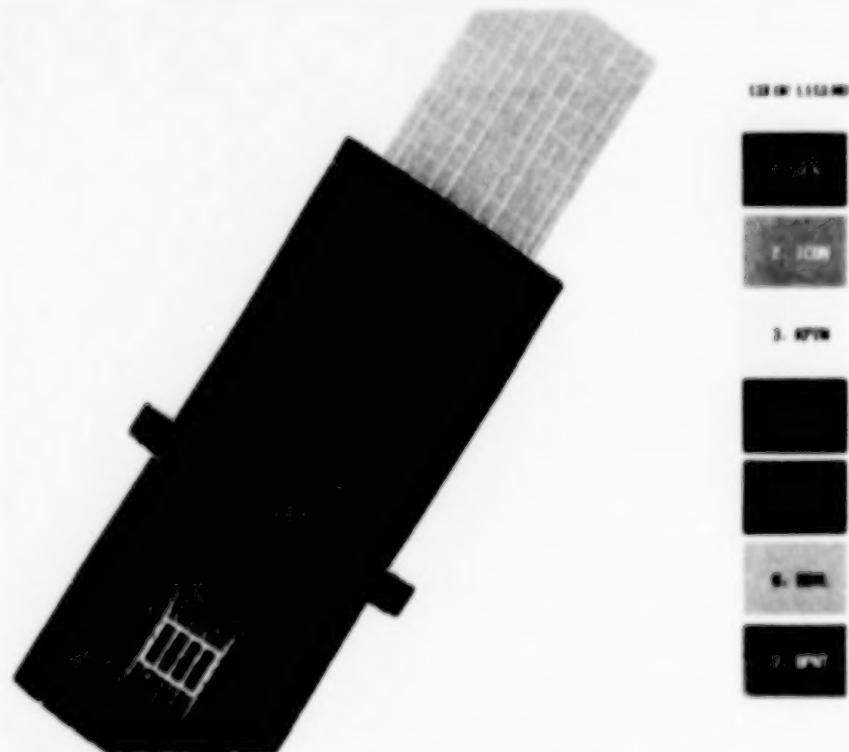


Figure 10 NASCAP/LEO model of PIX-II, showing the solar array sample mounted on rocket body.

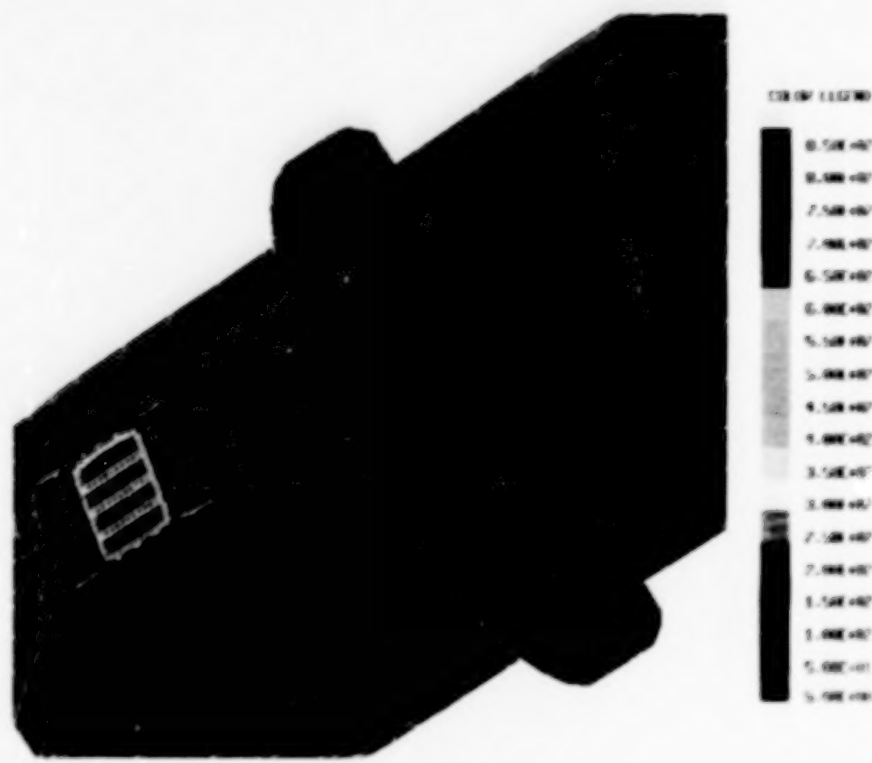


Figure 11 Surface potentials on the solar array sample with interconnects biased to 1,000 volts.

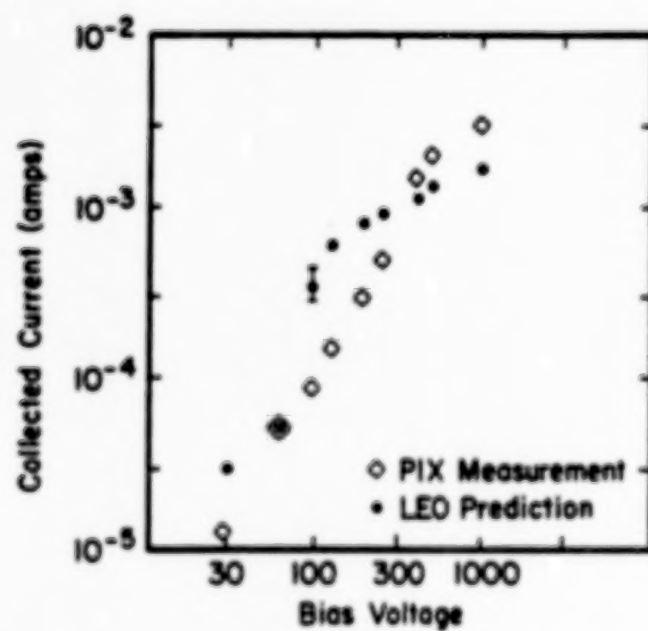


Figure 12 Calculated and measured current collected by the solar array as a function of bias voltage.



Figure 13 NASCAP/LEO model of SPEAR I, showing the rocket body floating at -8,000 volts and one sphere biased to 46,000 volts.

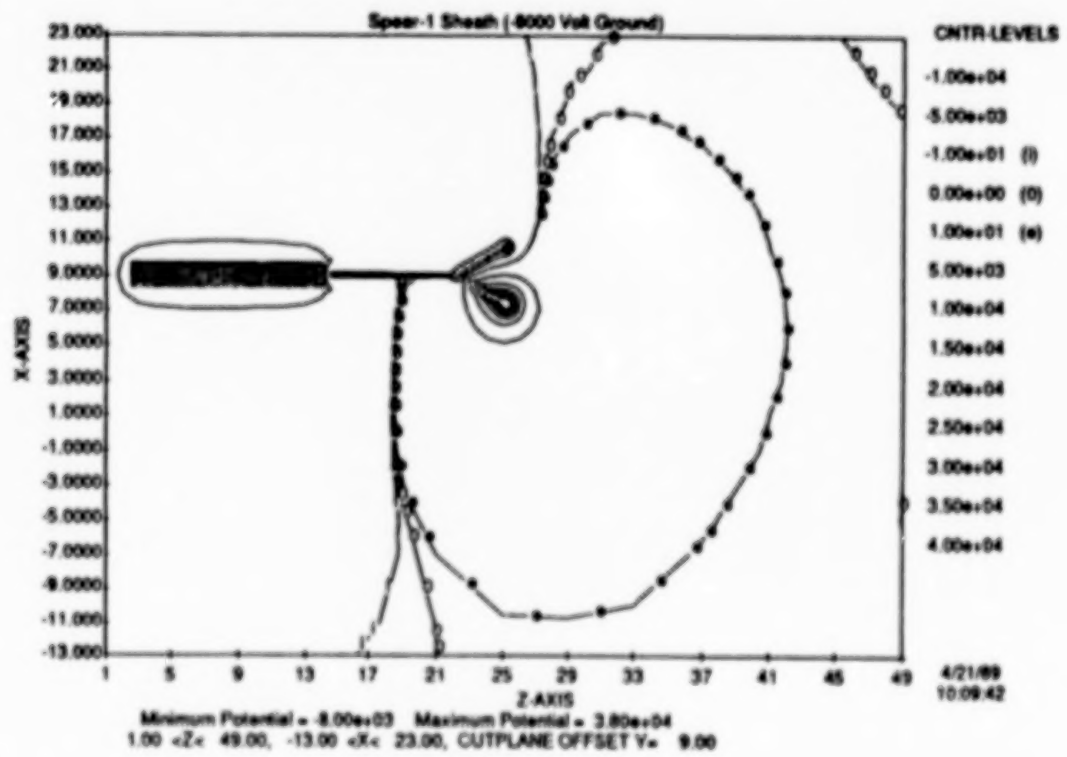


Figure 14 Sheath contour plot showing the asymmetric sheath formed about the probe. (Note that the dark blue region consists of potentials from -8,000 volts to -100 volts, while the bright red region consists of potentials from 100 volts to 38,000 volts.)

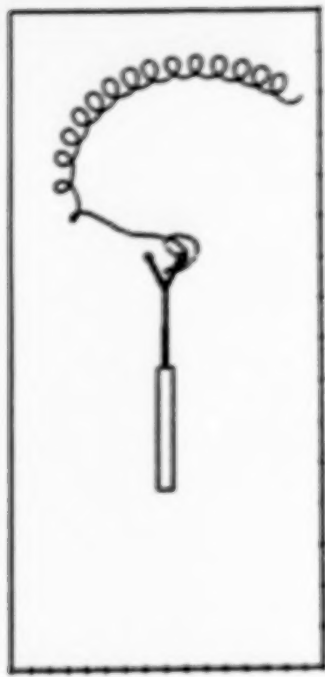


Figure 15 Trajectory of an electron collected by the probe in the asymmetric sheath.

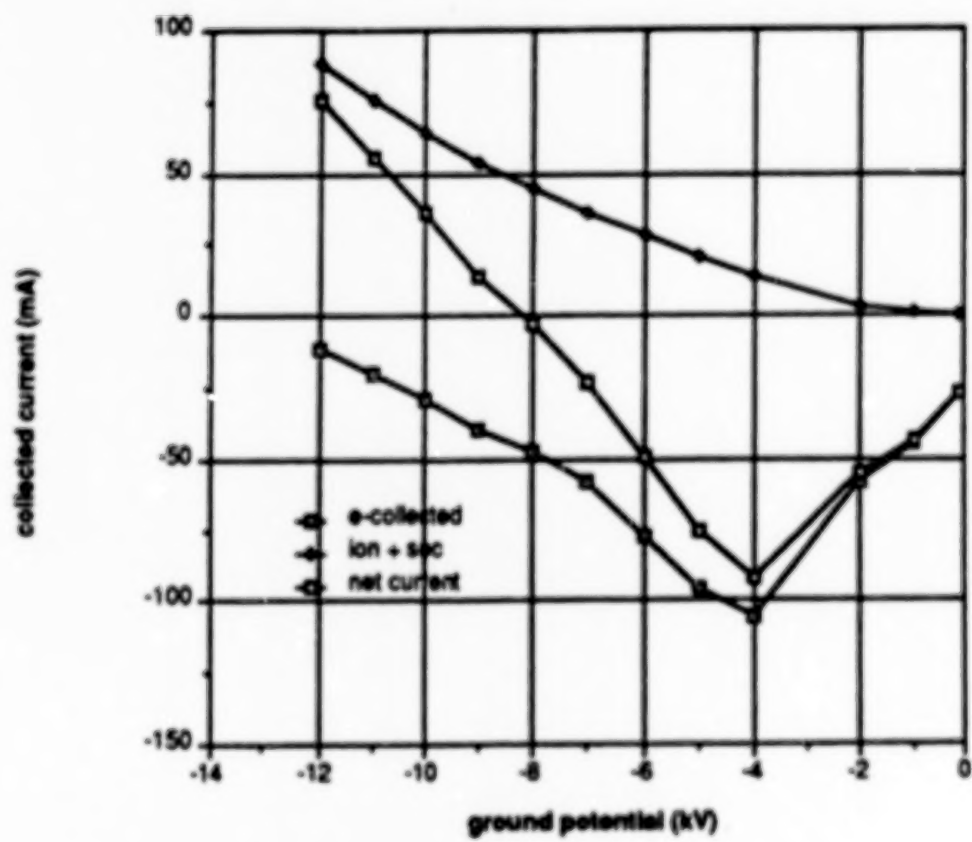


Figure 16 Electron current and secondary-electron-enhanced ion current collected as a function of spacecraft ground potential when 46 kV is applied to one sphere.

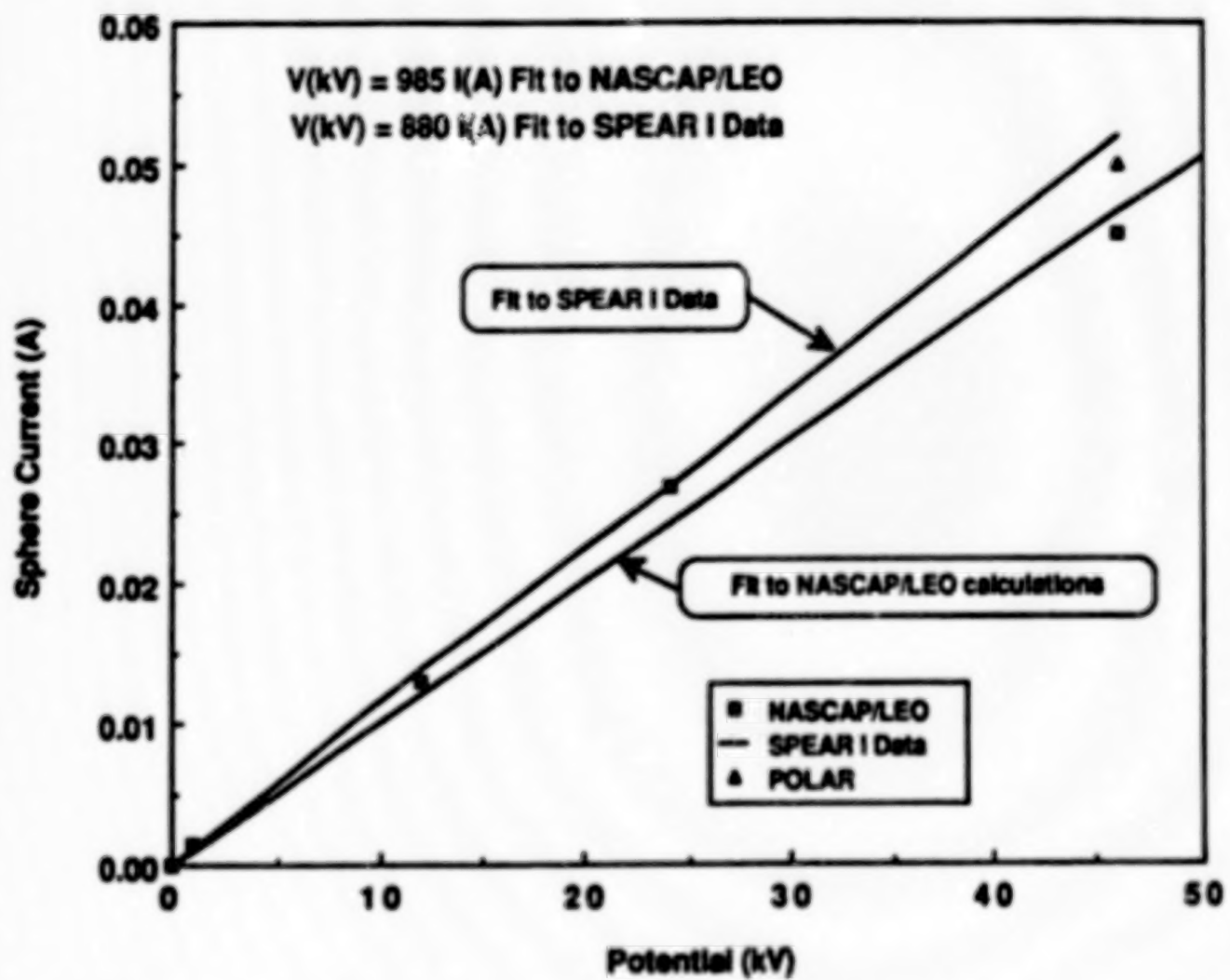


Figure 17 Observed and calculated current collected by the high-voltage sphere.

# The Environment Power System Analysis Tool Development Program

Gary A. Jongeward, Robert A. Kuharski,  
Eric M. Kennedy, Katherine G. Wilcox  
*S-CUBED / Maxwell Laboratories*

N. John Stevens, Rand M. Putnam  
*TRW*

James C. Roche  
*NASA/LeRC*

## Introduction

The Environment Power System Analysis Tool (EPSAT) is being developed to provide space power system design engineers with an analysis tool for determining system performance of power systems in both naturally occurring and self-induced environments. The program, which is funded by SDI/SLKT and directed by NASA/LeRC, is producing an easy to use CAE tool general enough to provide a vehicle for technology transfer from space scientists and engineers to power system design engineers. This paper presents the results of the project after two years of a three year development program.

The Strategic Defense Initiative (SDI) systems require the generation of very large power levels in space for defense applications. These power levels must be available, on demand, anytime in the 10 year mission life of the system requiring the power system to survive prolonged exposure to the space environment and then be fully functional. The space environment interacts with power systems in many ways including: ionization and bulk breakdown, plasma-induced surface flashover, oxygen erosion, meteor and debris damage, and radiation effects. Previously, engineers needing to assess the system impact of these interactions were forced to perform separate calculations and analysis for each interaction and then attempt to piece the intermediate results together. This made system analysis time consuming and unreliable and made extensive system tradeoff studies nearly impossible.

EPSAT is being developed to provide engineers of space power systems with system analysis capabilities. The program consists of four major areas. These are:

- (1) Identify the relevant power systems envisioned for SDI applications and determine which environment-power system interactions are most likely to be important in the operation of the space systems.

- (2) Develop a modern robust CAE tool to provide a natural framework to integrate newly developed or existing modeling software into a comprehensive analysis tool with a modern user interface.
- (3) Identify existing modeling codes and start development on new codes needed for modeling environment power system interactions. A separate detailed analysis phase will follow to determine the accuracy of the analysis codes and relevance of the interactions to the design of high power systems for the space environment.
- (4) Determine deficiencies in modeling capabilities, material properties, etc. relevant to environment-power system interactions and recommend corrective steps.

## **EPSAT**

A useful CAE tool provides engineers with the necessary design information for the systems under consideration. While this seems obvious, it places severe requirements on software design. SDI configurations are still in the conceptual design phase, hence power system designs, requirements, and planned applications evolve with time. A power system environment interactions CAE tool must be capable of absorbing changes and extensions quickly and reliably. To meet this need, EPSAT has been designed for change. The interface is user friendly and easily modified. The code is highly structured with calculational modules which can be altered or replaced. New modules can be added to give new results or build on results from other modules. All facets of the CAE tool, from the way information is presented to the user to the physical models used in the calculations, are easily changed. A unique architecture has been used to provide this capability and is shown in Figure 1.

The EPSAT approach separates the CAE tool into three distinct functional units: a *modern user interface* to present information, a *data dictionary interpreter* to coordinate analysis; and a *data base* for storing system designs and results of analysis

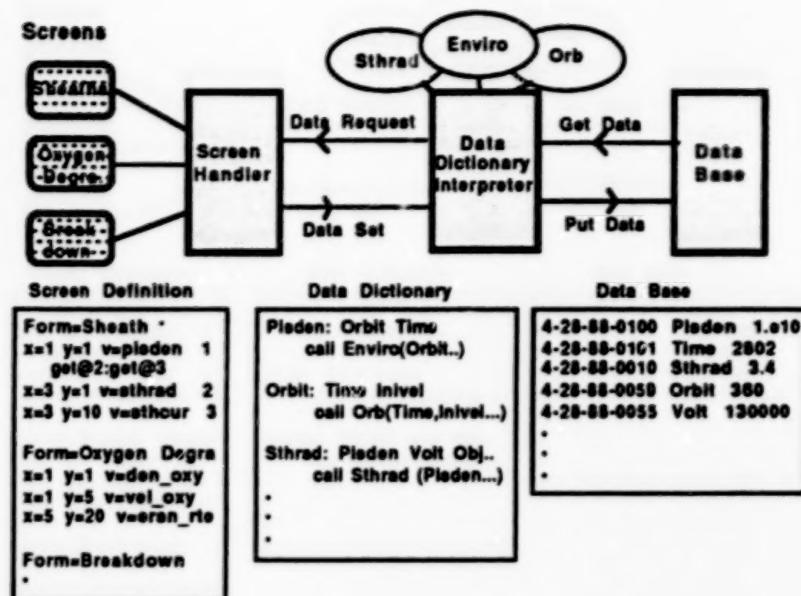


**Figure 1.** The modern design of EPSAT allows for extension and change. The *user interface* presents data to the design engineer through menus, screens, and graphics. Screen definition files tell the screen handler which data items are to be displayed on the screens. The *data dictionary interpreter* receives data requests from the screen handler and uses a rule book, the *data dictionary*, to find recipes to construct the desired data

The *user interface* is externally programmable through ASCII data files, which contain the location and type of information to be displayed on the screen. The information being displayed to the user can be changed while EPSAT is running. Besides aiding in development, this approach provides great flexibility in tailoring the look and feel of the code to meet individual user's needs. The *user interface* has utilities for table generation, line plotting, contour plotting, and perspective plotting as shown below in Figure 2.

To use the CAE tool, the user makes menu selections to display screens of information. These contain information such as the ambient plasma density. Table generation facilities provide a means to vary one variable and examine its effect on other variables. For example the ambient plasma density as a function of altitude or mission time could be generated using this utility. Tables can be viewed directly, saved as an ASCII file, displayed as a plot, or saved as a *Postscript* plot file. A similar utility generates contour plots for slices of data. If the user modifies a value on a screen the change is recorded and the screen is updated to reflect this change and any other changes in displayed quantities

which are dependent on the modified variable. This is the typical mode of interaction between the user and EPSAT; change a parameter (or vary it over a range for a plot or table) and examine the effect on dependent quantities. This ability of being able to vary any quantity and watch its effect on any other quantity is the power of the *data dictionary* approach used in EPSAT.

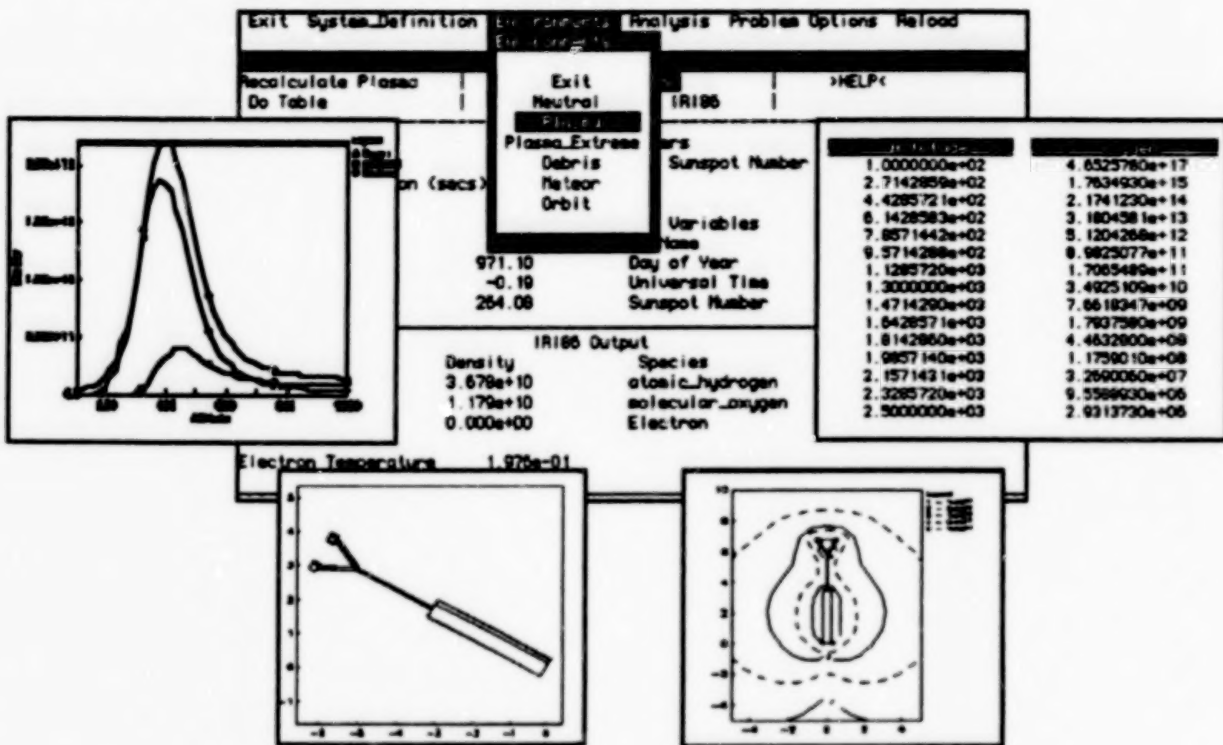


Figure 2. The EPSAT user interface presents information to the user through screens, line plots, perspective plots, contour plots and tables.

The *data dictionary interpreter* coordinates the analysis. It provides data requested by the user interface and insures that it is up to date with respect to all of the data on which it depends. This is accomplished by examining an ASCII file, the *data dictionary*, for recipes listing dependencies of data items and how to compute new values if required. If data needs to be computed then the appropriate analysis modules are called and their results stored in the *data base*. In this way complex multi-step calculations are reduced to a series of independent recipes each building on results determined by other recipes. Similarly, incorporation of new analysis modules is reduced to adding a recipe in the DDI containing the information on how the module is to be used. This increases both the speed of module incorporation and reliability.

## **Environment And Power System Interaction Models**

Plasma	Polar & Auroral Charging Ram/Wake Effects Turbulence
High Energy Radiation	Radiation Damage Single Event Upsets
Meteoroid/Debris	Punctures & Surface damage Sensor Erosion
Neutrals	Atmospheric Drag Oxygen Erosion Vehicle Glow
Electromagnetic Solar Radiation	Forces,Torques,Stresses Solar Degradation Thermal Effects
Self-Generated	Nuclear Radiation Outgassing Contamination Effluents High Voltage Interactions High Current Interactions

**Table 1.** Environment categories and power system interactions.

Table 1 shows the categories of environments and their corresponding effects on power systems. The size of this list reflects the many interactions a power system will experience. For each environment and interaction an appropriate simulation model must be identified, coded (unless one already exists) and incorporated into EPSAT. Calculational speed is an important factor in these modeling codes. EPSAT is intended for use in performing complex system tradeoff studies. Hence, large numbers of calculations consisting of parameter studies must be possible in a reasonable amount of time using a workstation. This restricts the models to engineering level approximations in which modeling fidelity is exchanged for the capability to model entire complex systems.

Table 2 shows the models currently in EPSAT along with additional models to be incorporated during the final year of the project.

## **Present Capabilities**

**Simplified Object Generation**

**Environment Models**

**Neutral**

**Plasma**

**Earth's Magnetic Field**

**Meteor**

**Debris**

**Orbit Generator**

**Interaction Models**

**Meteor/Debris Damage**

**Space Charge Sheaths**

**Sheath Ionization**

**Floating Potentials**

**Oxygen Erosion**

**Outgassing**

**Nozzle Plume Expansion**

**Plume Shadowing**

**Column Densities**

**Scattering**

## **Under Development**

**System Generation Module**

**Breakdown**

**Surface Flashover**

**Paschen**

**Plasma Induced**

**Neutral Interactions**

**Ionization**

**Radiation Environment**

**Surface Effects**

**Magnetic Field Interactions**

**Table 2 Power system-environment simulation models in EPSAT.**

## **Summary**

The high power systems envisioned for SDI applications will interact with their ambient and self generated environments more severely than the low power low voltage systems used to date. SDI power systems must be designed to survive many years in these environments and then operate in the environments on demand. The SDIO Space Power-Space Environment Effects Program is addressing this through the Environment Power System Analysis Tool, EPSAT, program. EPSAT will provide the design engineer with the capability to perform complex system tradeoff studies quickly and reliably. The unique design of EPSAT guarantees it will meet the evolving needs of space power system design engineers.



## Report Documentation Page

1. Report No. <b>NASA CP-3089</b>	2. Government Accession No.	3. Recipient's Catalog No.	
4. Title and Subtitle  <b>Current Collection From Space Plasmas</b>		5. Report Date  <b>December 1990</b>	6. Performing Organization Code  <b>ES53</b>
7. Author(s)  <b>N. Singh,* K. H. Wright, Jr.,** and N. H. Stone, Editors</b>		8. Performing Organization Report No.	
9. Performing Organization Name and Address  <b>George C. Marshall Space Flight Center Marshall Space Flight Center, AL 35812</b>		10. Work Unit No.  <b>M-644</b>	
12. Sponsoring Agency Name and Address  <b>National Aeronautics &amp; Space Administration Washington, DC 20546</b>		13. Type of Report and Period Covered  <b>Conference Publication</b>	
14. Sponsoring Agency Code			
15. Supplementary Notes  <b>Prepared by Space Science Laboratory, Science &amp; Engineering Directorate. *Dept. of Electrical &amp; Computer Engrg., University of Alabama in Huntsville, Huntsville, AL 35899 **Center for Space Plasma and Aeronomics Research, University of Alabama in Huntsville, Huntsville, AL 35899</b>			
16. Abstract  <p>The First Workshop on Current Collection from Space Plasmas was held at the Tom Bevil Center on the campus of The University of Alabama in Huntsville on April 24-25, 1989. The intent of the workshop was to assemble experts on various topics related to the problem of current collection for deliberations that would elucidate the present understanding of the overall current collection problem. This document contains papers presented at the workshop.</p>			
17. Key Words (Suggested by Author(s))  <b>Current Collection, High-Voltage Sheaths, Plasma Contactors, Beam Injection</b>		18. Distribution Statement  <b>Unclassified---Unlimited</b>	
Subject Category: 75			
19. Security Classif. (of this report)  <b>Unclassified</b>	20. Security Classif. (of this page)  <b>Unclassified</b>	21. No. of pages  <b>368</b>	22. Price  <b>A16</b>

NASA FORM 1626 OCT 86

For sale by the National Technical Information Service, Springfield, VA 22161-2171

NASA Langley, 1990

358

